Terahertz Spectroscopy and Applications II

J. Martyn Chamberlain
Chair/Editor

16-18 June 1999
Munich, Germany

SPIE

P

PROCEEDINGS
SERIES

Volume 3828

19991209 083

AQF00-03-0692

REPORT DOCUMENTATION PAGE		Form Approved OMB No. 0704-0188

Public reporting burden for this collection of information is estimated to average 1 hour per response, including the time for reviewing instructions, searching existing data sources, gathering and maintaining the data needed, and completing and reviewing the collection of information. Send comments regarding this burden estimate or any other aspect of this collection of information, including suggestions for reducing this burden to Washington Headquarters Services, Directorate for Information Operations and Reports, 1215 Jefferson Davis Highway, Suite 1204, Arlington, VA 22202-4302, and to the Office of Management and Budget, Paperwork Reduction Project (0704-0188), Washington, DC 20503.

1. AGENCY USE ONLY (Leave blank)	2. REPORT DATE 23 Novemberr 1999	3. REPORT TYPE AND DATES COVERED Conference Proceedings

4. TITLE AND SUBTITLE SPIE Conference on Terahertz Spectroscopy & Applications	5. FUNDING NUMBERS F61775-99-WF032

6. AUTHOR(S)

Conference Committee

7. PERFORMING ORGANIZATION NAME(S) AND ADDRESS(ES) University of Nottingham University Park Nottingham NG7 2RD United Kingdom	8. PERFORMING ORGANIZATION REPORT NUMBER N/A

9. SPONSORING/MONITORING AGENCY NAME(S) AND ADDRESS(ES) EOARD PSC 802 BOX 14 FPO 09499-0200	10. SPONSORING/MONITORING AGENCY REPORT NUMBER CSP 99-5032

11. SUPPLEMENTARY NOTES

12a. DISTRIBUTION/AVAILABILITY STATEMENT Approved for public release; distribution is unlimited.	12b. DISTRIBUTION CODE A

13. ABSTRACT (Maximum 200 words)

The Final Proceedings for SPIE Conference on Terahertz Spectroscopy & Applications, 16 June 1999 - 18 June 1999

This is an interdisciplinary conference. Topics will focus on terahertz science and technology, including: pulsed optical techniques for THz generation, intense terahertz sources, remote sensing of airborne pollutants, quantum optics, quantum coherent electronics, new concepts of fundamental sources including intersubband, exciton, tunnelling and plasma wave phenomena, and new fabrication and integration technologies for Terahertz components.

14. SUBJECT TERMS EOARD, Laser physics, terahertz electronics, terahertz technology	15. NUMBER OF PAGES 442
	16. PRICE CODE N/A

17. SECURITY CLASSIFICATION OF REPORT UNCLASSIFIED	18. SECURITY CLASSIFICATION OF THIS PAGE UNCLASSIFIED	19. SECURITY CLASSIFICATION OF ABSTRACT UNCLASSIFIED	20. LIMITATION OF ABSTRACT UL

NSN 7540-01-280-5500

Standard Form 298 (Rev. 2-89)
Prescribed by ANSI Std. 239-18
298-102

Terahertz Spectroscopy and Applications II

J. Martyn Chamberlain
Chair/Editor

The papers appearing in this book comprise the proceedings of the meeting mentioned on the cover and title page. They reflect the authors' opinions and are published as presented and without change, in the interests of timely dissemination. Their inclusion in this publication does not necessarily constitute endorsement by the editors or by SPIE.

Please use the following format to cite material from this book:
　　Author(s), "Title of paper," in *Terahertz Spectroscopy and Applications II*, J. Martyn Chamberlain, Editor, Proceedings of SPIE Vol. 3828, page numbers (1999).

Printed in the United States of America.

Contents

SESSION 5   ALL OPTICAL GENERATION AND IMAGING

SESSION 6   SPECTROSCOPY AND OTHER APPLICATIONS USING FAST PULSE SOURCES

SESSION 7   POSTER SESSION

Conference Committee

Conference Chair

J. Martyn Chamberlain, University of Nottingham (UK)

Organizing Committee

Paul Harrison, University of Leeds (UK)
Jennifer Griggs, University of Leeds (UK)
Karl Unterrainer, Technische Universität Wien (Austria)
Ekkehard Schomburg, University of Nottingham (UK)

Introduction

It is surprising that, almost at the end of the second millennium and some three centuries after Sir Isaac Newton provided evidence for the existence of an electromagnetic spectrum, there still remains a spectral region that is relatively inaccessible and under-exploited. Over the last few years, however, terahertz frequency science and technology have made significant advances and the entire field is now poised for a period of substantial growth. Recent developments in impulsive generation technologies have been matched by new advances in both novel electronic concepts and in the refinement of traditional devices and systems. In step with these technological activities, there has been a constant effort in the underpinning science — especially using new types of spectroscopic tools— that has provided a springboard from which to launch new devices and to improve the performance of existing systems.

The Conference on Terahertz Spectroscopy and Applications took place as part of the EOS/SPIE International Symposium at the ICM, Munich, Germany from 16–18 July 1999. Approximately 40 talks were given, together with a matching number of posters. The meeting was attended by approximately 80 people, drawn from both the "optical" and "electronic" traditions of the subject. The speakers provided overviews of their specific topics, which helped the audience to appreciate the significance and extent of the work under discussion. The discussion sessions after each talk were stimulating, and testified to the excellence of the presentations and the degree of interest aroused. The poster session proved to be exceptionally well-received, and in this context one of our sponsors (QMC Instruments Ltd.) is to be thanked for the refreshments that helped the conviviality of the occasion.

The papers that are contained in this volume are the majority of those presented in Munich; they have subsequently been refereed by the organizing committee and other experts. They cover the full range of topics considered at this meeting, and the editors (Paul Harrison and Ekkehard Schomburg) hope that they will serve as a reference point in the development of the field.

Finally, as chair of this lively and thought-provoking meeting, I would like to express my sincere thanks to the U.S. Department of the Air Force, European Office of Aerospace Research and Development, London, for their generous subvention that enabled the organizers to assist several speakers to attend. The organizations of SPIE and EUROPTO® are also thanked for help throughout the event and for technical assistance with the proceedings publication.

J. Martyn Chamberlain

SESSION 1

Intersubband and Intraband Sources

Electrically pumped Terahertz quantum well sources

Jérôme Faist
University of Neuchâtel, CH-2000 Neuchâtel, Switzerland
Jerome.Faist@iph.unine.ch, Michel.Rochat@iph.unine.ch, Mattias.Beck@iph.unine.ch

Abstract

Far-infrared ($\lambda = 88\mu m$) electroluminescence is investigated in quantum cascade structures. Narrow luminescence peak with a Full-Width at Half Maximum of 0.7meV are measured at low excitation currents ($30A/cm^2$) and low temperature (T = 5K). The temperature dependence of the luminescence efficiency is studied systematically up to 120K, showing the interplay between electron-electron and optical phonon emission.
Electroluminescence is also studied in a structure based on a diagonal (photon-assisted tunneling) transition and compared with the magnetotransport data. Wider luminescence peaks and intrinsic instabilities are observed.

Quantum cascade lasers based on intersubband transitions[1] have now demonstrated very high level of performances in the mid-infrared. We study here the application of the same technology to the far-infrared, where the lack of convenient sources is specially strong.
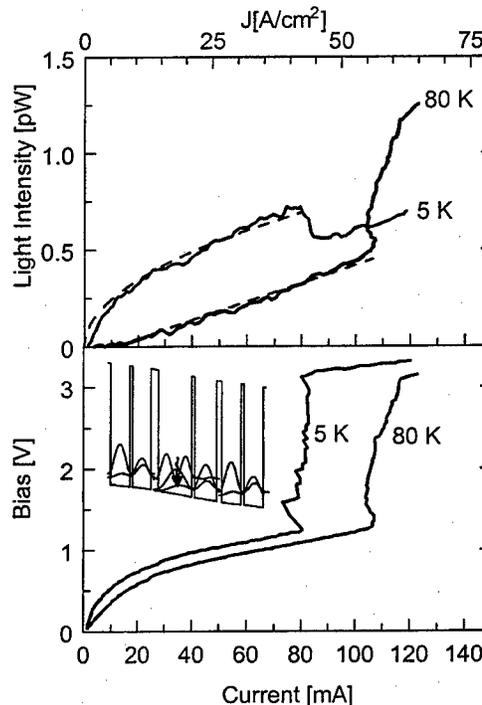
Fig. 1 Optical output power (top graph) and bias (lower graph) versus injected current. Inset: schematic band structure of the device

Our structure was grown by molecular beam epitaxy on a n-doped GaAs substrate and consists of 35 periods. As shown in the inset of Fig. 1 , one period of our structure consists of four GaAs quantum wells separated by thin Al$_{0.15}$Ga$_{0.85}$As tunnel barriers. The emission occurs in the 28nm well through a vertical transitions, i.e. the optical transition proceeds between two states with a strong spatial overlap.

For the experiments, the samples were processed into 450μm X 450μm mesas and the light coupled using a metal grating with a 15μm periodicity. The samples were mounted on the cold finger of a He flow cryostat, and the current driven in pulsed mode. The light was then collected by an off-axis parabolic mirror with an f/1.5 aperture and sent through a Fourier transform infrared spectrometer (FTIR) on a liquid-helium cooled Si Bolometer detector The entire optical path was purged by dry air to minimize water vapor absorption.

In Fig. 1, simultaneous measurements of the voltage and optical output power versus injection current performed are reported for temperatures of T = 5K (upper curve) and 80K (lower curve). In contrast to measurements performed on mid-infrared devices, the luminescence efficiency is not constant. At T=5K, the optical power rises sublinearly up to a current of I~80mA. The characteristic is more linear, with a lower efficiency, at T=80K. The spectral measurement show that the abrupt change in optical power above I=80mA (for T=5K) and 100mA (for T=80K), which is correlated with an abrupt increase of the applied voltage, arises when the ground state g of the injector is not anymore resonant with the upper state n=2 of the optical transition and a Negative Differential Resistance (NDR) occurs.

Spectral measurements of the luminescence were performed using the FTIR in the step-scan mode, the signal being detected with a lock-in amplifier. A few representative spectra taken for increasing injected currents at T=5K are displayed in Fig. 2. They show that the luminescence spectrum mainly consists of one narrow peak centered at a wavelength of λ=88μm. This peak is easily identified to correspond to the n=2 to n=1 transition in the 28nm well, since its measured photon energy of hv=14.1meV corresponds very well to the calculated value of the n=2 to n=1 transition energy.
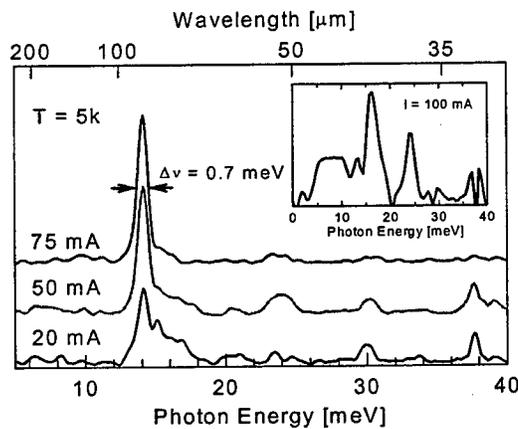
Fig 2 Electroluminescence spectra.

The FTIR allows us to spectrally resolve the luminescence peak and we measure a full width at half maximum of 0.7meV. The optical spectrum (inset of Fig. 2) in the region of negative differential resistance is extremely broad (>30meV) and features many additional peaks. The spectrum is consistent with a broad injection in many energy levels from electron population with a broad energy distribution. This very good correlation between the electrical and spectral characteristics in the same

device is a proof that the *electroluminescence arises from a resonant tunneling injection into the n=2 state and not from a heating of the electron gas.*

At low temperature, and in the limit of low injection current to prevent significant electron heating, optical phonon emission is forbidden and electron-electron scattering is the most efficient scattering mechanism. Our measurements are in very good agreement with this picture. Because the electron-electron scattering rate is approximately proportional to the electron density in the upper subband, the population (and the optical power) has a square root dependence on the injected current. As shown by the fit (dotted lines in Fig. 1), this is very well observed in our data.

The devices were also measured at higher temperatures. As shown in Fig. 3, intersubband electoluminescence is clearly visible in this structure up to temperatures of 100K. Above this temperature, the peak broadens significantly and the emission dissapears altogether at 120K.

Photon Energy [meV]
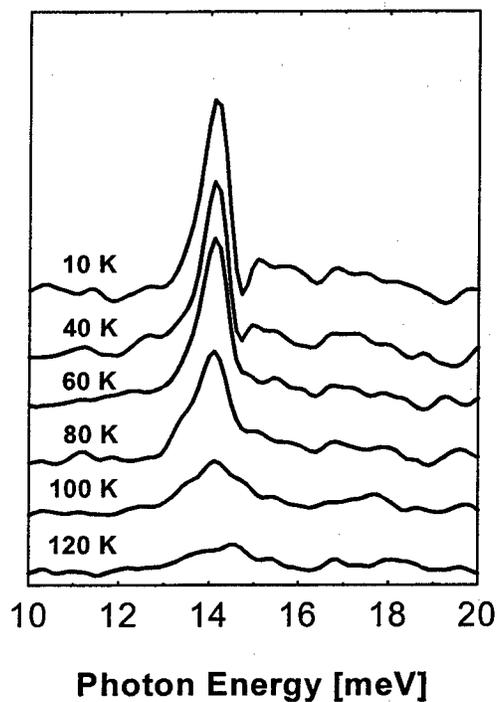
Fig. 3. Luminescence spectra as a function of temperature for a fixed current (65mA) The electroluminescence intensity decreases with increasing temperature and vanishes altogether at T = 120K
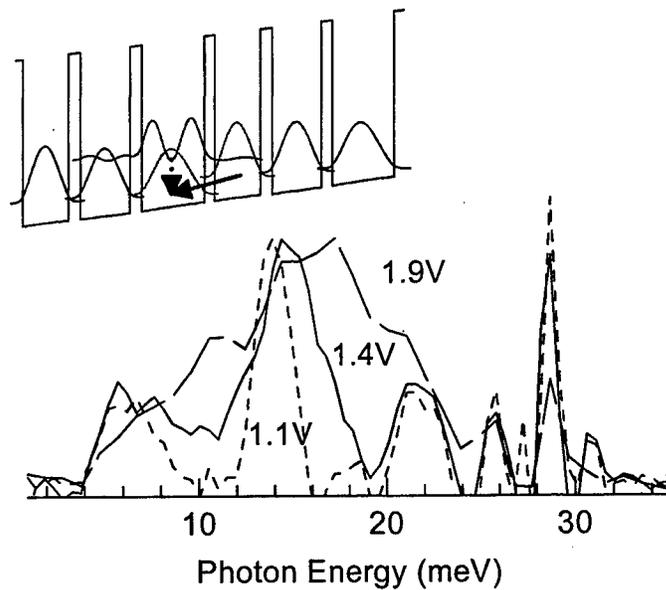
Fig. 4 Luminescence spectra for increasing currents in a structure based on a photon-assisted tunneling transition. We attribute the broad peak at hn = 14meV to the photon-assisted (interwell) transition, and the narrow peak at 29meV to the vertical (intrawell) transition. Inset: Schematic band diagram of the structures, with the arrows showing the two (interwell and intrawell) transitions

The same characterization was also carried over in a structure based on a diagonal transition (photon-assisted tunneling transition)[3]. The low temperature spectra show evidence of the vertical transition as well as the diagonal transition. Some electrical tuning of the luminescence is apparent in Fig. 4. It is limited however by the apparition of NDR at bias lower than ~1.1V. We believe that the relatively large width of the peak corresponding to the photon assisted tunneling transition is due to inhomogeneities in the applied electric field along the 50 periods of the structure.

References
1.   J. Faist, F. Capasso, D. L. Sivco, C. Sirtori, A. L. Hutchinson, and A. Y. Cho, Science **264**, 553 (1994)
2.   M. Rochat, J. Faist, M. Beck, U. Oesterle, M. Ilegems, Applied Physics Letters **73**, 3724, (1998)
3.   J. Faist, F. Capasso, C. Sirtori, D. L. Sivco, A. L. Hutchinson, and A. Y. Cho, Nature **387**, 777 (1997)

Long-wavelength High-power Quantum Fountain Unipolar Lasers in GaAs/AlGaAs Quantum Wells

Olivier Gauthier-Lafaye[a], Bruno Séguin-Roa [a], Francois. H. Julien [a], Gottfried Strasser[b],
Philippe Collot[c], Carlo Sirtori[c], and Jean-Yves Duboz [c]

[a]Institut d'Electronique Fondamentale, UMR CNRS 8822, University of Paris-Sud,
91405 Orsay, France.
[b]Institut für Festkoerperelektronik, Technische Universität Wien
Floragasse 7/1, 1040 Wien, Austria.
[c]Laboratoire Central de Recherches, Thomson-CSF, Domaine de Corbeville,
91404 Orsay, France.

ABSTRACT

High-power unipolar GaAs/AlGaAs lasers emitting in the 14-15 μm wavelength range under optical pumping by a pulsed CO_2 laser are investigated. Operation of edge lasers with side-facet pumping as well as broad-area lasers with normal-incidence pumping is demonstrated. We show that record high optical powers can be obtained from these quantum fountain unipolar lasers. Optical powers per facet as high as 6.6 W for edge lasers and 7.8 W for broad-area lasers are achieved with TM_{00} mode emission. Extended tunability of the lasing wavelength, $\Delta\lambda/\lambda\approx2.5\%$, is observed by varying the pump wavelength. Operating temperatures as high as 137 K are presently achieved. Application of quantum fountain unipolar lasers to CO_2 gas detection is demonstrated.

Keywords: unipolar lasers, infrared, intersubband transitions, quantum wells, semiconductors, optical pumping.

1. INTRODUCTION

Until recently, the available technology for developing infrared laser diodes above 5 μm wavelength relied on the electron-hole radiative recombination in narrow-gap semiconductors such as lead-salt materials.[1] In these bipolar devices, population inversion is achieved by injecting enough electrons and holes into the active region in order to fill the states close to Brillouin zone center. Population inversion is only local in k-space because of the opposite curvature of the conduction and the valence bands. The required carrier concentration dramatically increases with temperature as a consequence of the Fermi statistics. Narrow-gap semiconductor laser diodes suffer from strong non-radiative Auger recombinations. The activation energy of these Auger processes follows the band-gap energy and their efficiency grows like the cube of the carrier concentration. They become the dominant loss mechanism as the wavelength gets longer or the temperature higher. The adverse consequences of these Auger processes are the low output powers and operating temperatures characteristic of long-wavelength (bipolar) laser diodes.

The recent demonstration of quantum well unipolar lasers such as the current injection quantum cascade (QC) laser [2] or the optically pumped quantum fountain (QF) laser [3] opens new prospects for the development of high-power long-wavelength lasers operating above liquid nitrogen temperature. The infrared emission in these unipolar lasers arises from the radiative transition of electrons between confined subbands in the conduction band of the quantum wells. Because the subbands are parallel in reciprocal space, population inversion is global and the gain is concentrated in a narrow spectral band. With respect to bipolar laser diodes, much less carrier density is required for inversion. The role of Auger-like non-radiative channels remains negligible, which is favorable for achieving large optical powers and high operating temperatures. The non-radiative relaxation of electrons is indeed largely dominated by the very efficient scattering by optical phonons. Typical electron lifetimes in the excited state lay in the picosecond range and an efficient injection mechanism is required for achieving population inversion. In turn, quantum well unipolar lasers are potentially very fast devices.

In QC lasers, tunneling of electrons between injector/collector regions and the active quantum wells provides efficient current injection in the upper subband as well as fast depopulation of the lower subbands. In QF lasers, selective optical pumping from the ground subband is used to efficiently promote electrons in the upper subband.[4] The active region consists of quantum wells exhibiting three bound electron states. Electrons excited in the upper state radiate to the intermediate state, giving rise to the infrared emission. Population inversion as well as fast recycling of electrons into the ground state is provided by insuring a short lifetime of electrons in the intermediate state through an enhanced scattering with LO-phonons.[4] Although their operation imposes to use an external pumping source, QF lasers offer the advantage of a simplified design and have less stringent material requirements as compared to QC lasers. With no current flow, doping of the cladding layers and metal contacts are not necessary which results in low internal losses at long-wavelengths due to free-carrier absorption. In addition, the laser can be operated far above threshold with much less thermal penalty than in a current injection device. QF lasers are then expected to exhibit better performances in terms of output power than QC lasers at long-wavelengths above 10 μm. Powerful unipolar lasers are of interest for applications such as remote trace gas sensing units or LIDAR systems.

The first observation of intersubband luminescence in optically pumped quantum wells has been reported by Bales and co-workers.[5] In this work, the quantum well structure was designed for achieving intersubband emission at far-infrared wavelengths, i.e. at photon energies well below the optical phonon energy, in order to benefit from the long scattering times associated with acoustic phonon emission. Several studies have addressed the possibility of population inversion in this regime.[6,7,8] The QF laser scheme for emission at energy above the LO-phonon energy was first proposed in 1995.[4] Experimentally, intersubband spontaneous emissions have been observed at wavelengths of 14-15 μm in GaAs/AlGaAs coupled quantum wells under intersubband optical pumping by a cw CO_2 laser.[9,10,11] Observation of intersubband luminescences have also been reported under interband optical pumping at near-infrared wavelengths.[12,13] Population inversion in a QF laser scheme was first demonstrated in 1996 under optical pumping by an infrared free-electron laser and large stimulated gains have been measured at 12.5 μm wavelength.[14,15]. Lasing action was observed at λ = 15.5 μm in 1997 under optical pumping by a CO_2 laser.[16] This first Quantum Fountain unipolar laser delivered 0.6 W optical power per facet and a maximum operating temperature of 110 K has been achieved.

In this paper we review recent developments on QF lasers emitting in the 14-15 μm wavelength range under optical pumping by a pulsed CO_2 laser. We show that record-high output powers can be obtained by optimizing the QF laser design. We also demonstrate that the lasing wavelength can be tuned by as much as $\Delta\lambda/\lambda \approx 2.5\%$ simply by tuning the pump wavelength. We then discuss applications of the QF laser to CO_2 gas detection. Finally, we report on broad-area QF unipolar lasers and we show that outstanding performances can be achieved in terms of optical power and beam quality.

2. LASER DESIGN

Quantum Fountain unipolar lasers are optically-pumped three-level lasers. Their principle of operation is illustrated in Figure 1, which shows the conduction band profile of the quantum wells along the growth axis.
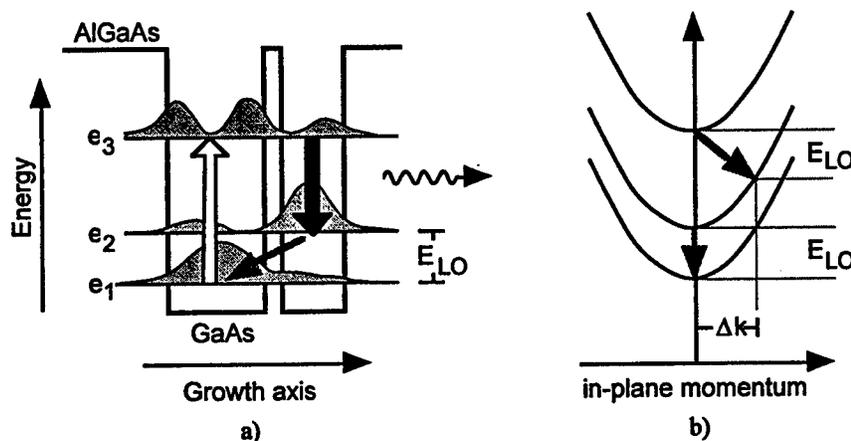
Figure 1: a) Conduction band profile of the active quantum wells of a quantum fountain unipolar laser, b) corresponding subband energy dispersion diagram. The arrows indicate non-radiative relaxation channels via LO-phonon emission. The LO-phonon energy in GaAs is $E_{LO}\approx36$ meV.

The active region consists of an asymmetric coupled quantum well structure (ACQW) formed by GaAs wells and AlGaAs barriers. The thickness and composition of the five layers (the two wells, the thin coupling barrier and the two outermost confining barriers) can be easily adjusted for obtaining three bound states at desired energies in the conduction band. The asymmetry of the structure, which is required for direct optical pumping of electrons from the ground state (e_1) to the second excited state (e_3), is obtained by using different well thickness. In order to populate the ground electron subband, n-doping of the structure is required either in the wells or in the barriers (modulation doping). The intersubband emission takes place between the second and first excited states ($e_3 \rightarrow e_2$). The emitted photons are down-converted from the pump photons by an energy equal to the energy spacing between the two lower subbands (e_2-e_1). The emission wavelength can be tuned within the mid-infrared spectral range through a proper choice of the structure growth parameters.

Population inversion in this three-level system can be achieved if the lifetime of electrons in the e_2 subband is made shorter than the scattering time, τ_{32}, between the e_3 and e_2 subbands. As shown in Ref[4], the scattering rates between subbands can be engineered through a proper choice of the subband energy separation. In particular, the structure can be designed to present an energy spacing between the first excited and ground subbands close to the LO-phonon energy as shown in Fig.1. In such a situation one expects the $e_2 \rightarrow e_1$ non-radiative relaxation to be fast because the phonon wavevector q transferred to the electrons ($|q|=|\Delta k|$) after emission of one LO-phonon is close to zero, i.e. the relaxation is vertical in reciprocal space. Indeed, in bulk semiconductors, the electron-LO phonon interaction rate varies as $1/q^2$ and one can expect a large enhancement of the intersubband scattering rate for zero-momentum phonons. In quantum wells, the situation is a bit more complicated because of the presence of confined phonon modes either guided in the layers (the slab modes) or at the interfaces (the interface modes or surface modes (SO)). A detailed analysis of the electron-phonon interaction for engineering the scattering rates between subbands in ACQW has been reported in Ref.[17]. At low carrier concentrations $\approx 1 \times 10^{11}$ cm^{-2}, typical scattering times are calculated to be $\tau_{21} \approx 0.4$ ps and $\tau_{32} \approx 1.9$ ps for an ACQW structure with $E_{21}=E_{LO}$ and $E_{31}=125$ meV. Although the scattering times are quite short, their large difference ensures population inversion. At larger carrier concentrations, i.e. for a Fermi energy at equilibrium above the ground subband, it is desirable to increase the energy of the second subband respective to the ground subband in order to minimize the thermal population of the e_2 subband. Under such conditions, τ_{21} is expected to increase but population inversion can still be maintained and large stimulated gains are predicted in optimized structures [18].

Based on these considerations, a laser sample has been designed for emission in the 14-15 μm wavelength range under optical pumping by a CO_2 laser. With respect to our first QF laser emitting at 15.5 μm wavelength,[16] the design is rather similar except for two modifications aimed at enhancing the modal gain of the laser. The number of active quantum well structures has been increased from 100 to 150 and the waveguide has been modified in order to achieve a large 81.1 % overlap of the TM mode within the active region. The waveguide structure grown by molecular beam epitaxy on an n-doped GaAs substrate consists of a 5 μm thick $Al_{0.9}Ga_{0.1}As$ cladding layer, followed by a 0.75 μm thick GaAs core layer, the 5.1 μm thick multi-quantum well layer and a 1.75 μm thick GaAs cap layer. The active structures separated by 20 nm thick $Al_{0.35}Ga_{0.65}As$ barriers, are asymmetric coupled quantum wells formed by a 7.9 nm thick GaAs wide well, a 1.13 nm thick $Al_{0.35}Ga_{0.65}As$ barrier and a 5.1 nm thick GaAs narrow well. The quantum wells are modulation doped resulting in a measured sheet carrier density of 2×10^{11} cm^{-2}. The transition energies are calculated to be 127 meV and 86.8 meV for $e_1 e_3$ and $e_2 e_3$ transitions, respectively. The $e_2 e_1$ energy spacing is 40.2 meV which is as desired slightly above the LO-phonon energy in GaAs (36 meV).

Because of the long emission wavelength, one major source of losses is the free-carrier absorption in the doped layers. Based on separate Fourier Transform Infrared (FTIR) spectroscopic measurements, we estimate the waveguide losses to be ≈ 20 cm^{-1} at the 14.5 μm emission wavelength. These losses are mainly attributed to free carrier absorption in the doped MQW active region. The experimental evolution with wavelength follows a λ^3 law. The measurements also reveal a two-phonon absorption band at 13.8 μm, which is attributed to the mixed-mode Al-Ga optical phonons in the thick $Al_{0.9}Ga_{0.1}As$ cladding layer.[19]

3. HIGH-POWER LASERS WITH SIDE-FACET PUMPING

The experimental arrangement used for side-facet optical pumping of the QF laser is shown in Figure 2. The laser samples are cleaved in 2.15 mm long bars and mounted on the cold finger of a variable temperature cryostat. Optical pumping is provided by a tunable Edinburgh MTL-3 mini-TEA CO_2 laser operated at 10 Hz repetition rate. The pump beam is focused

using a cylindrical lens onto the 2.15 mm-long side facet of the sample with a polarization parallel to the growth axis. The elliptical pump spot size is 5x0.4 mm^2 at the sample facet with the shorter axis perpendicular to the layer plane. The pump radiation coupled in the active region experiences strong attenuation by the $e_1 \rightarrow e_3$ intersubband absorption. At low pump intensity, the penetration length which defines the transverse extent of the gain region, is of the order of 10 μm. At pump intensities above 1 $MW.cm^{-2}$, the penetration length increases as a result of the $e_1 \rightarrow e_3$ absorption saturation. Lateral confinement of the emission is then provided by gain guiding in addition to index guiding at the interface between the side-facet and air. The emission is collected from one of the cleaved facets perpendicular to the side-facet with a f/1.2 ZnSe lens. Time-resolved detection is performed by a helium-cooled quantum well infrared detector (QWIP) with a cut-off wavelength of 18 μm and a sensitive area of 0.45x1.5 mm^2. The QWIP detector offers the advantage of a linear response even under intense irradiation.[20] Part of the incident pump beam is detected for reference purposes by a room-temperature HgCdTe photoconductor with a rise-time of ≈ 1 ns. The spectral response of both the detectors and the various optics has been carefully calibrated using our FTIR spectrometer.
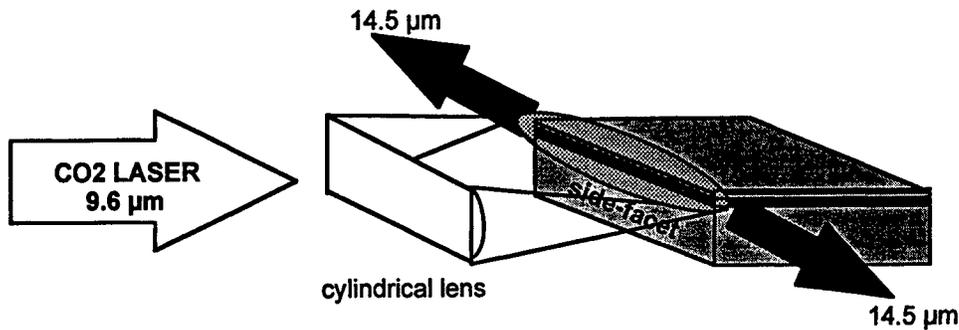
Figure 2: Side-facet optical pumping configuration.
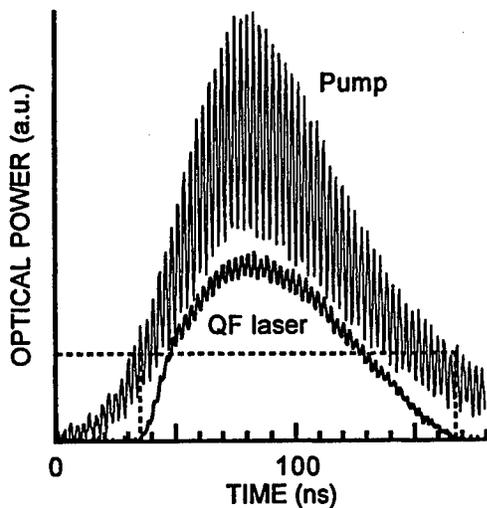
Figure 3: Oscilloscope traces of the 9.6 μm pump (top curve) and 14.5 μm QF laser (bottom curve) pulses. The QF laser is cooled at 20 K.
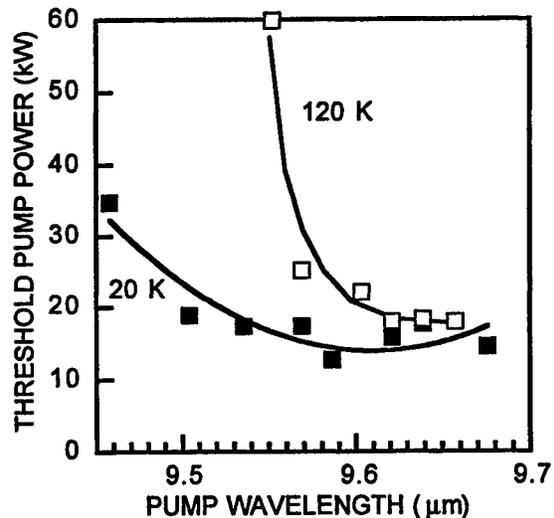
Figure 4: Pump power at threshold versus pump wavelength at a temperature of 20 K and 120K. The solid curves are guides for the eye.

Lasing action has been achieved at 20 K under optical pumping at 9.6 μm wavelength. Figure 3 shows typical oscilloscope traces of the pump and laser pulses. The pump pulse delivered by the multimode longitudinal CO_2 laser consists of micropulses with a 2.6 ns full width at half-maximum (FWHM) in a macropulse with 110 ns FWHM. As seen in Fig.3, the laser emission follows the pump signal above some threshold. The rise time of the QWIP signal is limited by electronics at 5 ns which is too slow to fully resolve the multimode beatings.

The pump threshold versus pump wavelength and sample temperature is reported in Figure 4. For temperatures between 20 and 77 K, the pump threshold is of the order of 33 kW at 9.46 μm. It decreases to 12 kW as the pump wavelength gets in closer resonance with the e_1-e_3 intersubband absorption near 9.6 μm. At 120 K, the minimum threshold ≈ 18 kW is achieved at a longer wavelength of 9.66 μm. This slight increase of the optimum pump wavelength is due to the red-shift of the intersubband resonance with temperature.[21] As seen, the minimum threshold is somewhat larger at 120 K than at 77 K. This increase is a consequence of the thermal population of the e_2 subband, which reduces available gain. Above 120 K, the intersubband resonance wavelength shifts to λ>9.7 μm which is outside the tuning range of our CO_2 laser over the 9P emission branch. Thus, a maximum operating temperature of 135 K has been achieved under optical pumping at 9.68 μm. We stress that the main intrinsic mechanism limiting the operating temperature is the gain reduction due to the thermal population of the second subband. Larger operating temperatures could be achieved by maintaining resonant pumping conditions. One way to increase the operating temperature is to slightly reduce the thickness of the wide GaAs quantum well in order to shift the pump absorption resonance to shorter wavelengths for compensating the temperature red-shift of the resonance.
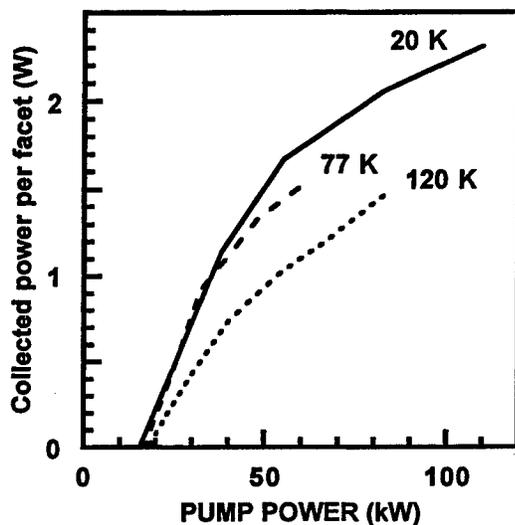
Figure 5: Collected power per facet versus the incident pump power at a temperature of 20, 77 and 120 K.
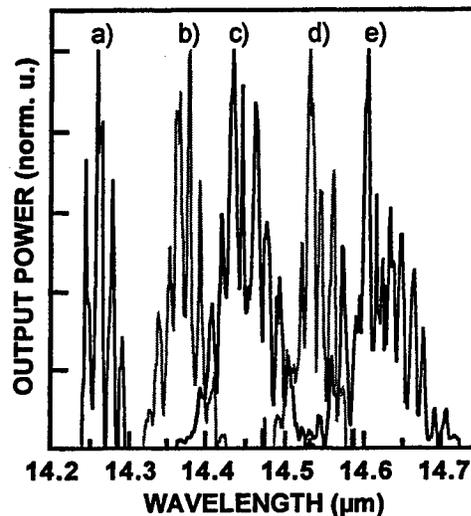
Figure 6: Normalized emission spectra of the QF laser operated 2 times above threshold at a temperature of 20 K. The pump wavelength is: a) 9.458 μm, b) 9.520 μm, c) 9.569 μm, d) 9.640 μm and e) 9.676 μm.

Figure 5 shows the collected power per facet versus the incident pump power at temperatures ranging from 20 up to 120 K. The pump wavelength was 9.6 μm at 20 K and 9.68 μm at 120 K. The curves are constructed from the time-resolved evolution of the pump and laser pulses after calibration of the detector response. The collected power per facet at 20 K reaches 2.3 W when the laser is operated at 7 times above threshold. The evolution with pump power is similar at 20 and 77 K. At 120 K, the collected power is of the order of 1.5 W when the laser is operated 4 times above threshold. Note that the power curve slope above threshold is smaller at 120 K than at 20 K, which stems from a lower differential gain due to the increased thermal population of the e_2 subband. To estimate the collection efficiency, we have performed separate beam divergence measurements of the QF laser emission. The divergence angle in the plane of the layer is found to be 26°, which corresponds to a beam waist at the output facet of the order of 10 μm. The divergence angle θ_z in the plane parallel to the growth axis could not be measured due to the limited aperture of the cryostat windows but is larger than 50°. Based on our calculations of the TM mode profile at the output facet, we estimate θ_z to be 60.4° following Ref[22]. The collection efficiency is then deduced to be 35%. Accounting for this factor, the optical power per facet is deduced to be as large as 6.6 W at 20 K.

Figure 6 presents normalized emission spectra of the QF laser operated 2 times above threshold at a temperature of 20 K. The pump wavelength has been varied between 9.458 and 9.676 μm. The resolution of the 60 cm-long infrared spectrometer

used for measurements is 0.4 cm^{-1}. As seen, the laser spectrum is typical of multimode longitudinal operation with a mode spacing of 0.69 cm^{-1} wavenumbers. Based on the device length, the group index deduced from the mode spacing is of the order of 3.4.[11] The major result of Fig. 6 is the large tunability of the peak lasing wavelength between 14.25 and 14.61 μm ($\Delta\lambda/\lambda \approx 2.5\%$) achieved by tuning the pump wavelength. This result is not the signature of a near-resonant Raman emission process since the shift of the laser photon energy respective to the pump is 0.72 instead of 1.[23] The tunability of the QF laser can be in fact attributed to layer thickness fluctuations during the long growth of the multiple quantum well layers. We have simulated the peak gain spectral position accounting for a one-monolayer thickness fluctuation of each of the quantum well layers and assuming a Gaussian distribution centered at the nominal thickness. The model predicts a relative energy shift of 0.7 in agreement with experiments. The tunability range is maintained at 77 K. Also seen in Fig. 6, the emission spectrum gets narrower as the emission wavelength is shifted to 14.2 μm. This is a consequence of the gain spectrum narrowing as the pump wavelength is tuned out of resonance. However, we cannot exclude the effect of increased internal losses as the emission wavelength gets closer to the mixed-mode Al-Ga two-phonon absorption band at 13.8 μm in the AlGaAs alloy cladding layer.[19]
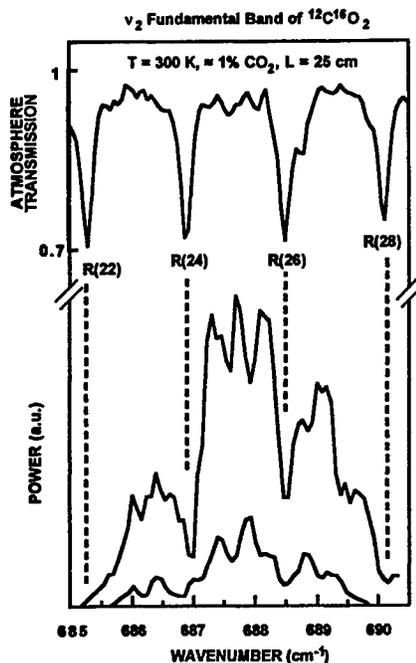
Figure 7: (top curve) FTIR transmission spectrum of ambient air containing 1% CO2 gas after 0.25 m propagation. The rotation-vibration absorption lines of the 0→ν_2 fundamental band of $^{12}C^{16}O_2$ are indicated in the figure. (bottom curves) Normalized emission spectra of the QF laser at a temperature of 20 K after 2.4 m propagation in ambient air. The laser is respectively operated at 3.6 (lower curve) and 10 times (upper curve) above threshold. The resolution of the dispersive spectrometer used for these measurements is 0.4 cm^{-1}.

The bottom curves of Figure 7 shows normalized emission spectra of the QF laser respectively operated 3.6 and 10 times above threshold at a temperature of 20 K. The propagation length between the laser and the detector is 2.4 m. As seen, holes develop in the emission spectrum. As shown in the top inset of Fig. 7, these holes reflect the fundamental 0-ν_2 rotation-vibration absorption lines of the CO_2 molecule. We have carried out separate experiments to assess the sensitivity of this atmospheric CO_2 gas detection technique. We used the QF laser. to measure the integrated transmission of a 3 cm long gas cell containing a mixture of CO_2 gas and air at atmospheric pressure. Preliminary results show that the detection limit could be well below 250 ppm.m of CO_2 gas concentration.

4. BROAD-AREA LASERS WITH NORMAL-INCIDENCE PUMPING

The side-facet pumping configuration offers the advantage of simplicity for coupling the TM polarized pump beam into the active layers. However, the pumping efficiency remains dramatically small. Based on simple geometric considerations, less than 1.5% of the incident pump energy is used to pump the QF laser. This figure may be largely overestimated since it does not account for the effective coupling of the pump into the waveguide, which is presently unknown. One way to enhance the pump efficiency is to make use of diffraction gratings patterned on top of the sample for normal-incidence coupling of the pump radiation. The diffracted waves inside the sample have a polarization component along the growth axis, which allows efficient coupling of the pump to the e_1e_3 intersubband transition. Besides, the normal-incidence pumping configuration is well suited for pumping broad-area lasers.
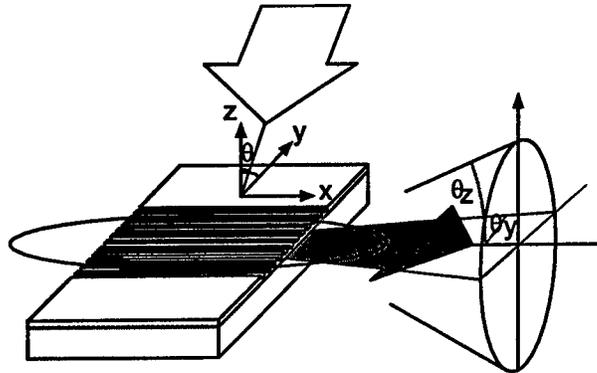
Figure 8: Experimental arrangement for grating-coupled QF lasers.

a)

b)
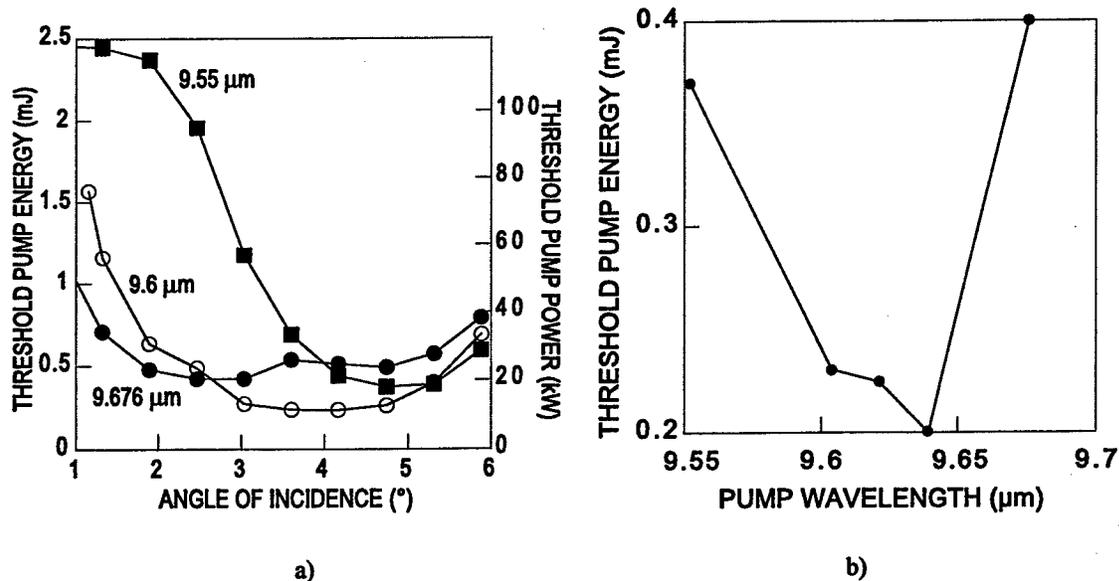
Figure 9: a) Dependence of pump threshold on the angle of incidence for three different wavelengths indicated on the figure. b) Minimum threshold pump energy versus pump wavelength.

The 1.75 μm thick GaAs cap layer has been used to pattern 1 mm wide transmission gratings by means of standard photolithographic and dry etching techniques. The grating period is 3.14 μm with a duty cycle of 0.7 and an etched depth of 1 μm. The grating efficiency (±1 diffraction orders) is calculated to be 35%.[24] After thinning the GaAs substrate, 1.5 mm long laser samples have been cleaved and mounted on the cold-finger of a liquid nitrogen cryostat. Figure 8 shows the experimental arrangement. A cylindrical lens is used to focus the CO_2 laser beam onto the sample surface with a spot size of 5x0.5 mm². Lasing action is achieved parallel to the grooves between the cleaved facets of the sample. It should be noted that the laser is gain guided and that the width of the active region along the y axis where positive gain occurs, increases

with pump intensity. The emission from one facet is collected with a f/1.1 ZnSe lens and then refocused onto the QWIP detector with a magnification factor of 4.

The angle of incidence of the pump radiation onto the surface of the sample, θ, is of critical importance for achieving good coupling efficiency and low thresholds. Figure 9.a) shows both the pump energy incident on the sample and the pump power at threshold versus angle of incidence for three pump wavelengths. As expected from grating theory, the angle of incidence corresponding to the minimum pump threshold is dependent on wavelength. Figure 9.b) shows the pump threshold energy as a function of pump wavelength. For each wavelength, the angle of incidence has been adjusted to minimize the threshold energy. The spectral evolution of the threshold exhibits a sharp resonance with a full width at half minimum of 1.8 meV. As seen, thresholds as low as 200 μJ are achieved at a pump wavelength of 9.64 μm. The corresponding threshold pump power is 8 kW. This threshold value is smaller than that obtained on 2.15 mm long QF lasers with side-facet pumping. It should be noted that the distributed optical losses in the present 1.5 mm long sample are increased from 5.6 to 8.5 cm^{-1}.
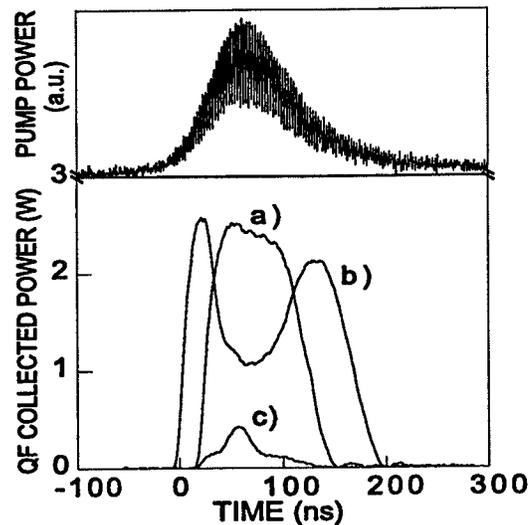
Figure 10: temporal evolution of a typical pump pulse at 9.64 μm wavelength (top curve) and of the QF laser power collected by the QWIP detector. θ is set at 3.3° to minimize pump threshold. The pump energy is 1.27 mJ for a) and 2.55 mJ for b) and c). For c), the detector has been moved by 0.5 mm along y-axis in the focal plane.

Figure 10 displays the multimode pump pulse and the corresponding temporal evolution of the QF emission at 14.7 μm wavelength. The pump wavelength is set at 9.64 μm and the angle of incidence has been adjusted for minimum threshold (8 kW). The energy of the pump pulse incident on the sample is 1.27 mJ for a) and 2.55 mJ for b) and c). The response of the QWIP detector at the emission wavelength has been carefully calibrated. Not shown in Fig.10, at pump energies below 1.2 mJ, the QWIP signal closely follows the pump pulse above threshold. At a pump energy of 1.27 mJ (curve a), the emission still follows the pump pulse above threshold but some saturation is visible at maximum. The collected power reaches 2.4 W at a pump power of 35 kW, i.e. 4.4 times above threshold. At higher pumping energy, the shape of the emission pulse is radically changed. As shown by curve b), the collected power follows the pump power at the initial and final stages of the pump pulse but an opposite behavior is observed for pump powers above 35 kW. The collected power drops by almost 50% at the peak of the pump pulse (120 kW). This behavior is attributed to a mode switching at higher pump powers from TM_{00} to TM_{01} and to the limited imaging area viewed by the detector. By moving the detector 0.5 mm away from its on-axis position along the y axis, an emission pulse is detected as shown by curve c). The pump threshold is of the order of 35 kW and the emission power grows with pump power. These results give clear indication that the laser switches to higher transverse mode under intense excitation. This effect is directly related to the intensity-dependent extent along the y axis of the active region in the present gain-guided laser. It should be noticed that the intrinsic response time of the QF unipolar laser is extremely fast since it is limited by the electron lifetime in the upper subband (0.7 ps). In the present experiments, the QWIP detector is not fast enough to resolve the micropulse structure of the QF laser emission induced by multimode laser pumping. The emission of the QF laser is expected to be a train of micropulses with less than 2.6 ns

FWHM. Mode-switching from TM_{00} to TEM_{01} is likely to occur within individual micropulses at pump powers exceeding 35 kW.

We have carried out separate measurements to estimate the output beam intensity profile. At pump energies below 1 mJ, the output mode is confirmed to be TM_{00}. The divergence angle in the layer plane, $\theta_y \approx 5°$, is remarkably small. The beam diameter at the output facet is deduced to be ≈ 120 μm. As seen, the in-plane divergence angle of the broad-area QF laser is a factor of 5 smaller than the value obtained for QF lasers with side-facet pumping. This low in-plane divergence is of course a consequence of the larger spatial extent of the active region along the y axis achieved with surface pumping with respect to side-facet pumping. However, we cannot exclude additional improvement of the mode quality, i.e. mode filtering, due to the presence of the top grating.[25] Because of the strong confinement of the TM emission along the growth axis, the divergence angle in the xz plane remains very large and could not be measured due to the limited aperture of the cryostat windows. We estimate $\theta_z \approx 60.4°$ as for side-facet pumped lasers. The collection efficiency is then deduced to be $\leq 53\%$ for the TM_{00} emission.
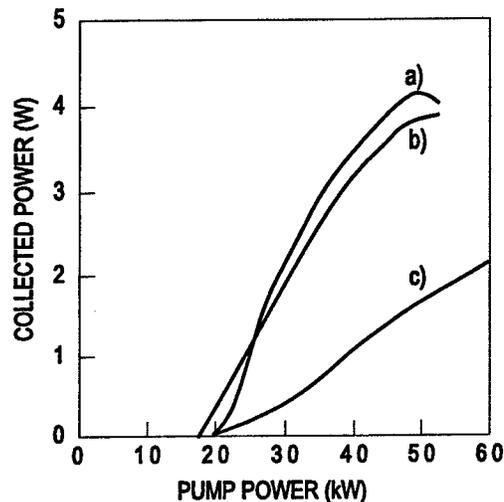
Fig 11: collected power versus pump power. The pump (emission) wavelength is 9.67 μm (14.8 μm), 9.64 μm (14.7μm) and 9.55 μm (14.55 μm) for curves a), b) and c), respectively. The angle of incidence $\theta \approx 2.6°$ has been adjusted for achieving large output powers.

Figure 11 shows the collected power versus pump power for three different pump wavelengths. For each pump wavelength, the angle of incidence of the pump radiation has been adjusted to achieve maximum output power under intense pumping. As seen, the threshold pump power is increased by almost a factor of 2 with respect to measurements at an angle of incidence optimized for low-threshold operation. For a pump power 3 times above threshold, the collected power reaches 4.16 W, 3.8 W and 1.7 W at a pump wavelength of 9.67 μm (a), 9.64 μm (b) and 9.55 μm (c), respectively. As for side-facet pumped QF lasers, the laser wavelength is found to be dependent on pump wavelength and is measured to be 14.8 μm, 14.7 μm and 14.55 μm for curves a), b) and c), respectively. The saturation visible in curve a) at large pump powers is attributed to the onset of the second transverse mode, which is not detected by the QWIP detector. Using a conservative value of 53% for the collection efficiency, the output power per facet of the QF laser operated in the TM_{00} mode is estimated to be at least 7.8 W for 48 kW pumping at 9.64 μm. This value sets a new record high for a semiconductor laser emitting at long mid-IR wavelengths. It should be noted that much higher output powers can be achieved under more intense pumping conditions. However, in this case the broad-area QF laser is multimode transverse.

5. CONCLUSION

In conclusion, we have reported on high-power unipolar GaAs/AlGaAs lasers emitting in the 14-15 μm wavelength range under optical pumping by a pulsed CO_2 laser. Operation of edge lasers with side-facet pumping as well as broad-area lasers with normal-incidence pumping has been demonstrated. We have shown that record high optical powers can be obtained from these quantum fountain unipolar lasers. Optical powers per facet as high as 6.6 W for edge lasers and 7.8 W for broad-area lasers are achieved with TM_{00} mode emission. Extended tunability of the lasing wavelength, $\Delta\lambda/\lambda \approx 2.5\%$, has been

observed by varying the pump wavelength. Applications to gas detection has also been investigated. The overall performances of QF lasers make them excellent candidates for applications such as remote gas sensing or LIDAR systems.

6. ACKNOWLEDGEMENTS

7. REFERENCES

1. M. Tacke, "New developments and applications of tunable IR lead salt lasers", Infrared Phys.Technol.. **36**, p.447 (1995).
2. J.Faist, F. Capasso, D. Sivco, C. Sirtori, A.L. Hutchinson, S. N. G. Chu and A.Y. Cho, "Quantum cascade laser", Science **264**, p.553 (1994).
3. O. Gauthier-Lafaye, P. Boucaud, F.H. Julien, S. Sauvage, S. Cabaret, J.-M. Lourtioz, V. Thierry-Mieg, R. Planel, " Long wavelength (≈15.5 micrometer) unipolar semiconductor laser in GaAs quantum wells", Appl. Phys. Lett., **71**, 3619 (1997); O. Gauthier-Lafaye, F. H. Julien, P. Boucaud, S. Sauvage,J.-M. Lourtioz, V. Thierry-Mieg, R. Planel, "Long-wavelength (15.5 µm) quantum fountain intersubband laser in GaAs/AlGaAs quantum wells", SPIE **3284**, p.224 (1998).
4. F.H. Julien, A. Sa'ar, J. Wang and J.-P. Leburton, "Optically pumped intersubband emission in quantum wells", Electron. Lett. **31**, p.838 (1995).
5. J. W. Bales, K. A. McIntosh, T. C. L. G. Sollner, W. D. Goodhue and E. R. Brown, "Observation of optically pumped intersubband emission from quantum wells", SPIE **1283**, p.74 (1990).
6. G. Sun and J. B. Khurgin, "Optically pumped four-level infrared laser based on intersubband transition in multiple quantum wells: feasibility study", IEEE J. Quantum Electron. **29**, p.1104 (1993).
7. V. Berger, "Three-level laser based on intersubband transitions in asymmetric quantum wells: a theoretical study", Semicond. Sci. Technol. **9**, p.1493 (1994).
8. A. Afzali-Kushaa, G. I. Haddad and T. B. Norris, "Optically pumped intersubband lasers based on quantum wells", IEEE J. Quantum Electron. **31**, p.135 (1995).
9. Z. Moussa, P. Boucaud, F.H. Julien, Y. Lavon, A. Sa'ar, V. Berger, J. Nagle and N. Coron, "Observation of infrared intersubband emission in optically pumped quantum wells", Electron. Lett. **31**, p.912 (1995).
10. Y. Lavon, A. Sa'ar, Z. Moussa, F. H. Julien and R. Planel, "Observation of optically pumped midinfrared intersubband luminescence in a coupled quantum well structure", Appl. Phys. Lett. **67**, p.1984 (1995).
11. F.H. Julien, Z. Moussa, P. Boucaud, Y. Lavon, A. Sa'ar, J. Wang, J.-P. Leburton, V. Berger, J. Nagle and R. Planel, "Intersubband mid-infrared emission in optically pumped quantum wells", Superlattices and Microstruct. **19**, p.69 (1996).
12. S. Sauvage, P. Boucaud, F.H. Julien, O. Gauthier-Lafaye, V. Berger, J.Nagle, "Intersubband photoluminescence of GaAs quantum wells under selective interband excitation", Appl. Phys. Lett. **71**, p.1183 (1997).
13. S. Sauvage, Z. Moussa, P. Boucaud, F.H. Julien, V. Berger and J. Nagle, "Room temperature infrared intersubband photoluminescence in GaAs quantum wells", Appl. Phys. Lett.**70**, p.1345 (1997).
14. O. Gauthier-Lafaye, S. Sauvage, P. Boucaud, F.H. Julien,R. Prazeres, F. Glotin, J.-M. Ortega,V. Thierry-Mieg, R. Planel,J.-P. Leburton and V. Berger, "Intersubband stimulated emission in GaAs/AlGaAs quantum wells: pump-probe experiments using a two-color free-electron laser", Appl. Phys. Lett. **70**, p.3197, (1997).
15. O. Gauthier-Lafaye, S. Sauvage, P. Boucaud, F.H. Julien, F. Glotin, R. Prazeres, J.-M. Ortega, V. Thierry-Mieg, R. Planel, "Investigation of mid-infrared intersubband stimulated gain under optical pumping in GaAs/AlGaAs quantum wells", J. Appl. Phys. **83**, p.2920 (1998).
16. O. Gauthier-Lafaye, P. Boucaud, F.H. Julien, S. Sauvage, S. Cabaret, J.-M. Lourtioz, V. Thierry-Mieg and R. Planel, "Long wavelength (≈15.5 micrometer) unipolar semiconductor laser in GaAs quantum wells", Appl. Phys. Lett. **71**, p.3619 (1997).
17. J. Wang, J.-P. Leburton, Z. Moussa, F.H. Julien and A. Sa'ar, "Simulation of Optically-Pumped Mid-Infrared Intersubband Semiconductor Laser Structures", J. Appl. Phys. **80**, p.1970 (1996).
18. J. Wang, J.-P. Leburton, F.H. Julien and A. Sa'ar, "Design and performance optimization of optically-pumped mid-infrared intersubband semiconductor lasers", IEEE Photonics Technol. Lett. **8**, p.1001 (1996).
19. S. Adachi, "GaAs, AlAs, and AlxGa1-xAs: Material parameters for use in research and device applications", J. Appl. Phys. **58**, p.R1 (1985).

20. J. Y. Duboz, E. Costard, J. Nagle, J. M. Berset, J. M. Ortega, J. M. Gerard, "Electron capture time measurements in GaAs/AlGaAs quantum-well infrared photodetectors: photoresponse saturation by a free-electron laser", J. Appl. Phys. **78**, p.1224 (1995).
21. P. Von Allmen, M. Berz, G. Petrocelli, F.-K. Reinhart, G. Harbeke, "Intersubband absorption in GaAs/AlGaAs quantum wells between 4.2 K and room temperature", Semicond. Sci. Technol. **3**, p.1211 (1988).
22. H.C. Casey and M.B. Panish, "Heterostructure Lasers", Academic Press, New York, (1978).
23. J. B. Khurgin, G. Sun, L. R. Friedman, R. A. Soref, "Comparative analysis of optically pumped intersubband lasers and intersubband Raman oscillators.", J. Appl. Phys. **78**, p.7398 (1995).
24. J. Y. Duboz, "Grating coupled intersubband transitions in microcavities" J. Appl. Phys. **80**, p.5432, 1996
25. R. J. Lang, K. Dzurko, A. A. Hardy, S. Demars, A. Schoenfelder, D. F. Welch, "Theory of grating confined broad area lasers", IEEE JQE **34**, p.2196, (1998)

The carrier dynamical issues for extending the operating wavelength of quantum cascade lasers

P. Harrison, K. Donovan, R. W. Kelsall, P. Kinsler

Institute of Microwaves and Photonics,
School of Electronic and Electrical Engineering,
University of Leeds, LS2 9JT, United Kingdom

ABSTRACT

Electron-longitudinal optic phonon and electron-electron intersubband scattering rates are calculated for a variety of quantum well systems. It is demonstrated that the internal quantum efficiency of a Terahertz radiative intersubband transition can be greater than in the mid-infrared at 4 K, however by room temperature has fallen to around 20%. A study of the internal quantum efficiency of a Terahertz energy intersubband transition in double and single quantum wells, has shown that the vertical intrawell transition is more efficient than the diagonal interwell transition.

Keywords: Terahertz, infrared, intersubband, quantum well, quantum cascade, lasers

1. INTRODUCTION

Besides higher powers, and higher temperatures of operation, one of the main development goals of quantum cascade lasers has been to extend their operating wavelength. Successive devices have moved this from the 4-8 μm centre of the mid-infrared,[1,2] through 11,[3] 13[4] and recently 17 μm.[5] It is clear that the potentially high returns of accessing the Terahertz (10-1 THz) or far-infrared (30-300 μm) are motivating workers to strive for much much longer wavelengths and recently Rochat[6] reported electroluminescence from a quantum cascade device at 88 μm which is deep into the Terahertz region (3.4 THz).

Quantum cascade lasers work via carrier scattering. Electrons enter a semiconductor layer stack through an emitter and cascade through successive active regions. Within any one particular active region the majority of the transitions are non-radiative and produce no photons. However the unique idea of carrier recycling and subsequent injection into the next active region compensates for the low efficiency and results in useful levels of output power. In principle, any one electron can produce many photons during a single passage through a device.

Whilst *stimulated emission* requires more electrons to be in an excited state than in the ground state, i.e., a population inversion, *optical gain* and subsequent lasing action relies upon reaching a particular photon density within the device. Both of these points are dependent upon the carrier dynamics. The former on the ratio of two scattering rates, see for example[7-9] and one factor in achieving the latter is the *internal quantum efficiency*. For any particular transition this is defined as

$$\eta = \frac{\text{spontaneous radiative emission rate}}{\text{total intersubband scattering rate}} \tag{1}$$

It gives a measure of the proportion of electron transitions from the upper to the lower subband which produce photons rather than non-radiative loss. The higher the number of photons produced the more readily threshold and lasing will be achieved.

In this work the potential operating performance of Terahertz quantum cascade lasers are compared with contemporary shorter wavelength mid-infrared devices from the viewpoint of the carrier dynamics within the active region.

Further author information: (Send correspondence to P.H.) E-mail: p.harrison@ee.leeds.ac.uk

Part of the EUROPTO Conference on Terahertz Spectroscopy and Applications II
Munich, Germany • June 1999 SPIE Vol. 3828 • 0277-786X/99/$10.00

17
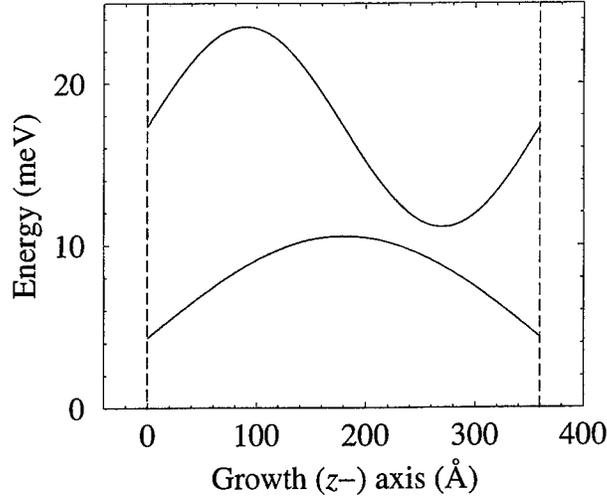
Figure 1. Ground and first excited state wave functions of a 360 Å wide GaAs quantum well surrounded by infinitely high barriers

2. THEORY

The mathematical expressions for the three most important scattering rates for electrons in quantum well subband systems are complicated: for example the electron-LO phonon scattering rate for an initial state wave vector k_i is of the form

$$\frac{1}{\tau_i} = \frac{\Upsilon''}{2} \int_{-\infty}^{+\infty} \frac{\pi |G_{if}(K_z)|^2}{\sqrt{K_z^4 + 2K_z^2 \left(2k_i^2 - \frac{2m^*\Delta}{\hbar^2}\right) + \left(\frac{2m^*\Delta}{\hbar^2}\right)^2}} \, dK_z \tag{2}$$

where $G_{if}(K_z)$ is a form factor involving the phonon wave vector K_z. The electron-electron scattering rate is of the form

$$\frac{1}{\tau_i} = \frac{m^* e^4}{\pi \hbar^3 (4\pi\epsilon)^2} \int \int_0^{2\pi} \int_0^{2\pi} \frac{|A_{ijfg}(q_{xy})|^2}{q_{xy}^2} \, P_j(\mathbf{k}_j) \, d\theta \, d\alpha \, dk_j \tag{3}$$

where $A_{ijfg}(q_{xy})$ is a form factor involving all 4 electron states involved in any one scattering event and q_{xy} represents the change in the relative wave vectors. And finally the spontaneous radiative emission rate is

$$\frac{1}{\tau_i} = \frac{e^2 \omega}{4\epsilon m^* c^2 W_z} O_{if} \tag{4}$$

where O_{if} is the oscillator strength. For more details on these expressions and information on how to implement them computationally see Harrison.[10]

Given their complexity it is difficult to derive any simple empirical understanding of the comparative behaviour of Terahertz intersubband transitions with the higher energy ones in the mid-infrared—a computational study is required. Whilst it is possible to gain valuable information with a careful analysis of the resulting scattering rates, it is more transparent to quantify a complete device design in terms of a single number—and a convenient one is the internal quantum efficiency, as defined above in equation 1 (the denominator is taken as the sum of all the above rates).

3. EFFECT OF REDUCED SUBBAND SEPARATION

The infinitely deep quantum well is a good example system in which to study the effect of altering the energy separation ΔE_{21} between two subbands, as this can easily be achieved by changing the well width, and it has the additional benefit of not altering the overlap of the wave functions. Fig. 1 gives an example of the wave functions of the lowest two eigenstates.
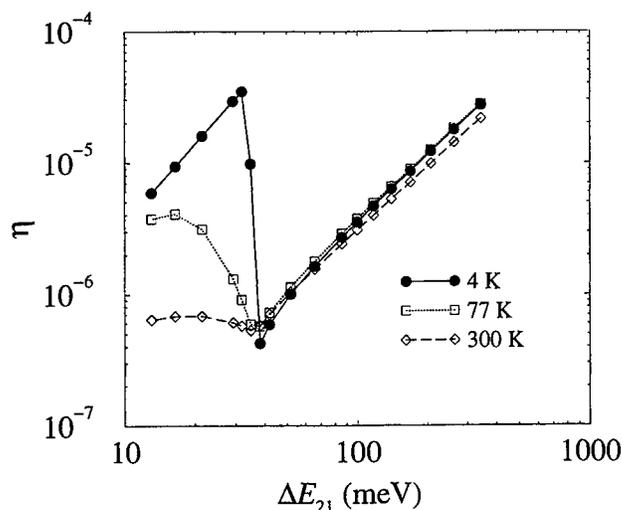
Figure 2. The effect of intersubband separation on the internal quantum efficiency η

Using the methods outlined above, the internal quantum efficiency was evaluated for the transition of electrons from the first excited state to the ground state, for equal populations in each subband of 10^{10} cm^{-2}. Fig. 2 displays the results for a variety of temperatures.

Moving from the higher subband energy separations typical of the mid-infrared ($\Delta E_{21} \gtrsim 100$ meV) to lower, the quantum efficiency decreases slightly as a function of temperature as well as showing a more dramatic decrease with energy separation. However when the LO phonon energy of 36 meV (in this example material of GaAs) is reached the curves show dramatic behaviour. At 4 K when the subband separation moves below the LO phonon energy, and the non-radiative competing mechanism of LO phonon emission is suppressed completely. Hence the internal quantum efficiency increases almost discontinuously and dramatically to levels even greater than in the mid-infrared. This is indicative of great potential for low temperature Terahertz lasers.

As the temperature increases the increase in the quantum efficiency as the subband separation is reduced below the LO phonon energy is still substantial but less impressive. This is due to LO phonon emission from the upper subband only being partially suppressed because of thermal broadening of the subband electron distributions. However even at 77 K the quantum efficiencies calculated are of similar magnitude to those in the mid-infrared and again indicate that from the viewpoint of the carrier dynamics lasing action at Terahertz frequencies should be as readily achieved as in the mid-infrared.

Similar results are expected for equivalent III-V polar materials which have comparative phonon structure.

4. OPTIMUM DEVICE GEOMETRIES

The early quantum cascade laser designs of Bell Labs., for example[2,1] had a 'diagonal' interwell radiative transition, see Fig. 3 (left). In this configuration the electrons in the upper laser subband were localised in one well, and underwent radiative transitions to a lower subband in an adjacent well. Whilst it offers the possibility of a small amount of tunability in the emission frequency, it was supposed that the oscillator strength of this interwell transition and hence the internal quantum efficiency was small. In addition it was expected that as the radiative transition samples the barrier it would suffer from inhomogeneous broadening, due to interface disorder and alloy fluctuations within the barrier. Later designs therefore tried the 'vertical' intrawell radiative transition, see for example,[3,11] as depicted in Fig. 3 (right).

From the theoretical expressions in Section 2 it is not at all obvious which of the two basic device geometries, whether vertical or diagonal is preferable. This view is evidenced in the literature with successful devices being
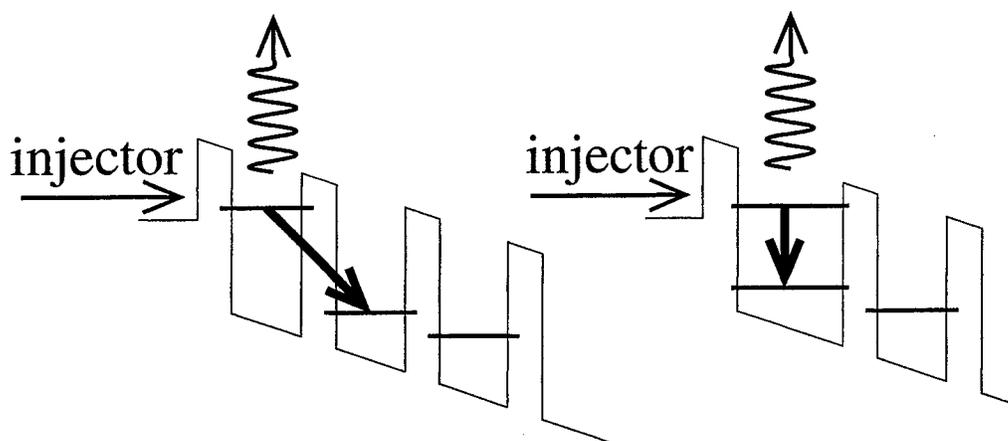
Figure 3. The two basic design geometries, diagonal radiative transitions (left) and vertical radiative transitions (right)
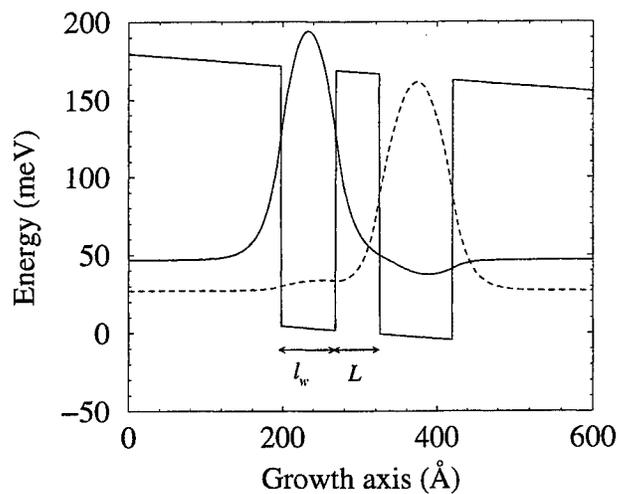
Figure 4. The lowest two eigenstates of a double quantum well structure with applied electric field
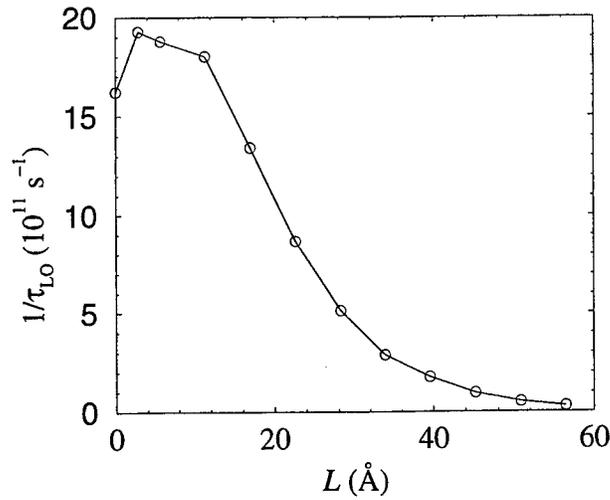
Figure 5. The electron-LO phonon emission rate from subband 2 to 1 as a function of the barrier width L
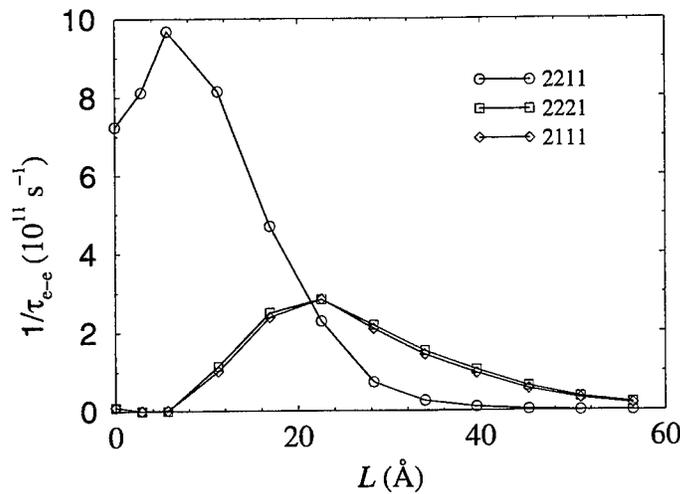
Figure 6. The electron-electron scattering rates from subband 2 to 1 as a function of the barrier width L

demonstrated with both vertical[12] and diagonal[13] radiative transitions. Both reports of far-infrared emission from quantum cascade devices were in the diagonal interwell configuration.[14,6]

Fig. 4 illustrates the 'test' system—the width L of the central barrier of the double quantum well was varied in order to alter the geometry from vertical $L = 0$ to increasingly more diagonal transitions. At each value of L the quantum well width l_w was adjusted in order to keep the subband separation fixed at 20 meV, this corresponds to a wavelength of 62 μm and a frequency of 4.8 THz which is taken as representative of the Terahertz band.

In order to evaluate the expression in equation 1 the electron-LO phonon, electron-electron scattering rates, together with the spontaneous radiative emission rates were calculated, as described in Section 2. Figs. 5, 6 and 7 display the results of these calculations, at 300 K, as a function of the central barrier width L, and for the electron populations of 10^{10} cm^{-2} in each subband. It can be seen that the electron-LO phonon, the *symmetric* 22-11 electron-electron and the electron-photon scattering rate all decrease as the barrier width increases. As the quantum
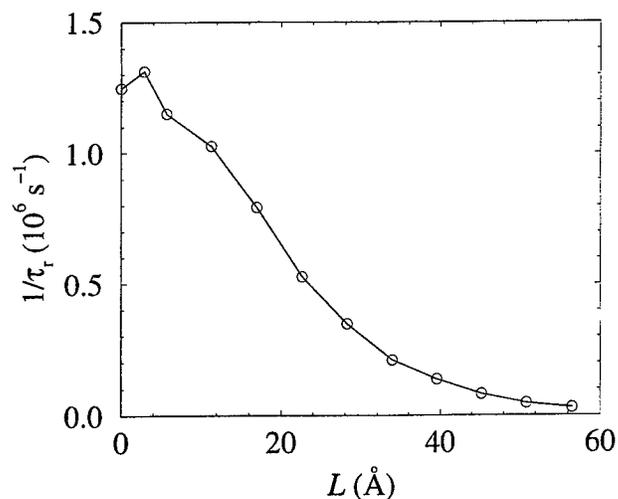
Figure 7. The spontaneous radiative emission rate from subband 2 to 1 as a function of the barrier width L
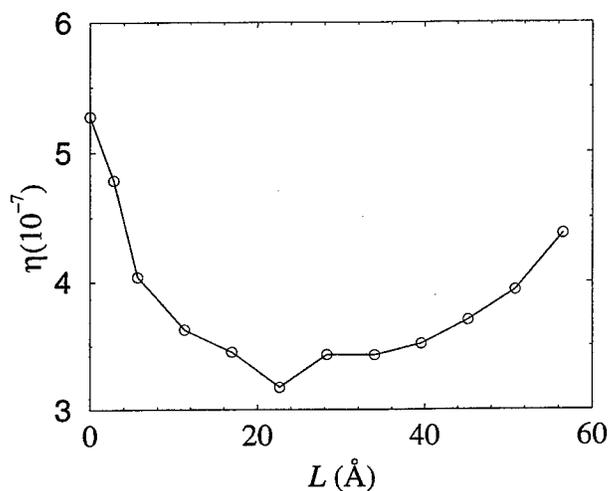
Figure 8. The internal quantum efficiency at 300 K as a function of the barrier width L

well width is adjusted to keep the subband separation constant then this effect is due entirely to the reduced overlap in the initial and final state wave functions.

The electron-electron scattering rate is the only one which shows any interesting behaviour. For a central barrier width L of zero, the system is actually a single quantum well, and with only a weak electric field ($4\,\text{kVcm}^{-1}$) is almost symmetric. Hence only the symmetric 22-11 electron-electron scattering rate is significant. As the barrier width increases though the system becomes more asymmetric and the other intersubband electron-electron transitions, the 22-21 and the 21-11, increase.

The combination of these different effects is summarised in Fig. 8—the internal quantum efficiency η as a function of the central barrier width L at 300 K. It can be seen that, over this L domain, the quantum efficiency is highest for a vertical intra-well transition. The calculations do indicate that comparative quantum efficiencies may be obtained at $L \gtrsim 60$Å, however additional non-radiative mechanisms due to alloy fluctuations in the barrier will become more

important at these large barrier widths and reduce the quantum efficiency.

Similar data is obtained at 4K and allows the conclusion to be drawn that vertical intrawell transitions have a higher quantum efficiency, at Terahertz energy subband separations, than diagonal interwell transitions.

5. IN SUMMARY

It has been shown that the internal quantum efficiency for radiative transitions between two subbands in GaAs at Terahertz frequencies is greater at low temperatures than that at mid-infrared wavelengths. It is comparable at 77 K and less at room temperature. Furthermore the internal quantum efficiency is higher for vertical intrawell transitions than diagonal interwell transitions at Terahertz frequencies.

ACKNOWLEDGMENTS

REFERENCES

1. J. Faist, F. Capasso, D. L. Sivco, L. Hutchinson, C. Sirtori, S. N. G. Chu, and A. Y. Cho, "Quantum cascade laser—temperature-dependence of the performance characteristics and high t_0 operation," *Appl. Phys. Lett.* **65**, p. 2901, 1994.
2. J. Faist, F. Capasso, D. L. Sivco, C. Sirtori, A. L. Hutchinson, and A. Y. Cho, "Quantum cascade laser," *Science* **264**, p. 553, 1994.
3. C. Sirtori, J. Faist, F. Capasso, D. L. Sivco, A. L. Hutchinson, and A. Y. Cho, "Long wavelength infrared ($\lambda \approx 11$ μm) quantum cascade lasers," *Appl. Phys. Lett.* **69**, p. 2810, 1996.
4. C. Sirtori, F. Capasso, J. Faist, D. L. Sivco, A. L. Hutchinson, and A. Y. Cho, "Quantum cascade unipolar intersubband light emitting diodes in the 8-13 μm wavlength range," *Appl. Phys. Lett.* **66**, p. 4, 1995.
5. A. Tredicucci, C. Gmachl, F. Capasso, D. L. Sivco, and A. L. Hutchinson, "Long wavelength superlattice quantum cascade lasers at $\lambda \approx 17$ μm," *Appl. Phys. Lett.* **74**, p. 638, 1999.
6. M. Rochat, J. Faist, M. Beck, U. Oesterle, and M. Ilegems, "Far-infrared (λ=88 μm) electroluminescence in a quantum cascade structure," *Appl. Phys. Lett.* **73**, p. 3724, 1998.
7. P. Harrison and R. W. Kelsall, "Population inversion in optically pumped asymmetric quantum well terahertz lasers," *J. Appl. Phys.* **81**, pp. 7135–7140, 1997.
8. P. Kinsler, P. Harrison, and R. W. Kelsall, "Intersubband terahertz lasers using four-level asymmetric quantum wells," *J. Appl. Phys.* **85**, pp. 23–28, 1999.
9. P. Harrison, P. Kinsler, K. Donovan, and R. W. Kelsall, "The carrier dynamics of terahertz intersubband lasers," *High Speed Electronic and Systems* , 1999. submitted.
10. P. Harrison, *Quantum wells, wires and dots: Theoretical and computational physics*, John Wiley and Sons, Ltd, Chichester, United Kingdom, 1999. to be published.
11. J. Faist, F. Capasso, C. Sirtori, D. L. Sivco, A. L. Hutchinson, and A. Y. Cho, "Continuous wave operation of a vertical transition quantum cascade laser above t=80 k," *Appl. Phys. Lett.* **67**, p. 3057, 1995.
12. C. Gmachl, F. Capasso, J. Faist, A. L. Hutchinson, A. Treddicucci, D. L. Sivco, J. N. Baillargeon, S. N. G. Chu, and A. Y. Cho, "Continuous-wave and high-power pulsed operation of index-coupled distributed feedback quantum cascade laser at $\lambda \approx 8.5 \mu$m," *Appl. Phys. Lett.* **72**, p. 1430, 1998.
13. C. Sirtori, P. Kruck, S. Barbieri, P. Collot, J. Nagle, M. Beck, J. Faist, and U. Oesterle, "Gaas/al$_x$ga$_{1-x}$as quantum cascade lasers," *Appl. Phys. Lett.* **73**, p. 3486, 1998.
14. B. Xu, Q. Hu, and M. Melloch, "Electrically pumped tunable terahertz emitter based on intersubband transition," *Appl. Phys. Lett.* **71**, p. 440, 1997.

Unipolar semiconductor lasers: new class of devices for the generation of mid-infrared radiation

Peter Kruck [a], Carlo Sirtori [a], Stefano Barbieri [a], Hideaki Page [a], Philippe Collot [a],

Julien Nagle [a], Mattias Beck [b], Jérôme Faist [b], Ursula Oesterle [c]

[a] Thomson-CSF, Laboratoire Central de Recherches, 91404 Orsay, France

[b] Institute of Physics, University of Neuchâtel, 2000 Neuchâtel, Switzerland

[c] Ecole Polytechnique Fédérale de Lausanne, Lausanne, Switzerland

ABSTRACT

Quantum cascade lasers are coherent light sources in the mid-infrared spectral region. They are based on resonant tunneling and optical transitions between discrete energy levels in the conduction band arising from size quantization in semiconductor heterostructures. QCLs have been demonstrated on GaInAs/AlInAs/InP and GaAs/AlGaAs outperforming existing semiconductor laser technologies in the mid-infrared spectral range (3.5 - 17 µm). The present paper reports the realization of a QCL based on GaAs/AlGaAs material designed with an emission wavelength of 9.3 µm. Specific properties inherent to this material system and their influence on laser operation are discussed in detail. The paper concludes with the presentation of a new waveguide concept, which offers considerable performance improvements.

Key words: semiconductor lasers, quantum wells, bandgap engineering

1. INTRODUCTION

Quantum cascade (QC) lasers are unipolar semiconductor lasers based on intersubband transitions [1]. The laser principle makes use of radiative transitions between discrete electronic states of the conduction band which arise from quantum confinement in semiconductor heterostructures grown by molecular beam epitaxy (MBE). The precise control of quantum well width and the tunneling barrier thickness allows the quantum engineering of electronic energy levels and level separation. Furthermore dipole matrix elements, lifetimes and scattering times between the levels can be tailored in order to obtain population inversion. Therefore the scheme differs in a fundamental way from semiconductor diode lasers, including quantum well lasers. In the latter conduction electrons and valence band holes are injected into the active region of a forward biased pn junction where they radiatively recombine across the band gap. In contrast to QC lasers, the band gap essentially determines the emission wavelength.

Since their first demonstration in 1994 QC lasers have shown tremendous performance improvements and have emerged as powerful coherent light sources for the mid-infrared region [2, 3]. The interest for semiconductor lasers operating in this spectral region, especially in the second atmospheric window, comes from various applications such as environmental sensing, combustion process control or industrial process control. Up to now the only commercially available semiconductor lasers emitting in this spectral range are lead-salt lasers [4]. However, their pulsed and continuous-wave (CW) operation characteristics are clearly surpassed by QC lasers designed with comparable emission wavelength. Other alternative mid-

24

Part of the EUROPTO Conference on Terahertz Spectroscopy and Applications II
Munich, Germany • June 1999 SPIE Vol. 3828 • 0277-786X/99/$10.00

infrared sources have also been developed, such as III-V compounds containing Sb [5], or type-II QCLs [6]. In this case photon emission occurs between an electron state and a hole state in a staircase of Sb-based quantum well structures. But all these competing concepts have not reached so far the performance of QCLs with respect to high temperature operation and range of accessible wavelengths.

The material system in which the QCL has been demonstrated and developed is the ternary alloy InGaAs/InAlAs grown lattice matched to InP substrates. Compared to other semiconductor compounds this material system offers mainly two advantages: firstly the high conduction band discontinuity (520 meV) and secondly the low refractive index substrate which can be used as lower cladding and which, hence, facilitates waveguide design and sample growth. Up to now InGaAs/AlInAs/InP based QC lasers have been realized which cover the spectral range between 3.5 and 17 μm with a considerable performance [7]. In pulsed mode and at cryogenic temperatures state of the art QCLs exhibit optical output powers of several hundred milliwatts, giving 'wall plug' efficiencies of nearly 10 % for the best devices reported [8]. Room temperature operation with peak optical power of more than ten milliwatts has been demonstrated in devices with emission wavelengths up to 11.5 μm [9]. Recent activities have tried to increase the maximum operating temperature for continuous wave (CW) operation by implementing e.g. binary InP top claddings, which optimize heat dissipation [10]. Furthermore the quantum cascade concept has been successfully combined with more refined cavity concepts such as destributed feedback (DFB) structures [11] or microcavity disk lasers to achieve monomode operation and low threshold current [12], respectively. Only recently spontanous far-infrared electroluminescence at λ=88 μm in a QC diode structures has been observed [13] confirming the wide range of accessible emission wavelengths of this innovative emitter concept.

2. GAAS/ALGAAS QUANTUM CASCADE LASERS
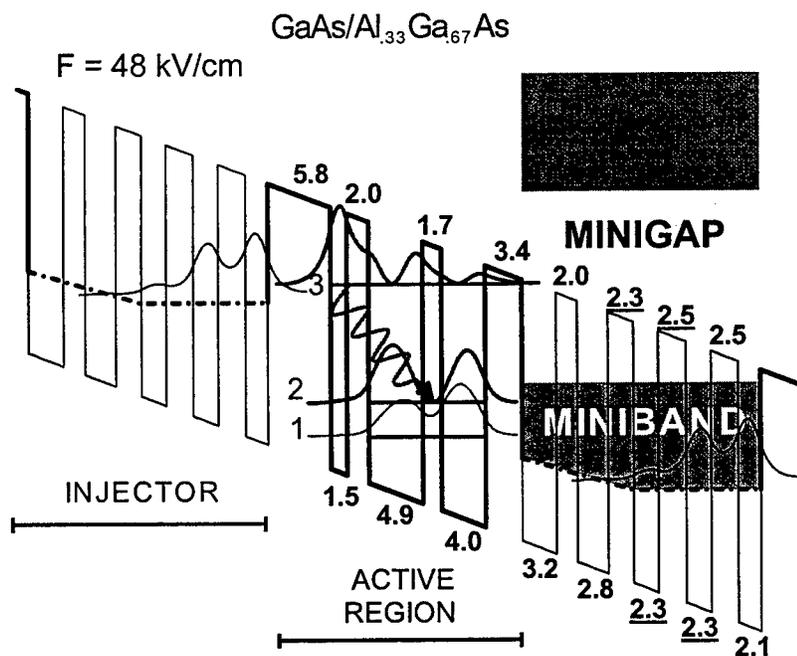
Fig. 1 Calculated conduction band structure of an active region enclosed between digitally graded injector regions. The relevant squared wave functions are shown. The wavy line indicates the transition (3-2) responsible for laser action. The thicknesses of the layers are indicated in nm. The underlined layers are silicon doped with a nominal concentration of n_{Si}= 4×10^{17}cm^{-3}.

Only recently we have demonstrated laser action in a QC structure made of GaAs/AlGaAs material designed with emission wavelength at 9.3 μm, confirming that the cascading scheme is independent of a specific heterostructure [14]. Furthermore the

use of this material system gives access to sophisticated device processing techniques. Fig. 1 shows a portion of the 30 period (active region plus digitally graded injector) active section of the GaAs/AlGaAs QCL. The active region of our laser structure is designed according to the anticrossed diagonal scheme with three GaAs quantum wells strongly coupled by thin $Al_xGa_{1-x}As$ barriers ($x = 0.33$). A detailled comparison between diagonal and vertical laser schemes based on InGaAs/InAlAs/InP material has shown that 'diagonal' QC lasers with comparable emission wavelength to our AlGaAs/GaAs QCL exhibit very low threshold current densities [15]. The aluminium content throughout the active region is $x = 0.33$, which corresponds to a Γ point discontinuity of about $\Delta E_c = 295$ meV. By this choice we can assume that lateral conduction band valleys in GaAs/AlGaAs have no major influence on device performance. Parasitic electron transfer to the lateral valleys would certainly deteriorate the material gain and would make it more difficult to achieve population inversion. The transition energy under the biasing conditions shown in Fig. 1 is $\Delta E_{32} = 132$ meV ($\lambda = 9.4$ µm). Under an external electric field of about $F = 48$ kV/cm the ground state of the graded injector alignes with the upper laser level $n=3$. At this point of operation electrons are resonantly injected through a 5.8 nm thick tunnel barrier into the upper laser level. Population inversion is achieved by the control of nonradiative relaxation channels (electron-optical-phonon scattering). A calculation for the present structure gives for the upper ($n=3$) and lower laser level ($n=2$) nonradiative lifetimes $\tau_3=1.5$ ps and $\tau_2=0.3$ ps, respectively.
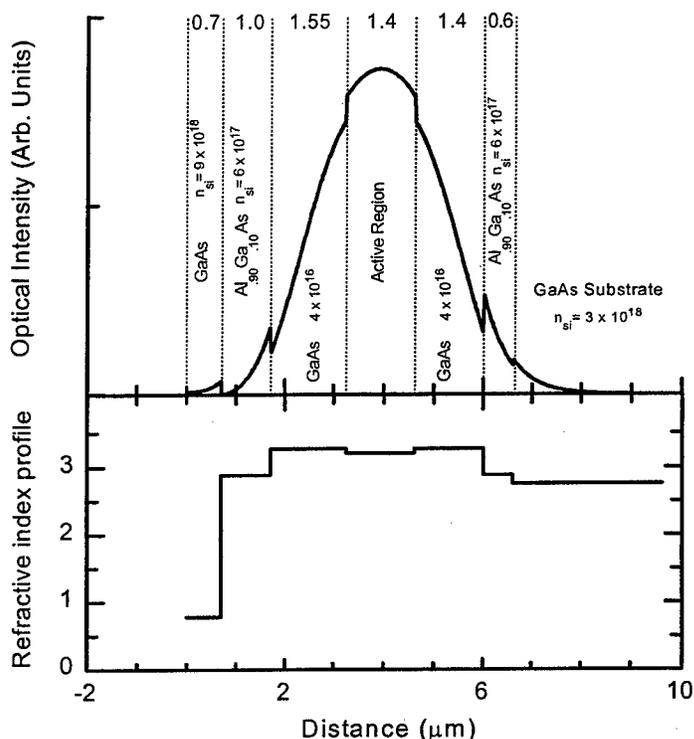
Fig. 2 Calculated optical intensity distribution of the fundamental TM mode of the waveguide structure (upper curve) and profile of the refractive index (lower curve). Only 4 % of the mode penetrate in the lossy $Al_{0.9}Ga_{0.1}As$ cladding layers.

The design of an appropriate waveguide demands extensive modifications compared to InGaAs/InAlAs QCLs grown on InP substrates. GaAs substrates have the largest index of refraction in the AlGaAs/GaAs heterostructure and, thus, cannot be used as lower waveguide cladding layer. A standard dielectric waveguide concept with micrometer thick $Al_xGa_{1-x}As$ cladding layers ($x>0.75$) on both sides of the active region would be difficult to implement for the following reasons: Firstly the waveguide design for a quantum cascade laser operating in the mid-infrared spectral region demands low doping concentration in order to keep waveguide losses due to free carrier absorption low. It is this mechanism which has the main influence on the threshold current density of GaAs/AlGaAs devices. The following equation displays the threshold condition

$$J_{th} = \frac{\alpha_W + \alpha_M}{g\Gamma} = \frac{\alpha_W}{g\Gamma} - \frac{\ln R}{g\Gamma}\frac{1}{L} \qquad (1)$$

where J_{th} is the threshold current density, α_W and α_M is waveguide and mirror losses, respectively, R the facet reflectivity (R = 0.26 for GaAs), g the gain coefficient, Γ the overlap factor between the mode and the active region and L the device length. The free carrier absorption becomes even more pronounced when the QCL is designed for emission at longer wavelengths, since in this spectral region the absorption strength increases with a λ^3 dependency. A second main drawback arises from the freeze-out of electrons at deep donor atoms in the $Al_xGa_{1-x}As$ cladding layers for typical operating temperatures. This freeze-out deteriorates the transport properties of the claddings. The donor ionization energy for a Si doped $Al_{0.9}Ga_{0.1}As$ alloy layer is E_{ion}= 65 meV. Therefore only a small fraction of electrons is released at cryogenic temperatures. Furthermore the mobility of an $Al_xGa_{1-x}As$ alloy layer is only few hundred cm^2/Vs at low temperatures, whereas it reaches some thousand cm^2/Vs in bulk GaAs. A higher doping level would improve the conductivity and reduce the series resistance introduced by the cladding layers. However this would also increase the waveguide losses and hence the threshold current.

According to these considerations we have, in a first approach, designed a waveguide structure which is based on thin $Al_{0.9}Ga_{0.1}As$ claddings and double sided plasmon-enhanced confinement. Fig. 2 shows the calculated mode profile and refractive index of our waveguide structure. On the bottom of the waveguide, a heavily doped substrate (n_{Si}=3×10^{18} cm^{-3}) pushes the mode towards the active region. This is counterbalanced by a heavily doped 0.7 µm thick GaAs n^{++} layer (n_{Si} = 9×10^{18} cm^{-3}) underneath the top contact. The core comprises the active region enclosed between two low doped µm-thick GaAs layers (n_{Si} = 4×10^{16} cm^{-3}). The $Al_{0.9}Ga_{0.1}As$ claddings (n_{Si} = 6×10^{17} cm^{-3}) only reside in the wings of the mode. Therefore only 4% of the waveguide mode overlap with the poorly conductive and lossy claddings. The reduced thickness makes sure that the series resistance of the alloy layers, especially at low temperature, is low. For a detailled description of the waveguide concept the reader is referred to ref. 14.

3. OPERATION CHARACTERISTICS
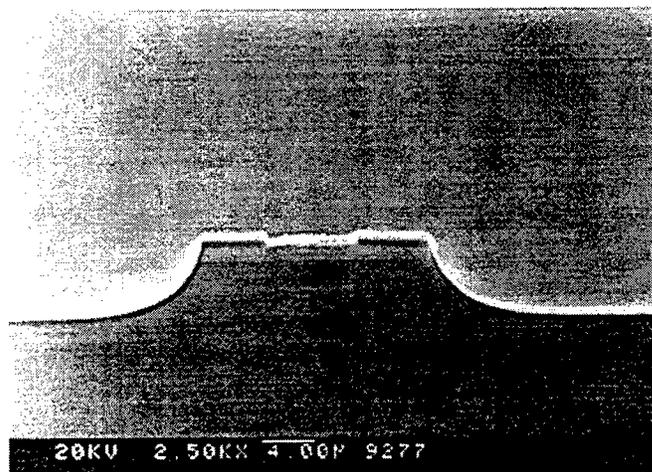
Fig. 3 Scanning electron micrograph of a cleaved facet of a ridge waveguide laser obtained after wet chemical etching.

The samples were processed into mesa etched ridge waveguides by optical contact lithography and deep wet chemical etching. Fig. 3 shows an SEM picture of the lateral profile obtained with a HCl : H_2O_2 = 80 : 4 etch solution. Typical etching rates of this etchant are in the range of 600 nm/min. After thinning down the substrate to 100 µm, a standard AuGe/Ni/Au contact is evaporated on the backside and alloyed at 400°C for one minute. For the insulation of the ridges a 300-nm-thick Si_3N_4 layer is deposited by a sputtering technique. Windows in the nitride are patterned on top of the ridges by reactive ion etching using a SF_6 plasma. For the top metallization 30 nm of titanium followed by 300 nm of gold are deposited on the top surface in an electron beam evaporation system. The top contact is not annealed in order to avoid any enhancement of waveguide losses. The lasers are then cleaved in bars of 1-3 mm length and the laser facets are left uncoated. Finally samples

are indium soldered epilayer up to Cu holders, wire bonded and mounted on the temperature controlled coldfinger of a helium cryostate. After cooling down to cryogenic temperatures in the dark we have measured current-voltage (I-V) and light-current (L-I) curves of a laser 1 mm long and 20 μm wide. In the measurement the device was driven with 100 ns long current pulses (0.1 ‰ duty cycle). The optical power versus drive current was obtained using a f/0.8 optical system and a room temperature calibrated HgCdTe detector. The lasers exhibit a strong dependence on external white light illumination. Fig. 4 shows the device characteristics under three different illumination conditions. The bold line refers to a measurement without illumination. The onset of the injection regime, which gives rise to the knee in the I-V characteristics, occurs at about V=8V. From the calculated bandstructure in Fig. 1we derive a voltage drop of ΔE=230 meV across one period. By multiplying the latter with the total number of periods N=30 one obtains an expected total voltage drop of 7 V, which is about 1 V below the measured value. We attribute this difference to the residual series resistance introduced by the cladding and contact layers. Threshold is reached at I_{th}=1.3 A. This corresponds to a current density of J_{th}=6.5 kA/cm^2.
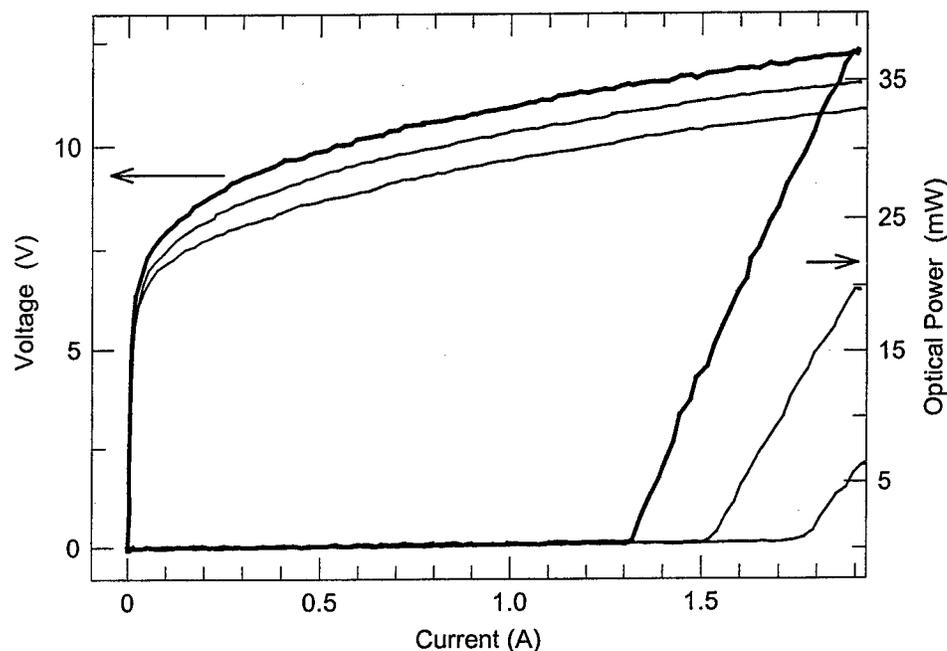
Fig. 4 Voltage versus current (I-V) and Light versus current (L-I) characteristic for a 1 mm × 20 μm device operating at 4 K in pulsed mode as a function of white light illumination. (bold line: no illumination before data acquisition, single lines: after subsequent illumination)

Illumination of the device with an external white light source before the measurements results in a strong persistent change of the L-I and I-V characteristics. The results obtained after subsequent illumination steps are plotted as single lines in Fig. 4. As a function of the exposure time the operation voltage for fixed current decreases. At the same time the threshold current moves from its 'dark' value I_{th}=1.3 A to higher values. With sufficient illumination we obtain a saturated threshold current of I_{th}=1.8 A (J_{th}=9.0 kA/cm^2) with a voltage of operation shifted 1.3V below its dark value. We attribute this behaviour to the release of electrons trapped at deep donor levels (*DX* centers) in the Al$_{0.9}$Ga$_{0.1}$As cladding. For x>0.22 the DX centre is the lowest energy level of the silicon donor atom [16]. The increase in carrier density after illumination improves the conductivity of the claddings, but enhances also the waveguide losses α_W due to a stronger free carrier absorption in the claddings. We have also performed temperature dependent I-V's and capacitance-voltage (C-V) measurements on test samples, composed of material identical to the Al$_{0.9}$Ga$_{0.1}$As claddings. The observed activation behaviour clearly identifies the DX centres as the source for the observed instability and excludes the presence of other impurities. A more refined analysis of the influence of DX centres on the performance of this laser structure will be published elsewhere [17]. Finally to exclude illumination effects coming from the active region, which is also composed of Al$_x$Ga$_{1-x}$As material with x = 0.33, we measured I-V and L-I characteristics of LED structures with an active region identical to the one in the laser structure, but without AlGaAs cladding layers. The data show no dependence on external white light illumination. Therefore we can assume that the gain mechanism

is independent of external illumination. This is also confirmed by the laser operation itself. We have calculated the product of slope efficiency $\eta=dP/dI$ (P: optical power) and threshold current density j_{th} after subsequent illumination steps. With

$$\eta = \frac{1}{2}\frac{h\nu}{e}N\frac{\alpha_M}{\alpha_M+\alpha_W}\left(1-\frac{\tau_2}{\tau_{32}}\right) \quad (2)$$

and the Equation (1) it is evident that the product $\eta \times j_{th}$ depends on the gain coefficient g, but is independent of the total losses $\alpha_T = \alpha_W+\alpha_M$. For fixed current ($I = 1850$ mA), which means fixed injection, we derive a gain coefficient g independent of external white light illumination. Fig. 5 shows the dependence of the slope efficiency and the threshold current density j_{th} as a function of the operating voltage for $I = 1850$ mA.
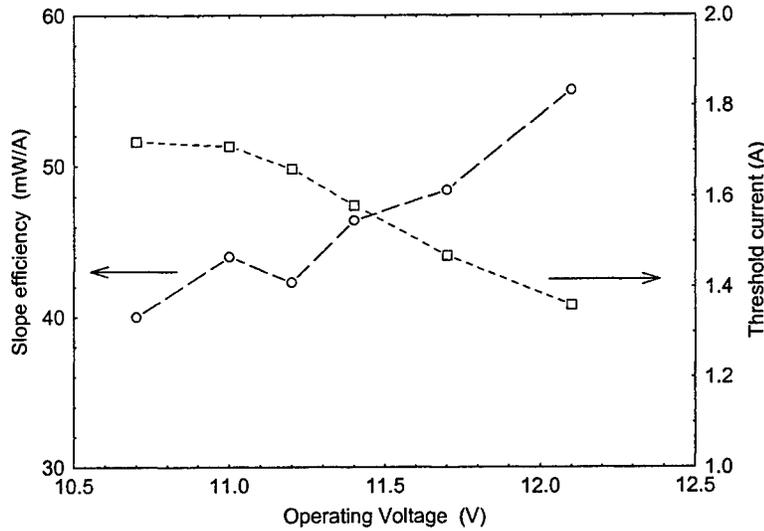
Fig. 5 Slope efficiency and threshold current density as a function of illumination derived from the L-I and I-V characteristics shown in Fig. 4 for an injection current of 1850 mA. We assume that the change of the operation voltage after each illumination step is a measure for the number of released carriers in the claddings. The product $\eta \times j_{th}$ is inversely proportional to the gain g. Our data confirm that g is independent of illumination within experimental error.

To determine the change of the waveguide losses $\Delta\alpha_W$ due to the release of carriers in the claddings, we have also measured high resolution subthreshold spectra for a constant injection current ($I = 1250$ mA) as a function of illumination using a Hakki-Paoli technique [18]. Illumination results in a striking damping of the Fabry-Perot fringes of the laser cavity. As is shown in ref. 19 the modulation depth of the fringes is proportional to the $R\exp(G_m-\alpha_W)L$, where G_m is the modal Gain $G_m=g\,\Gamma j$ (with R as the facet reflectivity and j the current density). From our data we derive a change $\Delta(G_m-\alpha_W)$ upon illumination, which is identical to the change $\Delta\alpha_W$ of waveguide losses since the optical gain g does not change as shown in the preceding section. The change in waveguide losses between dark and saturated illumination is $\Delta\alpha_W = 12$ cm^{-1}. Finally we can estimate the total waveguide losses $\alpha_T = \alpha_W+ \alpha_M$. From equation (1) and (2) we calculate the change of ΔJ_{th} and $\Delta(\eta^{-1})$ introduced by a change of waveguide losses $\Delta\alpha_W$. Ratioing with J_{th} and η^{-1}, respectively, gives the following identity

$$\frac{\Delta J_{th}}{J_{th}} = \frac{\Delta\alpha_W}{\alpha_T} = \frac{\Delta\left(\eta^{-1}\right)}{\eta^{-1}} \quad (4).$$

For fixed injection current ($I = 1850$ mA) we derive $\Delta(\eta^{-1})/\eta^{-1} = 0.3$ (see Fig. 4). A comparison of the equivalent ratio for the threshold current density gives the same value. With $\Delta\alpha_W = 12$ cm^{-1} and mirror losses $\alpha_M = 13$ cm^{-1} for a 1 mm long device we obtain $\alpha_W = 27$ cm^{-1}.

In order to improve laser performance and to avoid device instabilities due to the presence of DX centres in AlGaAs claddings we have designed and tested an alternative waveguide structure. The design is based on plasmon enhanced confinement only. High Al content AlGaAs cladding layers are suppressed. Two 1 μm n^{++} GaAs layers ($n_{Si} = 6 \times 10^{18}$ cm^{-3}) act now as cladding layers and provide the optical confinement. To avoid an increase of waveguide losses due to strong free carrier absorption, 3.5 μm thick low-doped GaAs spacer layers have been grown on both sides of the active region. Therefore only the wings of the mode overlap with the lossy GaAs cladding layers. The design of the active region is identical to the one shown in Fig. 1. As a consequence of the increase of waveguide dimensions the overlap factor Γ between optical mode and active region is reduced. In the present design this has been counterbalanced by increasing the number of periods to N=36. Simulations show that the symmetric design of the waveguide structure makes the mode profile less sensitive to slight deviations of doping concentrations during MBE growth compared to their nominal values. Fig. 6 shows the L-I and I-V characteristic of a laser device 2.5 mm long and 28 μm wide. Processing, mounting and operating conditions are identical to the ones previously described. At T=77 K threshold is reached at I_{th} = 3.2 A corresponding to J_{th} = 4.6 kA/cm^2. Maximum optical output powers up to P = 500 mW have been obtained. Laser operation in pulsed mode has been achieved up to T = 190 K. Under external white light illumination no changes of device operation have been observed. Preliminary measurements of the waveguide losses give an α_W in the order of 20 cm^{-1}. Therefore in comparison to waveguide designs using ternary alloy claddings the present design based on low doped binary GaAs could help to further reduce waveguide losses and to improve long wavelength operation of QCLs .
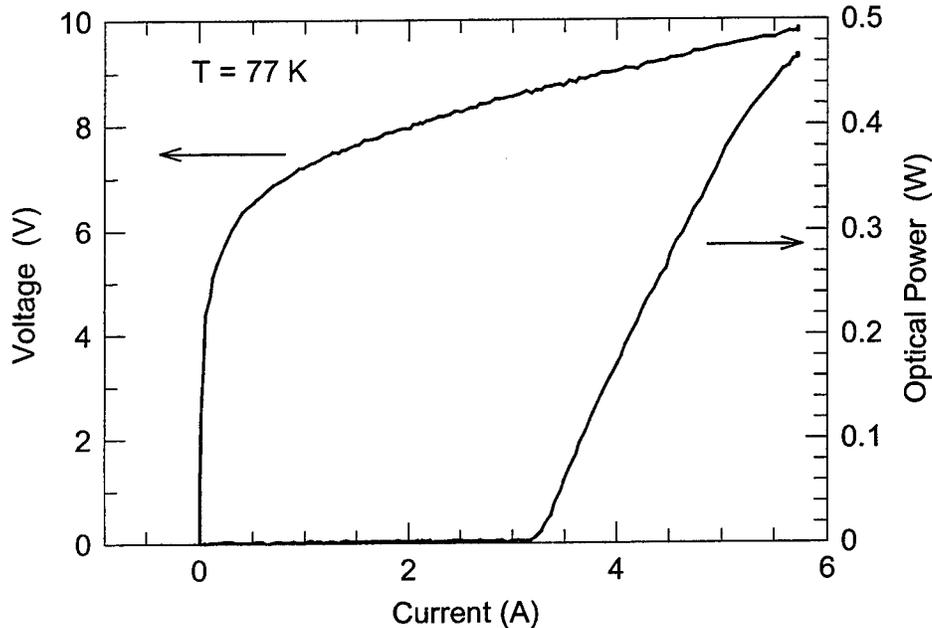
Fig. 6 Applied bias and measured optical peak output power from a single facet as a function of injected current for a laser 27 μm wide and 2.5 mm long. The device was driven in pulsed mode with 100 ns current pulses and 1 kHz repetition rate.

4. CONCLUSIONS

We have reported the performance characteristics of a GaAs/AlGaAs quantum cascade laser operating at 9.3 μm. For a waveguide design based on high Al content AlGaAs claddings a strong dependence of laser performance on external white light illumination has been observed. This effect is related to an increase of waveguide losses due to the ionization of electrons trapped in DX centres in the Si doped AlGaAs cladding layers. To avoid the illuminaton effect we have developed a new waveguide design entirely based on plasmon confinement in an aluminium free waveguide structure.

5. ACKNOWLEDGEMENTS

6. REFERENCES

1   J. Faist, F. Capasso, D.L. Sivco, C. Sirtori, A.L. Hutchinson, A.Y. Cho, Science **264**, 553 (1994)
2   J. Faist, A. Tredicucci, F. Capasso, C. Sirtori, D.L. Sivco; J.N. Baillargeon, A.L. Hutchinson, A.Y. Cho, IEEE J. Quantum Electron. **34**, 336 (1998)
3   C. Sirtori, J. Faist, F. Capasso, D.L. Sivco; A.L Hutchinson, A.Y.Cho, IEEE J. Quantum Electron. **33**, 89 (1997)
4   M. Tacke, Infrared Phys. Technol. **36**, 447 (1996)
5   Infrared Applications of Semiconductors - Materials, Processing and Device, In: M.O. Manasreh, T.H. Myers, F.-H. Julien (Eds.) MRS Proc. 450 (1997)
6   C.-H. Lin, R.Q. Yang, D. Zhang, S.J. Murr, S.S. Pei, A.A. Allerman, S.R. Kurtz; Electron. Lett. **33**, 598 (1997)
7   A. Tredicucci, C. Gmachl, F. Capasso, D.L.Sivco, A.L. Hutchinson, A.Y. Cho, Appl. Phys. Lett. **74**, 638 (1999)
8   C. Gmachl, A. Tredicucci, F. Capasso, A.L. Hutchinson, D.L. Sivco, J.N. Baillargeon, A.Y. Cho, Appl. Phys. Lett. **72**, 3130 (1998)
9   J. Faist, C. Sirtori, F. Capasso, D.L. Sivco; J.N. Baillargeon, A.L. Hutchinson, A.Y. Cho, IEEE Photon. Technol. Lett. **8**, 1100 (1998)
10   J. Faist, F. Capasso, C. Sirtori, D.L. Sivco, J.N. Baillargeon, A.L. Hutchinson, S.N.G. Chu, A.Y. Cho, Appl. Phys. Lett. **68**, 3680 (1998)
11   C. Gmachl, F. Capasso, J. Faist, A.L. Hutchinson, A. Tredicucci, D.L. Sivco; J.N. Baillargeon, S.N.G. Chu, A.Y. Cho, Appl. Phys. Lett. **72**, 1430 (1998)
12   J. Faist, C. Gmachl, M. Striccoli, C. Sirtori, F. Capasso, D.L. Sivco, A.Y. Cho, Appl. Phys. Lett. **69**, 2456 (1996)
13   M. Rochat, J. Faist, M. Beck, U. Oesterle, M. Ilegems, Appl. Phys. Lett. **73**, 3724 (1998)
14   C. Sirtori, P. Kruck, S. Barbieri, P. Collot, J. Nagle, M. Beck, J. Faist, U. Oesterle, Appl. Phys. Lett. **73**, 3486 (1998)
15   C. Sirtori, F. Capasso, J. Faist, A.L. Hutchinson, D.L. Sivco, A.Y. Cho, IEEE J. Quantum Electron. **34**, 1722 (1998)
16   P.M. Mooney, J. Appl. Phys. **67**, R1 (1990) and the references given in there
17   C. Sirtori, S. Barbieri, P. Kruck, M. Beck, J. Faist, U. Oesterle, V. Piazza, J. Nagle, IEEE Photon. Technol. Lett. In print
18   B.W. Hakki, T.L. Paoli, J.Appl. Phys. **46**, 1299 (1975)
19   J. Faist, F. Capasso, C. Sirtori, D.L. Sivco, A.L. Hutchinson, S.N.G. Chu, A.Y. Cho, Superlattices and Microstructures **19**, 337 (1996)

GaAs AlGaAs Intersubband MIR Lasers

L. Hvozdara, S Gianordoli, W. Schrenk, G. Strasser, K. Unterrainer and E. Gornik

Solid State Electronics Institute, TU Wien, Floragasse 7, 1040 Wien, Austria

ABSTRACT

We report on the design, growth and characterization of electrically pumped quantum cascade lasers (QCL) and LED's, based on the GaAs/AlGaAs material system. Intersubband and interminiband optical transitions within the conduction band of a heterostructure are used to achieve spontaneous emission and lasing action. Samples are grown using solid source molecular beam epitaxy (MBE). Transport measurements, infrared photocurrent spectral response, transmission and emission measurements are performed. Laser wavelengths above ten microns are achieved. Peak powers are in the 200 mW range. Laser operation up to 100K and threshold current densities below 15 kA/cm^2 are recorded. Ridge lasers exhibit multimode spectra, typical for Fabry-Perot resonators. Room temperature spontaneous emission is recorded, showing the feasibility of a room temperature operating QCL on the GaAs/AlGaAs material system.

Keywords: MID-infrared lasers, GaAs/AlGaAs, quantum cascade lasers, intersubband emitter, interminiband emitter

INTRODUCTION

The most recent development of the infrared technology is causing a great demand for compact, coherent mid-infrared light sources. Large numbers of potential applications in environmental monitoring, chemical analysis, process control and medicine are opened. Semiconductor technology offers small-scale compact, low bias lasers with special features, like CW-operation, tunability, electrical and optical modulation, q-switching or single mode operation. Common laser diodes, based on the radiative recombination across the bandgap of a direct semiconductor are covering spectral range from the ultraviolet to the near infrared. Lead salt lasers are reaching the mid-infrared band. These are the only semiconductor MID-infrared coherent sources available on the market. Quantum cascade lasers, based on intraband transitions are promising better performance (room temperature operation, longer wavelengths, simultaneous emission at different frequencies). Since the radiative transition is located in the conduction band (or valence band respectively) there is no requirement for a direct semiconductor. This opens a completely new field for application of the indirect semiconductors (namely silicon or silicon-germanium) in optoelectronics [1].

A possibility to achieve the population inversion in a system of quantum wells within the conduction band was theoretically predicted in 1971 [2]. Since 1994, when the first quantum cascade laser was demonstrated by Faist et al. [3] it became a viable coherent source in the mid-infrared spectral range. In 1996 above room temperature operation and peak powers of 100 mW [4], as well as CW operation above 110 K was reported [5]. In 1997 a QCL with distributed feedback [6] was introduced and tunability of a QCL was demonstrated [7]. A significant improvement in the performance of these mid infrared devices was the first superlattice laser based on interminiband optical transitions [8]. Lasing operation at room temperature in a remote doped superlattice laser was recorded [9]. Microdisk lasers with deformed quadrupole cross section have been reported recently [10]. All these results have been achieved using InGaAs/InAlAs lattice matched to InP.

The GaAs/AlGaAs material system offers very good lattice match over the whole range of Al concentrations in AlGaAs ternaries and a low amount of dislocations and defects in the substrates. Electrically pumped GaAs/AlGaAs intersubband emission was first demonstrated by our group [11] and Li et al. [12] at cryogenic temperatures and later on up to room temperature [13]. A lot of effort was put into the development of a quantum cascade laser based on GaAs/AlGaAs. Intersubband photoluminescence, stimulated emission and finally lasing in the long wavelength range was achieved by optical pumping using a free electron or a CO_2 laser [14]. The first electrically pumped GaAs/AlGaAs quantum cascade laser, emitting at 9.2 microns, was demonstrated by Sirtori et al. in 1998 [15].

32

Part of the EUROPTO Conference on Terahertz Spectroscopy and Applications II
Munich, Germany • June 1999 SPIE Vol. 3828 • 0277-786X/99/$10.00
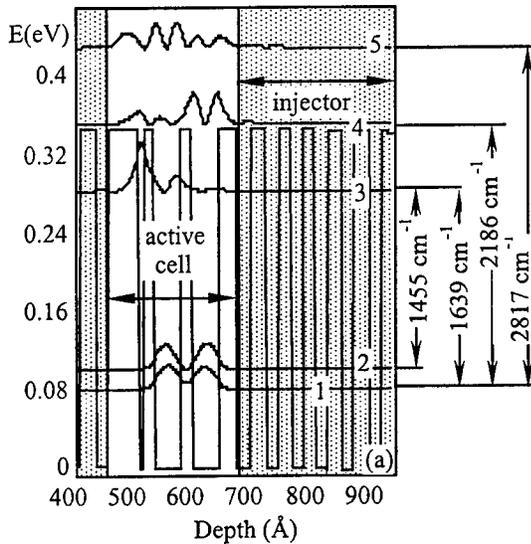
Figure 1a: Bandstructure of an intersubband emitter at flatband condition.
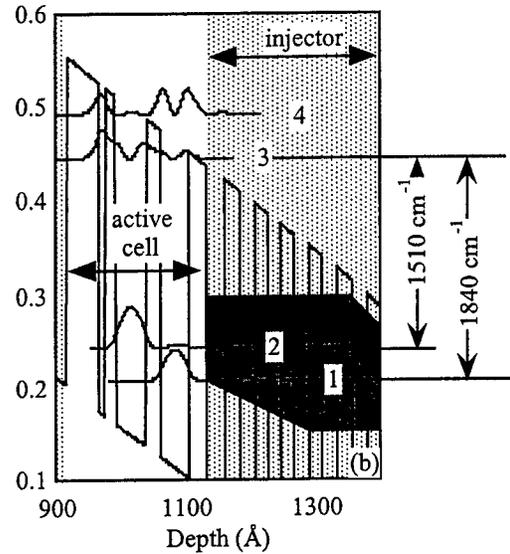
Figure 1b: Bandstructure of an intersubband emitter under 70 kV/cm bias, with corresponding energy spacing.

The first GaAs/AlGaAs intersubband emitters are using a three level laser scheme. The structure essentially follows the design rules given by Faist et al.[3], with the necessary changes due to a different material system. A triple quantum well serves as an active cell as seen in fig. 1a,b. The transition (3-2) is the radiative transition, where lasing should occur. Transition (2-1) is tailored to be in resonance with the LO-phonon energy (36meV) and serves for fast extraction of the electrons from level two. This mechanism maintains the population inversion, if sufficient injection into level three is provided. Single active cells are separated by superlattice injectors, that form a funnel shaped miniband under bias. An active cell of the first realized emitter, designed for investigation of a spontaneous emission at about 6.5 microns, is grown according to the following sequence: GaAs 10Å, AlGaAs 15Å, GaAs 45Å, AlGaAs 20Å and GaAs 45Å (fig.1). The aluminum fraction in the AlGaAs ternary is kept at x=0.45. The band offset for this Al concentration is largest and AlGaAs still behaves as a direct semiconductor. (The crossover of the Γ–valley and the X-valley occurs at Al fraction x=0.45). The structure is selectively doped in the injectors. The injectors are energetically aligned to collect the electrons - leaving the active cell at level one and to inject into level three of the following active cell (fig. 1b). A cascade of 25 periods of injectors and active cells, embedded between two n+ contact layers is grown. One electron successfully passing the cascade emits 25 photons.

For characterization, the samples are processed into 40*70 μm² mesas. AuGeNi contacts are evaporated, the mesas are soldered to a cold finger of a He cooled cryo-flow and wire
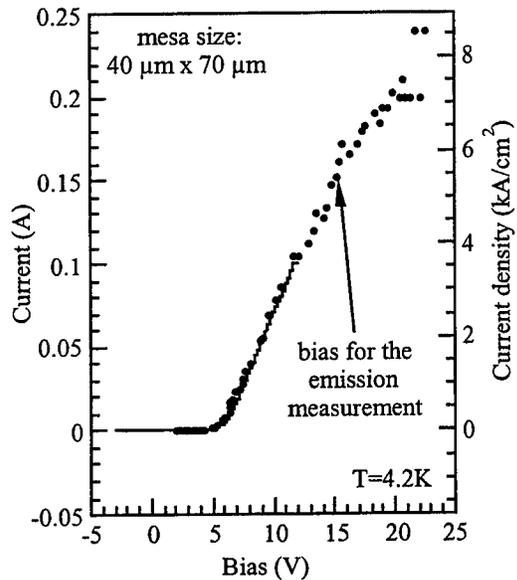
Figure 2: Current-voltage characteristic measured by quasistatic method (solid line) and by pulsed method (points). The arrow marks a working point of the emission measurements.

33

bonded. The current voltage characteristics (fig. 2) are recorded using a standard quasistatic (solid line) or pulsed (points) method respectively. The structure is designed to align at an external field of ~70kV/cm. Injectors align with the confined states in the wells, according to fig. 1b, enabling electron transport. The onset voltage of 6.4 volts, corresponding to the operational electric field of 68 kV/cm is in good agreement with the calculated operational electric field. The pulsed operation at small duty cycle protects the sample from thermal destruction at higher currents. The measurements are performed at liquid helium temperature.

The absorption spectra are obtained using a Fourier transform spectrometer (FTS) with a broadband light source and a LN_2 cooled MCT detector. The sample, grown on an undoped substrate, is polished, metallized and wedged on opposite facets, forming a slab waveguide. A wedging angle of 38° enables maximal light coupling. A multiple transition through the active region, enhances the absorption. Due to refraction on the tilted facet a non-zero component of the electric field in the growth direction is obtained. The transmission spectrum is shown in fig. 3 (upper curve). All three absorption minima are in agreement with the calculated level scheme (see fig. 1a and table 1). Small deviations from the model can be assigned to simplifications in the modeling and to thickness fluctuations. Photovoltaic response is measured using mesa structures. A broadband light source, is focused on the

Figure 3: Transmission spectrum and spectral response of an intersubband emitter in photovoltaic regime. At elevated temperature (2-3) transition can be observed.

Transition	wavenumbers [cm^{-1}]	
	meas.	calc.
1-2	168	188
1-3	1588	1633
1-4	2196	2153
1-5	2660	2730
2-3	1420	1433

Table 1 Calculated and measured energetic spacing at flatband conditions.

sample, the photovoltage response is amplified and fed into an FTS as a detector signal. Typical photovoltage spectra are shown in fig.3 (lower curves). The spectra measured at 4.2 K and at 25 K are showing three peaks, corresponding to transitions (1-3), (1-4) and (1-5). An additional peak at $1420 \, cm^{-1}$, corresponding to the transition (2-3), occurs above 100 K. An activation energy is required for population of the second state, therefore it occurs only at elevated temperatures. The temperature dependence of the ratio between the (1-3) and (2-3) peak heights yields an activation energy of 20±4 meV ($=188 \, cm^{-1}$), which is in a good agreement with the measured difference between the positions of (2-3) and (1-3) peaks in the spectra ($168 \, cm^{-1}$). Measured and calculated peak positions are compared in tab.1.

Electroluminescence spectra are shown in fig. 4 for both, 10 K and 300 K, respectively. The drive current is 165 mA (marked with an arrow in fig. 2). The main emission peak is centered around $1450 \, cm^{-1}$ (6.9 µm). This is in good agreement with the designed frequency ($1510 \, cm^{-1}$). An additional emission peak at $1850 \, cm^{-1}$, attributed to (3-1) optical transition can be observed. Detailed

Figure 4 Electroluminescence at 10K and 300K. Applied electric field marked in the I-V curve (fig 2).

analysis of the spectra reveals linewidth as narrow as 14 meV at 10 K, rising to 20 meV at room temperature (300 K). The narrow linewidth is assigned to the outstanding growth uniformity, and to the fact that the active cell is left undoped. Optical output lies in the 10 nW range. The sample exhibits a slight red shift (80 cm^{-1}) with increasing temperature. The polarization of the electroluminescence shows electric vector parallel to the growth direction (TM polarized), proving the selection rules for the intersubband transitions. In order to demonstrate the possibilities of the GaAs/AlGaAs emitters, various samples are grown and characterized. Emission frequencies over a range from 800 cm^{-1} to 1600 cm^{-1} (12.5μm to 6.25 μm) are achieved. The upper frequency limit is originating from the maximal achievable (and usable) band offset in the conduction band of a GaAs/AlGaAs heterostructure (~360meV). Relaxation mechanisms competing with the radiative transitions (like LO-phonon scattering) are limiting application of the above described three level system for low frequencies. A

Figure 5 Voltage dependence of the emission peak position for a sample with diagonal tunneling assisted transition.

possibility of the electrical tuning of the emission frequency (in the structure with tunneling assisted diagonal optical transition) shows the voltage dependence of the peak position in fig. 5. Tunability as high as 10 cm^{-1}/V is achieved in a structure designed for this purpose.

INTERMINIBAND CONCEPT

An alternative to the intersubband concept is an interminiband emitter, using a short period superlattice as an active cell. Electrons are injected into the second miniband of an intrinsic superlattice via an injector and they relax radiatively to the lowest miniband. The main advantage of this concept, compared to the intersubband concept, is higher oscillator strength of the radiative transitions across the miniband.

The studied emitter is designed following the rules given by Tredicucci et al. [9] and applying them to the GaAs/AlGaAs system. The conduction band are shown in fig. 6. The structure consists of an undoped eight period GaAs 58Å / AlGaAs 14Å intrinsic superlattice as an active cell. Miniband injector, bridging the active cell are locally close to the interface with the active cell. Doped regions are indicated by filled areas in fig.6. Dipoles, arising from the doping, act against the applied bias and flatten the minibands in active cell under the external electric field.

Another way to flatten minibands in the active cell under bias, is using aperiodic (chirped) superlattice [16]. A conduction band of this type of emitter is shown in fig. 7. This structure is designed to form a flat miniband under the applied electric field. The active cell consists of six quantum wells: GaAs **65Å**, AlGaAs 11Å, **61Å**, 12Å, **57Å**, 12Å, **51Å**, 13Å, **45Å**, 14Å, **43Å**, 24Å. It is designed to operate at 23 kV/cm. Active cells are bridged by funnel injectors., that are designed to inject only into the bottom of the second miniband of the active cell. This prevents transitions from higher states. The whole sample consists of 30 periods of alternating active cells and injectors.
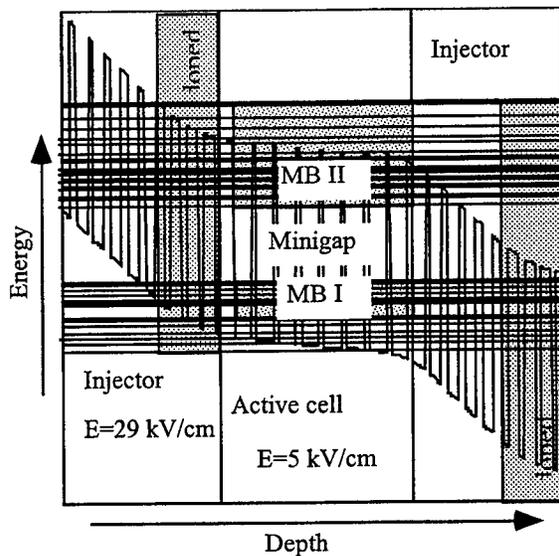
Figure 6 Conduction band of an interminiband emitter with remote doping.

Samples are wet chemical etched into 100 x 70 μm² mesas, TiAu contacts are sputtered chips are soldered to a heat sink and bonded. Characterization methods and the setup, used to investigate interminiband emitters, are comparable to those, used for characterization of the intersubband emitters. Samples are pulsed with 5 μs long pulses at 31 kHz repetition rate and currents up to 500 mA (~7kA/cm²). Measurements are performed at liquid helium temperatures up to room temperature. Total emitted powers are in the 10 nW range and the light is TM polarized. Emission spectra of the sample with a finite periodic superlattice are plotted for three different temperatures in fig. 8. Several overlapping emission peaks cover the range between 830 and 1400 cm⁻¹. The inset of fig. 8 shows the calculated energy dispersion of the investigated emitter. The solid lines represent the calculation for an infinite superlattice, while the dots denote the energies of the different states in the minibands for an eight period superlattice. Vertical transition energies (arrow marked in the inset) are plotted as dashed lines in fig. 8. The radiative transition between the two lowest superlattice minibands at about 110 meV can be observed up to room temperature. The electroluminescence spectrum recorded at low temperature shows additional, fully reproducible features. These peaks are attributed to the interminiband emission originating from vertical transitions from states in the upper minibands to states in the lower miniband.

The peaks between the dashed lines can't be attributed to any vertical transition, but self-consistent simulation show, that these transitions can be explained as diagonal transitions. The compensation of the external electric field using remote doping, as invented by Tredicucci et al. [9], is very sensitive to the doping concentrations. In addition it doesn't fully eliminate the influence of the external field in the active cells. As a result the dipole matrix elements of the diagonal optical transitions rise, and the peaks occur at corresponding positions in the spectrum. The second peak from the left in the 77K spectrum (fig.8) can only be interpreted as a diagonal optical transition between the second lowest state in the upper miniband and the highest state in the lower miniband. Simultaneous emission at more frequencies (fig.8) can be applied in the design of a "multicolor" GaAs/AlGaAs laser.

An emission spectrum of the interminiband emitter with an aperiodic (chirped) superlattice is in fig. 9. The emission peak is centered around 852 cm⁻¹. Compared to the
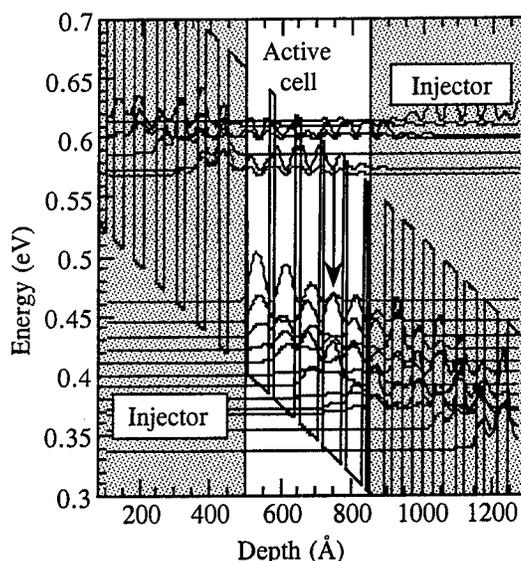
Figure 7 Conduction band of an emitter based on aperiodic (chirped) superlattice. The optical transition is arrow marked.
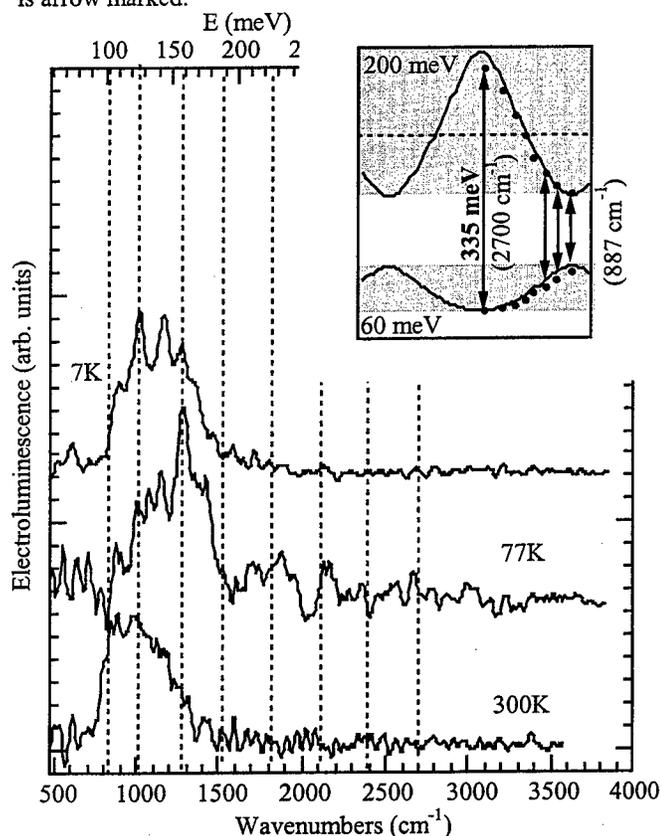
Figure 8: Emission spectrum of the interminiband emitter at three different temperature. The inset shows simulation of the active cell using the envelope function model (solid line) and self consistent calculation of the confined stated (dots).

emission spectrum of a periodic superlattice emitter (fig.8) it exhibits a much narrower peak (FWHM=121 cm^{-1}). The position of the peak is not sensitive to the variation of the electric field and the temperature. It is due to precise injection into the bottom of the upper miniband and due to a different concept of electric field compensation. An interminiband emitter based on the aperiodic superlattice appears to be better gain medium for fabrication of a GaAs/AlGaAs interminiband laser, compared to the emitter with a periodic superlattice.

Figure 9 Emission spectrum of an emitter based on an aperiodic superlattice

GaAs/AlGaAs QUANTUM CASCADE LASERS

A quantum cascade laser is essentially an intersubband emitter embedded into a resonator. The most important part of the optical cavity resonator is a waveguide cladding. A cladding material must be compatible with the GaAs/AlGaAs material system. It must provide a strong confinement of the guided mode in the gain medium and introduce low optical losses. In addition a high electrical conductivity (at room temperature and at cryogenic conditions) is required to provide a good admittance of the electrons to the gain medium.

The growth sequence of the waveguide, used in the described sample is given in tab. 2. Refractive indexes (dashed line) and the resulting mode profile (solid line) simulation is depicted in fig. 10. Two moderately doped GaAs cladding core layers are grown in order to centre the maximum of the intensity in the gain medium (fig. 10). Cladding layers, consisting of a high Al content (x=0.9), doped AlGaAs are embedding the gain medium with the core layers. The structure is grown on an n$^+$ doped GaAs substrate and capped by a highly doped GaAs layer, serving as a contact layer. The confinement factor is reaching 42% and the waveguide loss α=26 cm^{-1}.

The active zone is using the intersubband concept. It is designed to emit at 10 µm. Spacing between level three and level two is tailored to 124 meV (photon energy) and between level two and level one to 37 meV. The self-consistent simulation of the active cell and an injector is shown in (fig. 11). An active cell consists of three wells: GaAs **15Å**, AlGaAs 20Å, **49Å**, 17Å, **40Å**. Calculated dipole matrix elements for (3-1) and (3-2) optical transitions shows elimination of (3-1) transition, that would be spurious for the lasing action. Active cells are separated by funnel injectors (filled area in fig. 11).

Purpose	Material	Thickness	Doping
Cladding	AlGaAs, x=0.9	6000 Å	n_d=6e17 cm^{-3}
Gr. Layer	AlGaAs, x=0.33 to 0	300Å	n_d=2e18 cm^{-3}
Core	GaAs	14000 Å	n_d=4e16 cm^{-3}
Gain medium			
Core	GaAs	15500 Å	n_d=4e16 cm^{-3}
Gr. Layer	0 to x=0.33	300 Å	n_d=2e18 cm^{-3}
Cladding	AlGaAs x=0.9	10000 Å	n_d=6e17 cm^{-3}

Table 2 AlGaAs based waveguide composition.

The Al content in the AlGaAs barriers is set to x=0.33. The lasing transition is arrow marked and the injector is represented by the filled area. The gain medium of the sample contains 30 periods of alternating active cells and injectors.

Samples are wet chemical etched using H$_3$PO$_4$(85%): H$_2$O$_2$(30%): C$_2$H$_4$O$_2$ 20:8:20 (vol. parts), into 20 to 30 µm wide ridges. Chips are grinded to 100-150 micron thickness, AuGeNi contacts are evaporated on the back side and alloyed. TiAu non-alloyed top contacts are sputtered and extended over a PECVD deposited Si$_3$N$_4$ layer, forming a bonding pad. Ridges are cleaved into 1-2 mm long bars, soldered to a heat sink and installed in a He cooled cryo-flow.
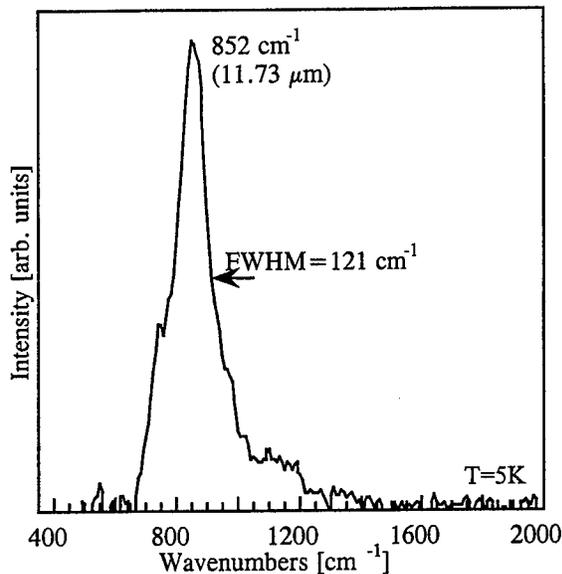
The samples are characterized using the same setup and methods as for characterization of the spontaneous emitters. Light is collected using f/0.75 optics and focused on a LN_2 cooled MCT detector. Pulsed signal is demodulated using correlation techniques. A fourier transform spectrometer in step scan mode, combined with correlation techniques is used to measure the emission spectra. The sample is pulsed with 1 μs long pulses at a repetition rate of 30 kHz to measure the spontaneous emission. The current density is 2800 A/cm^2 (well below the lasing threshold). The spectrum is centered at 978 cm^{-1} (10.2 microns) and full width half maximum is 139 cm^{-1}. This yields a relative peak width of 7, that is a typical value for this kind of emitter. The total output power lies in the 10 nW range.

To exceed the lasing threshold, pulses of 100ns duration at 5 kHz repetition rate and high current (up to 7.5A) are applied. Fig. 12. is showing the optical output characteristics (L-I) of a 1.55 mm long and 25 μm wide laser ridge. The lasing threshold, measured at 5K is 13.3 kA/cm^2. Peak output power is estimated to be in range of 200 mW per facet. Light is 100% TM polarized. The highest achieved operational temperature is 100 K. Maximum of the output power at this temperature decreases ten times, compared to the output at 5K. The emission spectrum of the same sample at 5K and 1.05*J$_{th}$ is shown in fig. 13. The multimode spectrum is centered at 9.78 μm (=1021.5 cm^{-1}). The linewidth of a mode is less then 0.5 cm^{-1} (limited by the
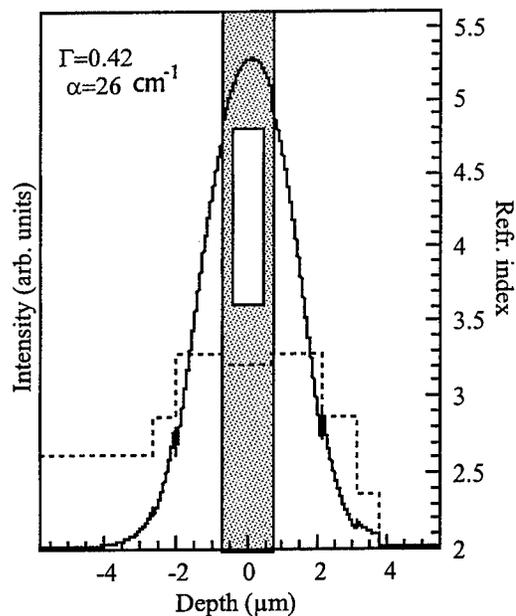
Figure 10: Mode profile (solid line) and refractive index (dashed line), in the waveguide.
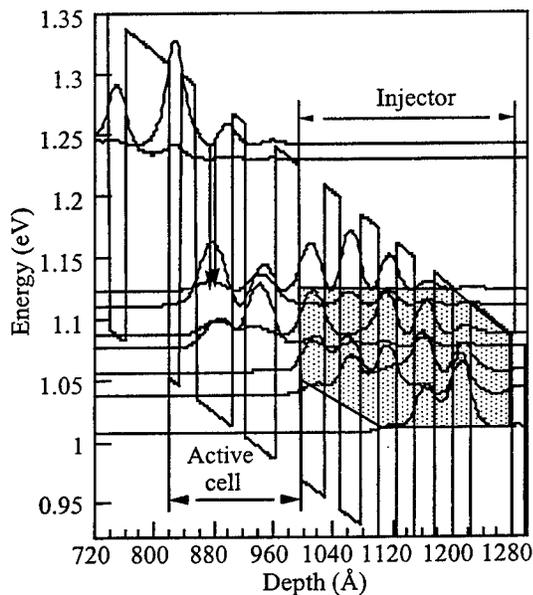
Figure 11: Conduction band of an active cell with applied electric field. Squared wavefunctions are plotted. Lasing transition is arrow marked. The shadowed polygon represents a funnel injector.
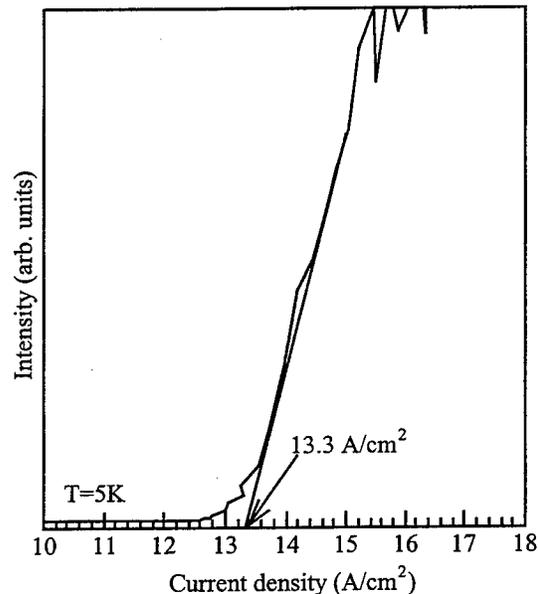
Figure 12: Output characteristics (L-I curve) of a 1.55 mm long laser, ridge, measured at 5K.

resolution of the FTS in step-scan mode). The average mode spacing is 0.95 cm^{-1}, that yields a group refractive index n_g=3.37. Additional modes appear, if the drive current is increased. No measurable spectral shift accompanied the variation of the drive current or the temperature.

CONCLUSIONS

In conclusion, we have realized intersubband and interminiband quantum cascade emitters on GaAs/AlGaAs material system. Mid infrared emission was demonstrated up to room temperature using both concepts for spectral range from 800 cm^{-1} to 1600 cm^{-1} (12.5 μm to 6.25 μm). Photovoltaic behavior of the structures was demonstrated above 77K, proving the possibility of application these structures for detection purposes. Tunability of the emission wavelength is demonstrated using a structure with tunneling assisted diagonal transition. The emission wavelength can be voltage tuned, over a range of 40 cm^{-1}. Ridge lasers with peak powers around 200 mW per facet are fabricated. A laser operating at 9.78 microns, at temperatures up to 100 K and the threshold current density of 13.3 kA/cm^2 is presented. All these results are promising high performance of the GaAs/AlGaAs mid-infrared coherent sources in the near future.

ACKNOWLEDGEMENTS

Figure 13: Laser spectrum. Ridge is 1.55 mm long. Group refractive index calculation yields a value of 3.37.

REFERENCES

[1] L. Friedman and R.A. Soref, Journal of Appl. Phys. **83**, 3480, (1998).

[2] R.F. Kazarinov and R.A. Suris, Sov. phys. Semicond. **5**, 207 (1971).

[3] J. Faist, F. Capasso, C. Sirtori, D.L. Sivco, A.L. Hutchinson and A.Y. Cho, Science **264**, 553 (1994).

[4] J. Faist, F. Capasso, C. Sirtori, D.L.Sivco, J.N. Baillargeon, A.L. Hutchinson, S.N.G. Chu and A.Y. Cho, Appl. Phys. Lett. **68**, 3680 (1996).

[5] C. Sirtori, J. Faist, F. Capasso, D.L.Sivco, A.L. Hutchinson, S.N.G. Chu and A.Y. Cho, Appl. Phys. Lett. **68**, 1745 (1996).

[6] J. Faist, C. Gmachl, F. Capasso C. Sirtori, D.L. Sivco, J.N. Baillargeon and A.Y. Cho, Appl. Phys. Lett. **70**, 2670 (1997).

[7] J. Faist et al., Nature **387**, 777 (1997).

[8] G. Scamarcio, F. Capasso, C. Sirtori, J. Faist, A.L. Hutchinson, D.L. Sivco and A. Cho, Science **276**, 773 (1997).

[9] A. Tredicucci, F. Capasso, C. Gmachl, D.L. Sivco, A.L. Hutchinson, A. Cho, J. Faist and G. Scamarcio, Appl. Phys. Lett. **72**, 2388 (1998).

[10] C. Gmachl, F. Capasso, E.E. Narimanov, J.U. Nöckel, A.D. Stone, J. Faist, D.L. Sivco and A. Cho Science **280**, 1556 (1998).

[11] G. Strasser, P. Kruck, M. Helm, J.N. Heyman, L. Hvozdara, E. Gornik, Appl. Phys. Lett. **71** (20), 2892 (1997).

[12] Y.B. Li, J.W. Cockburn, M.S. Skolnick, M.J. Birkett, J.P. Duck, R. Grey, G. Hill, Electron. Lett. **33**, 1874 (1997).

[13] P. Kruck, G.Strasser, M. Helm, L. Hvozdara, E. Gornik, Physica E 2, 449-452 (1998).

[14] O. Gauthier-Lafaye, P. Boucaud, F.H. Julien, R. Prazeres, F. Glotin, J.-M. Ortega, V. Thierry-Mieg, R. Planel, J.-P. Leburton, V. Berger, Appl. Phys. Lett. **70**, 3197 (1997).

[15] C. Sirtori, P. Kruck, S. Barbieri, P. Collot, J. Nagle, M. Beck, J. Faist U. Oesterle, Appl. Phys. Lett. **73**, 3486 (1998).

[16] A. Tredicucci, F. Capasso, C. Gmachl, D.L. Sivco, A.L. Hutchinson, A. Cho, Appl. Phys. Lett. **73**, 2101 (1998).

THz oscillators based on intraband transitions in bulk semiconductors.

V.N.Shastin, R.Kh. Zhukavin, A.V.Muravjov, E.E.Orlova, S.G.Pavlov

Institute for Physics of Microstructures of Russian Academy of Sciences

ABSTRACT

The operating principles and experimental results concerning far-infrared lasers based on the intersubband hot holes optical transitions in crossed electric and magnetic fields as well as on the optically excited intracenter shallow impurity states are reviewed and discussed. The analysis of the state of the art and the possible directions of the development of p-Ge hot hole intersubband transitions laser and the results of the recent theoretical and experimental investigations of new THz media based on impurity transitions in Si doped by phosphorus are presented.

Keywords: semiconductor, valence band, hot holes, laser, shallow impurity, silicon, germanium.

1. INTRODUCTION

It is well known that THz domain of the electromagnetic radiation ($\lambda^{-1} = \nu = 300 \div 30$ cm^{-1}, f = 10 ÷1 THz) has a great importance for spectroscopy of gases, liquids and condensed media. The frequencies of molecule rotations, solid state lattice vibrations, localized impurity states transitions in semiconductors and semiconductor structures as well as optical transitions between quantum well subbands lie in this region. Nevertheless the THz applications are limited up to the moment because of the lack of THz tunable effective sources of coherent radiation.

The conventional microwave tubes such as backward wave oscillators, magnetrons, clinotrons etc. need a smaller interaction circuit structure and narrower electron beam for higher operating frequencies (30 – 300 μm) for the generation of the THz waves. THz gyrotrons would require extremely large magnetic fields (hundreds kOe). Consequently, such devices can not be practically used. The working frequencies of semiconductor microwave devices such as IMPATT diode (f ≤ 0.4 THz), Gunn diode (f ≤ 0.15 THz) and resonance tunneling diode (f ≤ 1THz) are limited by the characteristic times of the basic processes such as the electron transit of an interaction region, ballistic heating, intervalley scattering and underbarrier tunneling correspondingly. Additionally RC cutoff problem becomes more prominent for higher frequencies. On the other hand the development of the gas quantum generators that successfully bridged optical and near infrared wavelength regions can not solve the problem to cover THz region because of the limited number and narrow widths of emission lines. Traditional band gap semiconductor lasers based on the interband transitions are less effective for lower frequencies and do not work for $\nu < 250$ cm^{-1}. The reasons mentioned above explain the high level of research activity aimed at the investigation of the new THz active media based on the intraband transitions in semiconductors and semiconductor structures. P-Ge lasers based on the hot hole intersubband transitions[1,2] and light hole Landau level transitions[3,4] in crossed electric and magnetic fields, as well as laser on shallow acceptor transitions in stressed Ge[5] can be regarded as a successes of such investigations in bulk semiconductors. It has been shown recently that highly nonequilibrium 2D electron subsystem in MQW heterostructures is perspective for THz stimulated emission on the intersubband quantum well transitions (Cascade-type[6] and Fountain- type[7] lasers). Bloch oscillation phenomena in quantum superlattices is an alternative rapidly developing direction in investigation of THz devices[8,9].

2. HOT HOLE INTERSUBBAND TRANSITIONS P-GE LASER

2.1. Theoretical background.

The degenerated valence band of Ge consists of light (l) and heavy (h) hole subbands (fig. 1) and l-h optical transitions determine THz radiation absorption in semiconductor with acceptor concentration $N_A \geq 10^{13}$ cm^{-3} at low temperatures. Intersubband absorption (amplification) coefficient α_{lh} on the frequency ω is proportional to the difference of the population densities of valence band subbands states $f_\alpha(p)$ ($\alpha = l, h$) averaged over the isofrequency surface

$$\alpha_{lh}(\omega) \sim f_h(p) - f_l(p); \quad \hbar\omega = \varepsilon_l(\vec{p}) - \varepsilon_h(\vec{p})$$

40

Part of the EUROPTO Conference on Terahertz Spectroscopy and Applications II
Munich, Germany • June 1999 SPIE Vol. 3828 • 0277-786X/99/$10.00
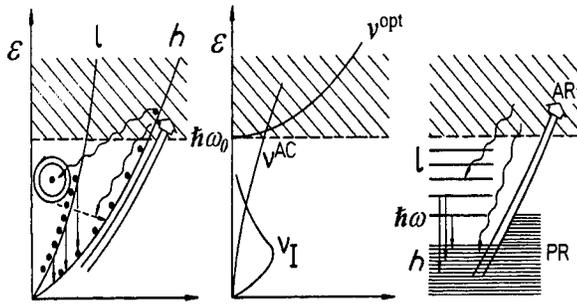
Fig. 1. Intersubband transitions ($\varepsilon_\alpha(p)$), scattering rates of holes ($\nu_\alpha(p)$) and inversion population mechanism scheme.
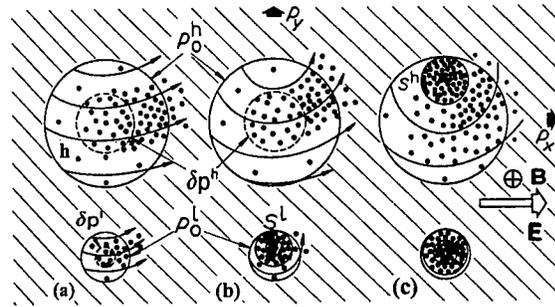
Fig. 2. Momentum-space hole trajectories and 3 characteristic types of distributions

Let us consider the hole distribution formed by their motion in the momentum space under applied crossed electric ($\vec{E}$) and magnetic ($\vec{B}$) fields and their scattering on optical (opt), acoustical (ac) phonons and on the coulomb (im) centers with characteristic frequencies ν_α^{opt}, ν_α^{ac}, ν_α^{im}.

$$\nu_\alpha = \tau_\alpha^{-1}(\varepsilon) = \nu_\alpha^{opt} + \nu_\alpha^{ac} + \nu_\alpha^{im}$$

For lattice temperatures $kT < \hbar\omega_0$ ($\hbar\omega_0 = 37$ meV - optical phonon energy in Ge), the optical phonons occupation numbers are negligible, their emission is spontaneous and thus has a threshold character. On the other hand for the holes energies $\varepsilon > \hbar\omega_0$ and moderate doping $N_A \leq 10^{15}$ cm^{-3} the optical phonon assisted scattering dominates

$$\nu_\alpha^{opt}(\varepsilon > \hbar\omega_0) >> \nu_\alpha^{ac}(\varepsilon), \nu_\alpha^{im}(\varepsilon).$$
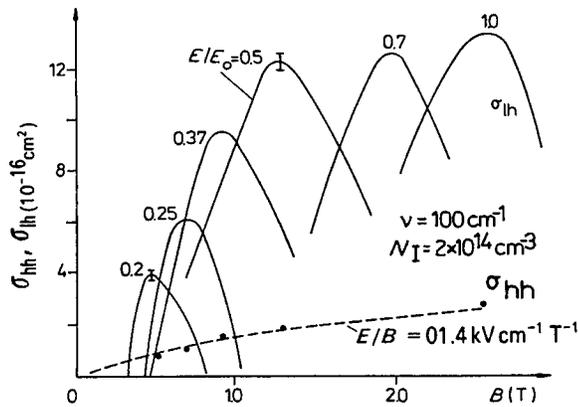
Fig. 3. Intersubband amplification (solid) and Drude-type absorption (dashed) cross-section as a function of fields. Monte-Carlo simulation for isotropic model of valence band.
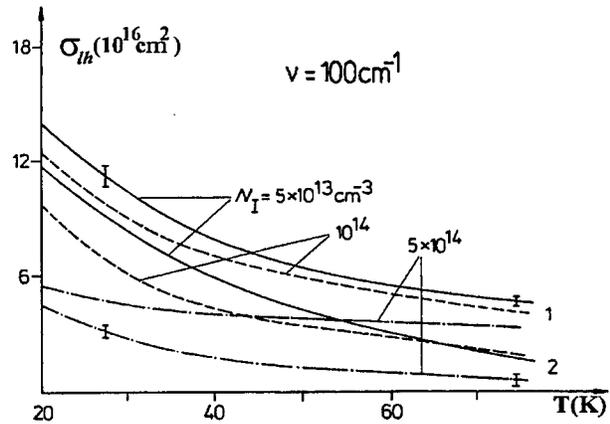
Fig. 4. Temperature dependence of amplification cross-section per hole for fixed frequency: (1) E=3.5 kV/cm, B=1.84 T; (2) E=1.75 kV/cm, B=0.92 T. Monte-Carlo simulation for isotropic model.

41

The ballistic heating of holes with $\varepsilon < \hbar\omega_0$ realizes when

$$\nu_\alpha \,(\varepsilon < \hbar\omega_0) << \omega_\alpha{}^c, \quad eE/p_\alpha{}^0 \leq \nu_\alpha{}^{opt}(\varepsilon > \hbar\omega_0),$$

where $\omega_\alpha{}^c = eB/m_\alpha c$ are cyclotron resonance (CR) frequencies of holes, while $p_\alpha{}^0=(2\ m_\alpha\ /\hbar\omega_0)^{1/2}$ - is a threshold optical phonon assisted scattering momenta. The three main variants can be distinguished according to the values of the holes drift energies

$$\text{a) } \varepsilon_\alpha{}^d > \hbar\omega_0, \quad \text{b) } \varepsilon_h{}^d > \hbar\omega_0 > \varepsilon_l{}^d, \quad \text{c) } \hbar\omega_0 > \varepsilon_\alpha{}^d$$

where $\varepsilon_\alpha{}^d = (p_\alpha{}^d)^2/2\ m_\alpha$, $\vec{p}_\alpha{}^d = m_\alpha c\ [\,\vec{E}\vec{B}\,]/B^2$.
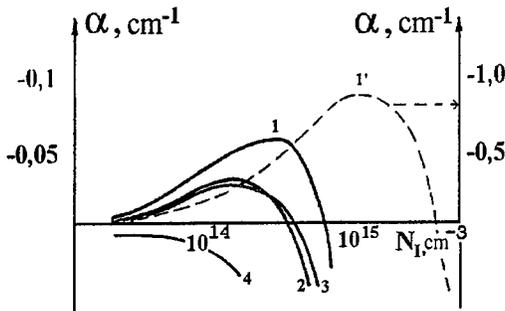
Fig. 5. Small signal gain versus hole concentration for fields E=1.7 kV/cm, B=1 T and temperature T=30 K for frequencies: (1) ν=100 cm^{-1}; (2) ν=50 cm^{-1}; (3) ν=200 cm^{-1}; (4) ν=25 cm^{-1}; (1' dashed) ν=100 cm^{-1} for Ω_l= 4π. Simplified model.
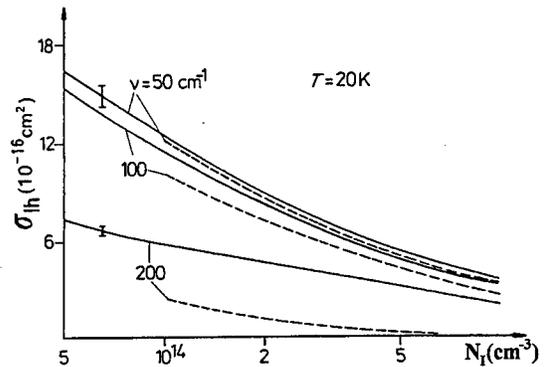
Fig. 6. Amplification cross-section per hole as a function of total number of Coulomb centers: (solid line) E=3.5 kV/cm, B=1.84 T; (dashed) E=1.75 kV/cm, B=0.92 T. Monte-Carlo simulation for isotropic model.
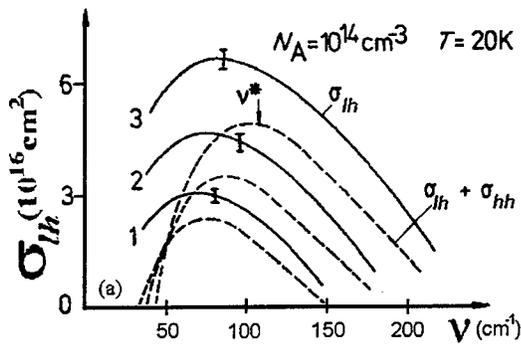
Fig. 7. Amplification cross-section per hole as a function of frequency for fields: (1) E=0.7 kV/cm, B=0.45 T; (2) E=1.2 kV/cm, B=0.9 T; (3) E=3.5 kV/cm, B=2.5 T. Monte-Carlo simulation for isotropic model.
Fig. 8. . Amplification cross-section for realistic anisotropic valence band of Ge.
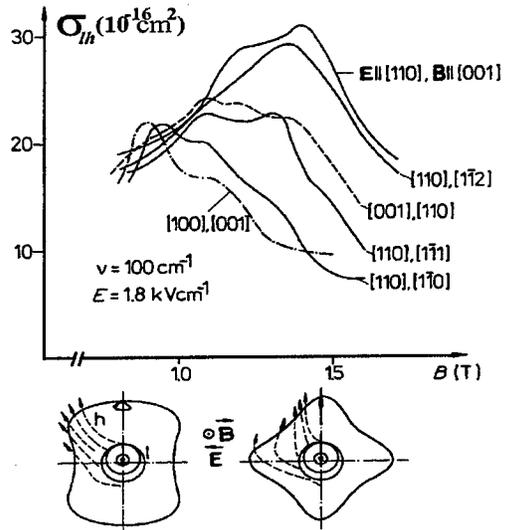
In the first case both types of holes exhibit the "streaming" motion. Their distributions are similar $f_h / f_l \sim (m_h/m_l)^{1/2}$ and slightly dependent on the magnetic field values. As a result $h \to l$ transitions lead to the absorption of THz radiation. In the second case there appears a set of light holes trajectories S_l, that does not intersect the border of the "active" $\varepsilon < \hbar\omega_0$ and "passive" $\varepsilon < \hbar\omega_0$ regions. Ballistic heating means that the life times of the heavy holes and light holes beyond the region S_l for $\varepsilon < \hbar\omega_0$ are controlled by their transit to the region of optical phonon scattering, while the life times on the S_l trajectories are controlled by acoustical phonons and Coulomb centers scattering. Thus S_l is the region of light holes accumulation (trap). Holes with $\varepsilon > \hbar\omega_0$, come, emitting the optical phonons, with equal probability to the states of heavy and light hole subbands, forming the area of pumping δ_α. It is determined by the holes transit beyond the passive region border. Fields increasing with constant ratio $E/B= const$ does not change the density of intensity of source of scattered holes $I_l(p) = I_h(p) = I(p)$, while the integral $I_\alpha d^3 p \sim \omega_h^c$ is increased. When δ_l covers the trap states, their population increase, $f_l \sim \omega_h^c$, while heavy hole subband states are depleted $f_h \sim (\omega_h^c)^{-2/3}$. Thus inverse population on $l\text{-}h$ transitions is formed. Field increasing ($\Delta\varepsilon > \hbar\omega_0$) causes the reduction of the pumping efficiency. In the case (c) heavy subband trap S_h appears and overpopulation of the light hole subband is suppressed. The optimum fields ratio in the isotropic model of Ge valence band ($m_l = 0.04\ m_0$, $m_h = 0.32\ m_0$, m_0– free electron mass) is $p^d_h \cong 0.7\ p^0_h$; $E/B \cong 0.14$ kV/cm × kOe =1.4 kV/cm × T.

2.2. Intersubband amplification.

The populations of light and heavy holes subband states and the amplification coefficient have been calculated using Boltzmann kinetic equation and Monte-Carlo simulating procedure both in the frame of classical approach. Calculation results are plotted on figure 3-9. Figure 3 presents small signal gain received by Boltzmann equation analytically using isotropic valence band in τ-approximation. Dashed curve on fig.3 shows $l\text{-}h$ small signal gain versus hole concentration, for the non-realistic case when light subband states with energies less then the optical phonon energy accumulate carries (maximum volume angle of S_l-trap $\Omega_l = 4\ \pi$). Substantially lager value of small signal gain for this case demonstrates the importance of the increasing of the S_l -trap volume, but Ω_l should not exceed 2π in germanium because of S_h appearance. Monte-Carlo simulations have been made both in isotropic fig. 4-8 and anisotropic fig.9 real model of the valence band of germanium accounting $h\text{-}h$ scattering by taking the double concentration of ionised Coulomb centers ($N_i = 2\ N$), where $N = N_i + N_h$ - hole concentration, $N_i/N_h \leq 0.1$. Hot holes small signal gain consists of two parts: α_{lh} - intersubband amplification/absorption coefficient and α_{hh} - collision absorption coefficient connected with heavy hole scattering on the optical phonons (non-vertical intrasubband optical transitions)

$$\alpha_h(v) = N\ (\sigma_{lh} + \sigma_{hh}),$$

where v- reciprocal wavelength of light, σ - cross-section of the absorption.
The calculations demonstrate that $l\text{-}h$ amplification can be realised in the wide range of the THz frequencies and working temperature can be increased up to the liquid nitrogen one. In p-Ge with acceptor concentration $N_A = (2 \div 3) \times 10^{14}$ cm^{-3} and low compensation $N_A \cong N$ one can get $l\text{-}h$ small signal gain $\alpha_{lh} = 0.15$ cm^{-1}. For frequency range $v= 100$ cm^{-1} optimum of doping is about $N_A =10^{14}$ cm^{-3} and for $v <100$ cm^{-1} it should be less. The angle of non-orthogonality between the total (including space charge correction) electric field and magnetic field is a very important parameter. Ballistic heating of holes under electric field component directed along magnetic field decreases the time of life of trapped holes and terminates $l\text{-}h$ amplification. The admissible angle θ of non-orthogonality should be less then 1-2°. Values and ratio of electric and magnetic fields appropriate for the maximum of the gain are presented on fig.3. For the wave number of light $v =100$ cm^{-1} the optimum values of fields are $E = 1.7$ kV/cm, $H = 12$ kOe and $E/H \cong 0.14$ kV /(kOe cm) ($p_h^d \cong 0.7\ p_h^0$). The increasing of the fields provides broader frequency range of $l\text{-}h$ amplification, but at the same time makes Drude absorption ($\sigma_{hh}(v) \sim v^2$) stronger. As result maximum of holes cross-section $\sigma_h = \sigma_{lh} + \sigma_{hh}$ is shifted to higher frequencies with field increasing. The simulations in the anisotropic model of the valence band reveal the optimal orientations of electric and magnetic fields according to the crystallographic orientation. It occurred that in the case of the drift motion of heavy holes directed along [111] or [110] crystallographic orientations one can get the largest volume of the light hole trap and higher amplification coefficient. Recently using Monte-Carlo simulating procedure the distribution functions and amplification cross-section have been analysed taking into account space charge effects[10]. It is shown that real space redistribution of holes strongly affects the $l\text{-}h$ amplification because of disturbances of field homogeneity and orthogonality. Simulations of non-linear regime yield the output power characteristics of p-Ge lasing. For high enough level of the intensity of the radiation the trap states are depleted by light. The amplification cross-section depends on the intensity as[2]

$$\sigma_{lh}(J) = \sigma_{lh}(0)\ (1 + J/ J_0)^{-1}\ ,$$

where $J_0= (2 \div 5)$ kW/cm^2

The stimulated emission intensity inside the resonator for the stationary case can be determined from the equation

$$\alpha_{lh}(J^*) = \alpha_L + \alpha_r + \alpha_{hh} + \gamma = \beta + \gamma \ ,$$

where γ (cm^{-1}) - the coefficient of the output coupling of stimulated emission, reduced to the unit of the length of the cavity. The output power of the unit volume of active medium $P^* = \gamma J^*$ has the maximum for $\gamma = (\beta \, \alpha_{lh}(0))^{1/2} - \beta$.

For $N = 1.5 \times 10^{14}$ cm^{-3} we get $\alpha_{lh}(0) \cong 0.12$ cm^{-1}, $\alpha_{hh} \cong 0.03$ cm^{-1} and $J_0 = 5 \times 10^3$ W/cm^2. It has to be mentioned, that the current density of holes practically does not depend on the value of field in the case of streaming type distribution: $j \cong 1.5 \times 10^{-12} \times N$ A/cm^2 and dissipation input power can be estimated as D $\sim (\omega_h^c)^{-1} \hbar\omega_0 N \cong 10^5$ W/cm^3. As a result we get the output power $P^* \cong 10$ W/cm^3 with the efficiency $\eta = P^*/D \cong 10^{-4}$.

2.3. Lattice absorption.

The most important factor limiting the working temperature and determining the threshold concentration of holes and pumping current is the host lattice absorption. Photon-phonon $\hbar\omega + \hbar\omega_p(q) = \hbar\omega_{p'}(q)$ combination ($\hbar\omega_p \cong 8$ meV, $\hbar\omega_{p'} \cong 20$ meV expected) yields two-phonon difference lattice absorption[11], that dramatically increases with temperature, being proportional to the occupation number of ω_p phonons. According to the experimental results[12] the lattice absorption in the purest Ge ($N \le 10^{11}$ cm^{-3}) is given by

$$\alpha_L(\nu, T) \cong \alpha_L^*(\nu) \exp(-T^*/T), \qquad \alpha_L^*(\nu) \sim \nu^2,$$

where $T^* \cong 80$ K, $\alpha_L^*(80$ cm$^{-1}) = 0.5$ cm^{-1}.

For $T \le 10$ K two-phonon lattice absorption should be negligible ($\alpha_L^* \le 10^{-3}$ cm^{-1}), but experiment reveals high enough residual absorption $\alpha_r = 10^{-2}$ cm^{-1} that can not be explained in terms of two-phonon difference process. Thus for total amplification we have to write down:

$$\alpha(\nu) = N(\sigma_{lh} + \sigma_{hh}) + \alpha_L + \alpha_r$$

Residual absorption doesn't depend on temperature below T = 10 K and substantially increases threshold hole concentration $N_{thr} = 10^{13}$ cm^{-3} and threshold current $j_{thr} = 15$ A/cm^2 being the main obstacle for CW lasing.

2.4. Valence band states Landau quantization.

Landau quantization has a very strong influence on *l-h* optical transitions in magnetic field because of the discrete character of light hole Landau level subbands and eigenfunctions orthogonality. In crossed electric and magnetic fields such orthogonality will be partly destroyed but the oscillatory behavior of optical characteristic still remains even in this case. The characteristic parameter of quantitative corrections is the ratio of drift energy of holes and CR energy $\hbar\omega_\alpha^c$. The calculation of the amplification in the frame of quantum approach imply the summation over all light and heavy hole Landau tubes[13]

$$\sigma_{lh}(\omega) \sim \sum_{nmp_z} \left| W_{lh}^{nm} \right|^2 \delta\left(\varepsilon_l^n - \varepsilon_h^m - \hbar\omega\right)\left[f_h^m(p_z) - f_l^n(p_z)\right] \ ,$$

where W_{lh}^{nm} - matrix element of optical transition between *n* and *m* Landau tubes.

The peculiarities of optical density of states appeared because of the crossing of light Landau level tube (n) and *l-h* optical transitions isofrequency $\omega_n^*(p)$ surface, that determines the line of frequency tuning of the maximum of the gain

$$\hbar\omega_n^* = \left[p_l^d + p_B(2n+1)^{1/2}\right]^2 / 2\overline{m} \ ,$$

where $\quad \overline{m}^{-1} = m_l^{-1} + m_h^{-1}, \qquad p_B = (\hbar eB/c)^{1/2}$, n=0,1,2...

The light hole tubes change their position in the momentum space under electric and/or magnetic fields and some of the tubes can be switched off/on since the *l-h* tunneling and Coulomb scattering rates having maximum just near $p = 0$. Thus the frequency skipping can be observed. L-h tunneling means that "initial" light and heavy hole states are mixed in crossed electric and magnetic fields. Such *l-h* hybridization has non-monotonically dependence on the light hole Landau level quantum numbers and leads to the corresponding corrections of lifetime for every of Landau level state[13-21]. The influence of quantum effect on lifetimes can be strong enough and yield the inversion population between different "light" hole Landau levels and as result additional amplification on the "light" hole cyclotron resonance and CR harmonics.

2.5. Shallow acceptor state effects.

The role of the doping impurities B, Al, Ga, In, Tl can not be reduced only to providing the necessary hole concentration and to the Coulomb scattering. Optical transitions between impurity states lie in the wavelength region of p-Ge laser radiation and can essentially influence the amplification. It was shown that the main recombination process in the conditions used is recombination assisted by spontaneous emission of optical phonons[22]. The bound states lifetimes are determined by the impact ionization processes making the cascade capture on acoustic phonons ineffective. It is shown, that the most shallow excited states are in the thermal equilibrium with the heavy holes $N_i/N \sim 10^{-3} \div 10^{-4}$, while the deeper ones accumulate about 10 % of the carriers in Ge:Ga that is much more (10^3) then for equilibrium distribution. It means that Ga acceptors give impact into the absorption on the level $\alpha \leq 4 \times 10^{-2}$ cm^{-1} for an acceptor concentration $N = 10^{14}$ cm^{-3}. The population of the impurity levels is changed by the growing laser radiation (fig. 9). The laser radiation

Fig. 9. Population of acceptor states, versus ionization energy for different intensities of laser radiation ($\lambda = 100$ µm)

with intensities close to saturation ($J \approx 1.5$ kW/cm^2) causes the ground acceptor state depletion, while excited states are not effectively ionized. The result is the inverse population of impurity states in nonlinear regime of the Ge:Ga laser. This model allowed to explain the details of the spectra of p-Ge laser, its dynamical behavior and the observed increase of the pumping current with the development of laser radiation. These investigations allowed to make a conclusion about the advantages of the deeper dopants (Be, Zn, Cu) for the increase of the small signal gain in p-Ge laser and reduction of excitation threshold.

2.6. Experiment.

Up to the moment l-h stimulated emission has been received on p-Ge doped by different elements[23-27] of III (Al, Ga, In, Tl) II (Be, Zn) and I (Cu) chemical groups of Mendeleev classification for the acceptor concentrations $N_A=10^{13} \div 10^{15}$ cm^{-3}. It was revealed that the optimum hole concentration for l-h lasing is $N^* =10^{14}$ cm^{-3} with threshold concentration $N^{th}=10^{13}$cm^{-3}. Binding energies of III group acceptors are relatively small (the energy range of ground states $\varepsilon_{g.s.} =11.1$-13.4meV) and the majority of centers are ionized (N$\cong$0.9N$_A$) by hot hole impact process. Deeper acceptors are less

Fig. 10. Ge:Ga laser band and the emission spectra.

ionized: for Ge:Be ($\varepsilon_{g.s.}$ =24.8 meV)- N≅0.8 N_A, Ge:Zn ($\varepsilon_{g.s.}$ =33 meV)- N≅0.5 N_A and for Ge:Cu ($\varepsilon_{g.s.}$ =43.2 meV)- N≤0.2 N_A depending on doping concentration and fields.

Positive results were obtained both for Faraday and Voigt configuration. From theoretical estimations one can expect not more then two times lower value of collision absorption cross-section for the light polarization directed along magnetic field that can be realized for Voigt configuration. But practically there are several factors connected with real space charge distribution (Hall and modified Sasaki-Shibuya (parallel Hall effect) effects in crossed $\vec{E} \perp \vec{B}$ fields). We consider that the latter has more influence on p-Ge lasing. It is an experimental fact that for the rectangular parallelepiped active body sample
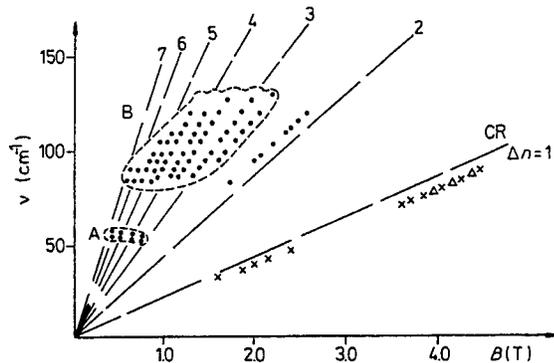
Fig. 11. Overall frequency tuning of germanium hot
hole lasers as a function of the magnetic field.
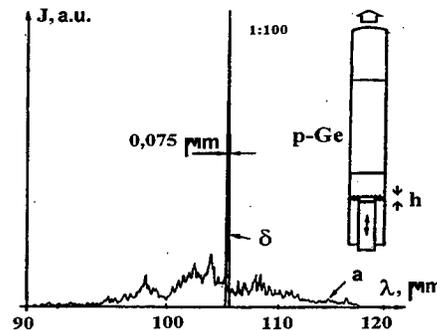
Fig. 12. Narrow line (δ) and broad band (a) regimes of
p-Ge laser.

with longer faces directed along [111] the crystal axis [111] $\perp \vec{B}$ configuration (Voigt) is preferable, while for [110] sample orientation better results one can get in [110] $\parallel \vec{B}$ configuration.

Light to heavy hole intersubband stimulated emission (SE) working temperature doesn't exceed T=25 K. The only data on lasing with working temperature as high as 60 K [28] concern special case of fields, as we guess the amplification on the transitions between light hole Landau levels with Δn=1,2 completes the *l-h* amplifications.

The SE pulse duration τ is restricted by the input energy dissipation leading to active body heating[29]. The pulse duration reached is τ≤10^{-5} sec in Ge:Ga and τ≤2×10^{-5} sec in Ge:Be and Ge:Zn active body samples immersed in liquid Helium[30]. The maximum of the repetition rate (R=10^3 Hz) and SE duty cycle 2,5 % have been reached[31,32] in Ge:Be samples with 5 mm³ active body and doping concentration 2×10^{13} cm⁻³. High quality of cavity was provided by internal reflectivity.

Typical bands of the applied field for stimulated emission are shown at Fig. 10. There are two parts of SE band for Ge:Ga laser with N_A-N_D≅(5÷8)×10^{13} cm⁻³ (N_D/N_A≅0.1): low field subband (A) and high field subband (B). Subband A provides a long wavelength emission and subband B – shorter one (compare Fig. 11). The first one is terminated for larger level of doping N_A-N_D>10^{14} cm⁻³. As it was estimated from SE temporal behavior small signal gain in commercial p-Ge:Ga does not exceed α=1.5×10^{-2} cm⁻¹ for subband A and α=3×10^{-2} cm⁻¹ for subband B. The output power P=(1÷2) W/cm³ for subband A and P=(5÷10) W/cm³ for subband B with efficiency η≤10^{-4} was registered. Laser characteristics are worse then one can expect from theoretical calculations and it is explained by the insufficient quality of germanium. This conclusion follows from the recent SE measurements with Ge samples of better quality grown and fabricated in LBL (E.E.Haller team). From the experimental data published the higher level of small signal gain α≈4×10^{-2} cm⁻¹ in Ge:Ga and α≈7×10^{-2} cm⁻¹ in Ge:Be and Ge:Zn can be estimated. Unfortunately direct measurements have not been performed yet.

Overall data of stimulated emission frequencies measured on Ge:A_{III} lasers with quasi-optical (non-selective) resonator are plotted on Fig. 11. P-Ge laser based on *l-h* transitions has a broad band (Δ ν≤ 20cm⁻¹) of SE and the spectral density of the laser intensity depends on active medium and cavity selectivity. SE spectrum has pronounced temporal behavior. It is started with shorter wavelength and tunes to the longer ones (Δλ ≤ 0.2λ) during the first microsecond. Points on Fig. 11 present the frequencies of SE intensity maximums versus magnetic field. Fan lines are expected positions of CR and CR harmonics frequencies from quasiclassical approach of Landau quantization.

CR and second harmonic of CR yield the mostly pronounced maximums. On the other hand it is occurred that SE lines for A subband in Ge: A_{III} medium are condensed just to the intracenter G-line while for B subband the spectrum for SE has similarity with the acceptor photoionization curve. Additionally in nonlinear regime of gain the another lines of SE that corresponds to the intracenter D, E optical transitions can appear.

The fine structure of the SE determined by the cavity mode composition consists of q-set (q≤500) of narrow Δν≈(πc₀τ)⁻¹ lines v_q=c₀(2L*n)⁻¹ q, tuned with the rate about 1 MHz/μs down[33]. Here 2L* is mode round trip, n– Ge refractive index, τ-

duration of the light pulse. Line tuning means that optical thickness of Ge sample increases under heating. We can substantially enhance the intensity of the lines by the intracavity frequency selection[34] (Fig. 12). It means that due to the fast cross-relaxation of light hole states trapped the mode competition is effective and single line regime of SE with $\Delta f \approx 1$ MHz can be realized with the served efficiency level. Fabry-Perot type frequency tunable selective mirror can be successfully used for this purpose.

2.7. Nowadays and future aspects.

Continuous-wave lasing, mode locking and THz spectroscopy are key points for further p-Ge laser development. Promising step toward CW lasing has been made by the introduction deeper acceptors. Following we have to increase the amplification cross section per hole and high quality slab or fiber type resonator with few millimeter cube active body volume has to be develop. One way to get larger cross section of amplification is to stress Ge sample. As it was shown uniaxial stressed Ge:Ga (P=200÷2000 bar) provides larger small signal and efficiency of lasing[23,35]. There is no theoretical model and Monte-Carlo simulations aimed to get understanding this phenomena except several suppositions. Under an external uniaxial compression the degenerated valence band is splitted on oblate and prolate constant energy ellipsoids of heavy and light holes in momentum space. This affects scattering rates on Coulomb centers and changes l-h Landau states hybridization enhancing the time of life of the light hole trap[17]. Additionally relative volume of S_l- trap slightly increases leading to high pump efficiency. At last the binding energy of shallow acceptor states are decreased by the valence band splitting for stressed- induced l-h gap $\Delta > \varepsilon_{g,s}$ ground state energy goes up $(\varepsilon_{g,s}(\Delta) \rightarrow \varepsilon_{g,s}(0)/2)$. Larger by factor two the amplification cross-section per hole can be expected and it settles the whole matter.

Recently it has been found that p-Ge laser can generate short pulses of far-infrared radiation, that is direct consequence of broad amplification spectrum and low dispersion. Self generation of strong intensity spikes with duration less then 80 ps was observed in paper[36] (fig. 13). Note, that this value was limited by the resolution of detecting equipment. The selfgeneration of short spikes of radiation has been interpreted as self-mode-locking of longitudinal modes of p-Ge laser. Taking into account the large relative width of the gain spectrum $\Delta\omega/\omega \sim 1$ the duration of the generated pulse of far-infrared radiation can be as short as~1ps. Also it was demonstrated in[37] that p-Ge active sample used as far-infrared optical amplifier
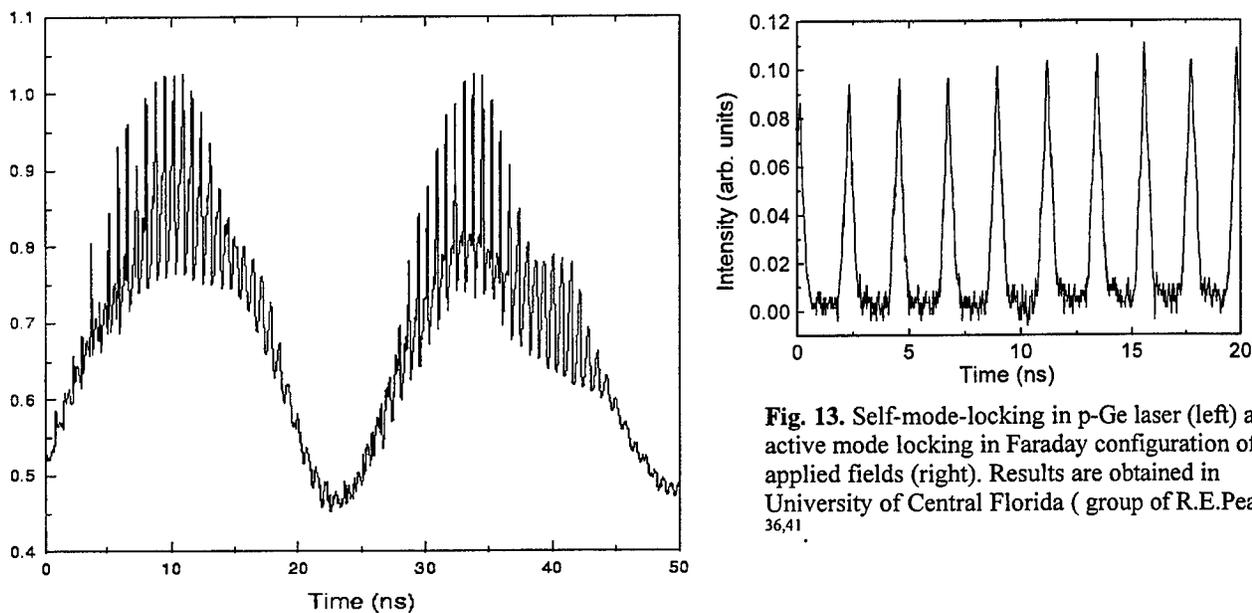
Fig. 13. Self-mode-locking in p-Ge laser (left) and active mode locking in Faraday configuration of applied fields (right). Results are obtained in University of Central Florida (group of R.E.Peale).[36,41]

transfers the subnanosecond dynamic of amplitude of input signal. Another few recent papers are devoted to the problem of active mode locking of p-Ge laser, where the train of short far-infrared pulses is generated by the p-Ge laser due to local modulation of the gain at the round trip frequency of the laser cavity[38-41]. The mechanism of gain modulation is based on high sensitivity of the gain to the degree of orthogonality of applied electric and magnetic fields. Thus RF electric field applied in the direction along magnetic field can effectively modulate the gain. Trains of emission pulses with 100-200 ps duration were obtained in ref.[38-41]. Recently active mode locking has been achieved in Faraday geometry of applied fields,

which is more flexible to modifications of gain modulation scheme and seems to be promising for the generation of picosecond duration pulses [41].

Besides using p-Ge laser like frequency tunable THz source the intracavity spectroscopy can be introduced. Such method has been successfully applied for THz intraband absorption investigation of 2D charge carriers in GeSi and GaAs\AlGaAs, GaAs\InGaAs MQW heterostructures[42]. The electromodulation of far infrared transparency under 2D carriers lateral transport was measured for the cryogenic temperature ($T \approx 10$ K) by the p-Ge laser output power. The heterostructures were introduced into the laser cavity. The high sensitivity of FIR ($\nu=50\div60$ and $80\div120$ cm^{-1}) transparency ($\Delta T/T=10^{-3}\div10^{-4}$) modulation induced by electric field applied to heterostructure has been reached. The intracavity modulation spectroscopy can be easy extended for other medium application. The list of devices can be widen by THz broad band p-Ge amplifier[37]. Mentioned above prove the perspectivity of hot hole germanium active medium for THz applications.

3. SILICON IMPURITY STATES INVERSE POPULATION AND FIR STIMULATED EMISSION.

3.1. Theoretical background.

The possibilities of inverse population on *l-h* and *l-l* transitions in crossed electric and magnetic fields and on impurity
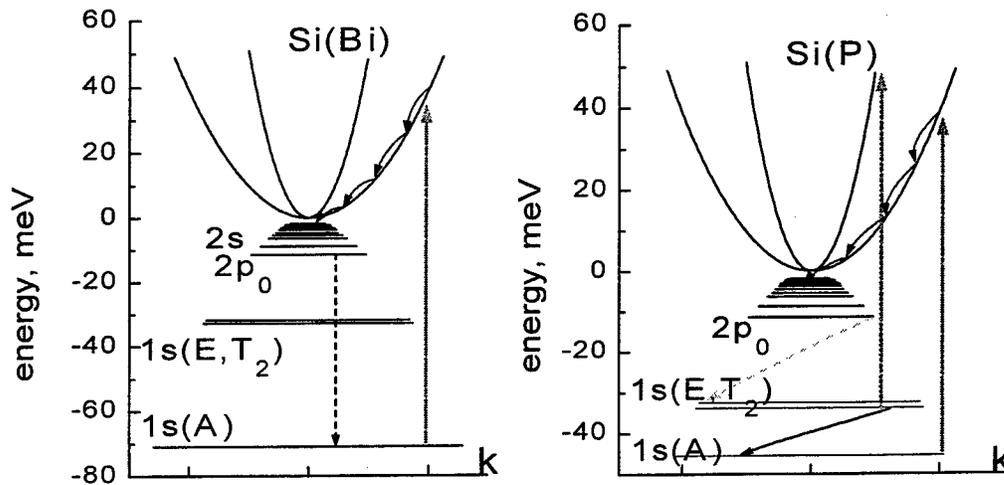
Fig. 14 Energy diagrams and transitions schemes for Si:Bi and Si:P with CO_2 laser pumping.

transitions, as well as low level of lattice absorption make silicon a perspective material for THz amplification. We will concentrate on the two schemes of inverse population of impurity states in silicon with optical CO_2 laser pumping, based on the electron-phonon interaction peculiarities (fig. 14).

The first is connected with the resonance interaction with optical phonons ($\hbar\omega_0 = \varepsilon_{ex.s.} - \varepsilon_{g.s.}$), that realizes in Si:Ga ($\hbar\omega_0 \approx$ 62 meV $\approx \varepsilon_{2p0} - \varepsilon_{g.s.}$), in Si:Bi ($\hbar\omega_0 \approx 59$ meV $\approx \varepsilon_{2p0} - \varepsilon_{g.s.}$). The fast transitions from the correspondent states ($\nu_{op} \approx 10^{12}$ sec^{-1}) accompanied by spontaneous emission of optical phonons ($\hbar\omega_0 >> kT$) cause the depletion of these states, while population of the higher excited states, formed mainly by the relaxation due to interaction with acoustical phonons ($\tau_\varepsilon \approx 10^{-10}$ sec for $T \approx 10$ K), is higher in the conditions of optical pumping.

Calculated population of impurity states in Si:Bi with CO_2 laser pumping is presented on fig. 15. The rates of acoustical phonon assisted transitions were estimated within hydrogenlike center model , the rate of optic phonon assisted transition from 2p0 state was estimated from the line shape of 1s→2p0 optical transitions. It is shown that the population inversion is realized under the conditions of optical pumping on the transitions ending the 2p0 Bi donor states from higher excited impurity states and continuum states with energies ($\varepsilon < kT$) as well, for the lattice temperatures $kT \leq \hbar\omega_0 / ln(\nu_{op}/\nu_i)$ (ν_i – optical ionization rate). For higher temperatures induced optical phonon assisted transitions populating the excited states are essential. The amplification up to 2 cm^{-1} (that exceeds the level of lattice absorption $\alpha_L < 0.1$ cm^{-1}) is expected in the

frequency range of $25 \div 100$ cm^{-1} for pumping intensities of CO_2 laser $I \geq 100$ W/cm^2 (10.6 μm), concentration of Bi donor centers $N_d \cong 10^{16}$ cm^{-3} and lattice temperatures up to 60 K.

The other population inversion scheme is possible due to the specific of acoustic phonon assisted relaxation to the shallow Coulomb centers (Si:P, Si:As, Si:Sb). It is essential, that the electron-phonon interaction is suppressed for the lower excited bound states due to the energy and momentum conservation laws. The acoustic phonon wave vectors q_{ij} corresponding to such transition $\hbar\omega_{ij} = \hbar q_{ij}v_s = \varepsilon_i - \varepsilon_j$ appears to be larger, than lower state localization in q-space. Corresponding states are longliving and can be overpopulated.

In the case of Si:P the inversion population of $2p_0$ state (lifetime in the order $10^{-7} \div 10^{-8}$ s) is expected under the photoionization by CO_2 laser radiation. The photoionization of donors in the LHe temperatures should cause the overpopulation of $2p_0$ state and THz amplification ($v = 168 \div 180$ cm^{-1}) on $2p_0 \rightarrow 1s(E)$, $2p_0 \rightarrow 1s(T_2)$ transitions[43].

3.2. Experiment.

Far-infrared spontaneous and stimulated emission from Si:P

Fig. 15. Population of impurity and continuum states in Si:Bi under CO_2 laser pumping I =100 W/cm^2, $N_d \cong 10^{16}$ cm^{-3} (N$_+$- ionized donor concentration).

Fig. 16. The dependence of the far-infrared spontaneous emission on the CO_2 laser pumping intensity for different doping concentration
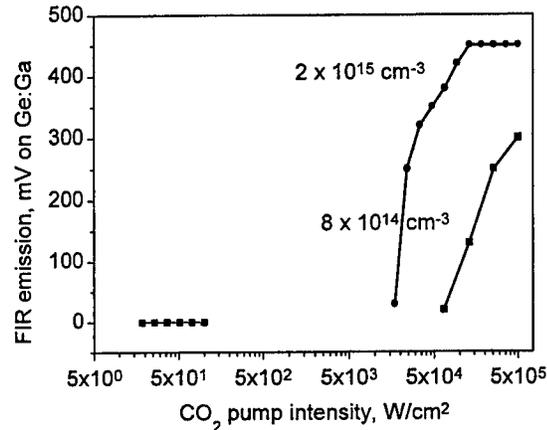
Fig. 17. A dependence of the far-infrared spontaneous (left) and stimulated (right) emissions from Si on the CO_2 laser pumping intensity

under CO_2 laser excitation have been investigated using Si crystals with doping concentrations $N_d = 0.9 \div 8 \times 10^{15}$ cm^{-3} and compensation level about 1%. The crystals were either grown by the float zone method or by the Czochralski method. Spontaneous emission signal versus pumping intensity is plotted on fig. 16. The dependence of the emission intensity and the photocurrent on the CO_2 laser intensity was close to linear up to 100 W/cm^2 laser intensity. Both of them increased with the doping level. The threshold growth of the emission signal was observed for the pumping intensities higher 10 kW/cm^2 for samples with the doping concentration around $N_D = 2 \times 10^{15}$ cm^{-3} (fig. 17). This dependence can be interpreted as a stimulated emission. The frequency range $150 \div 200$ cm^{-1} of the generation was estimated by using of the far-infrared filters[44]. It corresponds to expected $2p_0 \rightarrow 1s(E, T)$ transition. The threshold dependence was not observed for Si samples with doping level out of the range $8 \times 10^{14} \div 3 \times 10^{15}$ cm^{-3}, and the response was less then 50 mV. The unexpectedly high level of the threshold pumping intensity is explained by the excitation of D$^-$ centers (donors with extra electron). The reduction of the threshold intensity thus can be reached by compensation.

4. ACKNOLEGEMENTS.

5. REFERENCES.

1. A.A. Andronov, Yu.N. Nozdrin, V.N. Shastin, "Tunable FIR lasers in semiconductors using hot holes", Infrared Phys., 27(1), pp. 31-38, 1987.
2. V.N. Shastin, "Hot hole inter-sub-band transition p-Ge FIR laser", Opt. Quant. Electronics, 23(2), pp.S111-S131, 1991.
3. Yu.L. Ivanov, "Generation of cyclotron radiation by light hole in germanium", Opt. Quantum Electronics, 23(2), pp. S253-S265, 1991.
4. Yu.A. Mityagin, V.N. Murzin, S.A. Stoklitsky, A.P.Chebotarev, I.M.Melnichuk, "Wide-range tunable sub-millimetre cyclotron laser", Optical and Quantum Electronics, 23(2), pp. S307-S311, 1991.
5. I.V.Altukhov, M.S.Kagan, V.P.Sinis, "Spontaneous and stimulated emission of radiation from hot holes from uniaxially stressed germanium", Optical and Quantum Electronics 23, pp. S211-S216, 1991.
6. J. Faist, F. Capasso, D. L. Sivco, C. Sirtori, A. L. Hutchinson, and A. Y. Cho, "Quantum cascade laser", Science 264, pp. 553-556, 1994.
7. O. Gauthier-Lfaeye, P. Boucaud, F.H. Julien, S. Sauvage, S. Cabaret, J.-M. Lourtioz, V. Thierry-Mieg and R. Planel "Long wavelength (15.5 μm) unipolar semiconductor laser in GaAs quantum wells", Appl. Phys. Lett., 71, pp. 3619-3621, 1997.
8. K.F. Renk, E. Schomburg, A.A. Ignatov, J. Grenzer, S. Winnerl, K. Hofbeck, "Bloch oscillations and nonlinear transport in semiconductor superlattices", Physica B 244, pp. 196-200, 1998.
9. B.J. Keay, C. Aversa, S. Zeuner, S.J. Allen Jr, K.L. Campman, K.D. Maranowski, A.C. Gossard, U. Bhattacharya, M.J.W. Rodwell, "Virtual states, dynamic localization, absolute negative conductance and stimulated multiphoton emission in semiconductor superlattices", Semicond. Sci. Technol., 11, pp.1596-1600, 1996.
10. R.C.Strijbos, A.V.Muravjov and W.Th.Wenckebach, "Effect of space charge on electric field distribution in p-Ge hot hole lasers", Procc. Of the 9th Int.Conf. on Hot Carriers in Semiconductors, Chicago, USA, pp.627-629, 1995.
11. P. Bruesch, "Phonons: Theory and Experiments", part II, Springer-Verlag, Berlin (1986).
12. R.Brazis and F. Keilmann, "Lattice absorption of germanium in the far-infrared", Solid State Communications 70(12), pp. 1109-1111, 1989.
13. A.V.Murav'jov and V.N.Shastin, "Landau quantization and hot hole stimulated FIR emission in crossed electric and magnetic fields", Opt. Quantum Electron.,23(2), pp.S313-S321, 1991
14. S.Komiyama, S.Kuroda, I.Hosako, Y.Akasaka, N.Iizuka, "Germanium lasers in the range from far-infrared to millimeter waves", Opt. Quantum Electron.,23(2), pp.S133-S162, 1991
15. Yu.A. Mityagin, V.N. Murzin, S.A. Stoklitsky, "Quantum effects in submillimeter hot holes semiconductor lasers", Optical and Quantum Electronics, 23(2), pp. S287-S305, 1991.
16. Yu.A. Mityagin, V.N. Murzin, O.N. Stepanov, S.A. Stoklitsky, "Anisotropy and uniaxial stress effects in submillimeter stimulated emission spectra of hot holes in germanium in strong E⊥H fields", Semicond. Sci. Technol., 7, pp.b641-644, 1992.
17. Yu.A. Mityagin, V.N. Murzin, O.N. Stepanov, S.A. Stoklitsky, "Cyclotron resonance submillimeter laser emission in hot hole Landau level system in uniaxially stressed p-germanium", Physica Scripta, 49, pp.699-703, 1994.
18. S.A.Stoklitskiy, "Quantum states interaction in hot carriers accumulation and stimulated emission processes in p-Ge", Semicond. Sci. Technol., 7, pp.B610-B617, 1992.
19. S.Kuroda and S.Komiyama, "Far-infrared laser oscillation due to cyclotron emission in p-type germanium", Int.J.Infrared Millim. Waves, 12(7), pp.783-797, 1991.
20. C.Kremser, K.Unterrainer, E.Gornik, P.Pfeffer, W.Zawadzki, B.Murdin and C.R. Pidgeon, "Crossed-field hot-hole cyclotron resonance in p-Ge: non-parabolic and quantum effects", Semicond. Sci. Technol., 8, pp.S313-S316, 1993.
21. L.A. Reichertz, O.D. Dubon, G. Sirmain, E. Bruendermann, W.L. Hansen, D.R. Chamberlin, A.M. Linhart, H.P. Roeser, E.E. Haller, "Stimulated far-infrared emission from combined cyclotron resonances in germanium", Phys. Rev. B 56(19), pp.12069-12072, 1997.
22. A.V.Murav'ev, S.G.Pavlov, E.E.Orlova and V.N.Shastin, "Effects of shallow acceptors in a germanium hot-hole laser", JETP Lett., 59(2), pp. 89-93, 1994.
23. S.V.Demihovsky, A.V.Murav'ev, S.G.Pavlov, V.N.Shastin, "Stimulated Emission Using Shallow Acceptor States Transitions in Germanium", Semicond. Sci. Technol., 7, pp.b622-b625, 1992.

24. W. Heiss, K. Unterrainer, E.Gornik, W.L. Hansen, E.E. Haller, "Influence of impurity absorption on germanium hot-hole laser spectra", Semicond. Sci. Technol. **9**, pp. 638-640, 1994.
25. E. Bruendermann, A.M. Linhart, H.P. Roeser, O.D. Dubon, W.L. Hansen and E.E. Haller, "Miniaturization of p-Ge lasers: Progress toward continuous wave operation", Appl.Phys.Lett. **68**(10), pp. 1359-1361, 1996.
26. E. Bruendermann, A.M. Linhart, L. Reichertz, O.D. Dubon, W.L. Hansen, G. Sirmain and E.E. Haller, "Double acceptor doped Ge: A new medium for inter-valence-band lasers", Appl.Phys.Lett. **68**(22), pp. 3075-3077, 1996.
27. G. Sirmain, L.A. Reichertz, O.D. Dubon, E.E. Haller, W.L. Hansen, E. Bruendermann, A.M. Linhart, H.P. Roeser, "Stimulated far-infrared emission from copper-doped germanium crystals", Appl. Phys. Lett. **70**(13), pp.1659-1661, 1997.
28. L.E.Vorobjev, S.N. Danilov, Yu.V. Kochegarov, V.N. Tulupenko, D.A. Firsov, "Characteristics of far-infrared laser on hot holes in germanium in Voight and Faraday configurations of fields", Sov. Phys. Techn. Semicond. **31**(12), pp. 1474-1481, 1997.
29. A.V. Bespalov, . Schnellboegl, K.F. Renk, "Temperature dependence of gain and emission intensity of a far infrared broad band p-germanium laser", Proc. 18th Int. Quantum Electronics Conf., Vienna, Austria, PTh092, 1992.
30. E. Bruendermann, H.P. Roeser, W. Heiss, E. Gornik, and E.E. Haller, "High repetition rate far infrared p-type Germanium hot hole lasers", Appl.Phys.Lett. **67**, pp. 3543-3545, 1995.
31. E. Bruendermann, A.M. Linhart, L. Reichertz, O.D. Dubon, G. Sirmain, H.P. Roeser, O.D. Dubon, D.R. Chamberlin, W.L. Hansen E.E. Haller, "Tunable THz-laser for applications in FIR astronomy", Proc. 8th Int. Symposium on Space Terahertz Technology, Harvard/Boston, March, pp. 430-435, 1997.
32. E. Bruendermann, D.R. Chamberlin, and E.E. Haller, "Thermal effects in widely tunable germanium terahertz lasers", Appl.Phys.Lett. **73**, pp. 2757-2759, 1998.
33. E. Bruendermann and H.-P. Roeser, A.V. Muraviev, S.G. Pavlov, V.N.Shastin, "Mode fine structure of p-Ge intervalenceband laser measured by heterodyne mixing spectroscopy with an optically pumped ting gas laser", Infrared Phys. & Techn., **35**(1), pp. 59-69, 1995.
34. A.V.Murav'ev, I.M.Nefedov, S.G.Pavlov, V.N.Shastin, "Narrow-band tunable intra-valence-band p-germanium laser", Quantum Electronics, **23**, pp. 119-125, 1993.
35 I. Hosako, S. Komiyama, "P-type Ge far-infrared laser oscilation in Voigt configuration", Semicond. Sci. Technol., **7**, pp.b645-b648, 1992.
36 A. V. Muravjov, R. C. Strijbos, C. J. Fredricksen, H. Weidner, W.Trimble, S.H. Withers, S.G. Pavlov, V.N. Shastin, R.E. Peale, "Evidence for self-mode-locking in p-Ge laser emission", Appl. Phys. Lett., **73** (21), pp. 3037-3039, 1998.
37 A. V. Muravjov, S.H. Withers, S.G. Pavlov, V.N. Shastin, and R.E. Peale, " Broad band p-Ge optical amplifier of THz Emission", submitted to J. Appl. Phys., 1999.
38 J.N. Hovenier and A.V. Muravjov and S.G. Pavlov and V.N. Shastin, and R.C. Strijbos and W.Th. Wenckebach, "Active mode locking of a p-Ge hot hole laser", Appl. Phys. Lett., **71**(4), pp. 443-445, 1997.
39 J.N. Hovenier, T.O. Klaassen and W.Th. Wenckebach, A.V. Muravjov, S.G. Pavlov and V.N. Shastin, "Gain of the mode locked p-Ge laser in the low field region", Appl. Phys. Lett., **72**(10), pp. 1140-1142, 1998.
40 A.V. Muravjov, R. C. Strijbos, C. J. Fredricksen, S. H. Withers, W. Trimble, S.G. Pavlov, V. N. Shastin, R.E.Peale, "Pulse separation control for mode-locked far-infrared p-Ge laser", Appl. Phys. Lett., **74**(2), pp. 167-169, 1999.
41. A.V.Muravjov, S.H. Withers, R.C.Strijbos, S.G.Pavlov, V.N.Shastin and R.E.Peale, "Actively mode-locked p-Ge laser in Faradey configuration", submitted to Appl. Phys. Lett., 1999.
42. V.N. Shastin, R.Kh. Zhukavin, A.V. Muravjov, E.E. Orlova, S.G. Pavlov, V.Ya. Aleshkin, N.A. Bekin, B.N. Zvonkov, "Far-infrared hole absorption in $In_xGa_{1-x}As$/GaAs MQW heterostructures with δ-doped barriers", Physica Status Solidi (b), **204**, pp.174-177, 1997.
43. E.E. Orlova, R. Ch. Zhukavin, S. G. Pavlov, and V.N. Shastin, "Far-infrared active media based on impurity state transitions", Phys. Stat. Sol. (b) **210**, pp. 859-863, 1998.
44. H.-W. Hübers, K. Auen, S. G. Pavlov, E. E. Orlova, R. Kh. Zhukavin, and V. N. Shastin, "Population inversion and far-infrared emission from optically pumped silicon", **74**, pp. 2655-2657, 1999.

Investigation of Phosphorus Doped Silicon as a Possible Far-Infrared Laser Material

H.-W. Hübers[a], K. Auen[a], S. G. Pavlov[b], E. E. Orlova[b], R. Kh. Zhukavin[b], and V. N. Shastin[b]

[a] Institute of Space Sensor Technology and Planetary Exploration, DLR,
Rudower Chaussee 5, 12489 Berlin, Germany
[b] Institute for Physics of Microstructures, Russian Academy of Sciences,
Nizhni Novgorod GSP-105, 603600, Russia

ABSTRACT

The observation of spontaneous emission from phosphorus doped Si with a doping concentration of $0.9 \times 10^{15}\,cm^{-3}$ and $2 \times 10^{15}\,cm^{-3}$ is reported. Population inversion between the $2p_0$ state and the $1s(T)$ and $1s(E)$ states was achieved by optically pumping with a CO_2 laser. The spontaneous emission increased with pump power. Electrons could be excited from the $2p_0$ state into the conduction band due to the absorption of background radiation or radiation from a far-infrared probe laser. The frequency dependence of the absorption is in agreement with the cross section for photo ionization of a transition from the $2p_0$ state into the conduction band.

Keywords: semiconductor laser, terahertz, far-infrared, silicon

1. INTRODUCTION

Many scientific applications in the Terahertz (THz) frequency range require coherent, continuous wave, and frequency tunable radiation sources. They are needed for example in THz heterodyne receivers for astronomy and atmospheric remote sensing or fusion plasma diagnostics.[1, 2, 3] Other applications are in molecular and solid-state spectroscopy.[4, 5] Up to now far-infrared (FIR) gas lasers are used for these purposes. However, they are bulky and not tunable in frequency, which limits the application. For example, space based systems are very difficult to realize with gas lasers.

One of the key issues for THz frequency applications is the development of compact and frequency tunable radiation sources, which can deliver several microwatt output power in a continuous mode. Because of the prime importance many approaches have been made in order to develop new THz sources. They can roughly be divided into four groups. One approach is based on the extension of microwave technology, i.e. some kind of microwave oscillators (e.g. Gunn oscillator), which are multiplied by Schottky varactor diodes or heterostructure barrier varactors. The highest frequency generated with these sources is about 1 THz and the output power is slightly below 100 μW.[6] By downconversion of the radiation from two infrared lasers it is possible to generate about 1 μW up to 1 THz. But this falls off quite rapidly above 1 THz.[7] Another approach is the generation of coherent radiation in a heterostructure. When designed as a quantum cascade laser these devices emit in the infrared region (wavelength of 15 μm or shorter),[8] while devices based on Bloch oscillations operate up to about 100 GHz.[9] The frequency range in between is not covered by heterostructure devices. The fourth approach is the use of single crystalline material. Up to now lasing has been demonstrated in p-type Ge in crossed electric and magnetic fields and in uniaxially stressed Ge.[10, 11] The laser emission covers the range from about 3 – 6 THz. In this paper we describe experiments on a new mechanism for the generation of population inversion and far-infrared laser emission in phosphorus doped single crystalline silicon.

2. PRINCIPLE OF OPERATION

Optical pumping of a Si crystal with shallow, hydrogen like impurities is a possible mechanism to generate population inversion, because the cascade character of the phonon assisted relaxation allows efficient pumping of excited impurity states. However, the phonon assisted relaxation might cause problems, because it heats the crystal and therefore decreases the population inversion. Another complication arises from the fact that the absorption of radiation between two impurity states

falls in the same frequency region as a possible laser transition. Hence, the possibility of a laser transition in Si with shallow impurities depends on the details of the non-equilibrium population distribution of the optically pumped Si.

Si doped with phosphorus atoms is a promising candidate for the proposed laser mechanism. Irradiation by a CO_2 laser leads to the excitation from the 1s(A) ground state into the conduction band (Fig. 1). This is followed by a fast (10^{-12} s) relaxation via an optical phonon and a cascade of acoustic phonon assisted relaxation processes (10^{-10} s).[12] The $2p_0$ state with its lifetime $\tau_{2p0}=(3 - 5)\times10^{-7}$ s is longliving compared to the other excited states.[13] This is due to the restrictions of the momentum conservation law.[14] The lifetime was obtained from saturation experiments of the optical transition 1s(A)$\rightarrow$2p$_0$. Population inversion between the $2p_0$ and 1s(E,T) states is therefore expected under the conditions of optical excitation with a pumping rate $W>(\tau_{2p0}\times exp(-\Delta E/(k_BT_l)))^{-1}$, where ΔE is the energy gap between the 1s(A) and 1s(T,E) donor states, k_B is the Boltzmann constant and T_l is the lattice temperature. Calculations which take into account the optical excitation from the ground state and 1s(E), 1s(T) states and acoustic phonons assisted relaxation and excitation show that in Si:P crystals with a doping concentration around 10^{15} cm^{-3}, a crystal temperature $T_l<20$ K, and a pumping intensity ≥ 1 Wcm^{-2} amplification on the $2p_0\rightarrow$1s(E,T) transitions is possible. The expected gain is $\alpha=0.03$ cm^{-1}.[14]
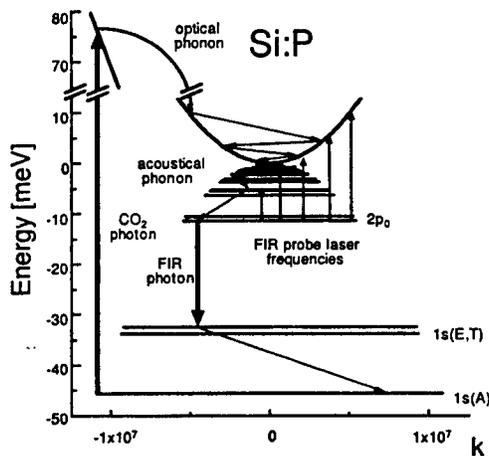
Fig. 1: Energy level diagram of Si:P with the proposed laser transition, the CO_2 pump transition and the FIR probe laser frequencies.
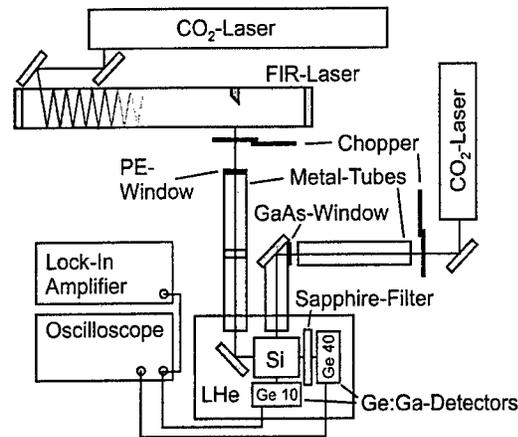
Fig. 2: Experimental set-up for the pump-probe experiments.

3. EXPERIMENTAL SET-UP

Seven Si crystals with phosphorus doping were tested. The parameters of the crystals are listed in Table 1. The doping concentration varies between 0.9 and 8×10^{15} cm^{-3}. One very pure crystal with a doping concentration below 10^{13} cm^{-3} was used as reference material. The crystals were either grown by the float zone method or by the Czochralski method. The compensation is in the about 1%.

Sample No.	Method of Growth	Resistivity [Ω cm]	Doping Concentration [10^{15} cm^{-3}]	Size [mm^3]	FIR beam along axis / length [mm]
1	Czochralski	5	0.9	6×6.5×7	[111] / 7
2	Czochralski	2	2	6×6.2×7	[111] / 7
3	Czochralski	>2000	< 0.006	5×5×7	[111] / 7
4	Float zone	5	0.9	5×5×7	[111] / 7
5	Czochralski	2	2	5×5×7	[111] / 7
6	Float zone	1.5	3	5×5×7	[111] / 7
7	Czochralski	0.5	8	5×5×7	[111] / 7

Table 1: The parameters of the investigated Si:P crystals.

The pump-probe experiment (see Fig. 2) consisted of a CO_2 laser, which excited a FIR gas laser transversely.[15] The FIR laser was optimized to operate at five different frequencies: 1.63 THz (lasing medium CH_2F_2), 2.52 THz (CH_3OH), 3.11 THz (CH_3OH), 4.25 THz (CH_3OH) and 5.24 THz (CH_3OD).[16] The typical output power was in the range from 0.1 mW to 1 mW. The FIR radiation was directed towards the Si sample by a metallic tube. The Si sample was immersed in liquid Helium (lHe) at a temperature of 4.2 K. At the entrance of the tube a polyethylene window was used to avoid the diffusion of water to the lHe. A second CO_2 laser was used to pump the Si sample. This laser was frequency tunable in the range from 9.2 - 9.8 μm and 10.1 - 10.9 μm. Via a mirror and metallic tubes its radiation was directed towards the sample. A GaAs window was used to prevent the diffusion of water vapor into the lHe vessel. The CO_2 radiation was chopped mechanically with about 480 Hz. By using different chopper blades it was possible to generate pulses with a minimum length of 2 – 3 ms. This lowers the heat load to the Si crystal. The CO_2 pump beam and the FIR probe beam were directed orthogonal to each other through the Si crystal. Two Ge:Ga detectors were integrated in the set-up. One with a resistivity of 10 Ωcm (Ge 10) was used for the detection and alignment of the CO_2 radiation and the other with a resistivity of 40 Ωcm (Ge 40) was used for the detection and alignment of the FIR radiation. To prevent the scattering of CO_2 radiation onto the Ge 40 detector a monocrystalline sapphire filter was used. The signals from the Ge 10 detector and from the Ge 40 detector were recorded with a Lock-in amplifier with the chopping frequency of the CO_2 pump laser as the reference. In addition, the signals were recorded with a 500 MHz digital oscilloscope.

The experiment for the generation of spontaneous emission was performed with a pulsed CO_2 laser in order to achieve higher pump power. This laser delivered pulses with a duration of 3 – 5 μs at a repetition rate of about 150 Hz. The principle set-up is shown in the inset of Fig. 6. The FIR emission was detected in orthogonal direction to the direction of the CO_2 pulse. Again, the CO_2 pulse was detected with the Ge 10 detector while the FIR emission was detected with the Ge 40 detector. A sapphire filter was used in front of the Ge 40 detector in order to block the CO_2 radiation. The FIR emission signal could be spectrally analyzed by inserting InSb, GaAs and KRS 5 filters in front of the Ge 40 detector.

4. FIR ABSORPTION BY OPTICALLY EXCITED SI:P

1. Absorption of background radiation

Optical excitation by CO_2 laser radiation leads to a population of the $2p_0$ state. From this state absorption into the conduction band is possible. In this section we describe the absorption of background radiation by optically excited Si. The background radiation was directed towards the Si sample by a metallic tube. Figs. 3a) and b) display the structure of a CO_2 excitation pulse (upper trace of Fig. 3a)) and the FIR signal (lower trace of Fig. 3a) and Fig. 3b)) from a Si:P crystal with a doping concentration of 3×10^{15} cm^{-3}. Due to the sign of the FIR signal on the Ge 40 detector it is an absorption signal. While the CO_2 pulse is smooth, a striking feature of the FIR pulse is that it consists of two components, one component with a time constant much less than 1 ms and the other with a time constant in the order of 1 ms. We interpret the fast component to be due to the absorption by transitions from the excited donor states into the conduction band (electronic absorption) which is a fast process. The slow component is due to lattice absorption of the Si lattice.
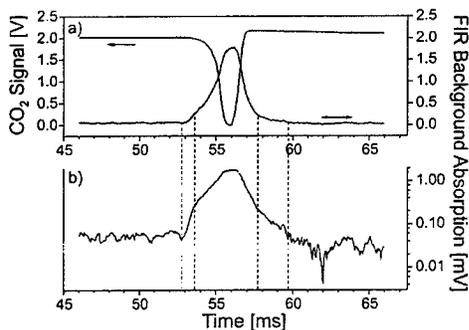
Fig. 3: a) Structure of the CO_2 pump pulse (upper trace) and the FIR pulse (lower trace) and b) structure of the FIR pulse in a logarithmic scale. Note the two components with different slopes.
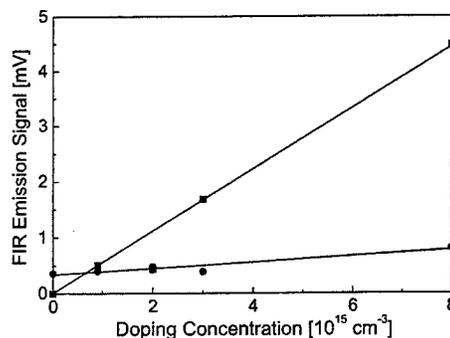
Fig. 4: Dependence of the FIR signal due to lattice absorption (circles) and electronic absorption (squares) on the doping concentration (samples 3 – 7).

In Fig. 4 the magnitude of the signals due to electronic absorption and due to lattice absorption are shown as a function of the doping density of the crystal. The signal due to electronic absorption increases linearly with the doping concentration while the signal due to lattice absorption is almost independent of the doping concentration. There is only one exception. For the sample with 2×10^{15} cm^{-3} donors (sample 5) the signal due to electronic absorption is smaller than expected. The reason for this is not quite clear. It might be a non-ideal crystal for example with too many dislocations. The interpretation of the FIR signal as absorption of background radiation is supported by the experimental findings that the absorption signal decreases by about a factor of three when the background is at a temperature of 77 K instead of 300 K and that the absorption signal saturates with increasing CO_2 pump power, because all electrons are excited. These experiments already demonstrate the possibility to populate the excited donor states by optical excitation with a CO_2 laser.

2. Frequency dependence of the absorption

In order to get the information which state is populated by the absorption of CO_2 laser radiation we have probed the population of the excited states with the radiation from a FIR gas laser. Since the energy separation of the $2p_0$ state and the minimum of the conduction band is 11.46 meV, the FIR radiation has to have a minimum frequency of 2.78 THz in order to lead to a direct absorption into the conduction band. However, as it is clear from Fig. 1 the probability for an absorption at a somewhat smaller frequency is quite high, since there is a quasi continuum just below the conduction band minimum. In fact, due to the high doping concentration the activation energy E_d of the donors is lowered. The lowering can be described by [17]

$$E_d = E_{d0} \left[1 - (N_D/N_{crit})^{1/3} \right] \quad , \tag{1}$$

where N_D is the doping concentration, N_{crit} is the critical donor concentration at which the activation energy vanishes ($\approx 1.1 \times 10^{18}$ cm^{-3} for Si) and E_{d0} is the activation energy for $N_D \ll N_{crit}$. For $N_D = 10^{15}$ cm^{-3} this yields an activation energy of 10.3 meV, corresponding to a lowering of the frequency where absorption can be expected to 2.5 THz. Therefore, radiation from the four laser lines with frequencies above 2.5 THz should be absorbed. Only at 1.63 THz the energy is not sufficient for an absorption into the conduction band and no corresponding impurity level is available for an absortion transition. As shown in Fig. 5 we observed absorption of the FIR probe laser at all laser frequencies above 2.52 THz but none at 1.63 THz, in agreement with the previously outlined arguments.

For a quantitative comparison the magnitude of the absorption signal, ΔS, has to be calculated. It depends on the cross-section for photo ionization, $\sigma(v)$, at the laser frequency, v, the difference in the population density, ΔN, between the $2p_0$ state and the conduction band, the length, L, of the Si crystal and the power, P_{FIR}, of the FIR probe beam. Division of the absorption signal by the FIR laser power yields the relative absorbed FIR power, which is a measure for the population difference between the $2p_0$ state and the conduction band. For a small absorption and low FIR power, i.e. saturation effects can be neglected, one has

$$\Delta S \approx \sigma(v) \, \Delta N \, L \, P_{FIR} \quad . \tag{2}$$

It is worth noting that the relative absorbed FIR power has two contributions: One is the absorption of FIR laser power and the other is the decrease of the spontaneous emission due to depopulation of $2p_0$ state. However, our calculations show that the latter effect is negligible, i.e., only 0.1 % of ΔS is due to the depopulation of the $2p_0$ state.

In Fig. 5 the relative absorbed FIR power is shown as a function of the probe beam frequency. The values for the 2 Ωcm crystal (sample no. 2) are about a factor of 1.9 bigger than for the 5 Ωcm crystal (sample no. 1). This is expected because the 2 Ωcm crystal has about twice the impurity concentration and for the same level of pump power about twice the number of electrons are excited into the $2p_0$ state. Also shown in Fig. 5 is the frequency dependence of the relative absorbed FIR power calculated according to Eq. 2. The cross section for photo ionization was calculated according to a model for a hydrogen like impurity state with the Coulomb factor included

$$\sigma(v) = \gamma \, (hv / E_b - 1) \, (hv / E_b)^{-5} \quad . \tag{3}$$

Here E_b is the binding energy of the impurity and $\gamma = 5.5 \times 10^{-14}$ cm^{-2} is a constant which depends on the effective mass of the electron and several constants of nature.[18] It is important to keep in mind that Eq. 3 is strictly valid only for the absorption from an s-type state into the conduction band. For an absorption from a p-type state the maximum shifts to a slightly higher

frequency. In addition, the binding energy of the $2p_0$ state has to be taken (11.46 meV). For the calculation of the relative absorbed FIR power a population difference of 0.3 % was assumed for both crystals. This value yield a good agreement between the measured data and the calculated absorption curve.

It is possible to estimate the population difference between the $2p_0$ state and the conduction band for the given experimental conditions. From power measurements at the exit of the metal tube and the reflection of FIR radiation from the surfaces of the Si crystal (ca. 30 %) the CO_2 power density entering the Si crystal can be estimated to be about 1 W/cm². For this value and a lattice temperature of 4.2 K our model yields an excitation of 0.36 % of the electrons from the phosphorus impurities into the $2p_0$ state. Furthermore, it follows from the model that the population of the conduction band is only about 1% of the population of the $2p_0$ state. Therefore, the difference between both is about equal to the population of the $2p_0$ state, i.e. 0.36 %. This is in excellent agreement with the value of 0.3 % obtained from the fit to the measured data.
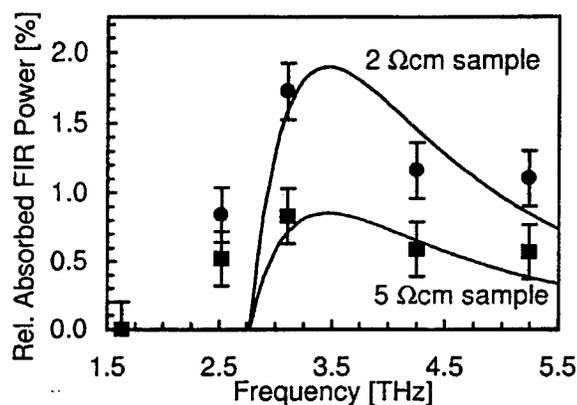
Fig. 5: Relative absorbed FIR power as a function of the probe laser frequency. The solid line is the calculated absorption curve.
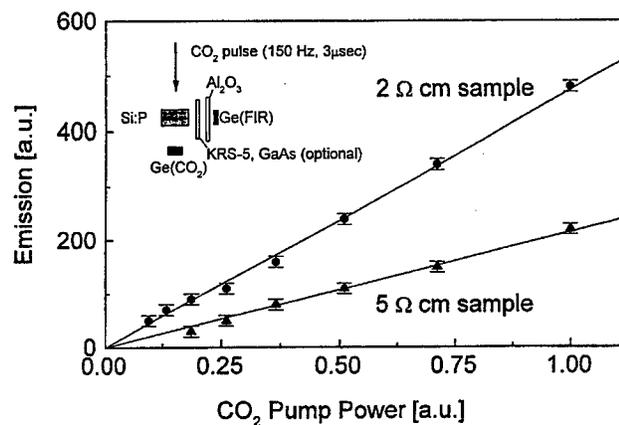
Fig. 6: Spontaneous emission as a function of the CO_2 pump power. In the inset a scheme of the experimental set-up is shown.

5. GENERATION OF SPONTANEOUS EMISSION

It was possible to generate spontaneous emission by using a pulsed CO_2 laser. This laser delivered more power than the cw CO_2 laser while the heat load to the crystal is not increased. Fig. 6 shows the results. The observed emission signal increases linearly with increasing pump power. As already seen in the absorption experiments the signal from the 2 Ωcm sample (no. 2) is about two times higher than that from the 5 Ωcm sample (no. 1) because of the two times higher doping concentration. In order to confirm that the emission originates from the $2p_0 \rightarrow 1s(E)$ (v=5.10 THz) and $2p_0 \rightarrow 1s(T)$ (v=5.41 THz) transitions, filters were introduced between the Si sample and the Ge 40 detector. At the low frequency side the KRS 5 filter cuts off frequencies below about 4.3 THz while at the high frequency side the GaAs filter has a 50 % absorption above 6.5 THz. Comparing the signals with and without the filters leads to the conclusion that the emission falls into the frequency region between 5 THz and 6 THz. The only transitions in this region are $2p_0 \rightarrow 1s(E)$ and $2p_0 \rightarrow 1s(T)$,[19] therefore the observed emission signal is spontaneous emission from these transitions (see also Ref. 20). However, the pump power was not sufficient to achieve stimulated emission.

6. CONCLUSION

We have demonstrated the possibility to achieve population inversion and spontaneous emission from optically pumped Si:P. Population inversion was achieved between the $2p_0$ state and the 1s(E) and 1s(T) states. Background radiation and the radiation from a FIR laser was absorbed by the $2p_0$ state, which could be populated due to the excitation with a CO_2 laser. The absorption signal consists of a fast electronic part and a slow part due to lattice absorption. The frequency dependence of the FIR laser absorption is in agreement with the frequency dependence of the cross section for a transition from the $2p_0$ state into the conduction band. Spontaneous emission was observed when pumping the Si crystal with a pulsed CO_2 laser. The

emission signal has a frequency between 5 THz and 6 THz as expected for the transitions from the $2p_0$ state to the 1s(E) and 1s(T) states. Since further optimization is possible, we conclude that phosphorus doped Si is a promising material for a FIR laser.

7. ACKNOWLEDGEMENTS

8. REFERENCES

1. H.-W. Hübers, G. W. Schwaab, and H. P. Röser, "A heterodyne receiver for the frequency range 1-6 THz", Proc. 30th ESLAB Symposium 'Submillimetre and Far-Infrared Space Instrumentation' ESA **SP-388**, pp. 159-162, 1996.
2. R. U. Titz, M. Birk, D. Hausamann, R. Nitsche, F. Schreier, J. Urban, H. Küllman, and H. P. Röser, "Observation of stratospheric OH at 2.5 THz with an airborne heterodyne system", Infrared Phys. Technol. **36**, pp. 883-891, 1995.
3. W. A. Peebles, D. Brower, Y. Jiang, L. Zeng, P. Pribyl, and P. King, "Compact, turn-key, terahertz, laser systems for fusion plasma diagnostics", Proc. of the 23rd Int. Conf. on Infrared and Millimeter Waves, pp. 284-286, Colchester, 1998.
4. G. A. Blake, K. B. Laughlin, R. C. Cohen, K. L. Busarow, D.-H. Gwo, C. A. Schmuttenmaer, D. W. Steyert, and R. J. Saykally, "The Berkeley tunable far infrared laser spectrometers", Rev. Sci. Instrum. **62**, pp. 1701-1716, 1991.
5. V. I. Ivanov-Omskii, "FIR laser spectroscopy of impurities insemiconductors", Infrared Phys. Technol. **1**, pp. 179-190, 1995.
6. R. Zimmermann, T. Rose, and T. Crowe, "An all solid state 1 THz radiometer for space applications", Proc. of the 6th Int. Symp. on Space Terahertz Technology, pp. 13-27, Charlottesville, 1995.
7. S. Matsuura, M. Tani, and K. Sakai, "Generation of coherent terahertz radiation by photomixing in dipole photoconductive antennas", Appl. Phys. Lett. **70**, pp. 559-561, 1997.
8. J. Faist, F. Capasso, D. L. Sivco, C. Sirtori, A. L. Hutchinson, and A. Y. Cho, "Quantum cascade laser", Science **264**, pp. 553-556, 1994.
9. E. Schomburg, S. Brandl, K. Hofbeck, T. Blomeier, J. Grenzer, A. A. Ignatov, K. F. Renk, D. G. Pavel'ev, Y. Koschurinov, V. Ustinov, A. Zhukov, A. Kovsch, and S. Ivanov, P. S. Kop'ev, Appl. Phys. Lett. **72**, pp. 1498-1500, 1998.
10. E. Bründermann, H. P. Röser, A. V. Muravjov, S. G. Pavlov, and V. N. Shastin, "Mode fine structure of the p-Ge intervalenceband laser measured by heterodyne mixing spectroscopy with an optically pumped ring gas laser", Infrared Phys. Technol. **1**, pp.59-69, 1995.
11. I. V. Altukhov, E. G. Chirkova, M. S. Kagan, K. A. Korolev, V. P. Sinis, and I. N. Yassievich, "Intracenter population inversion of strain-split acceptor levels in Ge", Proc. of the 23rd Int. Conf. on the Physics of Semiconductors, pp. 2677-2680, Berlin, 1996.
12. G. Askarelly and S.Rodriguez, "Recombination of electrons and donors in n-type germanium", Phys. Rev. **124**, pp. 1321-1328, 1961.
13. K.K. Geerinck, J. E. Dijkstra, J. N. Hovenier, T. O. Klaassen, W. T. Wenckebach, A. F. G. van der Meer, and P. W. Amersfoort, Nucl. Instr. and Meth. Phys. Res. A **341**, pp. 162-167, 1994.
14. E.E. Orlova, R. Ch. Zhukavin, S. G. Pavlov, and V.N. Shastin, "Far-infrared active media based on impurity state transitions", Phys. Stat. Sol. (b) **210**, pp. 859-863, 1998.
15. H.-W. Hübers, L. Töben, and H. P. Röser, "A far-infrared laser magnetic resonance spectrometer with permanent magnets", Rev. Sci. Instrum. **69**, pp. 290-293, 1998.
16. N. G. Douglas, "Millimetre and submillimetre wavelength lasers", Springer, Berlin, 1989.
17. E. F. Schubert, "Doping in III-V semiconductors", Cambridge University Press, Cambridge, 1993.
18. B. K. Ridley, "Quantum processes in semiconductors", Clarendon Press, Oxford, 1993.
19. A. K. Ramdas and S. Rodriguez, "Spectroscopy of the solid-state analogues of the hydrogen atom: donors and acceptors in semiconductors", Rep. Prog. Phys. **44**, pp. 1297-1387, 1981.
20. H.-W. Hübers, K. Auen, S. G. Pavlov, E. E. Orlova, R. Kh. Zhukavin, and V. N. Shastin, "Population inversion and far-infrared emission from optically pumped silicon", to appear in Appl. Phys. Lett., May 3rd, 1999.

The pulsed and mode-locked p-Ge THz laser: wavelength dependent properties.

T.O. Klaassen[a], N.J. Hovenier[a], W.Th. Wenckebach[a], A.V. Muravjov[b], S.G. Pavlov[b] and V. N. Shastin[b]

[a] Department of Applied Physics and DIMES, Delft University of Technology, P.O. Box 5046, 2600 GA Delft, The Netherlands

[b] Institute for Physics of Microstructures, Russian Academy of Sciences, GSP-105, Nizhny Novgorod 603600, Russia

ABSTRACT

Wavelength dependent properties of the p-Ge THz laser are reported for pulsed as well as for mode locked operation. The original small mirror laser outcoupler has been replaced by a mesh outcoupler, resulting in clear improvements of laser action. The optical output has been analysed using a grating spectrometer and fast Schottky diode detectors. For $0.25 \leq B \leq 0.6T$, 170-185 μm emission occurs. Laser action starts at short wavelength; during the pulse, longer wavelength components gain intensity, until simultaneous emission across the whole band occurs. With the mesh outcoupler instead of a small mirror, the small signal gain is found to increase, for instance from 0.015 cm^{-1} to 0.04 cm^{-1} at 172 μm . With the rf field modulation applied, 770 MHz mode locking of the laser is achieved at 172 μm, yielding a train of 100 ps FWHM pulses. For $0.5 \leq B \leq 1.4T$, 75-120 μm emission is observed, dependent on both B and E field. Time-and wavelength dependence is complicated; often an oscillatory behaviour of spectral components is seen. Although this effect complicates the formation of stable pulse trains under mode locked conditions, 140 ps pulses have been produced.

Keywords: p-Ge hot hole laser, THz emission, mode locking, small signal gain

1. INTRODUCTION

The p-Ge hot hole laser is as yet the only solid state laser with a strong and tunable broad band emission in the THz frequency range. A disadvantage of this source is the strong heating of the cryogenically cooled laser crystal, due to the necessary brute force laser excitation. As a consequence, only short pulsed operation is possible.[1] Lately, much effort has been put into the development of techniques to realise C.W. operation of this laser, in order to enable the use of this source for instance as local oscillator in THz heterodyne systems.[2-4] We have focussed our attention on the possibilities to employ this laser to create *very short* pulses, that could be used for time resolved experiments in which monochromatic THz radiation is needed.

Some time ago a possible method, based on Monte Carlo simulations, was discussed to actively mode lock the p-Ge laser.[5] Using the modulation technique proposed in that publication, actual mode locked operation was realised.[6,7] Peculiar properties of the optical output of this mode locked laser appear to be intimately related to the wavelength dependence of gain and pulse shape as observed for *long pulsed* operation.[8,9] Therefore in this paper we present results on the wavelength dependent properties of the optical output both for long pulsed as well as for mode locked operation. Also the influence of laser excitation conditions will be addressed. We show that we are able to produce trains of THz pulses pulses with a (FWHM) width shorter than 100 ps. Since our latest reports on this subject,[10,11] we have modified the laser cavity design, which has resulted in drastic changes in the optical output characteristics. Prelimenary results obtained with this new cavity will be compared with the earlier data.

The operation of the p-Ge hot hole laser is based on the acceleration of holes in $\vec{E} \perp \vec{B}$ fields at $T \leq 20$ K.[1] For the proper ratio of E and B fields, $E/B \approx 1.4$ kV/cmT, the heavy holes (hh) are accelerated up to energies above the optical phonon energy $\hbar \omega \approx 37$ meV , and therefore strongly scattered by optical phonons. A few percent of these

For further author information send correspondence to T.O.K.:
Email: tjeerd@hfwork1.tn.tudelft.nl; tel: ++31.15.2786136; fax: ++31.15.2783251.
WWW: http://duttcbs.tn.tudelft.nl/vs-hf/home.html

hh's are scattered into the light hole band. The light holes (lh) do not reach the optical phonon energy, and are thus not scattered, but accumulate on closed trajectories below the optical phonon energy. The resulting population inversion between the lh band and the hh band leads to stimulated emission in the 1.5-4.2 THz range. It must be noted that both bands are split up in discrete Landau levels by the action of the magnetic field. Because of the very short life time of the hh's, combined with the small Landau level splitting resulting from the large effective mass, the hh Landau levels merge to one broad band. Because of the longer life time of the lh's and the much larger Landau level (and electron spin-) splitting the lh band does exhibit a discrete structure. So, in fact, population inversion occurs between one or more lh Landau levels and the hh band. By increasing the amplitude of both E and B, the frequency of the laser emission tends to increase.
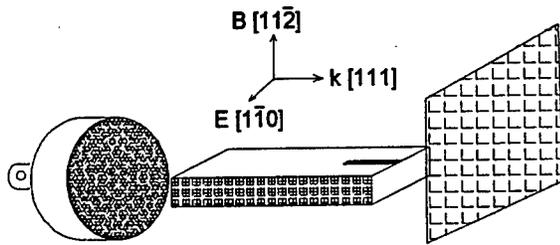
Figure 1. p-Ge laser cavity design.
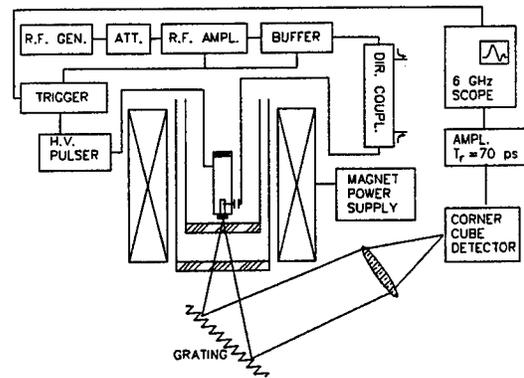
Figure 2. Schematic view of the experimental set-up

For proper action, $\vec{E}$ and $\vec{B}$ must be accurately perpendicular, as a small component of the electric field $\parallel \vec{B}$ causes an acceleration of the holes which is not restricted by the action of the Lorentz force. This enables the *light* holes to gain so much energy that they are also scattered by optical phonons, partly into the hh band, leading to the destruction of the population inversion. Being a disadvantage for normal laser operation, this very effect can be made usefull to obtain a modulation of the laser gain. With the application of a periodic electric field $\vec{E}_\nu \parallel \vec{B}$, the population inversion, and thus the laser gain, reaches a minimum at maximum amplitude of that field, i.e. twice per E_ν cycle. So, by choosing the frequency ν equal to *half* the laser cavity round trip frequency, a modulation of the gain at the round trip frequency is achieved; the essential prerequisite for active mode locking.[5]

2. EXPERIMENTAL DETAILS

2.1. Laser crystal

The laser sample used was cut from a single crystal of Ga doped Ge, with $N_{Ga} = 7.10^{13}$ cm^{-3}, in the form of a rectangular parallelepiped of $5 \times 7 \times 49.46$ mm^3. In the *former* cavity design two gold mirrors, evaporated on quartz substrates and isolated from the crystal by 10 μm Teflon films, were attached to the end faces of the sample. The smaller, 4 mm diameter, mirror covered only part of the end face: the laser radiation leaking out alongside this mirror was detected. In the *new* cavity design, shown in Fig. 1, this smaller end mirror has been replaced by a home made capacitive mesh outcoupler, covering the total end face of the crystal. This enables the detection of the laser emission originating from the very *center* of the laser crystal.

2.2. Experimental set-up

The high voltage electric excitation field $\vec{E} \parallel [1\bar{1}0]$ is applied to ohmic contacts covering two opposite lateral surfaces of the sample in pulses of a few μs long to avoid excessive heating. The magnetic field $\vec{B} \parallel [11\bar{2}]$ is applied perpendicular to the long axis and to $\vec{E}$. The rf field $\vec{E}_\nu \parallel \vec{B}$ for gain modulation is applied in short pulses too, synchronized

with the laser excitation, to additional ohmic contacts of 1×10 mm^2 on the other lateral sides of the sample. It must be noted, that employing the Voigt configuration, i.e. the optical axis perpendicular to both $\vec{B}$ and $\vec{E}$, is essential in order to use the present modulation technique. In the Faraday configuration (optical axis $\parallel \vec{B}$), which is often used to operate the p-Ge laser, the modulation electrodes would block the optical path.

As the optical length of the cavity is about $n_{Ge} \times 49.46$ mm ≈ 20 cm, the laser cavity round trip time equals 1.3 ns, i.e. the roundtrip frequency equals 772 MHz, and thus the frequency of the modulation field is choosen as $\nu = 386$ MHz.

Fig. 2 gives a schematic overview of the experimental set up. The High Voltage pulser consists of a large low inductance capacitor bank that can be switched on in two steps. Voltages up to 0.9 kV can be applied to the crystal within 30 ns, using a system of 5 parallel FET's. To obtain voltages up to 1.8 kV, a pre-step is applied using an IGBT switch with a risetime of $\leq$ 500ns. In this way, the electric field applied to the crystal is always raised within 30 ns from a value far below the active region (see Figs. 4 and 8) to the value needed for laser action.

For the gain modulation, a high voltage proof buffer amplifier with a 250W @ 386MHz. output was developed. The RF power is transferred to the Ge sample by a 50 Ω coaxial cable. Inside the home build Helium cryostat, as close as possible to the sample, a resonant circuit and transformer are situated to match the 10Ω resistance between the RF contacts to the 50Ω cable.
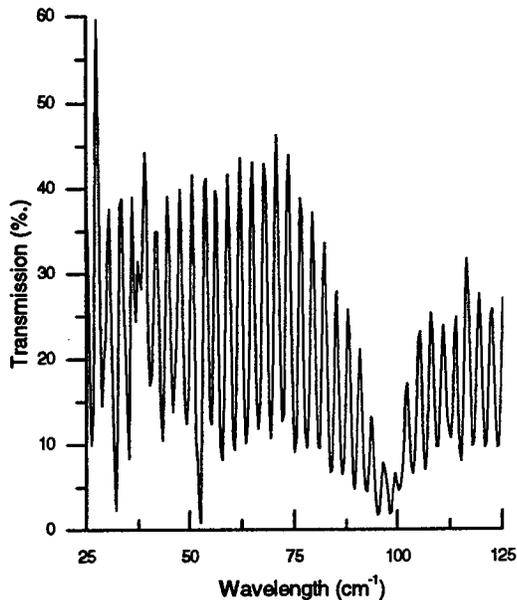
Figure 3. Room temperature transmission spectrum of the capacitive mesh outcoupler as determined with a FTIR spectrometer. The strong oscillatory wavelength dependent behaviour of the reflectivity is due to an etalon effect from the 0.45 mm thick Ge substrate.
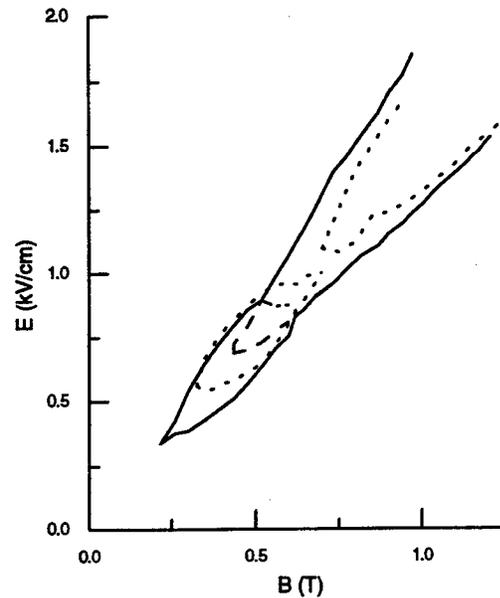
Figure 4. (E,B) field region for the p-Ge laser. Dotted curves show the actived regions with an outcouple mirror. Solid line: active regions with outcouple mesh. The dot-dashed and dashed curves indicate the long wavelength and short wavelength regions respectively.

The homogeneous electromagnet ($B_{max} \approx 1.3$T) with a 65mm bore, can be rotated to adjust the angle between E- and B-field to obtain optimum laser action. A z-cut quartz window at the bottom of the cryostat enables an easy outcoupling of the laser radiation. The spectrum of the laser output can be studied with a resolution of about 1% using either a 7.9 grooves/mm or a 4 grooves/mm Littrow grating. If possible, the optical path outside the cryostat is flushed with dry nitrogen in order to avoid water vapour absorption. This strong, wavelength dependent, absorption does not only cause an overall decrease in signal intensity, but also strongly distorts the shape of the laser emission spectrum.

The optical output is monitored with fast room temperature GaAs Schottky diode detectors (Faran Technology) or slower pyroelectric detectors. The signal is displayed using either a 0.5 GHz bandwidth, 2 GS/s, or a 1 GHz

bandwidth, 5 GS/s, oscilloscope to monitor the overall pulse envelope. For a detailed study of the waveform of individual pulses, a 6 GHz bandwidth real time oscilloscope was available. The overall response time of the electronic system was determined to be 100 ps.

2.3. Mesh outcoupler

The mesh outcoupler was designed to yield a maximum reflection of about 95 % at a wavelength of 100 μm. In Fig. 3 the transmission of the mesh, measured with a FTIR spectrometer at room temperature, is shown. Near 100 μm indeed a transmission minimum of about 5% is observed. Although the wavelength dependent transmission is strongly distorted by an etalon modulation resulting from the $\approx$ 0.45 mm thick Ge substrate, also near 53 cm^{-1} a transmission miniumum can be observed.

Because of the use of a capacitive mesh instead of a small mirror as outcoupling device for the laser cavity, a number of changes of the laser action can be expected. The absence of frequency selective elements in the former cavity, together with the inherently broad band nature of the intervalence band transition, caused laser action to occur simultaneously at a large number of longitudinal modes. Now, the strongly wavelength dependent reflectivity of the mesh will introduce a wavelength dependent modulation of the cavity round trip losses. As a minimum value for the reflection coefficient is needed in order to obtain laser action, this may influence both the active region of the laser as well as the shape of the emission spectrum as a function of E and B. The wavelength dependence of the mesh will favour laser action in certain regions, and suppress it in others. Secondly, in the former situation only the light leaking out of the cavity alongside the small outcouple mirror could be observed. That means that in the optical signal only light from transversal modes with a non negligible intensity at a distance of 2 mm or more from the center of the crystal was present.

With the present mesh outcoupler, the emission across the total transverse area of the laser is monitored. In fact, as one may expect the largest intensity to originate from the central part of the crystal, that emission will dominate the signal intensity. So, with the mesh outcoupler, the observed optical signal will be dominated by the contribution of the lowest order transversal mode of this cavity, probably the TEM$_{00}$ mode. This mode will most certainly experience a larger optical gain than the higher order transversal modes that were monitored with the mirror outcoupler.

3. EXPERIMENTAL RESULTS

3.1. Pulsed operation

3.1.1. Active region and emission spectra

Using a reflection grating in combination with a fast pyroelectric detector and/or a Schottky diode detector, the time- and wavelength resolved optical output of the laser has been studied throughout the E-B region where laser action is observed.In Fig. 4 this active region is shown. The solid line shows the results obtained with the new mesh outcoupler, whereas the dotted lines depict the active region observed under optimal conditions with the 4 mm diameter outcouple mirror. Clearly the active region observed with the mesh outcoupler is considerably extended compared to that with the mirror outcoupler. Also the gap in laser action earlier found around E= 1kV/cm has disappeared. However, the gap in the laser emission spectrum around 75 cm^{-1} remains. This gap is common for Ge:Ga hot hole lasers and due to optical absorption by the Ga impurities in the Ge crystal.[12] The range of the "high-field/short wavelength" region has extended towards much lower field, as shown by the long dashed curve. The "low-field/long wavelength" region (dot-dashed curve) has extended towards much lower field too, but seems to have shrunken somewhat at the high field side. Nevertheless, with this cavity, a region is found where laser action both at long and at short wavelength occurs. This overlap region near B=0.5 T is clearly seen in the low resolution spectra given in Fig. 5.

For B $\leq$ 0.6T laser action occurs in a nearly field independent wavelength range from 170- 185 μm. For B $\geq$ 0.45T the broad band laser emission occurs at wavelengths in the 80-130 μm range, the center wavelength gradually decreasing towards higher field. In Fig. 6 laser spectra for three E-B field combinations near the overlap region are given. These have been recorded with a higher spectral resolution than those in Fig. 5, and show the influence of the strong wavelength dependent reflectivity of the mesh that results from the etalon effect (see Fig. 3). The spectra show a peaked structure with a peak distance that equals the $\approx$ 2.8 cm^{-1} distance between the successive reflection maxima of the mesh. The low value of the reflectivity in the *minima* near 53 cm^{-1} ($\approx$ 60 %) indicates that certainly in that wavelength region laser action can only occur at the reflection *maxima*. Extrapolation towards

higher frequency proves that also around 90 cm^{-1} the laser output peaks at frequencies where maxima in the mesh reflectivity occur. Because the overall reflectivity in that frequency range is large, often also in between the maxima a finite emisssion intensity is observed. The regularity of the peaked structure is sometimes destroyed by residual water vapour absorption, as can be seen for instance near 93 cm^{-1}. It should be noted that the doublet structure in the B =1T spectrum in Fig. 5 is not the result of this effect. The splitting is much larger, about 10 cm^{-1}, and due to the occurrence of normal and "forbidden" spin-flip transitions.[13]
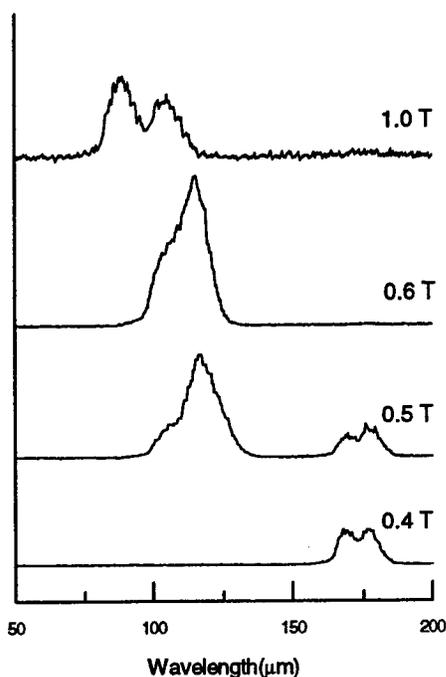
Figure 5. Low resolution laser emission spectra for various B-fields. Near B=0.5T the low- and high frequency emission ranges overlap.
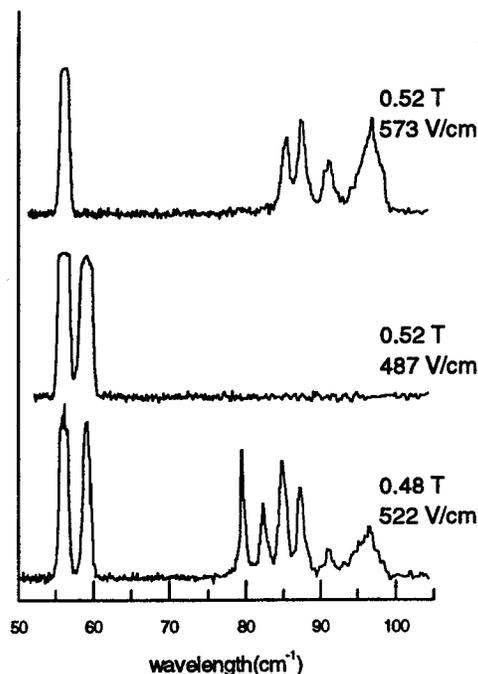
Figure 6. High resolution spectra for E and B near the overlap region. Intensity modulations are due to etalon effects in the mesh reflectivity

3.1.2. Time resolved experiments

For B=0.5 T the pulse shapes at three different wavelengths are shown by the solid curves in Fig. 7. These results were obtained with mirror outcoupling. The zero of the time scale coincides with the moment that the ≈ 3 μs long HV excitation pulse reaches the necessary amplitude to create a population inversion. Emission in a broad band occurs, but laser action starts at the short wavelength/high energy part of the spectrum, and shifts towards longer wavelengths during the optical pulse. At the end of the optical pulse, simultaneous emission across the total wavelength band occurs.From shot to shot, the relative intensities at these three wavelengths varies considerably, most probably due to longitudinal mode competition effects. The time delay versus wavelength remains however quite constant.

From the growth of intensity in the early part of these pulses, the wavelength dependent small signal gain $g_{(\lambda)}$ has been determined to be $g_{(172)}$=0.015 cm^{-1}, $g_{(177)}$=0.0026 cm^{-1} and $g_{(182)}$=0.0021 cm^{-1}. It must be noted that these values represent the *effective* gain, i.e. the actual (bare) gain reduced by, among others, reflection and outcouple losses. As these losses may well be in the order of 0.01 cm^{-1}, the wavelength dependence of the *bare* small signal gain may be not as strong as the above presented values suggest. The recent experiments with the mesh outcoupler indicate much larger values for the small signal gain, for instance at 171 μm a value of about 0.04 cm^{-1} has been observed. Also the time delay at that wavelength is reduced, i.e. from 350 ns, see Fig. 7, to 250 ns. As can be seen, the laser emission stops long before the end of the laser excitation. This is related to the strong heating of the crystal during excitation, which causes the laser gain to drop with time as a result of increasing lattice absorption and lh

phonon scattering.[14] To study the influence of lattice heating on the emission, a two-pulse excitation experiment has been carried out.
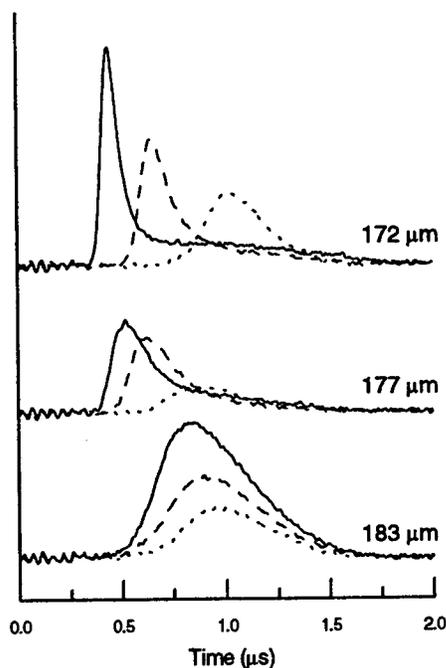
Figure 7. Shape of the optical pulses for B=0.5T at three wavelengths, as a function of the initial crystal temperature (see text for further explanation)
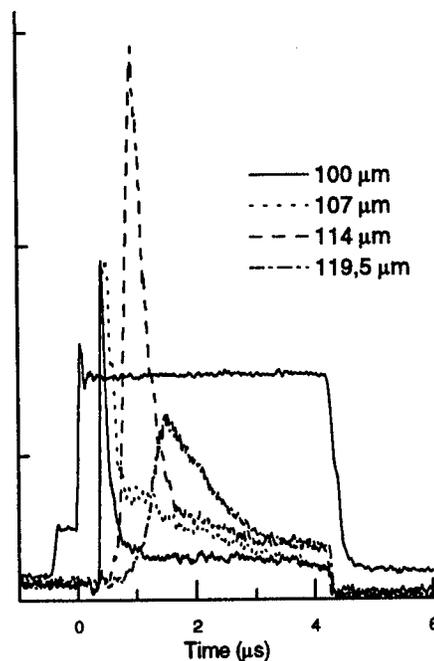
Figure 8. Wavelength dependent delay and pulse shape for B ≈ 0.7 T. The HV pulse is also indicated, showing the two-step increase in voltage.

The first E-field pulse, with a low enough amplitude to avoid laser action, heats up the crystal. By applying the second pulse at a well defined time delay after the first one, the initial lattice temperature of the crystal, at the moment of genuine laser excitation, can be increased in a controlled way. The solid curves in Fig. 7 have been taken at an initial temperature of T= 4.2 K (liquid Helium). The dot-dashed and dotted curves were measured at higher initial lattice temperatures, using this technique. Not unexpectedly, the time delay between excitation and start of laser emission increases and the small signal gain and peak intensity decrease with increasing temperature for all three wavelengths. However, the amount of change differs, with the result that at higher initial lattice temperature laser action starts at the *long* wavelength side of the spectrum.

In the high field region, effects similar to those found in the low field region, are observed. In general the small signal gain is found to be larger, and laser action can be sustained for a somewhat longer period, despite the fact that in this field region the power dissipation is much larger because of the necessary larger amplitude of the excitation field. Just like in the low field region, qualitatively the experimental results obtained with the mesh outcoupler are similar to those with the mirror outcoupler. The delay between HV pulse and start of laser action however is smaller and the small signal gain is higher. In Fig. 8 a typical result using the mesh outcoupler for B = 0.7 T is shown. Apart from the pulse shape of the optical output at four wavelengths, also the HV excitation pulse, is shown. The two step increase of the amplitude of the excitation pulse is clearly seen. The initial crystal temperature was T=4.2 K. The delay time is found to be now only about 350 ns instead of 700 ns with mirror outcoupling. Moreover, the duration of the optical pulse is much longer. Whereas formerly an ultimate duration of 3 μs could be realised at this B-field, with the mesh outcoupler, durations of up to 6 μs have been observed.The wavelength dependence of the time delay in the high field region is more complicated than in low field. In Fig. 9 an example for B=0.9T with mirror outcoupling is given. Laser action does start at the shortest wavelength, but the intensity at 103 μm shows two peaks as a function of time. Clearly some sort of mode competition with the 105 μm component occurs. In this shorter wavelength region, the delay of laser action does not depend in a simple way on the wavelength as is the case

63

in the low field region. In many circumstances laser action starts at an intermediate wavelength, with contributions at both shorter and longer wavelength developing after some time. In view of the results shown in fig. 7, this effect may quite well be related to the occurrence of a higher lattice temperature in this high field active region. The nature of the pulse to pulse variations of the intensities at different wavelengths, together with the odd temperature dependent effects, suggest that the optical pumping mechanisms as proposed earlier[15] are rather unlikely. They also seem to contradict the supposed homogeneous character of the inter valence band transition.[16] Besides these effects, especially with the mesh outcoupler, intensity oscillations on a time scale of about 20 ns are observed. Such oscillations, have also been observed by other authors,[17] and are probably related to beating of different transversal modes present within the cavity.[18] In Fig. 10 a detail of the optical pulse for B=0.4T (λ=172 μm) clearly shows these $\approx$ 20 ns oscillations. Also visible are oscillations with a 1.3 ns repetition time (= cavity roundtrip time) that result from auto-mode locking of the laser.
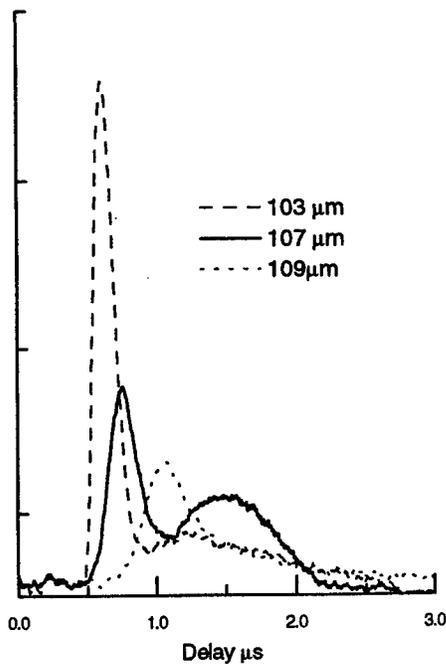
Figure 9. Shape of the optical pulses at B=0.9T for three wavelengths (mirror outcoupling) showing the peculiar time dependent intensity variations.
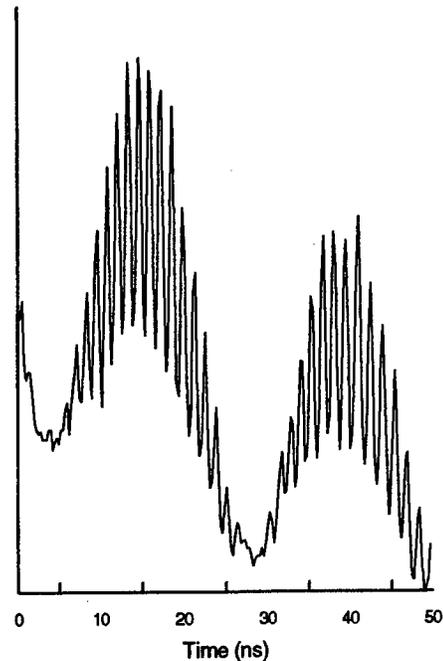
Figure 10. Detail of the optical pulse at B=0.4T (λ=172 μm), showing the $\approx$ 20 ns oscillations and the short pulse forming resulting from auto-mode locking.

3.2. Mode locked operation

With the modulation field $\vec{E}_{\nu}$ || $\vec{B}$ applied, active mode locking of the laser is achieved.[6,7] Both in the low and in the high B-field region the overall wavelength ranges are slightly smaller and the time delays slightly larger than observed for pulsed operation. This is possibly related to the disturbing effect of the rf modulation field on the start of laser action.[11]A detailed view on the time resolved output of the mode locked laser has been obtained using the 6 GHz bandwidth real time oscilloscope. In the early stage of laser action, see Fig. 11, a regular train of pulses with a separation equal to the 1.3 ns cavity round trip time, is observed. The increase of intensity of successive pulses reflects the small signal gain per cavity round trip of the optical pulse. Also a decrease of pulse width, typical for the build up period of mode locked operation, is observed. The small signal gain is found to be slightly larger than for normal pulsed operation at equal E and B fields. With the mesh outcoupler a small signal gain as high as 0.06 cm^{-1} has been observed for λ = 172 μm.

The rf field causes a considerable loss of gain in that part of the crystal which is situated in between the modulation electrodes, i.e. in 20% of the overall length of the active medium. The larger roundtrip gain under active mode

locking conditions clearly shows that the optical pulse does experience a substantial larger gain in the unmodulated part of the crystal than the quasi CW small signal gain as observed for normal pulsed operation. That suggests that the lifetime of the induced population inversion in that part of the crystal is a non-negligible fraction of the 1.3 ns cavity round trip time. This conclusion is corroborated by the observation that, under otherwise equal conditions, without the rf modulation applied, the small signal gain in the case of self mode locked operation can be nearly twice as large.[7]

Under saturated gain conditions, a train of constant amplitude, narrow pulses is observed, see Fig. 12. The wiggles in the tail of the pulses are the result of internal reflections in the detector unit, due to a slight impedance mismatch. In the low field region, the minimum width of these pulses is found to be about 100 ps FWHM. The electronic risetime of the detection system - Schottky diode, bias-T and amplifiers - has been determined to be about 100 ps. It is therefore conceivable that the actual minimum width of the pulses may even be shorter. In the high field regime, up till now, a minimum pulse width of 140 ps has been measured, using a different Schottky diode detector.
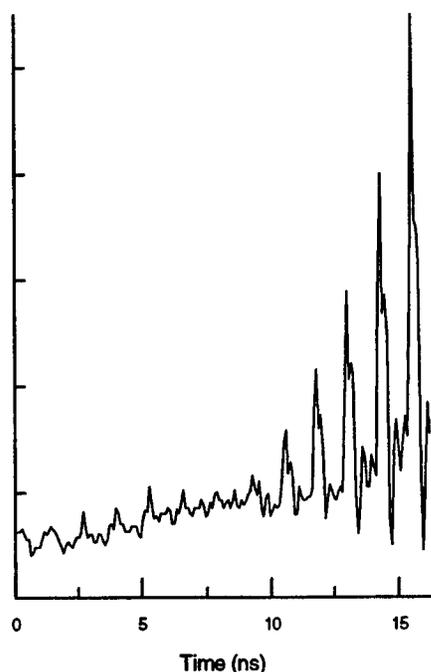
Figure 11. Single shot laser output for $\lambda \approx 172 \ \mu$m in the early start of laser action.
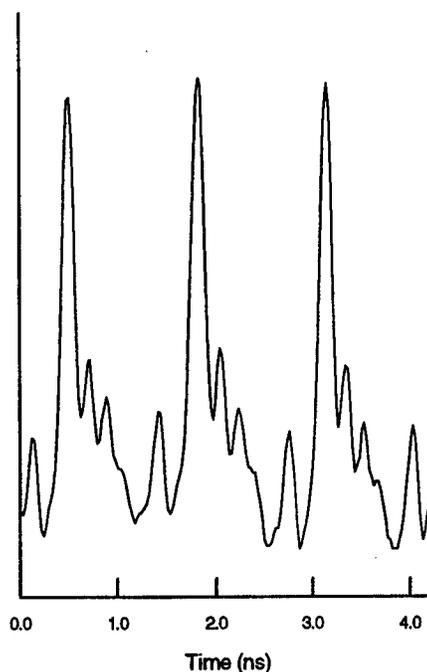
Figure 12. Pulse train in saturated gain region for $\lambda \approx 172 \ \mu$m

It must be noted that the mode locked pulses depicted in Fig.'s 11 and 12 represent "best typical" results. Because of the variation of emission wavelengths during laser action, the duration of stationary mode locking is rather limited. Consider for instance the yet best studied region near $\lambda \approx 172 \ \mu$m. Similar as for long pulsed operation, also under active gain modulation, the laser action in the 177-182 μm region is delayed with respect to that in the 172 μm region. The much smaller gain at these wavelengths is lowered even more by the disturbing effect of the rf modulation field. As a consequence, no genuine mode locking is observed for that wavelength region. Only a low intensity amplitude modulated output is seen, without the above described clear mode locking characteristics. As a result from the additional lowering of the gain in the long wavelength region due to the modulation field , proper mode locked action at 172 μm is sustained longer than would be expected from the time resolved experiments under long pulsed operation. Nevertheless, the duration of a properly behaving pulse train is only of the order of a few hundred nanoseconds.

In the high field region, similar effects occur. However, due to the even more complicated time dependence of the emission frequencies, the creation of a well behaving pulse train is more difficult.

4. CONCLUSION

The results of a time- and wavelength resolved study of the optical output of the pulsed and mode locked p-Ge hot hole laser, emitting in the THz range, have been reported. The system is able to produce trains of 100 ps FWHM pulses, but the time dependent variation of the emission wavelength *during* the laser excitation, still causes problems. Moreover, a faster detection technique should be employed to measure the actual width of the mode locked pulses. The introduction of a mesh outcoupler has lead to a number of improvements. Because now the central part of the cavity is monitored, the optical output has increased. The experimental results show clearly that in the center of the cavity the optical gain is much higher, leading to an increase of the E-B region for which laser action occurs. The delay of laser action after the start of the HV excitation pulse has diminished, the small signal gain is larger, and laser action is sustained for a longer time. Although the mesh introduces a wavelength dependent cavity roundtrip losses, strongly modulated by etalon effects, the emission remains very broad band.

5. ACKNOWLEDGMENT

REFERENCES

1. E. Gornik and A. A. Andronov, Eds.,Opt. Quantum Electron., vol. 23,Chapman and Hall, London, 1991,Special Issue on Far-infrared Semiconductor Lasers.
2. E. Bründermann, A.M. Linhart, H.P. Röser, O.D. Dubon, W.L. Hansen, E.E. Haller, "Miniaturization of p-Ge lasers: Progress toward continuous wave operation", Appl. Phys. Lett. vol. 68, pp. 1359–1361, 1996.
3. E. Bründermann, A.M. Linhart, L.A. Reichertz, H.P. Röser, O.D. Dubon, G. Sirmain, W.L. Hansen, E.E. Haller, "Double acceptor doped Ge: A new medium for inter-valence-band lasers" Appl. Phys. Lett. vol. 68, pp. 3075–3077, 1996.
4. E. Bründermann, D.R. Chamberlain, E.E. Haller "Thermal effects in widely tunable germanium terahertz lasers " Appl. Phys. Lett., vol. 73, pp. 2757–2759 , 1998.
5. R.C. Strijbos, J.G.S. Lok, and W.Th. Wenckebach, "A Monte Carlo simulation of mode-locked hot-hole laser operation," J. Phys. Condens. Matter, vol. 6, pp. 7461– 7468, 1994.
6. J.N. Hovenier, A.V. Muravjov, S.G. Pavlov, V.N. Shastin, R.C. Strijbos, W.Th. Wenckebach, "Active mode locking of a p-Ge hot hole laser ", Appl. Phys. Lett. vol. 71, pp. 443–445, 1997.
7. J.N. Hovenier, T.O. Klaassen, W.Th. Wenckebach, A.V. Muravjov, S.G. Pavlov, V.N. Shastin, "Gain of the mode locked p-Ge laser in the low field region", Appl. Phys. Lett. vol. 72, pp. 1140–1142, 1998.
8. J.N. Hovenier, M.C. Diez, T.O. Klaassen, W.Th. Wenckebach, A.V. Muravjov, S.G. Pavlov, V.N. Shastin, "Realisation of active mode locking of the p-Ge hot hole laser", Conference Digest 23rd International Conference on Infrared and Millimeter Waves, September 7-11, 1998, Colchester, Essex, U.K., Eds. T.J. Parker and S.R.P. Smith (ISBN 0 9533839 0 3) p. 37-9.
9. J.N. Hovenier, M.C. Diez, T.O. Klaassen, W.Th. Wenckebach, A.V. Muravjov, S.G. Pavlov, V.N. Shastin, "The p-Ge THz laser in low B-field: properties under pulsed and mode locked operation", Proceedings 6th IEEE International Conference on Terahertz Electronics THz98, 3-4 September 1998, Leeds, U.K., Ed. P. Harrison, (IEEE catalog no. 98EX171, ISBN 0 7803 4903 2) p.90-3.
10. T.O. Klaassen, J.N. Hovenier, M.C. Diez and W.Th. Wenckebach, A.V. Murav'jov, S.G. Pavlov and V.N. Shastin, "Wavelength dependent properties of the pulsed and mode locked p-Ge THz laser", Proceedings of the Annual Symposium IEEE/LEOS (Benelux Chapter), 26 November 1998, Gent, Belgium, (Eds. P. Demeester, R. Baets, A. Ackaert, V. Masquelin) ISBN 90-76546-01-0, pp. 161-164.

11. J.N. Hovenier, M.C. Diez, T.O. Klaassen, W.Th. Wenckebach, A.V. Muravjov, S.G. Pavlov, V.N. Shastin, "The p-Ge THz laser: properties under pulsed and mode locked operation", submitted to IEEE Trans. Micr. Theory Tech., Special Issue on Terahertz Electronics.

12. W. Heiss, K. Unterrainer, E. Gornik, W.L. Hansen, E.E. Haller, "Influence of impurity absorption on germanium hot-hole laser spectra", Semicond. Sci. Technol. vol. 9, pp. 638–640, 1994.

13. L.A. Reichertz, O.D. Dubon, G, Sirmain, E. Bründermann, W.L. Hansen, D.R. Chamberlain, A.M. Linhart, H.P. Röser, E.E. Haller, "Stimulated far-infrared emission from combined cyclotron resonances in germanium ",Phys. Rev. vol. B 56, pp. 12069– 12072, 1997.

14. S. Komiyama, S. Kuroda, I. Hosako, Y. Akasaka, N. Iizuka, " Germanium lasers in the range from far-infrared to millimeter waves " Opt. Quantum Electron. vol. 23 pp. S133–162, 1991.

15. S.V. Demihovsky, A.V. Murav'ev, S.G. Pavlov and V.N. Shastin "Stimulated emission using the tramsitions of shallow acceptor states in germanium" , Semicond. Sci. Technol. vol. 7, pp. B622– B625, 1992.

16. F. Keilmann and R. Till, "Nonlinear far-infrared response of passive and active hole systems in p-Ge," Semicond. Sci. Technol., vol. 7, pp. B633–B635, 1992.

17. A.V. Muravjov, R.C. Strijbos, C.J. Fredricksen, H. Weidner, W. Trimble, S.H. Withers, S.G. Pavlov, V.N. Shastin, R.E. Peale, " Evidence for self- mode-locking in p-Ge laser emission", Appl. Phys. Lett. vol. 73 pp. 3037–3039, 1998.

18. A.V. Bespalov , "Temporal and mode structure of the interband p-Ge laser emission", Appl. Phys. Lett., vol. 66, pp. 2703–2705, 1995.

SESSION 2

Electronic Sources

Two-terminal devices as fundamental solid-state terahertz oscillators

H. Eisele

Solid-State Electronics Laboratory, Department of Electrical Engineering & Computer Science
The University of Michigan, Ann Arbor, Michigan 48109-2122

ABSTRACT

The state-of-the-art radio frequency (RF) power levels at millimeter- and submillimeter-wave frequencies as well as the low-noise properties make GaAs tunnel injection transit-time (TUNNETT) diodes and InP Gunn devices prime candidates for fundamental solid-state terahertz oscillators. As examples, RF power levels of > 130 mW at 132 GHz, > 80 mW at 152 GHz, and > 1 mW at 315 GHz were measured with InP Gunn devices, whereas RF power levels of 100 mW at 107 GHz and > 10 mW at 202 GHz were measured with GaAs TUNNETT diodes. These experimental results as well as performance predictions for these devices at terahertz frequencies are reviewed and compared with the potential and the capabilities of other two-terminal devices such as impact avalanche transit-time (IMPATT) diodes and resonant-tunneling diodes (RTDs). The paper also summarizes advances in fabrication technologies as well as the application of more recent device principles and power-combining schemes.

Keywords: Gunn devices, millimeter-wave devices, millimeter-wave generation, millimeter-wave oscillators, oscillator noise, phase noise, submillimeter-wave devices, submillimeter-wave generation, submillimeter-wave oscillators, transit-time diodes.

1. INTRODUCTION

Reliable and compact radio frequency (RF) sources with low direct current (dc) power consumption are needed as a key component in rapidly emerging applications at submillimeter-wave frequencies such as upper atmospheric imagery, remote sensing, array receivers in radio astronomy, high-resolution near-object analysis, and ultra wide bandwidth intersatellite communications. Several types of solid-state devices are good candidates for these applications [1] as their power generation capabilities were demonstrated

E-mail: heribert@engin.umich.edu
Tel.: (734) 764-3354   Fax: (734) 647-1781

already at high millimeter-wave frequencies and beyond. The practical application of more recent as well as more "classical" principles [2], [3], [4] resulted in major advances of the device performance, which have also been enabled by materials of superior properties or quality as well as much improved processing technologies.

Rapid advances in the upper frequency limits [5]–[10] and RF power levels of three-terminal devices in amplifiers [11] as well as their ever-increasing use in systems applications are being reported up to millimeter-wave frequencies. Nonetheless, there have been a few practical demonstrations of fundamental oscillators with three-terminal devices above 100 GHz, and, in addition, only low RF power levels of much less than 1 mW were reported [12], [13]. Two representatives of two-terminal devices, *i.e.*, Gunn or transferred-electron devices (TEDs) and impact avalanche transit-time (IMPATT) diodes, are operated at higher oscillation frequencies than three-terminal devices and, together with vacuum tubes, still play quite an important role in systems applications.

This paper reviews the basic characteristics of different two-terminal devices as well as various approaches to continuous (CW) RF power generation at submillimeter-wave frequencies. It compares recent experimental results from InP Gunn devices and GaAs tunnel injection transit-time (TUNNETT) diodes above 100 GHz with performance predictions. The properties and capabilities of other potential candidates for solid-state fundamental sources, such as resonant-tunneling diodes (RTDs) and impact avalanche transit-time (IMPATT) diodes, are discussed with respect to the performance of TUNNETT diodes and Gunn devices.

2. TECHNOLOGY ISSUES

Generally, dc-to-RF conversion efficiencies decrease with frequency and, at high millimeter-wave frequencies, rarely exceed 10% [1]. Therefore, most of the dc input power needs to be dissipated as heat, and proper heat management

70

Part of the EUROPTO Conference on Terahertz Spectroscopy and Applications II
Munich, Germany • June 1999 SPIE Vol. 3828 • 0277-786X/99/$10.00

becomes as crucial a technological issue as appropriate low-loss circuits for extraction of the highest RF power levels from these devices. Selective etching technologies [1], [14] yield substrateless devices with low thermal resistances, particularly on diamond heat sinks, but also help minimize the skin-effect resistance as much as possible. These technologies enabled the recent experimental results above 100 GHz with state-of-the-art performance from Si IMPATT [15], GaAs IMPATT [14], [16] and GaAs TUNNETT [14], [17], [18] diodes as well as InP Gunn devices [14], [19], [20], the properties of which are discussed in subsequent sections. The use of diamond heat sinks or heat spreaders becomes mandatory when the highest RF power levels at millimeter- and submillimeter-wave frequencies need to be generated with these devices [1], [14].

3. RTDS AND OTHER QUANTUM-WELL DEVICES

Resonant tunneling through discrete energy levels of a so-called quantum well was first demonstrated in 1974 [4]. However, only after major advances in growth techniques, such as molecular beam epitaxy (MBE) or metalorganic chemical vapor deposition (MOCVD), in the 1980s were device structures suitable for oscillators grown and evaluated. As can be seen from Fig. 1, RTDs in the InAs/AlSb material system yielded the highest oscillation frequency of any fundamental solid-state RF source [21], [22], but RF power levels of, for example, 3 μW at 360 GHz and 0.3 μW at 712 GHz are low [22]. This makes it very difficult to employ standard phase-locking techniques either for frequency stabilization or in systems applications where the exact oscillation frequency must be known or be tied to a very accurate reference frequency. The negative differential resistance that is present in RTDs from dc to the highest oscillation frequencies causes RF sources with RTDs from any semiconductor material system to be prone to severe instabilities or bias oscillations and ultimately limits their RF power generating capabilities. Monolithic integration [23] and power combining [23], [24] was shown to alleviate some of these problems. Although an example of an RTD-based local oscillator (LO) for a receiver system was demonstrated [25], problems associated with RTDs have so far prevented their use in systems applications. Present measurement equipment offers only limited sensitivity, which degrades significantly at submillimeter-wave frequencies. Therefore, the low RF power levels from RTDs also severely restrict how accurately important oscillator characteristics such as free-running oscillator spectra and oscillation frequency vs. temperature or dc bias, can be determined.

A record dc-to-RF conversion efficiency of 50% at a microwave frequency of 2 GHz for an RF output power of 20 mW [26] was reported from a quantum well injection transit-time (QWITT) diode, which, in this case, basically was an RTD with a very short adjacent drift region. In contrast and shown in Fig. 1, dc-to-RF conversion efficiencies of RTDs at millimeter- and submillimeter-wave frequencies fall well below 1% and may indicate inferior impedance matching and/or significant losses from series resistances in ohmic contacts and circuit.
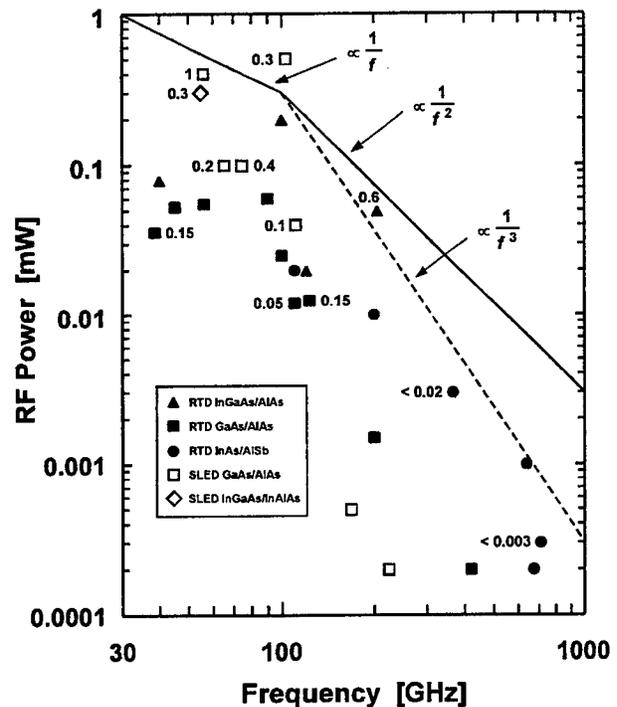
Fig. 1. Published state-of-the art results from RTDs and SLEDs in the 30–1000 GHz frequency range. Numbers next to the symbols denote dc-to-RF conversion efficiencies in percent, where applicable.

More recently, superlattice electronic devices (SLEDs) were demonstrated as millimeter-wave oscillators [27]–[30]. Except for a quasi-planar circuit in a WR-15/WR-6 waveguide combination [27], the devices were not mounted in a resonant cavity, but quasi-planar structures were contacted with different ground-signal or ground-signal-ground (GSG) probes for V-band (50–75 GHz) or W-band (75–110 GHz) [28]–[30]. As an example, the setup with a GSG probe for W-band is illustrated in Fig. 2 [30]. Recorded spectra of these SLEDs in free-running oscillators are not as clean as, for example, those of Gunn devices in free-running oscillators, but quite narrow-band for a nonresonant circuit or for very low quality factors Q, and this feature points to inherent device properties such as the

so-called Bloch oscillations. Reported RF power levels (and corresponding dc-to-RF conversion efficiencies), which are included in Fig. 1, were 0.4 mW (1%) at the fundamental frequency of 56 GHz, and 40 μW (0.1%) at the second-harmonic frequency of 112 GHz from the quasi-planar circuit configuration in a waveguide [27] as well as 0.5 mW at 103 GHz (0.3%) as measured with the GSG probe and a spectrum analyzer [30]. The length of the active region ranges approximately from 0.44 μm to 0.64 μm in these SLEDs, and, therefore, the higher oscillation frequency of 103 GHz is attributed to much narrower barriers of the quantum wells, which are only two monolayers of AlAs thick and cause a larger miniband width of 120 meV [30].
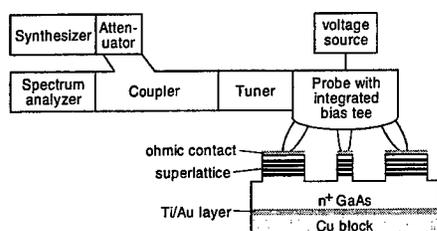
Fig. 2. Experimental setup for evaluation of SLEDs at W-band frequencies. After E. Schomburg et al. [30].

At comparable dc-to-RF conversion efficiencies, RF power levels from SLEDs are higher than those from RTDs, whereas they are still much lower than those from IMPATT and TUNNETT diodes as well Gunn devices at the same frequencies. These RF power levels P_{RF} were measured with two-terminal devices of quite different device areas A. Therefore, the RF power density Φ_{RF} (= P_{RF}/A) provides a fairer comparison of the power generating capabilities of various two-terminal devices and should be considered analogous to the performance comparisons quoted as RF power per gate length for three-terminal devices such as field-effect transistors (FETs) or high electron mobility transistors (HEMTs). Fig. 3 shows Φ_{RF} as derived from published state-of-the-art-results and device areas in the 30–1000 GHz frequency range for device types that, so far, have yielded measurable RF power levels above 200 GHz. As a result of high bias current densities and high dc-to-RF conversion efficiencies in IMPATT diodes, Φ_{RF} is by far the highest in Si and GaAs IMPATT diodes and exceeds that of RTDs, but also SLEDs, by typically more than two orders of magnitude up to D-band (110–170 GHz) frequencies. In addition, Φ_{RF} of GaAs TUNNETT diodes and Gunn devices exceeds that of RTDs and SLEDs up to the highest oscillation frequencies as well. Φ_{RF} of SLEDs from the GaAs/AlAs material system is only higher than that of RTDs from the same material system, but, quite importantly, SLEDs are not associ-

ated with the same severe restrictions [1], [14] that bias instabilities impose on device areas and, consequently, RF power generation capabilities of RTDs. As a consequence, higher RF power levels can be expected from SLEDs with larger areas in appropriate millimeter-wave circuits that match the accordingly lower device impedance levels to the RF load. Furthermore, the experimental result at 103 GHz [30] indicates the potential of reaching higher oscillation frequencies with SLEDs than with GaAs Gunn devices.
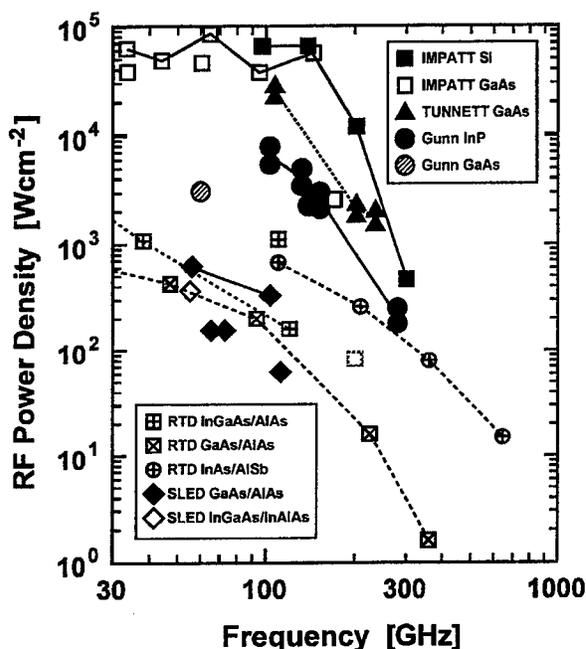
Fig. 3. RF power densities in two-terminal devices as derived from published state-of-the art results (Ranges given for InP Gunn devices and GaAs TUNNETT diodes due to uncertainties in device areas, lines between data points are only as a guide to the eye).

4. TRANSIT-TIME DIODES

Si IMPATT diodes were the first semiconductor devices to generate RF power above 300 GHz and, as shown in Fig. 4 (and in conjunction with Fig. 1 and Fig. 6), yielded the highest RF power levels from any solid-state fundamental RF source up to 300 GHz. Exemplary RF power levels (and corresponding dc-to-RF conversion efficiencies) of 50 mW (1.3%) at 202 GHz [31], 44 mW (1.2%) at 214 GHz [31], 50 mW (< 2%) at 217 GHz [32], [33], 50 mW (< 1%) at 245 GHz [33], 12 mW (< 0.5%) at 255 GHz [33], 7.5 mW (0.35%) at 285 GHz [34], 1.2 mW (< 0.05%) at 301 GHz [31], and 0.2 mW at 361 GHz [34] were measured at very high operating junction tempera-

tures of typically more than 300 °C with waveguide circuits at room temperature [32]. Higher RF power levels and oscillation frequencies were attained by cooling the heat sink of the diode and the waveguide circuit to 77 K (liquid nitrogen) and 4.5 mW (0.13%) at 295 GHz, 2.2 mW (0.047%) at 412 GHz were reported [35].
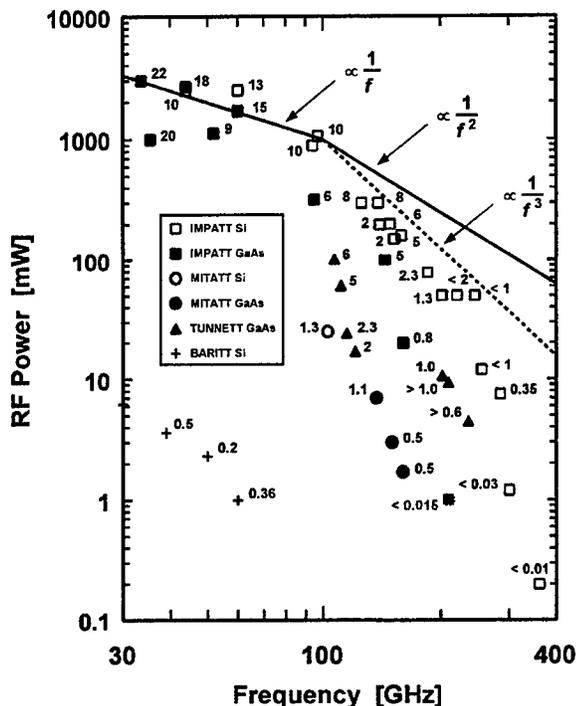
Fig. 4. Published state-of-the-art results from Si and GaAs transit-time diodes under CW operation in the frequency range of 30–400 GHz. Numbers next to the symbols denote dc-to-RF conversion efficiencies in percent.

Impact ionization as the carrier generation mechanism in IMPATT diodes creates more significant contributions to the noise than, for example, the mainly thermal noise in the domain formation process of Gunn devices [1], [2]. Therefore, IMPATT diodes are generally considered quite noisy although techniques are known how to minimize the noise contribution from impact ionization at the price of typically lower dc-to-RF conversion efficiencies [1], [2]. The noise properties of IMPATT diodes restrict their use as LO sources to either receiver applications where the highest sensitivity is not the primary concern or sensitive low-noise receivers in which the noise cancellation effect of subharmonically pumped mixers with well-balanced Schottky diodes is utilized [36].

TUNNETT diodes are based on a fast and quiet primary carrier injection mechanism [1], [2], which makes them another prime candidate for RF generation at high milli-

meter-wave and submillimeter-wave frequencies. RF power levels of 100 ± 5 mW and corresponding dc-to-RF conversion efficiencies of around 6% were measured with single-drift GaAs TUNNETT diodes in the fundamental mode at oscillation frequencies of 100–107 GHz [14], [17]. Excellent agreement was found between these experimental results and predictions [37] from simulation programs that employ an "equivalent" two-valley model for the conduction band in GaAs and solve the energy-momentum equations for electrons as well as the drift-diffusion equations for holes [38]. The same simulation programs also predicted that RF power levels on the order of 10 mW can be generated in the 240–280 GHz frequency range with GaAs single-drift TUNNETT diodes in the fundamental mode [38]. However, they also revealed that excellent ohmic contacts and low-loss circuits at these high-millimeter and submillimeter-wave frequencies are a primary prerequisite [38].

Power extraction at higher harmonic frequencies was investigated with Si [31], [39] and GaAs [40], [41] IMPATT diodes as well as GaAs TUNNETT diodes [14] [18]. Diode structures and properties suggest operation in second- or even third-harmonic mode for some of the aforementioned state-of-the-art results from Si IMPATT diodes above 200 GHz. As an example, the RF power of 1.2 mW at 301 GHz was thought to be generated at the third harmonic frequency [31]. However, for many other results at these high millimeter-wave frequencies no attempts to determine the exact mode of operation were reported.

Aforementioned GaAs TUNNETT diodes on diamond heat sinks were operated in a second-harmonic mode up to 237 GHz and yielded RF power levels exceeding 10 mW at 202 GHz, 9 mW around 210 GHz, and 4 mW around 235 GHz [18]. These power levels correspond to dc-to-RF conversion efficiencies around 1% at 202 GHz and 210 GHz as well as above 0.6% around 235 GHz [18]. Simulations using the same aforementioned two-valley energy-momentum programs revealed a mode of operation with a large modulation of the depletion region akin to that in high-performance varactor diodes. This mode of operation also explains the high up-conversion efficiencies, which exceeded 20% for the best results at 202 GHz, 210 GHz, and 235 GHz. Since this mode of operation exhibits its performance peak in these diodes below the maximum permissible bias current density [18], higher RF power levels and higher operating frequencies can be expected from TUNNETT diodes with shorter active regions and doping concentrations appropriate for higher current densities. The measured RF power levels and, particularly, conversion efficiencies of these TUNNETT diodes in a second-harmonic mode are comparable to those obtained from frequency multipliers where, for example, Schottky-barrier varactor diodes are driven by Gunn devices [42],

[43]. Fig. 5 compares these results from various frequency multipliers in the 100–1000 GHz frequency range with select results from GaAs TUNNETT diodes, InP Gunn devices and RTDs.
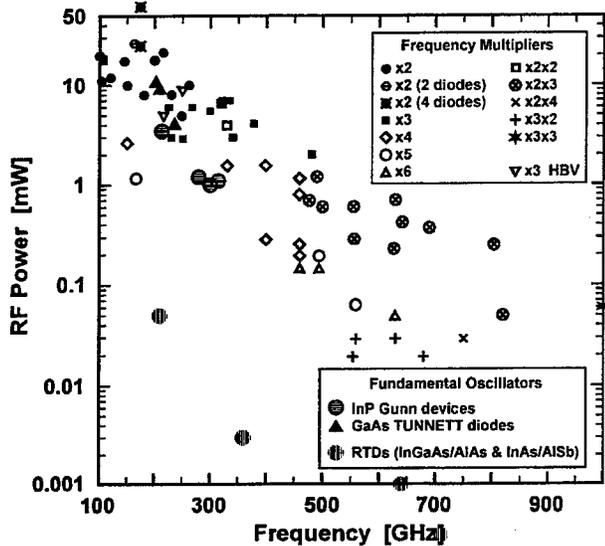
Fig. 5. Published state-of-the-art results from frequency multipliers with GaAs Schottky-barrier or InP-based heterojunction-barrier varactor diodes in the 100–1000 GHz frequency range in comparison with published state-of-the-art results from GaAs TUNNETT diodes, InP Gunn devices, and RTDs above 200 GHz.

Spectra were recorded from all TUNNETT diodes when they were operated as free-running oscillators at bias currents with significant RF power levels. They appeared to be very clean, and, as an example, an uncorrected phase noise of −94 dBc/Hz was determined at 500 kHz off the oscillation frequency of 209.377 GHz and at an RF power of 9 mW [18]. This phase noise correctly reflects values of well below −94 dBc/Hz in the fundamental mode at W-band frequencies [17], [14]. Since the phase noise is at the noise floor of the employed spectrum analyzer with a harmonic mixer, the corrected phase noise is estimated to be well below −98 dBc/Hz. TUNNETT diodes also yielded the lowest small-signal frequency-modulation (FM) noise measure reported from any oscillator with a two-terminal device [1], [14].

Contrary to preliminary results from GaAs TUNNETT diodes [14], [17], a very preliminary study of the properties of single-drift GaAs IMPATT diodes in a second-harmonic mode found that the measured spectra of free-running oscillators with these diodes [44] were clearly not as clean as those of free-running oscillators with TUNNETT diodes (or Gunn devices). This result was indeed expected from

approximately 7–8 dB higher values of the small-signal FM noise measure and at least 6 dB higher values of the large-signal FM noise measure of GaAs single-drift IMPATT diodes in the fundamental mode at W-band frequencies [1], [14]. Furthermore, dc-to-RF conversion efficiencies of, for example, 0.04% at 194 GHz [44], were inferior to those of the TUNNETT diodes in a similar circuit configuration [14], [18].

5. TEDS

Despite the rapid progress in three-terminal devices, TEDs still play a nearly indispensable role in transmitter applications or as low-noise local oscillators (LO) at millimeter-wave and submillimeter-wave frequencies, especially if electronic tubes or relatively bulky gas lasers need to be avoided. The typical configuration of an all solid-state LO source at submillimeter-wave frequencies consists of an oscillator with a GaAs or InP Gunn device at a medium millimeter-wave frequency of 60–150 GHz, which drives one or more stages of frequency multipliers with Schottky-barrier varactor diodes [36], [42], [43] or, more recently, heterojunction-barrier varactor diodes [45], [46]. The transferred-electron effect in Gunn devices depends only on bulk semiconductor material properties, i.e., the presence of at least two suitable energy minima in the conduction band, and more than ten semiconductor materials in the III-V and II-VI groups are known to exhibit such characteristics [2], [47], [48]. However, so far, only GaAs and InP have been exploited in commercially available devices for systems applications.

Favorable material parameters of InP, for example, include a higher thermal conductivity, a higher effective transit velocity, and, most importantly, much shorter energy relaxation and acceleration and deceleration times [47]–[52]. Relaxation times impose fundamental physical limits on the maximum operating frequencies of TEDs with short active regions, and these frequency limits have long been thought to be in the range of 100–130 GHz in GaAs and 200–230 GHz in InP [50]–[54]. The difference in the fundamental frequency limits is evident from Fig. 6 where a significant roll-off in the performance of GaAs Gunn devices occurs at around 80 GHz, whereas it sets in at least at twice this frequency for InP Gunn devices. The inherent material properties permit InP Gunn devices to reach higher operating frequencies and generate higher RF power levels [14], [47], [51], [55]. Therefore, this section mainly concentrates on the properties and characteristics of millimeter- and submillimeter-wave oscillators with InP Gunn devices.

InP TEDs with n^-n^+ layer structures and a current-limiting contact at the cathode side of the active region yielded the

highest dc-to-RF conversion at low to medium millimeter-wave frequencies and excellent performance up to D-band frequencies. Examples of RF power levels (and corresponding conversion efficiencies) are 380 mW at 57 GHz (10.6%) in the fundamental mode [52] as well as 175 mW (7%) at 94 GHz, 85 mW (3.8%) at 125 GHz, and 65 mW (2.6%) at 138 GHz in a second-harmonic mode [56], [57].

The highest RF power levels from any Gunn device above 100 GHz were achieved with devices that had an $n^+n^-n^+$ layer structure as well as a graded doping profile in the active region and were mounted on diamond heat sinks [14], [19], [47]. Operation in the fundamental mode was observed up to 165 GHz. As examples, RF power levels (and corresponding dc-to-RF conversion efficiencies) exceeded 200 mW (2.6%) at 103 GHz, [47], [49], [58] 130 mW (2.2%) at 132 GHz, 80 mW (1.4%) at 152 GHz, and 30 mW at 162 GHz [14], [47], [58]. These RF power levels are the highest reported to date from any Gunn device and, together with an excellent noise performance (to be discussed next), make InP Gunn devices ideally suited for driving high-performance Schottky diode frequency multipliers in sensitive terahertz receivers.
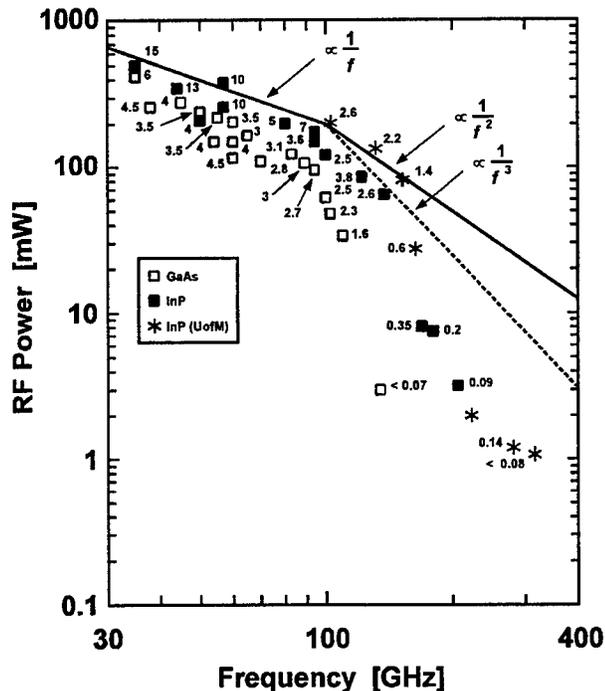
Fig. 6. Published state-of-the-art results from GaAs and InP Gunn devices under CW operation in the frequency range of 30–400 GHz. Numbers next to the symbols denote dc-to-RF conversion efficiencies in percent.

Uncorrected phase noise levels of less than –110 dBc/Hz at 103 GHz and 180 mW [58], less than –105 dBc/Hz at 132 GHz and 120 mW [19] as well as less than –100 dBc/Hz at 151 GHz and 58 mW [19] were all measured at an off-carrier frequency of 500 kHz and reflect the excellent low-noise properties of InP Gunn devices in free-running oscillators. They are typically near the noise floor of the employed spectrum analyzer with a harmonic mixer, and, therefore, corrected values are estimated to be at least 3–5 dB lower. They correspond to excellent values of the large-signal FM noise measure of 20–23 dB in the 95–155 GHz frequency range [1], [14]. Some devices with a current-limiting contact are known to have higher flicker-noise components in the spectra of free-running oscillators, which, in most cases however, are sufficiently suppressed by a phase-locked loop for frequency stabilization.

Operation in a second-harmonic mode somewhat overcomes the inherent fundamental frequency limit in Gunn devices, and RF power levels of more than 3.5 mW at 214 GHz, more than 2 mW around 220 GHz as well as more than 1 mW up to 315 GHz were measured in this mode of operation [20], [58]. The RF power levels above 300 GHz are the highest reported to date from any solid-state fundamental RF source and, as shown in Fig. 5, they approach those from frequency multipliers [42]. These RF power levels even exceed early performance predictions [51], [54], but the results of more recent simulations indicate that significant increases in RF power levels can be expected from more optimized device structures and circuits up to at least 320 GHz [59], [60]. Fig. 7 compares the experimental results in the fundamental mode as well as those in a second-harmonic mode with these recent predictions from detailed simulations [60] that employed a Monte Carlo-based harmonic balance technique [59]. Monte-Carlo simulations were originally used in the design of the D-band structures [61] and showed good agreement between performance predictions and measured results [59], [62]. Various device structures, which were designed for operation in a second-harmonic mode in the 200–310 GHz frequency range and had a doping gradient in the active region as shown schematically in the inset of Fig. 7, were investigated [60].

The measured RF power levels in the fundamental mode at D-band frequencies and the predicted RF power levels for operation in a second-harmonic mode at J-band (220–325 GHz) frequencies follow a clear $1/f^3$ roll-off. This trend evidently shows that substantial performance improvements can be expected from optimized device structures and waveguide circuits at J-band frequencies. This trend may also indicate that the transferred-electron effect in InP could be utilized even above 320 GHz and possibly up to 400 GHz with devices operating in a second- or third-harmonic mode. In addition, the experimental results from

InP Gunn devices above 220 GHz, but also recent results from GaAs Gunn devices in the fundamental mode at W-band frequencies [63], imply that the derivations of fundamental physical frequency limits for the transferred-electron effect in InP and GaAs should be revisited and re-investigated in greater detail.
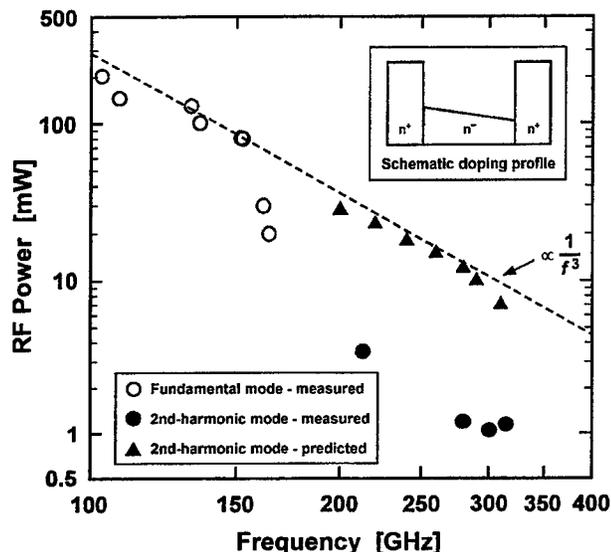
Fig. 7. Comparison of predicted [59], [60] and measured [20], [14] CW RF power levels from InP Gunn devices with an $n^+n^-n^+$ structure and a doping gradient in the active region as shown in the inset for the 100–320 GHz frequency range.

6. POWER COMBINING

Various power-combining techniques relevant to RF power generation at terahertz frequencies were investigated with most of the two-terminal devices discussed in this paper, such as RTDs [23], [24], IMPATT diodes [33], TUNNETT diodes [14], [17] as well as Gunn devices [14], [49], [58], and approaches to power combining at the device- or chip-level, circuit-level and beyond were reviewed in great detail elsewhere [55], [64], [65].

Recent experiments are based on somewhat classical approaches as well as novel principles. Power combing of two GaAs TUNNETT diodes [14], [17] or two InP Gunn devices [14], [49], [58] operating in the fundamental mode is straightforward in a simple in-line dual-cavity waveguide configuration and typically yields combining efficiencies above 80%. It increased the RF power levels available from InP Gunn devices to 305 mW at 106 GHz in W-band [49], 130 mW at 136 GHz [49], and 125 mW at 152 GHz in D-band [58] with typical combining efficiencies of more

than 80% at 106 GHz and 136 GHz [49] as well as more than 100% at 152 GHz [49], [58].

Spatial power combining of nine InP Gunn devices in an overmoded waveguide resonator resulted in the RF output power of 1.5 W at 61.4 GHz with a corresponding combining efficiency of 83% [66], [67]. Promising preliminary results at W-band frequencies in an appropriately scaled configuration with RF power levels around 450 mW and combining efficiencies around 52% at 98.8 GHz were also reported [67].

The number of oscillators is often limited in such approaches to power combining, but a novel principle in quasi-optical power-combining, that is, holographic power combining, helps overcome these limits. The advantages of holographic power combining are high combining efficiencies and no fundamental limits on the number of oscillators as well as a free choice of oscillator spacing for almost unrestricted heat dissipation [68]. This principle was applied to the power combining of five oscillators with GaAs Gunn devices in a linear array at 24 GHz [68], and, currently, more detailed experiments are being carried out using five oscillators with Si IMPATT diodes at V-band frequencies [69] also in a linear array.
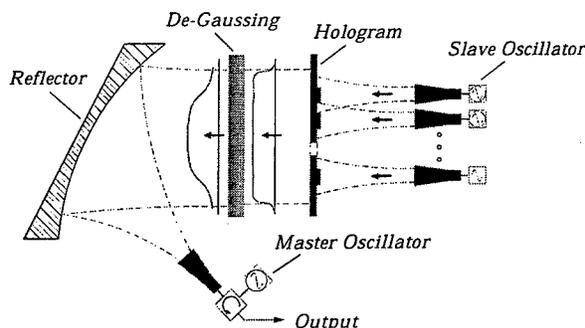
Fig. 8. Schematic of holographic power combining at millimeter- and submillimeter-wave frequencies [68], [69].

7. SUMMARY AND FUTURE TRENDS

RF power generating capabilities of several two-terminal devices were reviewed and compared. Compared to GaAs, InP is the better semiconductor material system to reach submillimeter-wave frequencies with Gunn devices. Experimental results from both GaAs and InP Gunn devices indicate that the fundamental frequency limit of the transferred-electron effect may be higher than previously thought. More detailed studies are necessary to determine the ultimate fundamental frequency limit, i.e., if InP Gunn devices are capable of generating significant RF power

levels in the 320–400 GHz frequency range. Nonetheless, simulations predict that substantial performance improvements are feasible in the 220–320 GHz frequency range, which may help eliminate one or two stages in a multiplier chain to reach terahertz frequencies.

As can be seen from the published results in Fig. 1, Fig. 4, and Fig. 6, the RF power levels from InP Gunn devices on diamond heat sinks are the highest reported to date from any solid-state fundamental RF source operated at room temperature and for frequencies above 300 GHz. Likewise, GaAs TUNNETT diodes are considered the second-most powerful solid-state fundamental RF source operated at room temperature and for frequencies above 200 GHz.

Reliable long-term operation requires the heat dissipation in the device to be minimized. Both Gunn devices and TUNNETT diodes on diamond heat sinks meet these requirements since the above-mentioned state-of-the-art-results were obtained at "cool" operating active-layer temperatures estimated to be generally below 200 °C, but most often well below 150 °C [17], [18], [20], [58].

Superconductor-insulator-superconductor (SIS) junctions or hot-electron bolometers are state-of-the-art mixing elements in receivers at submillimeter-wave frequencies. Either mixing element requires only modest LO power levels, and fixed-tuned circuits offer large bandwidths. Therefore, electronic tunability over a wide frequency range is one desired feature in submillimeter-wave local oscillators, but, so far, has not yet been addressed widely in fundamental RF sources at millimeter- and submillimeter-wave frequencies.

Other semiconductor material systems, such as GaN or InN, are known to exhibit a transferred-electron effect [47] which could be utilized for millimeter-wave Gunn devices. However, various Monte Carlo simulations predict its onset to occur in these semiconductor materials at five to more than ten times higher threshold electric fields than in InP [70]–[73]. Furthermore, much smaller values for the negative differential mobility at electric fields above twice the threshold field, as well as lower values for the low-field electron mobility, require much higher doping × length products for rapid domain formation than in GaAs or InP. Higher electric fields and, as a result, bias voltages, will enhance the RF power generating capabilities, but, together with higher doping × length products, may cause dc input power densities that are at least one order of magnitude higher than in InP and, even on diamond heat sinks, result in excessive overheating in the device. As a consequence, major advances in material growth, material characterization, and experimental verification of material properties and parameters, as well as appropriate device fabrication technologies, are required before the potential and capa-

bilities of any of these material systems can be fully assessed and eventually utilized.

ACKNOWLEDGMENTS

REFERENCES

[1] H. Eisele and G. I. Haddad, "Active Microwave Diodes", in *Modern Semiconductor Devices*, S. M. Sze, Ed., Ch. 6, John Wiley & Sons, New York, 1997, pp. 343–407.

[2] S. M. Sze, *Physics of Semiconductor Devices*, 2nd Ed., John Wiley & Sons, New York, 1981.

[3] L. Esaki and R. Tsu, "Superlattice and negative differential conductivity in semiconductors", *IBM J. Res. Develop.*, **14**(1), 1970, pp. 61–65.

[4] L. L. Chang, L. Esaki, and R. Tsu, "Resonant tunneling in semiconductor double-barriers", *Appl. Phys. Lett.*, **24**(12), 1974, pp. 593–595.

[5] H. Wang, R. Lai, Y. L. Kok, T. W. Huang, M. V. Aust, Y. C. Chen, P. H. Siegel, T. Gaier, R. J. Dengler, and B. R. Allen, "A 155-GHz monolithic low-noise amplifier", *IEEE Trans. Microwave Theory Tech.*, **46**(11), 1998, pp. 1660–1666.

[6] B. Agarwal, A. E. Schmitz, J. J. Brown, M. Matloubian, M. G. Case, M. Le, M. Lui, and M. J. W. Rodwell, "112-GHz, 157-GHz, and 180-GHz InP HEMT traveling-wave amplifiers", *IEEE Trans. Microwave Theory Tech.*, **46**(12), 1998, pp. 2553–2559.

[7] S. Weinreb, P. C. Chao, and W. Copp, "Full-Waveguide Band, 90 To 140 GHz, MMIC Amplifier Module", *IEEE MTT-S Int. Microwave Symp. Dig.*, Denver, CO, June 17–21, 1997, pp. 1279–1280.

[8] R. Lai, M. Barsky, T. Huang, M. Sholley, H. Wang, Y. L. Kok, D. C. Streit, T. Block, P. H. Liu, T. Gaier, and L. Samoska, "An InP HEMT MMIC

LNA with 7.2-dB gain at 190 GHz", *IEEE Microwave Guided Wave Lett.*, **8**(11), 1998, pp. 393–395.

[9] Q. Lee, B. Agarwal, D. Mensa, R. Pullela, J. Guthrie, L. Samoska, and M. J. W. Rodwell, "A > 400 GHz f_{max} transferred-substrate heterojunction bipolar transistor IC technology", *IEEE Electron Device Lett.*, **19**(3), 1998, pp. 77–79.

[10] D. Mensa, Q. Lee, J. Guthrie, S. Jaganathan, and M. J. W. Rodwell, "Transferred-substrate HBTs with 254 GHz f_τ", *Electron. Lett.*, **35**(7), 1999, pp. 288–290.

[11] Y. C. Chen, D. L. Ingram, R. Lai, M. Barsky, R. Grunbacher, T. Block, H. C. Yen, and D. C. Streit, "A 95-GHz InP HEMT MMIC amplifier with 427-mW power output", *IEEE Microwave Guided Wave Lett.*, **8**(11), 1998, pp. 399–401.

[12] Y. Kwon, D. Pavlidis, T. L. Brock, and D.C. Streit, "A *D*-band monolithic fundamental oscillator using InP-based HEMT's", *IEEE Trans. Microwave Theory Tech.*, **41**(12), 1993, pp. 2336-2344.

[13] S. E. Rosenbaum, B. K. Kormanyos, L. M. Jelloian, M. Matloubian, A. S. Brown, L. E. Larson, L. D. Nguyen, M. A. Thompson, L. P. B. Katehi, and G. M. Rebeiz, "155- and 213-GHz AlInAs/GaInAs/InP HEMT MMIC oscillators", *IEEE Trans. Microwave Theory Tech.*, **43**(4), 1995, pp. 927–933.

[14] H. Eisele and G. I. Haddad, "Two-terminal millimeter-wave sources", *IEEE Trans. Microwave Theory Tech.*, **46**(6), 1998, pp. 739–746.

[15] M. Wollitzer, J. Buechler, F. Schäffler, and J.-F. Luy, "*D*-band Si IMPATT diodes with 300 mW CW output power at 140 GHz", *Electron. Lett.*, **32**(2), 1996, pp. 122–123.

[16] M. Tschernitz and J. Freyer, "140 GHz GaAs double-Read IMPATT diodes", *Electron. Lett.*, **31**(7), 1995, pp. 582–583.

[17] H. Eisele and G. I. Haddad, "Enhanced performance in GaAs TUNNETT diode oscillators above 100 GHz through diamond heat sinking and power combining," *IEEE Trans. Microwave Theory Tech.*, **42**(12), 1994, pp. 2498–2503.

[18] H. Eisele, "Efficient second-harmonic power extraction from GaAs TUNNETT diodes above 200 GHz", *Electron. Lett.*, **34**(13), 1998, pp. 1324–1326 **and** *Electron. Lett.*, **34**(15), 1998, pp. 1531.

[19] H. Eisele and G. I. Haddad, "High-performance InP Gunn devices for fundamental-mode operation in *D*-band (110–170 GHz)", *IEEE Microwave Guided Wave Lett.*, **5**(11), 1995, pp. 385–387.

[20] H. Eisele, "Second-harmonic power extraction from InP Gunn devices with more than 1 mW in the 260–320 GHz frequency range", *Electron. Lett.*, **34**(25), 1998, pp. 2412–2413.

[21] E. R. Brown, C. D. Parker, A. R. Calawa, M. J. Manfra, C. L. Chen, L. J. Mahoney, and W. D. Goodhue, "High-frequency resonant-tunneling oscillators", *Microwave Optical Technol. Lett.*, **4**(1), 1991, pp. 19-23.

[22] E. R. Brown, J. R. Söderström, C. D. Parker, L. J. Mahoney, K. M. Molvar, and T. C. McGill, "Oscillations up to 712 GHz in InAs/AlSb resonant tunneling diodes", *Appl. Phys. Lett.*, **58**(20), 1991, pp. 2291–2293.

[23] M. Reddy, S. C. Martin, A. C. Molnar, R. E. Muller, R. P. Smith, P. H. Siegel, M. J. Mondry, M. J. W. Rodwell, H. Kroemer, and S. J. Allen, "Monolithic Schottky-collector resonant tunnel diode oscillator arrays to 650 GHz", *IEEE Electron Device Lett.*, **18**(5), 1997, pp. 218–221.

[24] D. P. Steenson, R. E. Miles, R. D. Pollard, J. M. Chamberlain, and M. Henini, "Demonstration of power combining at *W*-band from GaAs/AlAs resonant tunneling diodes", *Proc. 5th Int. Symp. Space Terahertz Technol.*, Ann Arbor, MI, May 10–12, 1994, pp. 756–767.

[25] R. Blundell, D. C. Papa, E. R. Brown, and C. D. Parker, "Resonant tunneling diode as an alternative LO for SIS receiver applications", *Electron. Lett.*, **29**(3), 1993, pp. 288–290.

[26] S. Javalagi, V. Reddy, K. Gullapalli, and D. Neikirk, "High efficiency microwave diode oscillators", *Electron. Lett.*, **28**(18), 1992, pp. 1699–1701.

[27] E. Schomburg, J. Grenzer, K. Hofbeck, T. Blomeier, S. Winnerl, S. Brandl, A. A. Ignatov, K. F. Renk, D. G. Pavel'ev, Yu. Koschurinov, V. Ustinov, A. Zhukov, A. Kovsch, S. Ivanov, and P. S. Kop'ev, "Millimeter wave generation with a quasi planar superlattice electronic device", *Solid-State Electron.*, **42**(7–8), 1998, pp. 1495–1498.

[28] E. Schomburg, S. Brandl, K. Hofbeck, T. Blomeier, J. Grenzer, A. A. Ignatov, K. F. Renk, D. G. Pavel'ev, Yu. Koschurinov, V. Ustinov, A. Zhukov, A. Kovsch, S. Ivanov, and P. S. Kop'ev, "Generation of millimeter waves with a GaAs/AlAs superlattice oscillator", *Appl. Phys. Lett.*, **72**(12), 1998, pp. 1498–1500.

[29] S. Brandl, E. Schomburg, R. Scheuerer, K. Hofbeck, J. Grenzer, K. F. Renk, D. G. Pavel'ev, Yu.

Koschurinov, A. Zhukov, A. Kovsch, V. Ustinov, S. Ivanov, and P. S. Kop'ev, "Millimeter wave generation by a self-sustained current oscillation in an InGaAs/InAlAs superlattice", *Appl. Phys. Lett.*, 73(21), 1998, pp. 3177–3119.

[30] E. Schomburg, M. Henini, J. M. Chamberlain, D. P. Steenson, S. Brandl, K. Hofbeck, K. F. Renk, and W. Wegscheider, "Self-sustained current oscillation above 100 GHz in a GaAs/AlAs superlattice", *Appl. Phys. Lett.*, 74(15), 1999, pp. 2179–2181.

[31] T. Ishibashi and M. Ohmori, "200-GHz 50-mW CW oscillation with silicon SDR IMPATT diodes", *IEEE Trans. Microwave Theory Tech.*, 24(11), 1976, pp. 858–859.

[32] N. B. Kramer and R.A. Johnson, "Generating power at mm-wave frequencies", *Microwaves & RF*, 23(5), 1984, pp. 243–249.

[33] K. Chang, W. F. Thrower, and G. M. Hayashibara, "Millimeter-Wave Silicon IMPATT Sources and Combiners for the 110-260-GHz Range", *IEEE Trans. Microwave Theory Tech.*, 29(12), 1981, pp. 1278–1284.

[34] M. Ino, T Ishibashi, and M. Ohmori, "C.W. oscillation with p⁺-p-n⁺ silicon IMPATT diodes in 200 GHz and 300 GHz bands", *Electron. Lett.*, 12(6), 1976, pp. 148–149.

[35] T. Ishibashi, M. Ino, T. Makimura, and M. Ohmori, "Liquid-nitrogen-cooled submillimeter-wave silicon IMPATT diodes", *Electron. Lett.*, 13(10), 1977, pp. 299–300.

[36] I. Mehdi, P. H. Siegel, D. A. Humphrey, T. H. Lee, R. J. Dengler, J. E. Oswald, A. Pease, R. Lin, H. Eisele, R. Zimmermann, and N. Erickson, "An all solid-state 640 GHz subharmonic mixer", *IEEE MTT-S Int. Microwave Symp. Dig.*, Baltimore, MD, June 7–12, 1998, pp. 403–406.

[37] H. Eisele, C-C. Chen, R. K. Mains, and G. I. Haddad, "Performance of GaAs TUNNETT diodes as local oscillator sources", *Proc. 5th Int. Symp. Space Terahertz Technol.*, Ann Arbor, MI, May 10–13, 1994, pp. 622–628.

[38] C-C. Chen, R. K. Mains, G. I. Haddad, and H. Eisele, "Numerical simulation of TUNNETT and MITATT devices in the millimeter and submillimeter range", *Proc. 4th Int. Symp. Space Terahertz Technol.*, Los Angeles, CA, March 30–April 1, 1993, pp. 362–376.

[39] M. Ohmori, T. Ishibashi, and S. Ono, "Dependency of the highest harmonic oscillation frequency on junction diameter of IMPATT diodes", *IEEE Trans. Electron Devices*, 24(12), 1977, pp. 1323–1329.

[40] H. Böhm, J. Freyer, M. Claassen, W. Harth, and T. Bauer, "Second harmonic power generation from GaAs IMPATT diodes at 210 GHz", *Int. J. Infrared Millimeter Waves*, 19(4), 1998, pp. 587–593.

[41] H. Böhm, J. Freyer, and M. Claassen, "CW harmonic power generation of GaAs IMPATT diodes above 200 GHz", *these proceedings*.

[42] A. V. Räisänen, "Frequency multipliers for millimeter and submillimeter wavelengths", *Proc. IEEE*, 80(11), 1992, pp. 1842–1852.

[43] T. W. Crowe, T. C. Grein, R. Zimmermann, and P. Zimmermann, "Progress toward solid-state local oscillators at 1 THz", *IEEE Microwave Guided Wave Lett.*, 6(5), 1996, pp. 207–208.

[44] H. Eisele, unpublished results.

[45] X. Mélique, C. Mann, P. Mounaix, J. Thornton, O. Vanbésien, F. Mollot, and D. Lippens, "5-mW and 5% efficiency 216-GHz InP-based heterostructure barrier varactor tripler" *IEEE Microwave Guided Wave Lett.*, vol. 8(11), 1998, pp. 384–386.

[46] X. Mélique, A. Maestrini, P. Mounaix, O. Vanbésien, D. Lippens, G. Beaudin, M. Favreau, J. M. Goutoule, and T. Nahri, "12% efficiency and 9.5 dBm output power from InP-based heterojunction barrier varactor triplers", to appear in *IEEE MTT-S Int. Microwave Symp. Dig.*, Anaheim, CA, June 13–19, 1999.

[47] H. Eisele, "Gunn or transferred-electron devices", in *Encyclopedia of Electrical and Electronics Engineering*, J. G. Webster, Ed., vol. 8, John Wiley & Sons, New York, 1999, pp. 523–537.

[48] H. Eisele, "Gunn device terahertz sources", to appear in *J. High-Speed Electronics Systems*, 1999.

[49] H. Eisele and G. I. Haddad, "Efficient power combining with *D*-band (110–170 GHz) InP Gunn devices in fundamental-mode operation", *IEEE Microwave Guided Wave Lett.*, 8(1), 1998, pp. 24–26.

[50] L. Wandinger, "mm-wave InP Gunn devices: status and trends", *Microwave J.*, 24(3), 1981, pp. 71–78.

[51] I. G. Eddison, "Indium phosphide and gallium arsenide transferred-electron devices", in *Infrared and Millimeter Waves*, Vol. 11, *Millimeter Components and Techniques, Part III*, Academic Press, Orlando, 1984, pp. 1–59.

[52] B. Fank, J. Crowley, and C. Hang, "InP Gunn diode sources", *Millimeter Wave Technology III*, SPIE **544**, 1985, pp. 22–28.

[53] P. A. Rolland, G. Salmer, E. Constant, and R. Fauqembergue, "Comparative frequency behavior of GaAs, InP, and GaInAs transferred-electron devices—derivation of a simple comparative criterion", *IEEE Trans. Electron Devices*, **28**(3), 1981, pp. 341–343.

[54] M. R. Friscourt and P.A. Rolland, "Optimum design of n+-n-n+ InP devices in the millimeter-range frequency limitation—RF performances", *IEEE Electron Device Lett.*, **4**(5), 1983, pp. 135–137.

[55] K. Chang, *Handbook of Microwave and Optical Components*, Vol. 2, John Wiley & Sons, New York, 1990.

[56] J. D. Crowley, C. Hang, R. E. Dalrymple, D. R. Tringali, F. B. Fank, and L. Wandinger, "140 GHz indium phosphide Gunn diode", *Electron. Lett.*, **30**(6), 1994, pp. 499–500.

[57] J. D. Crowley, R. E. Dalrymple, C. Hang, D. R. Tringali, F. B. Fank, and L. Wandinger, "InP Gunn diodes serve millimeter-wave applications", *Microwaves & RF*, **33**(3), 1994, pp. 143–146.

[58] H. Eisele, A. Rydberg, and G. I. Haddad, "Recent advances in the performance of InP Gunn devices for the 100–300 GHz frequency range", *Proc. 1998 IEEE 6th Int. Conf. Terahertz Electronics*, Leeds, United Kingdom, Sept. 3–4, 1998, pp. 66–68.

[59] R. Kamoua, "Monte Carlo-based harmonic balance technique for the simulation of high-frequency TED oscillators", *IEEE Trans. on Microwave Theory Tech.*, **46**(10), 1998, pp. 1376–1381.

[60] R. Kamoua, "Potential of second-harmonic power generation in InP Gunn oscillators above 200 GHz", *Proc. 4th Int. Conf. Millimeter Submillimeter Waves Applications*, San Diego, California, July 20–24, 1998, pp. 32–37.

[61] R. Kamoua, H. Eisele, and G. I. Haddad, "*D*-band (110–170 GHz) InP Gunn devices", *Solid-State Electron.*, **36**, 1993, pp. 1547–1555.

[62] H. Eisele and G. I. Haddad, "Recent advances in the performance of GaAs- and InP-based two-terminal devices as high-power millimeter-wave sources", *Proc. 4th Int. Conf. Millimeter Wave Far Infrared Science Technol.*, Beijing, China, August 12–15, 1996, pp. 2–5.

[63] I. Dale, J. R. P. Stephens, and J. Bird, "Fundamental-mode graded-gap Gunn diode operation at 77

and 84 GHz", *Proc. Microwaves 94*, London, United Kingdom, Oct. 25–27, 1994, pp. 248–251.

[64] K. Chang and C. Sun, "Millimeter-Wave Power-Combining Techniques", *IEEE Trans. Microwave Theory Techn.*, **31**(2), 1983, pp. 91-107.

[65] J. C. Wiltse and J. W. Mink, "Quasi-optical Power Combining of Solid-State Sources", *Microwave J.*, **35**(2), 1992, pp. 144–156.

[66] J. Bae, T. Unou, T. Fujii, and K. Mizuno, "Spatial power combining of Gunn diodes using an over-moded waveguide resonator at millimeter wavelengths", *IEEE Trans. Microwave Theory Tech.*, **46**(12), 1998, pp. 2289–2294.

[67] J. Bae, T. Unou, T. Fujii, and K. Mizuno, "Spatial power combining of Gunn diodes using an over-moded waveguide resonator at millimeter wavelengths", *IEEE MTT-S Int. Microwave Symp. Dig.*, Baltimore, MD, June 7–12, 1998, pp. 1883–1886.

[68] M. Shahabadi and K. Schünemann, "Holographic power combining: a new principle for millimeter- and submillimeter-wave power combining", *Proc. 26th European Microwave Conf.*, Prague, Czech Republic, Sept. 9-12, 1996, pp. 115–119.

[69] M. Höft, B. Schumann, R. Judaschke, and M. Shahabadi, "A 65-GHz holographic power combiner", to appear in *IEEE MTT-S Int. Microwave Symp. Dig.*, Anaheim, CA, June 13–19, 1999.

[70] J. Kolnik, I. H. Oğuzman, K. F. Brennan, R. Wang, P. P. Ruden, and Y. Wang, "Electronic transport studies of bulk zincblende and wurtzite phases of GaN based on an ensemble Monte Carlo calculation including a full zone band structure", *J. Appl. Phys.*, **78**(2), 1995, pp. 1033–1038.

[71] U. V. Bhapkar and M. S. Shur, "Monte Carlo calculation of velocity-field characteristics of wurtzite GaN", *J. Appl. Phys.*, **82**(4), 1997, pp. 1649–1655.

[72] S. Krishnamurthy, M. van Schilfgaarde, A. Sher, and A.-B. Chen, "Bandstructure effect on high-field transport in GaN and GaAlN", *Appl. Phys. Lett.*, **71**(14), 1997, pp. 1999–2001.

[73] E. Bellotti, B. K. Doshi, K. F. Brennan, J. D. Albrecht, and P. P. Ruden, "Ensemble Monte Carlo study of electron transport in wurtzite InN", *J. Appl. Phys.*, **85**(2), 1999, pp. 916–923.

Cw-harmonic power generation of GaAs-IMPATT diodes above 200 GHz

H. Böhm[*], J. Freyer, and M. Claassen

Technische Universität München
Lehrstuhl für Allgemeine Elektrotechnik und Angewandte Elektronik
Arcisstraße 21, D-80333 München, Germany

ABSTRACT

Cw-power generation from fundamental mode GaAs-IMPATT diodes is presently limited to frequencies well below 200 GHz. This restriction follows mainly from the losses in diode and resonator which exceed the negative resistance of the diode at elevated frequencies. However, the strong non-linearities of IMPATT diodes can successfully be used for harmonic mode operation to achieve rf-output power well above 200 GHz. For harmonic mode operation, the active device must be incorporated in a resonator which is terminated reactively at the fundamental frequency and on the other hand should be power matched at the harmonic frequency. The reactive termination of the fundamental wave can easily be achieved by a waveguide section with appropriate cut-off frequency. Matching at the harmonic frequency is aspired by the resonator geometry and a sliding short. The initial material for the applied GaAs-IMPATT diodes is grown by MBE technique. The devices are mounted on diamond heat sinks with extremely low parasitics to avoid additional losses. Experimental results are given for GaAs double-drift IMPATT devices above 200 GHz with 2 mW at 232 GHz and 1 mW at 242 GHz as best results. The experimental data are compared to theoretical simulations of both active device and applied resonator.

Keywords: GaAs-IMPATT diodes, harmonic mode operation, optimisation, experimental results

1. INTRODUCTION

IMPATT diodes deliver the highest output power at microwave and mm-wave frequencies, but cw-power generation of GaAs devices in the fundamental mode is limited to frequencies well below 200 GHz [1]. This is due to the oscillation condition which requires a negative dynamic device resistance which exceeds the loss resistances of the device contacts and the resonator. The negative diode resistance decreases with frequency and cannot be further enhanced by higher dc-current density because of thermal considerations. The principle of operation of IMPATT devices bases on periodic carrier generation by impact ionisation and following transit-time delay of drifting carriers. The primary advantage compared to other semiconductor transit-time devices is the initial phase lag of 90^0 due to the impact ionisation. This carrier generation process causes together with space charge modulation a strong non-linearity in the active region of the IMPATT diode which can successfully be applied for internal frequency multiplication in the oscillating device thus generating output power at harmonic frequencies above 200 GHz. This kind of power generation is denoted as harmonic power generation of IMPATT diodes. It is an obvious advantage of these self-pumped harmonic mode IMPATT-oscillators compared to frequency multipliers being driven by an external pumping source that no external pumping sources are required [2]. There exists only few work about these non-linear properties of IMPATT diodes [2,3,4], whereas for Gunn devices, harmonic mode operation is a well practised method to achieve output power at elevated frequencies [5,6].

In the following, the harmonic mode operation is explained, equivalent circuits at the fundamental and harmonic frequency are presented, a proposed optimum device structure for 250 GHz is given, and first experimental results with low parasitic mounting technique for this operation are summarised.

[*]Harald Böhm
e-mail: harald.boehm@ei.tum.de
Telephone: ++49 (0)89 289-22957
Fax: ++49 (0)89 289-22950

Part of the EUROPTO Conference on Terahertz Spectroscopy and Applications II
Munich, Germany ● June 1999 SPIE Vol. 3828 ● 0277-786X/99/$10.00

81

2. ACTIVE DEVICE

In order to study the principle of harmonic operation in IMPATT diodes, it is advantageous to adopt an idealised model of a Read-type device structure [7] although the final calculations are carried out using a large-signal drift-diffusion model (DDM) [8]. The basic approach is straightforward: In the avalanche region, fundamental as well as second harmonic field excitation are introduced into the Read equation. Following the further calculations for currents and voltages, equivalent circuits for the fundamental and harmonic operation can be derived as shown in Fig. 1.

At the fundamental frequency, the oscillation condition must be fulfilled which determines the frequency f_1 and amplitude U_1 of the internal pumping source. The capability of harmonic power generation is improved significantly by a large signal amplitude U_1 of the pumping source so that the active device is driven into non-linearities. This can be achieved by a nearly reactive termination of the device at the fundamental frequency so that the negative diode resistance $\mathrm{Re}\{Z_{D1}\}$ has only to compensate the total losses from both resonator and contacts R_{Loss1}. The load impedance Z_{L1} at the fundamental frequency should be purely reactive ($\mathrm{Re}\{Z_{L1}\} = 0$).

At the harmonic frequency, the active region of the device can be represented by an ideal current source I_{20} driven by the fundamental voltage U_1 and an internal admittance Y_{i2}. In this case, power matching instead of the compliance of an oscillation condition must be established to receive high harmonic rf-power. From this description, an essential difference in power generation at fundamental and harmonic frequencies can be concluded: With increasing frequencies, power generation at the fundamental frequency is limited to frequencies where the losses in both, diode and resonator, do not exceed the negative resistance of the active device. At the double frequency, however, output power can be achieved even if the losses are relatively high (see Fig. 1).

fundamental frequency	harmonic frequency
• **oscillation condition:** $$Z_{D1}+Z_{L1}+R_{Loss1}=0$$	• **power matching:** $$Z_{L2}=\left(R_{Loss2} + \frac{1}{Y_{i2}}\right)^{*}$$ • **available harmonic power:** $$P_{L2,max} = \frac{|I_{20}|^2}{8\,|Y_{i2}|^2 \cdot \mathrm{Re}\left\{\frac{1}{Y_{i2}}+R_{Loss2}\right\}}$$
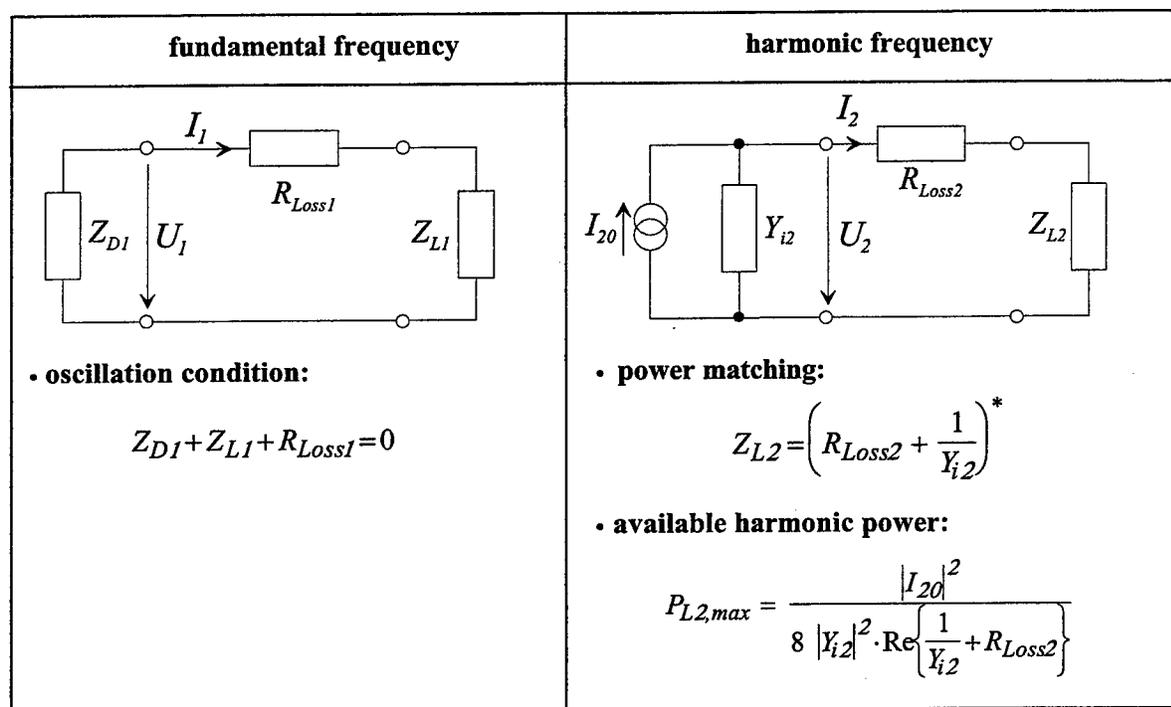
Fig. 1: The equivalent circuits of the self-pumped IMPATT device at the fundamental and harmonic frequency.

Fig. 2 shows doping concentration $N(x)$ and electric field distribution $E(x)$ of the investigated GaAs double-drift Read IMPATT diodes. For accurate calculations of the electrical characteristics of the applied devices, large-signal device simulators are used. The optimisation of the doping profile for the high field region was carried out by a Monte-Carlo model which takes into account Zener-tunneling and the non-stationary and non-local transport effects of the carriers [9]. In order to improve the electrical performance of IMPATT diodes, a compromise between low breakdown voltage of the active region and low Zener-tunneling (i.e. predominant carrier generation by impact ionisation) must be found. This

optimised doping profile can be applied for fundamental as well as for harmonic mode operation. Therefore, only the low field region must be modified for harmonic mode operation, appropriately (see Fig. 2). The doping profile of the two drift-regions was optimised with DDM adjusted by Monte Carlo simulations for the avalanche zone. The optimisation of the doping profile for maximum rf-output power at the double frequency $P_{L2,max}(U_{1,opt}, U_{2,opt}, \varphi_{opt})$ by DDM-simulations is rather time-consuming. The optimum operation point $(U_{1,opt}, U_{2,opt}, \varphi_{opt})$ can, however, also be found by only few DDM-simulations by optimising the current source I_{20} and the internal admittance Y_{i2}. This fast optimisation method is sufficiently accurate in all interesting operation points and can be applied successfully to other device structures.
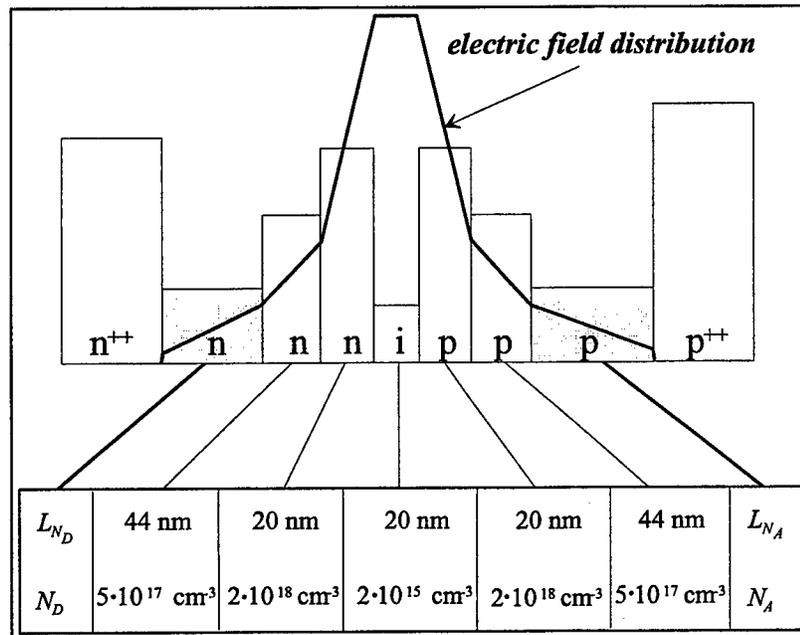
Fig. 2: GaAs double-drift Read IMPATT diode structure with doping profile and electric field distribution.

For self-pumped IMPATT diodes, a compromise between high fundamental voltage amplitude, bias stability, velocity saturation, and modulation of space charge region must be found. At the fundamental frequency, the negative diode resistance must compensate the total losses. Additionally, a high fundamental voltage must be obtained for efficient harmonic mode operation so that appropriate drift lengths are required. However, the injected convection current is smoothed during the transit time of the carriers within the drift regions so that very short drift lengths are preferred at the double frequency. Therefore, the length of the drift zones must be reduced with respect to the optimum length at the fundamental frequency in order to prevent the smoothing of the convection current. For harmonic mode operation from 210 GHz to 250 GHz drift lengths for electrons $L_{N,D}$ and holes $L_{N,A}$ of about 60 nm is considered to be advantageous (see Fig. 2). The electric field distribution must guarantee velocity saturation during the whole operation. Just punched through operation is advantageous for harmonic mode oscillators because of the additional modulation of the space charge region. The demanded punchthrough factor of about 1 can be obtained by a doping concentration of $N_A = N_D = 4 \cdot 10^{17} \text{ cm}^{-3}$. Modulation of the space charge region increases the rf-losses at the fundamental frequency and hereby lowers the rf-fundamental voltage. However, harmonic power generation is significantly improved due to the additional non-linear device capacitance.

Low-frequency instabilities in the bias circuit may appear in IMPATT devices at high fundamental voltage amplitude [10]. These bias oscillations are particularly troublesome for the harmonic mode operation due to the reactive load at the fundamental frequency. The high rf-voltage amplitude and the properties of carrier generation due to impact ionisation cause an rf-rectification that leads to a negative slope of the dynamic current-voltage characteristic as shown in section II of Fig. 3. In this range, the increasing bias current I_0 results in an enhanced oscillation amplitude that produces the back biasing due to rf-rectification. The negative slope of the dynamic current-voltage characteristic can induce bias oscillations at low frequencies and thus deteriorate the operation mode. Numerical investigations show that an increased doping concentration in the drift regions reduces the rf-rectification and prevents a negative slope.
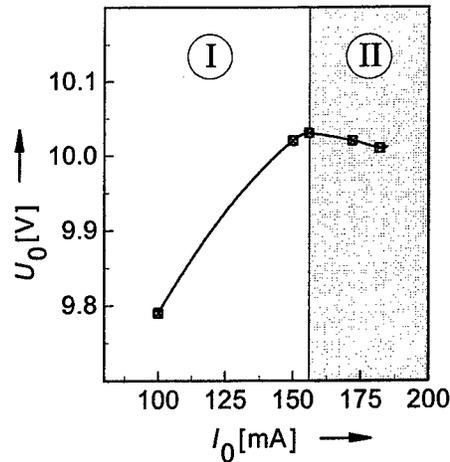
Fig. 3: Measured current-voltage characteristic which exhibits a negative slope in region II.

Absolute stability was calculated with optimised parameters for the doping concentration $N = N_A = N_D = 4 \cdot 10^{17}$ cm^{-3} and the appropriate drift lengths of $L_{N,D} = 64$ nm and $L_{N,A} = 60$ nm for the low field region as being shown in Fig. 2 with improved output power.

3. RESONATOR

For harmonic mode operation, the resonator should exhibit an inductive load at the fundamental frequency, whereas an appropriate load impedance for power matching is desirable at the harmonic frequency (Fig. 1). The resonators used for the experiments have a disc structure in a full height WR-06 waveguide (Fig. 4).
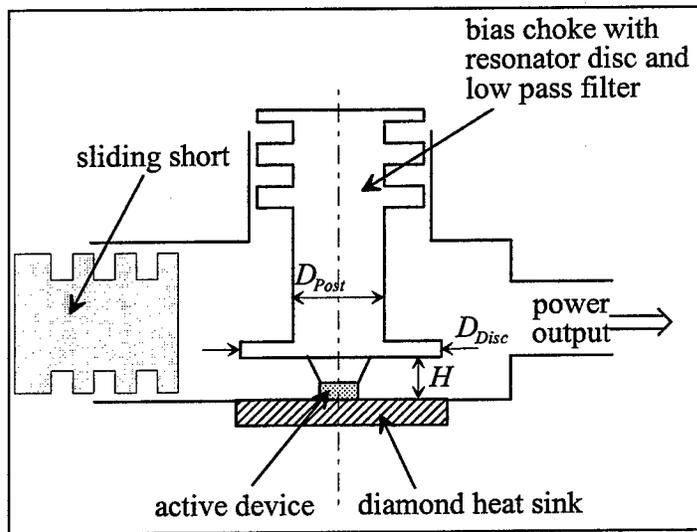
Fig. 4: A disc resonator in a full height WR-06 waveguide with sliding short on one side and a WR-04 waveguide section to achieve a reactive termination for the active device at the fundamental frequency.

Fine-tuning is accomplished by a sliding short. A WR-04 waveguide section at the end of the resonator cuts off all frequencies beyond 137 GHz leading to a nearly reactive termination for the active device at the fundamental frequency. The resonator impedance was numerically calculated by the help of a commercial finite element programme (HP-HFSS). Because of the inductive behaviour of the resonator, the load reactance X_{L2} increases with the increase of frequency but the internal reactance of the active device $X_{i2} = \text{Im}\{1/Y_{i2}\}$ decreases with the increase of frequency. Consequently, power

matching is not obtained with this resonator but some output power can always be extracted from the device at the harmonic frequency as characterised by the equivalent circuit in Fig. 1. The calculations of the load reactance show, however, that it exhibits resonances which can improve power matching.

4. EXPERIMENTAL RESULTS

In the experiment, a WR-06 disc resonator as described above with an integrated double-drift Read-type IMPATT diode is used. Contact losses of the active device can be reduced by the application of a Ti-Schottky contact on the highly doped n^+-layer whereas an ohmic contact was used for the highly doped p^+-contact layer. For reducing the thermal resistance, the active device is bonded on a diamond heat sink with a low parasitic mounting technique (see Fig. 5). This mounting technique is achieved with high precision and reproducibility and has been applied successfully for power generation in the mm-wave range [11].
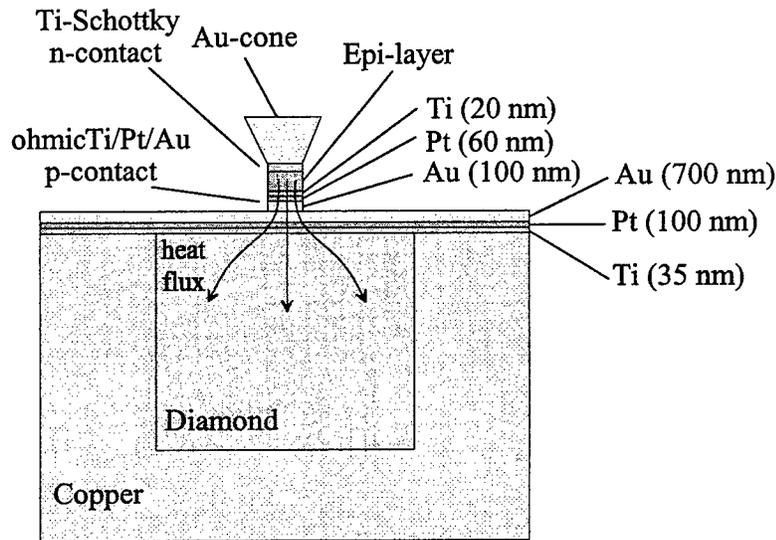
Fig. 5: Diamond heat sink with a low parasitic mounting technique of the active device.

The device area was optimised experimentally for high output power as a compromise between impedance matching, thermal considerations, and electrical performance. The diameters of the investigated double-drift IMPATT devices in the experiments are between 20 and 30 μm.

Two different doping concentrations $N_A = N_D = 1 \cdot 10^{17}$ cm^{-3} and $N_A = N_D = 2.5 \cdot 10^{17}$ cm^{-3} were investigated whereas the lengths of the both low field regions are $L_{N,A} = 60$ nm and $L_{N,D} = 64$ nm, respectively. The device with the doping concentration of $1 \cdot 10^{17}$ cm^{-3} was already successfully applied for the fundamental mode from 140 GHz to 170 GHz for dc-current densities from 50 kA/cm^2 to 100 kA/cm^2 [1]. For harmonic mode operation, lower frequencies and a reactive termination at the fundamental frequency are advantageous. Maximum output power of 2 mW could be obtained in cw-operation at 232 GHz (see Fig. 8). This is the frequency where the load reactance shows a minimum due to a resonance versus the frequency. Thus the aspired power matching could be improved accordingly.

As mentioned, bias oscillations are particularly troublesome for harmonic mode operation because of high fundamental voltages. Increasing the series resistance in the bias circuit could not sufficiently prevent bias oscillations. Thus the applied dc-current density had to be decreased to prevent the bias instabilities. Also operation at higher frequencies could prevent bias oscillations.

The total losses were determined by measurements of the dc-current for onset of oscillations in the frequency range from 110 GHz to 150 GHz. Following numerical calculations of the negative diode resistance with the DDM-programme determine the losses. The contact losses exceed the losses from the resonator. Therefore, the Ti-Schottky contact predominantly determines the behaviour of total losses and thus the losses decrease with the increase of frequency as being depicted in Fig. 6.
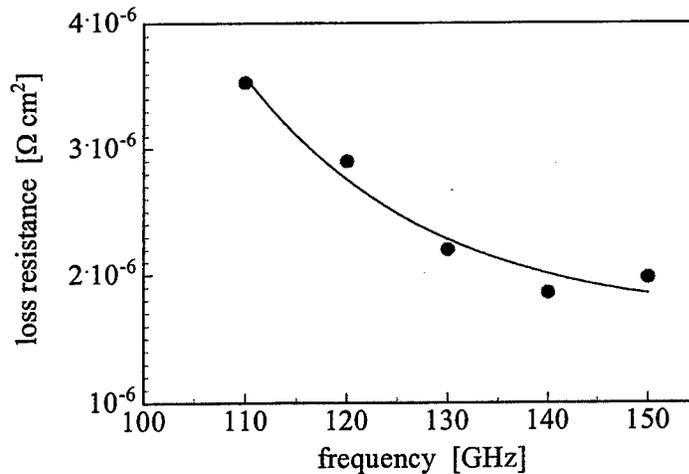
Fig. 6: Total losses from active device and resonator.

Further experimental investigations were carried out with doping concentrations of $2.5 \cdot 10^{17}$ cm^{-3}. 242 GHz was the highest frequency with a corresponding rf-output power of 1 mW. The output power was measured by a power meter and compared to measurements of a dry caloriometer. The frequency measurements were performed by a spectrum analyser which also guarantees single tone operation for the harmonic oscillators. The measured rf-output powers of the experimental results are summarised in Fig. 7. The theoretically predicted optimised diode structure with higher doping concentrations is concerned for future experimental investigations.
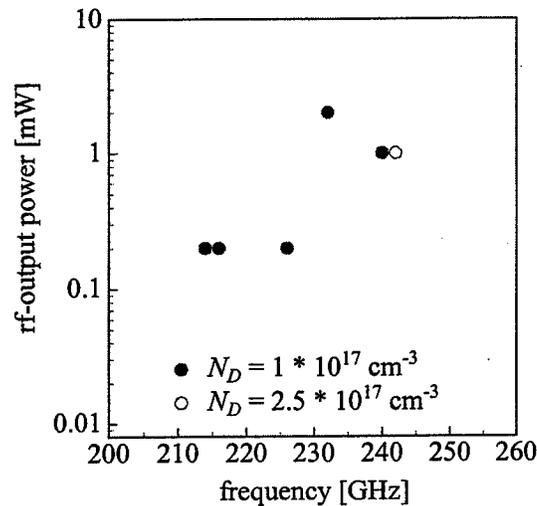
Fig. 7: Measured harmonic power generation from double-drift IMPATT diodes with different doping concentrations in the drift zones.

5. COMPARISON OF NUMERICAL AND EXPERIMENTAL RESULTS

The numerical calculation for the active device refers to the experimental data with a corresponding device diameter of 27 μm, a dc-current density j_0 of 55 kA/cm^2, and the loss resistances R_{Loss1}, R_{Loss2} of 0.5 Ω. For optimum harmonic operation at 232 GHz, a purely inductive resonator impedance of j·6 Ω is required at the fundamental frequency. A fundamental voltage amplitude of about 9 V results so that the negative diode resistance just compensates the total losses of 0.5 Ω. The internal current source amplitude $|I_{20}|$ amounts to 170 mA and the internal admittance Y_{12} to (57 + j 350) mS. This results in an attainable harmonic output power of $P_{L2,max}$ = 30 mW at 232 GHz. The corresponding resonator

impedance for power matching at the harmonic frequency would be $Z_{L2,opt} = (1 + j\,3)\,\Omega$. A resonator structure with a disc diameter D_{Disc} of 800 μm, a post diameter D_{Post} of 500 μm, and a post height of H = 20 μm as being shown in Fig. 4 was applied in the experiment. The impedance at the harmonic frequency could only be tuned to the value of about $(0.4 + j\,8)\,\Omega$ which is fairly far from the above calculated load impedance $Z_{L2,opt}$. It results in a calculated output power of 1.7 mW. This findings fit quite well to the experimental result, where an output power of 2 mW was obtained. The calculations of the output power P_{L2} at the double frequency versus the load impedance Z_{L2} are shown in Fig. 8.
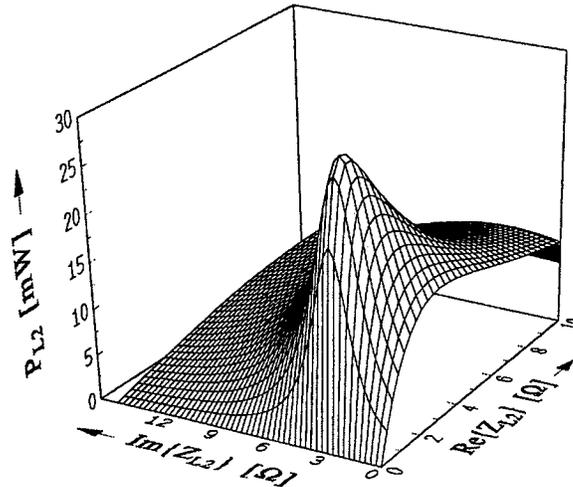
Fig. 8:
Output power P_{L2} at 232 GHz versus load impedance Z_{L2}.

6. CONCLUSION

In this work, theoretical and experimental investigations concerning power generation by second harmonic operation of self-pumped IMPATT diodes are described. The active device is characterised by a time-domain drift-diffusion model. The applied disc-type resonator structure is investigated by a commercial simulation programme. Using a low parasitic mounting technique for the active devices, up to 2 mW cw-output power at 232 GHz was obtained.

7. ACKNOWLEDGEMENTS

8. REFERENCES

1. Freyer, J., Tschernitz, M., Grothe, H., Harth, W., „GaAs transit-time devices for frequencies above 140 GHz", Proc. of 3rd International Workshop on Terahertz Electronics, Zermatt, Switzerland, pp. 22-33, 1995

2. Claassen, M., Böhm, H., „Harmonic mode operation of GaAs-IMPATT devices above 200 GHz", 3rd International Kharkov Symp.: Physics and Engineering of Millimeter and Submillimeter Waves, Kharkov, Ukraine, pp. 142-144, 1998

3. Rolland, P. A., Vaterkowsky, J. L., Constant, E., Salmer, G., „New modes of operation for avalanche diodes: Frequency multiplication and upconversion", IEEE MTT-24, pp. 768-775, 1976

4. Mouthaan, K., „Non-linear characteristics and two-frequency operation of the avalanche transit-time oscillator", Philips Res. Rept, 25, pp. 33-67, 1970

5. Barth, H., „A wideband backshort-tunable second harmonic W-band Gunn oscillator", IEEE MTT-S Int. Microwave Symp. Dig., pp. 334-337, 1981

6. Eisele, H., „Second-harmonic power extraction from InP Gunn devices with more than 1 mW in 260-320 GHz frequency range", Electron. Lett. 34, (25), pp. 2412-2413, 1998

7. Read, W. T., „A proposed high-frequency, negative resistance diode", Bell Sys. Tech. J., 37, pp. 401-446, 1958

8. Gaul, L., Claassen, M., „Pulsed high-power operation of p$^+$pnn$^+$-avalanche diodes near avalanche resonance for mm-wave oscillators", IEEE Trans. Electron Dev., ED-41, (8), pp. 1310-1318, 1994

9. Liebig, D., Schünemann, K., „Cellular automaton particle simulation and sensitivity analysis of GaAs-MITATT-diodes for operation at 200 GHz", International Journal of Electronics and Communications (AEÜ), **52**, (5), pp. 229-234, 1998

10. Brackett, C. A., „The elimination of tuning-induced burnout and bias-circuit oscillations in IMPATT oscillators", The Bell System Technical Journal, **52**, (3), pp. 271-306, 1973

11. Benz, C., Freyer, J., „Pulsed GaAs-IMPATT oscillator up to 200 GHz", Proc. 23rd Int. Conf. Infrared and Millimeter Waves, Colchester, UK, pp. 34-36, 1998

Millimetre wave emission from current oscillations in semiconductor superlattices: Present status and future prospects

E. Schomburg

Institut für Experimentelle und Angewandte Physik, Universität Regensburg, Universitätsstr. 31,
D-93040 Regensburg, Germany
electronic mail: ekkehard.schomburg@physik.uni-regensburg.de

ABSTRACT

Recent results of millimetre wave generation with doped GaAs/AlAs superlattices are reviewed. The wide-miniband superlattices show negative differential conductance caused by Bloch oscillations of the miniband electrons. The millimetre wave emission is due to current oscillations driven by travelling dipole domains. The oscillation frequency is given by the ratio of the domain velocity and the superlattice length. The experimental results show that the oscillation frequency increases with increasing peak drift velocity, which strongly depends on the miniband width. Current oscillations in GaAs/AlAs superlattices up to a frequency of 103 GHz at a power level of about 0.5 mW are reported. The superlattice oscillator will be compared with resonant tunnelling diode oscillators and Gunn diode oscillators. The possibility of using different material systems for the superlattices will be discussed.

Keywords: superlattice, millimetre wave generation, current oscillation, travelling dipole domains

1. INTRODUCTION

A semiconductor superlattice, as proposed by Esaki and Tsu [1], is a periodic repetition of quantum wells separated by narrow barriers; the quantum well and the barrier layers are obtained by using different semiconductor materials (e.g. GaAs and AlAs). A new band structure, consisting of minibands separated by minigaps, is formed due to a strong coupling between wave functions of adjacent quantum wells. Esaki and Tsu predicted a current-voltage characteristic with a negative differential conductance for transport along the superlattice axis. Current-voltage characteristics with a negative differential conductance for superlattices were observed by different groups [2]. The aim of this paper is to discuss recent results of microwave emission from self-sustained current oscillations in semiconductor superlattices with wide minibands.

2. THE SUPERLATTICE DEVICE

A typical superlattice, grown by molecular beam epitaxy on a n$^+$ GaAs substrate, is considered consisting of 120 periods, each of 4.9 nm thick GaAs and 1.3 nm thick AlAs layers, and doped with silicon (about 1x10^{17} cm^{-3}). The superlattice has a miniband width of 22 meV. On top of the superlattice, a n$^+$ GaAs cap layer was grown for the formation of ohmic contacts. The superlattice was embedded between graded layers of gradual composition and doping level in order to match the band structure of the superlattice to the n$^+$ GaAs layers.

A typical device [3], prepared from the superlattice structure, is shown in Fig.1. The superlattice device had two mesas, one with a small and another with a large area, on the n$^+$ GaAs substrate. The mesas were provided with ohmic contacts on top. Using a high-frequency probe tip, the mesas were connected to a 50-Ohm coaxial cable for transmission of both the direct and the high-frequency current. The mesa with the smaller area acted as an active element, while the large-area mesa was a series resistance in order to connect the active mesa to the contact. Direct and high-frequency current were separated by a bias tee. The current-voltage characteristic was measured by an I-V curve tracer and the millimetre wave radiation was monitored by a spectrum analyser.

Part of the EUROPTO Conference on Terahertz Spectroscopy and Applications II
Munich, Germany ● June 1999 SPIE Vol. 3828 ● 0277-786X/99/$10.00

89
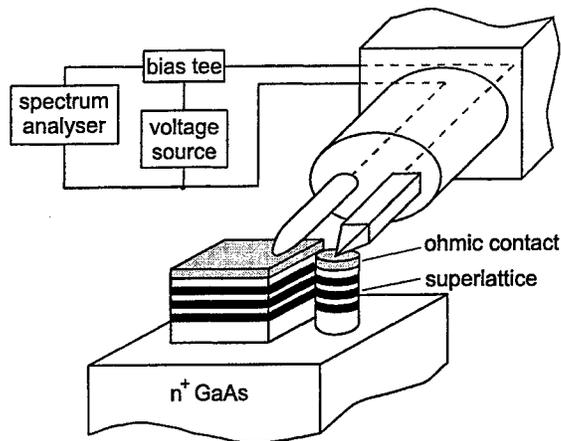
Fig.1: Experimantal set-up.

The current voltage characteristic (Fig.2) of the 22-meV superlattice device (superlattice with a miniband width of 22 meV) showed ohmic behaviour at small voltages and a negative differential conductance above a critical voltage (~0.7 V), corresponding to the peak current. For voltages larger than the critical voltage the current changed in jumps followed by smooth parts. For positive voltages, microwave emission was observed immediately after the first current jump, while in negative direction no emission was found. A peak drift velocity of about 7×10^5 cm/s was estimated from the peak current.

The superlattice device showed an emission spectrum (Fig.3) with a fundamental frequency near 5 GHz and higher harmonics. The line at the fundamental harmonic had a width of less than 1 MHz. A maximum power of the oscillator of about 0.1 mW was obtained corresponding to an efficiency from dc to high-frequency power of about 1 %.

3. MINIBAND TRANSPORT, NEGATIVE DIFFERENTIAL MOBILITY AND TRAVELLING DOMAINS

Electrons, which populate the energetically lowest miniband, are responsible for the transport properties of the superlattice. In a weak electric field (Fig.4a) applied parallel to the superlattice axis, a miniband electron is accelerated until an inelastic scattering process occurs; afterwards it is accelerated again. The drift-velocity field characteristic shows ohmic behaviour. At high electric fields (Fig.4b) a miniband electron can reach the top of the miniband and experience Bragg reflection. The miniband electron oscillates (with the Bloch frequency $\omega_B = eE_0a/\hbar$, where e is the
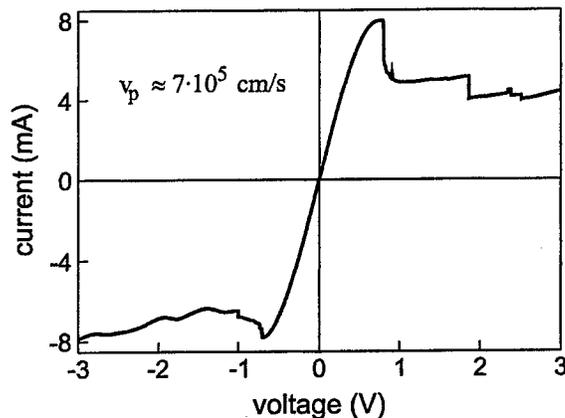
Fig.2: Current-voltage characteristic of a 22-meV superlattice device.
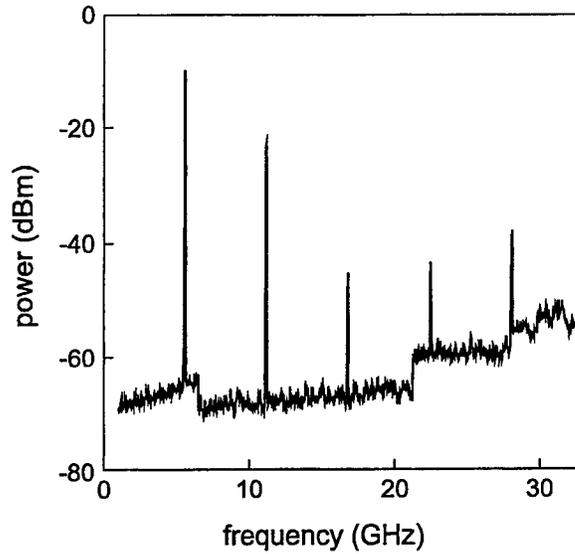
Fig.3: Spectrum from a 22-meV superlattice device.

elementary charge, $\hbar$ Planck's constant, a the superlattice period and E_0 the electric field) along the superlattice axis (Bloch oscillation [4]) over several periods before it looses energy by an inelastic scattering process (i.e. $\omega_B > \tau$, where τ is an average intraminiband relaxation time). All miniband electrons perform Bloch oscillations independently, i.e. without a phase relation to each other. The Bloch oscillation leads to a field-induced localisation of miniband electrons. This localisation increases with increasing the field strength; therefore, the drift motion becomes slower with increasing electric field and negative differential mobility occurs. The drift velocity-field characteristic (Fig.4c) is given for a tight binding miniband dispersion relation by [1]

$$v_D = v_p \frac{2\omega_B\tau}{1+\left(\omega_B\tau\right)^2},$$

(1)

where v_p is the peak drift velocity. The peak drift velocity occurs for a critical field E_c (onset of the negative differential mobility), where $\omega_B\tau = 1$. The differences between the current-voltage characteristic (Fig.2) in the region of negative differential conductance and a current-voltage characteristic expected from the velocity-field characteristic (Fig.4c) with a completely smooth slope indicates the occurrence of space charge instabilities and the formation of travelling domains.

A spatially homogeneous field distribution becomes unstable if a voltage in the region of negative differential velocity is applied to the superlattice. A domain is formed near the cathode, travels through the superlattice and grows until a dynamic equilibrium between drift and diffusion processes is reached. Fig.5 shows results [5] of a calculation of the spatial carrier and field distribution inside the 22-meV superlattice with a self-consistent drift-diffusion model [6] taking into account Eq.1. The domain has a shape of a dipole consisting of a small accumulation layer followed by a wider depletion layer. In the domain, the electric field reaches a value which is several times the critical field, while outside the domain the electric field is below the critical field (which prevents the occurrence of a second domain before the first one disappears). The domain travels towards the anode with an almost constant domain velocity of about 0.7 v_p. At the anode, the domain is annihilated. This process is repeated periodically and leads to current oscillations [7] in the external circuit. The oscillation frequency found for the 22-meV superlattice is very close to the transit frequency of the domains, about 0.7 v_p/L, where L is the length of the superlattice. The width of the domain is a third of the superlattice length. Accordingly, the current oscillation is not sinusoidal, which is in good agreement with the experimental observation of higher harmonics.
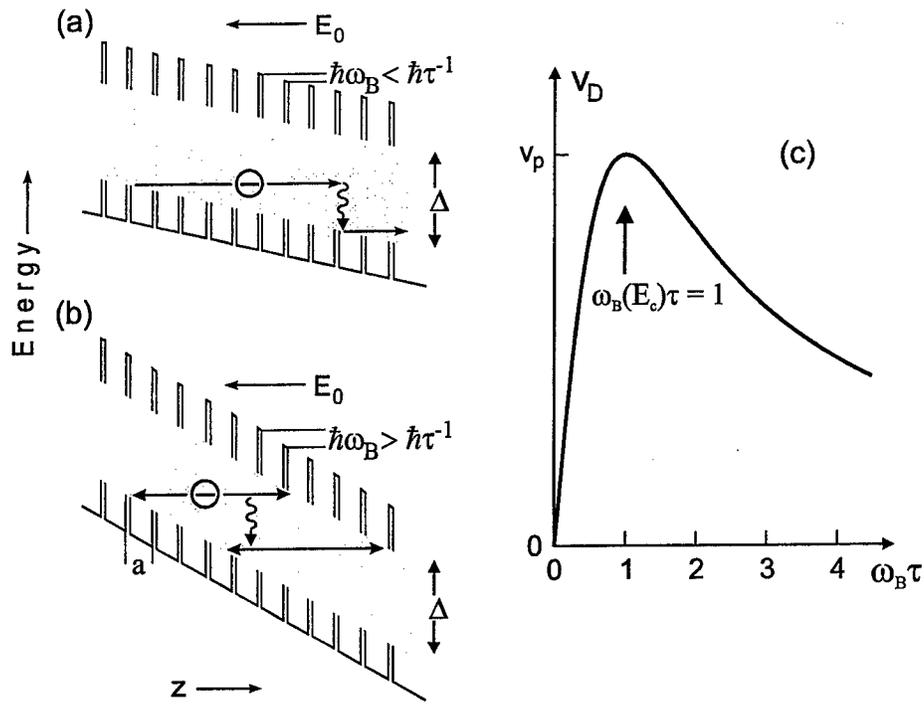
Fig.4: Electron in a superlattice at low (a) and high (b) electric fields; drift velocity-field characteristic (c).
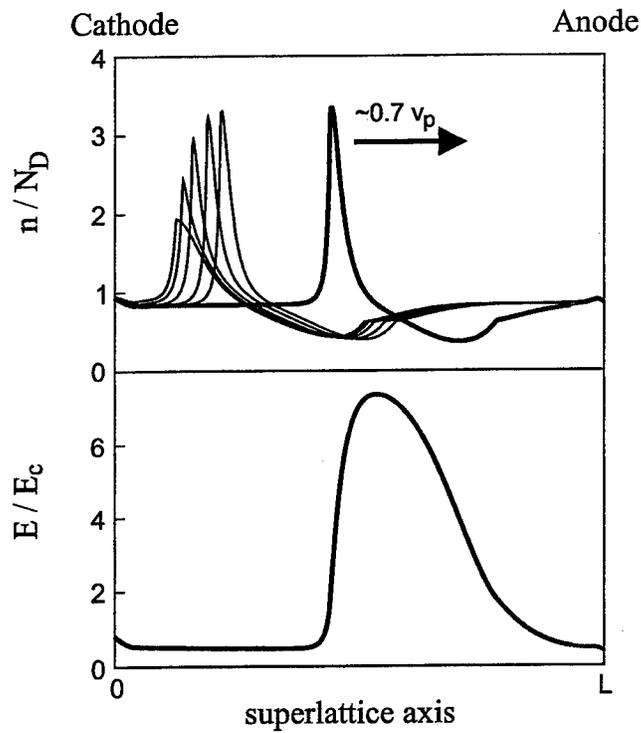
Fig.5: Carrier and field distribution along the superlattice axis.

4. CURRENT OSCILLATION IN SUPERLATTICES WITH DIFFERENT MINIBAND WIDTHS

Current-voltage characteristic and microwave emission for several superlattice devices, each with a different miniband width and the same length, was investigated [8, 9]. The miniband width was obtained by adjusting the well and barrier thickness in each superlattice. It was found that the peak drift velocity v_p increased from $2 \cdot 10^5$ cm/s, for a 16-meV superlattice device, up to $75 \cdot 10^5$ cm/s for a 120-meV superlattice device. The critical field in the superlattices was almost independent of the miniband width, and had a value of ~14 kV/cm. Fig.6a shows the peak drift velocity divided by the period of the superlattice (v_p/a) as function of the miniband width Δ for the different superlattices (points in Fig.6a). The experimental result is compared with calculations of the peak drift velocity with a semiclassical model for miniband transport, which takes into account inelastic and elastic intraminiband relaxation [10],

$$v_p = \frac{\Delta a}{4\hbar} \frac{I_1\left(\dfrac{\Delta}{2kT}\right)}{I_0\left(\dfrac{\Delta}{2kT}\right)} \left(\frac{v_\varepsilon}{v_\varepsilon + v_{el}}\right)^{\frac{1}{2}} \tag{2}$$

where v_ε is the inelastic scattering rate, v_{el} the elastic scattering rate, k Boltzmann's constant and $\hbar$ Planck's constant. Our analysis (solid line in Fig.4a) delivers $v_\varepsilon/(v_\varepsilon+v_{el}) \sim 0.25$. A similar value was reported for undoped superlattices studied by time-of-flight measurements [11]. In the semiclassical model [10], the average intraminiband relaxation time is $\tau = [v_\varepsilon(v_\varepsilon+v_{el})]^{-1/2}$; accordingly, a value of the elastic scattering rate of $15 \cdot 10^{12}$ s^{-1} and of the inelastic scattering rate of $5 \cdot 10^{12}$ s^{-1} is estimated. It is suggested that the inelastic scattering in the superlattices at room temperature is due to interaction with optical phonons, while the elastic scattering is caused by the roughness of the interfaces between the GaAs and AlAs layers.

The oscillation frequency of the current oscillation in the different superlattices increased with increasing miniband width (from 2 GHz for the 16-meV superlattice up to 103 GHz for the 120-meV superlattice). The highest
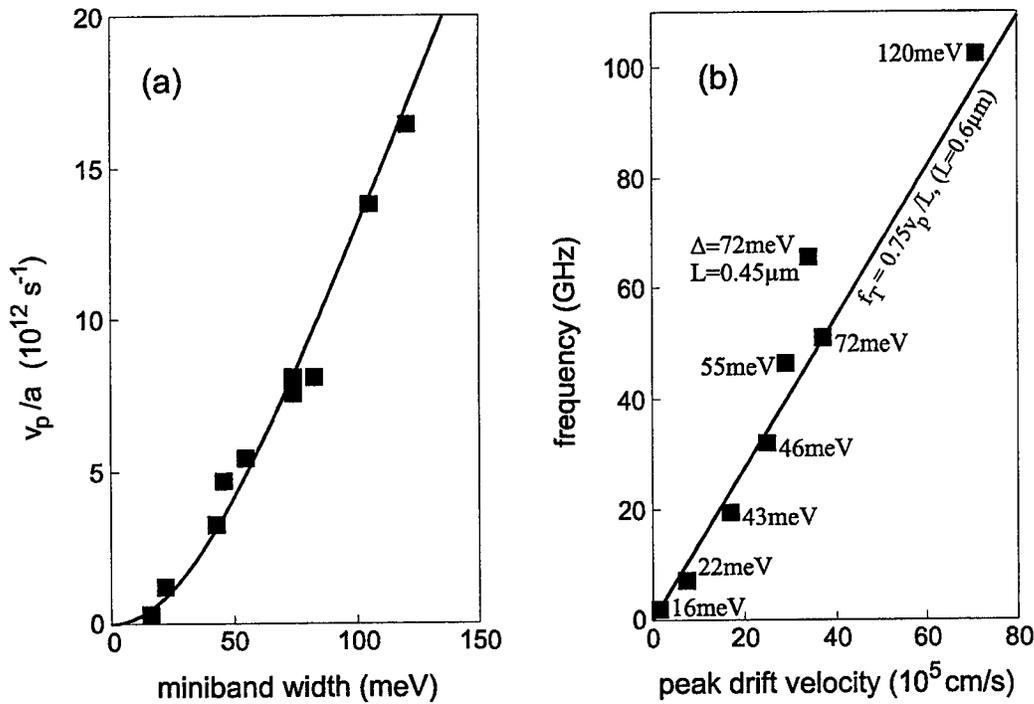
Fig.6: (a) Ratio of v_p/a versus the miniband with; (b) oscillation frequency of superlattices with different miniband widths.

output power was about 0.5 mW [9] (at 103 GHz) for the 120-meV superlattice. The fundamental harmonics of the superlattices showed different linewidths in the range from about 3 MHz (16-meV superlattice) to less than 10 kHz (46-meV superlattice). At present, we have no explanation for the different linewidths.

In Fig.6b the oscillation frequency versus the peak drift velocity is plotted (squares are experimental points). The straight line, calculated by the expression for the transit frequency $f_T = 0.75\, v_p/L$ (L = 0.6 μm), described well the dependence of the experimental data for superlattices with about the same length. For the 72-meV superlattices with a different length, it was found [3, 8] that a decrease of the length led to an increase of the oscillation frequency (from 53 GHz to 65 GHz), although the shorter superlattice had a slightly smaller peak drift velocity than the longer one. The dependence of the oscillation frequency from both, the peak drift velocity and the length, corresponds to the behaviour expected from domains travelling through the superlattice.

5. THE FREQUENCY LIMIT OF THE NEGATIVE DIFFERENTIAL MOBILITY

The analysis of the experimental results indicates that the negative differential mobility is the origin of travelling domains and the current oscillations. It is an important question for the device operation, up to which frequencies a negative differential mobility occurs. Therefore, the frequency dependence of the small-signal mobility, μ_ω (Fig.7), using one dimensional moment-balance equations, was investigated [12] for a constant inelastic scattering rate ($v_\varepsilon = 5 \cdot 10^{12}$ s^{-1}) and different ratios v_{el}/v_ε. For the calculation a static electric field at the maximum of the negative differential mobility ($\omega_B\tau = 1.7$) was chosen. The small-signal high-frequency mobility converges for small frequencies to the value of the negative differential mobility obtained from the velocity-field characteristic (Eq.1). The largest negative value of μ_ω was found in the absence of elastic scattering ($v_{el}/v_\varepsilon = 0$). The mobility remains negative up to a frequency above 1 THz. Elastic scattering reduces the value of the negative small-signal mobility at small frequencies. The analysis of the static transport parameter of our superlattices were consistent with $v_{el}/v_\varepsilon \approx 2$. For this ratio, μ_ω was almost constant up to a frequency of about 1 THz. Therefore, we suggest that the intrinsic properties of a GaAs/AlAs superlattices give, in principle, the feasibility for generation of radiation up to nearly 1 THz. A more refined experimental set-up is necessary for the observation of generation of THz radiation with a superlattice.
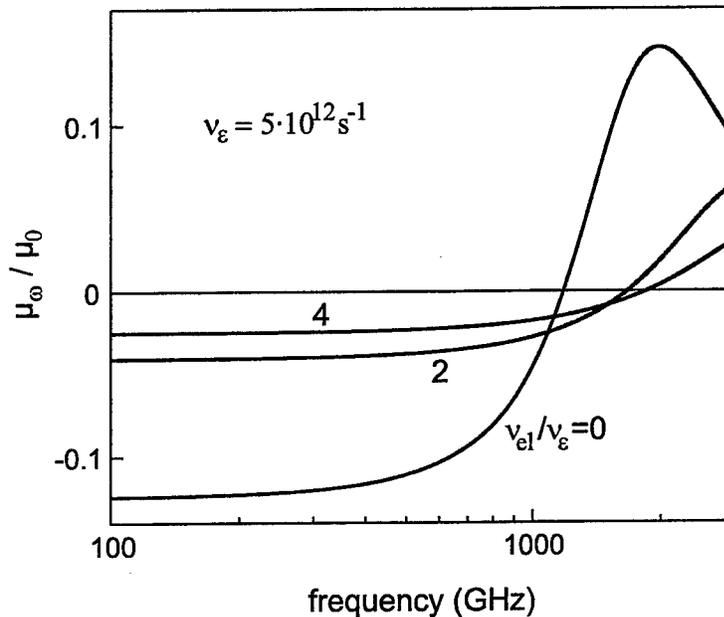
Fig.7: Frequency dependence of the small-signal high-frequency mobility normalised to the static low-field mobility.

6. FUTURE PROSPECTS

In comparison to the 120-meV superlattice device, an oscillator based on a GaAs-AlAs resonant tunnelling diode produced an order of magnitude less power (15 μW at 112 GHz [13]) at about the same efficiency. The steep slope in the negative differential conductance region of a resonant tunnelling diode makes it necessary to use devices with a diameter well below 10 μm in order to obtain a negative conductance in a range that allows a stable operation of the oscillator. Such a limit does not exist for a superlattice device because the negative differential conductance occurs over a range of several volts (Fig.2), which makes the device impedance much more suitable for matching to an external circuit. Experimental results suggest that a superlattice device oscillator can reach output powers of more than several milliwatts by using a device with a larger area and by an appropriate matching of the device impedance to the impedance of the external circuit. However, more experimental investigations are necessary to determine the superlattice device impedance.

The superlattice device can exhibit a current oscillation at a higher fundamental frequency than a GaAs Gunn diode. The fundamental frequency of a Gunn diode is limited to below 100 GHz [14] by the characteristic times (~1 ps [14]) for the electron transfer from a central conduction band minimum with high mobility to satellite minima with low mobility. To our knowledge, the highest observed frequency of a GaAs Gunn diode in fundamental mode operation was 83 GHz [15]. A fundamental frequency above 100 GHz was demonstrated with the 120-meV superlattice device. This is possible due to the short intraminiband relaxation time, which determines that the negative differential mobility exists up to submillimetre wave frequencies (Fig.7). Operation of a superlattice oscillator, optimised with respect to miniband width and length, well above 100 GHz should therefore be possible.

It is suggested that a further increase of the operation frequency can be obtained by using different material systems. For example, in comparison to a GaAs/AlAs superlattice, an InGaAs/InAlAs superlattice, with the same quantum well and barrier thickness, has the advantage of a larger miniband and, therefore, of a higher drift velocity; this is due to lower effective electron masses of the constituent materials and a lower barrier height. Accordingly, a higher oscillation frequency is expected for optimised InGaAs/InAlAs superlattices compared to GaAs/AlAs superlattices. Up to date, the highest oscillation frequencies observed for an InGaAs/InAlAs superlattice were 55 GHz [16] and 74 GHz [17]. Furthermore, InGaAs/InAlAs superlattices offer the possibility to interact with optical radiation in a wavelength range (1.3 μm) used for fibre transmission lines; this is due to an appropriate bandgap of this material system. Recently, it was reported [18] that an InGaAs/InAlAs superlattice oscillator can be injection-locked by an optical signal (modulated with a microwave signal having a frequency close to the frequency of the free running superlattice oscillator) in the 1.3 μm wavelength range. This experiment shows the potential of superlattice devices to interconnect the optical and millimetre wavelength range.

7. CONCLUSION

In conclusion, recent results of the development of superlattice devices as novel solid-state source for the generation of millimetre wave radiation were reported. Due to the short intraminiband relaxation time, a GaAs/AlAs superlattice device shows current oscillations above 100 GHz. The oscillation frequency can be adjusted over more than two orders of magnitude (1 - 100 GHz) by the miniband width and length of the superlattice. A 100-GHz oscillator based on the superlattice device had a much larger output power than the best reported GaAs-AlAs resonant tunnelling diode oscillator and was operated in a fundamental harmonic mode at higher frequencies than a GaAs Gunn oscillator. Superlattice devices based on the InGaAs/InAlAs material system are promising with respect to higher oscillation frequencies and opto-electronic applications.

8. ACKNOWLEDGEMENT

9. REFERENCES

[1] L.Esaki and R.Tsu, IBM J. Res. Dev. **14**, 61 (1970).

[2] A.Sibille, J.F.Palmier, H.Wang, and F.Mollot, Phys. Rev. Lett. 64, 52 (1990); F.Beltram, F.Capasso, D.L.Sivco, A.L.Hutchinson, S.-N.G.Chu, and A.Y.Cho, Phys. Rev. Lett. **64**, 3167 (1990).

[3] E.Schomburg, S.Brandl, K.Hofbeck, T.Blomeier, J.Grenzer, A.A.Ignatov, K.F.Renk, D.G.Pavel'ev and Yu.Koschurinov, V.Ustinov, A.Zhukov, A.Kovsch, S.Ivanov, and P.S.Kop'ev, Appl. Phys. Lett. **72**, 1498 (1998).

[4] F.Bloch, Z. Physik **52**, 555 (1928); C.Zener, Proc. Roy. Soc. London Ser. A **145**, 523 (1934).

[5] K.Hofbeck et al., to be published (1999).

[6] T.Blomeier, E.Schomburg, K.Hofbeck, J.Grenzer, S.Brandl, I.Lingott, A.A.Ignatov, K.F.Renk, D.G.Pavel'ev, Yu.Koschurinov, B.Melzer, V.Ustinov, S.Ivanov, and P.S.Kop'ev, phys. stat. sol. (b) **204**, 485 (1997).

[7] K.Hofbeck, J.Grenzer, E.Schomburg, A.A.Ignatov, K.F.Renk, D.G.Pavel'ev, Yu.Koschurinov, B.Melzer, S.Ivanov, S.Schaposchnikov, and P.S.Kop'ev, Phys. Lett. A **218**, 349 (1996).

[8] E.Schomburg, T.Blomeier, K.Hofbeck, J.Grenzer, S.Brandl, I.Lingott, A.A.Ignatov, K.F.Renk, D.G.Pavel'ev and Yu.Koschurinov, B.Ya.Melzer, V.M.Ustinov, S.V.Ivanov, A.Zhukov, and P.S.Kop'ev, Phys. Rev. B **58**, 4035 (1998).

[9] E.Schomburg, M.Henini, J.M.Chamberlain, D.P.Steenson, S.Brandl, K.Hofbeck, K.F.Renk, and W.Wegscheider, Appl. Phys. Lett. **74**, 2179 (1999).

[10] A.A.Ignatov, E.P.Dodin, and V.I.Shashkin, Mod. Phys. Lett. B **5**, 1087 (1991).

[11] C.Minot, H.LePerson, J.F.Palmier, and F.Mollot, Phys. Rev. B **47**, 10024 (1993).

[12] E.Schomburg, J.Grenzer, K.Hofbeck, T.Blomeier, S.Winnerl, S.Brandl, A.A.Ignatov, K.F.Renk, D.G.Pavel'ev, Yu.Koschurinov, B.Melzer, V.Ustinov, A.Zhukov, A.Kovsh, S.Ivanov, and P.S.Kop'ev, Solid-State Electronics **42**, 1495 (1998).

[13] E.R.Brown and C.D.Parker, Phil. Trans. R. Soc. Lond. A **354**, 2365 (1996).

[14] For a recent review see: H.Eisele and G.I.Haddad, IEEE Trans. Microwave Theory Tech. **46**, 739 (1998), and references therein.

[15] K.Akamatsu, A.Yokohata, S.Kato, N.Ohkubo, and M.Ohmori, Proc. of the 19th International Conference on Infrared and Millimeter Waves, Sendai, Japan, ed. by K.Sakai and T.Yoneyama, p.89 (1994).

[16] S.Brandl, E.Schomburg, R.Scheuerer, K.Hofbeck, J.Grenzer, K.F.Renk, D.G.Pavel'ev, Yu.Koschurinov, A.Zhukov, A.Kovsch, V.Ustinov, S.V.Ivanov, and P.S.Kop'ev, Appl. Phys. Lett. **73**, 3117 (1998).

[17] J.F.Palmier, C.Minot, J.C.Harmand, A.Sibille, D.Tanguy, and E.Penard, Superlatt. Mictrostruct. **25**, 13 (1999).

[18] J.F.Cadiou, J. Guena, E.Penard, P.Legaud, C.Minot, J.F.Palmier, H.LePerson, and J.C.Harmand, Electron. Lett. **30**, 1690 (1994).

Electronic devices for non-linear applications at Terahertz frequency

D. Lippens

Institut d'Electronique et de Microélectronique du Nord (IEMN), UMR 8520, Université des Sciences et Technologies de Lille, Avenue Poincaré, BP 69, 59652 Villeneuve d'Ascq Cedex, France

ABSTRACT

The recent advances in telecommunication and teledetection systems are creating a demand for system developments in the upper part of the millimetre wave spectrum and beyond that available in this frequency range. It is thought that novel device schemes, relying on quantum effects, will play an increasing role in this development. At last, new micromachining technologies are currently being developed for these wavelengths not only for the fabrication of passive components but also for active devices. This paper gives an overview of the Terahertz components, currently fabricated at IEMN, which are aimed at operating in THz receivers. This concerns mixers and harmonic multipliers, engineered for ultra-fast electron dynamics and strongly reactive and resistive non linearities. Special attention has been paid to high performance InP-based Heterostructure Barrier Varactors (HBV's) for harmonic multiplication, Double Barrier Heterostructure Resonant Tunnelling Diodes (DBH-RTD's) for fundamental generation and T-gate Schottky's for sub-harmonic mixing. Novel ideas will be presented in order to control the particle and displacement currents and to overcome the intrinsic and extrinsic limitations.

Keywords: Terahertz range, Non linear devices, Heterostructure Barrier varactors, Schottky diodes, Resonant Tunnelling Diodes, harmonic multipliers, sub-harmonic mixers

1. INTRODUCTION

High speed non linear semiconductor devices are key components for advanced electronic systems in the Terahertz region that handle analogue signals at frequencies typically between 100 GHz and 1 THz. These devices appears vital to the continued growth of this maturing research area which has now a long and respectable history. The study of earth atmosphere using millimetre or submillimetre spectroscopy and radio-astronomy is particularly representative of the activity in this field. Recently, tremendous strides have been made which are based on advanced epitaxial and processing techniques including epitaxial and planar integration, the development of heterostructures and the emergence of micromachining techniques. The purpose of this paper is to illustrate this evolution which affects no only the active devices but also their environment and hence the external circuits. Most important is the fact that heterostructure semiconductors can now be produced as highly perfect crystals and this provides a natural basis for the fabrication of highly non linear devices.

The structuring of semiconductors on the micron scale with a high perfection is manifested in a number of important ways. Firstly, one can take advantage of the so called quantum-size effects when the De Broglie wavelength for electron compare to the system dimension. Also, the growth of multi-layered structures opens the way to combine individual samples so that the electrical characteristics can be tailored depending of the targeted application, with respect to the power handing or frequency capabilities notably. To complete our picture of the context, it is also important to mention that advanced processing techniques including microstructuring of semiconductor dielectric and metallic heterostructures has brought a profound change in Terahertz technology driven largely by the concern of low cost system development. In this paper, I will try to give an overview of these transitions which are now spawning widespread research and development of III-V based integrated devices.

For further author information
Email: Didier.Lippens@IEMN.univ-Lille1.fr

Part of the EUROPTO Conference on Terahertz Spectroscopy and Applications II
Munich, Germany • June 1999 SPIE Vol. 3828 • 0277-786X/99/$10.00

97

Such devices include Resonant Tunnelling Diodes (RTD's)[1-11] which can operate at room temperature as fundamental solid state source, Heterostructure Barrier Varactors (HBV's) [13-26] which now compete with conventional Schottky varactors for harmonic multiplication, and Heterostructure Schottky diodes for mixing [28-31]. In terms of passive circuits components, this concerns membrane-like transmission elements for electromagnetic waves, surface micromachined access regions. Section 2 deals with Resonant Tunnelling Diodes intended to operate as fundamental solid state sources. Heterostructure Barrier varactors are considered in section 3 for harmonic multiplication while section 4 will be devoted to the studies on Schottky diodes for subharmonically pumped mixers

2. RESONANT TUNNELLING DIODES

Basically, the advantage of using semiconductor heterojunctions are numerous from the device physics to the technological points of view. In particular, a band gap engineering approach is possible for alleviating most of the trade-offs which have to be satisfied in the design and in the fabrication of Terahertz devices. On the other hand, on the short scale, new physical effects are involved with notably the occurrence of quantum effects when electron wavelength compares to the structure dimension. Resonant Tunneling Diodes are representative of this new class of quantum devices [1-2]. The generic structure consists of a Double Barrier Heterostructure. This creates a quantum well whose quantum levels can be occupied through a tunneling process. The conjunction of a tunneling process, enhanced by a resonance effect, and of quantum size effects give rise to strong nonlinearity in the current voltage characteristics with negative differential resistance effects [4-9]. However, to be observed at room temperature with a significant contrast between the on -resonance and off -resonance state, one of the first requirement is to shrink the barrier dimension in order to increase by this means the quantum probabilities. Also, as a consequence, the life time of trapped carriers on the quasi-bound state becomes very short, on picosecond or subpicosecond scales. This means that the relevant time constant involved in the resonant tunneling process can be kept short with the associated benefit of an intrinsic high frequency capability. To summarize at this stage, a resonant tunneling diodes is potentially able to operate at very high frequency provided the barrier thicknesses (Lb) are thin enough, in practice less than 2nm. In addition, this increase (exponential dependence with Lb) in the tunneling quantum transmission probabilities results in a dramatic increase in the current density. In terms of rc time constant, where the resistive part is due to the quantum conduction mechanisms, this means that this increase in the associated conductance benefits a high cut off frequency. Conversely, the current contrast is decreased and one of the key feature in the design of high performance RTD's is to preserve a high peak-to valley current ratio while maintaining a high current density.

With these requirement in mind, let us now consider the choice of a material system which are mainly InP-based or GaAs based starting from a semi-insulating substrate for subsequent planar integration. The first demonstration of pronounced negative differential conductance effects was demonstrated in the AlGaAs/AlAs with concentration of aluminum between 0.3 and 0.7. For the former content the conduction discontinuity at the GaAs /$Al_{0.3}$ $Ga_{0.7}$ heterointerface was quite low in the 200-300 eV range. Increasing the aluminum contents results in a increase in ΔEc. However, we are facing the problem -X cross over Γ. This should be also verified if a AlAs barrier is used. In practice however the thickness of the barrier plays an important role in the respective importance of tunneling mechanisms through the X or the Γ states. Therefore for thin barrier it is found that AlAs /GaAs heterostructures is the better choice for a Terahertz operation.

Another advantage stems from the fact that pseudomorhic layers can be grown which incorporates locally a certain content of Indium increasing by this way the discontinuity between the narrowest gap material and the widest gap one. Such a band gap engineering via the pseudomorphic growth of InGaAs layer is illustrated in Figure 1 which shows the epitaxial sequence of a resonant tunneling aimed at operating at millimetre wave frequency. The quantum well also contains an InGaAs perturbation and the overall structure can be compared to triple well double barrier structure. Before any processing techniques, it is often preferable to carry out some calculations in order to have some estimate of the current density identified as a key figure of merit first and of the characteristic peak and valley voltage. This can be performed by means of self consistent calculation of the band bending first followed by the modeling of the quantum transmission probabilities. The last stage is the derivation of the Current-voltage curve via the computation of the integral of current. Figure 2 shows typical results computed for a RTD for a room temperature operation. In the present case, the onset of conduction is immediate with a quasi-linear rise in the current value at increasing voltage. At the peak voltage the current suddenly decreases over practically one Volt before increasing again. The peak current density is 200 kA /cm^2.

Contact layer	$In_{0.53}Ga_{0.47}As$	$>1\times10^{19}$ at.cm-3	5000 Å
Cladding layer	$In_{0.53}Ga_{0.47}As$	1×10^{18} at.cm-3	1000 Å
Spacer	$In_{0.53}Ga_{0.47}As$	n.i.d	50 Å
Barrier	AlAs	n.i.d	17 Å
Well	$In_{0.53}Ga_{0.47}As$	n.i.d	10 Å
	InAs	n.i.d	25 Å
	$In_{0.53}Ga_{0.47}As$	n.i.d	10 Å
Barrier	AlAs	n.i.d	17 Å
Spacer	$In_{0.53}Ga_{0.47}As$	n.i.d	50 Å
Cladding layer	$In_{0.53}Ga_{0.47}As$	1×10^{18} at.cm-3	1000 Å
Contact layer	$In_{0.53}Ga_{0.47}As$	$>1\times10^{19}$ at.cm-3	5000 Å
Buried layer	InP	5×10^{18} at.cm-3	5000 Å

Fe-doped Semi-Insulating InP substrate

Figure 1 Epitaxial sequence for a RTD in InP-based technology
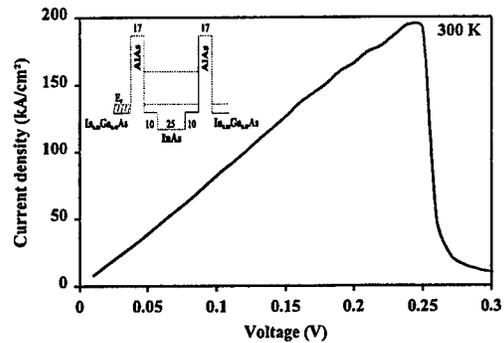
Figure 2 : Illustration of band gap engineering for RTD's in inset . Calculated current-voltage characteristic

The next step in the optimization is the fabrication of the devices which has to be planarly integrated. It was early recognized that the conventional whisker-contacted technology which was of great help to radioastronomy development cannot be used for a broader application range. Basically, the planar integration of such devices face two major difficulties. The first one is that the devices has to be integrated by defining small area. An order of magnitude is $1\mu m^2$. Contacting this very small active region to the external circuit has also to be made by means of low parasitic interconnecting techniques. In practice this implies the use of air bridge contacting technology which is quite common in MMIC technology especially for coplanar lines but require a real skill on micron and submicron scale. To illustrate the difficulty of such an integration by means of a an air bridge we show in Figure 3 the Scanning Electron Micrograph of a RTD interconnected to the external circuit with an evaporated air bridge. Thick metallisation are necessary for mechanical stability and low contacting resistance reasons. Figure 4 gives the current-voltage characteristic which can be compared to the calculated data (Figure 2).
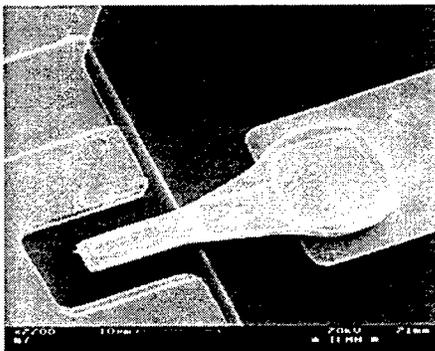
Figure 3 SEM of a RTD planar integrated
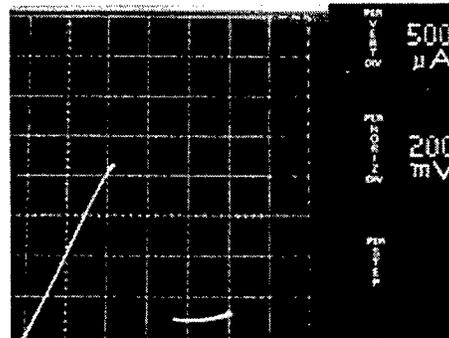
Figure 4 Current-voltage characteristics measured at 300K

3. HETEROSTRUCTURE BARRIER VARACTORS

At the end of 1980's, several research groups were involved in nonlinear applications of Resonant Tunnelling Diodes which were outlined above. Besides the effort devoted to fundamental generation, several attempts [9-11] have been also made to take advantage of the Negative Differential Conductance effects for harmonic multiplication In this context, it was soon recognised that the non linear feature of the diode capacitance characteristic also influences the overall efficiency. Subsequently, E. Kollberg and A. Rydberg [13] were the first to propose the concept of a single barrier varactor in 1989 with the acronym, at that time, of Quantum Barrier Varactor. For generic structures however, namely those consisting of a heterostructure barrier, sandwiched between two cladding layers, the electrical behaviour was found to be comparable to that of Schottky varactor diodes. Quantum effects affect mainly the leakage current characteristics due to tunnelling of

carriers through the heterostructure barrier. This is not the case for HBV structure which include two quantum wells on each side of the blocking barrier for which quantum size effects play a major role.

Basically, It can be seen that Heterostructure Barrier Varactors have potential advantages over their Schottky counterparts and very promising results have been reported in the literature [14-23]. The key advantage is the symmetry of the capacitance-voltage characteristic about zero Volt. Such symmetry improves dramatically the functionality of devices since only odd harmonics are generated in harmonic multiplication. Symmetrical C-V relationship can also be achieved with back-to-back Schottky's but its was shown that self-biasing effects impede the variation of elastance when the devices are driven in a large signal regime [24]. Secondly, several degrees of freedom are afforded by the use of semiconductor heterojunctions and novel structures, notably those making use of a quantum well/barrier or a delta doping configuration can be fabricated to tailor the C-V characteristics. Another important advantage stems from the fact that the devices can be vertically stacked during epitaxy. This epitaxial integration is a welcome feature in terms of voltage handling and capacitance levels.

However, HBV's exhibit some drawbacks. First of all, the epitaxial quality is of prime importance and highly perfect epilayers has to be grown. Sometimes the efforts made in order to improve the device performances by elegant band gap engineering are ruined by a high leakage current through defect-assisted spurious tunnelling effects. Also, it is difficult to achieve high barrier heights, of typically 0.7 eV, by comparison with the built-in potential of Schottky barrier. Finally, we have only ohmic contacts which complicate device integration especially for small-area devices.

In order to illustrate the design rules, let us consider the epitaxial material depicted in Figure 5 grown by gas source molecular beam epitaxy, starting from a semi-insulating Fe-doped InP substrate. Two basic $In_{0.53}Ga_{0.47}As$ /$In_{0.52}Al_{0.48}As$ /AlAs /$In_{0.52}Al_{0.48}As$ /$In_{0.53}Ga_{0.47}As$ layered structures were series integrated during the same epitaxy. It can be shown [25] that the device characteristics scale with epilayer complexity. Hence, the voltage breakdown is twice that of the single barrier device whereas the capacitance is half the value for one barrier. The design of epilayers was carried out by means of an in-house Schrödinger and Poisson equations solver. For a given epilayer sequence, the code permits us to compute the band bending profile along with the electron wave-function with the purpose to reduce drastically the leakage current while maintaining a high capacitance ratio.

InGaAs	5×10^8 cm^{-3}	500nm
InGaAs	1×10^7 cm^{-3}	300nm
InGaAs	Undoped	5nm
InAlAs	Undoped	5nm
AlAs	Undoped	3nm
InAlAs	Undoped	5nm
InGaAs	Undoped	5nm
InGaAs	1×10^7 cm^{-3}	300nm
InGaAs	5×10^8 cm^{-3}	500nm
InP Substrate		

X2

Figure 5 Growth sequence for HBv's in Dual barrier configuration
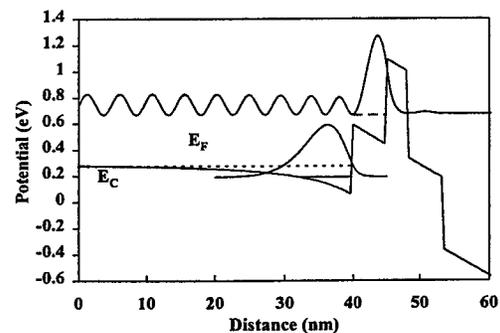
Figure 6 Conduction band profile calculated self consistently by solving Schrödinger and Poisson equations

Figure 6 illustrates this theoretical approach of the conduction (I-V curve) and storage mechanisms (C-V relationship). We plotted the conduction band edge as a function of distance for a one-barrier device biased at 4 V having the growth parameters listed in Figure 5. An accumulation region forms in front of the heterostructure barrier in a quasi-triangular quantum well. A computation of the sheet carrier density, n_s, via the electron wavefunction as a function of voltage is a direct calculation (after derivating n_s with respect to voltage) of the expected C-V characteristic. To illustrate the conduction mechanisms, we have also plotted the wave-function corresponding to the leakage current via a tunneling mechanism [26]

This tunneling process explains the conduction mechanisms at moderate voltages. In contrast, the breakdown conduction, around 6 V for the device under consideration, is due to impact ionization. It is worth-noting that this characteristic tunneling energy is several hundred meV (>600meV) and hence is much higher than the relevant energy value involved in a GaAs technology. For instance, the relevant characteristic energy would be about 180 meV for a $GaAs/Al_{0.7}Ga_{0.3}As/GaAs$. This is the fundamental reason why the voltage handling of InP-based diodes is dramatically improved. In practice an improvement of a factor of three can be pointed out (6V instead of typically 2 V). Figure 7 shows the device layout.
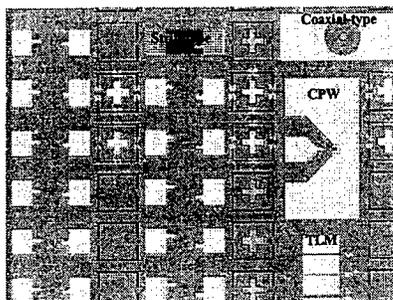
Figure 7 Layout of fabricated HBV's in
InP based technology
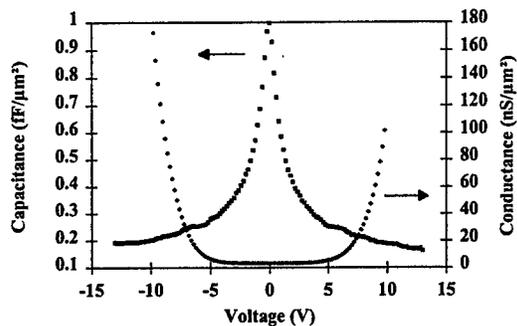
Figure 8 Illustration of non linearity
for a Dual Barrier Heterostructure

Figure 8 displays the nonlineraty achieved experimentally for two barriers in series which correspond to a Dual Heterostructure Barrier Varactor (DHBV). The symmetry in the C-V characteristic is excellent. This is advantageous for efficiently rejecting the even harmonics as shown in section 5. The zero-bias voltage is $1fF/\mu m^2$. The capacitance ratio is 6:1 Also plotted in Figure 8 is the voltage dependence of the conductance of the device. Note the unit of the conductance in $nS/\mu m^2$. The voltage handling of such a device is thus remarkable with a "safe" peak-to-peak operating voltage range of at least 20 V. In addition to the careful design of the blocking barrier, special attention has also to be paid to the adjacent layer that greatly influences the trade-off between current saturation effects [27] and achievable capacitance ratio. The former can be overcome by increasing the doping concentration. The latter is related in first approximation to the ratio between the barrier thickness (the screening length has also to be taken into account for a better estimate) and the depletion layer thickness as seen in the following section in GaAs technology. Also, some band gap engineering has to be implemented to increase the conduction band offset. Turning now to the device technology challenges, firstly we have to mention that several stages can be distinguished aimed at the characterisation of devices at the wafer level or in a multiplier block. On the other hand, it seems preferable to fabricate a set of devices by varying their topology. Towards this goal, we included in the mask set a large variety of configuration in the device area and in the level of planar integration. From figure 7 which is an optical view of the layout prior to the implementation of the air bridges, three kinds of devices have been patterned on the mask set. The simplest is of coaxial-type. It consists of a mesa-etched circular-shaped device with a concentric ring shaped side contact. It is used for rapid assessments of current-voltage and capacitance-voltage characteristics without the requirement of an air-bridge contacting technology
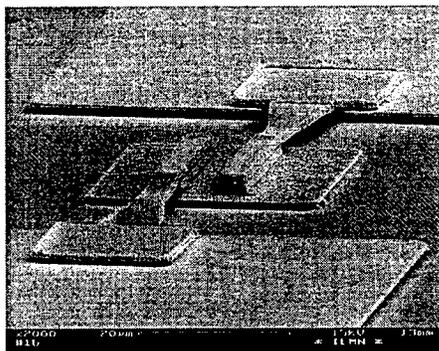
Figure 9 Scanning Electron Microphotograph for a
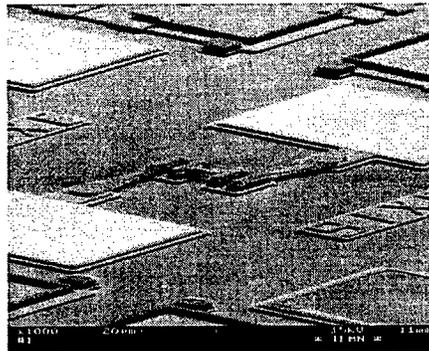
Figure 10 SEM of a device with eight integrated barriers

quadruple barrier device.

Conventional fabrication technologies were employed with sequential Ni/Ge/Au/Ti/Au overlay for the ohmic contact fabrication and $H_3PO_4/H_2O_2/H_2O$ solution for the wet etching of isolation mesa taking advantage of the high selectivity between InGaAs and InP. For the metallisation of the air-bridges, we employed either an electroplating technique or evaporation procedure. For the latter option, we developed a pyrolyzation technique of photo-resists which results in a convex shaped temporary mold for thin metal film evaporation.

The main purpose of the small signal measurements was to derive an equivalent circuit of devices for the subsequent harmonic balance simulations. The intrinsic nonlinear capacitance-voltage characteristics can be measured without de-embedding techniques by means of coaxial type configuration not only at low frequency but also at a frequency corresponding to the pump frequency (@83.3 GHz for the application reported in the present work). On the other hand it is worth mentioning that this kind of preliminary experiments gives some estimate of the series resistance on the basis of the impedance analysis. Experimentally, we measured a few ohms, the exact value depending on the area, despite the fact that large anode contacts were used. In addition, TLM measurements by means of the resistance ladder were performed yielding a resisivity of typically $1 \times 10^{-7} \Omega \, cm^2$. This clearly shows the benefits of using a low band gap InGaAs contacting layer and high doping concentration ($\sim 5 \times 10^{18} \, cm^{-3}$). This means that the contact resistance is less than 1Ω for an area greater than $10\mu m^2$. Subsequently, the CPW test pattern was used to deduce the equivalent circuit for airbridge-contacted devices. In that case, we must include the extrinsic elements which are, in a first approximation, the self inductance due to the air bridge and the pad-to-pad capacitance. The self-inductance resonates with the capacitance elements notably the diode capacitance which can be tuned either by a change in the bias voltage or in the diode area (Figures 11 and 12). This well defined resonance which can be carefully recorded, provided the measurements are performed in a broad band, permits us to derive a complete equivalent circuit without ambiguity.
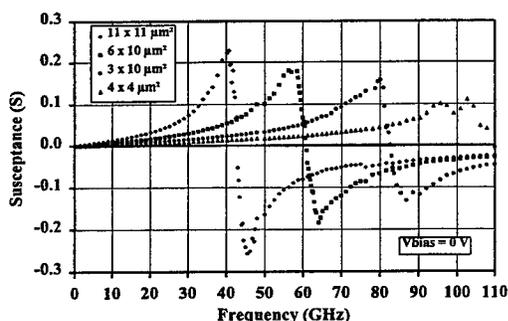
Figure 11 Small signal impedance mesaurements for HBV's for various diode areas
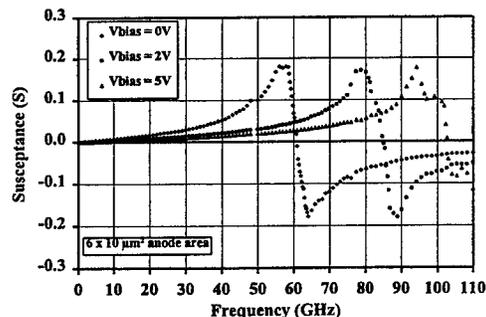
Figure 12 . Influence of bias voltage on resonance effects

By means of this procedure we have measured the series resistance which is the key parameter for achieving a high cut-off frequency and hence high device performance: Rs =3.8 Ω for a $30\mu m^2$, 2.5 Ω for 60 μm^2 and 2.2 Ω for a 121 μm^2 device. One can note that the series resistance does not scale with area as expected when the spreading resistance plays the major role. From the data extracted from the both types of measurements (coaxial- and CPW-type) an estimate of the cut-off frequency of the diodes can be obtained. We thus calculate f_c = 1.5 THz and 2.1 THz respectively for DBH's of 60 and 30 μm^2 area from the small signal measurements.

The multiplier block used for the tripler measurements at 250 GHz is a crossed wave guide type mount with a design in a similar fashion to the Archer's one with wave-guides coupled through a low-pass stripline filter. The pump power incident in the full-height WR-8 waveguide is fed to the planar integrated diode through a stripline E-plane transition and through the low pass filter implemented on a 75 μm-thick quartz substrate. Impedance matching at the pump power is achieved using two sliding non contacting backshorts. The output was also equipped with two backshorts. On the other hand, the multiplier block differs from that of the Archer's tripler design by the full-height output waveguide where the diode chip is mounted in a flip-chip technology using a conductive epoxy. For mounting purpose, the diode samples were first thinned to

a thickness of about 100μm by a HCl wet etching and then diced into discrete devices. The overall chip dimensions are thus 100x220x100 μm³.
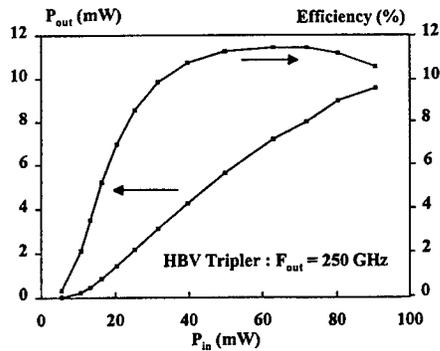
Figure 13 Performance achieved at ENS with a 6μm diameter device
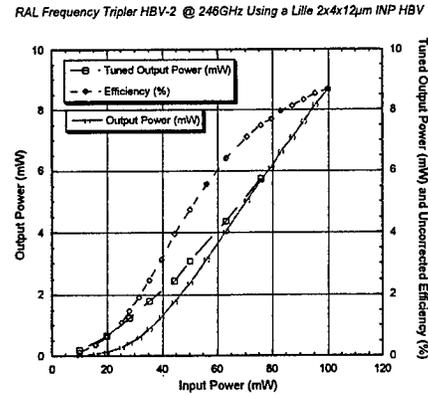
Figure 14 Performance measured at RAL. 4x12μm² Finger-shaped contact

In comparison to our previous experiment with 2x12μm² samples reported previously [17] with 5% efficiency and 5mW output power at 216 GHz a significant increase in efficiency and frequency capability has been achieved. The new low-loss block multiplier can explain this improvement. On the other hand, the influence of device impedance which is varied by changing the device areas is now clear. In the RAL experiment (Figure 14), large area devices have been used (48μm²). No saturation effects in the output power variation versus input power can be seen and it is believed that much higher power could be delivered at higher pump level. In the ENS/OBS experiments (Figure 13) smaller area devices have been tested (28 μm²). Under these conditions the devices can be driven at reduced power in non linear regime. At last, let us mention that in this later case the output waveguide was WR 4 and this permitted us to measure the second harmonic content which was found to be -25 dB below the third harmonic. This very good rejection of the even harmonic is a direct consequence of the excellent symmetry in the capacitance-voltage characteristics. In the short term, it is believed that this very good performances with simultaneously high output power and efficiency can be further improved with the rf testing of eight barrier samples.

4. SCHOTTKY DIODES

The third key component in ultra high frequency nonlinear electronics is the Schottky diode which is notably used in heterodyne reception at room temperature. In that case, we take advantage of the exponential variation of current versus voltage under bias condition for down converting the rf signal. At increasing frequency, one of the main difficulty stems from the lack of local oscillator which deliver sufficient power for optimal operation. As a consequence, it may be wise to use a mixer that is pumped at half the rf frequency and to mix the rf signal with the second harmonic. Such subharmonically pumped mixers have exhibited excellent performances over the past at millimetre wavelengths with conversion efficiency only slightly worse than comparable fundamental mixers. Successful operation of subharmonically pumped mixers requires a antiparallel configuration for mounting the diodes with a very good circuit balance. In particular, the associated diodes and the parasitics due to interconnecting elements must have identical characteristics. At ultra high frequencies, this balance can be very difficult to reach, especially for whisker contacted diodes. For this reasons, the planar integration of the devices is essential for successful operation at Terahertz frequency while maintaining a low parasitic environment. This is one of the main difficulties for the development of high performance subharmonic mixers. In additions a number of improvement has to be brought in the devices conception and fabrication. On one hand, the series resistance has to be as low as possible for increasing the device cut-off frequency. This implies notably to use narrow gap for access region. In this case, it is possible to drastically decrease the buit-in potential of the Schottky contact with the associated benefit of a limited pump power.

In the following section, I will try to illustrate these various issues by considering first the design of epilayers. It is now well know that a low resistance ohmic contact requires a low gap material. This generally in contrast to the fabrication of high

threshold voltage Schottky contact for which it is imperative to deposit the metal on wide gap semiconductor. On the other hand, using a low gap material is often synonymous with electron high mobility and of high doping concentration. The flexibility afforded by the use of heterojunction cannot be denied. Let us now consider two kinds of epilayers which permits us to point out the limitations of such band gap engineering especially with respect to the ideality factor. In Figure 15, we plotted for comparison the current-voltage characteristics calculated in (a) with a InGaAs active layer in (b) when a thin InAlAs layer is inserted between the schottky contact and the InGaAs layers. All epilayer are assumed lattice matched to the InP substrate with a Aluminium concentration of 0. 47 and 0.48 respectively. In both cases, the doping concentration in the InGaAs layer is 2×10^{17} cm^{-3} for a nominal thickness of 0.1 μm. The access region consist of a 1or 2 μm thick $In_{0.47}Ga_{0.53}As$ layer doped to 1×10^{19} cm^{-3}. As expected the introduction of a surface wide gap material modulates the threshold voltage, which in practice could be varied between 0. 15 and 0. 7 eV. The former corresponds to a full InGaAs epilayer with a steep increase in the current-values for an onset of conduction close to 0.1 V. Under reverse bias the conduction is stopped but the threshold voltage for impact ionisation is limited. With the insertion of an InAlAs layer all the relevant voltages are pushed to higher values but to the detriment of the non linearity of the conduction characteristics. Therefore, there exist a trade-off in the conduction behaviour of the devices and the next stage is to study in what extent these variations in the ideality factor and buit-in potential influence the performance of the subharmonic mixer in terms of conversion efficiency and noise temperature.
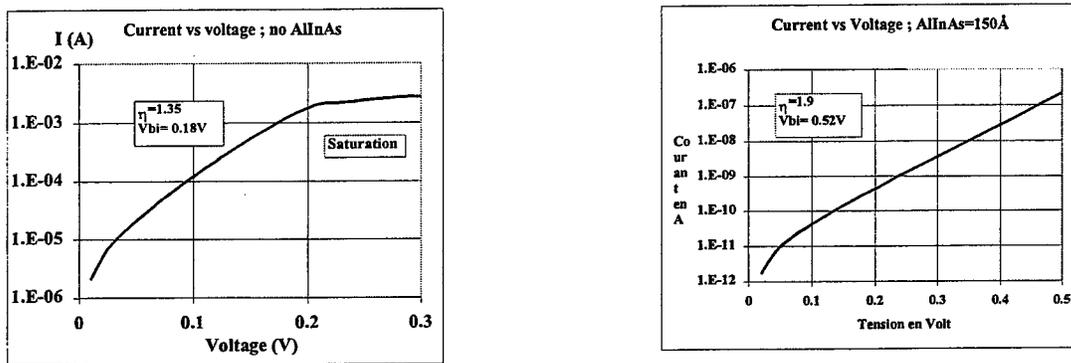
(a) 0.1μm-thick InGaAs/1μm-InGaAs/ SI InP substrate   (b) 0.02-thick InAlAs/ 0.1μm thick InGaAs /SI InP

Figure 15 Current-voltage characteristics calculated by self consistently solving the Poisson and Schrödinger equations

Turning now to the design of the subharmonically pumped mixer, we plot in Figure 16 the variation of the conversion efficiency for a room temperature subharmonic operation for various values of ideality factors. It can be seen that an increase in the values of η does not degrade the down conversion efficiency but the optimum pump power is accordingly increased. For the present simulation carried out by means of the commercial software Microwave Design System® of HP, the built-in potential was 0. 25 V. With a value for η of 1. 4 the optimum required local oscillator would be -2 dBm (less than 1mW. In contrast, any increase in η degrades the noise properties by typically 1dB in the range investigated with an average value of 10 dB (Figure 17).
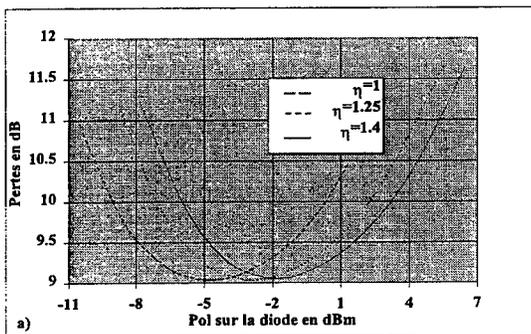
Figure 16 Conversion efficiency versus pump power   Figure 17 Influence of the ideality factor on the noise figure
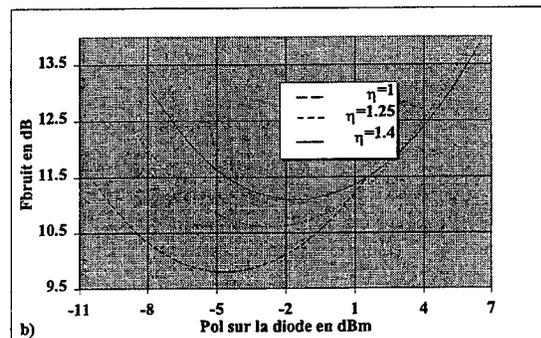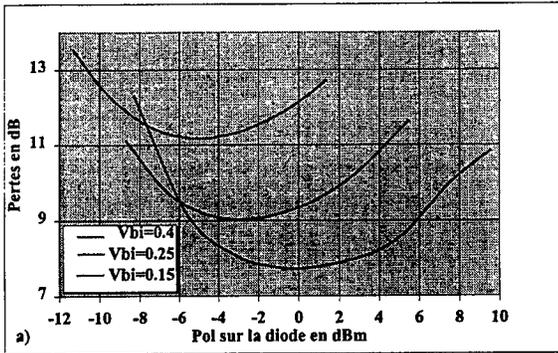
Figure 18 Conversion efficiency as a function or the pump power with the buit-in potential as a parameter
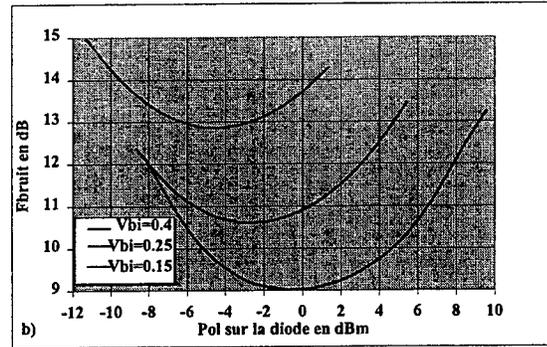
Figure 19 Noise Figure versus LO power for various values of built-in potentials

The role played by the built in potential in the achievement of good performance is illustrated in Figure 18 (conversion efficiency) and in Figure 19 (Noise Figure). It can be noted that the counterpart of any decrease in the threshold for conduction offset is a degradation of both in conversion efficiency and noise temperature. Again a trade-off is necessary to establish between the required pump power and the targeted performances. In order to get a further insight into the impact of the technology let us now consider the processing techniques on the basis of a planar integration of the devices. Most of the guides lines discussed previously can also be applied to the fabrication of Shottky's but several specific points have however to be taken into account. The first one is the necessity to shrink drastically the lateral dimension of the diodes to met the requirement first of a low capacitance and secondly to decrease as far as possible the series resistance. In fact, various contributions can be identified in the overall series resistance and notably the resistance of contact metal and the spreading resistance. For the latter, is can be demonstrated that a huge improvement can be obtained by implementing finger-shaped contacts rather than circular shaped anodes surrounded by an ohmic contact in very close proximity. In addition, the overall area should be in the $1\mu m^2$ range, this means that the lateral dimension are on submicron scale. Similar criteria are encountered for High Electron Mobility transistors and the topology implemented for the realisation of High speed HEMT can be adapted for the fabrication of Terahertz Schottky notably the T-gate or Mushroom gate topology. Another key point is the parasitic capacitance whose influence was pointed in several studies [28-29]. Various contributions can be foreseen but with a major contribution due to the pad-to pad capacitance. In order to decrease this parasitic term is to use the surface channel approach which consist in a deep surface etching so that the self sustaining air bridge is crossing a wide air gap. On the basis of these fabrication guide lines, extremely small area Schottky diodes can be fabricated in a an antiparallel configuration. Figure 20 shows a Scanning electron microphotograph of the mould which served for fabricating the T gate. The patterning was performed by means of a LEICA HRPG with a nominal width for the gate of 0.1 μm. The T shape was obtained making use of a bi-layered MMA/PMMA resist profile. For the fabrication of air bridge, temporarily sustained by a resist layer, and for the definition of pillar on the circuit side we used some variations of dose in order to write the mould for the whole interconnecting metallisation and contact material in one step (Figure 21).
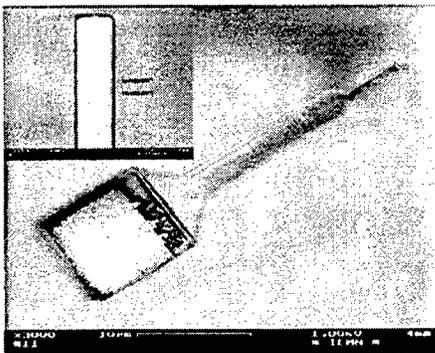
Figure 20 SEM of the mould which is used for processing in one step the contacting and interconnecting elements
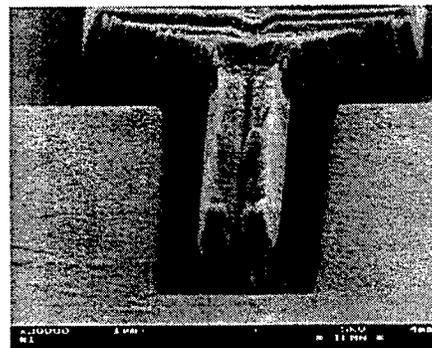
Figure 21 SEM view of the T shaped Schottky contact

105

Figure 22 show a Scanning Electron Microphotograph of a Schottky diode planar integrated in a Coplanar waveguide configuration in order to wafer probe the devices up to 110 GHz. These measurements of the air bridges contacted devices over a quite broad band permits one to define the lumped circuit elements which can be subsequently used for harmonic balance simulations. Similar resonance effects than those found for HBV devices can be pointed out. In the frequency dependence of the small signal impedance seen at the two terminals whose resonant frequency can be of great help for accurate determination of lumped elements. For large signal analysis the diodes can be integrated in an anti-parallel scheme as exemplified in Figure 23. Two diodes are facing each other and are interconnected by two pads. A surface micromachining stage etching deeply into the Semi-insulating InP substrate lowered as explained above the parasitics capacitance. These kind of devices relying on an InP technology have been successfully fabricated in several laboratories over the world and have shown promise for the down conversion under subharmonically condition at 200 and 500 GHz [31].
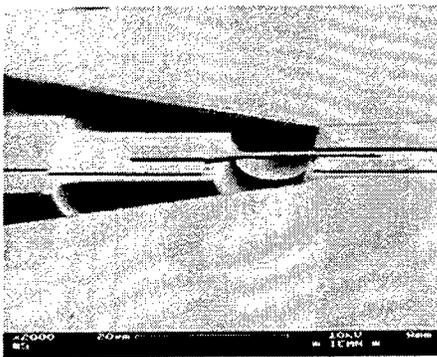
Figure 22 SEM of a single Shottky device in a Coplanar Wave-Guide configuration
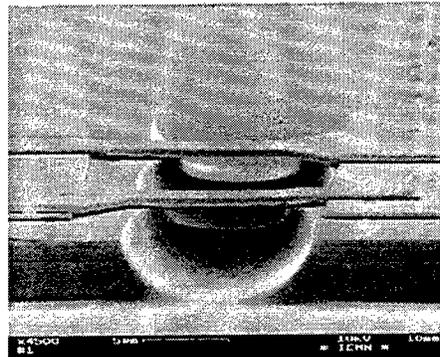
Figure 23 SEM of an antiparallel diode scheme planarly integrated

5. CONCLUSION

In conclusion, the Terahertz field has now experience a profound change resulting from the recent advances in the growth of multi-layered heterotructure on short scales and in planar integration techniques. For each non linear functions involved in heterodyne reception and more generally in reception head, some novel devices can be implemented which now compete in terms of frequency capability and/or power delivering with respect to more conventional devices. The use of semiconductor heterostructures appears vital in the improvement of performances for the enhancement of functionality. This is notably the case for resonant tunnelling diodes whose barrier control enables now to fabricate high current devices in excess of 100 kA/cm^2 while preserving a high contrast between the on-and off-resonant states. So far RTD's have no solid state competitor for operating in the submillimetre wave range. In counterpart the delivered power is in the microwatt range at submillimetre wavelengths. HBV's do not suffer frm this power limitation and have exhibited record performance in the upper part of the millimeter wave spectrum. Extension of these studies to higher frequencies is envisaged but some scaling rules for the doping concentrations and dimensions has to be fulfilled. Heterostructure Schottky's have shown very promising results for subhramonivcally pumped mixers aimed at operation in the 500-600 GHz frequency band. The use of heterotructure in conjunction with low gap materials appears favourable to limit the pump signal for driving the devices in non linear regime. It is believed that further improvement can be achieved by a three dimensional integration of the devices making advantge of epitaxial stacking and air bridging techniques.

6. ACKNOWLEDGMENT

7. REFERENCES

1. M. Reddy at al. "Monolithic Schottky Collector Resonant Tunnelling Diodes Arrays to 650 GHz", IEEE Electron Devices letters, Vol. **18**, N°5, 1997

2. E. R. Brown, J. R. Söderström, C.D. Parker, L.J. Mahoney, K.M. Molvar, and T.C. Mc Gill, 3Oscillations up to 712 GHz in InAs/AlSb Resonant Tunnelling Diodes3, Appl. Phys. Lett.; **58**, pp. 2291-2293, 1991

3. J. R. Södersrtöm, E. R. Brown, C. D. Parker, L. J. Mahoney, J.Y. Yao, T.G. Anderson and T.C. Mc Gill," Growth and Characterization of High current density, High speed In/AlSb Resonant tunnelling Diodes", J. Appl. Phys., **58**, pp. 275, 1991

4. T.P.E. Broekart, W. Lee, and C.G. Fonstad, "Pseudomorphic $In_{0.53}Ga_{0.47}As$/AlAs /InAs Resonant Tunnelling Diodes with peak-to-valley ratios of 30 at room temperature", Appl. Phys. Lettes, **53**, pp. 1545-1548, 1988

5. D. Z. Y. Ting, M. L. Jackson, D.H. Chow, J.R. Söderström, D. A. Collins, and T. C. Mc Gill, "X-point tunnelling in AlAs/GaAS Double Barrier Heterostructures", Solid State Electronics, **32** , pp. 1513, 1989

6. T. S. Moise, Y.C. Kao, A. J. Katz, T.P. Broekaert, and F.G. Celio, "Experimental sensitivity analysis of pseudomorphic InGaAs/AlAs Resonant Tunnelling Diodes", J. Appl. Phys. **78**, pp. 6305, 1995

7. H. Kitabayashi, T. Waho, and M. Yamamoto, "Resonant interband tunnelling current in InAs/AlSb/GaSb/InAs Double Barrier Diodes", J. Appl. Phys., **84**, pp. 1460, 1998

8. H. Kitabayashi, T. Waho, and M. Yamamoto,3'Resonant Interband Tunnelling current in InAs/AlSb/GaSb,/InAs diodes with extremely thin AlSb barrier layers", Appl. Phys. Lett., **71**, pp; 512, 1997

9. E. R. Brown, W.D. Goodhue, and C.A. Correa, "Harmonic multiplication using resonant tunneling", J. Appl. Phys. Vol. **64**, pp. 4248, October 1988

10. A. Rydberg, and H. Grönqvist,"Quantum well High efficiency millimeter-wave frequency multiplier", Electronics Letters, Vol. **25**, pp. 348-349, 1989,

11. R. Bouregba, D. Lippens, L. Palmateer, E. Bockenhoff, M. Bogey, J.L. Destombes, A. Lecluse,",Frequency multiplication using resonant tunneling diodes with output at submillimeter wavelengths", Electronics Letters, Vol. **26**, pp. 1804-1805, October 1990

12. C. H. Page, "Harmonic multiplication with ideal rectifiers", Proceedings of the IRE, Vol. **46**, pp. 1738-1740, October 1958

13. E. Kollberg, and A. Rydberg, " Quantum-barrier-varactor diodes for high-efficiency millimeter wave multipliers", Electronics Letters, Vol. **25**, pp. 1696-1697, December 1989

14 A. Rydberg, H. Grönqvist and E. Kollberg," Milllimeter - and Submillimeter-Wave Multipliers using Quantum Barrier-Varactor (QBV) Diodes", IEEE Electron Device Letters, Vol. **11** pp. 373-375, September 1990

15. D. Choudhury, M.A. Frerking and P. D. Batelaan, "A 200 GHz Tripler using a single barrier varactor", IEEE Transactions on microwave Theory and Techniques, Vol. **41**, pp. 595-599, April 1993

16. J. Stake, L. Dillner, S.H. Jones, C.M. Mann, J. Thornton, J.R. Jones, W.L. Bishop, and E. Kollberg "Effects of self heating on planar heterostructure Barrier varactor diodes", IEEE Transactions on Electron Devices, pp. 179-182, Vol. **45**, 11, November 1998

17. X. Mélique, C. Mann, P. Mounaix, J. Thornton, O. Vanbésien, F. Mollot, and D. Lippens, "5mW and 5 % efficiency 216 GHz InP-based Heterostructure barrier varactor tripler", IEEE Microwave and Guided Wave Letters,Vol. **8**, pp. 384-386, November 1998

18. A. Rahal, R.G. Bosisio, C. Rogers, J. Ovey, M. Sawan, and M. Missous, "A W-band medium power multistack quantum barrier varactor frequency multiplier", IEEE Microwave and Guided Wave Letters, Vol. **5**, pp. 368-370, November 1995

19. J.R. Jones , W.L. Bishop, S.H. Jones, and G.B. Tait, "Planar multibarrier 80/240 GHz Heterostructure Barrier Varactor triplers", IEEE Transactions on Microwave Theory and Techniques, Vol. **45**, pp. 512-518, April 1997

20. K. Krisnamurthi, S.M. Nilsen, and R.G. Harrison, "GaAs Single-barrier varactors for millimeter-wave triplers: guidelines for enhanced performances", IEEE Transactions on Microwave Theory and Techniques, Vol. **42**, pp. 2512-2516 , December 1994

21. A. Rahal, E. Boch, C. Rogers, J. Ovey, and R.G. Bosisio, "Planar multistack quantum barrier varactor tripler evaluation at W-band, Electronics letters, Vol. **31**, pp. 2022-2023, 1995

22. K. Krisnamurthi and R.G. Harrison, "Millimeter-wave frequency tripling using stacked heterostructure Barrier Varactor on InP", IEEE Proc. Microwave Antennas Propagation, Vol. **43**, pp. 272-276, August 1996

23. A. V. Räisänen, T. J. Tolmunen, M. Natzic, M. A. Frerking, E. Brown, H. Grönqvist and S. M. Nilsen, " A single barrier quintupler at 170 GHz", IEEE Transactions on Microwave Theory and Techniques, Vol. **43**, pp. 685-688, March 1995

24. R. F. Bradley, A. R. Kerr, and N. Erikson, "Why don't back-to-back abrupt junction frquency triplers work", Proceedings of the eight International Symposium on Space Terahertz Technology, Havard Smithsonian, Cambridge, March 1997

25. E. Lheurette, P. Mounaix, P. Salzenstein, F. Mollot, and D. Lippens,"High performance InP-based Heterostructure barrier varactors in single and stack configuration", Electronics Letters, Vol. **32**, pp. 1417-1418 July 1996

26. R. Havart, E. Lheurette, O. Vanbésien, P. Mounaix, F. Mollot and D. Lippens, "Step-like heterostructure barrier varactor", IEEE Transactions on Electron Devices, Vol. **45**, November 1998

27. E. Kollberg, T.J. Tolmunen, M. A. Frerking, and J. East, " Current saturation in submillimeter wave varactors" IEEE Transactions on Microwave Theory and Techniques, Vol. **40**, pp. 831-838

28. R.E. Muller, S. C. MartinR.P. Smith, S.A. Allen, M. Reddy, U. Battacharaya, and M.J. W. Rodwell, "Electron beam lithography for the fabrication of air-bridged, submicron Schottky collectors", J. Vac. Sci. Technol. , **12**, pp. 3668-3672, 1994

29. C.M. Mann, "mixers for the millimetre, submillimetre and Terahertz regions, Procceedings 28 th European Microwave Conference, Amsterdam, 1998

30. K. Hong, P. F. Marsh, G.I.Ng, D. Pavlidis, and C.H. Hong, "optimization of MOVPE grown InAlAs/InGaAs planar heteroepitaxial Schottky diodes for Terahertz applications", IEEE trans. On Electron Devices, **41**, pp. 1489-1497, 1994

31. I. Medhi, S.C. Martin, R.J. Dengler, R.P. Smith, and P.H. Siegel, "Fabrication and performance of planar Schottky diodes with T-gate-like anodes in 200 GHz subharmonically pumped waveguide mixers", IEEE Microwave and Guided Wave Letters, **6**, pp. 49-51, 1996

Highly non linear capacitance in quantum well/barrier heterostructures : application to harmonic multiplication at Terahertz frequency

V. Duez[a] , M. Henini[b], O. Vanbésien[a], M. Chamberlain[b], and D. Lippens[a]

[a]Institut d'Electronique et de Microélectronique du Nord, UMR CNRS 8520, Département Hyperfréquences et Semiconducteurs, Université des Sciences et Technologies de Lille, Avenue Poincaré BP 69, 59652 Villeneuve d'Ascq Cedex, France
[b]The University of Nottingham, University Park, Nottingham NG7 2RD, United Kingdom

ABSTRACT

In this communication, we report on the design and the fabrication of quantum well barrier varactor structures with state of the art results in terms of capacitance ratio over a narrow voltage range. Basically, the fact to consider is a barrier cladded by two quantum wells with respect to a single barrier heterostructure. It has several consequences for the non linear character of the device. The capacitance mechanism is governed at low voltage by the electron population rates of the quantum well rather than the conventional depletion mode process. A true band gap capacitance engineering is here demonstrated with three kinds of structures either in the InP material system with a InGaAs/InAs/AlAs heterostructure or in the GaAs material system with GaAs/InGaAs/AlAs pseudomorphic epilayers and lattice matched AlGaAs/GaAs/AlAs heterojunctions. Self-consistent simulations, based on the solution of Poisson and Schrödinger coupled equations system, were performed in order to calculate the electron wave function and the conduction band bending. High capacitance ratios can be predicted depending on material parameters and structure geometry. Test samples were then fabricated and rf tested. The devices exhibit very high capacitance ratios in excess of 5:1 over a 1Volt range.

Keywords: Heterostructure barrier varactor, harmonic multiplication, Terahertz frequency, GaAs material system, InP material system, Schrödinger-Poisson solver, quantum capacitance.

1. INTRODUCTION

Heterostructure barrier varactors (HBV)[1] now compete with Schottky barrier varactors with record performance at millimeter wave frequency in tripling operation. Their electrical properties, namely a sharp non-linearity and a symmetrical capacitance-voltage characteristic about zero volt, greatly enhance the functionality of devices since only odd harmonics are generated. Various results for HBV triplers have been reported in literature between 200 and 280 GHz for GaAs based devices[2-3]. Recently, we report record performances in terms of maximum efficiency (12.3 %) and output power (in excess of 9 mW) at 247.5 GHz[4-5] for an InP material system based structure which consisted of two InGaAs/InAlAs/AlAs barriers epitaxially stacked. Further developments are now necessary to further improve the non-linearity of the devices aimed at operating at terahertz frequency in the context of a reduced drive power. Towards this goal, we report here on the design and the fabrication of quantum well barrier structures with state-of-the-art results in terms of capacitance ratio over a narrow voltage range.

Basically, the fact to consider is a barrier cladded by two quantum wells with respect to a single barrier heterostructure. It has several consequences for the non linear character of the device. First, electrons occupy the two-dimensional density of states of the quantum wells under equilibrium. As a consequence at zero bias, the blocking barrier is sandwiched in very close proximity by two highly populated regions while maintaining a moderate doping level in the adjacent layers. The associated benefit is an expected increase in capacitance ratio. The capacitance mechanism is governed at low voltage by the electron population rates of quantum well and not by a conventional depletion mode process. At last, there exist numerous degrees of freedom opening the way of a band gap capacitance engineering. In this communication, the idea is demonstrated with three kinds of structures either in the InP-based material system with InGaAs/InAs/AlAs heterostructure[6-7] or in the GaAs based

---

For further author information

V.D : Email : Valerie.Duez@IEMN.univ-lille1.fr

108

Part of the EUROPTO Conference on Terahertz Spectroscopy and Applications II
Munich, Germany ● June 1999 SPIE Vol. 3828 ● 0277-786X/99/$10.00

system with GaAs/InGaAs/AlAs epilayers grown under pseudomorphic conditions[8] and lattice matched AlGaAs/GaAs/AlAs heterojunctions.

The paper is organized as follows : In part 2, the self consistent Poisson-Schrödinger solver is briefly described. Part 3 is devoted to the design of diodes in both GaAs and InP material system. Experimental results of devices fabricated[9] and rf tested[10] are presented and discussed in Part 4. Part 5 contains concluding remarks.

2. NUMERICAL PROCEDURES

A heterosrructure barrier varactor consists typically of a wide band gap semiconductor sandwiched by two symmetrical n-type epilayers having a smaller band gap. The central barrier prevents conduction through and over the heterojunction while each cladding layer can be depleted under reverse and forward bias conditions. The key figures for capacitance non linearities in varactor structures are namely the maximum capacitance at equilibrium and the capacitance ratio extension upon voltage. To reach terahertz frequency operation, one has to maximize the former and to minimize the latter since less drive power for harmonic multiplication is available at a few hundreds of GHz. In conventional devices, as in Schottky varactors, the capacitance ratio is dominated by the saturation capacitance value obtained generally by the depletion of a moderately doped layer. Here the idea is to increase the capacitance at equilibrium by means of quantum wells and the associated two dimensional density of states which allow us to decrease significantly the electric field screening lengths. Moreover, the capacitance modulation at low voltages will be governed by the escape of carriers from these quantum wells with the result of a steep decrease compared to a conventional depletion regime. Since the growth of III-V semiconductors gives us the opportunity of a true band gap engineering, we will examine in the next section the potentialities of three material systems, respectively the InP-based InGaAs/InAs/InAlAs/AlAs heterostructure, the GaAs-based pseudomorphic GaAs/InGaAs/AlAs heterostructure and the GaAs-based lattice matched AlGaAs/GaAs/AlAs heterostructure.

For an accurate treatment of both quantum mechanisms and classical depletion effects and of their impact on the capacitance-voltage characteristics of these quantum well varactor devices, a self-consistent solver for the potential and the charge distributions throughout the device is necessary[11-12]. Here, the main difficulty that faces us is the superimposition of regions of different dimensionality both in space or in the energy domain as it is exemplified in the schematic band profile given in Figure 1. Therefore, a code giving the solution of the unidimensional Schrödinger-Poisson coupled system of equations combined with a two or three dimensional determination of carrier densities depending on confinement conditions has been developed.
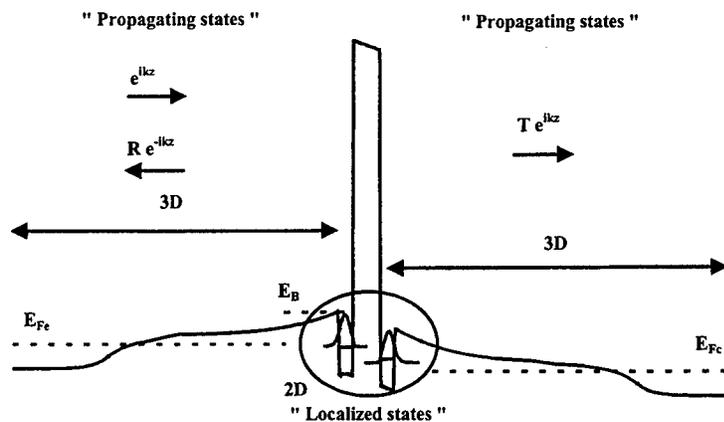
Figure 1 : Schematic of the conduction band profile for a quantum well-barrier heterostructure. Space and energy domains are defined depending on the confinement conditions.

First a discretized form of the Poisson equation is solved using a variable spatial discretization mesh[13]. This allows us to treat simultaneously large regions such as the cladding layers as well as potential perturbations on the monolayer scale :

$$\frac{\partial}{\partial z}\left(\varepsilon(z)\frac{\partial}{\partial z}V(z)\right) = -q\left(N_D^+(z) - N_A^-(z) + p(z) - n(z)\right) \qquad (1)$$

As boundary conditions, we use Dirichlet conditions on both sides in the emitter and collector regions which are considered at equilibrium (Thomas-Fermi approach). The applied bias voltage is thus defined by the energy difference between the corresponding emitter and collector Fermi levels. The calculation procedure makes use of a (over)relaxation method to accelerate convergence.

To determine space charge effects, we need an accurate description of the free carrier density. To this aim, the solution of the time-independent Schrödinger equation, using the effective mass approximation according to the n-type material constituting the heterostructure, is calculated by using the following equation :

$$-\frac{\hbar^2}{2}\frac{\partial}{\partial z}\left(\frac{1}{m_e^*(z)}\frac{\partial}{\partial z}\varphi(z)\right) + V(z)\varphi(z) = E_z\varphi(z) \qquad (2)$$

When considering the structure under investigation, two approaches have been developed. On one hand, we used an eigenvalue solver for carriers trapped within the quantum well-barrier region which can be considered as a closed system. This model used a standard matrix approach with zero wave-function values at the boundaries on the variable spatial mesh already defined for Poisson's equation. However, since the emitter and collector region are three dimensional, open system, a solution has been developed to calculate the current density flowing through the device with plane wave boundary conditions. Here, a classical Runge-Kutta method is used.

The overall carrier distribution is then considered as the superimposition of both the two and three dimensional states, as shown in Figure 1 :

$$n(z) = n_{2D}(z) + n_{3D}(z) \qquad \text{with}$$

$$n_{2D}(z) = \sum_i \frac{m^*kT}{\pi\hbar^2} Ln\left(1 + \exp\left(\frac{E_F - E_i}{kT}\right)\right)|\psi_i(z)|^2 \qquad \text{for } E \leq E_b$$

and $\qquad\qquad\qquad\qquad\qquad\qquad\qquad\qquad\qquad\qquad\qquad\qquad\qquad\qquad (3)$

$$n_{3D}(z) = \frac{1}{2\pi^2}\left(\frac{2m^*}{\hbar^2}\right)^{3/2}\int_{E_b}^{\infty}\frac{E - E_c(z)}{1 + \exp(\frac{E - E_F}{kT})}dE \qquad \text{for } E \geq E_b$$

This carrier profile is then injected into the Poisson equation and the procedure is repeated until convergence is obtained. In a final step, once the potential profile and carrier concentrations are known, capacitance and current density can be derived. For the former, it is defined as the accumulated carrier density evolution with bias voltage (equivalent to the depleted charge density owing to electro-neutrality conditons) :

$$C(V) = q\frac{\partial n_s(V)}{\partial V} \qquad (4)$$

The current density is defined by :

$$J(V) = \frac{qm_e^*k_BT}{2\pi^2\hbar^3}\int T(E,V)F(E,V)dE$$

with

$$F(E,V) = ln\left(\frac{1 + \exp((E_F - E)/k_BT)}{1 + \exp((E_F - qV - E)/k_BT)}\right) \qquad (5)$$

110

T(E,V) is the global transmission from the emitter to the collector, and F(E ,V) is termed the "supply function" which describes the balance between emitter and collector carrier streams. At this point, let us mention that this approach has the advantage to include both tunneling and thermionic current contributions.

3. STRUCTURE DESIGN

3.1 InP material system : InGaAs/InAs/AlInAs/AlAs heterostructure

A typical growth sequence of an InP-based quantum well-barrier heterostructure is given in Figure 2. The barrier consists of a step-like $In_{0.52}Al_{0.48}As$ (5 nm)/AlAs (3 nm)/$In_{0.52}Al_{0.48}As$ (5 nm) heterojunction. The conduction band offset between InGaAs and AlAs is 1.2 eV. We have shown previously the advantages gained by this barrier scheme (effective barrier height > 600 meV) to prevent parasitic conduction and in terms of increased power handling[6]. The barrier is sandwiched successively by two 5 nm-thick InAs wells undoped, two 300 nm-thick $In_{0.53}Ga_{0.47}As$ adjacent layers doped 10^{17} cm^{-3}, and two contact layers doped 5×10^{18} cm^{-3}. Figure 3 shows a comparison of the calculated capacitance-voltage (C-V) and current-voltage (J-V) characteristics at room temperature with or without the InAs wells.

It is immediately apparent that one can note improvements both in terms of capacitance- and current-voltage characteristics when InAs wells are inserted. Indeed, the onset of conduction is shifted towards higher voltages of about a factor of 2 if we consider a reference value of 5 $A.cm^{-2}$ for the current density. Moreover, the maximum capacitance is increased from 2.4 $fF.\mu m^{-2}$ up to 3.3 $fF.\mu m^{-2}$ while keeping an equivalent saturation capacitance around 0.4 $fF.\mu m^{-2}$. This appears consistent with the fact that the minimum capacitance is governed by the full depletion of the 300 nm-thick InGaAs layer here equal for both devices.

GaInAs	5×10^{18} cm^{-3}	3000 Å
GaInAs	1×10^{17} cm^{-3}	3000 Å
InAs	u-d	50 Å
InAlAs	u-d	50 Å
AlAs	u-d	30 Å
InAlAs	u-d	50 Å
InAs	u-d	50 Å
GaInAs	1×10^{17} cm^{-3}	3000 Å
GaInAs	5×10^{18} cm^{-3}	5000 Å
Substrat InP SI		
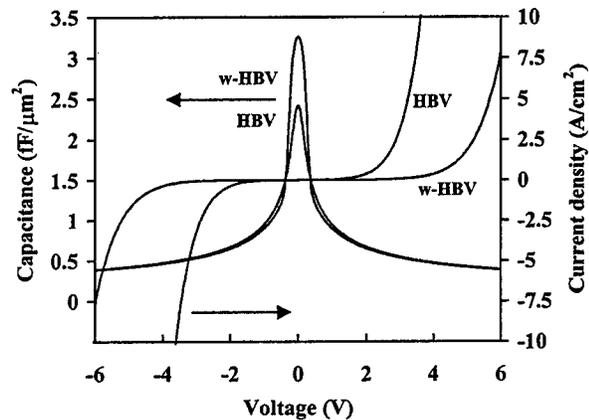
Figure 2 : Typical growth sequence for an InP-based quantum well-barrier varactor structure. The Indium content is 52 % in InAlAs and 53 % in InGaAs.

Figure 3 : Comparison of calculated C-V and J-V characteristics at room temperature for InP-based HBV with or without InAs quantum wells.

In order to determine the cause of these improvements in the C-V and I-V characteristics of the quantum well-barrier structure, let us consider the diagrams of the conduction profiles and charge densities plotted in Figure 4a at a bias point very close to equilibrium conditions (V = 10 mV) and in Figure 4b for V = 1 V. In Figure 4a, the electrons are strongly localized within the quantum wells, thus forming quasi-degenerate semiconductor regions. As a consequence the length for electric field screening (L_S) is expected to be very short, whereas much wider L_S's are found in conventional barrier devices. In such a case, there is no counterbalance against the repelling effect of the barrier. Under bias, the pre-well structure is progressively fed by the adjacent layer which plays the role of a reservoir according to 2D-density of states and Fermi -Dirac statistics. Correlatively, the carriers are escaping from the post-well structure until this quantum well is empty. At this stage, the operation mode becomes classical with full depletion of the cladding layer reached at ~6V. As a consequence the capacitance ratio is improved for the quantum-well barrier heterostructure with a value close to 8.5 :1 compared to 6.2 :1 for the conventional device.
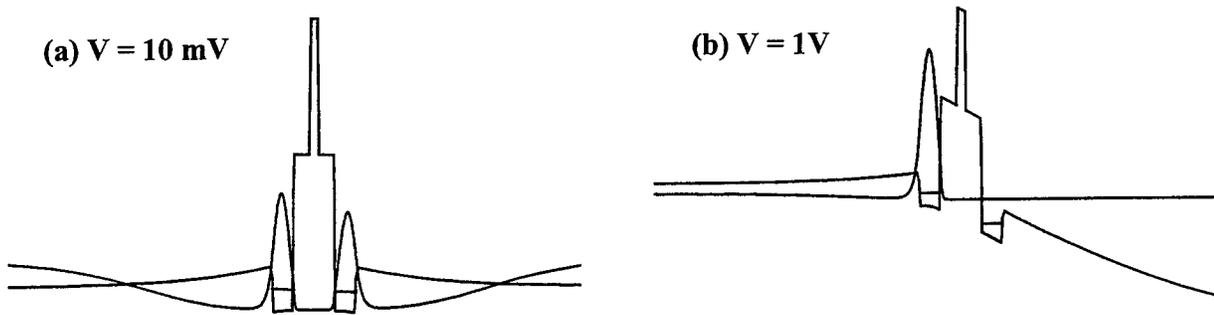
(a) V = 10 mV

(b) V = 1V

Figure 4 : Schematic conduction band profiles and charge densities for the quantum well-barrier heterostructure, (a) V = 10 mV (equilibrium conditions), (b) V = 1V.

The shift in voltage of the conduction threshold is also a consequence of the carrier localization in the InAs pre-well. Indeed, incoming carriers stored in the pre-well experience a higher barrier height compared to carriers delocalized in the InGaAs layer since the ground state of the well is buried below the InGaAs conduction band edge. Consequently, the effective barrier height increases and a higher voltage is required in the case of the quantum well-barrier structure to obtain transmission conditions comparable to the single barrier structure.

3.2 GaAs material system : pseudomorphic GaAs/InGaAs/AlAs heterostructure

It appears nowadays that GaAs base heterostructure barrier varactors suffer from several drawbacks to be used as harmonic multiplier at millimeter wavelengths. For example, using the classical GaAs/AlAs heterojunction, the leakage current, and associated thermal effects[14], due to parasitic conduction via the X valley of AlAs is difficult to control. Starting from a 1 eV conduction band discontinuity between GaAs and AlAs, one finds experimentally effective barrier heights close to 200 meV. As a consequence for single barrier structures, onset of conduction is often found below 2V. Nevertheless, high non-linear capacitance can be obtained also using this material system with very narrow evolution around zero volts which appears to be a welcome feature for very high frequency operation in the context of a reduced drive power.

GaAs	$2x10^{18}$ cm^{-3}	5000 Å
GaAs	$1x10^{17}$ cm^{-3}	3000 Å
InGaAs	u-d	50 Å
AlAs	u-d	100 Å
InGaAs	u-d	50 Å
GaAs	$1x10^{17}$ cm^{-3}	3000 Å
GaAs	$2x10^{18}$ cm^{-3}	1 μm
Substrat GaAs SI		
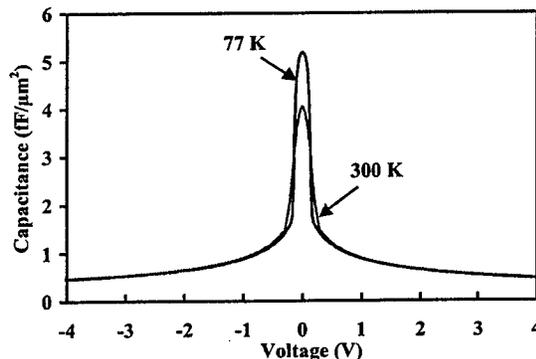
Figure 5 : Epitaxial sequence for a GaAs base quantum-well barrier heterostructure under pseudomorphic conditions. Indium content is 30 %

Figure 6 : Calculated C-V characteristics at 300 K and 77 K for the GaAs base quantum well-barrier heterostructure.

Figure 5 gives the epitaxial sequence of a GaAs-based GaAs/InGaAs/AlAs quantum-well barrier heterostructure varactor under pseudomorphic growth conditions. The Indium content in the well is 30 %. This design is equivalent to the InP-based structure described in the previous section. The sole difference is the AlAs barrier width here limited to 10 nm. This is a compromise between the blocking capability of the barrier which depends on the ability of electrons to tunnel through it and the targeted capacitance value at zero bias. For the latter, the thinner the barrier, the higher the capacitance but higher the tunneling also. Figure 6 shows the calculated capacitance voltage characteristic at 300 K. The maximum capacitance is here

close 4 fF.μm^{-2} and the capacitance ratio higher than 10 :1 at 4 V. At 77 K, one can note that the influence of the wells is strengthened. Indeed, the decrease in temperature tends to increase the localization of carriers closer to the Fermi level and to trap more efficiently the electrons thus reducing the screening effect. A maximum capacitance higher than is 5 fF.μm^{-2} is thus obtained whereas the saturation capacitance is not modified as depletion mechanisms are temperature independent. Moreover, a plot of $\delta C/\delta V$ shows clearly that the non linearity is significantly enhanced compared to room temperature operation.

3.3 GaAs material system : lattice matched AlGaAs/GaAs/AlAs heterostructure

Keeping in mind that closer the localization to the barrier, higher the maximum capacitance, a new idea is under development involving both Nottingham and Lille universities. As shown in Figure 7 and 8, the idea is to use GaAs well instead of InGaAs or InAs. Indeed, the confinement strength is enhanced due to the higher effective mass of carriers in the well. The cladding layers are here made of AlGaAs with various Al content, whereas GaAs reservoirs are very highly doped (10^{19} cm^{-3}) to counterbalance the effect of the GaAs/AlGaAs heterointerface and ensures an efficient feeding of the GaAs wells. Moreover it tends to reduce the series resistance which is one of the key factor to reach terahertz frequencies. At last, the main advantage is to take advantage of a lattice matched heterostructure with the benefit of very high quality epilayers.

GaAs	1.10^{19} cm^{-3}	500 nm
Al$_x$Ga$_{1-x}$As X=0.1 ; 0.2 ; 0.3	1.10^{17} cm^{-3}	300 nm
GaAs	nid	5 nm
AlAs	nid	8 to 12 nm
GaAs	nid	5 nm
Al$_x$Ga$_{1-x}$As X=0.1 ; 0.2 ; 0.3	1.10^{17} cm^{-3}	300 nm
GaAs	1.10^{19} cm^{-3}	1μm
GaAs SI Substrate		
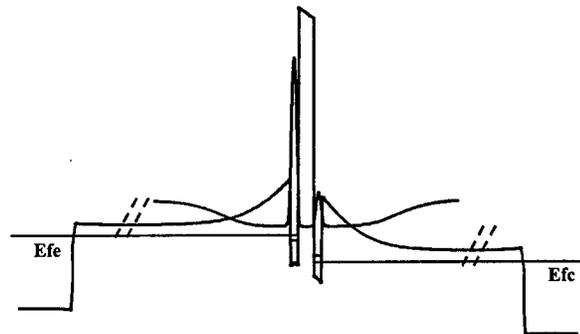
Figure 7 : Epitaxial sequence for the lattice matched AlGaAs/GaAs/AlAs quantum well-barrier heterostructure barrier varactor

Figure 8 : Band bending profile and carrier concentration for the AlGaAs/GaAs/AlAs heterostructure barrier varactor
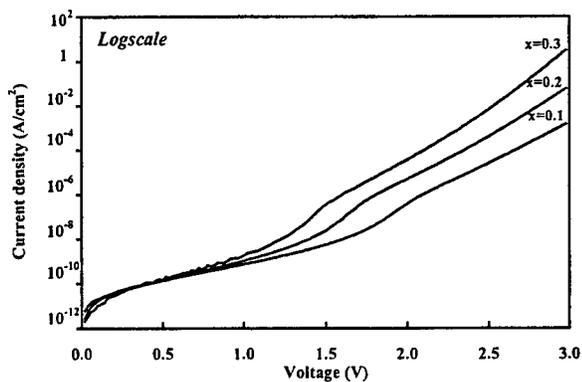
Figure 9 : Calculated current-voltage characteristics for the lattice matched AlGaAs/GaAs/AlAs quantum well-barrier heterostructure barrier varactor as a function of Al content
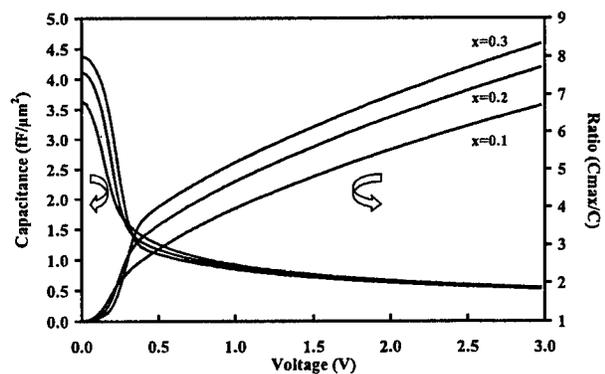
Figure 10 : Calculated capacitance-voltage characteristics and capacitance ratio variation upon voltage for the lattice matched AlGaAs/GaAs/AlAs quantum well-barrier heterostructure barrier varactor as a function of Al content

Simulated results for such structures as a function of Al content of cladding layers are given in Figures 9 and 10. As it can be seen in Figure 9, current density values can be maintained at very low values up to 2 V irrespective of Al content. It has to be mentioned that our calculations do not take into account conduction phenomena through X valleys in AlAs which can be an important parameter in this type of structures. Indeed as the structure is biased, the barrier exhibits a triangular shape. Conduction through X states in the quasi-virtual triangular well, thus formed, can increase drastically the transmission of the barrier[15]. Nevertheless, preliminary estimates of the apparent barrier height shows that the device could be driven safely up to 2 V.

Turning now to the capacitance-voltage characteristics displayed in Figure 10, one can note that the maximum capacitance, with values ranging from 3.5 to 4.5 ff.μm^{-2}, increases with Al concentration in the cladding layer. This result is consistent with the idea of a reinforcement of confinement conditions in the GaAs well. As for the non-linearity, we obtain a steep decrease of the capacitance with a capacitance ratio that reaches almost 5 :1 at 1V for an Al content of 30 %. Based on these considerations, this type of heterostructure barrier varactor appears to be a promising candidate for tripling operation in the terahertz range owing to a accurate control of thermal effects induced by parasitic conduction phenomena.

4. EXPERIMENT

Several devices have been grown, fabricated and tested. Details on the technological procedures are beyond the scope of this communication and can be found elsewhere[4,9-10]. State of the art results have been obtained both in InP and GaAs technologies. Figure 11 shows the experimental capacitance-voltage characteristics obtained respectively with (a) an InGaAs/InAs/AlInAs/AlAs heterostructure and (b) a pseudomorphic GaAs/InGaAs/AlAs heterostructure whose growth sequences are given in Figures 2 and 5.
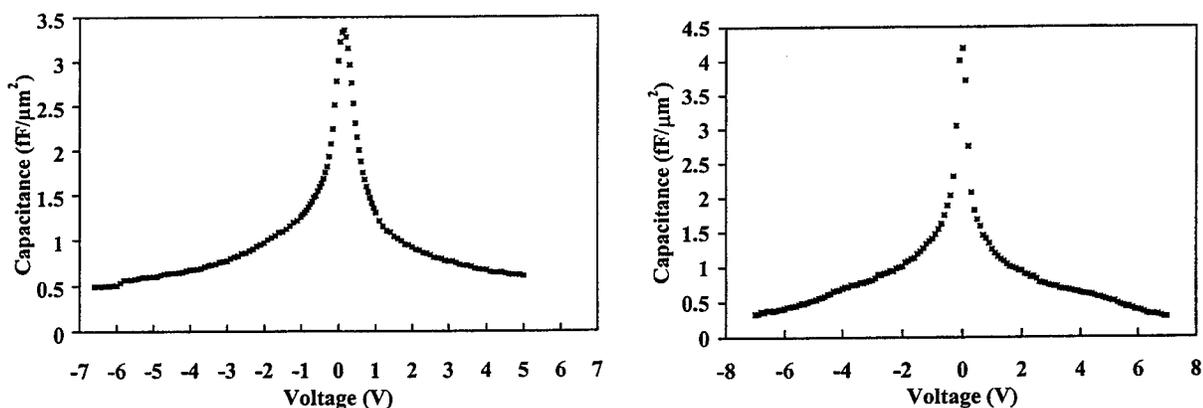
Figure 11 : Experimental capacitance-voltage characteristics at room temperature for quantum well-barrier heterostructure varactors, (a) in InP technology (diameter 10 μm) and in GaAs technology (diameter 7μm).

With respect to InP based technology, the overall capacitance ratio has been measured 7 :1 with a maximum capacitance of 3.5 fF.μm^{-2}. On GaAs, the maximum capacitance is close to 4.5 fF.μm^{-2} with a capacitance ratio of 10 :1 at 7 V. Note the steep decrease in this last case, with a ratio close to 4 :1 at 1V. As it is illustrated in Figure 12, the drawback of GaAs based devices is the relatively high level of conduction. In fact, different conduction regimes can be identified. First at low voltages, typically less than 2 V, the barrier plays perfectly its role with a small leakage current. A second regime between 3 and 6 V can be attributed to different tunneling paths including conduction through X states. At higher voltages, the tunneling current increases drastically as the barrier height is lowered and finally breakdown due to impact ionization occurs. A study of the different tunneling contributions to the total current density is under investigation by means of low temperature measurement. Preliminary results show successive kinks in the second regime attributed to different localization effects involving both quantized states of the pre-well and virtual states above the triangular barrier. Let us mention that these problems do not occur in InP-based materials with very low conduction levels compared to the GaAs material system and with the associated benefit of negligible thermal effects when the diode is driven in a large signal regime[6].
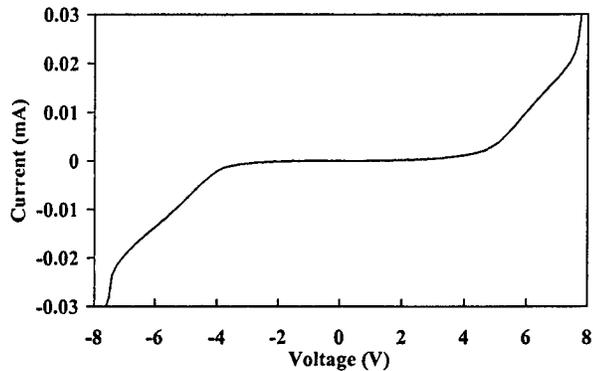
Figure 12 : Experimental current voltage characteristic for the GaAs based GaAs/InGaAs/AlAs hetrostructure barrier varactor at room temperature (diameter 7 μm)
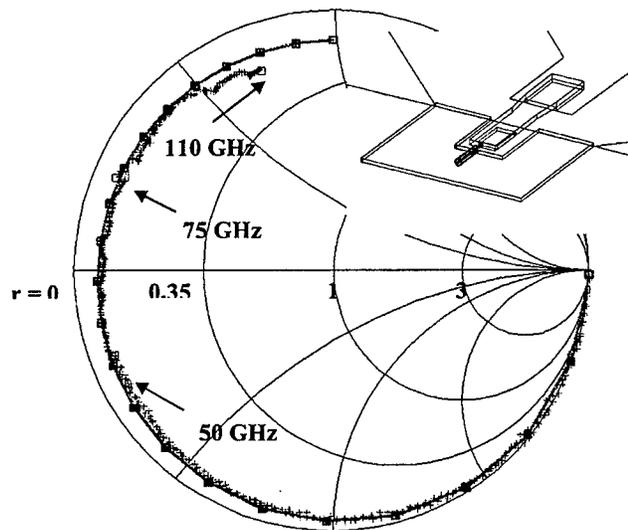
Figure 13 : Illustration of scattering parameters de-embedding up to 110 GHz which combines electromagnetic and circuit simulations to extract the small-signal equivalent circuit from measurements. (Diode area 6x10 μm²)

As a final point, let us mention that these C-V and I-V characteristics were accompanied by scattering parameter measurements to derive the frequency capabilities of the devices. An illustration of de-embedding of scattering parameter measurements is shown in Figure 13. To extract a small-signal equivalent circuit which includes both extrinsic and intrinsic elements, electromagnetic simulations of the diode environment combined with a circuit approach which incorporates the intrinsic elements determined experimentally with a second set of measures have been used. The comparison between experiment and simulation is satisfactory and allows us to estimate cut-off frequencies for our devices in excess of 2 THz. The crucial parameter is here the series resistance of the devices, depending on their geometry. Several technological studies have been undertaken to optimize this parameter, a key issue for high frequency operation.

5. CONCLUSION
In this communication, we have presented different ways to increase the capacitance non-linearity of heterostructure barrier varactor diodes. The common feature of these structures, both in terms of GaAs and InP technologies, is the use of quantum wells grown on both sides of the blocking barrier. By taking benefit of the two dimensional density of states and of the associated decrease of electric field screening lengths, capacitance-voltage characteristics have been tailored with respect to applications in the terahertz frequency domain. Based on a self-consistent solution of the Schrödinger-Poisson system of equations, the main result is the existence of a quantum-capacitance regime, which leads to very narrow C-V curves about zero-volt and a capacitance ratio in excess of 5 :1 over one volt extension. These ideas have been tested successfully with the fabrication of state of the art devices both with InP and GaAs material system with respectively capacitance ratio of 7 :1 and 10 :1.

The discrete devices which have been tested in tripling operation have shown excellent results in terms of output power and efficiency at 250 GHz[5]. To go further, preliminary studies on non linear transmission lines periodically loaded by heterostructure barrier varactors involving soliton propagation are currently under investigation for tripling or quintupling operation in order to reach terahertz frequencies.

6. ACKNOWLEDGEMENTS

7. REFERENCES

1. E.L. Kollberg and A. Rydberg, „Quantum barrier varactor diode for high efficiency millimeter wave multipliers", Electron. Lett., **25**, 1696-1698, 1989
2. D. Choudury, M.A. Frerking and P.D. Batelaan, „A 200 GHz Tripler using a single barrier varactor", IEEE Trans. on MTT, **41**, pp. 595-599, 1994
3. A. Rydberg, H. Grönqvist and E. Kollberg, „Millimeter and Submillimeter Wave Multipliers using Quantum Barrier Varactor (QBV) Diodes", IEEE Elec. Dev. Lett., **11**, pp. 373-375, 1990
4. X. Mélique, C. Mann, P. Mounaix, O. Vanbésien, F. Mollot and D. Lippens, „5 mW and 5 % efficiency 216 GHz InP based heterostructure barrier varactor tripler ", IEEE Micro. Guid. Wav. Lett., **8**, pp. 384-387, 1998
5. X. Mélique, A. Maestrini, E. Lheurette, P. Mounaix, M. Favreau, O. Vanbésien, J.M. Goutoule, G. Beaudin, T. Nähri and D. Lippens, „12 % efficiency and 9.5 dBm output power from InP-based heterostructure barrier varactor triplers at 250 GHz ", IEEE-MTT Symposium, Anaheim, California, June 1999
6. R . Havart, E. Lheurette, O. Vanbésien, P. Mounaix, F. Mollot and D. Lippens, „Step-like heterostructure barrier varactor", IEEE Trans. Elec. Dev., **45**, pp. 2291-2297, 1998
7. E. Lheurette, X. Mélique, P. Mounaix, F. Mollot, O. Vanbésien and D. Lippens, „Capacitance engineering for InP-based heterostructure barrier varactor ", IEEE Elec. Dev. Lett., **19**, 338-340, 1998
8. V. Duez, X. mélique, O. Vanbésien, P. Mounaix, F. mollot and D. Lippens, „High capacitance ratio with GaAs/InGaAs/AlAs heterostructure quantum well-barrier varactors ", Electron. Lett., **34**, pp 1860-1861, 1998
9. E. Lheurette, P. Mounaix, P. Salzenstein, F. Mollot and D. Lippens, „High performance InP based heterostructure barrier varactors in single and stack configuration ", Electron. Lett., **32**, pp. 1417-1418, 1996
10. X. Mélique, J. Carbonell, R. Havart, P. Mounaix, O. Vanbésien and D. Lippens, „ InGaAs/InAlAs/AlAs heterostructure barrier varactors for harmonic multiplication", IEEE Micro. Guid. Wave Lett., **8**, pp. 254-256, 1998
11. J.P. Sun, R.K. Mains, W.L. Chen, J.R. East and G.I. Haddad, „C-V and I-V characteristics of quantum well varactors", J. Appl. Phys., **72**, pp. 2340-2346, 1992
12. Y. Fu, L. Dillner, J. Stake, M. Willander and E. Kollberg, „ Capacitance anlysis for AlGaAs/GaAs and InAlAs/InGaAs heterostructure barrier varactor diodes", J. Appl. Phys., **83**, pp. 1457-1462, 1998
13. I-H. Tan, G.L. Snider, L.D. Chang and E.L. Hu, „A self-consistent solution of Schrödinger-Poisson equations using a non-uniform mesh", J. Appl. Phys., **68**, pp. 4071-4076, 1990
14. J. Stake, L. Dillner, S.H. Jones, C.M. Mann, J. Thornton, J.R. Jones, W.L. Bishop and E. Kollberg, „Effects of self-heating on planar heterostructure barrier varactor diodes", IEEE Trans. Elec. Dev., **45**, pp. 179-182, 1998
15. J.J. Finley, R.J. Teissier, M.S. Skolnick, J.W. Cockburn, G.A. Roberts, R. Grey, G. Hill, M.A. Pate and R. Planel, „Role of the X minimum transport through AlAs single-barrier structures", Phys. Rev. B, **58**, pp. 10619-10628, 1998

SESSION 3

Other Novel Sources
and Devices

Generation and detection of THz waves with photomixers

S. Verghese, K. A. McIntosh, and E. K. Duerr

Lincoln Laboratory, Massachusetts Institute of Technology, Lexington, MA 02420-9108, USA

ABSTRACT

Two low-temperature-grown GaAs photomixers were used to construct a transmit-and-receive module that is frequency agile over the band 25 GHz to 2 THz, or 6.3 octaves. A photomixer transmitter emits the THz difference frequency of two detuned diode lasers. A photomixer receiver then linearly detects the THz wave by homodyne down conversion. The concept was demonstrated using microwave and submillimeter-wave photomixers. Compared to time-domain photoconductive sampling, the photomixer transceiver offers improved frequency resolution, spectral brightness, system size, and cost.

Keywords: photomixers, gallium arsenide, submillimeter waves

1. INTRODUCTION

Measurements that require coherent, continuous-wave (cw) illumination in the terahertz frequency range typically rely on microwave tubes, molecular-gas lasers, or harmonic upconversion of fundamental sources. A tunable coherent solid-state source would enable high-resolution molecular spectroscopy to be performed with much simpler instrumentation than is currently available. Also, recent advances in terahertz receivers based on superconducting bolometers have created a compelling need for a tunable local oscillator (LO) with output power $> 1\,\mu W$ from roughly $0.5-3$ THz.[1-3]

Photomixers are compact, all-solid-state sources that use a pair of single-frequency tunable diode lasers to generate a THz difference frequency by photoconductive mixing in low-temperature-grown (LTG) GaAs.[4,5] Typical output power levels range from 1 to $0.1\,\mu W$ from 1 to 2 THz, respectively. At MIT Lincoln Laboratory, photomixers are being optimized for use with cryogenic terahertz receivers. Recently, a demonstration of a 630-GHz photomixer LO coupled to a superconductor-insulator-superconductor receiver resulted in a double-sideband noise temperature of 331 K.[6] A schematic diagram of this experiment is shown in Fig. 1(a). At other institutions, photomixers are being used as sources to perform high-resolution (~ 1 MHz) transmission spectroscopy of molecular gases. Figure 1(b) shows a typical arrangement in which the output of a photomixer passes through a gas cell and is then detected by a liquid-helium-cooled bolometer. Such configurations using photomixers have been used to measure fine structure in the rotational spectra of molecules such as sulfur dioxide[7] (SO_2) and acetonitryl[8] (CH_3CN).

In the time domain, photoconductive sampling has been used by many groups for terahertz spectroscopy in free space and on transmission lines. These systems consist of two fast photoconductive switches that are excited by a mode-locked laser and are coupled to each other via antennas or transmission line. Until recently, there had not been a demonstration of photoconductive sampling for detection of cw THz waves using photomixers. This paper describes a photomixer transceiver that performs photoconductive sampling in the frequency domain. For spectroscopy applications that require narrow linewidth (< 1 MHz), this technique can offer significant improvement in frequency resolution and spectral brightness over time-domain sampling. Furthermore, the system is coherent, widely tunable, and can be compact—using inexpensive laser diodes that are fiber coupled to the photomixer-transmitter and receiver chips.

2. MICROWAVE EXPERIMENT

Figure 2(a) is a diagram of the experimental setup that was used to test the concept at microwave frequencies. The combined light ($\lambda \approx 850$ nm) from a pair of distributed-Bragg-reflector laser diodes is split in half and fiber coupled to each photomixer. Each LTG-GaAs photomixer comprises a 20×20-μm active region with 0.2-μm-wide interdigitated electrodes with gap spacings of 0.6 μm for the transmitter and of 0.4 μm for the receiver. The photomixers used epitaxial layers of LTG GaAs grown by molecular-beam epitaxy on GaAs substrates and had photocarrier lifetimes of 0.2-0.3 ps.[9] The transmitter is dc biased through a broadband bias tee and therefore develops an ac current across

Corresponding author: S. Verghese (simonv@ll.mit.edu)

118

Part of the EUROPTO Conference on Terahertz Spectroscopy and Applications II
Munich, Germany • June 1999 SPIE Vol. 3828 • 0277-786X/99/$10.00
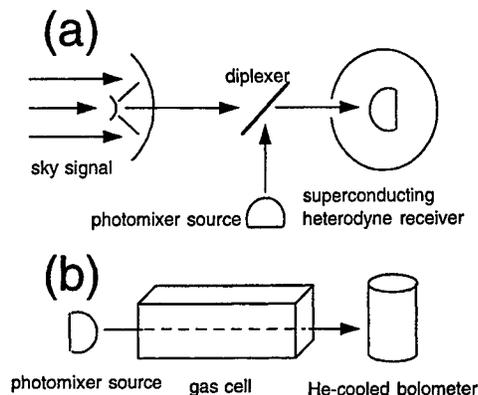
Figure 1. Two examples of applications that use LTG-GaAs photomixers. (a) Schematic of a photomixer transmitter used as a frequency-agile local oscillator for a submillimeter-wave heterodyne detector. (b) Schematic of a photomixer transmitter used for gas spectroscopy.

the electrodes when the photoconductance is modulated at the difference (beat) frequency of the two laser beams. Some of the resulting microwave power is launched onto a coplanar waveguide which transitions into a 50-Ω coaxial line that is connected in similar fashion to the receiver, which is unbiased. At the receiver end, the optical beating periodically raises the photoconductance such that a small amount of unipolar current flows out through the bias tee and into the dc current amplifier. This action is equivalent to homodyne detection of the rf electric field. Figure 2(b)(i) shows that the homodyne signal scales approximately linearly with the dc-bias voltage—or incident electric field—while the transmitted power 2(b)(iii) measured with a spectrum analyzer scales quadratically in voltage.

In contrast to a photoconductive switch driven with a pulsed laser, the photomixer rf impedance is relatively high during cw illumination $Z_t = V_t/I_t \approx 10 - 30\,\mathrm{k\Omega}$. Here V_t is the dc voltage across the transmitter that generates a dc photocurrent I_t when illuminated by two lasers. In the limit of mismatched impedances, the dc current measured at the receiver is proportional to the transmitted rf voltage.[10] The phase of the rf voltage is measured by dithering the difference in path length of the two arms with a short delay line. Then, the receiver is a linear detector of the transmitted wave in the same sense that time-domain sampling performs a linear detection of the transmitted voltage pulse. Contrast this with the power measured by a direct detector (such as in a scalar spectrum analyzer). In that case, the measured signal is proportional to the magnitude squared of the transmitted voltage and all phase information is lost. The symbols in Fig. 2(b) result from a calculation of the homodyne-detected signal using as input parameters the transmitter bias voltage and the dc photoconductances of the transmitter and receiver. Agreement between theory and measurement is close, in part because there are no free-space beams and associated coupling losses.[11]

3. SUBMILLIMETER-WAVE EXPERIMENT

Two antenna-coupled photomixers were used to test a quasioptical version of the photomixer transceiver (Fig. 3(a)) at terahertz frequencies. Such an implementation, for example, could be used for measuring the transmission of trace gases through an air column. Planar log-spiral antennas were patterned in Ti/Au films by optical lithography on the LTG-GaAs surface. Electron-beam lithography was used to define an 8×8-μm active area with 0.2-μm-wide electrodes at the drive point of the antenna. The electrodes were separated by 0.8-μm gaps for the transmitter chip and by 1.5-μm gaps for the receiver. The photomixers were mounted on silicon-hyperhemisphere lenses so that they opposed each other, separated by 6 cm. The emitted radiation from two tunable cw Ti:sapphire lasers was combined with a beam splitter. Half of the combined beam passed through a variable delay line and was coupled into a fiber
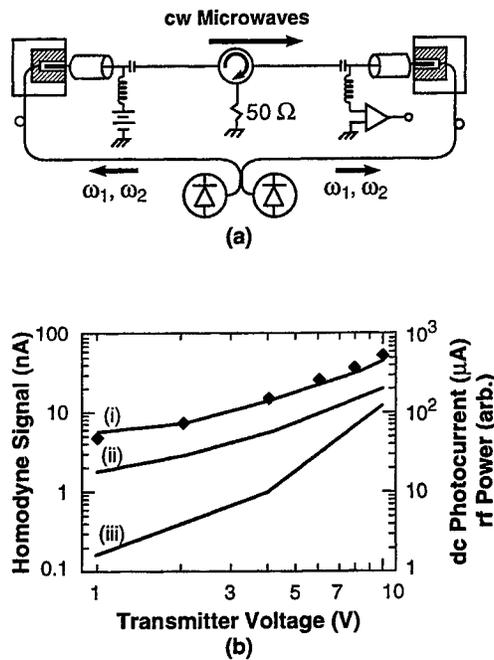
Figure 2. (a) Schematic of the microwave measurement system. Two laser diodes are combined and coupled via optical fiber to two photomixers. The photomixers are connected via 50-Ω coaxial line, separated by an isolator. The transmitter is dc biased and a dc current amplifier measures the homodyne-detected current. (b) (i) Measured homodyne signal as a function of the dc-voltage bias on the transmitter chip. The symbols show the calculated homodyne signal. (ii) Measured dc photocurrent. Note how its shape tracks the homodyne signal. (iii) Measured rf power from the transmitter using a spectrum analyzer (not shown).

that was pigtailed to the receiver. The other half passed through a chopper before entering a fiber that was coupled to the transmitter. Each photomixer was pumped by approximately 35 mW of optical power and the transmitter was dc biased at 15 V resulting in a dc photocurrent of 300 μA.

Figure 3(b) shows the homodyne signal amplitude as a function of frequency. The signal is relatively flat to 600 GHz and then rolls off until it is detectable with a signal-to-noise ratio of $\sim$ 3 at 2 THz.[12] With higher-power photomixers optimized for high-frequency operation, this upper frequency should extend beyond 2 THz.[5] At low frequencies ($<$ 1 THz), the ratio of the signal to the background noise was high and the measurement was dominated by multiplicative noise from the lasers. Residual intensity noise on the laser was a few percent, caused by the fluctuations on the Ar pump laser. The current source driving the diode lasers used for the microwave experiment described above contributes relative intensity noise $<$ 10^{-4} in a 200-kHz noise bandwidth. A second noise contribution arises from frequency jitter of the lasers. Since this system is highly coherent, standing waves are always present. Standing waves provide a mechanism for converting frequency jitter to amplitude noise on the detected homodyne signal. Most of these effects could be mitigated by using Gaussian reimaging optics and stabilized lasers.

4. PHASE-SENSITIVE TRANSMISSION MEASUREMENT

An important capability of the photomixer transceiver is the measurement of amplitude and phase of the transmitted electric field. This allows measurement of the real and imaginary components of the linear response of a medium (e.g. $\epsilon_1 + i\epsilon_2$) or of a device (e.g. complex S-parameters). A transmission measurement through an inductive-mesh filter[13] was performed to demonstrate this capability. Figure 4 shows the amplitude and phase of the electric-field transmission coefficient $|\tau(\omega)| \exp i\phi(\omega)$ as a function of detuning frequency between the two lasers. The amplitude $|\tau|$ was determined by dithering the offset in zero-path difference and obtaining the ratio of the fringe amplitudes with the sample in and out of the beam. The inset in Fig. 4(a) shows the fringe pattern with the mesh in the beam
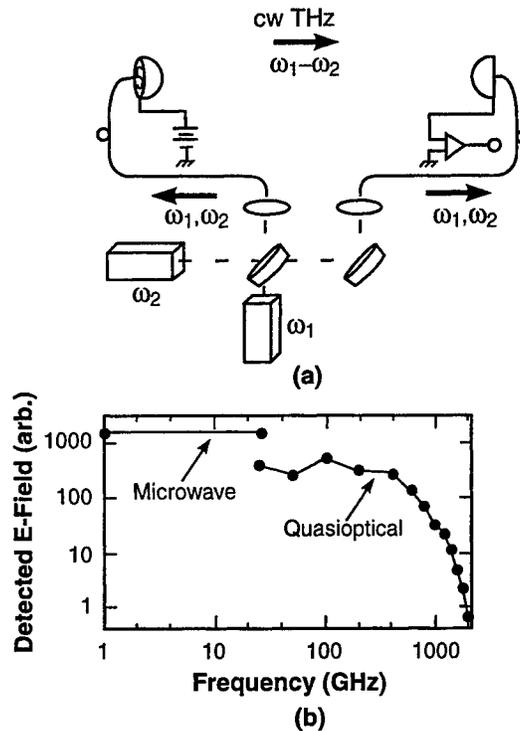
Figure 3. (a) Schematic of the quasioptical implementation. Two cw Ti:sapphire lasers were used since their tuning range exceeded that of the available diode lasers. A pair of tunable diode lasers was used previously (unpublished) with this setup. (b) Homodyne signal plotted versus the difference frequency between the two lasers. Between the microwave and quasioptical systems, the photomixer transceivers covered over three orders of magnitude in frequency.

(i) and out of the beam (ii). The phase $\phi = \omega(d_1 - d_2)/c$ was determined by measuring the change in path between zeroes in the fringe pattern. For high frequencies, where noise is an issue, these quantities are better estimated by Fourier transforming the fringe patterns to extract phase and amplitude values.

An approximate theory for a two-dimensional inductive mesh was derived by Lee *et al.*[14] The theory assumes a transmission-line model in which the incident wave experiences a normalized shunt admittance of value $2Y$. Then, the complex transmittance for the electric field is simply $\tau(\omega) = 1/(1+Y(\omega))$. The expression for Y was phenomenologically developed from numerical simulations

$$Y(\omega) = (-j)(\beta - \frac{1}{\beta}) \left[\frac{\frac{a}{c} + \frac{1}{2}(\frac{a}{\lambda})^2}{\ln \csc(\frac{\pi \delta}{2a})} \right] \tag{1}$$

where $\beta = (1 - 0.41\delta/a)/(a/\lambda)$, $\delta = (a - c)/2$, $a = 318\,\mu m$ is the pitch of the mesh, and $(a - c) = 25\,\mu m$ is the width of the wires that form the mesh.[13] The solid lines in Fig. 4(a) and 4(b) show curves that were calculated using equation (1). The general trends in the calculated curves are reproduced by the transceiver measurements. The signal-to-noise ratio in these data was high and the values were reproducible. The scatter between points was systematic and presumably resulted from standing waves in the present quasioptical system.

5. DISCUSSION

It is instructive to compare some of the features of the photomixer transceiver to more established techniques for terahertz spectroscopy.

Fourier-transform infrared (FTIR) spectrometers are often used for infrared analysis of gases with resolving power $\lambda/\delta\lambda \approx 10^4$ or higher. For the far-infrared and submillimeter bands, an equivalent resolving power demands long
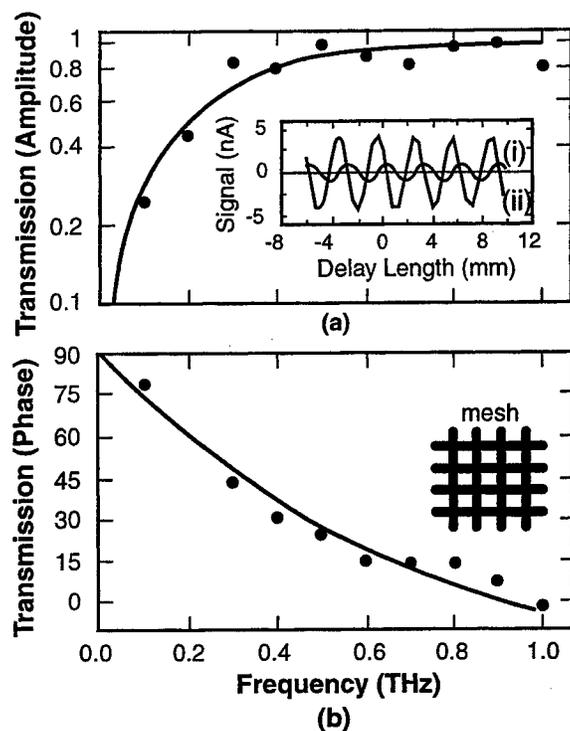
Figure 4. (a) Measured transmission coefficient for the propagating electric field incident on a wire-grid mesh. The solid line shows a theoretical calculation of the transmission. (Inset) Measured fringe pattern at 100 GHz for the mesh in (i) and out (ii) of the beam. (b) Measured phase delay incurred by the wave from propagating through the mesh. The solid line is calculated.

travel for the scanning mirror. For example, resolving a 1-THz feature with 100-MHz resolution ($\lambda/\delta\lambda \sim 10^4$) requires a mirror travel of 1.5 m. For a typical spectrometer designed for high resolving power, the maximum available power in this band is 2×10^{-11} W.[15] Such low power requires a liquid-helium-cooled detector. This is in contrast to $\sim 10^{-6}$ W available from a photomixer in a band that is less than 1 MHz wide. Already, researchers have used photomixers with bolometers to perform gas spectroscopy with resolution ($\lambda/\delta\lambda \sim 10^6$) that would require > 100 m of mirror travel in a FTIR spectrometer.[7,8] The photomixer transceiver should offer an equivalent capability, but with the size and cost advantages of a compact, room-temperature system.

In time-domain sampling, a train of wide-bandwidth pulses with low duty cycle ($\sim 10^{-4}$) carries the THz radiation. The peak pulse power is relatively high and the receiver switch acts like an ultrafast boxcar integrator with high signal-to-noise ratio. However, the power available in a 1-MHz band is reduced by a factor as large as the duty cycle (typically $\sim 10^{-4}$) compared to that available in an equivalent photomixing experiment.[16] Furthermore, without continuous tuning of the laser cavity length, the minimum frequency resolution is the free spectral range of the laser cavity (typically ~ 80 MHz for mode-locked Ti:sapphire lasers). In frequency-domain sampling with photomixers, it is the homodyne action of the receiver that restricts the noise bandwidth in the same fashion as for a lock-in amplifier. Hence, there is a tremendous reduction in noise bandwidth compared to using a direct detector such as a bolometer and the photomixer receiver does not need cooling to enhance its sensitivity.

6. CONCLUSIONS

In summary, a technique has been demonstrated at microwave (0.1–26.5 GHz) and submillimeter-wave frequencies (25 GHz–2 THz) for photoconductive sampling in the frequency domain using photomixers and cw lasers. With more optimized photomixers,[17] the upper frequency range is expected to exceed 3 THz.

Many of the applications that have been suggested for time-domain systems (e.g. T-ray imaging and other linear spectroscopy) could in principle be performed with the photomixer transceiver.[18] The system described in this paper is being upgraded to use higher-efficiency photomixers with resonant antennas. The laser system will be improved by using diode seed lasers that drive a semiconductor optical amplifier. Higher performance antennas are being developed that should improve the prospects for using photomixers in point-sensing spectrometers and as local oscillators in THz heterodyne receivers.

ACKNOWLEDGMENTS

REFERENCES

1. M. Bin, M. C. Gaidis, J. Zmuidzinas, T. G. Phillips, and H. G. LeDuc, "Quasi-optical SIS mixers with normal metal tuning structures," *IEEE Trans. Appl. Supercond.* **7**, pp. 3584-3588, 1997.

2. C.-Y. E. Tong, R. Blundell, D. C. Papa, J. W. Barrett, S. Paine, X. Zhang, J. A. Stern, and H. G. LeDuc, "A fixed tuned low noise SIS receiver for the 600 GHz frequency band," *Proc. 6th Intl. Symp. Space THz Tech.*, pp. 295-304, California Institute of Technology, Pasadena, CA, 1995.

3. B. S. Karasik, M. C. Gaidis, W. R. McGrath, B. Bumble, and H. G. LeDuc, "A low-noise 2.5 THz superconductive Nb hot-electron mixer," *IEEE Trans. Appl. Supercond.*, **7**, pp. 3580-3583, 1997.

4. K. A. McIntosh, E. R. Brown, K. B. Nichols, O. B. McMahon, W. F. DiNatale, and T. M. Lyszczarz, "Terahertz photomixing with diode lasers in low-temperature-grown GaAs," *Appl. Phys. Lett* **67**, pp. 3844, 1995.

5. S. Verghese, K. A. McIntosh, and E. R. Brown, "Highly tunable fiber-coupled photomixers," *IEEE Trans. Microw. Theory Tech.* **45**, pp. 1301-1309, 1997.

6. S. Verghese, E. K. Duerr, K. A. McIntosh, S. M. Duffy, S. D. Calawa, C.-Y. E. Tong, R. Kimberk, and R. Blundell, "A photomixer local oscillator for a 630-GHz heterodyne receiver," submitted to *IEEE Microw. Guided Wave Lett.*, 4 January 1999.

7. A. S. Pine, R. D. Suenram, E. R. Brown, and K. A. McIntosh, "A terahertz photomixing spectrometer: Application to SO_2 self broadening," *J. Mol. Spectrosc.* **175**, pp. 37-47, 1996.

8. P. Chen, G. A. Blake, M. C. Gaidis, E. R. Brown, K. A. McIntosh, S. Y. Chou, M. I. Nathan, and F. Williamson, "Spectroscopic applications and frequency control of submillimeter-wave photomixing with distributed-Bragg-reflector diode lasers in low-temperature-grown GaAs," *Appl. Phys. Lett.* **71**, pp. 1601-1602, 1997.

9. K. A. McIntosh, K. B. Nichols, S. Verghese, and E. R. Brown, "Investigation of ultrashort photocarrier relaxation times in low-temperature-grown GaAs," *Appl. Phys. Lett.* **70**, pp. 354-356, 1997.

10. S. Verghese, K. A. McIntosh, S. D. Calawa, W. F. DiNatale, E. K. Duerr, K. A. Molvar, "Generation and detection of coherent terahertz waves using two photomixers," *Appl. Phys. Lett.* **73**, pp. 3824-3826, 1998.

11. For a detailed analysis of a photomixer in a transmission line see: E. R. Brown, F. W. Smith, and K. A. McIntosh, *J. Appl. Phys.* **73**, pp. 1480, 1993.

12. The signal-to-noise ratio was estimated by chopping (1.5 kHz) the optical beam coupled to the transmitter and monitoring the rms fluctuation in the signal on a lock-in amplifier with a 300-ms postdetection bandwidth.

13. Electroformed wire mesh, 80 copper lines/inch, 0.00098-inch wire width. Buckbee-Mears, St. Paul, MN 55101.

14. S.-W. Lee, G. Zarrillo, and C.-L. Law, *IEEE Trans. Antennas Propag.* **30**, pp. 904, 1982.

15. See, for example, the Magna series of FTIR spectrometer from Nicolet Corporation, 5225 Verona Road, Madison, WI 53711. Assumptions for the maximum power estimate are: Glow-bar color temperature 1473 K, unity emissivity, lossless spectrometer, optical throughput (etendu) 0.005 sr-cm^2, resolution bandwidth 100 MHz.

16. The spectral-brightness factor is the duty cycle (10^{-4}) if time-domain and frequency-domain sampling are performed with identical antennas of a given radiation resistance that is impedance matched to the photoconductor resistance during illumination. In practical systems, an impedance match is difficult to accomplish with cw photomixing, and the realizable advantage for photomixing in spectral brightness will be closer to $\sim 10^2$.

17. S. Verghese, K. A. McIntosh, and E. R. Brown, "Optical and terahertz power limits in low-temperature-grown GaAs photomixers," *Appl. Phys. Lett.* **71**, pp. 2743-2745, 1997.
18. M. C. Nuss, *IEEE Circuits Devices Mag.* **12**, pp. 25, 1996.

DFG THz-wave generation in DAST using dual wavelength Ti:Al$_2$O$_3$ laser

Maya Mizuno[a], Kodo Kawase[b], Syunichi Soma[a], Hidenori Takahashi[a], Yoshiharu Urata[b], Satoshi Wada[b], Hideo Tashiro[b] and Hiromasa Ito[a,b]

[a]Research Institute of Electrical Communication, Tohoku University, 2-1-1 Katahira, Sendai 980-8577, Japan

[b]Photodynamics Research Center, The institute of Physical and Chemical Research (RIKEN), 19-1399 Koeji, Nagamachi, Aoba, Sendai, 980-0868 Japan,

ABSTRACT

Recently, we grew organic ionic-salt crystals of 4-dimethylamino-N-methyl-4-stilbazolium-tosylate (DAST) with extremely large nonlinearity, and also realized dual wavelength oscillation of an electronically tuned Ti:Sapphire laser. In this report, the generation of a coherent THz-wave from DAST crystal was demonstrated for the first time by the difference frequency generation of a dual-wavelength oscillating Ti:Sapphire laser.

Keywords: nonlinear optics, THz-wave, long pulse, difference frequency generation, nonlinear crystal, organic ionic salt, DAST, electronic tuning, Ti:Sapphire laser, dual wavelength.

1. INTRODUCTION

The generation of coherent and widely tunable THz-wave radiation is of interest for a variety of applications in basic and applied physics, communication, and life sciences. Soon after the invention of the laser, many pioneering works had been conducted for tunable THz-wave generation. These included generating tunable submillimeter waves using nonlinear difference frequency mixing between two laser sources[1,2], although the observed conversion efficiency was poor. These efforts ended in the mid-1970's, primarily due to the invention of molecular gas submillimeter lasers.

In the past few years, THz-wave generation and detection have attracted much attention from both theoretical and applied points of view[3,4,5]. Most studies have utilized the ultrabroad bandwidth characteristics of mode-locked subpicosecond laser pulses, sacrificing their temporal coherence as a result. On the other hand, the study of widely tunable THz-wave or submillimeter-wave sources have been developed by means of the photo mixing[6,7] and optical parametric oscillation methods[8,9,10].

Recently, we grew the very efficient organic nonlinear crystal 4-dimethylamino-N-methyl-4-stilbazolium-tosylate (DAST)[11], and also realized dual wavelength oscillation of an electronically tuned Ti:Sapphire laser[12]. Among nonlinear crystals, DAST is known as the most efficient THz rectification medium[13]. In this report, a coherent terahertz (THz) wave was generated using DAST

Part of the EUROPTO Conference on Terahertz Spectroscopy and Applications II
Munich, Germany • June 1999 SPIE Vol. 3828 • 0277-786X/99/$10.00

125

by the difference frequency between two oscillating wavelengths of an electronically tuned Ti:Sapphire laser.

2. EXPERIMENTAL SETUP

The organic ionic salt crystal DAST, which was invented and patented by H. Nakanishi[14] et al., is an extremely promising material with the highest nonlinear and electro-optic coefficients. In addition, DAST is suitable for high-speed modulation and detection, and THz-wave radiation, because of its low dielectric constant[15,16,17]. The production of ultra broadband THz radiation from DAST was reported using optical rectification with a sub-ps laser pulse as the source[18]. In our laboratory, we have conducted studies on growing single large, high-quality DAST crystals and using them for ultrahigh-speed optical devices. We have developed a stable, reproducible way of growing crystals using the fixed seed crystal method. The crystal used in this report was 12×11×2mm. The optical rectification experiment to evaluate the 2nd order nonlinear coefficient was also performed using DAST, and the obtained value was d_{11} = 313 pm/V, which is almost 10 times larger than d_{33} for LiNbO$_3$.
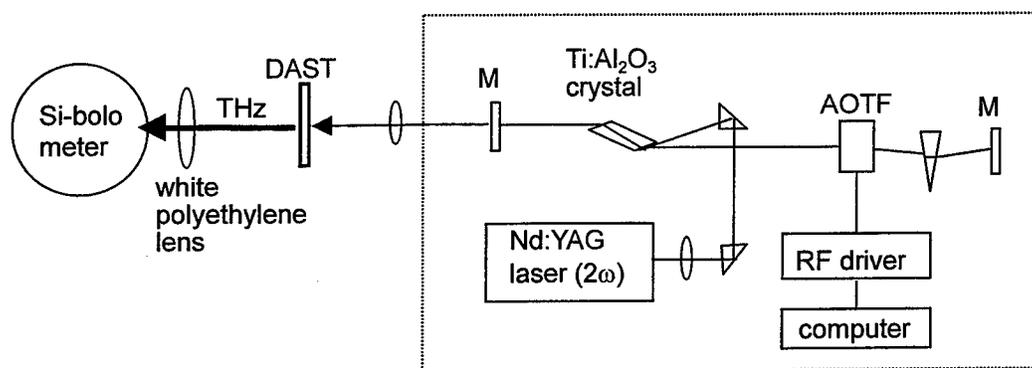
Fig. 1 The experimental setup for generating THz-waves from a DAST crystal using the difference frequency between dual oscillating wavelengths of an electronically tuned Ti:Sapphire laser.

The experimental setup for generating THz-waves is illustrated in Fig. 1. An electronically tuned Ti:Sapphire laser operated with dual wavelengths was utilized as the light source for difference frequency generation (DFG). Two wavelength can be controlled electronically by adjusting the two rf frequencies supplied to the AOTF (acousto-optic tunable filter) crystal inside the laser cavity. In this experiment, the wavelengths, pulsewidth, energy, and repetition rate of the Ti:Sapphire laser were 796.8nm and 799.9nm, 40ns, 600μJ/pulse, and 10Hz, respectively. The simultaneous dual wavelength oscillation was confirmed by sum-frequency (399.2nm) generation using a barium borate (BBO) crystal. An example of the spectrum of the dual wavelength oscillation is shown in Fig. 2. The laser beam was focused to ~0.5mmφ spot on the DAST surface using a lens with f = 300mm. The THz-wave generated was focused into the 4K Si-Bolometer with a white polyethylene lens (f = 60mm).
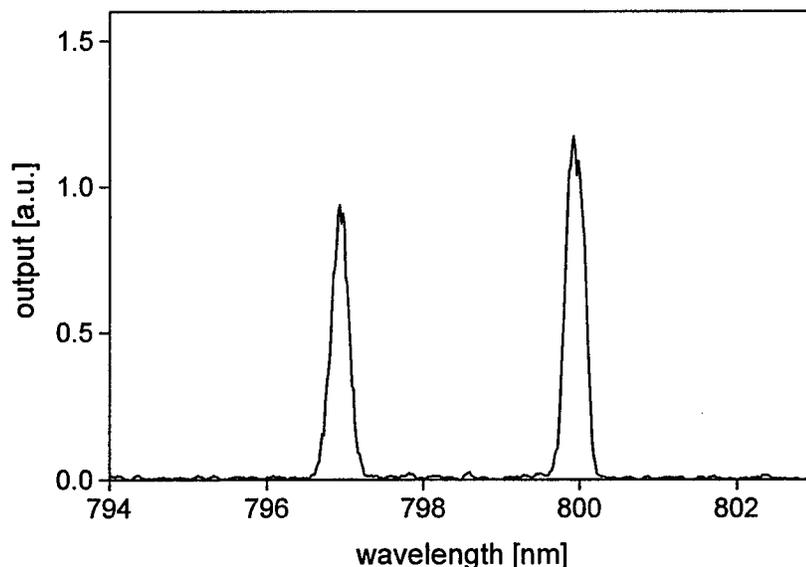
Fig. 2 An example of the spectrum of the dual wavelength oscillation of the electronically tuned Ti:Sapphire laser. The simultaneous oscillation of both wavelengths was proven by the sum-frequency generation using a BBO crystal.

3. EXPERIMENTAL RESULTS

The obtained THz-wave output was 80fJ/pulse (2.5μW at peak). The wavelength was measured using a scanning Fabry-Perot etalon consisting of two metal mesh plates with a 65μm-grid as shown in Fig. 3. The displacement between the two periods was 214μm, which corresponds directly to the difference frequency between the two incident laser wavelengths in Fig. 2. The linewidth of the THz-wave is decided by the laser's purity which is closely related to the resolution of the AOTF. Therefore, narrower THz linewidth can be obtained using a AOTF with higher resolution.

Fig. 4 shows the temporal characteristics of the incident laser pulse and the generated THz-wave pulse. A Schottky barrier diode detector[19] was utilized to monitor the THz-wave pulse shape. The pulse widths of the laser (40ns) and THz-wave (32ns) indicated that the dual-wavelengths (796.8nm and 799.9nm) from the Ti:Sapphire laser oscillated almost simultaneously. It should be mentioned that we have also tried the same experiment using other crystals, such as $LiNbO_3$, $LiTaO_3$, KTP, and GaP, but only DAST generated a detectable THz-wave output, proving its high conversion efficiency.
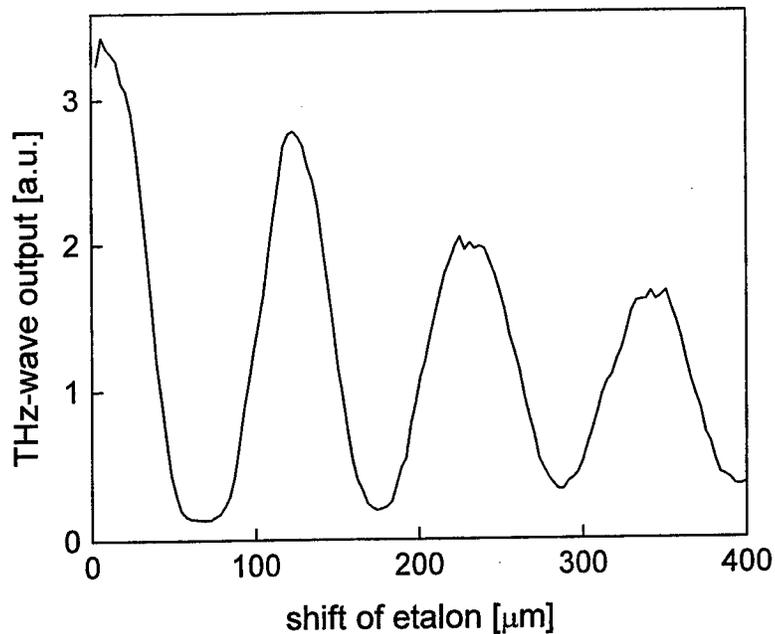
Fig. 3 A typical THz wavelength measurement using a scanning Fabry-Perot etalon consisting of metal mesh plates.
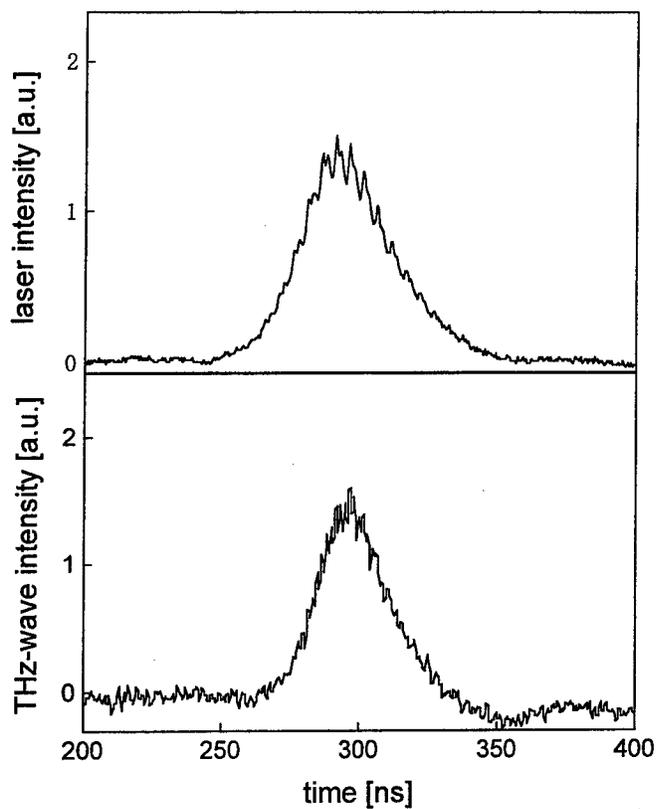
Fig. 4 The temporal characteristics of the incident laser pulse (upper line) and the generated THz-wave pulse (lower line). A Schottky Barrier Diode detector monitored the THz-wave pulse shape.

Polarization characteristics of the generated THz-wave were measured using a rotating wire grid polarizer as shown in Fig. 5. In the upper and the lower figure, the polarization direction of two laser beams are parallel to the a-axis and b-axis of the DAST crystal, respectively. The polarization of the generated THz-waves are parallel to the a-axis irrespective of the incident polarization direction, because the electronic and ionic polarization mainly contributes in the direction of the a-axis.
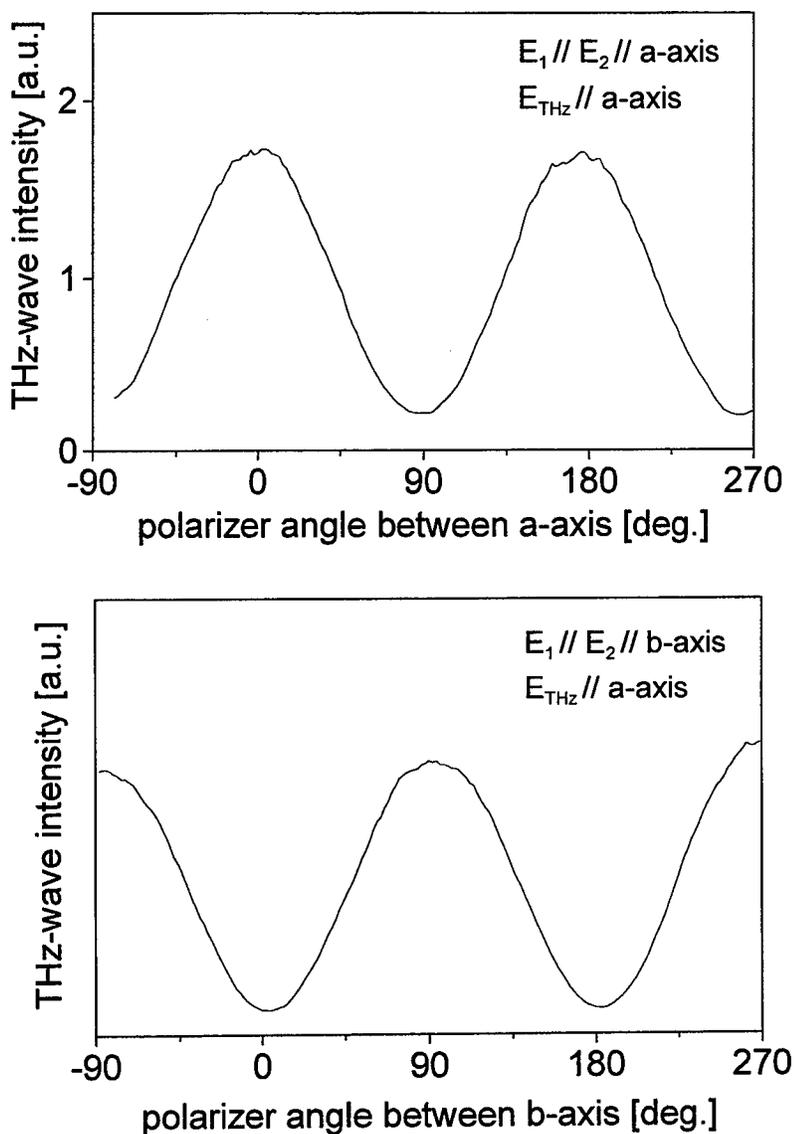
Fig. 5 Polarization of the THz-wave. In the upper and the lower figure, the polarization direction of two laser beams are parallel to the a-axis and b-axis of the DAST crystal, respectively. The polarization of the generated THz-waves are parallel to the a-axis in both cases.

In conclusion, we have demonstrated coherent, longpulse THz-wave (wavelength: 214μm, frequency: 1.4THz, pulsewidth: 32ns) generation from DAST using the difference frequency between dual oscillating wavelengths of an electronically tuned Ti:Sapphire laser. In the 32ns THz pulse width, there exist almost 5×10^4 wave train, giving higher coherency than the THz radiation by femto second laser pulses. Since it is possible to vary the two wavelengths of this laser between 700-900nm, a widely tunable THz-wave is easily obtained.

References

[1] F. Zernike, Jr., and P. R. Berman, Phys. Rev. Lett. **15**, 999 (1965).

[2] R. Morris and Y. R. Shen, Phys. Rev. A **15**, 1143 (1977).

[3] P. R. Smith, D. H. Auston, and M. C. Nuss, IEEE J. Quantum Electron. **24**, 255 (1988).

[4] M. van Exter and D. Grischkowsky, IEEE Trans. Microwave Theory Tech. **38**, 1684 (1990).

[5] D. M. Mittleman, R. H. Jacobsen, and M. C. Nuss, IEEE J. Sel. Topics in Quantum Electron. **2**, 679 (1996).

[6] E. R. Brown, K. A. McIntosh, K. B. Nichols and C. L. Dennis, Appl. Phys. Lett. **66**, 285 (1995).

[7] S. Matsuura, M. Tani, K. Sakai, Appl. Phys. Lett. **70**, 559 (1997).

[8] K. Kawase, M. Sato, T. Taniuchi, and H. Ito, Appl. Phys. Lett. **68**, 2483 (1996).

[9] K. Kawase, K. Nakamura, M. Sato, T. Taniuchi, and H. Ito, Appl. Phys. Lett. **71**, 753 (1997).

[10] J. Shikata, M. Sato, T. Taniuchi, H. Ito, and K. Kawase, Opt. Lett. **24**, 202 (1999).

[11] S. Sohma, H. Takahashi, T. Taniuchi, and H. Ito, paper accepted to J. Chem. Phys.

[12] S. Wada, K. Akagawa, and H. Tashiro, Opt. Lett. **21**, 731 (1996).

[13] T. J. Carrig, G. Rodriguez, T. S. Clement, and A. J. Taylor, Appl. Phys. Lett. **66**, 10 (1995).

[14] H. Nakanishi, H. Matsuda, S. Okada, and M. Kato, Proc. the MRS Int. Mtg. Adv. Mater. **1**, 97 (1989); Japan Patent No. 1716929 (1986).

[15] F. Pan, G. Knopfle, Ch. Bosshard, S. Follonier, R. Spreiter, M. S. Wong, and P. Gunter, Appl. Phys. Lett. **69**, 13 (1996).

[16] R. Spreiter, Ch. Bosshard, F. Pan, and P. Gunter, Opt. Lett. **22**, 564 (1997).

[17] U. Meier, M. Bosch, Ch. Bosshard, F. Pan, and P. Gunter, J. Appl. Phys. **83**, 3486 (1998).

[18] T. J. Carrig, G. Rodriguez, T. S. Clement, and A. J. Taylor, Appl. Phys. Lett. **66**, 121 (1995).

[19] T. Suzuki, J. J. Chang, T. Nozokido, Y. Kuwano, and K. Mizuno, Proc. 17th Int. Conf. Infrared and Millimeter Waves, pp.210-211, December 1992.

Terahertz photonic microstructures for electrooptic modulator applications

Richard M. De La Rue,

Optoelectronics Research Group, Department of Electronics and Electrical Engineering, University of Glasgow, Glasgow G12 8LT, Scotland, U.K.

r.delarue@elec.gla.ac.uk

The prospects for using photonic bandgap effects in suitably fabricated 1D waveguide photonic microstructures to enhance the strength of the electrooptic interaction at terahertz frequencies are considered. Both ferroelectric and electrooptic semiconductors are assessed. More work will be required, both on measuring material properties and in the conception and fabrication of new device structures.

Introduction

We have previously described (1) the principles according to which a narrowband, low power consumption electrooptic modulator for terahertz frequency operation could be constructed in a 'standard' Pockels effect electrooptic material such as single domain ferroelectric crystal lithium niobate ($LiNbO_3$). The modulator takes the form of a terahertz frequency resonant cavity, in which high reflectivity DBR photonic microstructures are used to provide the mirrors. The THz DBR photonic microstructure is formed by using two quite different cross-sections of THz image waveguide. We now re-examine the predictions of this earlier work and briefly consider its possible extension to other materials such as lithium tantalate, strontium barium niobate and potassium niobate.
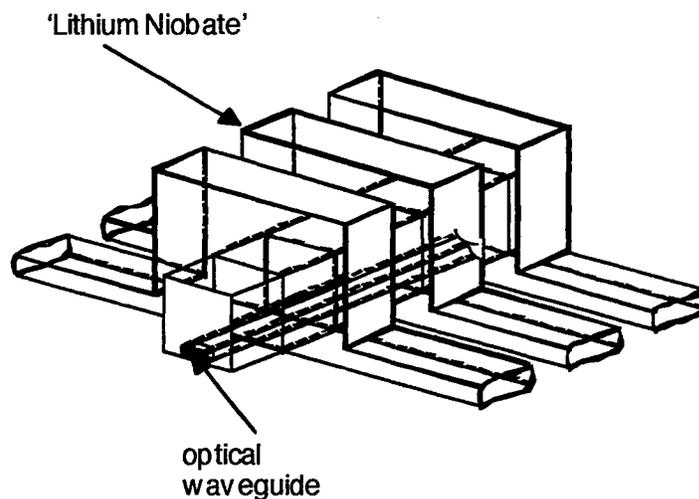
Fig. 1: part of a terahertz modulator DBR mirror stack, showing alternating waveguide cross-sections in each period and the location of the optical waveguide.

III-V semiconductors are well-established as the basis both for high microwave-frequency generation and for a range of optoelectronic device functions, including efficient light generation and detection. They also exhibit a strong linear electrooptic (Pockels effect) and, in suitable structures, both the Franz-Keldysh electroabsorption effect of bulk semiconductors and enhanced electroabsorption in the form of the quantum confined Stark effect (QCSE). Moreover, novel physical processes and new bandgap-engineered device structures continue to appear in III-V semiconductors. Already substantial levels of terahertz electromagnetic wave generation via sub-

Part of the EUROPTO Conference on Terahertz Spectroscopy and Applications II
Munich, Germany • June 1999 SPIE Vol. 3828 • 0277-786X/99/$10.00

131

picosecond pulse generation have been demonstrated in III-V semiconductors - e.g. at levels sufficient for T-ray imaging purposes. The presentation will therefore also consider issues relevant to Terahertz frequency photonic microstructure-based electrooptic modulators realised in III-V semiconductors. It will include some deliberately speculative ideas on connecting electrooptic modulation to novel methods for generating narrow-band Terahertz frequency drive oscillations.

Photonic crystals and waveguide optoelectronic devices in the sub-Terahertz to Terahertz regime.

One interesting area of potential applications for the photonic crystal approach has already received a significant amount of attention. This area can be identified in frequency terms as ranging from the microwave part of the electromagnetic spectrum, up to at least 10 THz. One important characteristic feature of practically the whole of this range is that the refractive index of a significant range of materials is much larger than the refractive index at optical frequencies. This feature means that strongly photonic bandgap behaviour is available from a correspondingly bigger range of materials. The creation of microwave frequency photonic crystals at the 1D, 2D and 3D levels - and their exploitation within conventional microwave frequency waveguides or elsewhere - has been an interesting exercise for a number of reasons. It can be argued that a new push has been given to what was apparently a mature field, at least at the lower end of the frequency spectrum, but also that, in some measure, microwave frequency photonic crystals and bandgap structures have been around for a long time.

The present paper is concerned with applying a particular simplification of the photonic crystal concept, which we label as the waveguide 1D photonic microstructure, to the anticipated requirement for electrooptic modulators operating at frequencies well in excess of 100 GHz. This might well be considered as a premature development, but our belief is that the intellectual challenge is of sufficient interest to make it worthwhile. The most immediate benefit would probably come at frequencies towards the bottom end of the decade between 100 GHz and 1 THz, but so far the conceptual approach fits most readily towards the top end of this decade. The most obvious factor to reduce the minimum frequency of operation would be the discovery of an alternative electrooptic crystal material with at least comparable electrooptic coefficients to those of lithium niobate, but possessing a significantly higher dielectric constant. It would also be required that the material would show comparably low dielectric absorption losses at the desired operating frequency.

Sub-Terahertz to Terahertz electrooptic modulators in lithium niobate

Electrooptic modulators are now widely used in large-capacity fibre-optical communications systems. Such modulators can provide amplitude or phase modulation - or a chosen combination of both. While direct modulation of the current supplied to a semiconductor diode injection laser is still the most widely used approach for fibre-optical communications, such current modulation can induce substantial levels of frequency chirp alongside the desired pure amplitude modulation effect. Chirp can have a major negative impact on the transmission of high bit-rate data pulse streams along dispersive fibres because of the consequent pulse spreading. But chirp can be eliminated, or compensated for, by a variety of techniques - which include modifying the voltage bias levels applied to the electrodes of an external electrooptic modulator.

For external amplitude modulation at bit-rates up to 10 Gigabits/s, the 'standard choice' is a fibre-pigtailed waveguide modulator, realized in lithium niobate and having an essentially Mach-Zehnder configuration. Both annealed proton-exchange and titanium-diffused waveguide technologies are used in currently commercial devices. (Since the light from a semiconductor laser is usually strongly polarised, polarisation independent operation is not usually an issue at this stage.) Research on techniques for extending the capability of lithium niobate based electrooptic modulators to baseband modulation rates in excess of 50 GHz is now reasonably mature. The main

ingredient in achieving such a large modulation bandwidth has been to shape the total device structure so that a substantial part of the electromagnetic energy propagating along the electrodes of the modulator is in the 'air' outside the lithium niobate electrooptic medium. This configuration enables the velocity of the electromagnetic mode to be matched reasonably closely to the inherently much larger velocity of the optical frequency waves propagating in the waveguide regions embedded in the electrooptic substrate. The issues associated with obtaining *non*-baseband operation at centre frequencies up to at least 100 GHz, and with restricted bandwidth, have also received some attention.

But the eventual limitation on modulator bandwidth is simply the increasing propagation losses of the electromagnetic travelling wave supported by the metal electrode structure. Increasing the thickness of the metallisation cannot eliminate the effects of the progressively smaller skin depth. In our previous paper, we examined the possibility of extending the operation of lithium niobate electrooptic modulators to frequencies as high as 1 THz. The main arguments presented were that:

a) at a frequency of about 1 THz, the electric field strength associated with reasonable total electromagnetic power levels supported in a properly designed high refractive index dielectric waveguide becomes comparable with that associated with a typical electrode structure at the same power level.

b) that a simplified form of waveguide photonic microstructure could increase the strength of modulation, simply by providing a cavity with a moderately high Q-factor.

The choice of lithium niobate for modulators at 1 THz remains a natural one because of its established position in guided-wave optoelectronics, because of its large electrooptic coefficients and high dielectric constant. It now also seems reasonably certain that the terahertz frequency electromagnetic wave propagation losses are sufficiently small, at moderately low temperatures, for compact resonator structures based on the waveguide photonic microstructure approach to be quite feasible.

Fig. 1 shows a simplified schematic of the previously proposed terahertz DBR (distributed Bragg reflector) mirror section based on dielectric image waveguide in lithium niobate. Two such mirrors with a moderate number of periods (say seven), together with an appropriate length of unmodulated spacer section, can provide a usefully high-Q resonator for the modulating terahertz frequency electromagnetic wave. The waveguide DBR is made up of alternate sections (Fig. 2 and 3) of waveguide with substantially different levels of electromagnetic confinement and, therefore, quite different effective refractive indices. For TM waves the terahertz waveguide is monomode and has its maximum electric field strength exactly where required to give the strongest modulation of light supported in an optical waveguide on the continuous flat surface of the image guide and adjacent to its ground plane. It may be worth remarking on the similarity of the terahertz image guide proposed here to a structure described - and realised experimentally, by Qian et al (2). But the principle difference between the two dielectric loaded cavity geometries is also important for our application in electrooptic modulation. Nevertheless, much the same geometry as ours, suitably scaled and in an appropriately chosen low-loss dielectric medium, could be used for the low-noise electronic oscillator application described by Qian et al (2).
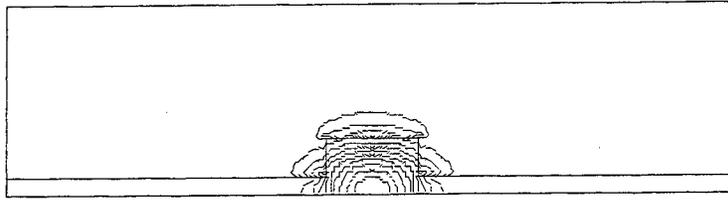
Fig. 2: Cross-section and modal field pattern plot of 'lithium niobate' image guide with monolithic slab-coupled rib format. The rib cross-sectional dimensions are 20 μm height and 50 μm width on a 10 μm thick slab, at a free-space wavelength of 300 μm. The effective refractive index of the guided mode is 5.1.
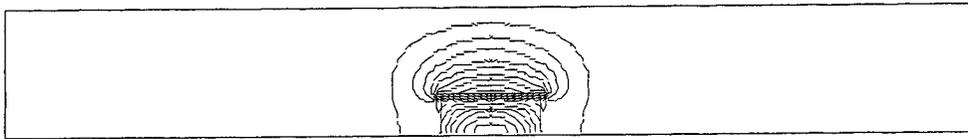
Fig. 3 Cross-section and modal field pattern plot of 'lithium niobate' image guide with rib-only format and rib cross-sectional dimensions of 15 μm height and 40 μm width, at free-space wavelength of 300 μm. The effective refractive index of the guided mode is 2.5.

At terahertz frequencies, the problem of coupling the electromagnetic wave into the modulator is also a significant challenge. If the terahertz electromagnetic wave source is a reasonably well-collimated free-space propagating beam, a system of plastic lenses could be used to focus the beam onto one end of the lithium niobate image guide. But the modal cross-section is only about one-sixth of the free-space wavelength in its larger dimension. This suggests that it would also be desirable to incorporate a two-dimensionally tapered horn section into the input end of the modulator image guide - and, possibly, to use a lensed input face. Alternatively, the terahertz wave might be delivered along another waveguide or it might be generated 'electronically' at a suitable location within the modulator, e.g. if the objective were to generate widely spaced frequency sidebands around an optical carrier.

(With a suitable modulation format, the carrier might itself be substantially suppressed).

Sub-terahertz to terahertz electrooptic modulators in ferroelectric crystals other than lithium niobate

Lithium niobate has a demonstrated capability for use in moderately large cross-point switch arrays and for optical amplification via rare-earth doping. Although the available gain is quite modest, particularly if one means *net* gain, research has led to multi-section lasers with the capability of actively mode-locked operation and monolithically integrated in the lithium niobate, although external pumping was still required. Lithium niobate electrooptic devices for both polarisation control and polarisation scrambling are already important and acousto-optic tunable filters in lithium niobate could yet become a very useful component in WDM systems.

Another area of increasing importance for lithium niobate is periodically-poled lithium niobate (PPLN) - which is now of particular interest as a 'bulk' material for second harmonic generation (SHG) with solid-state lasers - with more general processes such as parametric conversion also of interest. These factors all add up to a fairly strong niche position for lithium niobate within optoelectronics - and *guided wave* optoelectronics in particular. Although electrooptic devices based on lithium *tantalate* clearly also have commercial potential, the properties of lithium tantalate are either, in most respects, not significantly different from those of lithium niobate (e.g. the electrooptic coefficients) or are substantially inferior. Lithium tantalate is significantly less strongly piezoelectric than lithium niobate and has a much lower Curie temperature. But as a direct

consequence of its lower Curie temperature, lithium tantalate has considerably larger pyroelectric coefficients. This is an advantage for thermal sensing applications but may be more problematic from the point of view of performance and device processing in environments where charge build-up on crystal wafers or device surfaces is likely to accompany quite moderate temperature changes. Satisfactory waveguide technologies for lithium tantalate are not so well established and it is considerably more difficult to grow large single-crystal boules of the material. Unlike the situation for lithium niobate, 3 inch (7.5 cm) diameter boules of lithium tantalate are not currently available commercially. One well-known positive feature of lithium tantalate is its much larger threshold for significant photorefractive effects. This superior resistance to photorefractive effects has led to competitive work being carried out on SHG in waveguides fabricated in lithium tantalate - although MgO-doped lithium niobate has been successfully used to achieve at least comparable performance and optical power handling capability.

A number of other inorganic ferroelectric materials, e.g. potassium titanyl phosphate (KTP), show a potentially useful electrooptic effect and there has been work both on electrooptic and nonlinear waveguide devices in this material. Other materials of potential interest are potassium niobate (3) and strontium barium niobate (4). Potassium niobate has three distinct refractive index values around 2.2 and a reported value of around 1000 for one of its dielectric constants, while one of its electrooptic coefficients has a clamped value of 360×10^{-12} m.V^{-1}, more than ten times the largest value in lithium niobate. Strontium barium niobate has quite similar values for the same parameters, but different crystal symmetry. Such remarkably strong electrooptic effects are unlikely to come without penalty. Both materials are clearly strongly dispersive for electromagnetic waves, increasing velocity mismatch effects. Strong dispersion is also likely to imply greater electromagnetic propagation losses. At this stage in the development of terahertz technology, it appears that there is a need for a serious study to measure the propagation losses for terahertz electromagnetic waves in various electrooptic crystals.

Electrooptic modulators using III-V and II-VI semiconductors:??

We now consider another group of alternative possible materials for electrooptic modulation in the sub-terahertz to terahertz regime. In particular it is appropriate to consider electrooptically active semiconductors, e.g. crystals of the III-V and the II-VI compounds. Depending both on the specific compound and on the method by which they are produced, crystals and epitaxial layers of these materials may appear in either wurtzite (hexagonal symmetry) or zinc-blende (face-centred cubic symmetry) form. Although one phase may be the strictly stable one, for a particular compound, the other phase may be a long lasting metastable one. Under certain 'abnormal' conditions, crystals having the simple cubic rock-salt structure are also a possibility.

Because of their widespread use in optoelectronics and electronics more generally, it is appropriate to consider firstly the III-V semiconductors gallium arsenide (GaAs) and indium phosphide (InP) and, implicitly, the various heterostructure combinations which are more-or-less routinely grown on substrates of either of these two crystal semiconductors. Both InP and GaAs are piezoelectric, albeit rather weakly so, and have useful magnitude electrooptic coefficients. The latter coefficients are more than an order of magnitude smaller than the largest electrooptic coefficients in ferroelectric crystals such as lithium niobate and lithium tantalate (5). But the apparent disadvantage is substantially recouped because of the cube-law dependence of the electrooptic change in refractive index on the refractive index - and the much larger refractive index of GaAs, InP and the related heterostructure compounds typically grown on substrates of these crystals.

The simplified relationship for the change in refractive index produced when an electric field is applied to a Pockels effect material is:

$$\Delta n = -\frac{n^3}{2} . r$$

The Pockels effect is linear in the applied electric field, E - and requires the crystal to be non-centrosymmetric and correctly oriented. It has the vital feature of being 'instantaneous' at frequencies up to and beyond the optical range.

In the context of electrooptic modulation, GaAs and InP are important for several reasons. They show only a small amount of refractive index dispersion over practically the whole range of frequencies up to the optical region, so that the velocity mismatch between microwave travelling waves supported by a broadband co-planar transmission line electrode and guided optical waves is not inherently large. It is also possible to integrate the electrooptic function with other important functions of a III-V semiconductor based monolithic integration technology, e.g. light emission, photodetection and drive/detection electronics. Although this kind of integration is still not routine, basic principles have been demonstrated. But there is a further aspect of these semiconductors to mention, the electroabsorption effect known as the Franz-Keldysh effect, which occurs in bulk semiconductors – and the quantum-confined Stark effect (QCSE) which is typically produced in multiple quantum well (MQW) epitaxial structures. These structures have thin (2 to 10 nm thick) layers of GaAs or InGaAs with barrier layers of AlGaAs or InGaAsP – and may be grown lattice-matched, strained or pseudomorphically. If the photon energy is carefully tuned into the region just below the bandgap energy, the quadratic term in the electrooptic effect can become much larger and therefore enhance the refractive index modulation substantially by comparison with the Pockels effect alone.

But the III-V semiconductors cover a much wider range of compounds - and there has recently been an upsurge of interest in the group III nitrides, in particular gallium nitride (GaN) and epitaxial heterostructures containing ternary and binary layers based on AlN, GaN and InN. Research has been most strongly focused on blue light emitting diodes and current injection diode lasers. Historically, work on growing epitaxial films of AlN on sapphire was primarily motivated by their potential use in ultrasonics (6). Although it is clear from its crystal symmetry and significant piezoelectricity that AlN must be a Pockels medium, I have not been able to locate information on the magnitude of the electrooptic effect in the nitride semiconductors, so their use in the present context must be speculative. Multiple quantum well containing devices based on excitonic behaviour could be more interesting. II-VI compounds tend to have somewhat larger electrooptic coefficients than the III-Vs. As an example, ZnTe has a quoted value for r_{41} of more than 4×10^{-12} m.V^{-1}, together with a refractive index of just below 3 at a wavelength of 1 μm (5). So II-VI compound crystals should also be given some attention.

We now attempt a limited comparison of the properties of different candidate materials for use in Terahertz electrooptic modulators. Fig. 4 and Fig. 5 show the results of computations using F-wave (7) for the dominant TM mode of image guides on a perfectly conducting plane, inside the box dictated by computational requirements. The dielectric material from which the guide is made is assumed to have a 'bulk' refractive index of 3. This value is in the middle, approximately, of the range which applies for the various semiconductors. As with our previous calculations for the material 'lithium niobate', the slab-coupled rib of Fig. 4 gives a high modal effective refractive index which is 2.65 here, approaching that of the bulk material. Likewise, the rib-only structure of Fig. 5 has smaller cross-sectional dimensions and a considerably lower effective index value of 1.48.
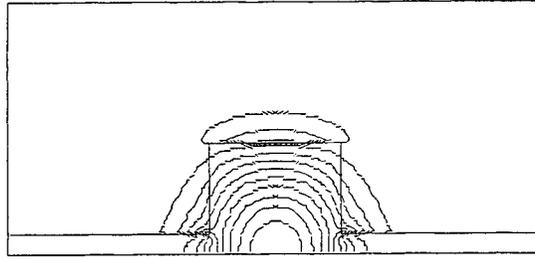
Fig. 4: Cross-section of dielectric image waveguide with slab-coupled rib format and dominant TM mode field pattern for medium with a refractive index of 3. Taking the free-space wavelength of the electromagnetic wave as $300\,\mu$m (i.e. a frequency of 1 THz), the guide cross-sectional dimensions are slab-height $15\,\mu$m, additional rib height $65\,\mu$m and rib width of $100\,\mu$m. The effective refractive index of the guided mode is 2.65.
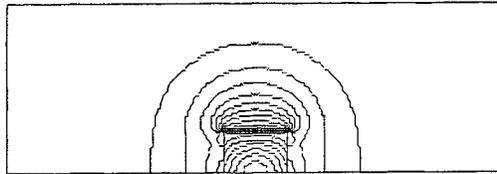
Fig. 5: Cross-section of dielectric image waveguide with rib-only format and dominant TM mode field pattern for medium with a refractive index of 3. At a free-space wavelength of $300\,\mu$m, the rib-guide cross-sectional dimensions are height $35\,\mu$m and width of $50\,\mu$m. The effective refractive index of the guided mode is 1.48.

Taking account of the cross-sectional dimensions, the electromagnetic confinement is approximately five times lower in Fig. 4 for the generic semiconductor than in Fig. 2 for the archetypal ferroelectric. The combination of more than an order of magnitude smaller electrooptic

Δn and much weaker confinement clearly suggest that the semiconductor cannot compete with the ferroelectric. But the semiconductor may be much less dispersive and its electromagnetic absorption in the terahertz regime is probably also much smaller. So competitiveness may be partially restored in favour of the semiconductor. My view is, however, that one should look to carrier density modulation effects and/or quantum confinement or excitonic effects for strong terahertz-optical interactions in semiconductors. Resonant PBG-based terahertz structures could still be of value in conjunction with such interactions in semiconductors.

Generation of terahertz frequency electromagnetic oscillations for application to electrooptic modulators

The generation of even modest power levels of coherent electromagnetic oscillation is already quite difficult once the frequency required goes above 100 GHz. We must therefore recognise the severity of the situation at 1 THz. For potential applications such as short distance free-space communications, it will be essential to have efficient conversion of input electrical dc or low-frequency ac power into terahertz wave power. It will also be desirable to have a direct modulation capability so that communications signals can be imposed directly on the terahertz carrier.

Strong excitation of terahertz acoustic phonons has been demonstrated in AlN/GaN superlattices under very short pulse laser illumination. This suggests that, because the medium is also piezoelectric, significant Terahertz electromagnetic wave generation should be possible. Nevertheless, the overall conversion efficiency from electrical input power to output from the laser

will still be very low. The possibility of even modest conversion efficiency in carrier injection devices using inter-subband transitions (8) makes this approach potentially attractive – and the possibility of direct electrical modulation is also important for communications applications. QC laser operation at frequencies as low as ~3 THz has been reported, but only at cryogenic temperatures. One can speculate that further 'bandgap engineering' will be beneficial – going beyond the already high sophistication of the QC laser or discovering a superior semiconductor material combination for such lasers or related inter-subband structures. Resonantly extracting the terahertz frequency component from the fluctations in carrier density which occur in mode-locked semiconductor lasers could also be useful.

Conclusions

The prospects for using photonic bandgap effects in suitably fabricated 1D waveguide photonic microstructures to enhance the strength of the electrooptic interaction at terahertz frequencies have been considered. Both ferroelectric and electrooptic semiconductors have been assessed. More work will be required, both on measuring material properties and in the conception and fabrication of new types of device structure, if good electrooptic performance is to be achieved.

References

1. R.M. De La Rue, M.R.S. Taylor, K. Li, M. Sasaki, T. Hori and M. Izutsu, "TeraHertz frequency regime waveguide photonic microstructures for electro-optic modulation", 6th IEEE Terahertz Electronics Conference, Leeds, U.K., pp.106-109, 2nd-4th Sept (1998).
2. Y. Qian, R. Coccioli, F-R. Yang and T. Itoh, Passive and active component design using PBG, 6th IEEE Terahertz Electronics Conference, Leeds, U.K., pp. 42-45, 2nd-4th Sept (1998).
3. M.Zgonik et al., J. Appl. Phys., **74**, pp.1287-1297, (1993).
4. J.M. Marx et al., Appl. Phys. Lett., **67**, pp. 1381-1383, (1995).
5. I.P. Kaminow and E.H. Turner, 'Linear Electrooptical Materials', chapter 15 of CRC Handbook of Lasers, Ed. By R.J. Pressley, (1971).
6. K.Tsubouchi et al., IEEE Trans. Sonics and Ultrasonics, **SU-32**, pp. 634-644, (1985).
7. F-wave IV by M.R.S. Taylor, available on the internet at http://eeapp.elec.gla.ac.uk/ .
8. P. Harrison et al., Quantum well intersubband transitions as a source of terahertz radiation', 6th IEEE Terahertz Electronics Conference, Leeds, U.K., pp.74-77, 2nd-4th Sept (1998).

Tunable solid-state terahertz-wave sources: New ideas and prospects

S. A. Mikhailov

Max-Planck Institut für Physik komplexer Systeme, Nöthnitzer Str. 38,

D-01187 Dresden, Germany

ABSTRACT

An idea to build a solid-state analog of vacuum travelling and backward wave tubes operating in the THz frequency range has long been discussed in the literature. Experiments directed to the realization of this idea using the radiative decay of grating-coupled two-dimensional (2D) plasmons in semiconductor heterostructures have been made since 1980, however the intensity of emitted radiation remains too low so far. A general theory presented here describes the main physical phenomena underlying the operation principle of this kind of devices, and answers the two most important practical questions: why the devices have not worked properly, and what should be done to improve their characteristics. Particular attention is given to recently proposed ideas of using the quantum-wire (or quantum-dot) gratings, instead of commonly employed metal ones. The use of the new type of gratings is shown to lead to a substantial reduction of the threshold velocity of amplification, and to a very large enhancement (by a few orders of magnitude) of the gain. Physically, this is a consequence of the resonant interaction of plasma waves in the 2D electron layer and in the quantum-wire (quantum-dot) grating. Specific recommendations on how to build a tunable semiconductor travelling wave tube are formulated, unsolved theoretical problems are discussed.

Keywords: Smith-Purcell effect; Quantum wells, quantum wires, quantum dots; Current driven plasma instability; Two-dimensional plasmons; Amplification and generation of terahertz radiation.

1. INTRODUCTION

Recent advances in modern semiconductor technology have made it possible to realize high-quality semiconductor structures with low-dimensional electron systems (ES): quantum wells, quantum wires, quantum dots. It became also possible to combine quantum wells, wires and dots in more complicated structures consisting in, for instance, a two-dimensional (2D) electron layer and an adjacent quantum wire (or quantum dot) array, Figure 1. If a strong direct current is passed through the 2D electron layer in the direction perpendicular to the (quantum-wire) grating strips (the direction of the current is of no importance in the case of a quantum-dot grating), the structure resembles the geometry of the Smith-Purcell experiment,[1] and one could expect a generation of electromagnetic waves from the structure with the frequency

$$\omega/2\pi \simeq v_0/a, \tag{1}$$

where v_0 is the drift velocity of electrons and a is the grating period. Physically, the effect is due to a current-driven instability of 2D plasmons in the 2D electron layer: plasmons derive their energy from the current and convert it to the energy of electromagnetic radiation by means of the grating coupler. The operating frequency of such type of amplifier or oscillator would fall in the terahertz range (from $\simeq 0.3$ THz to a few THz).

An idea to use the Smith-Purcell effect in low-dimensional semiconductor structures for a creation of tunable solid-state sources of terahertz radiation has long been discussed in the literature. A number of far-infrared emission experiments have been directed to the realization of this idea.[2-7] A weak radiation has been actually observed, but its frequency depended not on the drift velocity v_0, but on the density of 2D electrons $n_2{}^*$. With a good accuracy the frequency of radiation has been shown to coincide with the frequency of 2D plasmons

$$\omega = \omega_{p2}(q) = \left(2\pi n_2 e^2 q/m_2\epsilon\right)^{1/2} \tag{2}$$

Further author information: E-mail: sam@mpipks-dresden.mpg.de

*Under certain conditions some drift velocity dependence of the emission spectra have been observed in Refs.[8,9]

Part of the EUROPTO Conference on Terahertz Spectroscopy and Applications II
Munich, Germany • June 1999 SPIE Vol. 3828 • 0277-786X/99/$10.00

139
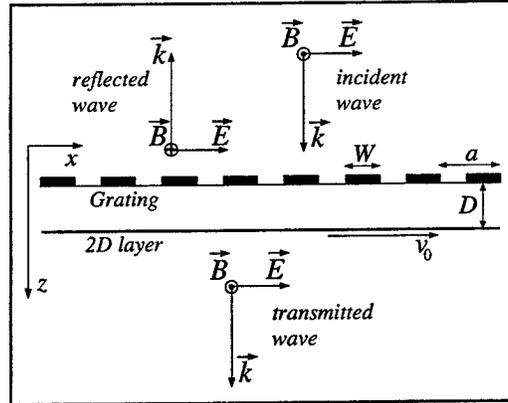
Figure 1. The structure under consideration (side view): a 2DES with a flowing direct current (the drift velocity v_0), and an adjacent grating coupler in the form of a quantum wire (or quantum dot) array.

with the wave-vector

$$\mathbf{q} = \mathbf{G}_m = (2\pi m/a, 0), \quad m = \pm 1, \pm 2, \dots, \tag{3}$$

determined by reciprocal lattice vectors $\mathbf{G}_m$. Here e and m_2 are the charge and effective mass of 2D electrons, respectively, and ϵ is the dielectric permittivity of the surrounding medium. In addition, the intensity of the emitted radiation turned out to be very low to be promising for device applications. The problem of building tunable semiconductor far-infrared sources based on low-dimensional electron structures – solid-state analogs of the travelling wave tube – remains to be solved so far.

A theory of plasma instabilities in 2D electron systems has been developed by Krasheninnikov and Chaplik.[10] They showed, in particular, that in order to observe the current-driven plasma instability in low-dimensional semiconductor structures, the drift velocity of 2D electrons should exceed a threshold value which is determined, roughly, by the condition,

$$v_0 > v_{\text{th}} \approx \omega_{p2}(q)/q. \tag{4}$$

For typical experimental parameters[2-7] ($n_2 \simeq 1 \times 10^{11}$ cm^{-2}, $a \simeq 1$ μm, $q \simeq 2\pi/a$) Eq. (4) gives $v_{\text{th}} \simeq 5.5 \times 10^7$ cm/s, which requires very strong driving electric fields. On the other hand, the average drift velocity v_{av} of 2D electrons is restricted by scattering. The dominant scattering mechanism of 2D electrons in a strong electric field is the emission of LO phonons. Estimating v_{av} in a GaAs sample with $\hbar\omega_{LO} = 36$ meV and $m_2 = 0.067$ one gets

$$v_{\text{av}}^{LO} \simeq (\hbar\omega_{LO}/2m_2)^{1/2} \approx 2.1 \times 10^7 \text{ cm/s} \tag{5}$$

(the experimentally measured value $v_{\text{av}}^{LO} \approx 1.9 \times 10^7$ cm/s agrees well with this estimate, see Ref.[8]). The estimate (5) gives the *upper bound* of the drift velocity of 2D electrons in the considered structures. Thus, in order to satisfy the condition $v_0 > v_{\text{th}}$ one should find the ways of a substantial reduction of the threshold velocity. This could be achieved by using the structures with smaller 2D electron densities, submicrometer periods $a \simeq 0.1$ μm and/or by exciting the higher 2D plasmon harmonics ($m = 2, 3, \dots$). This leads, however, to an essential decrease of amplitudes of the transmission (reflection, absorption) resonances.

In all experimental studies so far only the *metal* gratings has been used for coupling the plasma oscillations in the 2DES with external electromagnetic field. It has been recently shown[11,12] that the problem outlined above can be solved by using the *quantum wire* (or *quantum dot*) grating, instead of the commonly employed metal ones. The plasma parameters of quantum wires or dots (the plasma frequency ω_{p1}, the scattering rate γ_1) are of the same order of magnitude as in the 2DES, and falls in the THz range. Due to the resonant interaction of plasmons in the 2DES and in the grating the resonance amplitudes can be enhanced by a few orders of magnitude.[11,12] Due to this *resonant* Smith-Purcell effect one can effectively use the excitation of higher 2D plasmon harmonics in samples with low 2D electron density and with short (submicrometer scale) grating periods. As a result, the threshold velocity of

amplification can be reduced down to experimentally achievable values, and the gain of the structure can be increased by a few orders of magnitude compared to the structures with metal gratings.

In this paper we present a general theory which describes the main physical phenomena underlying the operation principle of the considered type of devices, formulate specific recommendations on how to build a tunable semiconductor "travelling wave tube", and discuss further unsolved theoretical problems.

2. THEORY

In this Section we follow, mainly, the general approach developed in Ref.[12] We consider the scattering of light on the structure "grating coupler – 2DES" shown in Fig.1. The grating coupler is treated as an infinitely thin conducting layer with an electron density

$$N_1(x)\delta(z) = \sum_k n_1(x - ak)\delta(z), \tag{6}$$

placed in the plane $z = 0$. The continuous function $n_1(x)$ is assumed to be zero at $|x| > W/2$ and an arbitrary nonzero function at $|x| < W/2$, where W is the width of the grating strips and a is the grating period. The conducting layer (2DES) is placed in the plane $z = D$ and is described by the frequency, wave-vector, and drift-velocity dependent conductivity $\sigma_{2D}(q, \omega, v_0)$. Electromagnetic wave is assumed to be incident upon the structure along the z axis with the electric vector being polarised in the x direction, perpendicular to the grating strips. A strong direct current is flowing in the 2DES in the x-direction. The system is infinite in the y direction, and the background dielectric constant ϵ is uniform in all the space.

The total electric field $\mathbf{E}^{tot}$ in all the space satisfies the Maxwell equations,

$$\nabla \times (\nabla \times \mathbf{E}^{tot}) + \frac{\epsilon}{c^2}\frac{\partial^2 \mathbf{E}^{tot}}{\partial t^2} = -\frac{4\pi}{c^2}\frac{\partial}{\partial t}\left[\mathbf{j}^{1D}(x)\delta(z) + \mathbf{j}^{2D}(x)\delta(z - D)\right] \tag{7}$$

with scattering boundary conditions at $z \to \pm\infty$. We expand the solution in Fourier series over reciprocal lattice vectors, apply the boundary conditions at the planes $z = 0$ and $z = D$, use the relation $j_{x,G}^{2D} = \sigma_{2D}(\mathbf{G}, \omega)E_{x,G}^{tot}|_{z=D}$ between the current in the 2DES and the total electric field at the plane $z = D$, and finally come to the following integral equation for the total electric field $E_x^{tot}(x) \equiv E_x^{tot}(x, z = 0)$ at the plane $z = 0$ of the grating

$$E_x^{tot}(x) = E_0 W(0, \omega) + \left(\frac{\partial^2}{\partial x^2} + \frac{\omega^2 \epsilon}{c^2}\right)\int_{cell}\frac{dx'}{W}\vartheta(x')L(x - x')E_x^{tot}(x'). \tag{8}$$

Here E_0 is the amplitude of the electric field in the incident wave, the kernel $L(x - x')$ is determined by the expressions

$$L(x - x') = \frac{2\pi i f\langle\sigma_{1D}(\omega)\rangle}{\omega\epsilon}\sum_\mathbf{G}\frac{W(\mathbf{G}, \omega)}{\kappa_G}e^{i\mathbf{G}\cdot(\mathbf{r}-\mathbf{r}')}, \tag{9}$$

$$W(\mathbf{G}, \omega) = 1 - \left(1 - \frac{1}{\epsilon_{2D}(\mathbf{G}, \omega)}\right)e^{-2\kappa_G D}, \tag{10}$$

$\epsilon_{2D}(\mathbf{G}, \omega)$ is the (relative) "dielectric permittivity" of the 2DES,

$$\epsilon_{2D}(\mathbf{G}, \omega) = 1 + \frac{2\pi i\kappa_G}{\omega\epsilon}\sigma_{2D}(\mathbf{G}, \omega), \tag{11}$$

$\langle\sigma_{1D}(\omega)\rangle$ is the local conductivity of electrons in the grating strips, averaged over the area of the strip, $\langle\ldots\rangle = \int(\ldots)dx/W$,

$$\vartheta(x) = n_1(x)/\langle n_1(x)\rangle \tag{12}$$

is a normalized electron density in the grating strip, $f = W/a$ is the geometrical "filling factor" of the grating, and

$$\kappa_\mathbf{G} \equiv \kappa_G = \sqrt{G^2 - \omega^2\epsilon/c^2}, \quad \text{Im } \kappa_G < 0. \tag{13}$$

From this point on we apply a more general approach to the solution of Eq. (8) than that of Ref.[12] Let $O_n(x)$ be a set of orthogonal functions at the interval $|x| < W/2$, which satisfy the conditions

$$\int \frac{dx}{W} \vartheta(x) O_n(x) O_m(x) = \delta_{mn}. \tag{14}$$

Let us expand the unknown electric field $E_x^{\text{tot}}(x')$ (at $|x'| < W/2$) over the orthogonal functions $O_n(x)$,

$$E_x^{\text{tot}}(x') = \sum_{n=0}^{\infty} C_n O_n(x'). \tag{15}$$

Substituting (15) into Eq. (8), multiplying it by $\vartheta(x) O_m(x)$ and integrating over dx we get an infinite set of equations

$$\sum_{n=0}^{\infty} M_{mn} C_n = E_0 W(0, \omega) \delta_{m0}, \tag{16}$$

where the matrix M_{mn} has the form

$$M_{mn} = \delta_{mn} + \frac{2\pi i f \langle \sigma_{1D}(\omega) \rangle}{\omega \epsilon} \sum_{\mathbf{G}} W(\mathbf{G}, \omega) \kappa_G \beta_m(\mathbf{G}) \beta_n^*(\mathbf{G}), \tag{17}$$

the factors $\beta_m(\mathbf{G}) = \langle \vartheta(x) O_m(x) e^{i\mathbf{G} \cdot \mathbf{r}} \rangle$ are determined by the density profile function $\vartheta(x)$, and the star means the complex conjugate. If the matrix equation (16) is solved (i.e. the coefficients C_n are found), we obtain the electric field $E_x^{\text{tot}}(x')$ inside the grating strips (at $|x'| < W/2$). Equation (8) then gives the field $E_x^{\text{tot}}(x)$ at all x, and the problem is completely solved. So, in order to get the solution, we need to invert the matrix M_{mn}, Eq. (17).

Equation (16) is solved by truncating the matrix M_{mn} to a finite size $N \times N$. In Ref.[12] the problem was solved approximately, assuming that $N = 1$, i.e. $C_0 = E_0 W(0, \omega)/M_{00}$ (a justification and physical consequences of this approximation have been also discussed in[12]). Here we make the next step, keeping two terms in the expansion (15). The final result for the transmission and reflection amplitudes of the structure assumes the form

$$t(\omega) = 1 + r(\omega) = \frac{1}{\epsilon_{2D}(0, \omega)} \left(1 - \frac{2\pi f \langle \sigma_{1D}(\omega) \rangle}{c\sqrt{\epsilon} \tilde{\zeta}(\omega)} \right), \tag{18}$$

where the response function

$$\tilde{\zeta}(\omega) = \frac{1}{W(0, \omega)} \left(M_{00} - \frac{M_{10} M_{01}}{M_{11}} \right) \approx \epsilon_{2D}(0, \omega) \left(M_{00} - \frac{M_{10} M_{01}}{M_{11}} \right) \tag{19}$$

differs from that used in Ref.[12] by the terms proportional to $M_{10} M_{01}$. In formulas (18), (19) we have used that both the period of the grating a and the distance between the 2DES and the grating D are small compared to the wavelength of radiation. The transmission, reflection and absorption coefficients are determined, as usual, by the formulas $T(\omega) = |t(\omega)|^2$, $R(\omega) = |r(\omega)|^2$, and $A(\omega) = 1 - R(\omega) - T(\omega)$.

In the rest of the paper we apply the results of the theory to an analysis of the transmission spectra of the structure shown in Figure 1 with a quantum-wire or a metal grating. We assume a semielliptic density profile

$$\vartheta(x) = (4/\pi)\sqrt{1 - (2x/W)^2}, \tag{20}$$

a Drude-type model for the average conductivity of electrons in the grating

$$\langle \sigma_{1D}(\omega) \rangle = \frac{n_1 e^2}{m_1} \frac{i}{\omega + i\gamma_1}, \tag{21}$$

and a hydrodynamic model for $\sigma_{2D}(\mathbf{q}, \omega, v_0)$,

$$\sigma_{2D}(\mathbf{q}, \omega, v_0) = \frac{i\omega n_2 e^2/m_2}{(\omega - \mathbf{q}\mathbf{v}_0)(\omega - \mathbf{q}\mathbf{v}_0 + i\gamma_2)}, \tag{22}$$

where n_i, m_i, and γ_i are the average electron density $(n_1 = \langle n_1(x) \rangle)$, the electron effective mass, and the phenomenological momentum relaxation rate in the grating $(i = 1)$ and in the 2DES $(i = 2)$, respectively (numerical parameters correspond to a GaAs-based semiconductor heterostructure). The relaxation rate of electrons in the grating γ_1 is determined by the quasi-elastic scattering of electrons by impurities and acoustic phonons. The electron relaxation rate in the 2DES γ_2 is determined by the same scattering mechanisms in the low-field regime, and by strongly inelastic scattering of electrons (due to emission of optical phonons) in strong electric fields. The relaxation rates are considered as phenomenological parameters of the theory, which can be extracted from experimentally measured low-field and high-field electron mobilities of the structure.

3. RESULTS

3.1. No current; absorption

Figures 2 and 3 demonstrate the frequency dependent transmission coefficients of the structure *"metal* grating – 2DES" (Fig. 2) and *"quantum-wire* grating – 2DES" (Fig. 3), under the condition when no current is flowing in the 2DES, $v_0 = 0$. In both cases one sees a number of resonances associated with a few lowest 2D plasmon harmonics and, in the case of the quantum wire grating, – with the grating plasmon. The most important characteristic feature of the quantum-wire grating structures is the larger amplitude of the resonances. Comparing Figures 2c and 3 one sees that they are stronger by at least one order of magnitude than in the metal grating structures. This is due to the resonant interaction of plasmons in quantum wires and in the 2DES. Indeed, the plasma frequency in metals is 3-4 orders of magnitude larger than the 2D plasmon frequency; therefore, the metal grating completely screens the plasma oscillations in the 2DES, and the coupling efficiency of the metal grating turns out to be rather low. The plasma frequency in quantum wires is of the same order of magnitude as in the 2DES; due to the resonant interaction of the plasmons the coupling efficiency of the grating resonantly increases by orders of magnitude. This is the main effect which leads to the dramatic improvement of device characteristics at finite v_0 in structures with the quantum-wire grating.

Another important feature of the transmission spectra of Figures 2 and 3 is an oscillating dependence of the amplitudes of resonances on the geometrical filling factor $f = W/a$. Under certain conditions some 2D plasma modes disappear at all (e.g. Fig. 2a, the mode $m = 2$). The largest values of the oscillator strengths can be obtained if the geometrical parameters of the (quantum-wire) grating satisfy the conditions

$$W/a = j_{0,s}/\pi m, \quad D/W \ll 1/4j_{0,s}, \quad s = 1, 2, \ldots, \tag{23}$$

where m is the 2D plasmon mode index and $j_{0,s}$ are zeros of the Bessel function $J_0(x)$.[†]

3.2. Finite current; amplification

3.2.1. Structure 2DES – metal grating

Now we consider the transmission of far-infrared radiation through a grating coupled 2DES at finite drift velocities $v_0 \neq 0$. Figure 4 demonstrates the general behaviour of the transmission spectra $T(\omega, v_0)$ of the structure with the *metal* grating. The drift velocity v_0 changes from $U \equiv v_0/v_{F2} = 0$ for the curve a up to $U = 8$ for the curve b (v_{F2} is the Fermi velocity of 2D electrons in the 2DES). For parameters of Figure 4 the Fermi velocity of 2D electrons is about 3.3×10^7 cm/s, so that the value of $U = 8$ corresponds to the drift velocities far beyond the experimentally achievable limit (5). Nevertheless, we analyse the curves in Figure 4 in order to understand physics of the considered effects. The methods of substantial reduction of threshold velocities are discussed below.

When $v_0 = 0$ (the curve a in Figure 4) one sees a number of resonances associated with 2D plasmon harmonics (2), see Figure 2. When v_0 increases, the 2D plasmon modes are splitted and assume the form of the Doppler shifted 2D plasmon resonances,

$$\omega \approx \pm\omega_{p2}(G_m) \pm G_m v_0. \tag{24}$$

[†]For a quantum-dot grating with the square lattice of dots $[G_{m,n} = 2\pi(m,n)/a]$ a similar condition exists. In particular, one can show that the oscillator strength of the (m, n)-th plasmon harmonic is proportional to $J_{3/2}^2(2\pi\sqrt{m^2 + n^2}R/a)$, where R is the radius of the dots. Thus, the (m, n)-th mode disappears if the argument of the Bessel function here coincides with zeros of $J_{3/2}(x)$.
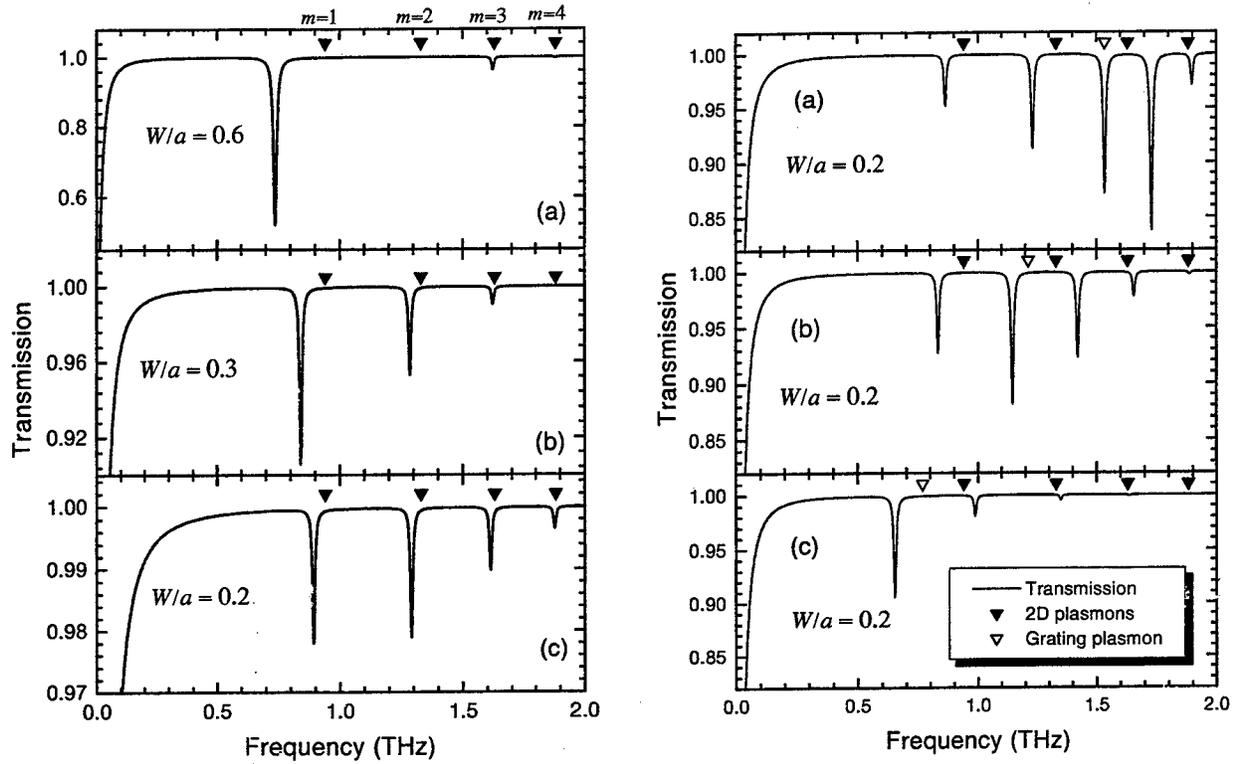
Figure 2. The transmission spectra of the structure "metal grating – 2DES" at different values of W/a. Geometrical parameters: $a = 1~\mu$m, $D = 60$ nm. Parameters of the 2D layer: $n_2 = 3 \times 10^{11}$ cm^{-2}, $\gamma_2 = 0.7 \times 10^{11}$ s^{-1}, $m_2 = 0.067$ (the mobility $\mu_2 = 375000$ cm^2/Vs). The grating parameters ($n_1 = 6 \times 10^{18}$ cm^{-2}, $\gamma_1 = 1.1 \times 10^{14}$ s^{-1}, $m_1 = 1$) correspond to a typical (Au) grating coupler. The dielectric constant is $\epsilon = 12.8$. Triangles show the calculated positions of the 2D plasmon harmonics (2) for $m = 1, \ldots, 4$.

Figure 3. The transmission spectra of the structure "quantum wire grating – 2DES" at different values of the grating plasmon frequency $\tilde{\omega}_{p1}$ at $a = 1~\mu$m, $D = 60$ nm, and $W = 0.2~\mu$m. Parameters of the 2D layer and the dielectric constant ϵ are the same as in Figure 2. Parameters of the grating: $\gamma_1 = 0.7 \times 10^{11}$ s^{-1}, $m_1^* = 0.067$, the electron density: (a) $n_{s1} = 4 \times 10^{11}$ cm^{-2}, (b) $n_{s1} = 2.5 \times 10^{11}$ cm^{-2}, (c) $n_{s1} = 1 \times 10^{11}$ cm^{-2}. Triangles show the calculated positions of the 2D plasmon harmonics (2) for $m = 1, \ldots, 4$, open triangles show the positions of the grating plasmon.

When v_0 becomes sufficiently strong, one of these modes,

$$\omega \approx -\omega_{p2}(G_m) + G_m v_0, \tag{25}$$

becomes unstable, and the transmission coefficient of the structure at the frequency (25) exceeds unity, – the wave is amplified. It is these conditions that correspond to the standard Smith-Purcell effect. One sees that in order to get the amplification of radiation, the drift velocity should exceed a threshold value roughly determined by the inequality

$$v_0 > v_{th}^m \simeq \omega_{p2}(G_m)/G_m \tag{26}$$

(more accurate estimate of v_{th} is given in[12]). The condition (26) was fulfilled in the Smith-Purcell experiment[‡], as well as in vacuum travelling wave amplifiers. In semiconductor structures, however, the threshold velocity is typically

---

[‡]In Ref.[1] the energy of electrons in the beam was 300 keV, the grating period 1.67 μm, and the bulk plasma frequency in the beam $\omega_p \simeq 1.5 \times 10^8$ s^{-1}. The ratio $v_0/v_{th}^{m=1}$ can then be estimated as $v_0/v_{th}^{m=1} \simeq 6 \times 10^6$.
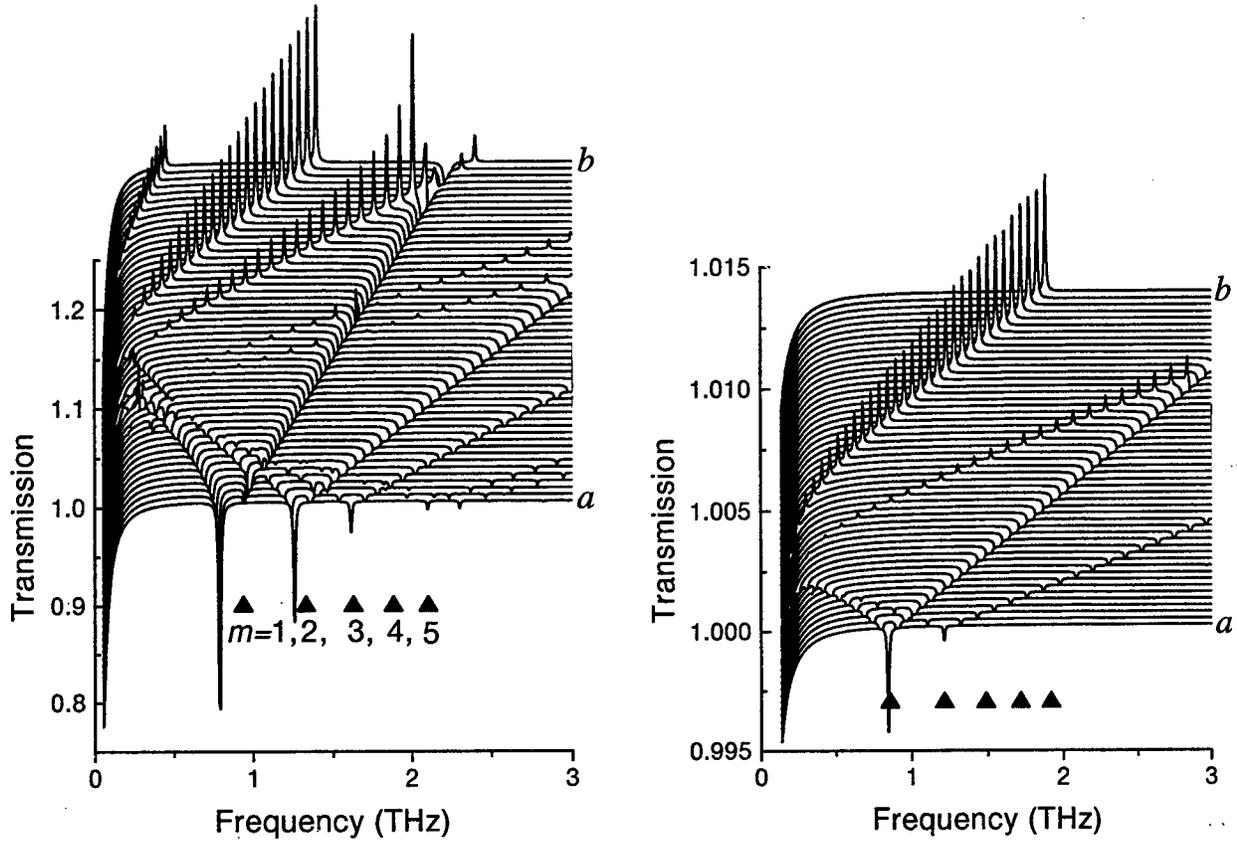
Figure 4. The transmission spectra of the structure "metal grating – 2DES" at different values of the dimensionless drift velocity $U = v_0/v_{F2}$: $U = 0$ for the curve a, and $U = 8$ for the curve b. Parameters of the structure: $n_2 = 6 \times 10^{11}$ cm^{-2}, $\gamma_2 = 0.7 \times 10^{11}$ s^{-1}, $m_2 = 0.067$; $n_1 = 6 \times 10^{18}$ cm^{-2}, $\gamma_1 = 1.1 \times 10^{14}$ s^{-1}, $m_1 = 1$; $\epsilon = 12.8$; $a = 2$ μm, $W = 0.6$ μm, $D = 80$ nm. Triangles show the calculated positions of the 2D plasmon harmonics (2) for $m = 1, \ldots, 5$.

Figure 5. The same as in Figure 4 but for $n_2 = 1 \times 10^{11}$ cm^{-2}, $a = 0.4$ μm and $W = 0.12$ μm.

essentially larger than the limiting value (5), which explains the very low intensity of the emitted THz radiation in experiments made so far. For instance in Ref.[7] (a GaAs/AlGaAs heterostructure with a metal grating, $n_2 = 5.4 \times 10^{11}$ cm^{-2}, $a = 2$ μm and $a = 3$ μm, the mobility of 2D electrons $\mu = 4 \times 10^5$ cm^2/Vs and the maximum driving electric field ~ 7.5 V/cm) the estimated drift and threshold velocities were $v_0 \approx 3 \times 10^6$ cm/s and $v_{th}^m \approx 1.8 \times 10^8/\sqrt{m}$ cm/s, respectively.

One could try to reduce the threshold velocity of amplification in structures with metal gratings by changing parameters of the system. As seen from the estimate (26), v_{th}^m decreases if

- the density of 2D electrons n_2 goes down,

- the grating period a goes down,

- the 2D plasmon harmonic index m goes up.

Compared to parameters of Figure 4, both the density of electrons n_2 and the grating period a can be reduced by at least one order of magnitude (the structures with such parameters have been experimentally realized, see e.g.[8,13]). Exploring the excitation of modes with $m = 2, 3, 4$, instead of the fundamental mode $m = 1$, one could reduce, in principle, the threshold velocity of amplification down to experimentally achievable values.
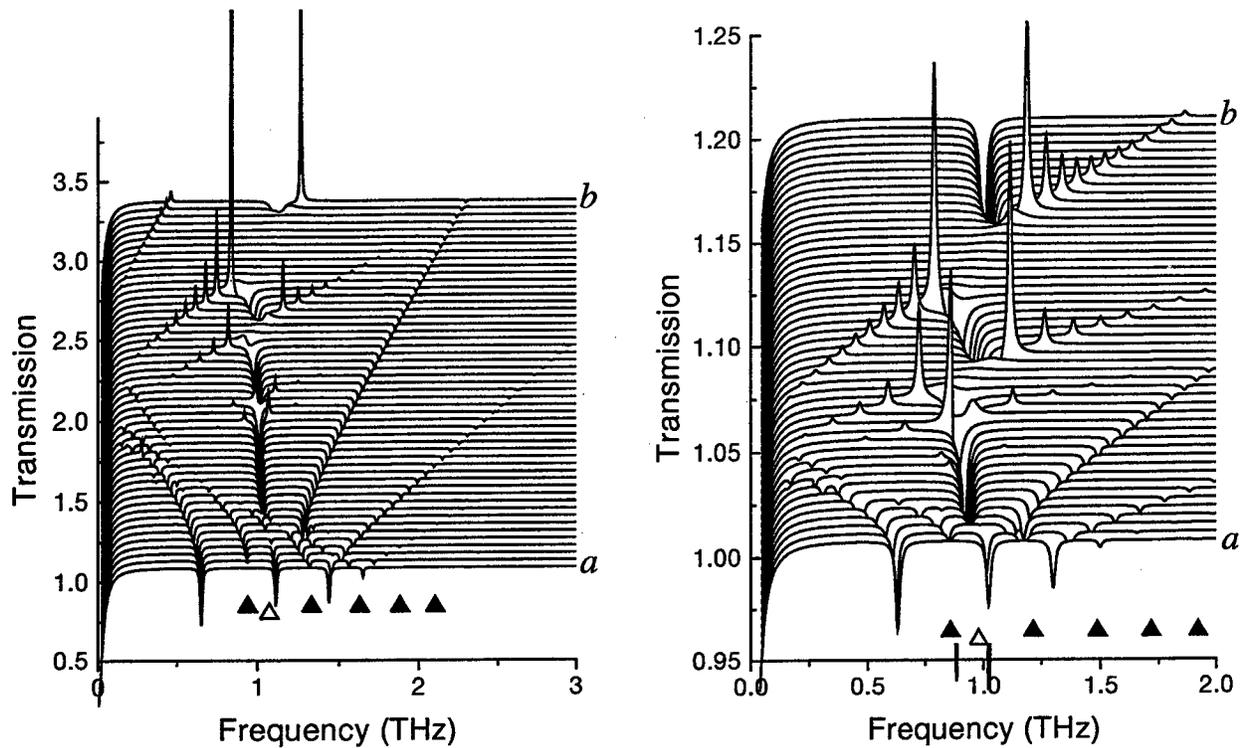
Figure 6. The transmission spectra of the structure "quantum-wire grating – 2DES" with the same parameters of the 2DES and the same *geometrical* parameters of the grating as in Figure 4, but for $n_1 = n_2 = 6 \times 10^{11}$ cm^{-2}, $\gamma_1 = \gamma_2 = 0.7 \times 10^{11}$ s^{-1}, and $m_1 = m_2 = 0.067$. Black triangles – the calculated frequencies (2) of the 2D plasmons, open triangle – the calculated frequency of the grating plasmon. The curve a corresponds to $U = 0$, the curve b – to $U = 8$.

Figure 7. The transmission spectra of the structure "quantum-wire grating – 2DES" with $n_1 = n_2 = 1 \times 10^{11}$ cm^{-2}, $\gamma_1 = \gamma_2 = 1.3 \times 10^{11}$ s^{-1}, $m_1 = m_2 = 0.067$, and $a = 0.4$ μm, $W = 0.12$ μm, $D = 20$ nm. Black triangles – the calculated frequencies (2) of the 2D plasmons, open triangle – the calculated frequency of the grating plasmon. The curve a corresponds to $U = 0$, the curve b – to $U = 8$.

On this way, however, another difficulty arises. As seen from Figure 4, the higher the mode index m, the smaller the amplitude of resonances. The same is valid for structures with smaller electron density and grating period: the smaller n_2 and a, the smaller the amplitude of resonances. This can be seen from comparison of the transmission spectra in Figures 5 and 4 (note a very large difference in the vertical axis scales in the Figures).

Does this mean, that the aim to build a solid-state analog of travelling wave tubes based on the low-dimensional electron systems is unattainable? Hopefully, not.

Fortunately, nature proposes a nice possibility to overcome this difficulty. As we have seen above, in semiconductor structures one can realize a new type of *resonant* grating couplers – the quantum-wire, or quantum-dot gratings. In structures with such gratings the amplitude of resonances substantially increases, and finally, one gets a pronounced reduction of threshold velocities and a large enhancement of the gain.

3.2.2. Structure 2DES – quantum-wire grating

Figure 6 demonstrates the transmission spectra of the structure "quantum-wire grating – 2DES". The physical parameters of the 2DES (n_2, γ_2, and m_2), as well as the geometrical parameters of the grating (a, W, and D) are
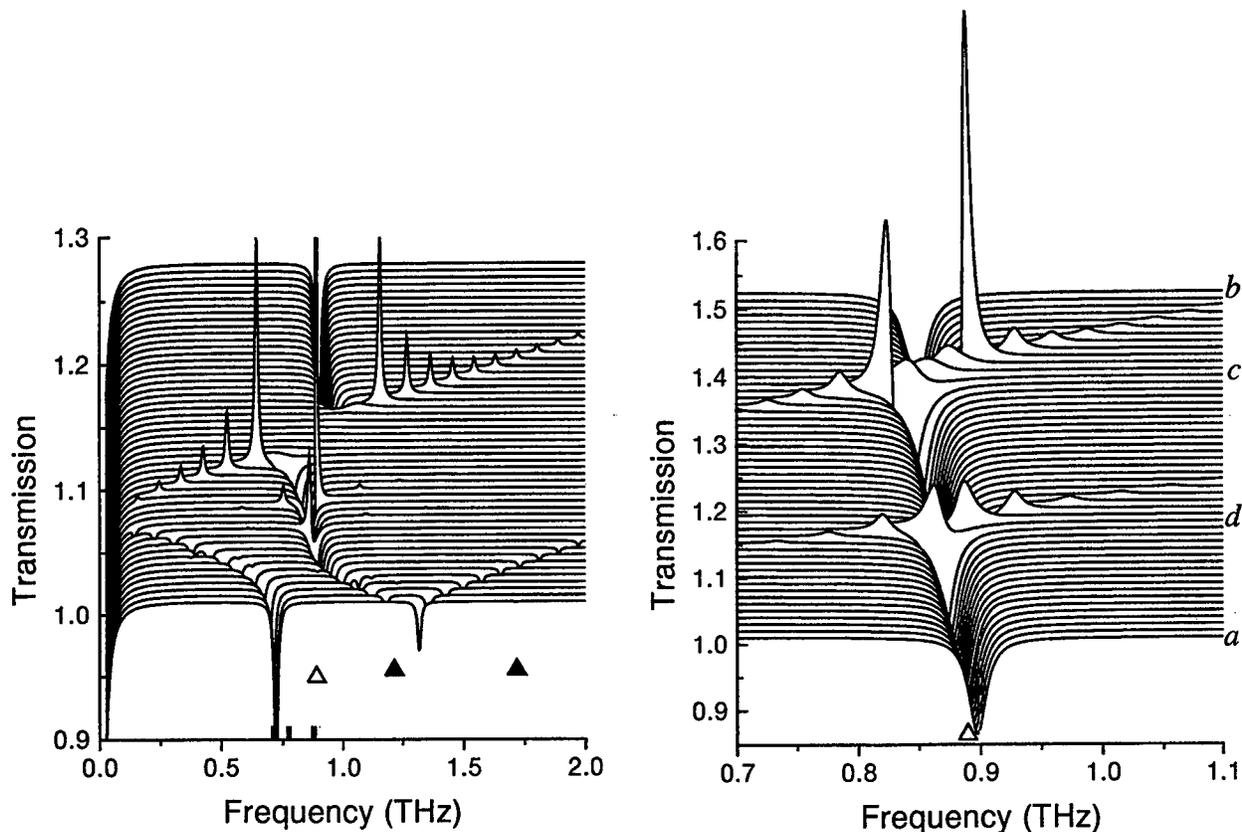
Figure 8. The transmission spectra of the structure "quantum-wire grating – 2DES" with $n_1 = 0.8 \times 10^{11}$ cm^{-2}, $n_2 = 1 \times 10^{11}$ cm^{-2}, $\gamma_1 = \gamma_2 = 1 \times 10^{11}$ s^{-1}, $m_1 = m_2 = 0.067$, and $a = 0.2$ μm, $W = 0.106$ μm, $D = 20$ nm. Black triangles – the calculated frequencies (2) of the 2D plasmons, open triangle – the frequency of the grating plasmon. The curve a corresponds to $U = 0$, the curve b – to $U = 6$. The Fermi velocity in the 2DES is $v_{F2} = 1.37 \times 10^7$ cm/s.

Figure 9. The transmission spectra of Figure 8 on an enlarged scale. The curve a corresponds to $U = 1.1$, the curve b – to $U = 2.1$.

the same as in Figure 4. The physical parameters of the grating (n_1, γ_1, and m_1) are chosen to be similar to those of the 2DES.

In addition to the drift-velocity dependent 2D plasmon resonances, a new, drift-velocity independent resonance, associated with the quantum-wire grating plasmon, appears in Figure 6. Due to the resonant interaction of the grating plasmon with the 2D ones, the amplitude of the unstable 2D plasmon resonances increases near their intersection with the grating plasmon. As a result, a huge enhancement of amplification of THz radiation is seen for the modes with $m = 2$, $m = 3$, and even for the higher modes with $m = 5$ and $m = 6$. Figure 6 thus clearly demonstrates that employing the quantum-wire grating one can effectively use the higher 2D plasmon harmonics and hence reduce the threshold velocity.

Figure 7 demonstrates the transmission spectra of the structure "quantum-wire grating – 2DES" with a smaller value of the 2D electron density and a shorter grating period. A resonant enhancement of the gain is also seen in the Figure, and the threshold velocity is substantially reduced compared to Figure 6.

Figures 8 and 9 provide another example of the transmission spectra of the structure. A substantial amplification of radiation can be seen already at *experimentally achievable values* of the drift velocity of 2D electrons: the group of curves d in Figure 9 (the unstable 2D plasmon mode with $m = 3$) corresponds to $v_0 \approx 1.9 \times 10^7$ cm/s. The
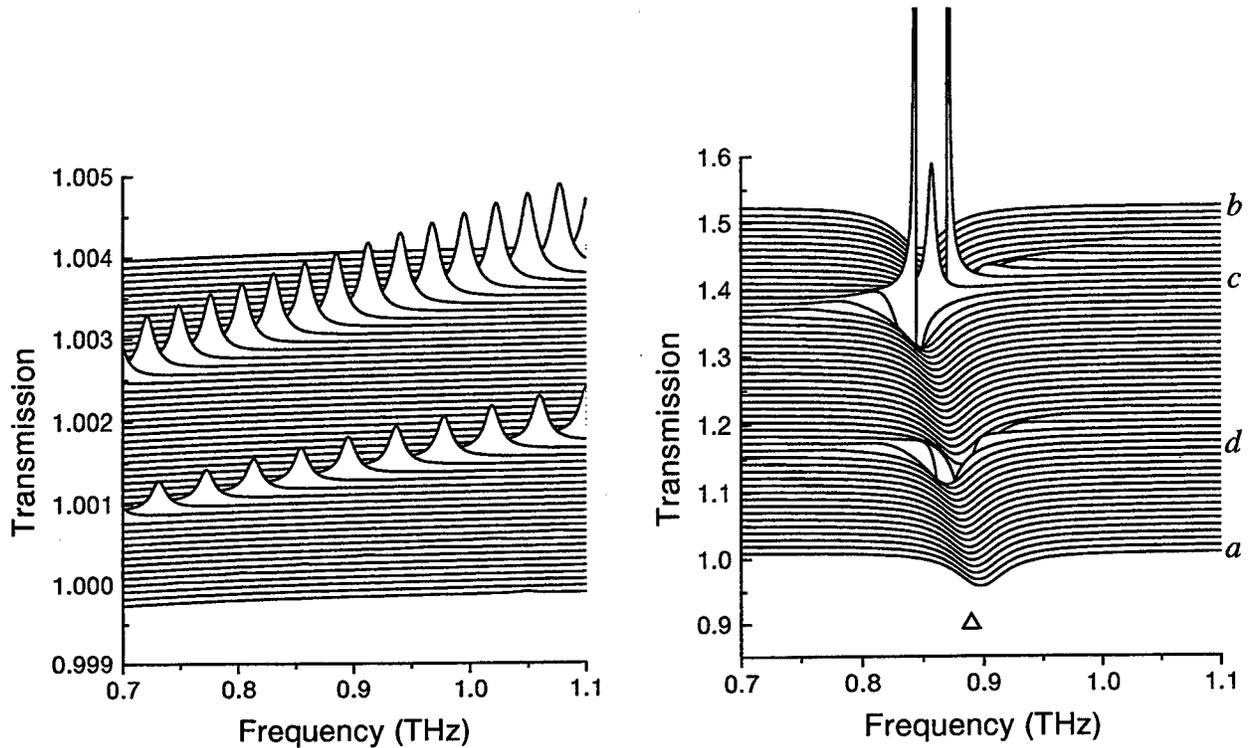
Figure 10. The same as in Figure 9 but for the metal-grating structure. Note the very large difference in the vertical axis scales in this Figure and in Figure 9.

Figure 11. The same as in Figure 9 but for $\gamma_1 = \gamma_2 = 3 \times 10^{11}$ s^{-1}.

threshold velocity *can be reduced further* by using 2DES's with 2D electron density below $n_2 = 1 \times 10^{11}$ cm^{-2} (see Ref.[12]). Another possibility *substantially to reduce* the threshold velocity (roughly, by a factor of two) consists in using the *counter-streaming* electron flows in adjacent low-dimensional electron layers. The structures with two close separately contacted 2DES's have been experimentally realized, e.g., in Ref.[14]

It should be emphasized ones more that the large absolute value of the gain in Figure 9 is due exclusively to the use of the *quantum-wire* grating. Figure 10 shows the transmission spectra of a grating-coupled 2DES with the same parameters of the 2DES and the same geometrical parameters of the grating, as in Figure 9, but for the *metal*-grating structure. One sees resonant features related to the unstable 2D plasmon modes with $m = 2$ and 3, but the value of the gain is about *two orders of magnitude smaller* than in the case of the quantum-wire grating!

Finally, we discuss the influence of the relaxation rates γ_1 and γ_2 on the transmission spectra of the structure "2DES – quantum-wire grating". In Figure 11 we show the transmission spectra, similar to those of Figure 9, but for the three times larger values of the relaxation rates γ_1 and γ_2 ($\gamma_1 = \gamma_2 = 1 \times 10^{11}$ s^{-1} in Figure 9 and $\gamma_1 = \gamma_2 = 3 \times 10^{11}$ s^{-1} in Figure 11). The amplification resonance associated with 2D plasmon mode $m = 3$ (curves d) disappears, while that corresponding to the mode $m = 2$ still exists, although in a narrower frequency range. One can show that the m-th 2D plasmon harmonic is unstable, and hence the transmission coefficient at the corresponding frequency exceeds unity, if the condition

$$\gamma_1 \gamma_2 < \tilde{\omega}_{p1} \omega_{p2} (G_m) |m|^{-1} J_1^2 (\pi f m) \exp(-2|G_m|D) \qquad (27)$$

is satisfied (the semielliptic density profile in the wires (20) is assumed). Equation (27) explains the difference between the spectra of Figures 9 and 11.

Equation (27) provides the estimate of the upper boundary of the relaxation rates (the lower boundary of the 2D electron mobilities) at which the amplification of THz radiation can still be observed in structures with quantum wire gratings.

4. DISCUSSION

4.1. How to build a tunable semiconductor terahertz-wave amplifier?

Now we can answer the two most important practical questions: Why the semiconductor devices based on the discussed principle did not work so far? and What should be done to build a successfully working semiconductor analog of the travelling (backward) wave tubes?

The semiconductor devices which have been studied so far did not work properly because the average drift velocity of 2D electrons in semiconductors is strongly restricted by the emission of LO phonons, Eq. (5), but the required threshold velocity of amplification substantially exceeded this value (at parameters used in experiments). The threshold velocity could be reduced by using the structures with lower electron density in the 2DES and shorter periods of the grating, but the amplitudes of the unstable plasma resonances (the gain) becomes negligibly small in the structure with commonly employed metal gratings. In fact, as seen from the above analysis, the LO phonon emission by 2D electrons in strong electric fields leaves practically no hope for the realization of a solid-state travelling wave tube on the basis of commonly employed structures "2DES – *metal* grating". The use of the resonant interaction of plasma waves in the 2DES and in the *quantum-wire* (or similar) grating (the *resonant* Smith-Purcell effect) provides a possible solution of this problem.

How to build a successfully working semiconductor terahertz-wave amplifier (oscillator) based on the grating coupled low-dimensional electron system shown in Figure 1? A set of specific recommendations listed below gives an approximate outline of requirements which should be met in order to build a successfully working device.

- The grating coupler must be made out of a material with plasma parameters (ω_{p1}, γ_1) similar to those of the 2DES. This can be a *quantum-wire, quantum-dot, antidot, etc*, grating.

- The grating period a should be as small as possible: the threshold velocity essentially depends on and decreases with a.

- The optimal values of the ratio W/a are given by Eq. (23).

- The distance between the 2DES and the grating should be as small as possible, $D \ll W$.

- The density of electrons in the 2DES should be sufficiently small (below $\simeq 1 \times 10^{11}$ cm^{-2}).

- The relaxation rates γ_1 and γ_2 should satisfy the condition (27).

The last question which should certainly be discussed concerns the tunability of the devices with quantum-wire or similar gratings. Because of the use of the resonant interaction of plasmons in such structures the tunability range of this kind of devices is certainly narrower than it could be in structures with metal gratings. This is the price for the substantial reduction of the threshold velocity and the enhancement of the gain. Nevertheless, as seen from the above discussion, the operating frequency can be tuned within approximately 20-30% around the average frequency (determined by the plasma frequency in the quantum wires) by means of the applied current (see Figure 9). In addition, the grating plasma frequency itself can be varied by changing the density of electrons in wires with the help of an additional metal gate.[15] Combining these two methods of tuning the operating frequency one can expect a rather wide tunability range of the terahertz-wave amplifiers (oscillators) with quantum-wire or similar gratings.

4.2. Problems to be solved

The physical ideas presented in this theory can be developed further with the aim to find *the best conditions* for the device operation. The following problems can be formulated and solved:

- *Different low-dimensional electron systems:*

    – 2DES – quantum dot grating;

- 2DES – antidot grating;
- a system of "antirings"[11] – a periodic array of quantum dots placed inside antidots within the same 2DES plane;
- many-layer superlattice structures;
- quantum wire array – crossed quantum wire grating;
- other low-dimensional electron systems.

- *Low-dimensional electron structures with counter-streaming electron flows;*

- *"Gratings" with a violated periodic symmetry.* An analysis of this problem may be of a great practical importance in connection with possible realization of the discussed ideas in a system "2DES – an array of *self-assembled* quantum dots".[16,17]

- *Influence of external (e.g. magnetic) fields on the amplification of THz radiation in the structures with quantum-wire (or similar) gratings.* This may give additional possibilities to control the operation characteristics of the device.

- *An analysis of more comprehensive models for the conductivity of the 2DES:* Influence of nonlocal, quantum-mechanical, electron scattering and electron heating effects.

5. SUMMARY

We have presented a complete theory of terahertz-wave amplifiers based on low-dimensional electron structures with quantum-wire (or similar resonant) gratings. We hope that this work will stimulate new experimental research in semiconductor terahertz-wave electronics and will finally lead to a creation of semiconductor analogs of the travelling and backward wave tubes.

ACKNOWLEDGMENTS

REFERENCES

1. S. J. Smith and E. M. Purcell *Phys. Rev.* **92**, p. 1069, 1953.
2. D. C. Tsui, E. Gornik, and R. A. Logan *Solid State Commun.* **35**, p. 875, 1980.
3. E. Gornik, R. Schwarz, G. Lindemann, and D. C. Tsui *Surf. Sci.* **98**, p. 493, 1980.
4. R. A. Höpfel, E. Vass, and E. Gornik *Phys. Rev. Lett.* **49**, p. 1667, 1982.
5. R. A. Höpfel, G. Lindemann, E. Gornik, G. Stangl, A. C. Gossard, and W. Wiegmann *Surf. Sci.* **113**, p. 118, 1982.
6. N. Okisu, Y. Sambe, and T. Kobayashi *Appl. Phys. Lett.* **48**, p. 776, 1986.
7. K. Hirakawa, K. Yamanaka, M. Grayson, and D. C. Tsui *Appl. Phys. Lett.* **67**, p. 2326, 1995.
8. C. Wirner, C. Kiener, W. Boxleitner, M. Witzany, E. Gornik, P. Vogl, G. Böhm, and G. Weimann *Phys. Rev. Lett.* **70**, p. 2609, 1993.
9. E. Gornik, W. Boxleitner, V. R. kopf, M. Hauser, C. Wirner, and G. Weimann *Superlatt. & Microstruct* **15**, p. 399, 1994.
10. M. V. Krasheninnikov and A. V. Chaplik *Zh. Eksp. Teor. Fiz.* **79**, p. 555, 1980.
11. S. A. Mikhailov and N. A. Savostianova *Appl. Phys. Lett.* **71**, p. 1308, 1997.
12. S. A. Mikhailov *Phys. Rev. B* **58**, p. 1517, 1998.
13. D. Weiss, M. L. Roukes, A. Menschig, P. Grambow, K. von Klitzing, and G. Weimann *Phys. Rev. Lett.* **66**, p. 2790, 1991.
14. T. J. Gramila, J. P. Eisenstein, A. H. MacDonald, L. N. Pfeiffer, and K. W. West *Phys. Rev. Lett.* **66**, p. 1216, 1991.
15. D. Heitmann and J. P. Kotthaus *Physics Today* **46/6**, p. 56, 1993.
16. D. Leonard, M. Krishnamurthy, C. M. Reaves, S. P. Denbaars, and P. M. Petroff *Appl. Phys. Lett.* **63**, p. 3203, 1993.
17. M. Fricke, A. Lorke, J. P. Kotthaus, G. Medeiros-Ribeiro, and P. M. Petroff *Europhys. Lett.* **36**, p. 197, 1996.

Plasmon Based Terahertz Laser Without Population Inversion.

K.Kempa[a], P. Bakshi[a], M. Ciftan[b], E. Gornik[c], K. Unterrainer[c], G. Strasser[c] and C. Rauch[c]

[a]Department of Physics, Boston College,Chestnut Hill, MA, USA

[b]Department of Physics, Duke University,Durham, NC, USA

[c]Institute for Solid State Electronics and Microstructure Center, TU Wien, Austria

ABSTRACT

We propose here a class of quantum well structures designed to achieve a coherent generation of THz radiation through a plasma instability. This can be achieved, without population inversion, if a dynamical inhomogeneity is built into the active region of the structure. We show, through self-consistent calculation of the non-equilibrium steady state, that such structures can be inherently unstable against growing charge fluctuations under a variety of conditions, including lack of population inversion. Preliminary calculations of the I-V characteristics of such structures are in good agreement with experimental results.

Keywords: terahertz radiation, quantum well structures, plasma instability, population inversion

1. INTRODUCTION

Conventional lasers require a sufficient population inversion in the carrier distribution, to achieve the dominance of the downwards radiative transitions. Such population inversion is however difficult to achieve in semiconductor nanostructures due to the presence of very fast electron-phonon and electron-electron scatterings[1]. We have proposed plasma instability based approaches[2-6] in a variety of systems, to obtain THz radiation. These also require population inversion[2-6]. Thus achieving population inversion is presently the most serious obstacle in obtaining a THz laser, and therefore schemes which do not require population inversion are very attractive. We have recently proposed a novel scheme to obtain a plasma instability without population inversion[7]. We show there, that this scheme does not require population inversion if in addition to a plasmon bath, there is a region where a dynamic charge inhomogeneity can develop[7]. Here, we suggest specific quantum well structures for a practical implementation of this novel idea.

We propose here a structure in which the plasmon reservoir is in the form of a wide parabolic quantum well, and a properly designed adjoining potential well is the location of the dynamic charge inhomogeneity. Under bias, a dc current flows through this structure. However, due to the non-linear dynamics arising from the charge inhomogeneity, the current is repeatedly interrupted, and induces oscillations in the plasmon reservoir. These charge oscillations generate coherent electromagnetic radiation at the same frequency.

2. PLASMA INSTABILITIES

If a current flows through a plasma, plasma waves can grow by drawing energy from the current under appropriate circumstances. This phenomenon is called the current driven plasma instability, and is well known in gaseous plasmas[8]. Certain types of such instabilities have already been used to generate and amplify electromagnetic waves in gaseous plasmas. We have investigated[2] the feasibility of generating analogous instabilities in a variety of lower dimensional solid state systems. In general, a direct transfer of energy from a dc current into a plasma mode of an homogeneous system requires that the carrier velocities exceed a certain threshold. This threshold velocity in uniform solid state systems is prohibitively high[2], of the order of the Fermi velocity V_F. High mobility modulated wires[3] or lateral surface superlattices[4] require lower drift

Part of the EUROPTO Conference on Terahertz Spectroscopy and Applications II
Munich, Germany • June 1999 SPIE Vol. 3828 • 0277-786X/99/$10.00

151

thresholds, but are diffucult to fabricate. In bounded (statically inhomogeneous) quantum well systems one can achieve instability by selective injection and extraction of carriers[4,5]. This rests, however, on the existence of the hard to achieve population inversion in the carrier distribution between the injected and extracted subbands[6]. Experimentally plasma instability has not yet been seen in the semiconductor structures, due to the difficulties stated. However, we note that a radiative decay of incoherent plasmons has been observed[9] in semiconductor heterostructures, in a wide temperature range (up to room temperature), and in the presence of bulk doping.

3. PROPOSED STRUCTURES

In Ref.7 it was shown that an instability, without population inversion occurs if a small dynamic charge region is created in a uniform electron plasma, and which has a response given by a susceptibility of a form $f(\ ) = 2i\ \ _p$ where $_p$ is the bulk plasma frequency, and >0. A general system was proposed, to model this dynamic charge region, consisting of a small potential well capable of accumulating electrons, with a variable potential barrier on one side which acts as a non-linear gate. Such a system will exhibit the desired form of the susceptibility[7].

With these results in mind we now propose *specific semiconductor nanostructures* which should have the desired properties. A typical structure under bias is shown in Fig.1.
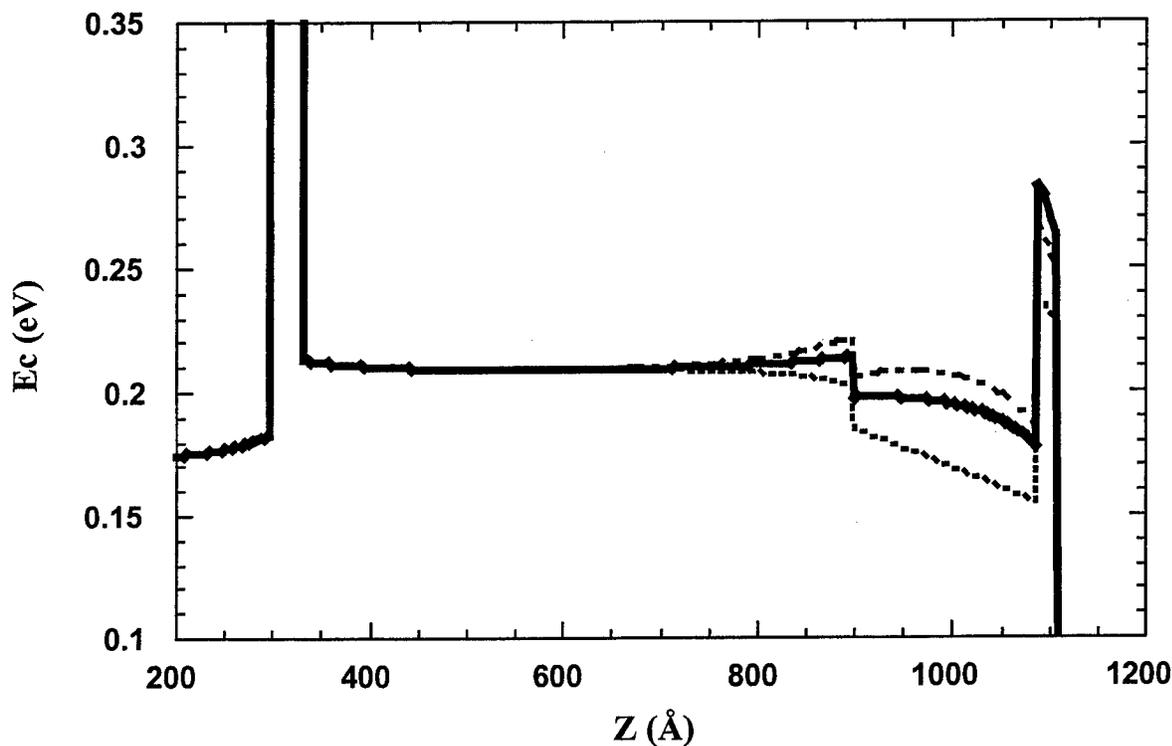
Fig.1 The energy of the conduction band edge E_C vs distance, z, in Å. The electrons are confined by this potential only in the z-direction (the growth direction), and are free to move in the plane perpendicular to this growth direction. The solid line represents the potential calculated assuming that the total charge density inside the pocket corresponds to an effective quasi-Fermi level there at 0.205eV. The corresponding potential for the fully filled pocket is shown as the dashed-dotted line, while the dotted line represents the potential of the empty pocket.

The lines represent the energy of the conduction band edge vs distance, z. The different values of the edge energy along z are due to a varying Al content in the AlGaAs alloy. The electrons are confined by this potential only in the z-direction (the growth direction), and are free to move in the plane perpendicular to this growth direction. The structure consists of a narrow barrier, separating the doped region to the left (left reservoir) from the parabolically profiled active region. The curvature of this parabolic confining potential has been chosen so that the Kohn's resonance (plasmon of the parabolic region) is at 12 meV. Immediately to the right of the parabola is a linearly graded region of the pocket. Finally, a narrow barrier separates the pocket from the outside doped region (right reservoir). This barrier and the pocket, together, simulate the dynamic inhomogeneity region, discussed above. The Fermi level of the left reservoir is at 0.22eV, and of the right reservoir at 0 eV, i.e the bias voltage is 0.22V. The solid line represents the potential calculated assuming that the total charge density inside the pocket corresponds to an effective quasi-Fermi level there at 0.205eV. The corresponding potential for the fully filled pocket is shown as the dashed-dotted line, while the dotted line represents the potential of the empty pocket. The corresponding electron charge densities are shown in Fig.2, and were obtained using the self-consistent Thomas-Fermi method[10].
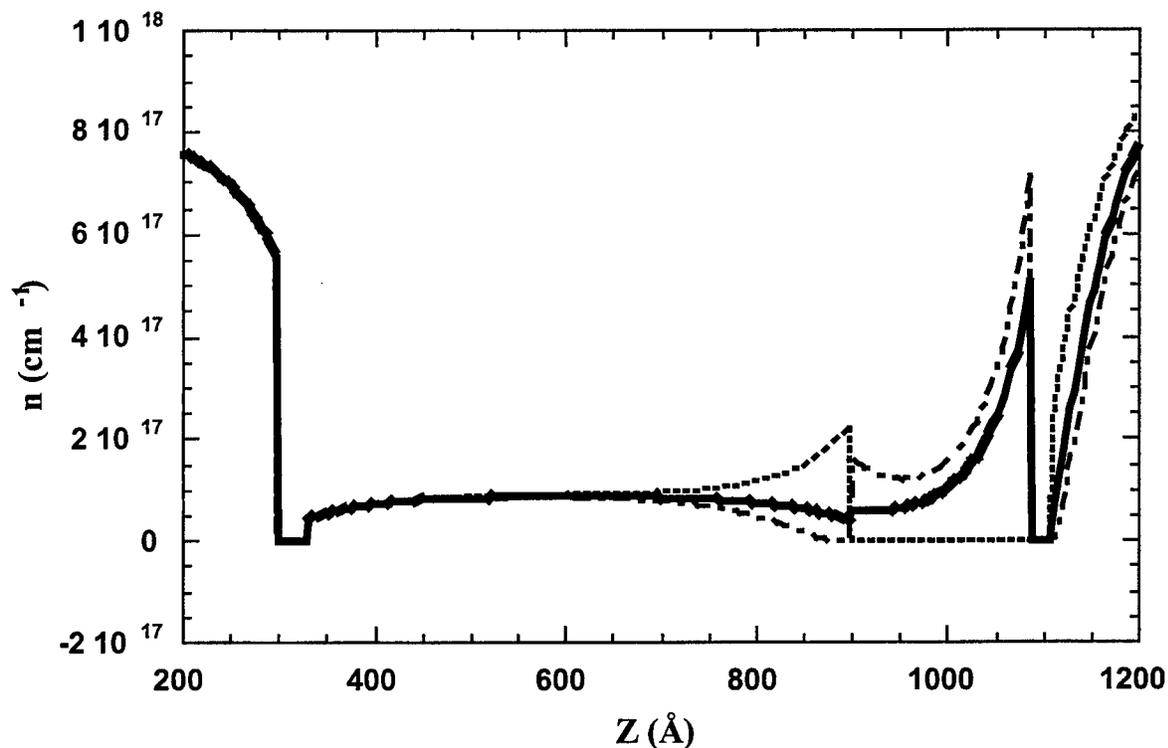
Fig.2 The electron charge densities corresponding to the self-consistent potentials of Fig.1 (notation as in Fig.1).

4. PLASMA RESPONSE

To calculate the possibility of an instability in this structure, we employ the RPA formalism described in detail in. Ref.11. We assume the potential represented by the solid line in Fig.1, and populate the subbands so that there is *no population inversion*. We calculate the single particle eigen states and wave functions in an extended zone, so as to allow a current to flow through the structure (complex wave functions). We find a robust instability at Re(h)≈ 13.7 meV, with Im(h)≈ 1.5 meV. This is a strong instability of the prime mode of the parabolic quantum well (there is an expected slight depolarization of the resonance from the 12 meV). To prove that this is indeed a dynamic inhomogeneity induced instability, we next

eliminate the pocket region. The results in this case show that the instability indeed disappears. We found that this instability strongly depends on the shape of the self-consistent potential (and of course on the presence/absence of the pocket), but is relatively insensitive to the subband population scheme in the pocket. In the calculation above, we assumed the "worst case scenario" of all subbands below the Fermi level being fully occupied. The instability exists for partial subband populations (still without population inversion), and also exists if a population inversion is assumed.

The instability calculations predict only an onset of divergent charge oscillations. Usually, in the case of the conventional instabilities, the non-linear effects quickly saturate such a divergency so that macro-charge oscillations do not develop. However, in our structure non-linear effects should support large charge oscillations. To see this, assume that initially the pocket is empty. Then the corresponding potential is shown by dotted line in Fig.1. As the pocket fills with electrons from the left, the potential approaches the shape given by dash-dotted line of Fig.1. In the process, however, the potential wedge, which rises even faster, strongly reduces the charge in-flow into the pocket. As the inflow of charge into the pocket diminishes, the current outflow through the right barrier (practically unchanged) begins to empty the pocket. Consequently the screening decreases, causing the potential to approach again the dotted line of Fig.1. This, in turn, lowers the wedge, and with the in-flow of charge into the pocket, the new cycle begins. This periodic charge build-up in the pocket occurs at the expense of the charge in the parabolic region, and will enhance charge "sloshing" there. This is clearly visible in Fig.2. This charge "sloshing" will enhance the instability, provided that it is fast enough. In turn, the instability about an intermediate bias (solid line in Fig.1) assures that the macro-charge oscillations do not decay to this quasi-equilibrium state. This is the essence of the dynamic inhomogeneity.

The resulting charge oscillations are dipole active (q->0), *and will emit electromagnetic radition at the frequency of the coherent plasma mode*. The structure should be built into a narrow (a few · m of diameter) mesa post. Then the post will act as a Hertz dipole antenna. To enhance the efficiency of the plasmon-radiation conversion, an efficient antenna arrangement could be constructed, e.g. "bow-tie".

5. PRELIMINARY EXPERIMENTAL RESULTS

For an experimental realization of these ideas we have begun the design, growth, and characterisation of speciffic quantum well structures, along the lines of section 3. The following two structures have been grown, and their I-V characteristics have been measured. The two structures are identical, except that one has a quantum well pocket, which represents the dynamic inhomogeneity. This allows us to investigate the role played by this dynamic inhomogeneity. The structures are similar to the one in Fig.1, except that the pocket region is deeper (pure GaAs), the barriers are much thinner (8 Å and 11 Å) to allow a significant current flow through the structure, and the size of the active region is smaller (480Å for the parabolic regin and 80Å for the pocket).

The measured I-V characteristics for the structure with the quantum well pocket are shown in Fig.3, to be contrasted with the results for the other structure shown in Fig.4.

154
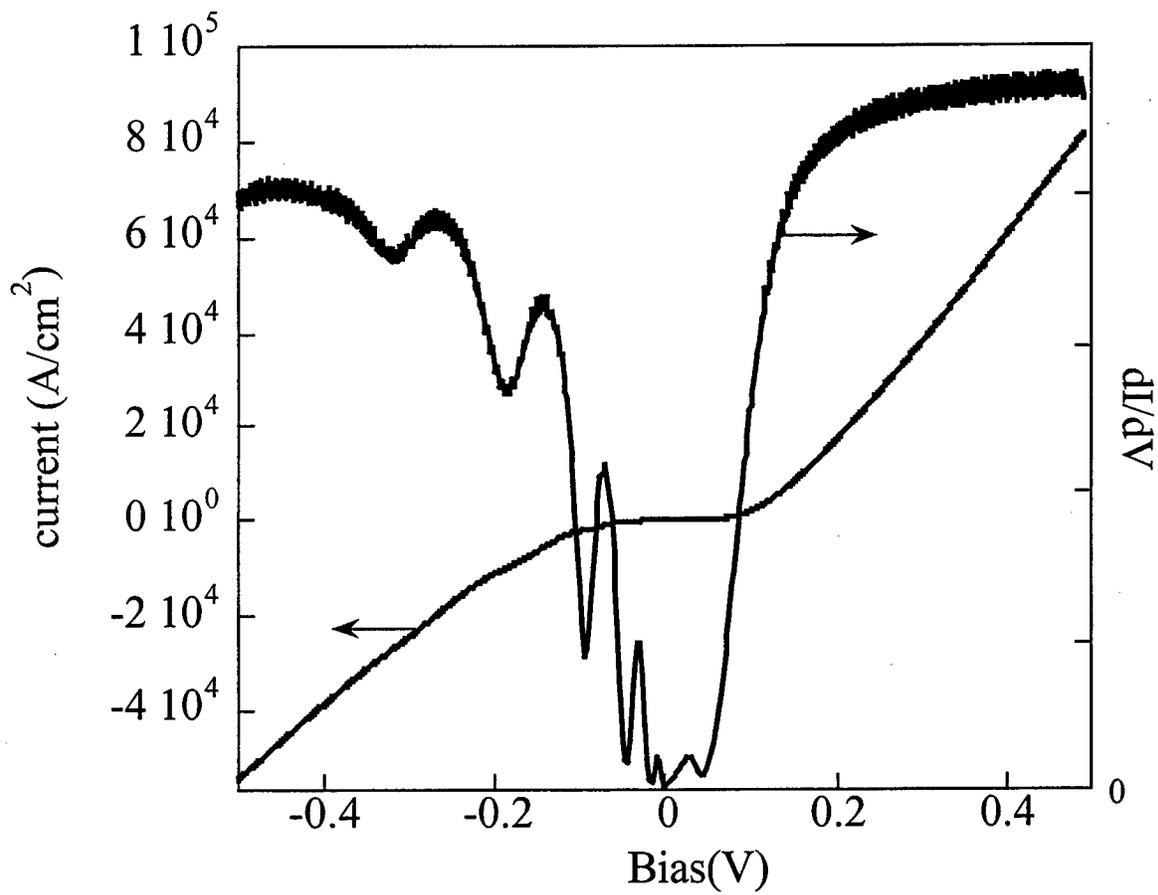
Fig.3. Current density and its derivative vs bias for a structure with the pocket region.
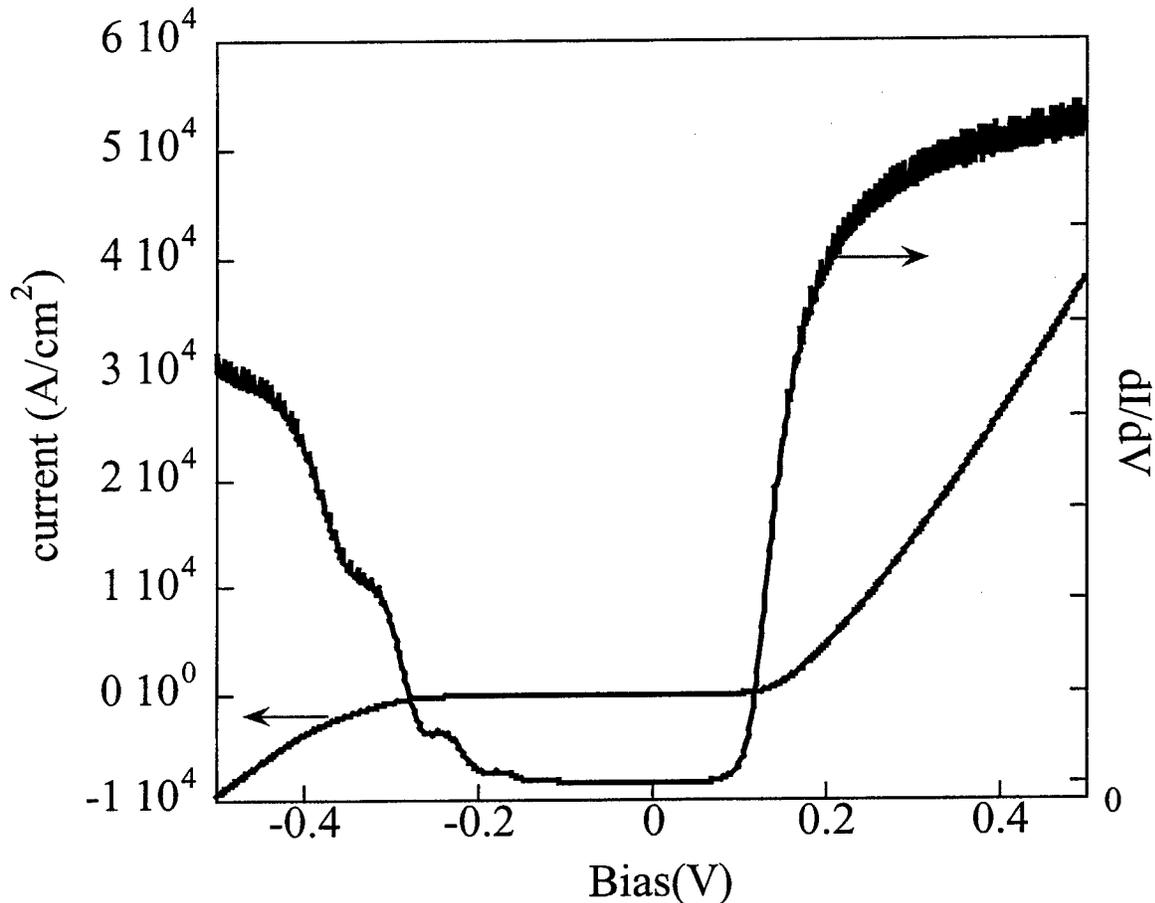
Fig.4. Current density and its derivative vs bias for a structure without the pocket region.

There is a dramatic difference in the two cases, reflecting a diffrent dynamics of the two structures under bias. At corresponding biases, the structure with the pocket has a much larger current, and the differential conductance has much more pronaunced oscillations in Fig.3.

To develop a quantitative understanding of these results, we have begun microscopic calculations of the steady state non-equilibrium transport through
these structures. We have developed a fully self-consistent computational scheme to accomplish this[6,12]. The eigenstates are determined by the Schroedinger-Poisson scheme, the subband populations by rate balance equations, inter-subband transfer rates through a RPA self-energy calculation, and the injection-extraction rates by the transfer matrix for complex energies. We have obtained preliminary results for the I-V characteristics of these structures (for the forward bias). Comparison with the experimental results (Figs. 5 and 6) shows good agreement. Further studies will be conducted to fully understand the dynamics of these structures.
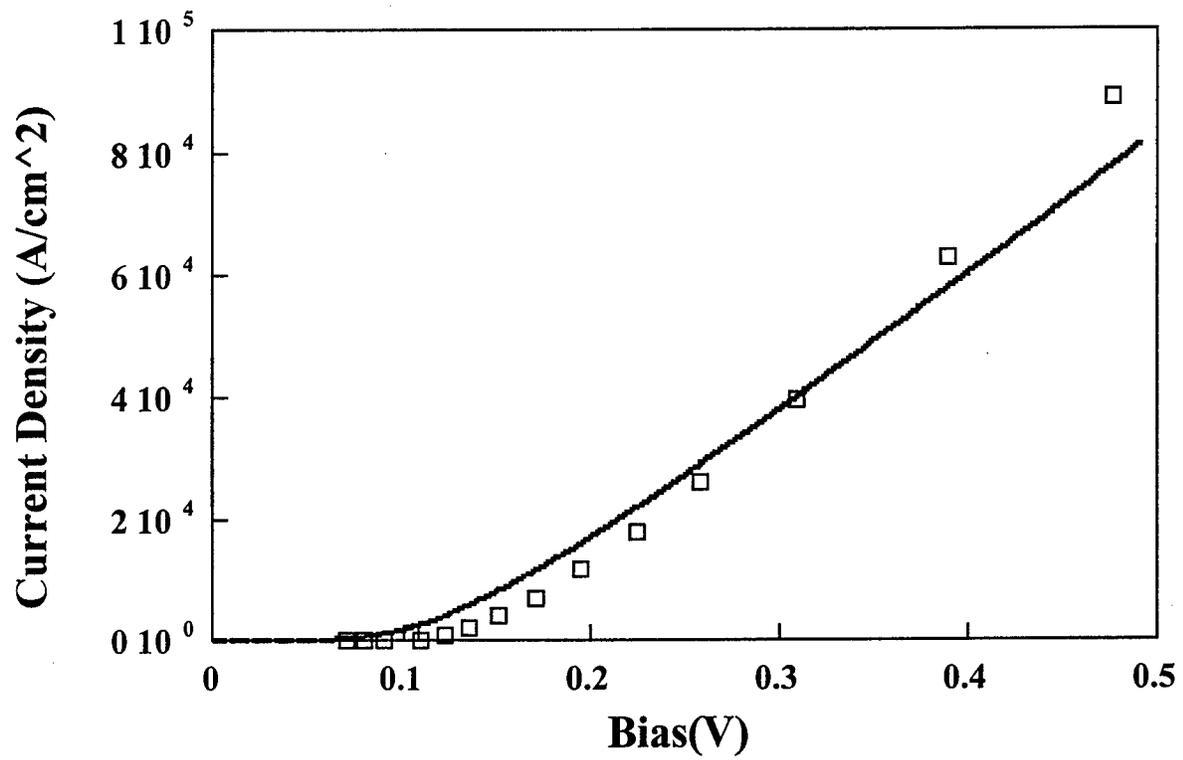
Fig.5. Current density vs bias for a structure with the pocket region. Experiment (solid line) and calculation (squares).
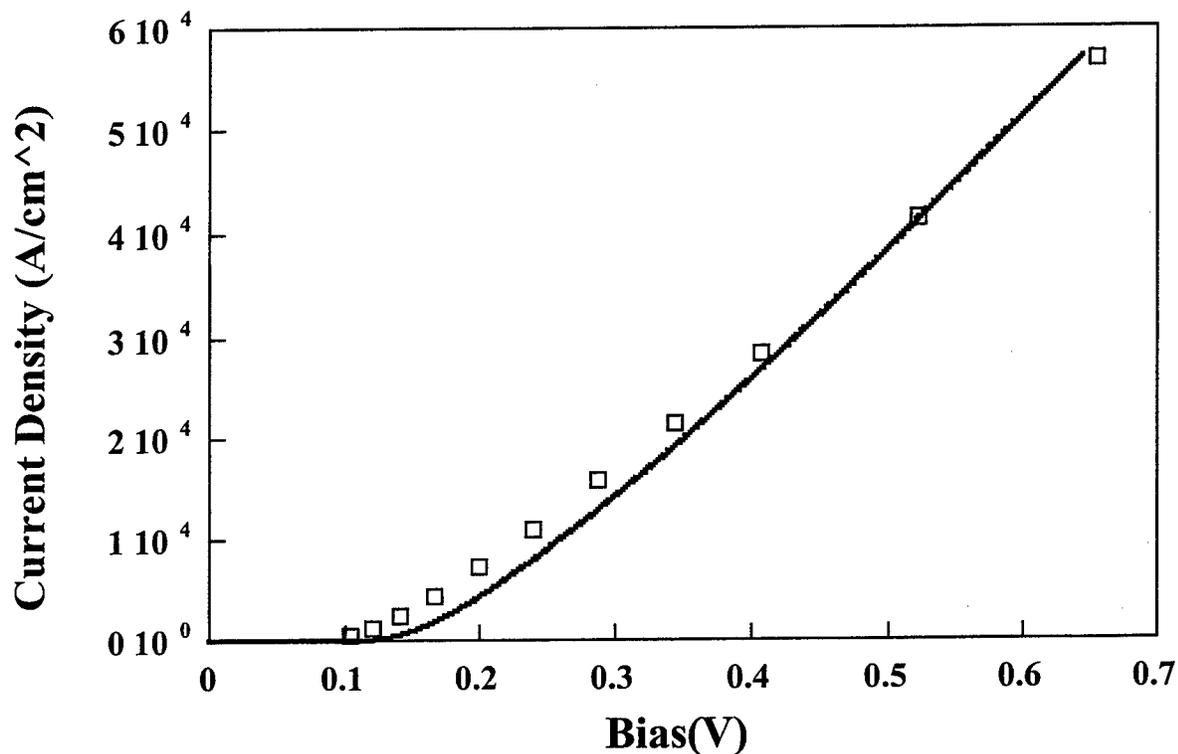
Fig.6. Current density vs bias for a structure without the pocket region. Experiment (solid line) and calculation (squares).

6. CONCLUSIONS

In conclusion, we have proposed a class of structures to achieve a coherent generation of THz radiation. This approach is based on the *stimulated emission of coherent plasmons*, which can be achieved *without a population inversion*, if a *dynamical inhomogeneity* is built into the active region of a structure. The THz radiation is emitted by the oscillating charges associated with the coherent plasmon generation. Our preliminary self-consistent calculations of the non-equilibrium steady state for the I-V characteristics of such structures are in good agreement with the experimental results.

REFERENCES

1. P. Hyldgaard, and J.W. Wilkins, Phys. Rev. **B55**, 6889 (1996).
2. P. Bakshi, J. Cen, and K. Kempa, J. Appl. Phys. **64**, 2243 (1988); J. Cen, K. Kempa, and P. Bakshi, Phys. Rev. B **38**, 10051 (1988); P. Bakshi, J. Cen and K. Kempa, Solid State Commun. **76**, 835 (1990); H. Xie, K. Kempa and P. Bakshi, J. Appl. Phys.**72**, 4767, (1992).
3. K. Kempa, P.Bakshi, and H. Xie, Phys. Rev. B **48**, 9158, (1993).
4. P. Bakshi and K. Kempa, *Superlattices and Microstructures*, **17**,363 (1995) .
5. K. Kempa, P. Bakshi, and E. Gornik, *Phys. Rev. B* **54**, 8231 (1996).

6. K. Kempa, P. Bakshi, C. Du, G. Feng, A. Scorupsky,G. Strasser, C. Rauch, K. Unterrainer, E. Gornik, J. Appl. Phys. **85**, 3708 (1999)

7. K. Kempa, P. Bakshi and M. Ciftan (to be published)

8. B. Mikhailovskii, *Theory of Plasma Instabilities*, Vol. 1,Consultant Bureau, New York, (1974); N. Krall and A. Trivelpiece, *Principles of Plasma Physics*, (McGraw-Hill, New York, 1973).

9. M. Vossebuerger, H.G. Roskos, F. Wolter, C. Waschke, H. Kurz, K. Hirakawa, I. Wilke, and K. Yamanaka, J. Opt. Soc. Am. **B13**, 1045 (1996); K.D.Maranowski, A.C.Gossard, K.Unterrainer, E.Gornik, Appl. Phys. Letters **69**,3522 (1996); R. Kersting, K. Unterrainer, G. Strasser, H.F. Kauffmann, E. Gornik, Phys. Rev. Lett., **79**,3038 (1997).

10. W. R. Frensley, Rev. Mod. Phys. **62**, 745 (1990).

11. K. Kempa, D.A. Broido, C. Beckwith, and J. Cen, Phys. Rev. B **40**, 8385 (1989); K. D. Tsuei, W.W. Plummer, A. Liebsch, E. Pehlke, K. Kempa and P. Bakshi, Surf. Sci. **247**, 302 (1991).

12. P. Bakshi and K. Kempa (to be published)

SESSION 4

Free Electron Laser
and Other Spectroscopies

Free electron laser studies of carrier lifetime and lifetime design in semiconductors and ionic crystals

C. R. Pidgeon[a], J-P. Wells[a,b], I. V. Bradley[a,b] and B. N. Murdin[c]

[a]Physics Department, Heriot Watt University, Edinburgh EH14 4AS, UK
[tel: 0131 451 3022; fax: 0131 451 3136; email: c.r.pidgeon@hw.ac.uk]
[b]FOM Institute 'Rijnhuizen', P.O. Box 1207, NL-3430 BE Nieuwegein, The Netherlands
[c]Physics Department, University of Surrey, Guildford GU2 5XH, UK

ABSTRACT

A brief review is given of pump-probe carrier lifetime studies with the free electron laser at FOM-Rijnhuizen (FELIX), emphasising work on mid-infrared interband recombination in narrow gap semiconductors. We compare results on the lead salt system with earlier work on HgCdTe and As-rich InAs/InAsSb strained layer superlattices, where we have studied the suppression of Auger recombination by band structure engineering. The Auger coefficient for either the lead salt structures or the As-rich strained layer superlattice is suppressed by some 2 orders of magnitude by comparison with HgCdTe of an equivalent bandgap composition. In addition we have made time resolved studies of local modes in ionic crystals, where non-radiative decay plays an important role in the optical pumping cycle of laser gain media. We have studied the local modes created upon the introduction of a light impurity, in particular the H- ion, in CaF_2 in the spectral region 700 to $1200 cm^{-1}$. We have employed a two pulse photon echo experiment to remove the inhomogeneous broadening of the vibrational ensemble and measure the transverse relaxation time (the vibrational dephasing).

Keywords: Free electron laser, Auger suppression, low dimensional semiconductors, localised modes, photon echo.

1. INTRODUCTION

As is well known, the ability to control the Auger recombination rate in narrow gap systems by band structure engineering[1-3] is of considerable interest for many device applications since in most cases this is the limiting effect on the device performance.[4-6] Low threshold non-linear devices controlled by cw lasers, and high sensitivity mid-infrared detectors and emitters need large excess carrier lifetimes; whereas applications such as laser mode locking, ultra-fast radiation detectors and optical switches require recovery times to be as short as possible. In particular, In(As,Sb) SLSs offer infrared detector and emitter applications beyond 10μm, since the type II band offset gives a superlattice structure with an effective bandgap substantially lower than either of the constituents. [3,7] At present T_o, the threshold current temperature coefficient of mid-IR laser diodes, is limited by intrinsic Auger scattering processes, preventing room temperature laser operation at wavelengths longer than about 3μm in any materials system.

We have earlier reported the utilisation of rf linac-pumped free electron lasers (FELs) to study Auger recombination, and particularly the deliberate suppression of this process, in arsenic-rich $InAs/InAs_{1-x}Sb_x$ strained layer superlattices (SLSs) at room temperature near 10μm. A direct comparison with measurements on epilayers of $InSb$[8,9] and bulk HgCdTe (see below, Fig. 3 and Ref. 22) of a similar bandgap shows that the Auger processes have been substantially suppressed (the Auger coefficient, C_1, is about two orders of magnitude smaller) in the As-rich alloy case as a result of both the quantum confinement and strain splittings in the SLS structure[8]. Our measurements have been made on As-rich In(As,Sb) SLSs, where both the shift of the band gap to longer wavelengths and the internal photoluminescence efficiencies have been found to be greater than for the Sb-rich SLSs, and efficient photo- and electroluminescence has been observed covering a wavelength range of 4-11μm.[3]

The lead salts are of interest both fundamentally, because of their novel band structure, and from a device point of view since they are widely used in mid-infrared (MIR) optoelectronic emitters and detectors. A particular feature of this system – i.e. their near "mirror" conduction and valence bands – has been cited as potentially leading to much

162

Part of the EUROPTO Conference on Terahertz Spectroscopy and Applications II
Munich, Germany • June 1999 SPIE Vol. 3828 • 0277-786X/99/$10.00

smaller Auger scattering rates than found in III-V material systems. However, theory predicts that there may nevertheless still remain a substantial contribution to this unwanted recombination process through intervalley scattering[10-13], although later theories[11-13] including more realistic band structure pictures suggest that this should not be as serious as originally predicted[10]. Understanding accurately how the recombination processes change with carrier density is important for emission devices which operate far from equilibrium, and in particular in the continuing quest for the development of compact MIR room temperature lasers. A recent design study suggesting the possibility of cw room temperature MIR operation of GaSb/PbSe/GaSb double heterostructure lasers[14] depends critically on the theoretical prediction of a low value of Auger coefficient, C^{13}. Although considerable research has been done on the recombination processes, with the exception of one report[15] almost all previous work has utilised techniques using relatively long pulse or cw radiation, and experimentally reported values for C vary over an order of magnitude[15-17].

We have recently made direct pump-probe measurements of radiative and non-radiative recombination in epilayers of PbSe under high excitation with an rf linac-pumped (ps) free electron laser (FELIX), in the temperature range 30 to 300K (see below and Ref. 24) For temperatures below 200K and carrier densities above the threshold for stimulated emission, stimulated recombination represents the most efficient recombination mechanism with kinetics in the 50-100ps regime, in good agreement with earlier reports[15,18,19]. Above this temperature Auger recombination dominates on a 0.1-2ns time scale. The sophistication of a 3-beam pump-probe experimental technique described below has enabled an analysis of the decay at times longer than 100ps, in terms of the non-parabolic anisotropic band structure of the lead salts, to give the Auger coefficient, C, quantitatively over a wide temperature range, 30-300K. The results are in good agreement with theory for non-parabolic, anisotropic bands[20,21] and non-degenerate statistics[11], and confirm that the original parabolic band calculations[10] underestimated the measured lifetime by more than an order of magnitude[11-13,15]. Finally the Auger results for the lead salts are compared with earlier measurements taken at FELIX[22] for $Hg_{1-x}Cd_xTe$ of a composition such that the bandgap for the two semiconductors is the same at T = 100K[22]. It is found that C for PbSe is between one and two orders of magnitude lower than for $Hg_{1-x}Cd_xTe$ over the whole temperature range for comparable values of bandgap. This results in domination of stimulated radiative recombination even at quite low carrier concentrations.

2. EXPERIMENT

The samples were (111)-oriented epitaxial layers of PbSe on insulating substrates (BaF_2). They were grown by molecular beam epitaxy (MBE) under ultra-high vacuum conditions[23]. The samples were ~ 2μm thick with an n-type carrier concentration of $3.2 \times 10^{17} cm^{-3}$ and mobility of $28,070 cm^2 V^{-1} s^{-1}$ at 77K. The wavelength-degenerate pump-probe experiments were performed with the Dutch free electron laser (FEL) in Utrecht (FELIX), which operated with pulse trains ('macropulses') typically of length 4μs and at a repetition rate of 5Hz. The macropulse consisted of a train of 'micropulses', each of width adjustable between 2ps and 10ps, with a pulse separation of 40ns. It was shown previously[8,22] that over the range of excited electron concentrations used throughout this study, the carrier temperatures approach the lattice temperature to within 2% in less than 3ps, resulting in a temperature increase in the sample of only ~0.02K per pulse. Hence, we have neglected heating effects and, for recombination processes which occur in less than about 20ns (see below), we have treated the interpretation in the same way as for a "single pulse" experiment.

The macropulse fluctuations of FELIX depend strongly on the required performance of the machine and can be of order 10%. In order to obtain a good signal noise ratio in the MIR regime, we have utilised a pump-probe setup which compensates for these macropulse fluctuations. The experimental arrangement is a 3 beam pump-probe setup shown in Fig. 1. From the original pump pulse both a probe beam and a reference beam are split off by ZnSe beamsplitters. The reference beam is delayed by 20 ns (6 m) and back-reflected on the beamsplitter with an −1 telescope onto the probe beam position.

The probe and reference beams follow the same optical path, transmit through the sample at the same position and are both detected by the same (77K) MCT detector. It is assured independently that both have the same signal size. The
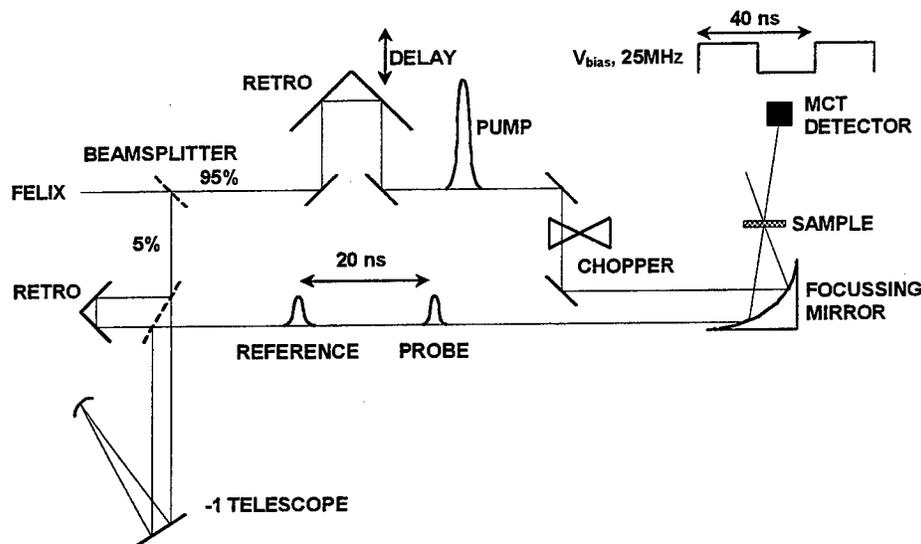
Fig. 1. Schematic diagram of the three-beam pump-probe experimental setup, utilising a modulation technique to determine the relative transmission of the probe beam as a function of delay time as described in the text (after Ref. 24)

detector bias is modulated with 25 MHz, synchronised with FELIX. This results in signals with opposite sign for the probe and the reference beams. When the system is in balance (no pump is applied), the integrating electronics show an apparant output signal of the detector which is zero. In the experiment the pump beam is chopped with 2.5 Hz frequency (every other pump pulse is blocked) and the signal fed into a boxcar integrator in the toggle mode. The result is a signal/noise ratio better than 0.1%, even when the fluctuations from macropulse to macropulse are several percent. The three beams were focussed on the sample using an f=25cm parabolic mirror, resulting in a spotsize of 100 microns. The sample was mounted in a flow cryostat (4-300K). The effective pump and probe energy fluences per micropulse were estimated to be 350 and $10\mu J/cm^2$ respectively, including losses due to beam splitters and optics. The relative transmittance of the probe was measured directly as a function of optical delay, t_{delay}, between pump and probe pulses.

Band filling as the pump radiation is absorbed causes a strong dynamic blue shift in the IR absorption edge (the dynamic Moss-Burstein shift or DMS) and leads to pronounced bleaching near the excitation frequency. Recovery times in the range 20-800ps were found, and shown to be strongly dependent on the sample temperature and the excited carrier density[24]. In agreement with previous workers[15] we have found that at room temperature and at the pump intensities (excited carrier densities) used here the recombination is dominated by Auger scattering. Below 200K stimulated recombination represents the most efficient recombination mechanism with kinetics in the 100ps regime. At times longer than 100ps, the Auger process takes over in the absence of stimulated recombination. For all temperatures the net recombination rate in the high excitation regime is a fundamental property of the material, and not defect related[13]. Analysis of the recovery of the probe absorption leads to a quantitative determination of the temperature dependence of the threshold concentration for stimulated emission and the Auger coefficient as described below.

3. ANALYSIS

In order to interpret the pump-probe data, where the experiment determines the probe transmission as a function of delay with respect to the pump beam, we need to convert the measured transmission into values of excited carrier

concentration, N_e (the procedure is described in detail in Refs. 8 and 24). The rate of decay of $N_e(t)$ with pump-probe delay can then be extracted directly and Auger recombination coefficients can be obtained by fitting $N_e(t)$ with a simple rate equation. The recovery time of the bleaching depends on the photon energy, $h\nu$, due to the carrier concentration dependent relaxation process. The value of N_e at complete bleaching corresponds to the carrier density required to separate the electron and hole quasi Fermi energies by an amount equal to the pump photon energy, and increases monotonically with $h\nu$. We assume that the carriers thermalise rapidly compared with the recombination rate, in which case the concentration becomes determined: every value of transmission corresponds to a unique electron and hole quasi-Fermi energy and thus a unique excited carrier concentration, since the electron and hole concentrations are equal. With the measured lifetimes substantially longer than the pulse duration (5ps), the generation rate is zero during the probe pulse delay time and the recombination rate, γ, which is some function of N_e (t), can be measured unambiguously.

We may similarly neglect the pulse duration (i.e. the probe pulse shape function $I(t)$ is effectively a delta function) when calculating the sample transmission:

$$T \approx (1-R)^2 \exp[-\alpha(t_{delay})d] . \tag{1}$$

We have assumed that the absorption coefficient, α, while time dependent, is approximately constant through the probed region of the sample (the initial concentration is spatially uniform for complete bleaching). R is the sample reflectivity and d the thickness. The dependence of the transmission on the reflectivity is complicated by the different values for the top PbSe layer, the bottom BaF_2 layer and the interface between the epilayer and the substrate. This problem is removed in our signal processing method where we take the ratio of the measured difference in the probe and reference transmission to the reference transmission. In this way the dependence of the reflectivity is removed leaving us with an expression relying solely on the change in the absorption coefficient, $\Delta\alpha$, resulting from the pump:

$$\frac{T_{probe} - T_{reference}}{T_{reference}} = \frac{(1-R)^2[\exp\{-(\alpha_o + \Delta\alpha)d\} - \exp(-\alpha_o d)]}{(1-R)^2[\exp(-\alpha_o d)]} = \exp[-(\Delta\alpha)d] - 1 .$$

The procedure is then to use a knowledge of the non-spherical, non-parabolic band structure (see below), which determines the (final and initial) electron and hole energies, E_e and E_h, for electron-hole pair creation at a given photon energy, and also the density of states functions, g_e and g_h. One then takes a range of values of electron Fermi energy, and computes the corresponding hole Fermi energies and electron and hole excited carrier concentrations from the relation:

$$N_e = \int_{E_c}^{\infty} f_e(E)g_e(E)dE = \int_{-\infty}^{E_v} f_h(E)g_h(E)dE , \tag{2}$$

where f_e and f_h are the Fermi occupation probability functions for the electron and hole respectively, and E_c and E_v are the band edge energies for the conduction and valence bands. At the same time, each assumed value of electron Fermi energy determines a unique value of α (and hence T) from the relation:

$$\alpha = \frac{\sigma}{h\nu}\{1 - f_e(E_e) - f_h(E_h)\}J_{cv}(E) , \tag{3}$$

where $J_{cv}(E)$ is the joint density of states, and the absorption cross-section, σ, is determined by fitting the theoretical transmission obtained with the equilibrium Fermi energy to the small signal absorption spectrum taken with a Fourier transform spectrometer. This is carried out in in terms of the appropriate energy band structure for the theoretical fit. We estimate the overall error in deriving the carrier concentration from the pump-probe measurement is about 30%, leading to an error in the Auger coefficient of about 60%.

As described in Refs. 8, 22 and 24, it is necessary to have a detailed knowledge of the band structure of the crystal. Then from equations (1) to (3) we can calculate the value of the excited carrier concentration, $N_e(t_{delay})$, corresponding to each value of transmission, $T(t_{delay})$. As described previously, we have also included the effect of small refractive index changes arising from a shift in the plasma frequency[22].

For the data at room temperature, and for the results at lower temperatures in the regime <u>below</u> the threshold value of N_e for stimulated emission, the data was analysed with a simple rate equation for radiative and non-radiative decay, including terms depending on the Shockley-Reed, radiative and Auger recombination coefficients, A, B and C respectively, for a <u>non-degenerate</u> N_e distribution:

$$\frac{dN(t)}{dt} = AN(t) + BN^2(t) + CN^3(t) \ . \tag{4}$$

This equation was solved and fitted to the decay curves[24]. It was found in all cases that Auger recombination dominated and the other terms were negligible, and in particular that the N_e^3 dependence expected for a non-degenerate carrier distribution gave a very good fit to the data. A similar result was obtained in the 300K case in Ref. 15. The value of C obtained by this fitting procedure is shown plotted over the full temperature range 30-300K in Fig. 2. Excellent agreement between theory and experiment is obtained with the Auger process for inter-valley scattering in the approximation of non-degenerate statistics, but it is clearly essential to include a realistic non-parabolic band structure[11]. The difference between the parabolic and non-parabolic approximations is most clearly seen in the low temperature regime where the Auger coefficient drops markedly between 77K and 30K. Finally the Auger results for the lead salts are compared with earlier measurements taken at FELIX for $Hg_{0.795}Cd_{0.205}Te$ (experiment and theory[22,25]) and $Hg_{0.744}Cd_{0.256}Te$ (theory[25]). Since there is such extremely good agreement to the theory for non-parabolic bands with the isotropic Kane model, the latter curve (with the same bandgap as PbSe at 100K - i.e. $\lambda_G \sim 7\mu m$) is taken for comparison between the two materials. It is found that C for PbSe is between one and two orders of magnitude lower than for $Hg_{1-x}Cd_xTe$ at comparable values of bandgap. Stimulated emission was not observed in the earlier $Hg_{0.795}Cd_{0.205}Te$ measurements even at the lowest temperatures used, but it is possible that it might be achieved in material of precisely the same bandgap as PbTe (i.e. x = 0.256) and with the higher FELIX intensities available with the current optical set-up. We estimate the threshold carrier concentration for this material would be about $8\times10^{17}cm^{-3}$, which is some four times greater than achieved in the earlier experiments[22]).

One other clear difference between the two systems is in the dependence of C on temperature. Both PbSe and $Hg_{1-x}Cd_xTe$ (of this composition) are anomalous in that the bandgap <u>decreases</u> with lowering temperature. However, in the case of $Hg_{1-x}Cd_xTe$, because of the low ratio of electron to heavy hole effective mass arising from the Kane band structure, which decreases further with decreasing bandgap, the threshold for Auger recombination drops with reducing temperature. This bandgap dependence dominates over the change of the occupation function with temperature. By contrast, the ratio of electron to hole effective mass for PbSe is approximately unity over the whole range of values of E_G. In this case reducing the temperature below threshold quenches the Auger recombination.

166
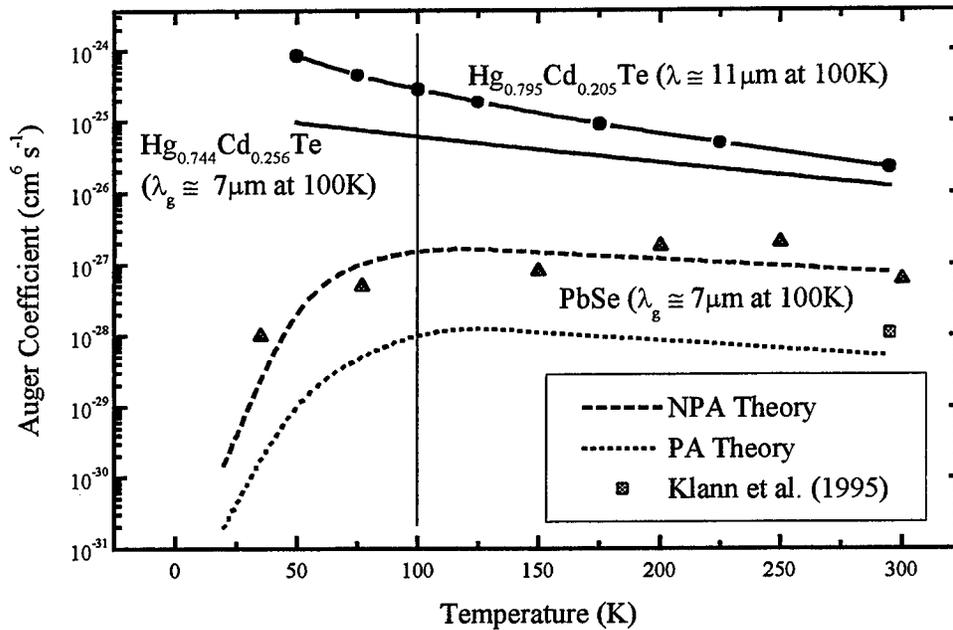
Fig. 2. PbSe: Auger coefficient C vs temperature for n-type Pbse - solid triangles, after Ref. 24; solid square Ref. 15. The dashed line is the theoretical curve for a nondegenerate distribution and nonparabolic bands (NPA) after Ref. 12; the dotted line is from the same paper in the parabolic band (PA) approximation. $Hg_{1-x}Cd_xTe$: Auger coefficient C vs temperature for $Hg_{0.795}Cd_{0.256}Te$ - circles. The solid lines are the theooretical curves for two compositions for the Kane model of nonparabolic, spherical bands, after Ref. 24. The energy gap for PbSe and $Hg_{0.744}Cd_{0.256}Te$ is the same ($\sim 7\mu m$) at T = 100K.

In summary, we have utilised a ps free electron laser to measure directly the Auger recombination rates as a function of photo-excited carrier concentration in PbSe over a wide temperature range (30-300K). The rate is approximately constant between 77K and 300K with a value $C = 2 \times 10^{-28} cm^6 s^{-1}$, and then drops to a value $C = 1 \times 10^{-28} cm^6 s^{-1}$ at 30K. Good agreement is obtained with theoretical calculations for non-parabolic, non-spherical energy bands in the non-degenerate limit for the excited carrier concentration[11]. Good agreement is also obtained with the room temperature value for C reported previously, and we confirm the earlier result that for temperatures below 200K and carrier densities above the threshold for stimulated emission, stimulated recombination represents the most efficient recombination mechanism[15]. We have determined the threshold carrier concentration for stimulated emission over the same temperature range, 30-300K, and this occurs at carrier concentrations somewhat lower than would be the case for bulk materials with the Kane band structure. This is in accord with the finding that C for PbSe is between one and two orders of magnitude lower than for InSb or $Hg_xCd_{1-x}Te$ of comparable values of bandgap. The small Auger coefficients in the lead salts are mitigated to some extent by the relatively heavy anisotropic effective masses and valley degeneracy, which would tend, by contrast, to higher threshold carrier concentrations than for HgCdTe or III-V materials of comparable bandgap (assuming comparable internal losses).

We confirm the conjecture made recently that Auger recombination in IV-VI semiconductors in the wavelength range of 3-5μm will not prevent quantum structures of these materials achieving room temperature laser operation[14]. Rather, it is the problems of insufficient electron and hole confinement and low thermal conductivity from

traditionally used materials, PbEuSeTe, PbSrSe of PbSrS, that have to be overcome by the utilisation of novel structures such as GaSb/PbSe/GaSb[14].

4. DYNAMICS OF HYDROGENIC LOCALISED VIBRATIONAL MODES

The presence of H⁻ ions in an otherwise perfect crystal destroys the translational symmetry of the lattice and at the same time modifies its normal modes of vibration. As a consequence of the fact that force constants between the substitutional (or for that matter, interstitial) H⁻ ion and its neighbours are similar to those between neighbouring hosts lattice ions and that the hydrogen impurities are very light; the modified vibrational modes fall outside the maximum band mode frequency for the perfect lattice and cannot be transmitted throughout the crystal. Thus, they are highly spatially localised around the defect and are known as *localised vibrational modes* [26].

The development of near infrared solid state lasers, based around for example $3d^2$ configuration ions such as Cr^{4+} and V^{3+}, is hampered by heavy quenching of the optical excitation by non-radiative relaxation at room temperatures. Recent studies have shown the importance of local mode vibrations of the optically active center in mediating the non-radiative multiphonon relaxation process [27]. We report on pump-probe and photon echo experiments on the localised vibrational modes of ionic hydrogen in CaF_2 and $LiYF_4$ crystals using FELIX output in the ten micron region. These systems are attractive for their simplicity, the only possible non-radiative path being into the lattice band modes.

Few previous studies have investigated the relaxation of ionic hydrogen and only Davison and coworkers have used pulse lengths shorter than the relaxation time of the local mode itself [28]. These workers used the Stanford FEL to study the energy relaxation time (T_1) of the substitutional hydrogen local mode in CaF_2 with a standard two pulse, pump-probe technique. A value of 45 picoseconds was derived from the pump-probe data and compared with the 6 ps value for an interstitial mode. By contrast, we have employed a three pulse pump-probe technique (as described above) to perform saturation measurements on H⁻ local modes in $LiYF_4$ using FELIX. Unlike CaF_2:H⁻, the linear absorption spectroscopy of $LiYF_4$:H⁻ is not well studied; indeed there is currently no information published in the literature. We have performed our own FTIR transmission experiments which reveal two local modes at frequencies of 1122.5 and 1173.2 cm⁻¹. These transitions give 50-70% absorption depths most suitable for excitation by the FEL pulse and a 10 Kelvin energy relaxation time for the 1122.5 cm⁻¹ mode has been measured to be T_1=2.7 ps. This is significantly shorter than the time measured for the substitutional mode in CaF_2 where the hydrogen is tetrahedrally bonded. A possible explanation is that the symmetry of the H⁻ local vibration is lower in $LiYF_4$ allowing it to be more strongly coupled to the lattice band modes. This appears consistent with the observed linewidth of the local mode resonance which appears homogeneously broadened even at the lowest available temperature of 4.2 Kelvin.

The substitutional H⁻ local mode in CaF_2 gives rise to a single resonance at a frequency of v=965 cm⁻¹ at low temperatures, associated with the transition to the triply degenerate n=1 state of the anharmonic oscillator. Whilst this feature appears as a sharp (0.3 cm⁻¹) transition at low temperatures, this linewidth is dominated by inhomogeneous broadening effects due to crystalline imperfections and other strains created during the growth of the crystal itself. We have employed a two pulse photon echo experiment to remove the inhomogeneous broadening of the vibrational ensemble and measure the transverse relaxation time (the vibrational dephasing). In this regime the exciting infrared radiation is tuned to the 965 cm⁻¹ resonance and the pump and a single probe beam crossed in the sample. The pulse excites a coherent superposition of anharmonic oscillator states within the vibrational ensemble which then begin to dephase due to the effects of crystal inhomogeneity. The second pulse, which is delayed in time from the pump pulse, initiates rephasing through inversion of the dephased dipole moments of the individual anharmonic oscillators. This results in a coherent burst of radiation (a super-radiant pulse) delayed in time from the second pulse by the exact amount of time the second pulse is delayed from the first. The echo emerges from the sample in a unique direction given by the wavevector matching conditions $|2k_2-k_1|$. The intensity of the echo is then measured as a function of the optical delay of the probe pulse (as shown in Figure 3). This signal displays both modulations (or beats) and non-exponentiality; evidence of vibrational up-pumping which can occur when the laser bandwidth exceeds (as it does in this case) the vibrational anharmonicity.
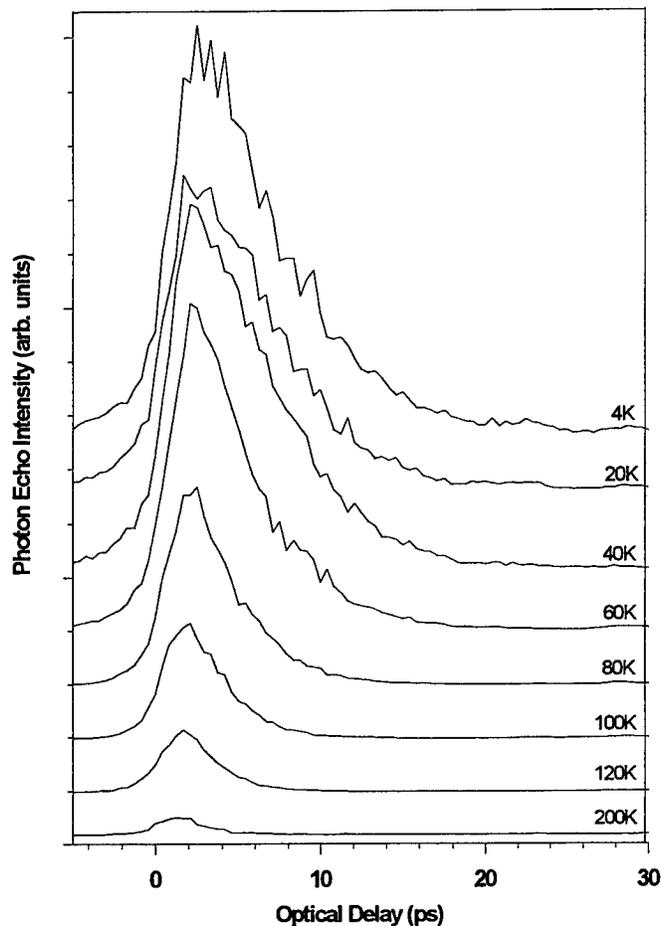
Fig. 3. Temperature dependence of the vibrational photon echo decay as a function of optical delay for the localised vibrational mode in $CaF_2:H^-$.

The echo technique measures the homogenous dephasing which has contributions from both the pure dephasing and the vibrational lifetime. Thus, the combination of both techniques allows one to separate out and study the pure dephasing component (T_2^*). The echo intensity measured for the $CaF_2:H^-$ local mode is extremely large, an effect which may be attributed to the substantial H^- ion dipole polarisability [4] of 30.2 $Å^3$. This makes the H^- local mode an extremely valuable probe of incoherent and coherent effects associated with vibrational relaxation in ionic crystals. It may also be possible to use the vibrational dephasing of H^- local modes as a probe of the transition to the glassy state in mixed fluorite crystals and further work continues in this area.

ACKNOWLEDGMENT

REFERENCES
1. E. R. Youngdale, J. R. Meyer, C. A. Hoffman, F. J. Bartoli, C. H. Grein, P. M. Young, H. Ehrenreich, R. H. Miles and D. H. Chow, Appl. Phys. Lett. **64**, 3160 (1994).

2. S. R. Kurtz and R. M. Biefeld, Appl. Phys. Lett. **66**, 364 (1995); S. R. Kurtz, R. M. Biefeld and L. R. Dawson, Phys. Rev. **B51**, 7310 (1995).

3 P. J. P. Tang, M. J. Pullin, S. J. Chung, C. C. Phillips, R. A. Stradling, A. G. Norman, Y. B. Li and L. Hart, Semicond. Sci. Technol. **10**, 1117 (1995).

4 A M. White, Infrared Phys., **25**, 729 1985).

5 T. Ashley, A. B. Dean, C. T. Elliot, A. D. Johnson, G. J. Pryce, A. M. White and C. R. Whitehouse, Semic. Sci. Technol. **8**, 386 (1993); and, Appl. Phys. Lett. **64**, 2433 (1994).

6 K. L. Vodopyanov, H. Grainer, C. C. Phillips and T. J. Tate, Phys. Rev. **B46**, 13194 (1992).

7 S. R. Kurtz and R. M. Biefeld, Phys. Rev. **B44**, 1143 (1991).

8 C.M.Ciesla,B. N. Murdin, C. R. Pidgeon, C. C. Phillips, R. A. Stradling, M. Livingston, I. Galbraith, D. A. Jaroszynski, C. J. G. M. Langerak, P. J. Tang and M. J. Pullin, J. Appl. Phys. **80**, 2994 (1996).

9. V. Chazapis, H. A. Blom, K. L. vodopyanov, a. g. Norman and C. C. Phillips, Phys. Rev. **B52**, 2516 (1995).

10. P. R. Emtage, J. Appl. Phys. **47**, 2565 (1976)

11. O. Ziep, O. Mocker, D. Genzow and K. H. Hermann, Phys. Stat. Solidi **90b**, 197 (1978).

12. M. Mocker and O. Ziep, Phys. Stat. Solidi **115b**, 415 (1983).

13. R. Rosman and A. Katzir, IEEE J. Quant. Electron. **QE-18**, 814 (1982)

14. Z. Shi, Appl. Phys. Lett. **72**, 1272 (1998).

15. R. Klann, T. Hofer, R. Buhleir, T. Elsaesser and J. W. Tomm, J. Appl. Phys. **77**, 277 (1995); J. W. Tomm, M. Mocker, T. Kelz, T. Elsaesser, R. Klann, B. V. Novikov, V. G. Talalaev, V. E. Tudorovskii and H. Bottner, J. Appl. Phys. **78**, 7247 (1995).

16. K. Lischka and W. Huber, J. Appl. Phys. **48**, 2632 (1977).

17. T. X. Hoai and K. H. Herrmann, Phys. Stat. Solidi **83b**, 465 (1977).

18. R. Klann, R. Buhleier, T. Elseasser and A. Lambrecht, Appl. Phys. Lett. **59**, 885 (1991).

19. R. Klann, T. Hofer, R. Buhleier, T. Elsaesser and A. Lambrecht, Appl. Phys. Lett. **61**, 2866 (1992).

20. D. L. Partin, IEEE J. Quant. Electron. QE24, 1716 (1988)

21. M. Tacke, Infrared Phys. Technol., 36, 447 (1995).

22. C. M. Ciesla, B. N. Murdin, T. J. Phillips, A. M. White, A. R. Beattie, C. J. G. M. Langerak, C. T. Elliott, C. R. Pidgeon and S. Sivananthan, Appl. Phys. Lett. **71**, 491 (1997).

23. G. Springholz and G. Bauer, Appl. Phys. Lett. **60**, 1600 (1992).

24. P. C. Findlay, C. R. Pidgeon, R. Kotitschke, a. Hollingworth, B. N. Murdin, C. J. G. M. Langerak, A. F. g. van der Meer, C. M. Ciesla, J. Oswald, a. Homer, G. Springholz and G. Bauer, Phys. Rev. **B58**, 12908 (1998).

25. A. R. Beattie and A. M. White, J. Appl. Phys. **79**, 802 (1996).

26. R.C. Newman, 'Infra-red Studies of Crystal Defects' Taylor and Francis, London , (1973).

27. D.M. Calistru, S.G. Demos and R.R. Alfano, Phys. Rev. Lett. **78**(2) (1997), 374.

28. C.P. Davison, J.A. Campbell, J.R. Engholm, H.A. Schwettman and U. Happek, J. Lumin. **76&77** (1998) 628.

29. S. Malli and G. Fraga, 'Many Electron Systems: Properties and Interactions' Saunders, Philadelphia, (1968).

Free-electron laser studies of intra-acceptor transitions in GaAs :a potential far-infrared emission system

M.P.Halsall, P.Harrison[a], H.Pellemans[b], C.R.Pidgeon[c]

Department of Physics, UMIST, Manchester, M60 1QD, UK
[a]The Institute of Microwaves and Photonics,University of Leeds,
Leeds, LS2 9JT U.K.)
[b]FOM-instituut voor Plasmafysica, 3430 BE Niewegeibn,The Netherlands
[c]Department of Physics, Heriot-Watt University, E14 4AS, U.K.

ABSTRACT

Normal dopant species in III-V semiconductors form shallow donors or acceptors whose atomic-like transitions (e.g. the 1s-2p transition) have energies of the order of 3-20meV which corresponds to the Terahertz region of the spectrum. It has been suggested that these levels could be utilised in an impurity based THz laser system Developing a solid-state THz source from such a technology will require engineering of the energy levels to favour radiative recombination. In this paper we report initial experiments to measure the 1s-2p scattering rate for holes bound to Beryllium acceptors in a bulk GaAs epilayer using the European free electron laser facility FELIX. Two absorption lines were studied the so-called D and C lines at 167cm^{-1} and 184cm^{-1} corresponding to 1s-2P transitions of the Beryllium acceptors. At high pump powers these lines were saturated and it was possible to perform Pump-probe measurements to observe the recovery of the absorption as a function of time. The temperature dependence of the decays was also measured. The D and C transitions were found to decay with lifetimes of 360ps and 440ps respectively. This represents the first direct measurement of these transition lifetimes which are much longer than those reported for intersubband scattering (typically 10-100ps). The results are highly encouraging and support the concept of an impurity based Terahertz device for room temperature operation.

Keywords:Free-electron laser, Terahertz spectroscopy, Intra-acceptor transitions, GaAs

1.INTRODUCTION

Semiconductor quantum dots are currently attracting a great deal of attention for both the physical phenomena they exhibit and their potential for a range of opto-electronic applications, such as temperature stable thresholdless lasers and normal incidence intersublevel detectors. In effect quantum dots are `artificial atoms' which confine the charge carriers in all dimensions and whose properties can be manipulated by changing their size and shape. The fabrication of semiconductor dots is still relatively immature and although techniques using `self-assembly' in highly lattice mismatched heterosystems offer the potential for improving structural quality, there is still some way to go before the quality inferred from standard characterisation procedures can match that of quantum wells. In particular, broad photoluminescence emission lines are indicative of a wide variance in dot size and the large Stoke's shift between emission and absorption suggests at localised exciton states at defects. The desirable properties of quantum dots relate to the fact that the carriers are confined along all spatial directions. Such confinement removes band dispersion as occurs in bulk and in-plane dispersion as occurs in quantum well systems. Thus in principle the emission lines from systems of dots should be very narrow, as in atomic systems, such as hydrogen and sodium vapour lamps. There is another semiconductor alternative to the artificial atom. Namely quantum confined impurities in semiconductor heterostructures. These have all the properties of quantum dots, i.e., confinement in all spatial directions but with the additional benefit of fabrication with contemporary molecular beam epitaxial (MBE) techniques. The energy levels of impurities can be tuned structurally be placing
"delta"-layers within quantum well systems, see for example Fig. 1a. Aiming such technology towards a light emitting device would require engineering of the energy levels to favour radiative emission. It is interesting to introduce the analogy of a free hydrogen atom at this point. Like the hydrogen atom, the energy levels of the impurity can be described by a principle quantum number n and a quantised orbital angular momentum l with radiative transitions between levels allowed for $\Delta l = \pm 1$. Thus a hole or electron in the 2p level can collapse to the 1s ground state by emitting a photon. Thus for a hydrogenic impurity in a crystal lattice if the 2p excited state could be populated then the carrier could scatter to the ground state and emit a photon and such a transition might be utilised in a solid state laser. However, unlike the hydrogen atom for an impurity state an extra loss mechanism would be that charge carriers in the 2p state could scatter non-radiatively with the lattice population of acoustic phonons, into the lower energy 2s state. Electrons in the 2s level have, obviously, a very

Part of the EUROPTO Conference on Terahertz Spectroscopy and Applications II
Munich, Germany • June 1999 SPIE Vol. 3828 • 0277-786X/99/$10.00

171

long radiative lifetime with respect to transitions to the 1s ground state. Hence they are very susceptible to scattering by other carriers or phonons, which could lead to the beneficial repopulation of the higher angular momentum states or to detrimental ionisation. The latter reducing the system's quantum efficiency. The aim of the described research is to take the first steps in assessing such an impurity transition for applications in light emitters, the long term aim being be to electrically pump the impurity energy levels with a semiconductor quantum well heterostructure.

The typical energy level spacing within impurities, i.e., tens or several tens of meV, is within the mid- to far-infrared (FIR) region of the spectrum. Currently there is much interest in bridging this 'Terahertz gap' of frequencies which lie between traditional electronic and optical technologies[1]. The fastest electronic devices, HEMTs and double barrier resonant tunnelling diodes can oscillate in circuits at frequencies up to several hundred GHz. Meanwhile optical devices, generating photons via electronic transitions can operate down to around 15 THz. In between lies the terahertz (1-10 THz) or far-infrared (300-30μm) region of the spectrum which is believed to have many applications, the most important including short-range wireless communications, such as wireless LANs, and active imaging. The use of far-infrared or terahertz frequencies for active imaging has been demonstrated for security purposes, both baggage and personnel scanning, but perhaps most exciting is the possibility for medical imaging[2]. TeraHertz waves are a viable alternative to X-rays and devices have the potential for low power consumption and compactness.

As mentioned above any device utilising internal impurity transitions could be fabricated using established MBE technology. The most well developed Quantum Well (QW) technology is that based on the GaAs/AlGaAs system. In principle either donors or acceptors could be used to form the energy levels of a device. However in practice the greater binding energy of acceptors makes them attractive candidates as they can have their transition energies moved over a wider range by varying the quantum confined environment of the impurity. In addition the transition energy could exceed the LO phonon energy, thus significantly reducing this non-radiative loss mechanism. In the GaAs/Al$_x$Ga$_{1-x}$As system, Beryllium is a commonly used acceptor; Beryllium is relatively stable with respect to diffusion and in bulk has a binding energy of 26 meV. Previous studies[3,4] of Be doped GaAs/AlGaAs QWs have observed the theoretically predicted increase in the acceptor binding energy with increased confinement; up to a binding energy of 50meV. Thus confined Beryllium acceptor states neatly span the 20-60μm wavelength. Another important aspect of such a technology is that impurity states (unlike intersubband emission) do not have any inconvenient selection rules concerning the orientation of the electric field vector of the interacting radiation. Thus an impurity based device could be used as the basis of a large area surface emitting structure. If Beryllium is to be used in such devices an understanding of the recombination kinetics of the acceptor excited states is essential to that end we present here the first reported spectroscopic study of the 1s-2p scattering rate for Be atoms in bulk GaAs using the European Free Electron Laser Infrared eXperiment (FELIX) in Rijnhausen, the Netherlands.

2. THEORY

The energy levels of an acceptor in GaAs are illustrated in figure 1. The states of a shallow acceptor in Sphalerite semiconductor can be thought of as spin 3/2 atom with levels split by the cubic crystal field. Thus there are several none-degenerate 2p states which could be utilised in a device.

$$1\,S_{3/2}\,\Gamma_8$$
$$2\,P_{3/2}\,\Gamma_8$$
$$2\,S_{3/2}\,\Gamma_8$$
$$2\,P_{5/2}\,\Gamma_8$$
$$2\,P_{5/2}\,\Gamma_7$$

Valence band
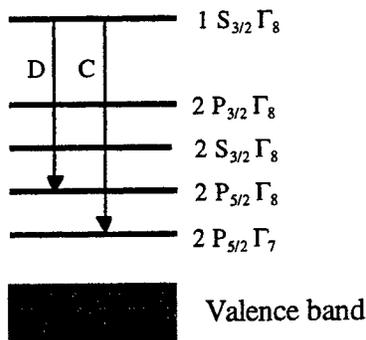
Figure 1. Acceptor energy levels in GaAs, the transitions giving rise to the D and C lines studied here are as marked in the figure.

3. SAMPLE PREPARATION

For these preliminary experiments a 1μm thick GaAs epilayer doped uniformly with Be to concentration of 10^{16} Be/cm^3 was used, corresponding to 10^{12} Be/cm^2. The sample was grown by the conventional MBE technique and was selected as showing excellent optical and structural properties. To confirm the presence of the acceptors conventional linear far-infrared spectroscopy was conducted. To obtain linear spectra the sample was polished into a wedge shape to prevent Fabry-Perot fringing and mounted over a 2mm aperture inside a continuous flow He cryostat, three pieces of sample were stacked to improve the absorption signal. The spectra were taken by a Bruker FTIR spectrometer with the sample at 4.2K and illuminated by a Hg lamp source. Figure 2 shows the linear absorption from this sample in the region 100-200cm^{-1} (12-24 meV). The spectrum in figure 2 has been normalised by dividing the spectrum with a reference spectrum taken at elevated temperature after the acceptors have thermalised and no absorption is expected. Thus the vertical axis corresponds to absorption change relative to the reference spectrum. The two prominent absorption lines are the so called D and C lines of the Be acceptors corresponding to the $1S_{3/2}\Gamma_8$ - $2P_{5/2}\Gamma_8$ and $1S_{3/2}\Gamma_8$ - $2P_{5/2}\Gamma_7$ transitions respectively as described in the theory section. The two observed lines are centred on 167cm^{-1} and 183 cm^{-1} and the observed energy positions correspond well to those reported by Lewis et al[5] for a similar Be doped GaAs epilayer.
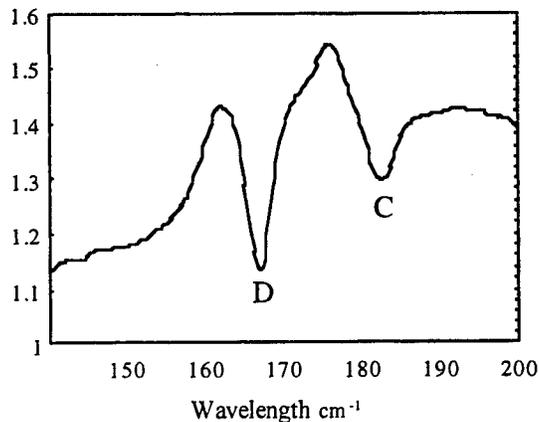
Figure 2. Linear absorption spectrum of Be doped GaAs epilayer taken at 4.2K

These lines were found to thermalise completely by 70K in agreement with those observed by previous workers. Once the sample had been shown to exhibit the expected behaviour pump-probe experiments could be attempted.

4. EXPERIMENTAL

In order to study the time dependence of the intra-acceptor transitions in GaAs it is necessary to have an intense source of far-infrared light which will cover the wavelength region 20-60μm continuously. For many years one of the main limitations of Terahertz spectroscopy has been the lack of such sources of THz radiation. Molecular lasers exist that operate in the far infra-red but are limited to specific wavelengths, whereas picosecond lasers fitted with parametric oscillators currently only work down to the region of approximately 15μm (20 THz). This leaves a whole stretch of the electromagnetic spectrum in which currently neither solid state nor gas laser lasers can cover continuously. This (500Ghz-20THz) region corresponds to the terahertz gap which many researchers are trying to bridge in the way described in the introduction. It is in this region that the free electron laser (FEL) comes into its own as the only intense tuneable source of such radiation. The FELIX facility in Rijnhausen, The Netherlands has recently been shown[6] as an effective means of performing far-infrared time domain spectroscopy on solid state systems for potential THz devices - such as intersubband scattering in GaAs/AlGaAs quantum wells. In order to measure the 2p-1s scattering time for Be acceptors in GaAs the sample, mounted as described in section 3, was taken to the FELIX facility.

The FELIX facility (in the 60μm region of the spectrum) produces 30ps long micro-pulses 40ns apart, each micropulse energy is approximately 0.1μJ giving a peak power of the order of 30kW. The micropulses are contained in a 10μs long macropulse with a repetition rate of 10Hz. To measure the 1s-2p scattering time the technique of pump-probe was employed. In contrast to systems involving continuous distributions of carriers such as intersubband absorption in quantum wells, the system studied here is a two level in acceptors which are isolated from each other. In a simple two level system

the pump-probe technique essentially measures the inter-level scattering time directly, i.e. the absorption change observed at a time t after excitation by the pump beam is proportional to the fraction of holes still remaining in the upper state at this time. However, the absorption changes for a realistic areal doping density are expected to be relatively small (perhaps a few percent). The major problem in detecting pump-probe signals using FELIX when the absorption change is small is the large pulse power variation of the free electron laser. Therefore, the pump-probe experiments were performed in the balanced pump-probe set up as originally implemented at FELIX by van der Meer et al and extended to longer wavelength by Chamberlain et al[7]. The experimental set up is illustrated in figure 3.
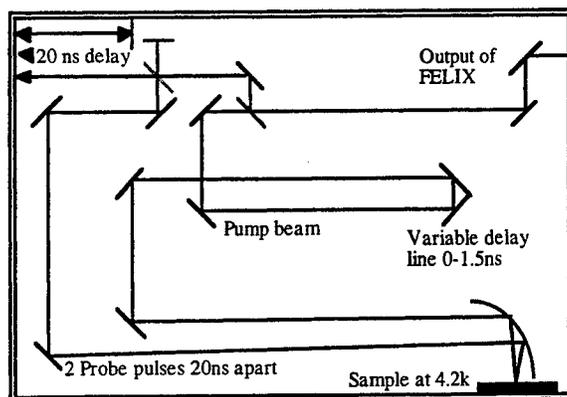
Figure 3. Experimental set up for balance pump-probe experiment.

The sample was mounted inside a continuous flow cryostat with polythene windows and cooled to 4.2K. As already mentioned the major source of noise in pump probe experiements with FELIX is the large pulse power variation. In the balanced pump-probe experiment this problem is overcome by the use of two probe pulses in the following way. A reference pulse is created and split again, one reference pulse is delayed by (a constant) 20ns. A Liquid He cooled photoconductive Ge:Ga detector is biased using a 25Mhz signal synchronised to FELIX. The phase of this signal is adjusted so that the maximum and minimum bias coincides with the probe and reference pulse respectively and thus the two signals are subtracted within the detector to zero. The original pump pulse is now scanned by a variable delay line to precede the probe pulse. The pump-probe signal is then measured as a function of pump-probe time to a resolution of 30ps as limited by the bandwidth of FELIX when operating at 60μm. The two probe beams and the pump beam were focused to approximately 5mm diameter spots which were brought to coincidence at the front of the sample. A difference in angle of incidence for the pump and probe beams assisted in the rejection of the pump beam signal at the detector. The pump probe signal was then measured as the delay line scanned the reference beam through a 1ns delay line.

5. RESULTS
Preliminary scans of the 160-200cm^{-1} (60-50μm) using FELIX clearly showed the absorption lines to be studied (figure 4). The line at 165 cm^{-1} is due to acoustic phonon absorption.
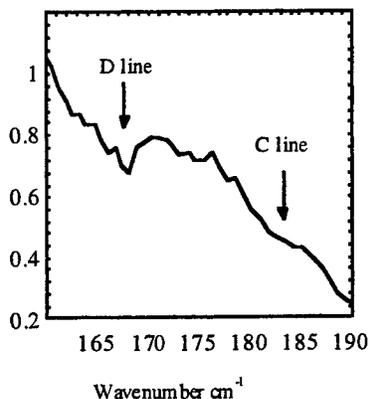
Figure 4. Sample transmission as measured by FELIX

The spectrum in figure 4 was taken at full laser power and some bleaching of the D line was observed (approximately 30%). Balanced pump probe was then performed on this signal using a probe pulse of approximately 10% of the pump beam. The pump-probe signals for the D and C lines as a function of delay are shown in figure 5a and 5b.
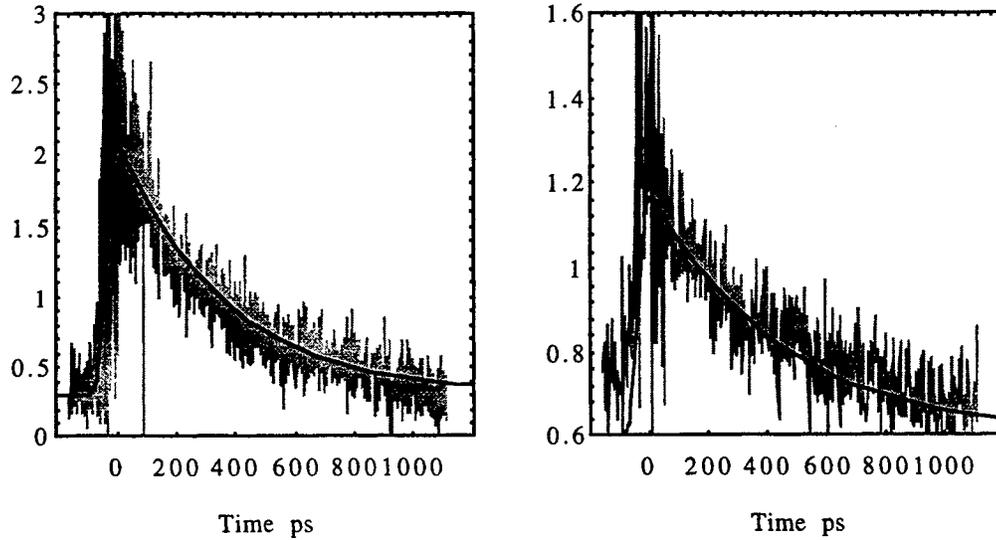
Figure 5a (left) and 5b (right). The pump probe signal for the C (fig. 5a) and D (fig. 5b) line 1s-2p intra-acceptor transitions in GaAs:Be. The solid curve is calculated by a rate model according to the lifetimes for the C line of 360ps and for the D-line 440ps as described in the text.

The two-level rate equation for a homogeneously broadened system is[7]

$$\frac{dN_{2P}}{dt} = \frac{\sigma}{\hbar\omega} I(t)(N_{1S} - N_{2P}) - \frac{N_{2P}}{\tau} \quad (1)$$

Where N_{1S} and N_{2P} are the number of acceptors with holes in the 1S and 2P states respectively, σ is the absorption cross section, τ is the lifetime of the transition and I(t) is the intensity of the laser pulse with time which is taken to be a gaussian with width 30ps (the pulse length of FELIX when operated at 60µm). the absorption change observed is calculated as

$$A = \int_{-\infty}^{+\infty} \frac{\sigma}{\hbar\omega} I(t - t_d)(N_{1S} - N_{2P}) dt \quad (2)$$

To solve this we have considered N_{1S} and N_{2P} to be the fraction of acceptors in the respective states we can put $N_{1S} + N_{2P} = 1$ and adjusted the cross section term to achieve the degree of bleaching of the transition observed in the transmission scan figure 4. Equation 1 was then solved numerically to obtain τ. Using this process the solid lines in figure 5 were generated as fits with τ=360±10ps for the D-line and τ=440±20ps for the C-line. The temperature dependence of the D-line transition rate was also studied and found to be constant within experimental error up to a temperature of 40K at which point some thermalisation of the acceptors was evident.

6. DISCUSSION AND CONCLUSIONS

The results presented in the previous chapter are, as far as the authors are aware, the first measurement of the intra-acceptor transitions for a shallow acceptor in a conventional semiconductor. Therefore, whilst the observed lifetimes are in line with expectations, we simply observe that these transition rates are an order of magnitude longer than those observed for typical intersubband transitions (typically 10-100ps[6]). As was discussed in the introduction, intersubband transitions for optical emission suffer from strong competing non-radiative transition routes. In contrast the system studied here is essentially a two level system in which continuous loss of energy via successive single acoustic phonon interaction cannot occur. Moreover, the stability of the transition with temperature is also in line with our predictions and encouraging for optical

applications. Obviously it will also be important to generate and observe photon emission from the studied transitions in order to assess whether the observed decays are radiative. A detailed study of this system, both theoretical and experimental, including studies of delta doped quantum wells and Terahertz generation by optical pumping of the acceptor states, is in preparation.

7. ACKNOWLEDGEMENTS

8. REFERENCES

1. J.M. Chamberlain and R.E. Miles, editors.
' New directions in terahertz technology',
Kluwer, Dordrecht, 1997.

2. M.May 'T-rays spell sharper, safer images'
New Scientist, pp. 22-24, 24 May 1997.

3. D.Gammon, R.Marlin, W.T. Masselink, and H.Morkoc.
' Raman spectra of shallow acceptors in quantum well structures.'
Phys. Rev. B, **33** no 86 pp 2919-2922. 1986

4. A.A.Reeder, J.M.Mercy and B.D.McCombe
'Effects of confinement on shallow donors and acceptors in GaAs/AlGaAs Quantum wells'
IEEE J. Quant. Electronics **24** no8 pp.1690-1697. 1988

5. R.A.Lewis, T.S.Chang, M.Henini and J.M.Chamberlain.
'Energy states of Be in GaAs' Phys. Rev. B, **53** no19 pp 12829-12834.

6. B.N. Murdin, G.M.H. Knippels, A.F.G. van der Meer, C.R. Pidgeon, C.J.
G.M. Langerak, M.Helm, W.Heiss, K.Unterrainer, E.Gornik, N.J. Hovenier,
and W.Th. Wenckebach.
'Excite-probe determination of the intersubband lifetime in wide
GaAs/AlGaAs quantum wells using a far-infrared free electron laser.'
Semicond. Sci. Technol, 9 pp1554-1557, 1994.

7. B.E.Cole, C.J.G.M.Langerak, B.N.Murdin, C.D.Bezant, J.M.Chamberlain, C.R.Pidgeon,
M.Henini and V.Nakov.
'Saturation absorption studies of intersubband relaxation rates in a p-GaAs/AlGaAs Qw using a free
electron laser'
Physica E, 1998 Vol 2, No1-4 pp.181-185.

Suppression of LO phonon scattering in "quasi" quantum wires and dots.

B.N. Murdin

Department of Physics, University of Surrey, Guildford, GU2 5XH, U.K.
(fax, + 44 1483 876781, email b.murdin@surrey.ac.uk)

ABSTRACT

We review recent work on the scattering of electrons in doped quantum wells in high magnetic fields. Picosecond time-resolved far-infrared measurements have allowed the determination of scattering lifetime between Landau levels as a function of applied field in quantum wells and bulk material. The measurements show a clear suppression of the cooling rate when the Landau level spacing is equal to the phonon energy, and thus the results provide unambiguous evidence for the phonon bottleneck.

Picosecond time-resolved far-infrared measurements have allowed the determination of scattering lifetime between Landau levels as a function of applied field in quantum wells and bulk material. The magnetic field quantises the motion of the electrons in the perpendicular plane and the density of states mimics that of a quantum dot in the case of a quantum well sample ($B \parallel$ growth) or a quantum wire in the case of bulk sample. These "quasi" quantum wires and dots have an easily variable confinement scale, and are far more homogeneous than spatially confined systems. For example, in rectangular quantum wires the density of states follows

$$\rho = \frac{\left(2m^*\right)^{\frac{1}{2}}}{\pi\hbar} \frac{1}{L_x L_y} \sum_{l,m}\left(E - E_{l,m}\right)^{-\frac{1}{2}}$$

and for a Landau quantised wire

$$\rho = \frac{\left(2m^*\right)^{\frac{1}{2}}}{\pi\hbar} \frac{1}{\pi L_B^2} \sum_{n}\left(E - E_n\right)^{-\frac{1}{2}}$$

where the magnetic confinement length L_B is related to the cyclotron frequency ω_c by

$$\hbar\omega_c = \frac{\hbar e B}{m^*} = \frac{\hbar^2}{2m^*} \cdot \frac{2}{L_B^2}$$

Quasi wires and dots therefore present a way of testing ideas about low-dimensional semiconductor systems (LDS), and we review here our recent results on intraband cooling lifetimes. Understanding of intraband lifetimes is essential for the design of optoelectronic devices based on LDS, e.g. devices based on the intraband transitions themselves such as Quantum Cascade require long excited state lifetimes and a fast lower state depopulation. *Inter*band lasers require a fast cooling of electrons to the band edge, and recent interest in quantum dots (QD) has provoked debate over the existence and relative importance of the so-called phonon bottleneck in the intraband cooling. Intraband scattering occurs from the interaction of carriers with the lattice (phonons), with impurities, and among themselves.

One of the primary scattering mechanisms in semiconductors is the emission of longitudinal optic (LO) phonons. However this process is resonant, and the cooling of carriers by LO emission in quantum dot structures may be inhibited when the level separation is not equal to the phonon energy, $\hbar\omega_{LO}$, thus reducing the interband emission efficiency. There have recently been a significant number of experiments which have attempted to measure the intraband lifetimes in quantum dot systems[1-5], and the results are somewhat inconsistent, but this may well be due to slightly differing sample structure and also to differing measurement techniques. There are many groups who have reported fast cooling times from near-IR interband measurements and attributed this to a number of competing processes. One such process is Auger scattering where the energy is taken away by charge carriers which have little or no quantum-confined energy restriction e.g. heavy holes or barrier electrons. The problem remains to quantify the speed of these processes and develop a model which successfully predicts which is dominant. One way to discriminate between processes is by doing far-IR intraband measurements on n-type doped samples.

Part of the EUROPTO Conference on Terahertz Spectroscopy and Applications II
Munich, Germany • June 1999 SPIE Vol. 3828 • 0277-786X/99/$10.00

177

These give the pure scattering rate due to electron-confined electron and electron-phonon cooling, and eliminate the electron-hole and electron-barrier electron Auger mechanisms.

There has at present been no published literature on far-IR measurements on quantum dots, and this is probably due to the difficulty of growing highly homogeneous samples. Typical self-organised dot samples exhibit several PL lines under high laser pump intensity, and the narrowest of the reported lines is around 15meV wide, separated by about 75meV. This would lead to a far-IR transition which is at least 20% broad (assuming the PL lines involve heavy hole states with negligible separation).

In order to try to fill in this gap we have performed picosecond-resolved, far-IR pump-probe spectroscopy on doped, quasi quantum dots. Our results show unequivocal evidence for a phonon bottleneck, and indicate that the size of the suppression of non-resonant scattering (bottlenecking) as compared with resonant LO scattering may be 2 orders of magnitude. As already stated this may not be the dominant effect in interband experiments (or on spatially quantised dots) and further experiments are planned where photo-excited carriers are added to the system to quantify their effect.
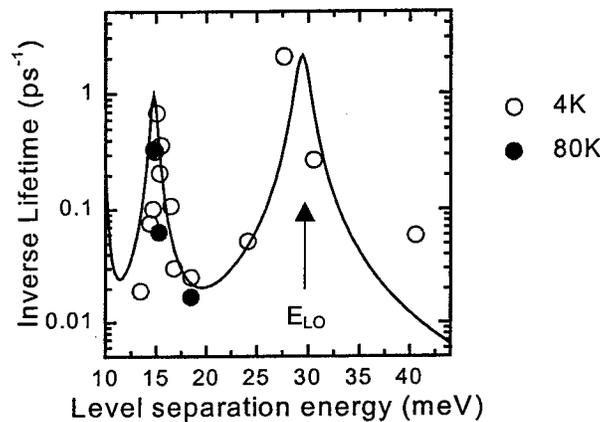
Figure 1. Resonant cooling in an InAs/AlSb QW as a function of magnetic field. After Ref [7].

Several experiments have provided results in different regimes of intraband scattering. There are essentially 3 pathways for the relaxation to occur. The first is by direct, resonant LO phonon emission. This occurs when a pair of Landau levels is separated by the phonon energy, and has been observed in InAs quasi dots (Fig 1) to be of order 1 ps when $\Delta l = 1$ [6,7]. This increases to order 10 ps for $\Delta l = 2,3$ [6-9] due to the reduction in matrix element (Fig 2), and this shows that modification of the LO scattering rate may be possible by modification of the electronic wavefunctions. The increased joint density of states in quasi-wires means that measurement of the resonant LO scattering lifetime is difficult.
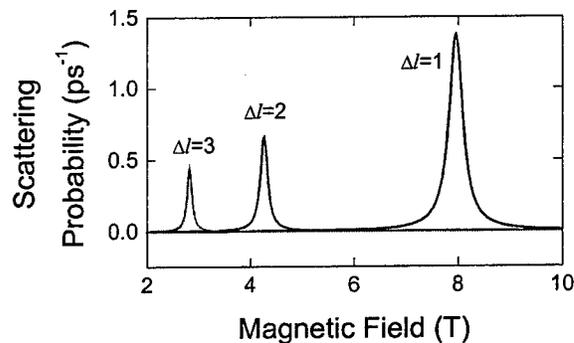
Figure 2. The matrix elements of the LO phonon emission in a InAs quasi quantum dot, calculated from a 14 band quantum well **k.p** calculation, showing the effect of varying the electron wavefunctions on the peak scattering rate. After Ref [7].
The second relaxation pathway is via a combination of electron-electron (e-e) scattering followed by electron-LO phonon emission (e-LO). This may occur in quasi wire away from the LO phonon resonance since the 1D density of states always

allows e-LO to occur, though not necessarily at the zone centre. The electrons are fed by e-e into those states which can be scattered by the phonons. Work in this regime on bulk n-InSb [10] showed Landau lifetimes of approximately 0.1ns. A similar regime may be reached in quasi dots when the excitation is less than the phonon energy, but higher levels are resonant. This was the case for most previous work on GaAs quantum wells[11-13], where lifetimes of >1 ns have been seen. The lifetime in these cases is determined by the slowest of the 2 stages in the decay, and from the observation that $\tau \propto 1/n$ this appears to have been the e-e part.

Finally LO phonon scattering may be suppressed, as in quasi-dots away from LO-phonon resonance. Relaxation must take place via e-LO from the wings of the (broadened) Landau levels, or via some other weak process such as e-LA or multi-phonon scattering. As for the above, the precise times are likely to be governed by the level structure and linewidth. Carriers may have extremely long lifetimes compared with resonant e-LO in the same sample, ranging from 10ps for lower mobility InAs samples (i.e. larger linewidths)[6] up to order 100 ps for higher mobilities[7-9].

In order to study the dependence of the LO phonon supression effect on the degree of confinement as the transition is made from dots to wires, we chose to investigate the lead-salts[14]. In this system the LO phonon energy is much lower than for InAs, which enabled us to easily probe the situation in which the level separation is greater than the LO phonon energy. The samples used were a bulk epilayer of PbTe, a wide parabolic p-n-p doping well of PbTe and a quantum well of PbTe/Pb$_{1-x}$Eu$_x$Te. The three samples allow comparison of the effects of no z-confinement (i.e. a "quasi" wire), weak, and strong z-confinement respectively. All samples had wide cyclotron resonance linewidths and therefore even though the experiments were performed away from the LO phonon resonances, the suppression is much weaker than for the high mobility InAs sample. However, a clear increase in the lifetime was observed from the bulk to wide well to narrow well, in line with the above discussion.

In summary, useful insight in to the intraband scattering rates in low dimensional semiconductor heterostructures may be gained from the Landau-confined analogues. Results have been obtained in n-type narrow and wide gap semiconductor systems. We are currently extending these results to find the effect of hole concentration by fs-pulsed photo-excitation

REFERENCES

1. U. Bockelmann and G. Bastard, *Phys. Rev.* **B 42**, 8947 (1990)
2. H. Benisty, C M. Sotomayor-Torres and C. Weisbuch, *Phys. Rev.* **B 44**, 10945 (1991)
3. T. Inoshita and H. Sakaki, *Phys. Rev.* **B 46**, 7260 (1992)
4. K. Mukai, N. Ohtsuka, H. Shoji and M. Sugawara, *Phys. Rev.* **B 54**, R5243 (1996)
5. R. Heitz, A Kalburge, Q. Xie, M. Grundmann, P. Chen, A. Hoffmann, A. Madhukar and D. Bimberg, *Phys. Rev.* **B 57**, 9050 (1998)
6. Vaughan T A, Nicholas R J, Langerak C J G M, Murdin B N, Pidgeon C R, Mason N J, Walker P J, *Phys. Rev.* **B 53**, 16481-16484, (1996).
7. B.N. Murdin, A.R. Hollingworth, M. Kamal-Saadi, R.T. Kotitschke, C.M. Ciesla, C.R. Pidgeon, P.C. Findlay, H.P.M. Pellemans, C.J.G.M. Langerak, A.C. Rowe, R.A. Stradling and E. Gornik, *Phys Rev* **B 59** R7817 (1999)
8. BN Murdin, CM Ciesla, CJGM Langerak, RA Stradling, M Kamal-Saadi, E Gornik, CR Pidgeon, *Phys. Stat. Sol. b* **204**, 155 (1997).
9. SK Singh, BD McCombe, J Kono, SJ Allen Jr, I Lo, WC Mitchel, and CE Stutz, *Phys Rev.* **B 58**, 7286 (1998).
10. E Gornik, TY Chang, TJ Bridges, VY Nguyem, JD McGee and W Muller, *Phys. Rev. Lett.*, **40**, 1151-1154, (1978).
11. Maran I, Seidenbusch W, Gornik E, Weimann G, Shayegan M, *Semi. Sci. Technol.*, **9**, 700-703, (1994).
12. Heiss W, Auer P, Gornik E, Pidgeon C R, Langerak C J G M, Murdin B N, Weimann G, Heiblum M, *Appl. Phys. Lett.*, **67**, 1110-1112, (1995).
13. LS Muratov, MI Stockman, LN Pandey, TF George, WJ Li, BD McCombe, JP Kaminski, SJ Allen and WJ Schaff, *Superlatt and Microstruct* **21** 501 (1997).
14. B.N.Murdin, C.M.Ciesla, P.C.Findlay, C.J.G.M.Langerak, C.R.Pidgeon, J.Oswald, G. Springholz and G.Bauer, Submitted to *Semicond. Sci. and Tehnol.* (1999)

Measurements of magnetic resonance and high-frequency conductivity at low temperatures and high magnetic fields

J.M. Schrama[a], E. Rzepniewski[a], A. Ardavan[a], R. Edwards[a], A.-K. Klehe[a], A. Kornilov[b] and J. Singleton[a]

[a]Physics Department, University of Oxford, Clarendon Laboratory, Parks Road, Oxford OX1 3PU, UK
[b]Lebedev Center for Research in Physics, Leninskii Prospekt 53, Moscow 117924, Russia

ABSTRACT

We describe a range of techniques developed by the Oxford group for use in conjunction with the Millimetre-wave Vector Network Analyser in measurements of magnetic resonance and high-frequency conductivity, at extremely low temperatures and high magnetic fields. Included are a variety of resonant cavity techniques. The cylindrical geometry is used to produce high-Q tuneable cavities, ideally suited to measurements of the frequency and temperature dependence of, for example, cyclotron resonance of carriers in GaAs-(Ga,Al)As heterojunctions. A family of rectangular cavities has been designed specifically for measurements of the angle-dependent high-frequency conductivity of organic molecular metals; these systems allow us either to rotate the whole cavity (containing a sample) in the external magnetic field, thus measuring the dependence of a particular component of the conductivity tensor on magnetic field orientation, or to rotate the sample within the cavity, thus measuring different components of the magneto-conductivity. We also describe a non-resonant measurement using a pressure cell with optical access permitting experiments at up to 1.8 GPa. Examples of data obtained from each technique are included.

Keywords: Millimetre-waves, solid state physics, MVNA, techniques

1. INTRODUCTION

For the past few years, the Correlated Electron Systems Group in the Clarendon Laboratory, Oxford, has used a Millimetre-wave Vector Network Analyser (MVNA)[1] extensively as a millimetre-wave source and detection system. In this paper, we describe some of the ways that we have developed to interface the MVNA to the high magnetic field, very low temperature environment in which our experiments are performed.

2. OPERATION OF THE MVNA

2.1. Principles of operation

At the heart of the MVNA are two carefully matched yttrium-iron-garnet (YIG) oscillators, S_1 and S_2.[2] By varying the current driving the YIGs, they can be made to oscillate at any frequency between 8 and 18 GHz.

The frequency, F_{GHz}, of the first source, S_1, is chosen by the user. The signals from S_1 and S_2 are mixed and the difference frequency is compared with a reference from a programmable synthesiser generating a MHz frequency, F_{MHz}. A feedback loop driving S_2 maintains a frequency difference of F_{MHz} between the two sources. In this way the sources are tied; S_2 follows S_1 as the user varies the frequency F_{GHz}.

The source S_1 drives a Schottky diode (labelled in Fig. 1 as HG for Harmonic Generator). This device acts as a transducer, emitting radiation at the frequency of the current it carries. The Harmonic Generator derives its name from the fact that it has non-linear current-voltage characteristics; it is driven by a voltage oscillating sinusoidally at a frequency F_{GHz}, but the current through it is made up of a range of Fourier components. Thus a comb of millimetre-wave frequencies, $F_{mm} = NF_{GHz}$, is radiated, where N is an integer.

Corresponding author: J.M. Schrama, E-mail: marije.schrama@magd.ox.ac.uk

180

Part of the EUROPTO Conference on Terahertz Spectroscopy and Applications II
Munich, Germany • June 1999 SPIE Vol. 3828 • 0277-786X/99/$10.00
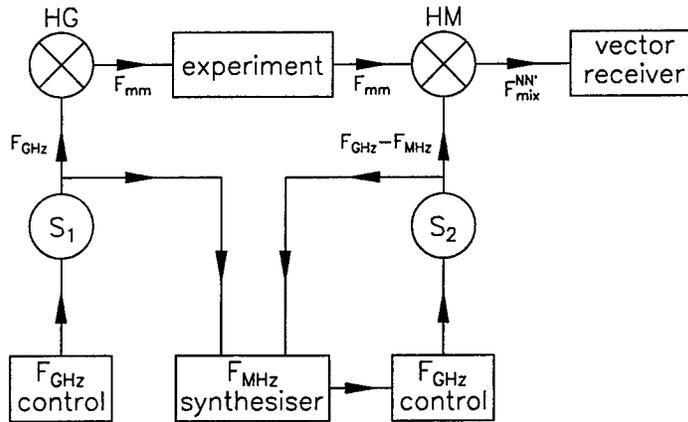
Figure 1. A schematic of the principle of operation of the MVNA.

The millimetre waves are sent through the experiment (or the device under test), where they are attenuated and pick up a phase change of $\delta\phi_N$. They are incident on another Schottky diode, HM (for Harmonic Mixer), which is driven by S_2 at a frequency $F_{\mathrm{GHz}} - F_{\mathrm{MHz}}$. This diode also has non-linear current-voltage characteristics, matched as closely as possible to HG. The millimetre waves transmitted through the experiment mix with the harmonics of the HM driving frequency, $N'(F_{\mathrm{GHz}} - F_{\mathrm{MHz}})$. A comb of difference frequencies, $F_{mix}^{NN'}$, is generated,

$$F_{mix}^{NN'} = NF_{\mathrm{GHz}} - N'(F_{\mathrm{GHz}} - F_{\mathrm{MHz}}) = (N - N')F_{\mathrm{GHz}} + N'F_{\mathrm{MHz}} \tag{1}$$

The amplitude of the signal at the frequency $F_{mix}^{NN'}$ is proportional to the amplitude of the millimetre wave of frequency $F_{mm} = NF_{\mathrm{GHz}}$ arriving at HM, and its phase is

$$\phi_{mix}^{NN'} = N\phi_1 + \delta\phi_N - N'\phi_2 \tag{2}$$

where ϕ_1 and ϕ_2 are the phases of the sources S_1 and S_2 respectively.

A subset of these frequencies, those for which $N = N'$ and $F_{mix}^{NN} = NF_{\mathrm{MHz}}$, are in the MHz range; the rest are GHz frequencies. The phases are $\phi_{mix}^{NN} = N(\phi_1 - \phi_2) + \delta\phi_N = \delta\phi_N$, since S_1 and S_2 are phase locked, and the amplitudes are proportional to the amplitude of the millimetre wave of frequency $F_{mm} = NF_{\mathrm{GHz}}$ transmitted through the experiment. One of these radio-frequency signals is chosen in the Vector Receiver. Its frequency is stepped down by mixing with signals from programmable synthesisers that are synchronised with the F_{MHz} synthesiser. Its amplitude and phase, and hence the amplitude and phase of the corresponding transmitted millimetre wave, are measured by a lock-in amplifier. Thus, the MVNA measures both the amplitude and the phase of a millimetre-wave signal transmitted through an experiment, employing only solid state electronics.

2.2. Details of operation

The difference frequency

The Vector Receiver can function at either of two frequencies, $NF_{\mathrm{MHz}} = 9.010488$ (usually used when $N \leq 3$) or 34.010488 MHz (usually used when $N > 3$). The choice of difference frequency, F_{MHz}, therefore depends on the harmonic used. For example, measurements made using the second harmonic, $N = 2$, would employ a difference frequency of $F_{\mathrm{MHz}} = 9.010488/2 = 4.505244$ MHz. For measurements using $N = 5$, $F_{\mathrm{MHz}} = 34.010488/5 = 6.8020976$ MHz. Control software calculates the appropriate difference frequency and programs the synthesiser automatically.

Frequency stabilisation

The MVNA has a frequency stabilisation input; the frequency F_{GHz} can be varied by up to ± 100 MHz by applying a voltage in the range -10 V to +10 V. A frequency counter (such as an EIP575) can be programmed to output a voltage proportional to the difference between its input frequency and a reference set by the user. This voltage is fed back to the stabilisation input, locking F_{GHz} to the reference frequency.

The stabilisation input can also be used to lock the phase rather than the frequency. This is useful if a measurement is being performed in a cavity whose quality factor, and hence resonant frequency, is changing significantly over the course of the measurement. The procedure makes use of the fact that the phase of the wave in the cavity remains constant when it is at resonance, even if the resonant frequency changes (see Section 4.2). An external lock-in amplifier is connected to the output of the Vector Receiver. F_{mm} is tuned such that the cavity is at resonance. The external lock-in is phased to the output of the Vector Receiver, so that the out-of-phase component reads zero. The out-of-phase analogue output of the external lock-in is fed back to the stabilisation input. If the cavity's resonant frequency varies from the measurement frequency, the external lock-in detects an out-of-phase component; its output stabilises F_{mm} back to the cavity's resonant frequency, where the out-of-phase component is restored to zero. The lock-in time constant and gain can be adjusted for optimum results.

This procedure does not work if there are other factors causing phase drift in the measurement; one example is the variation in length of the waveguides that couple the cavity to HG and HM.

Sweeps

At a harmonic N, the measurement frequency can be swept continuously from $8 \times N$ GHz to $18 \times N$ GHz. Any frequency between 8 GHz and about 350 GHz is accessible with a suitable choice of N. The dynamic range is about 120 dB for $N = 4$. This falls by 5 or 6 dB each time N is increased by 1.

The control computer can perform continuous sweeps of frequency within a certain harmonic; the frequency F_{GHz} is monitored using a frequency counter with an accuracy of ~ 100 Hz. This is a very powerful feature, allowing rapid evaluation of the frequency response of the experiment or device under test. This can give a user an instant measurement of the quality factor of a cavity and the amplitude of any millimetre-wave leaks, for example, or of the cut-off frequency of a section of micro-machined waveguide.[3]

Alternatively, the frequency F_{GHz} can be locked to the counter and the experiment's response can be measured while an external parameter, such as magnetic field or antenna angle, is swept.

The millimetre-wave heads

The performance of the Schottky diodes can be optimised for certain harmonics. The heads HG and HM come in pairs suitable for use at certain ranges of harmonics. Some of the pairs can be biased with a d.c. current to optimise their response at a certain frequency. Some heads also have a tuning screw which can be used to optimise the coupling of the diode to the waveguide. These heads are less suitable for use in frequency sweeps than the alternative broadband heads, because the coupling depends strongly on frequency and so the signal strength varies greatly over the course of a sweep.

2.3. The MVNA as a spectrometer in solid state physics

The experiments carried out by the Oxford group are, for the most part, concerned with the millimetre-wave properties of materials at low temperatures and high magnetic fields. These conditions can only be generated in confined spaces inside cryostats and magnet bores. The MVNA provides a source and a detector, both operating at room temperature. The millimetre waves must interact with the sample inside the cryostat for a measurement to be possible; the sample must be coupled to the millimetre wave heads by waveguides.

The solutions of Maxwell's equations with boundary conditions corresponding to the presence of a waveguide are different from the free space solutions in several important respects.[4] There is a frequency below which radiation is not transmitted (the cut-off frequency), and above this frequency, only certain discrete field distributions are allowed in the transverse direction (perpendicular to the direction of propagation). These transmitted modes fall into two classes, transverse electric (TE_{mn}) and transverse magnetic (TM_{mn}); the indices m and n are the number of half wavelengths in the field distribution in each of the transverse directions.
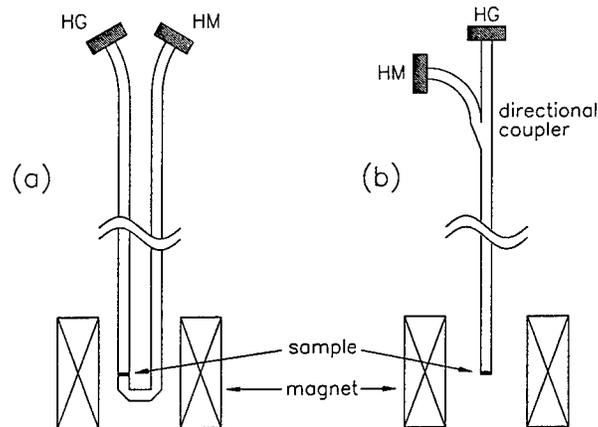
Figure 2. Schematics of the (a) transmission and (b) reflection experiments.

A waveguide can be terminated at both ends, such that it contains an integer number of half wavelengths along its length. In this configuration, it can support resonant standing wave at a particular frequency. These resonant cavity modes are indexed in the same way as their "parent" modes, TE_{mnp} and TM_{mnp}, with the extra index, p, indicating the number of half wavelengths contained between the terminations.

2.4. Measurements

In any experiment, the source emits millimetre waves, which are guided into the cryostat where the sample interacts with them, after which they are guided back out of the cryostat to the detector. The sample can interact with millimetre waves passing it in a travelling waveguide mode or it can be placed in a cavity where it interacts with a resonant millimetre-wave field. In the following Sections, these two approaches and the associated experimental apparatus are described in detail.

3. TRANSMISSION AND REFLECTION MEASUREMENTS

Fig. 2 shows schematics of apparatus used to measure the transmission and reflection of a sample.

3.1. Transmission

In the transmission set-up, the sample is placed across the waveguide in the external steady magnetic field centre. Millimetre waves emitted from the source HG are incident on the sample, and a certain proportion are transmitted through it. The transmitted waves are guided around a U-bend at the bottom of the insert and back up to the detector, HM, where their amplitude and phase are measured.

The sample must cover a large proportion of the cross-sectional area of the waveguide, otherwise much of the signal will be transmitted around the sample without interacting with it. If the sample is small, it should be mounted on a metallic diaphragm with a hole covered by the sample. In practice, it is usually necessary to fix the sample with conductive paint. Any paints and glues used in the set-up should be tested in the absence of the sample to ensure that they do not themselves contribute features to the spectra.

3.2. Reflection

The reflection set-up employs a single waveguide and a directional coupler. The wave from the source is guided down to the sample, which is again positioned in the external magnetic field centre. The reflected wave is guided back up and coupled, via the directional coupler, to the detector, where its amplitude and phase are measured.
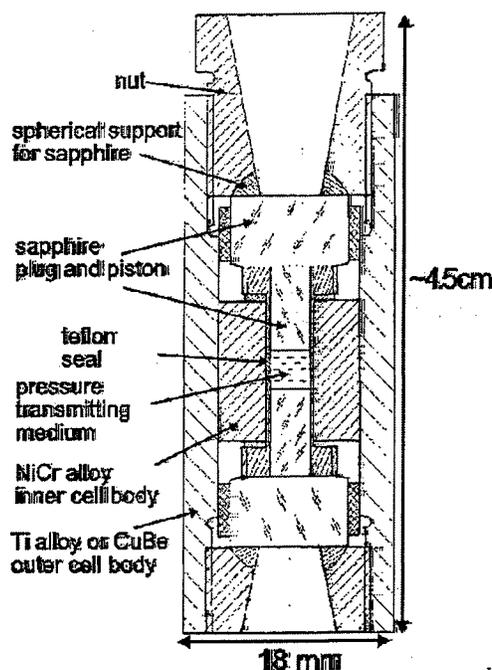
Figure 3. Schematic representation of the "Kornilov cell".[6] This cell was specially designed for millimetre wave experiments at low temperatures and high magnetic fields.

3.3. High pressure measurements

The transmission geometry can be combined with an optical pressure cell to allow non-resonant measurements of the millimetre-wave transmission of samples at high pressures, low temperatures and high magnetic fields. Pressure is a fundamental thermodynamic variable that causes a controlled volume change of a physical system. Varying the pressure allows us to, for example, adjust the bandstructure or carrier correlations in a material[5]; such pressure-induced changes can be observed through the measurement of cyclotron resonance.

Cyclotron resonance measurements under pressure are made possible by an optical cell developed by A. Kornilov, Lebedev Institute, Moscow, Russia.[6] This cell is a piston-cylinder cell, in which the pistons and the supporting plugs on both ends of the cell have been replaced by cylindrical sapphire windows (see Fig. 3). The cell body is of a common two cylinder design, with an inner cylinder of NiCr-alloy wedged into an outer supporting cylinder of beryllium-copper or titanium alloy. The practical pressure limit of the cell is 1.8 GPa. The cell is small enough (outer diameter 18 mm, length about 4.5 cm) to be integrated into a waveguide circuit that can be inserted into a ^{3}He cryostat inside the bore of a superconducting magnet. Whereas diamond anvil cells or most other optical pressure cells generally have a very restricted area of optical access that will cause diffraction problems for the long wavelengths used in MVNA experiments,[7] the "Kornilov cell" overcomes this drawback by making the whole inner diameter of the cell of 3.7 mm optically accessible. The cell is suitable for measurements at frequencies exceeding 40 GHz. Its upper frequency limit is the absorption band of sapphire (10 THz – 150 THz). We selected silicon-oil as the pressure transmitting medium for our measurements, as this fluid does not react with our samples and shows no absorbency in the broad energy range investigated.

We performed the first cyclotron resonance studies of high mobility two-dimensional hole systems (GaAs-(Al,Ga)As heterojunction) under pressure. Fig. 4 shows a resonance spectrum under pressure taken in transmission mode. The signal to noise ratio over the whole field scan and the quality of the fit verify the suitability of the cell for this kind of measurement. These measurements were used to determine the change of effective mass in the two-dimensional hole systems with pressure.[5]
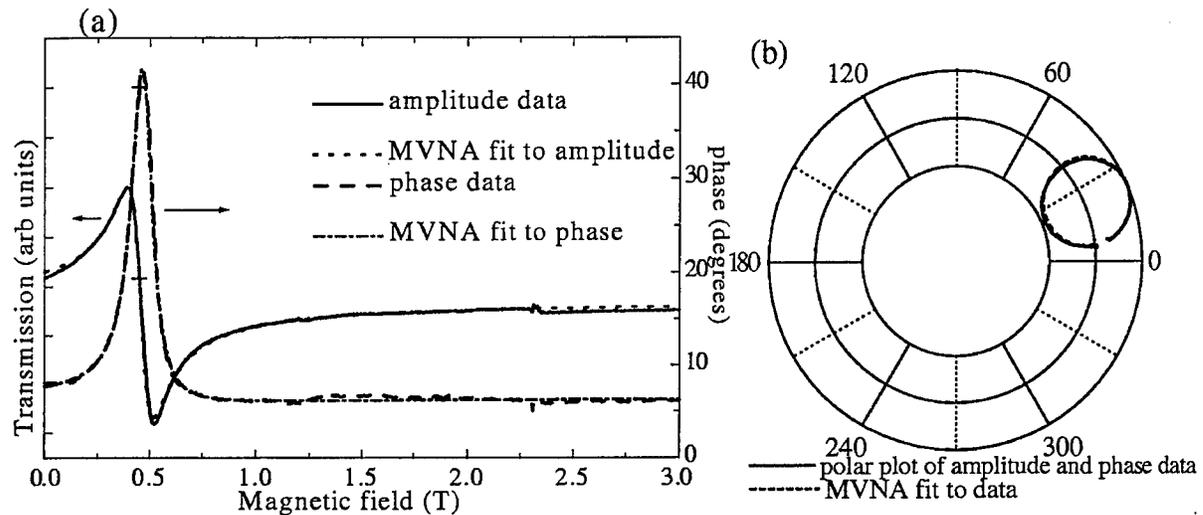
Figure 4. Transmission spectrum and MVNA fit for a high mobility GaAs/(Al,Ga)As heterojunction (NU 942)[5] at P = 0.95 GPa, T = 4.2 K and f = 63.912 GHz. (a) Transmission and phase versus magnetic field. (b) Polar plot of amplitude and phase.

3.4. Advantages and disadvantages of non-resonant measurements

Non-resonant measurements are easy to set up and quick to perform. They allow the millimetre-wave properties of a sample to be studied over a wide range of frequencies.

However, under certain circumstances, the interpretation of the results of non-resonant measurements often proves to be rather difficult. The problems arise because the electrodynamic environment around the sample is poorly defined, and may even change during a measurement. A sample in a transmission insert provides a reflection point in the waveguide, setting up a standing wave. The sample therefore experiences a mixture of oscillating electric and magnetic fields that depends critically on the properties of the sample. If, during a magnetic field sweep, the properties of the sample change, for example if the charge carriers undergo cyclotron resonance, then the sample's electromagnetic environment can change drastically, changing the nature of the measurement.

A resonant cavity can provide a stable and well defined electromagnetic environment, which circumvents these problems, while increasing the sensitiviy of a measurement by several orders of magnitude.

4. CAVITY MEASUREMENTS

The simple cavities introduced in Section 2.3 are not particularly useful in real experiments because they provide no mechanism for exciting a field inside the cavity and there is no indication of how to make a sample interact with such a field. These issues will be discussed in this Section.

4.1. Exciting a mode: coupling to the cavity

An electromagnetic wave incident on a metallic surface induces currents in the metal.[4] These currents screen the bulk of the metal from the wave and re-radiate the reflected wave. A resonating cavity can be thought of as a box in which an electromagnetic wave is constantly reflected from each metallic surface. The surfaces of the cavity carry oscillatory currents which sustain the oscillatory fields. For a given millimetre-wave field distribution, the current density is perpendicular to the local magnetic field direction, and the magnitude of the current is largest in parts of the walls coincident with magnetic field antinodes.

Since the currents in the cavity walls are exactly sufficient to contain the millimetre-wave field, a "missing current" will radiate as the corresponding current would in the absence of the millimetre-wave field; if a

hole to the outside is made in the cavity wall at one of the points at which the current density is large, the hole will radiate. This provides a mechanism for coupling energy both into and out of a resonant cavity. A millimetre wave of the correct frequency, when incident on such a hole from outside, will contribute energy to the resonant millimetre-wave field inside the cavity. Holes through which energy can be supplied or radiated are known as coupling holes.

It is clear that the position of the coupling holes is critical. Coupling holes in certain positions can excite only certain modes; modes with no current density at the coupling hole position cannot be excited. This property allows the cavity to act as a filter. Broadband radiation incident on the coupling hole will excite a particular mode, with a well defined frequency, inside the cavity. Radiation can be coupled out of the cavity through another coupling hole. The emitted radiation will have the same spectrum as the radiation inside the cavity; the higher the quality factor, the narrower the transmitted intensity peak will be around the resonant frequency.

4.2. Frequency response

A cavity has the same resonant behaviour as an LCR circuit or a damped simple harmonic oscillator. The generalised equation of motion is

$$\frac{\partial^2 x}{\partial t^2} + \gamma \frac{\partial x}{\partial t} + \omega_0^2 x = E_0 e^{-i\omega t} \tag{3}$$

In the case of a resonant cavity, x represents the amplitude of the electromagnetic wave inside, γ is a damping constant, ω_0 is the resonant frequency and $E_0 e^{-i\omega t}$ is the amplitude of the in-coupled wave. The steady state solution is

$$x = E_0 \frac{(\omega_0^2 - \omega^2) + i\omega\gamma}{(\omega_0^2 - \omega^2)^2 + \omega^2\gamma^2} e^{-i\omega t} \tag{4}$$

The amplitude is

$$|x| = \frac{E_0}{\sqrt{(\omega_0^2 - \omega^2)^2 + \omega^2\gamma^2}} \tag{5}$$

and the phase, ϕ, is given by

$$\tan\phi = \frac{\omega\gamma}{\omega_0^2 - \omega^2} \tag{6}$$

Fig. 5 shows the amplitude and phase of the signal transmitted through a real cavity, similar to the one described in Section 5.1.

The quality factor

A cavity of a given geometry can be excited in a number of different modes. Each mode has a resonant frequency and a quality factor, Q, defined as[8]

$$Q = 2\pi \frac{\text{(Energy stored)}}{\text{(Energy lost per cycle)}} \tag{7}$$

4.3. The size-dependent properties of a cavity

The energy is stored in the electromagnetic field, and scales with the volume of the cavity. In an empty cavity, the only losses are due to currents induced in the metallic walls by the millimetre-wave field and radiation from the coupling holes.[9] For a cavity with small coupling holes, the losses scale with the surface area. Consequently, smaller cavities tend to have lower quality factors.

For a given geometry and mode, the resonant frequency increases as the cavity dimensions decrease. The resonant frequency of the TM_{mnp} or TE_{mnp} mode in a rectangular cavity of dimensions $a \times b \times c$ is

$$f_0 = \frac{1}{2}\sqrt{\frac{\left(\frac{m}{a}\right)^2 + \left(\frac{n}{b}\right)^2 + \left(\frac{p}{c}\right)^2}{\mu\epsilon}} \tag{8}$$

The frequencies of cylindrical modes are not so easily expressed; graphs of the resonant frequencies against cavity dimensions are available in many textbooks (see, for example, Fig. 8.7 in Poole[9]).
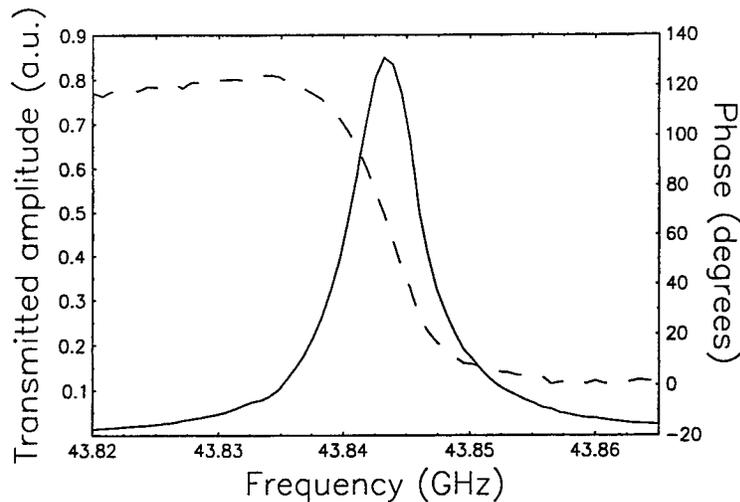
Figure 5. A sweep of frequency across the TE_{012} mode of a cylindrical cavity, showing the amplitude (solid line) and phase (dashed line) of the transmitted wave.

4.4. Measuring the properties of a sample

The millimetre-wave field distribution in a resonating cavity is well known[9]; some regions experience an oscillating electric field, others experience an oscillating magnetic field. It is therefore possible to choose a location inside the cavity at which to place a sample, dependent on what kind of measurement is to be made.

Consider the selection rules governing two kinds of magnetic resonance, electron spin resonance and cyclotron resonance. In each case, the particle energy levels are split by application of a steady magnetic field **B**, into Zeeman levels and Landau levels respectively. Transitions between Zeeman levels are excited by an oscillatory magnetic field perpendicular to **B**, while transitions between Landau levels are excited by an oscillatory electric field perpendicular to **B**. A sample can be positioned in different places in the cavity depending on whether a measurement is to be made of its response to oscillatory magnetic or electric fields.

A sample placed inside a cavity becomes part of the resonant system. If the properties of the sample change, the properties of the resonator are affected. In general, as the properties of a sample change, the resonant frequency changes, $\omega_0 \to \omega_0 - \Delta\omega_0$, and the the quality factor changes, $Q \to Q - \Delta Q$.

For a sample with a complex permittivity $\epsilon = \epsilon' + i\epsilon''$ in an electric field antinode, $\Delta\omega_0 \propto \Delta\epsilon'$ and $\Delta Q \propto \Delta\epsilon''$.[10] For a sample with a complex susceptibility $\chi = \chi' + i\chi''$ in a magnetic field antinode, $\Delta\omega_0 \propto \Delta\chi'$ and $\Delta Q \propto \Delta\chi''$.[11] In certain circumstances, it is possible to evaluate the quantities $\epsilon(\omega_0)$ and $\chi(\omega_0)$ by measuring $\Delta\omega_0$ and ΔQ when the sample is introduced into the cavity. Klein and Donovan[10] have evaluated the effect of an arbitrary spheroidal conducting sample on the cavity properties, using a cavity perturbation approach.

4.5. The experiments performed in Oxford

The effects of interest to the Oxford group are, for the most part, magnetic-field-induced changes in the millimetre-wave properties of materials. A sample is placed inside a cavity and the cavity's properties are measured as a function of applied magnetic field. The sample's properties as a function of magnetic field are deduced.

It is, in principle, possible to lock the MVNA to the resonant frequency of a cavity (see Section 2.2). In most of the experiments described here, this procedure was not possible. The problem arises from the fact that it is necessary to couple the cavity to the millimetre-wave heads using long lengths (~ 1.5 m) of stainless steel waveguide, along which there is a temperature change of about 270 K. The appreciable

thermal expansion coefficient of the stainless steel leads to a drift in the phase of the measured signal as the temperature distribution along the waveguides varies. Since the guided wavelengths at the frequencies used are of the same order as the length change of the waveguides, this effect is important.

Our cavity measurements are carried out at fixed frequencies, with the frequency of the MVNA locked to an EIP575 microwave counter. This technique is satisfactory if the changes in the cavity properties are small throughout a measurement (i.e. $\Delta Q/Q \ll 1$ or $\Delta\omega_0$ is small compared to the frequency width of the cavity resonance). Under these conditions, changes in the amplitude of the millimetre wave in the cavity are proportional to ΔQ and the change of phase of the signal, $\Delta\phi$, is proportional to $\Delta\omega_0$. If the changes are not small, there is mixing between the phase and amplitude signals.[11]

4.6. Advantages and disadvantages of resonant measurements

The millimetre-wave field inside a resonant cavity is stable and well defined, offering an elegant solution to the most serious problems affecting non-resonant measurements. At the same time, the sensitivity of a measurement can be increased by a large margin using a cavity. The sample is part of a resonator; even small changes in the sample's properties can have a large effect on the behaviour of the resonator.

The use of cavities as an experimental tool is not straightforward. They need to be carefully designed and accurately constructed. The frequencies at which measurements can be made are limited to the cavity's resonant frequencies, and the effect of a sample on the cavity mode must be considered. In the following sections, several cavities, designed specifically for use with the MVNA in solid state spectroscopy, are described.

5. CYLINDRICAL CAVITIES

In the TE_{011} mode of a cylindrical cavity, the oscillatory magnetic field forms a torus around the cavity axis with the electric field looping it.[9] The azimuthal mode number is zero; the mode is azimuthally symmetric. There is an electric field antinode at $(r, z) = (0.48r_0, 0.5z_0)$. There are magnetic field antinodes at $(r, z) = (0.48r_0, 0)$ and $(0.48r_0, z_0)$. There are therefore two possible coupling configurations for this mode, with coupling holes either on the endplates or in the barrel walls. If the cavity is coupled through the endplates, it is also possible to excite higher TE_{01p} modes.

5.1. Tuneable cylindrical cavities

The study of how the magneto-optical properties of a material vary with frequency is of interest and can be performed with comparative ease in the transmission and reflection geometries. However, in a cavity measurements can only be made at the discrete frequencies at which the cavity resonates. To overcome this problem, the the frequency at which a particular mode resonates should be variable by the experimenter.

The fact that a good electrical connection between the endplates and the barrel is not required for the TE_{01p} modes in a cylindrical cavity means that it is possible to replace one endplate with a close-fitting plunger. The dimension z_0 can be varied and the resonant frequency of a particular mode can then be tuned continuously. Fig. 6 shows a mechanism designed to allow the length of a cylindrical cavity to be varied. A plunger is mounted on a screw that moves up and down along the cavity axis as it is rotated. The screw is coupled by gears to a vertical drive rod, which exits the cryostat parallel to the waveguides. By rotating the drive rod, the length of the cavity can be changed *in situ* inside the cryostat. This means that it is possible to measure a sample at a range of frequencies without repeatedly warming and cooling the system, which is a time-consuming procedure that some samples do not tolerate. A further feature of this design is that the barrel and plunger sections (shaded in Fig. 6) can be replaced with sections of a different diameter, whilst retaining the tuning mechanism. In this way, tuneable cavities that operate over different frequency ranges can be made.

The first barrel-plunger combination had a diameter of 9 mm. Its TE_{011} mode is tuneable from about 45 GHz to 70 GHz when empty, with a peak Q of 7000 at 4.2 K. Measurements made with this cavity are described in the next Section. A second barrel-plunger combination was manufactured later with a diameter of 6.5 mm; this cavity can be tuned from about 60 GHz to 80 GHz with a quality factor between 7000 and 10000.
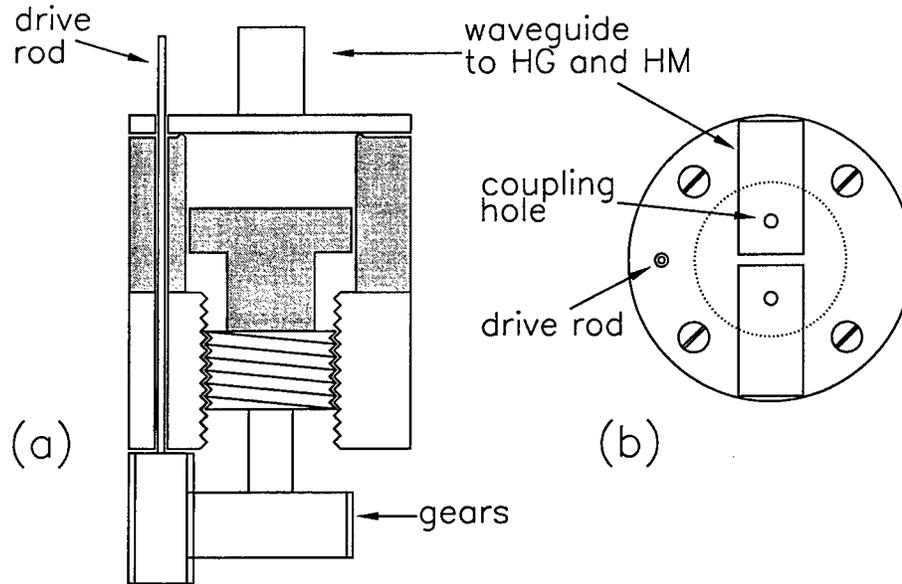
Figure 6. A schematic of the tuneable cavity mechanism. (a) vertical cross section, (b) top view.

5.2. Measurements of the frequency-dependence of the coupled cyclotron resonance in GaAs-(Al,GaAs) hole systems

Using the tuneable cavity system, we carried out a detailed study of cyclotron resonance in p-type GaAs-(Al,GaAs) heterojunctions.[12] The presence in the samples of two hole spin subbands with different effective masses suggests that two cyclotron resonances should be observed. In some samples, however, it is found that only a single resonance is observed over a wide range of conditions of applied magnetic field and temperature. This single resonance is seen to split into two as the temperature and measurement frequency are varied. Using the tuneable cavity system, we were able to measure the cyclotron resonance lineshapes with unprecedented accuracy over the temperature and magnetic field ranges of interest. These results stimulated the formulation of a theory describing the interactions between the two hole populations; the theory predicts that under certain circumstances, the cyclotron motion of the two populations becomes coupled, resulting in the observation of a single resonance. Fig. 7 shows an example of the results of our measurements. The amplitude transmission of the cavity is shown as a function of the applied magnetic field, B. In (a) the high-field cyclotron resonance can be seen increasing in strength as the measurement frequency increases from 51.7 GHz to 66.7 GHz. The solid lines represent experimental data and the dotted lines are fits to the theory, demonstrating excellent agreement (the deviations from the dotted lines in (b) are due to quantum oscillations, periodic in $1/B$; these are only visible because of the very high sensitivity of the measurement). From these data, we were able to extract the detailed parameters of the intersubband interactions.[12]

5.3. Cylindrical cavities: a summary

Cylindrical cavities are useful for measurements requiring a stable and well-known electromagnetic environment around the sample. They are easy to construct, have high quality factors and can be made to be tuneable. One of the disadvantages of cylindrical cavities is that their modes, even for low mode numbers, are not particularly well separated in frequency space. When a highly perturbing sample is placed inside, it causes mixing between the cavity modes. The resulting electromagnetic environment is very unstable; cylindrical cavities are not suitable for measurements of such samples.
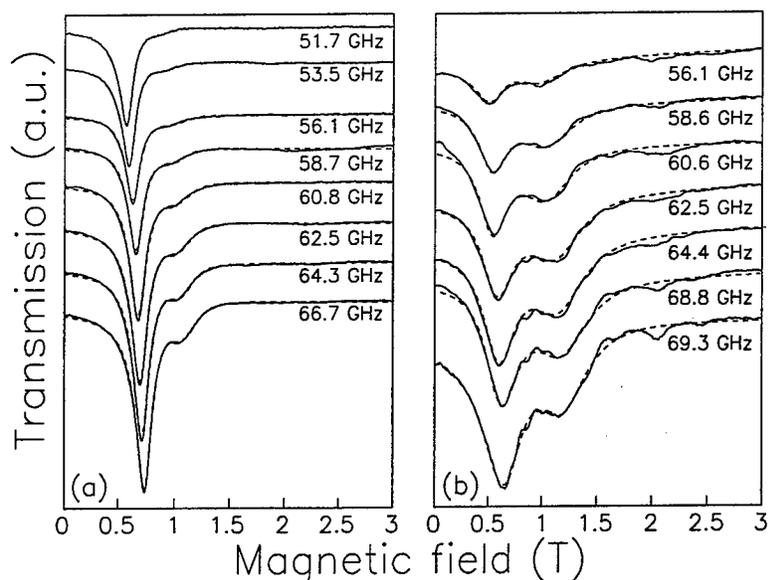
Figure 7. Amplitude transmission of the cylindrical cavity as a function of magnetic field and measurement frequency for two p-type GaAs-Al,GaAs heterojunctions. The temperature is 500 mK.

6. RECTANGULAR CAVITIES FOR MEASUREMENTS OF BEDT-TTF SALTS

Quasi-two-dimensional organic molecular metals based on the molecule BEDT-TTF[13] form one class of materials difficult to measure in cylindrical cavities because of their relatively high conductivities. We have designed several systems based around rectangular cavities specifically for measurements involving these samples.

6.1. The rotating rectangular cavity

The d.c. and low frequency properties of metallic salts based on the organic molecule BEDT-TTF have been studied extensively.[14] The salts form a range of interesting groundstates, including superconductivity and spin-density and charge-density waves. Although they are chemically complex, their electronic structure turns out to be remarkably simple. The availability of very high quality single crystals means that they provide interesting systems in which to study the fundamental physics of metals.

The very high conductivity in certain directions is the source of difficulty in cavity measurements; the millimetre-wave field can be strongly perturbed in the presence of a sample. There are several measures that can be taken in these circumstances. The cavity mode should be carefully selected to be robust (i.e. well separated in frequency from other modes, to avoid mixing). The position and orientation of the sample can be chosen to minimise the perturbation of the millimetre-wave field. A metallic sample with a short skin depth will almost completely expel the millimetre-wave from its bulk; depending on the shape of the sample, this might perturb the mode greatly. In the case of highly anisotropic metals, it is sometimes possible to align the sample in the millimetre-wave field such that this effect is avoided. The rectangular TE_{102} mode provides a suitable environment from both points of view; it is well separated from other modes, while at the same time it provids a choice of locations for the sample in the millimetre-wave field.

6.2. Fermi surface traversal resonance

As a consequence of their reduced dimensionality, many of the properties of BEDT-TTF salts vary in interesting ways depending on the orientation of a steady external magnetic field. In measurements of the high frequency properties, however, it is important that the millimetre-wave field rotates with the sample; if the
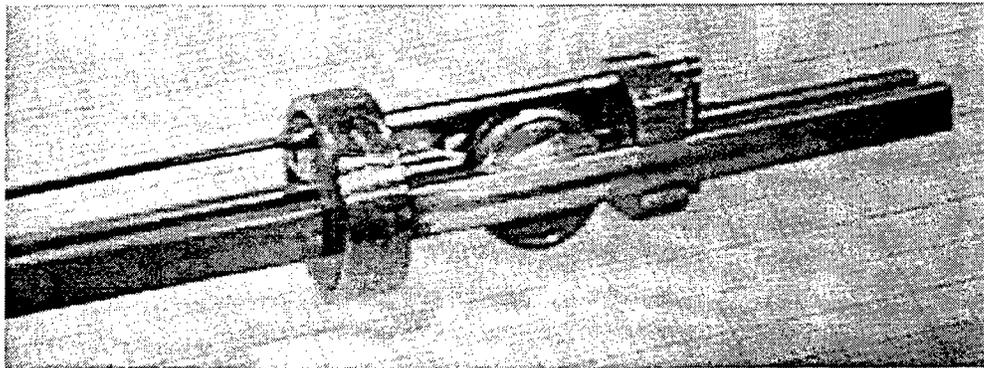
Figure 8. The rotating rectangular cavity apparatus, showing the waveguides, the cavity mounted inside the gear and the worm drive.

sample moves with respect to the millimetre-wave field, the nature of the measurement is changed. Thus the cavity must rotate with the sample through the external magnetic field.

Fig. 8 shows a photograph of the apparatus with which we can perform such measurements. Two waveguides are visible; these lead to the source and detector heads outside the cryostat. The rectangular cavity is mounted inside a gear driven by a worm drive; the whole cavity can be rotated to an arbitrary angle from outside the cryostat. The sample is placed in the cavity in an antinode of the oscillatory magnetic field **H**, such that **H** is parallel to the highly-conducting quasi-two-dimensional planes of the sample. Oscillatory circulating currents are induced in the plane perpendicular to **H**; hence they always have a component in the low conductivity direction (i.e. perpendicular to the high-conductivity planes). The skin depth in this regime is rather larger than the sample dimensions and the millimetre-wave field penetrates the sample completely.[15] The currents induced in the sample dissipate power from the cavity's millimetre-wave field, and for small changes, the change in the cavity's quality factor is proportional to the change in the sample's conductivity. The cavity system therefore allows a particular component of the sample's bulk conductivity to be measured at GHz frequencies.[15]

Using equipment similar to this, Ardavan *et al.* measured a new effect, Fermi surface traversal resonance (FTR),[15] arising from the periodic motion of carriers across the open sections of Fermi surface commonly found in BEDT-TTF-based metals. This observation has lead to renewed interest in the dynamics of carriers at the Fermi surface in magnetic fields and the development of two distinct and complementary theories of FTR.[16]

6.3. Superconducting order parameter in κ-(BEDT-TTF)$_2$Cu(NCS)$_2$

In the previous Section, we described a system allowing us to measure a particular conductivity component as the steady magnetic field orientation is varied. The rectangular geometry also allows us to measure different conductivity components, by rotating the sample with respect to the millimetre-wave field inside the cavity (i.e. by rotating the sample within the cavity). We have designed a system in which the sample is placed on a quartz rod inside the cavity, such that it is positioned in the **H**-field antinode, as in the measurement of FTR. The rod can be rotated from outside the cryostat, such that the plane of the sample remains perpendicular to the steady magnetic field. Thus the orientation of **H** within the highly-conducting planes can be varied. In such an arrangement, the induced circulating currents always have the same interplane component; however, the direction of the inplane component of the induced current can be changed by rotating the sample. In this way, variations of the inplane properties as a function of azimuthal angle can be studied.[18]

We have used this kind of measurement geometry to measure the anisotropy of the superconducting order parameter in the superconductor κ-(BEDT-TTF)$_2$Cu(NCS)$_2$. Fig. 9(a) shows the transmission of the cavity as a function of magnetic field for a range of sample orientations. The dip in transmission (corresponding to a peak in the absorption in the sample) is associated with the superconducting transition; its position and size
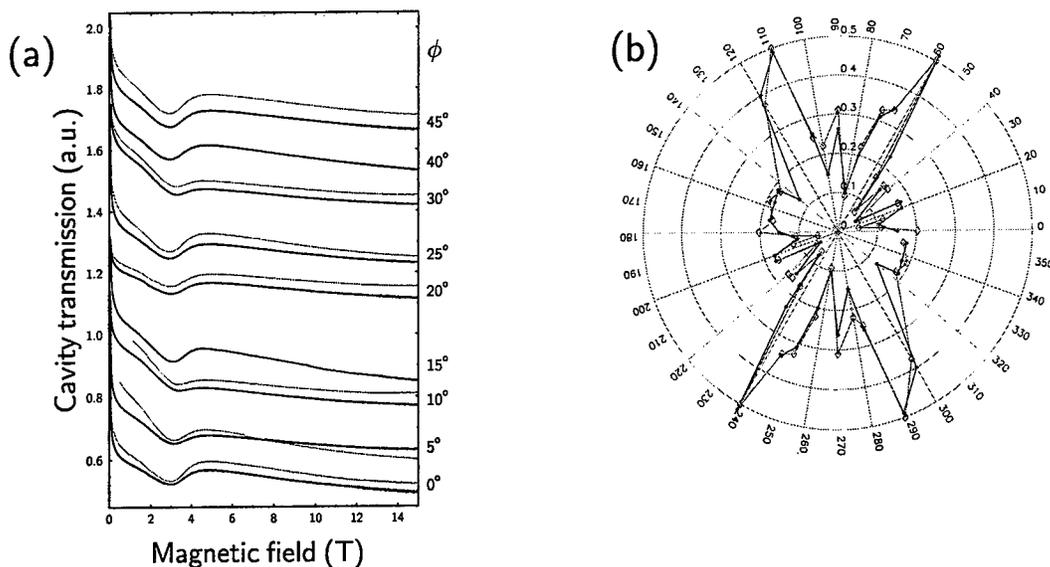
Figure 9. (a) Cavity transmission versus applied magnetic field for a range of sample orientations, ϕ. The temperature is 1.4 K and the measurement frequency is 70 GHz. (b) The normalized amplitude of the dip associated with the superconducting transition as a function of the sample orientation.

are angle dependent. Fig. 9(b) is a polar plot of the normalised dip amplitude. The X-shaped dependence of this parameter reflects the underlying symmetry of the order parameter, which is in turn thought to be defined by the form of the Fermi surface.[17] The plot in Fig. 9(b) bears a striking resemblence to recent theoretical predictions of the order parameter by Schmalian.[17] This experiment is described in more detail by Schrama et al..[18]

6.4. Extremely low temperatures

The experiments described so far in this paper have been performed to temperatures as low as 500 mK using ^{3}He cryostats. We can extend this limit to about 100 mK using a small dilution refrigerator that we have modified to accept waveguides. The cooling power of the dilution refrigerator becomes small at such low temperatures, and so it is necessary to minimise all heat leaks. The waveguides must be broken and thermally anchored at the 4.2 K stage, without allowing coupling between the source and detection sides. This equipment has been used to measure spin resonance in the quasi-one-dimensional antiferromagnet, Cs_2CuCl_4.[19,20]

New cavities that we are currently developing to work at sub-100 mK temperatures and over the whole millimetre-wave frequency range will raise the possibility of exploring exciting new physical effects that are only accessible at extremes of magnetic field and temperature.

7. CURRENT DEVELOPMENTS

We have described the techniques that are already established and used regularly by the Oxford group. The development of new techniques is continuing and there are several projects currently in progress which will extend the capabilities of the system still further.

7.1. Very-far-infrared measurements

A recent addition to the MVNA system has been a pair of Gunn diode local oscillators. At very high harmonics, the power generated by the Schottky diode heads becomes small, with a corresponding loss of

signal. In place of the Schottky diodes, Gunn diodes can be used with harmonic generators, oscillating at a fundamental frequency tuneable over a small range around 100 GHz. With this system, measurements can be made at frequencies of up to 800 GHz. Waveguides and cavities become impractically small when designed for use at such high frequencies; quasi-optical techniques are in development.

7.2. Dielectric systems

The obvious way of confining and guiding radiation is to use metallic cavities and waveguides. In the millimetre-wave region, however, it is possible to make waveguides and resonators out of purely dielectric materials. The advantage of dielectric systems is that they can be used in pulsed magnetic fields, where the rate of change of the external field would cause excessive heating and mechanical forces in equivalent metallic components. Apparatus is being developed for use in explosive driven flux compression magnets, which can generate peak fields of 1000 Tesla.[21] A metallic system would be entirely unusable in these magnets, where the rate of change of magnetic field exceeds 10^8 Tesla per second.

REFERENCES

1. Produced by P. Goy and M. Gross, AB Millimetre, 52 rue Lhomond, 75005 Paris, France.
2. P. Horowitz and W. Hill, The Art of Electronics, Second edition, *CUP* (1989).
3. G.M. Parkhurst, J.W. Digby, A. Ardavan, M. Schrama, C.E. Collins, R.E. Miles, R.D. Pollard, J.M. Chamberlain, J. Singleton, N. Cronin, J.W. Bowen, L.S. Karatzas, D.P. Steenson and S. Davies, accepted for presentation at the Fourth Int. Conference on Millimetre and Submillimetre Waves and Applications, San Diego, July 1998, and in press.
4. For solutions of Maxwell's equations in waveguides, see Baden and Fuller, Microwaves, *Pergamon Press* (1969) Chapters 4 and 5.
5. G.L.B. Verschoor, J.M. Schrama, A.V. Semeno, A. Kornilov, A.-K. Klehe, A. Ardavan, J. Singleton, P. Goy, J.M. Chamberlain, M. Henini and T. Cheng, *Physica B* **256-258**, 359 (1998).
6. A.V. Kornilov, V.A. Sukhoparov and V.M. Pudalov, Proc. Joint XV AIRAPT & XXXIII *EHPRG Int. Conf. on High Pressure Science and Technology*, Warsaw, Poland, 11-15 Sept., 1995, pages 63-65.
7. M. Eremets, High Pressure experimental methods, *OUP*, 1996.
8. See, for example, B.I. Bleaney and B. Bleaney, Electricity and Magnetism, Third edition, *OUP* (1990), Chapter 9.
9. C.P. Poole, Electron Spin Resonance, *Interscience Publishers* (1967), Chapter 8.
10. Olivier Klein, Steve Donovan, Martin Dressel and George Grüner, *International Journal of Infrared and Millimetre Waves* **14** 2423 (1993).
11. C.P. Poole, Electron Spin Resonance, *Interscience Publishers* (1967), Chapter 20.
12. See B.E. Cole, F.M. Peeters, A. Ardavan, S.O. Hill, J. Singleton, W. Batty, J.M. Chamberlain, A. Polisskii, M. Henini and T. Cheng, *J.Phys.: Condens. Matter* **9** 3163 (1997), and references therein.
13. Bis(ethylenedithio)tetrathiafulvaline is an organic molecule also known as BEDT-TTF or ET.
14. T. Ishiguro, K. Yamaji and T Saito, Organic Superconductors, *Springer Verlag*, (1998).
15. A. Ardavan, J.M. Schrama, S.J. Blundell, J. Singleton, W. Hayes, M. Kurmoo, P. Day and P.Goy, *Phys. Rev. Lett* **81**, 713 (1998).
16. A. Ardavan, J.M. Schrama, S.J. Blundell, J. Singleton, A. Semeno, P. Goy, M. Kurmoo and P. Day, this conference.
17. Jörg Schmalian, *Phys. Rev. Lett* **81**, 4232 (1998).
18. J.M. Schrama, E. Rzepniewski, A. Ardavan, J. Singleton, M. Kurmoo, P. Day and P. Goy, this conference; *Phys. Rev. Lett.* submitted.
19. J.M. Schrama, A. Ardavan, R. Coldea, J. Singleton, A.V. Semeno, P.J. Gee and E. Rzepniewski, *presented at the 13th International Conference on High Magnetic Fields in Semiconductor Physics (Semimag 13), Nijmegen, 10-14 August 1998*, and Physica B **256-259**, 637-640 (1998).
20. J.M. Schrama, E. Rzepniewski, P.J. Gee, A. Ardavan, R. Coldea, J. Singleton, J. Suto, and A.V. Semeno, *Proc. of the International Conference on Physical Properties at High Magnetic Fields (Tallahassee, Florida, October 1998)*, in press.
21. J.S. Brooks, C. Mielke, J. Cothern, J. Simmons, Bechtel Group, UNSW Group, Sarov Group, LANL Group, *Physica B* **246-247** 50 (1998); C.M. Fowler, *Physicalia Mag.* **19** 261 (1997).

Photon-induced transport through mesoscopic structures using nano-ploughed Josephson junctions

A. W. Holleitner[a], F. Simmel[a], B. Irmer[a], R. H. Blick[a], and J. P. Kotthaus[a]
M. Bichler[b] and W. Wegscheider[b]

[a]Center for NanoScience and Sektion Physik, Ludwig-Maximilians-Universität,
Geschwister-Scholl-Platz 1, 80539 München, Germany

[b]Walter Schottky Institut, Technische Universität, Am Coulombwall, 85748 München, Germany

ABSTRACT

A new technique is presented enabling the combination of highly transparent superconducting weak links with mesoscopic devices. These can serve as on-chip millimeter wave sources working at frequencies in the range of $10-100$ GHz suitable for photon-assisted transport experiments. We use a modified AFM tip to plough grooves into superconducting material, thus defining Josephson junctions. The weak links are easily integrated within mesoscopic structures such as quantum point contacts or quantum dots with high accuracy in alignment. In combination with a quantum point contact we observe a bolometric photoconductance signal. Embedding these versatile millimeter wave sources in single and multiple quantum dot structures enables us to investigate photon-assisted transport phenomena and their modifications due to near-field effects.

Keywords: Mesoscopic systems, Josephson junctions, photon-assisted tunneling

1. INTRODUCTION

At low temperatures the transport properties of small electron islands are dominated by the so-called Coulomb blockade (CB) phenomenon which is due to the mutual electrostatic repulsion of the electrons. In the Coulomb blockade regime, the energy needed to add additional electrons to the island exceeds the thermal energy by several orders of magnitude. However, by carefully changing the energy of the island using gate electrodes it is possible to add electrons to the system one by one. In semiconductors such islands can be defined electrostatically within the two-dimensional electron gas (2DEG) of a GaAs/AlGaAs heterostructure. Due to the large Fermi wavelength of electrons in a 2DEG, the classical Coulomb blockade is modified by quantum mechanical effects. For this reason these "quantum dots" are often also termed "artificial atoms". Just like for real atoms the energy level structure of quantum dots can be analyzed using several spectroscopic techniques. Furthermore, linking quantum dots together can lead to the formation of "artificial molecules". Beside these fundamental investigations, quantum dots can also be regarded as ultimate electronic devices. They are discussed as single electron transistors, electrometers or even as the basis of a future solid state quantum computer.

Whereas many experiments on the DC transport properties of quantum dots have been performed in the last decade,[1] only few experiments have dealt with high frequency (HF) spectroscopy of these systems. This partly is due to the fact that HF experiments on quantum dots are extremely challenging. Low-temperature techniques have to be married with microwave technology. We therefore employ a new technique – "nano-ploughing"[2] – to define a superconducting weak link close to quantum dot systems. Driven in the AC Josephson regime the weak link irradiates millimeter waves with a voltage-tunable frequency. Positioning the HF source in close proximity to the quantum dot has the great advantage that one does not have to feed externally generated microwaves into the cryostat in which the experiment is performed. Additionally, near-field effects may lead to new phenomena not observable in conventional experimental setups. Whereas the emphasis of our work lies on PAT through quantum dots, nano-ploughed weak links can serve as on-chip millimeter wave sources for any other mesoscopic structure as well.

194

Part of the EUROPTO Conference on Terahertz Spectroscopy and Applications II
Munich, Germany • June 1999 SPIE Vol. 3828 • 0277-786X/99/$10.00

2. FABRICATION OF NANO-PLOUGHED JOSEPHSON JUNCTIONS

The definition of an on-chip radiation source is achieved by utilizing the nano-ploughing technique. To form a nano-plough, an ordinary AFM tip is modified by electron beam deposition (EBD) (Fig. 1). In the EBD process, high dense carbon can be grown on top of a common Si tip by focusing the beam of a scanning electron microscope at the appropriate position.[3] The resulting EBD tips are non-brittle and have a hardness comparable to diamond.[4,5] Furthermore, they can be grown up to 500 nm long and 50 nm wide enabling us to scratch 50 nm wide trenches into metal films of several hundred nanometers thickness.[6]
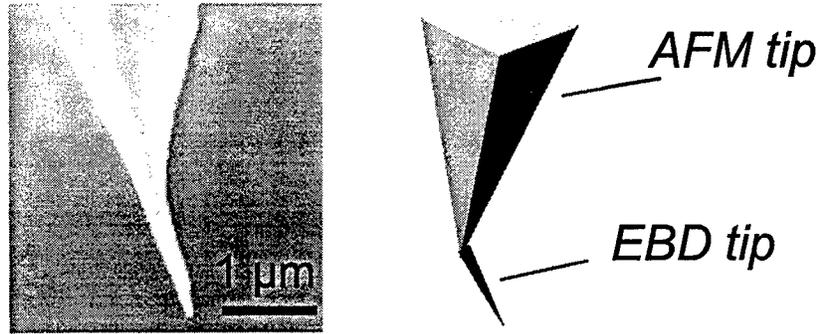
Figure 1. A nano-plough is an ordinary AFM tip modified by electron beam deposition. On the left an SEM micrograph of such a tip is shown, a schematic can be seen on the right. The EBD tip is deposited in a slight angle with respect to the AFM tip in order to achieve a good ploughing performance.

For the fabrication of Josephson junctions we use thin Aluminum films. Bulk Aluminum becomes superconducting below ≈ 1.2 K and can be easily patterned and deposited on semiconductor substrates using standard lithographic techniques. Structuring with a nano-plough is possible with great accuracy in alignment and shape of the ploughed trench. An example for a scratched Al-film can be seen in Fig. 2.
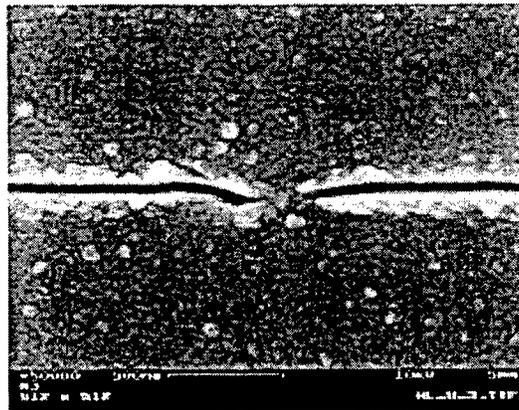
Figure 2. A nano-ploughed Josephson junction in an Aluminum film. This junction is of the Dayem bridge type (cf. Fig. 3). The bridge has a cross-section of approximately 200×200 nm^2.

In contrast to the well-known tunnel-type Josephson junctions (Fig. 3 (a)) the junctions fabricated with the nano-plough are so-called microbridges with a much lower normal state resistance $R_n \approx 0.1 - 1$ Ω. In our work

we mainly concentrate on Dayem microbridges (Fig. 3 (b)) and the variable thickness bridge (VTB) (Fig. 3 (c)).[7,8] Although the superconducting condensates on both sides of the junction are not separated by a tunneling barrier, the Josephson effect is observable: This is due to the dimensions of the microbridges ($\sim$ 100 nm) which are much smaller than the superconducting coherence length ($\xi_{Al} \approx 2.9$ μm). The superconductors are only "weakly linked".

Weak links or microbridges have several advantages as compared to tunnel junctions, especially for their use as microwave sources[8]: the low value of R_n leads to a higher critical current ($j_c \approx 10^6$ A/cm^2) and therefore to a larger output power in the AC Josephson regime. Furthermore, the small intrinsic capacitance of microbridges do not shunt the junction at higher frequencies as is the case for tunnel junctions. A detailed analysis of the different nano-ploughed weak link types has been given in Refs. 2,6.
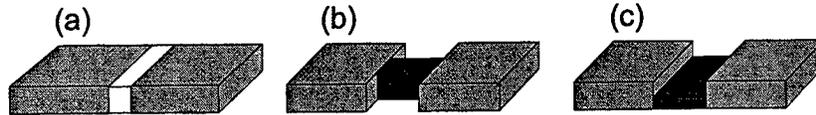
Figure 3. Different types of Josephson junctions: (a) A tunnel junction where two regions of superconducting material are separated by an insulating barrier, usually an oxide. The other two junctions are of the microbridge type: (b) A Dayem bridge, where the two superconducting regions are connected via a constriction, and (c) a varaiable thickness bridge (VTB) in which the film thickness of the superconductor is varied. In both cases the resulting constrictions are smaller than the superconducting coherence length.

3. NANO-PLOUGHED WEAK LINKS IN THE AC JOSEPHSON REGIME

According to the famous Josephson relation,[9] application of a finite voltage V over a weak link leads to an AC current with frequency $f = 2eV/h$, i. e. approximately 500 MHz/μV. Therefore, these structures should serve as perfectly tunable on-chip millimeter wave sources which are used for photon-assisted transport experiments through quantum dot systems. Typical energies for such systems are on the order of 100 μV (excitation energies) up to several meV (CB charging energies) which correspond to frequencies in the GHz regime.
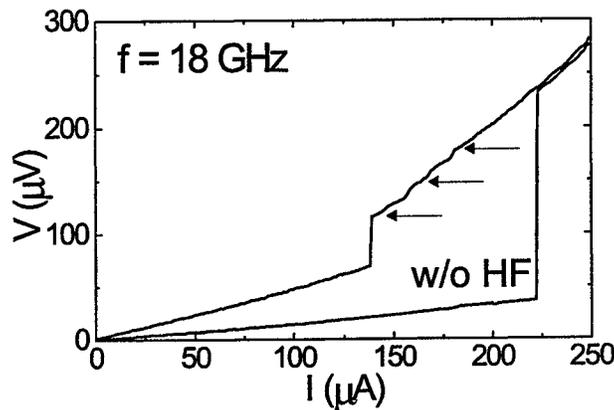
Figure 4. The IV-curve of a nano-ploughed Josephson junction with and without external HF irradiation. The IV-curve is strongly modified under the influence of microwaves. The step-like features indicated by the arrows appear at voltages separated by $hf/2e$. This identifies them as Shapiro steps.

We have performed several tests to check the HF properties of our nano-ploughed microbridges. All experiments have been done in a ^{3}He/^{4}He dilution refrigerator with a base temperature of $T = 25$ mK. In Fig. 4 the influence

of external microwave irradiation on the IV-curve of a nano-ploughed microbridge is displayed. The external HF radiation of $f = 18$ GHz is generated with an HP 87311A microwave source and transduced on the sample using an antenna. Without HF irradiation we obtain the usual Josephson IV-curve. Under the influence of the HF field instead, step-like features appear, resembling Shapiro steps.[10,11] These steps are separated by $hf/2e$ and can be attributed to photon assisted transport of Cooper pairs through the junction. This clearly indicates that the junction is indeed in the AC Josephson regime.

A more direct test of the irradiation capabilities of a nano-ploughed weak link is shown in Fig. 5. For this measurement, a quantum point contact (QPC) is defined electrostatically in the 2DEG of a GaAs/AlGaAs heterostructure using the common split-gate technique. Application of negative voltages to the gates leads to the formation of a ballistic one-dimensional channel which shows the familiar quantized conductance steps.[12,13] In Fig. 5 the last conductance step is shown with and without a voltage applied over a nano-ploughed superconducting microbridge defined on the surface of the heterostructure. The difference signal is also displayed. It can be understood as the bolometric response of the QPC to microwave irradiation which causes an asymmetric heating of the 2DEG on both sides of the contact.[14,15]
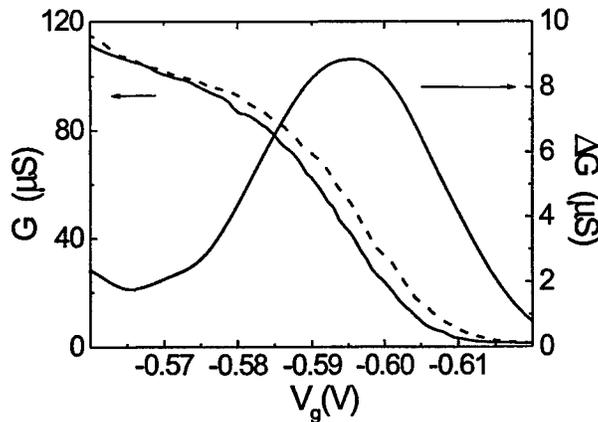
Figure 5. Last conductance step of a quantum point contact with (dotted line) and without (solid line) Josephson radiation emitted by a nano-ploughed weak link. Both curves refer to the left axis. Also shown is the difference signal (reference to right axis) which is a typical bolometric photoconductance signal of a microwave-irradiated QPC.

4. PHOTON-ASSISTED TRANSPORT THROUGH MULTIPLE QUANTUM DOTS

Under the influence of microwave irradiation, photon-sidebands emerge in the conductance oscillations of a quantum dot in the CB regime. Conventionally, the resonance condition for transport through a quantum dot system is the alignment of the discrete chemical potential of the quantum dot with the Fermi levels of the connecting leads. Absorption or emission of photons can also lead to non-resonant transport processes which occur at energies shifted by an integer multiple of the photon energy $n\hbar\omega$. In a multiple quantum dot system, additional resonance conditions have to be fulfilled between the individual quantum dots.

Applying microwave radiation to such a multiple quantum dot can lead to most interesting new transport phenomena. In Fig. 6 (a) a photon-assisted transport process through a double quantum dot is shown. Without microwaves, transport through the system is blocked. However, application of HF radiation can induce an electronic interdot transition in which an electron is transferred from the left to the right dot. When this electron tunnels into the right reservoir, the double dot is refilled from the left reservoir. The net result is a photon-induced current.
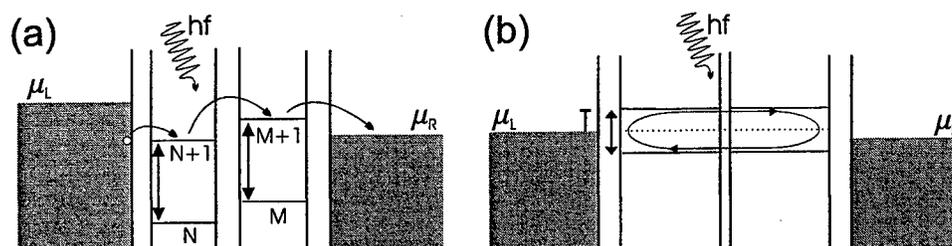
Figure 6. Photon-induced transport processes in a double quantum dot: (a) Photon-assisted tunneling through the double dot in the weak coupling limit. (b) Rabi oscillations due to interaction of an electron in a quasi-molecular state with the high-frequency radiation. In the strong coupling regime the energy levels of the quantum dot system are tunnel-split by the tunnel-coupling T.

If the two quantum dots are coupled more strongly (Fig. 6 (b)), an artificial molecule can be formed. Two formerly aligned individual quantum dot energy levels split up into a "bonding" and an "anti-bonding" molecular state. Interaction of an electron occupying such a state with microwave radiation can lead to the formation of Rabi oscillations. In resonance with the microwaves, the electron of the artificial molecule then switches between the two tunnel-split states. This effect may be exploited to gain information about the electronic wave function in the system.[16] An example for a typical structure we use is shown in Fig. 7. A Josephson junction can be defined close to a triple quantum dot structure utilizing the nano-ploughing technique.
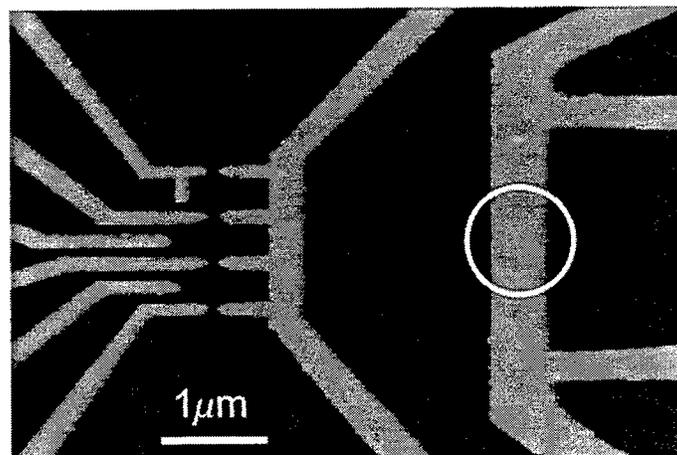
Figure 7. AFM-picture of a triple quantum dot structure made of Aluminum gates (left) prior to the ploughing step. After nano-ploughing the electrode on the right (position indicated by a circle, it can serve as an on-chip millimeter source.

Besides the great versatility of the on-chip radiation sources we expect a modification of the HF transport experiments due to near-field effects. As is well known from far-infrared spectroscopy of low-dimensional electron systems, radiation usually only couples to the collective center of mass modes of the electrons. This is the statement of the generalized Kohn theorem. However, this is only valid when the radiation is treated in a far-field approximation. Adopting a "local" picture of photon-assisted transport (Fig. 8) one could well imagine to circumvent Kohn's theorem and obtain spectral information on quantum dots not attainable in ordinary setups.
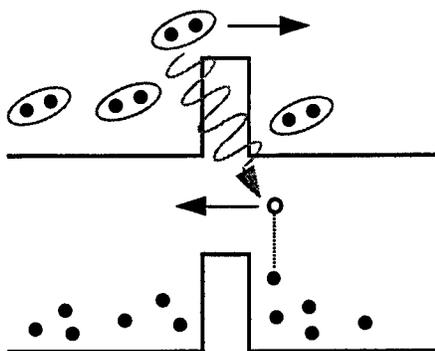
Figure 8. Principle of Josephson radiation-induced transport: Cooper pairs tunneling through the Josephson junction emit photons. Electrons in the 2DEG 50 − 100 nm below the surface absorb these photons and can thus tunnel through the tunneling barrier.

5. CONCLUSION

We have presented a new technique – "nano-ploughing" – to define superconducting weak links in close proximity to mesoscopic semiconductor structures. In the AC Josephson regime the weak links can be used as on-chip millimeter wave sources. With these sources, high-frequency spectroscopy of mesoscopic systems can be performed. A modification of photon-induced transport phenomena due to near-field effects is expected.

ACKNOWLEDGEMENTS

REFERENCES

1. L. P. Kouwenhoven, C. M. Marcus, P. L. McEuen, S. Tarucha, R. M. Westervelt, and N. S. Wingreen, "Electron transport in quantum dots," in *Mesoscopic Electron Transport*, H. Grabert, J. M. Martinis, and G. Schon, eds., Kluwer Academic, Dordrecht, 1997.
2. B. Irmer, R. H. Blick, F. Simmel, W. Goedel, H. Lorenz, and J. P. Kotthaus *Appl. Phys. Lett.* **73**, pp. 2051–2053, 1998.
3. M. Wendel, B. Irmer, J. Cortes, J. Kotthaus, A.Lorke, and E. Williams *Superl. Microstr.* **20**, p. 349, 1996.
4. H. Lorenz, J. Lechner, and I. Eisele *Surface and Coatings Technology* **47**, p. 746, 1991.
5. C. Davis, G. Amaratunga, and K. Knowles *Phys. Rev. Lett.* **80**, p. 3280, 1998.
6. B. Irmer, F. Simmel, R. H. Blick, and J. P. Kotthaus *Superl. Microstr.* **25**, 1999.
7. T. Klapwijk and J. Mooij *ASC* **74**, p. 858, 1974.
8. K. K. Likharev *Rev. Mod. Phys.* **51**, p. 101, 1979.
9. B. Josephson *Phys. Lett.* **1**, pp. 251–253, 1962.
10. A. H. Dayem and R. J. Martin *Phys. Rev. Lett.* **8**, pp. 246–249, 1962.
11. S. Shapiro *Phys. Rev. Lett.* **11**, pp. 80–82, 1963.
12. B. J. van Wees, H. van Houten, C. W. J. Beenakker, J. G. Williamson, L. P. Kouwenhoven, D. van der Marel, and C. T. Foxon *Phys. Rev. Lett.* **60**, p. 848, 1988.
13. D. A. Wharam, T. J. Thornton, R. Newbury, M. Pepper, H. Ahmed, J. E. F. Frost, D. G. Hasko, D. C. Hasko, D. C. Peacock, D. A. Ritchie, and G. A. C. Jones *J. Phys. C* **21**, p. L209, 1988.
14. R. A. Wyss, C. C. Eugster, J. A. del Alamo, and Q. Hu *Appl. Phys. Lett.* **63**, pp. 1522–1524, 1993.
15. R. A. Wyss, C. C. Eugster, J. A. del Alamo, Q. Hu, M. J. Rooks, and M. R. Melloch *Appl. Phys. Lett.* **66**, pp. 1144–1146, 1995.
16. R. H. Blick, D. W. van der Weide, R. J. Haug, and K. Eberl *Phys. Rev. Lett.* **81**, pp. 689–692, 1998.

SESSION 5

All Optical Generation
and Imaging

THz-Imaging: Fundamentals and Biological Applications

Martin Koch

Institut für Hochfrequenztechnik, TU Braunschweig, D-38106 Braunschweig, Germany

ABSTRACT

In the beginning of this article we briefly outline the working principle of terahertz imaging. This relatively new technique is based on THz time-domain spectroscopy and has the potential to lead to the first portable far-infrared imaging spectrometer. For such a spectrometer many applications can be foreseen in the fields of biology, medicine, chemistry and material science. Here we present two biological applications. First we show that THz-imaging is an ideal tool for dendrochronology as it allows us to obtain density profiles of wood specimen. Secondly, we monitor water take up in plants after plant water stress.

Keywords: THz spectroscopy, dedrochronology, plant water stress.

1. INTRODUCTION

Today innumerable modern imaging techniques provide a great wealth of information for biological, medical and material science applications. While some of theses techniques are more or less mechanical, including those which belong to the field of scanning probe microscopy, most imaging techniques use electromagnetic radiation in the visible and near-infrared region of the spectrum to obtain spatially-resolved information on an object. Important examples for these optical techniques are confocal and laser scannig microscopy, optical tomography, thermography and infrared imaging. Also microwaves are widely used for imaging purposes. They provide less spatial resolution which nevertheless is still sufficient for many applications. Typical examples include ground penetrating radar and synthetic aperture radar.

Until recently however the far-infrared region located between the infrared and the microwave region of the electromagnetic spectrum was not accessible to imaging. This spectral gap ranging form 0.1 to about 10 terahertz (THz) was closed only recently by THz time-domain spectroscopy [1-3]. This young technique makes use of the ease with which ultrashort optical pulses can nowadays be obtained. The optical pulses can "drive" little photoconductive dipole antennas much faster than this would be possible with the fastest electronic ac-devices available to date. The impulsive laser excitation results in the emission of few-cycle THz bursts with a typical bandwidth of several terahertz. These THz pulses can be detected with a second antenna of similar design which again is gated by ultrashort laser pulses.

Nuss and coworkers were the first to further develop this emitter-receiver scheme to a stage were 2-dimensional images of objects a few centimeters in diameter could be taken [4]. Since this first demonstration in 1995 even new dimensions such as THz tomography and THz near-field imaging have been explored [5].

In the beginning of this article we briefly recollect the working principle of a THz imaging setup [6]. Subsequently some examples for THz imaging on biological objects are given: namely density mapping of wood and water take up in plants.

2. PRINCIPLE OF THz IMAGING

A typical THz imaging setup is shown in Fig.1. It consists of two photoconductive dipole antennas which are gated by 100 femtosecond laser pulses. The pulses are delivered by a $Ti:Al_2O_3$ laser with a repetition rate of 80 MHz. They can be delayed with respect to each other by two optical delay lines. The one on the detector side is typically realized via a stepper motor for coarse alignment, the other one uses a fast shaker oscillating at typical frequencies of 10 to 20 Hz. When an optical pulse hits the biased emitter antenna, a short electrical pulse is triggered. According to Maxwell's law the emitted electromagnetic field is given by the derivative of this current spike. If the electrical pulse rises fast enough the emitted electromagnetic field has strong components in the THz region [6]. The THz pulse which leaves the emitter antenna is precollimated by a silicon lens and then guided by off-axis parabolic mirrors to form an intermediate focus through which
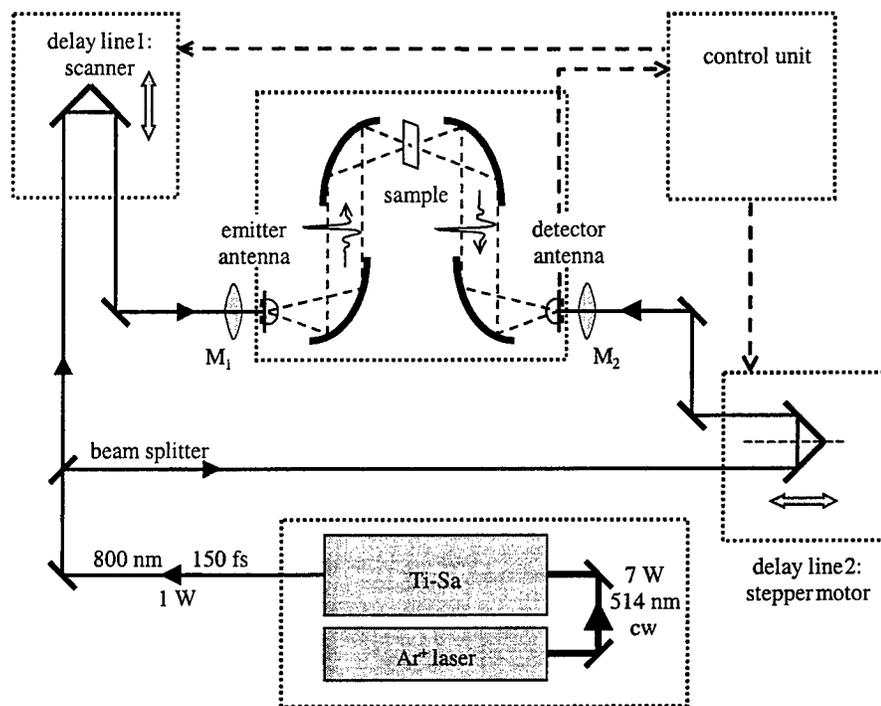
Figure 1: Schematic drawing of the THz imaging setup.
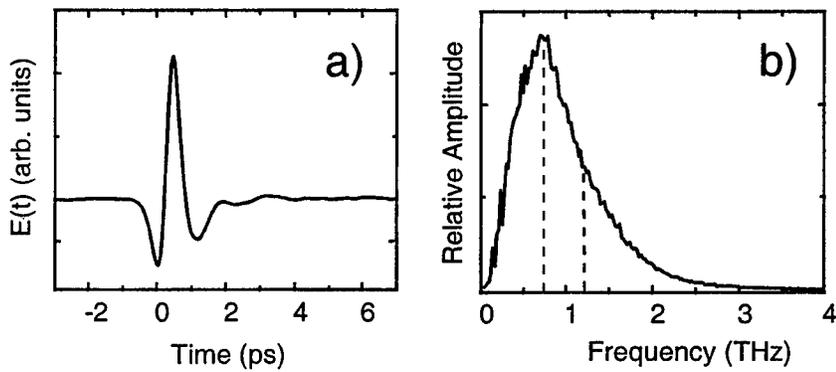
Figure 2: a) Typical THz waveform. b) Fourier transform of the waveform in a). The dashed vertical lines enclose the area over which the spectral integration is performed (0.75 to 1.2 THz for the wood images shown below).

the sample is scanned in a raster pattern. The transmitted radiation is then focused onto the receiver antenna which is made of a semiconductor material with a very short carrier lifetime, i.e. radiation damaged silicon-on-sapphire or LT-GaAs. Like the emitter antenna this detector antenna is gated by an ultrashort laser pulse. In the detector chip the excited carriers are not accelerated by an external bias-field but jiggle back and forth in the field of the incident THz pulse. During their short "life" they contribute to a net current which is monitored as a function of the time delay between the two gating pulses. Using this sampling technique a THz waveform can be obtained.

A typical example of a THz waveform is shown in Fig. 2a. As can be seen in part b) of this figure its spectrum has useful components up to 2.5 THz. With the fast shaker many waveforms can be acquired every second. Several of these waveforms are averaged, subsequently Fourier-transformed and finally spectrally integrated over a certain range (vertical lines in Fig. 2b) [7]. This integration value is translated into a gray value to obtain a pixel. Using this scheme several pixels can be acquired per second; a whole image of 100 x 100 pixels typically requires several minutes. For a more detailed discussion on the THz imaging setup the reader should refer to Ref. 4,5,8.

3. DENSITY MAPPING OF WOOD

An important parameter of wood is its density. On a macroscopic scale density fluctuations as well as the overall density define the quality of a piece of wood. If its quality is too poor a piece might not be used for construction. In a sawmill planks and boards are being sorted based on a mechanical test of their flexibility and an x-ray examination.

Even more interesting from a scientific point of view are the small scale density fluctuations associated with year rings. They tell us a story about climate changes and forest fires in recent history. The investigation of year rings represents an own field of research which is called dendrochronology. It is thus no wonder that over the past 50 years many techniques have been developed to study the density of wood with sub year ring resolution. Early techniques are the hardness feeler [9], a pin which is pressed into wood with a defined pressure, and the acid-corrosion method [10] in which the wood is „burned" by sulfuric acid and subsequently scrutinized with an optical microscope. Later more sophisticated techniques have been developed, including the investigation with X-rays known as radiodensitometry [11,12], gravitometric-volumetric studies [13] and the sandblasting method [14].

In order to test if THz imaging might be an interesting alternative to these existing techniques we have studied several wood samples with a size of 14 x 14 x 1.7 mm cut from different trees. As water heavily absorbs at THz frequencies all samples are pre-dried in an oven to remove surplus water. However, during the experiment in ambient air the wood humidity amounts to 12% in weight.
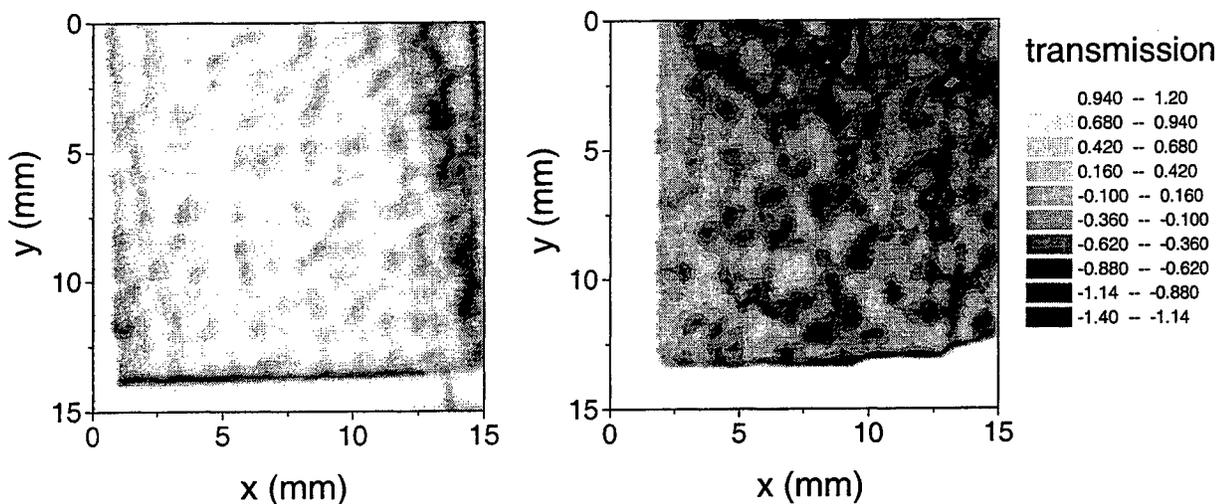
Figure 4: THz images of a piece of balsa (left) and a piece of bongossi (right).

Since the central question is whether refractive index and absorption in the THz range vary with density, we first investigate a piece of balsa wood which is an extremely light and bongossi which is a quite heavy and dense wood. Balsa (ochroma pyramidale) is found in the tropical parts of America. It is of grey-white colour and its density varies between 0.1 and 0.25 g/cm³. Bongossi (lophira alata) is a west african wood, which is famous for its robustness. After being dried this dark brown-violett wood has an average density of 1.0 g/cm³. Both, balsa and bongossi do not show clearly visible year rings.

Fig. 4 shows the THz images of the two wood samples. Regions of low transmission are plotted darker. From a comparison of the two images it is obvious that the overall absorption of the dense bongossi wood is much higher. This is a first indication that the optical density in the THz range scales with wood density.

To test the suitability of THz imaging for dendrochronology we investigate a piece of beech wood (fagus sylvatica). This wood shows pronounced year rings clearly visible to the naked eye and has a mean density of 0.72 g/cm³. As can be seen form the THz image (left part of Fig. 5) the year rings can also be resolved at THz frequencies (vertical structures). The darker areas represent late wood which is less transparent due to its larger density. Early wood on the other hand with its large cell lumina is more transparent and appears brighter. In addition, rays can be observed as horizontal structures.
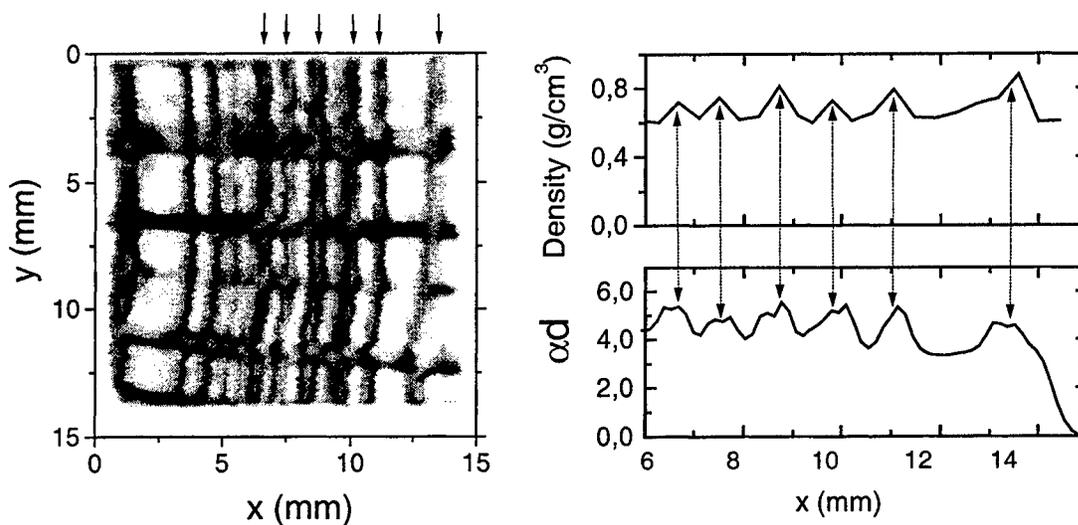
Figure 5: Left part: THz image of a piece of beech wood. Right part: Density profile (upper part) obtained with the gravitometric-volumetric method and absorption profile (lower part) extracted from a defined area of the THz image in the left part (see text).

In order to translate the THz image of Fig. 5 into a density map we need to calibrate the transmission data to the real wood density. The latter is determined with the gravitometric-volumetric method, .i.e., the samples are cut into slices of approximately 400 μm thickness the density of which is then determined by measuring their volume and their weight.

The upper right of Fig. 5 shows the density profile of the area from x=6 to 15 mm and y=0 to 4.5 mm. Slices are cut along the y-direction resulting in an integration of the density over y. Clearly several peaks can be observed. They correspond to regions of late wood which have been marked by the little arrows in the left part of the figure. Ignoring losses due to reflection (we estimate that they are below 3%) the transmission data for the same area have been transformed into optical thickness αd according to Beer's law. The optical density data which are plotted in the lower right of Fig. 5 are integrated from y=0 to 4.5 mm to be comparable to the density data. A clear correlation between the gravitometric-volumetric data and the THz data can be observed. A maximum in the density coincides with a maximum in absorption as indicated by the arrows. The relation between absorption and density is obtained by extracting a couple of data points from each plot and plotting the values for the density n versus the corresponding optical density data. A linear fit of this plot (not shown here) leads to n=0.145 αd g/cm³. This relationship can be used to directly translate THz transmission images of beech into a density map. For our piece of beech wood we determine density variations between 0.4 and 1.4 g/cm³ (see Ref 15 for a color reproduction).

It should be noted that also the refractive index varies with wood density. The average index of refraction in the THz region can be estimated form the temporal delay of the main THz spike that is observed when a wood sample is introduced into the beam path. We find the following refractive index for the different specimen: ochroma pyramidale 1.08; lophira alata 1.49; fagus sylvatica: 1.39 to 1.42.

In conlcusion THz imaging might serve as a useful alternative method to map density profiles of wood with sub-tree ring resolution. The THz technique has advantages over other techniques as it is nondestructive and THz radiation does not represent any danger (as opposed to x-rays used in radiodensitometry). Since THz radiation is highly sensitive to water it could be used to reveal water depots in wood an other biological specimen; a task which can not be performed by radiodensitometry or the sandblasting method. In the next section we make use of this advantage and investigate the water take up in living plants.

4. WATER STATUS OF PLANTS

A quantitative determination of the water status in living plants is desired by plant breeders and plant physiologists. Despite this need there is no noninvasive method to determine the water content of a transpiring leaf. As we will see below THz imaging might be the ideal tool for this purpose.

Plant water status is not only of economic importance but also of great interest form the viewpoint of basic research; many problems in plant physiology remain to be solved. In particular, the mechanisms responsible for water flow in plants are not fully understood. While it is commonly accepted that capillary forces alone can not explain water transport up to the top of tall trees, the well established cohesion theory is questioned from time to time. This theory assumes that water is "sucked" to the top of trees as a consequence of the water loss caused by the transpiration in the leaves. This transpiration which is triggered by sunlight accounts for 90 % of the total amount of water consumed by a plant. Although THz spectroscopy on plants will not allow us to extract water flow rates (which anyway are different in different parts of the plant and depend on a variety of parameters) it might give some indications on the validity of the cohesion theory. As we will see in the following, the THz method also allows us to measure the "refill time" of a leaf after the plant has experienced plant water stress and to make quantitative statements about the total amount of water taken up by a leaf.

The species studied here are vine, ginkgo and sunflower. Before the experiments the plants have not been watered for a period of about two weeks. In order to scan a living leaf through the THz focus we have developed a special holder which allows us to clamp it softly (Fig. 6). Since the normal lab illumination is not intense enough to trigger adequate transpiration the plants are additionally illuminated by a special UV-Lamp during the measurements.

In inset in Fig. 7 shows the transmission image of a part of a vine leaf. The dark areas represent regions of low transmission. These areas correspond to the veins in the leaf. As they are thicker they contain more water and hence lead to higher absorption. To monitor the water take up in a leaf we do not take a complete image but restrict ourselves to a line scan. By increasing the number of waveforms averaged per data point we can further reduce experimental noise. A complete line scan thus takes approximately five minutes to obtain.

Fig. 7 shows the spatially resolved transmission directly before watering and for two different times after watering. The data are normalized by assuming that transmission through air (see very left in the inset of Fig. 7) is 100%. They are not corrected for reflection losses. The two pronounced minima visible in Fig. 7 correspond to two of the veins. After watering
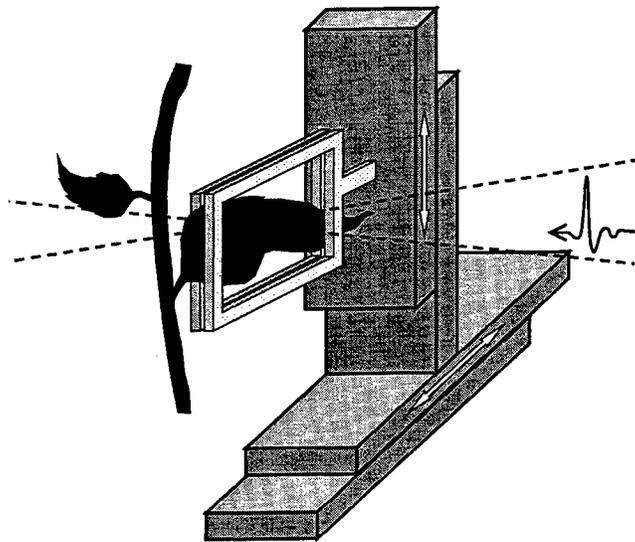
Figure 6: Schematic drawing of the special holder developed to clamp a leaf.

the overall transmission drops as water is sucked back into the leaf. This can be seen most clearly at the positions of these minima. It should be noted that the position of the minima varies slightly form scan to scan. This is due to the fact that the a "living" leaf cannot be grasped too tightly in order not to squeeze or damage it. Therefore small lateral displacements may occur form scan to scan.

Fig. 8 shows the temporal evolution of the transmission at the positions of the two veins. The transmission drops as time goes by. For both curves the dynamics can be fitted quite well by an exponential decay with a time constant of 110 minutes. This time constant can be regarded as the "refill time" after plant water stress. Such information has not been obtained with other techniques such as nuclear magnetic resonance.

The refill effect is also observed with the ginkgo plant and the sunflower, although not as pronounced [16]. It is not observed when the UV lamp is switched off during the experiment. In this case the plants do not transpire enough, if at all. This observation can be interpreted as another indication for the validity of the cohesion theory.

In principle THz spectroscopy along these lines will allow us to make quantitative statements about the total amount of water taken up be a leaf after plant water stress. Future investigations will focus on this point [16].

We would like to point out that recently also two other groups started to investigate plant leaves with microwaves [17, 18].

5. ACKNOWLEDGEMENTS
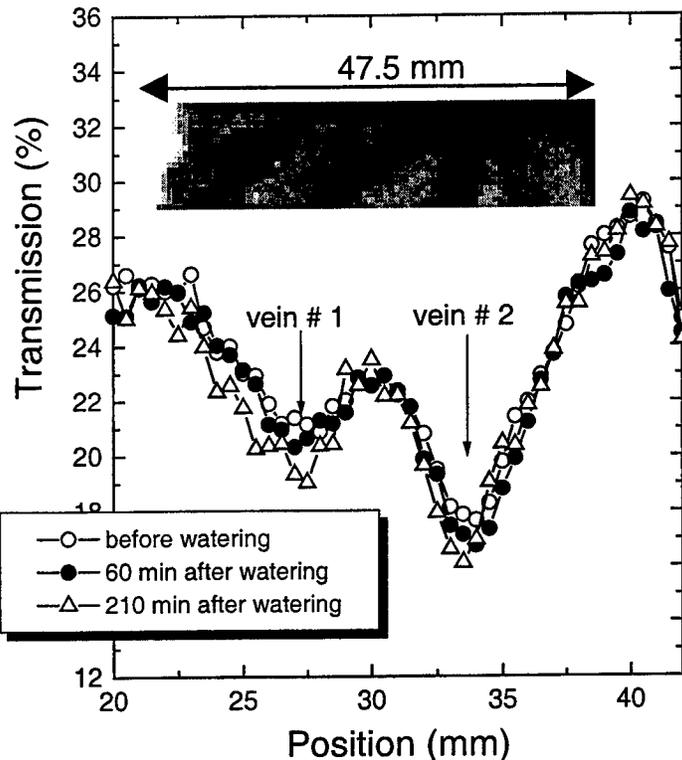
Figure 7: Spatially resolved transmission for different times after watering the plant. Inset: transmission image of a part of a vine leaf.
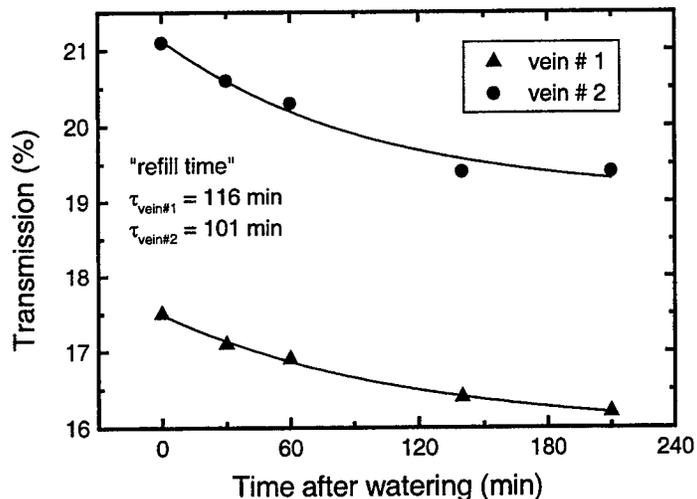
Figure 8: Transmission through the leaf at the positions of the two veins as a function of time.

6. REFERENCES

1. P. R. Smith, D. H. Auston, and M. C. Nuss, IEEE J. Quant. Elec., **24**, 255 (1988).
2. M. van Exter and D. Grischkowsky, IEEE Trans. Microwave Th. Tech., **38**, 1684 (1990).
3. L. Xu, X.-C. Zhang, and D. H. Auston, Appl. Phys. Lett., **61**, 1784 (1992).
4. B.B. Hu, and M.C. Nuss, Opt. Lett. **20**,1716 (1995).
5. S. Hunsche, D.M. Mittleman, M. Koch, and M.C. Nuss, IEICE Trans. Electron. **E81-C**, 269 (1998).
6. P. Uhd Jepsen, R. H. Jacobsen, and S. R. Keiding, J. Opt. Soc. Am. B, **13**, 2424 (1996).
7. Note, that the spatial resolution (typically 0.3-0.5 mm) depends critically on the spectral range over which the integration is performed.
8. D.M. Mittleman, R.H. Jacobsen, M.C. Nuss, IEEE Journal of Selected Topics in Quantum Electronics **2**, 679 (1996)
9. H. Mayer-Wegelin, Allg. Forst- und Jadgzeitung **122** (1950).
10. J. Kisser, and I. Lehnert, Mitt. Österr. Ges. Holzforschung, Wien (1951).
11. H. Polge, Wood Science and Technology **12**, 187 (1978).
12. D. J. Cown, and B.C. Clement, Wood Science and Technology **17**,91 (1983).
13. O. Lenz, E. Schär, and F.H. Schweingruber, Holzforschung **30** 114 (1976).
14. G. Lesnino, Wood Science and Technology **28**, 159 (1994).
15. M. Koch, S. Hunsche, P. Schumacher, M.C. Nuss, J. Feldmann, and J. Fromm, Wood Science and Technology **32**, 421 (1998).
16. I. Libon, M. Hempel, M. Koch, J. Fromm, N.E. Hecker, and J. Feldmann, unpublished.
17. G. Rehm, U. Guckenberger, K. Huber, and H. Brand, Proceedings of the 5th International Workshop on Terahertz Electronics, Grenoble, France, September (1997).
18. S. Hadjiloucas, L.S. Karatzas, and John W. Bowen, IEEE Transact. on Microwave Theory and Techn. **47**, 142 (1999).

Applications of Terahertz (THz) Technology to Medical Imaging

DD Arnone, CM Ciesla, A Corchia, S Egusa, and M Pepper
Toshiba Research Europe Ltd., Cambridge Research Laboratory, 260 Science Park, Milton Road, Cambridge CB4 4WE U.K

JM Chamberlain, C Bezant
Department of Physics , University of Nottingham, Nottingham NG7 2RD U.K.

EH Linfield
Department of Physics , Cavendish Laboratory, University of Cambridge, Cambridge NG7 2RD U.K

R Clothier, N Khammo
Queens Medical Centre, University of Nottingham, NG7 2RD U.K.

ABSTRACT

An imaging system has been developed based on pulses of Terahertz (THz) radiation generated and detected using all-optical effects accessed by irradiating semiconductors with ultrafast (fs-ps) pulses of visible laser light. This technique, commonly referred to as T-Ray Imaging or THz Pulse Imaging (TPI), holds enormous promise for certain aspects of medical imaging. We have conducted an initial survey of possible medical applications of TPI and demonstrated that TPI images show good contrast between different animal tissue types (muscle, fat, kidney, skin, cartilage). Moreover, the diagnostic power of TPI has been elucidated by the spectra available at each pixel in the image, which are markedly different for the different tissue types. This suggests that the spectral information inherent in TPI might be used to identify the type of soft and hard tissue at each pixel in an image and provide other diagnostic information not afforded by conventional imaging techniques. Preliminary TPI studies of pork skin show that 3D tomographic imaging of the skin surface and thickness is possible, and data from experiments on models of the human dermis are presented which demonstrate that different constituents of skin have different refractive indices. Lastly, we present the first THz image of human tissue, namely an extracted tooth. The time of flight of THz pulses through the tooth allows the thickness of the enamel to be determined, and is used to create an image showing the enamel and dentine regions. Absorption of THz pulses in the tooth allows the pulp cavity region to be identified. Initial evidence strongly suggests that TPI may be used to provide valuable diagnostic information pertaining to the enamel, dentine, and the pulp cavity.

Keywords: THz imaging, THz spectroscopy, medical imaging, tooth, skin
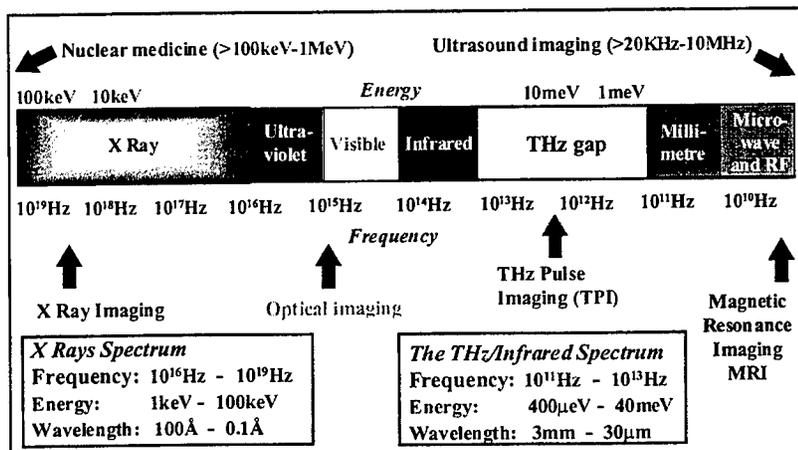
Figure 1. Medical Imaging and the Electromagnetic Spectrum.

1. TPI VERSUS CONVENTIONAL MEDICAL IMAGING TECHNOLOGIES

In the thirty odd years since the first appearance of coherent light, lasers have become almost commonplace. However, there remains one region of the electromagnetic spectrum - the so-called 'Terahertz Gap' - where bright, coherent sources of radiation do not exist (Fig. 1). Terahertz (THz) typically includes frequencies between 0.1THz to 20THz, where $1THz=10^{12}Hz$, or in units of wavelength $\lambda=3mm$ to $15\mu m$. Over the last decade, advances in ultrafast pulsed visible and near-infrared lasers have lead to coherent generation and detection of sub-

Part of the EUROPTO Conference on Terahertz Spectroscopy and Applications II
Munich, Germany ● June 1999 SPIE Vol. 3828 ● 0277-786X/99/$10.00

209

picosecond, broadband (0.05THz-10sTHz) pulses using commercially available technology. Recently, a new imaging technique has been developed based on pulses of THz radiation generated and detected using photoconductive[1] or electro-optical[2] effects with visible pulses (fs-ps) from Ti:Sapphire lasers. This technique commonly referred to as T-Ray Imaging or THz Pulse Imaging (TPI) holds enormous promise for a wide variety of applications. One area of potentially great significance is the application of TPI to medical imaging. Traditional techniques such as X-Ray radiography and computed tomography (CT), magnetic resonance imaging (MRI), ultrasound, and radioisotope imaging are capable of penetrating deep into the body and providing detailed images which represent many years of effort by the medical imaging community. As competition with such accomplishments would be difficult at this early stage of development, applications of TPI should focus initially on specific areas where THz light might have imaging and diagnostic capabilities not afforded by the conventional imaging techniques, such as the potential ability of TPI to distinguish between certain types of healthy and abnormal soft tissue. Its penetration depth for various tissue types, as well as its ability to distinguish between different tissue types, will therefore dictate the utility of THz in medical investigations. The ultimate goal of TPI is to provide high quality images that contain diagnostic information not readily available with other techniques. TPI could provide such information for certain medical applications where it might have distinct advantages over X-Ray, MRI, and ultrasound because of a) its possible diagnostic capabilities arising from the spectral information available at each pixel in the image, and also due to b) the *multiplicity of contrast mechanisms available in TPI.* At each pixel in an image, one can plot:

1. The absorption coefficient $\alpha(\omega)$ over the entire frequency bandwidth of the THz pulse: *panchromatic absorption image,*
2. The absorption coefficient $\alpha(\omega)$ at a fixed frequency ω or over a limited frequency range covered by the THz pulse: *monochromatic absorption image,*
3. Thickness of the object: *time-of-flight image,* or
4. Refractive index $n(\omega)$ at a fixed frequency or over the entire bandwidth: *refractive index image.*

We illustrate these unique and powerful attributes of TPI below in a series of examples relevant to medical imaging.

2. DESCRIPTION OF TPI

2.1. Fundamentals and Description of Current System

A TPI system based on difference frequency generation of THz pulses (bandwidth ~ 0.3THz-2.7THz) and electro-optic detection via the ac Pockels effect[2] has been developed at the Cambridge Research Laboratory (CRL) of Toshiba Research Europe Ltd. (TREL) (Fig. 2). Generation of THz pulses is based on difference frequency mixing arising from the second order susceptibility $\chi^{(2)}$ of a semiconductor crystal (here <110> ZnTe). Ultrafast red (λ_{vis} =800nm) visible pulses with a temporal width of ~70fs have a frequency bandwidth in excess of 10THz. Exciting a crystal having large $\chi^{(2)}$ with such an ultrafast visible pulse produces a time-dependent polarisation where the different visible frequencies beat against each other to create a polarisation P_{NL} at the difference frequency, ω_{THz}:

$$P_{NL}(\omega_{THz})=\chi^{(2)}E(\omega_{vis1})E(\omega_{vis2}), \tag{1}$$

where $\omega_{THz}=|\omega_{vis1}-\omega_{vis2}|$, and ω_{THz}, ω_{vis1}, ω_{vis2} are the THz and visible frequencies, respectively. This time varying polarisation emits a pulse of THz electromagnetic radiation that contains a broad range of frequencies from dc up to the bandwidth of the visible radiation.

Conventional detectors for THz radiation rely on liquid helium cooled bolometers, which measure only the intensity of the radiation, have a background limited sensitivity, and do not provide any phase information. Using mechanisms that are similar to those responsible for the generation of broadband THz pulses, it is now possible to directly and coherently measure the THz electric field in the time domain with high sensitivity at room temperature, without any requirement for cooling
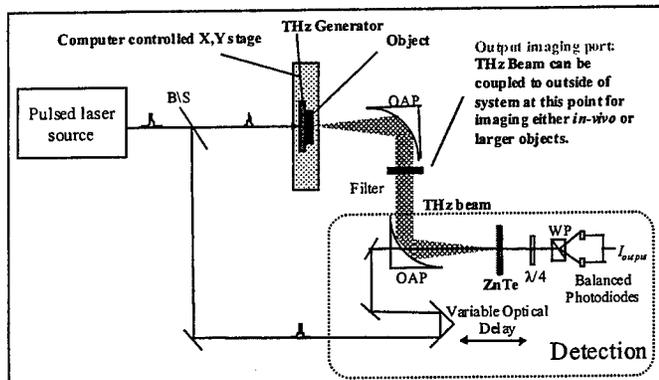
Figure 2. TPI Imaging Platform. The Entire System is Controlled by a DeskTop PC. Further Explanation of Symbols in Text.

of components. The technique being used at TREL-CRL uses the linear electro-optical effect known as the ac Pockels effect[2]. A THz pulse incident on an electro-optical medium (again <110> ZnTe) induces birefringence that is proportional to the amplitude of the THz electric field. This birefringence is readily probed using a visible (probe) beam that experiences a retardation on propagation through an electro-optic medium that is measured with inexpensive and commercially available visible wavelength components and photodetectors. Due to the instantaneous response of the electro-optical material, electro-optical sampling (EOS) in principle has an extremely high bandwidth with a flat frequency response, and allows a direct measurement of the amplitude, phase and spatial distribution of the THz electric field.

The system is shown schematically in Fig. 2. The main components of the system are (a) femtosecond (fs)-pulsed visible laser, (b) THz generator, (c) coupling optics for the THz beam, and (d) time-resolved EOS measurement of the THz pulses. The visible laser source is a commercial ultrafast pulsed Ti:Sapphire oscillator pumped by a diode laser-driven cw solid state laser. The Ti:Sapphire oscillator is tunable over the 750-890nm range, producing short pulses down to 50fs, with a maximum power of ~1W. The visible beam is split in to two equal parts by a beam-splitter (B/S); one part of the beam is used for generating the THz and the other portion is used for detection. The THz is generated using difference frequency mixing in a semiconductor by focussing the visible beam to a 250μm diameter spot using a concave mirror (f=250mm, not shown in Fig. 2). We have found that for optimum generation of THz using difference frequency mixing, the semiconductor is mounted normal to the visible beam, with an adjustment for the azimuthal angle in order to maximise $\chi^{(2)}$. In this geometry the THz is emitted in transmission through the semiconductor and the waist of the visible beam determines the size of the THz source. The emitted THz diverges from this small source, and is collimated by an f=30mm off-axis parabolic mirror (OAP).

For the EOS detection, a second OAP (f=30mm) focuses the THz beam onto the EOS detection crystal, which is <110> ZnTe for all experiments. <110> ZnTe has a large electro-optic coefficient, thus giving a high detection sensitivity, and is also transparent at λ_{vis} =800nm and in the THz, thus permitting a long interaction length between the THz and visible fields. The retardation experienced by the visible pulse arising from the Pockels effect in <110> ZnTe is measured using the combination of a quarter wave-plate (λ/4), a polarisation-splitting (Wollaston (WP)) prism and a balanced photodetector assembly. With no THz field present, the linearly polarised visible (probe) beam passes through the ZnTe with a negligible change in its polarisation. After passing through the quarter wave-plate, the beam polarisation is transformed from linear to circular, and then the Wollaston prism spatially separates the vertical and horizontal components of the polarisation. For a perfectly

circularly polarised beam the components are equal in intensity. The two beams are detected using a balanced photodiode pair, where the output current is equal to the difference in the photocurrents from the two diodes. In the presence of a THz signal, the change in the ZnTe refractive index retards the probe beam, changing the polarisation state from linear to elliptical. Thus, the intensities of the vertical and horizontal beams following the Wollaston prism are no longer equal, and a non-zero photocurrent is measured. Due to the linear shift of the ZnTe refractive index with THz electric field, the output current is proportional to the magnitude of the THz electric field. Neglecting propagation effects in the ZnTe and assuming a delta function-like probe pulse, the instantaneous

Figure 3. Time and Frequency Domain Data Available at Each Pixel in TPI Image.

response of the Pockels effect allows the THz electric field to measured in the time domain simply by varying the arrival time of the THz and probe pulses at the ZnTe detector. This is achieved using a mirror mounted on a computer-controlled delay

stage; moving the mirror back increases the probe path length, and thus delays the arrival of the visible pulse at the ZnTe, allowing the THz pulse waveform to be measured at a later time.

Mounting the object on the rear of the generation crystal, and stepping both the object and the generation crystal through the visible generation beam performs imaging. An X-Y translation stage (see Fig. 2) allows THz spectra to be recorded at each pixel in the image (see Fig. 3). Time domain data is displayed on the PC computer screen, or frequency domain data may be examined at each pixel in the image by applying a fast Fourier transform to the time domain data. *This ability to provide the THz spectral fingerprint of the object at each pixel in its image is one of the major advantages of TPI relative to X-Ray, MRI, and other conventional imaging technologies.* Spatial resolution of 200μm is common in the TREL TPI system illustrated here, limited by diffraction in the far field. Better resolution may be achieved by near field imaging of thin objects (several hundred μm thick and located several hundred μm from the generation crystal); near field imaging is not diffraction limited, and spatial resolution is dictated largely by the diameter of the visible beam in the generation crystal, which can be made 50μm or less.

2.2. TPI System Development

For imaging of larger objects or those that are not easily accessible or easily mounted on the generation crystal, more sophisticated THz and/or visible optics may be used to couple THz into and out of the object under study. In this way, it will be possible to perform TPI on a wide variety of objects, large and small, *in vivo*. In addition, the system in Fig. 2 can be made more compact and durable in a variety of ways using new innovations. A significant part of our current work focuses on developing such systems for the future. We are also concerned with design and fabrication of new semiconductors for much larger visible to THz conversion efficiency, which will produce higher THz power levels and enable us to penetrate through thicker objects. Similar effort is being devoted to new detection schemes to improve signal- to-noise ratios and hence increase image quality and acquisition times.

3. CONTRAST IN TPI BETWEEN DIFFERENT SOFT TISSUE TYPES: PANCHROMATIC ABSORPTION IMAGING AND DIAGNOSTIC INFORMATION AT EACH PIXEL

3.1. Differentiation Between Tissue Types

As a precursor to the examination of abnormal or diseased tissue, we have investigated contrast in TPI between different types of normal tissue. Initial 2D panchromatic (0.3THz-2.7THz) TPI images of pork samples obtained from a local butcher and containing a variety of different tissue types - muscle, fat, and kidney - are shown in Fig. 4b, along with the corresponding visible photograph of the sample in Fig. 4a. The excellent contrast seen between the different types of tissue in the TPI image, as well as the ability of the relatively low power (average power ~1.1μW, peak energy ~*fJ*) THz pulses to pass through these different tissue types (typically 2mm in thickness) are very encouraging for future medical applications. These images were obtained by plotting the peak THz electric field of the transmitted pulse (Fig. 5a) as a function of X-Y position on the sample. Fourier transforming the time domain data leads to the spectral plots of transmission vs. frequency such as that in Fig. 5b, which may be obtained for each pixel in the image. Fig. 5b demonstrates that variations in absorption (transmission) occur across the THz range for each of the tissue types imaged. Moreover, the spectra for different tissue types are markedly different across the THz range probed, allowing the tissue type to also be identified from the absorption spectra. Similar differences in the THz spectra of thin chicken

Figure 4. Visible (a) and THz (b) Images of Different Soft Tissue Types in Pork Sample.

muscle, skin, and cartilage have also been measured (Fig. 6). *This work suggests that different soft tissue types may have characteristic spectral fingerprints in the THz range.* Besides the diagnostic information that may be contained in these spectra, the differences in absorption at a given THz frequency yield monochromatic images at different frequencies that

allow the operator to optimise the contrast between different soft tissue types. However, this preliminary work should be qualified by the fact that the samples were partially dry due to the nature of these initial measurements. The ability to distinguish between different types soft tissue types, suggested by the data above, may lead after further development work to the use of TPI in certain medical applications where the imaging of abnormal or diseased tissue is not adequate using X-Rays or financially feasible using MRI.
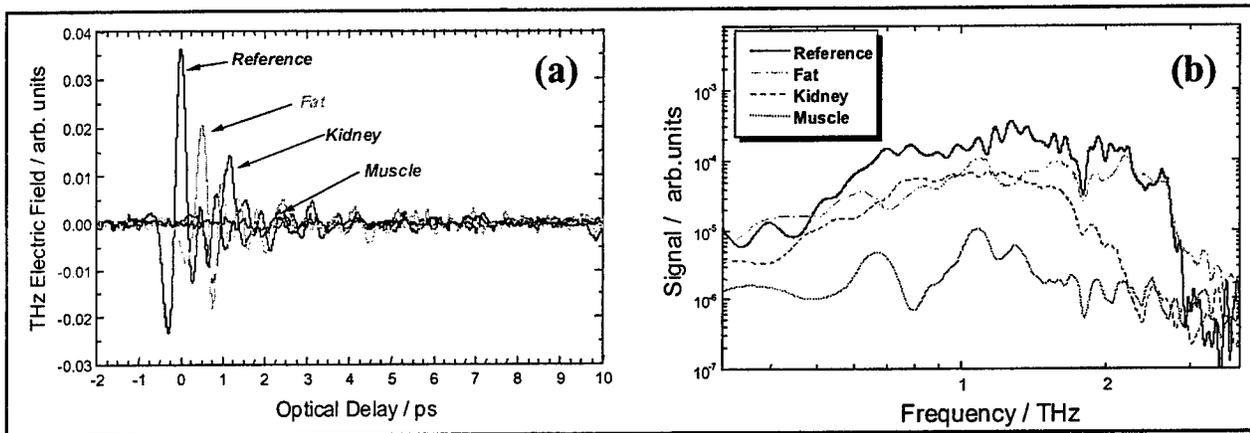
Figure 5. (a) Time Domain Data Used to Produce Panchromatic Image of Soft Tissues, and (b) THz Spectral Fingerprints of Different Soft Tissues for Thin Pork Sample.
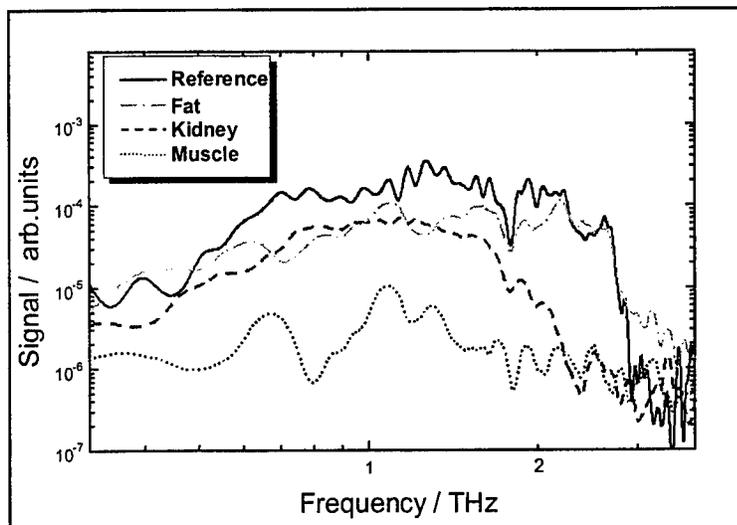
Figure 6. THz Spectral Fingerprints of Different Tissues for Chicken Sample.

3.2. Preliminary Studies of Model Dermis Systems

Current work is addressing the issue of differentiation between various types of fully moisturized tissue. Preliminary work (Fig. 7) on model dermis systems[3] stored in bovine calf serum and recorded several hours after removal from an incubator suggests that THz radiation readily penetrates such samples with 0.5-1.5mm thickness, despite the low average power levels used (1μW). Moreover, excellent reproducibility is observed between two nominally identical dermis samples (Fig. 7). In addition, the refractive indices of various tissue types and substances can be reconstructed from the time delay of the pulse as it travels more slowly through the tissue relative to air (Fig. 8). Preliminary work (Fig. 8) suggests that the refractive indices of the serum (~3.9), dermis with serum (1.4), and water (~2.2) all differ in the 0.3THz-2.7THz range. It should therefore be possible to determine a tissue type not only from its absorption of THz light, but additionally from its refractive index n(ω) which can also be extracted from TPI. Besides this useful diagnostic information, variation in n(ω) between different tissue types is also the basis of yet another image contrast mechanism in TPI (see Eq. (2) below).
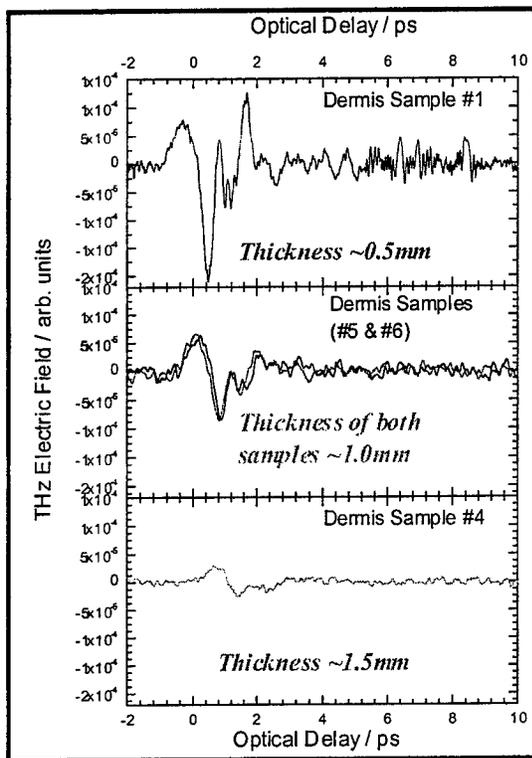
Figure 7. THz Transmission Through Different Thickness Model Human Dermis.
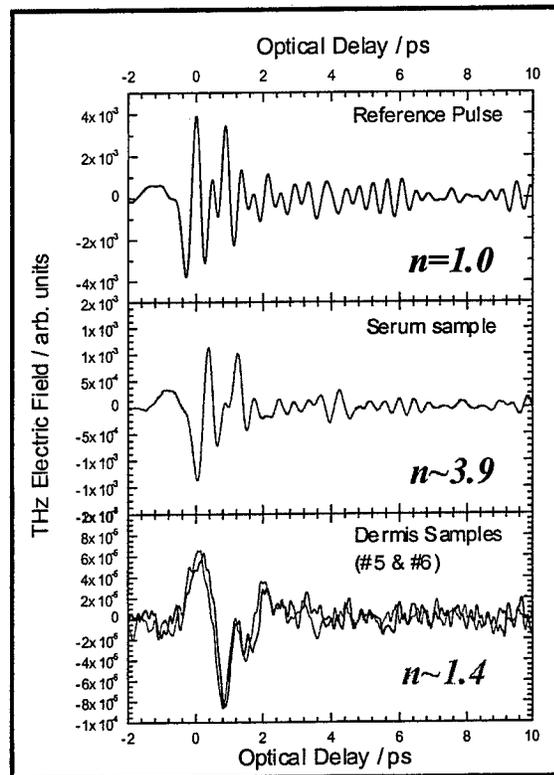
Figure 8. THz Transmission through Skin Constituents Including Serum, and Model Dermis in Serum. *n* is the Index of Refraction, Which is Different for the Different Materials.

4. 3D MAPPING OF SKIN THICKNESS USING TPI: TIME-OF-FLIGHT IMAGING
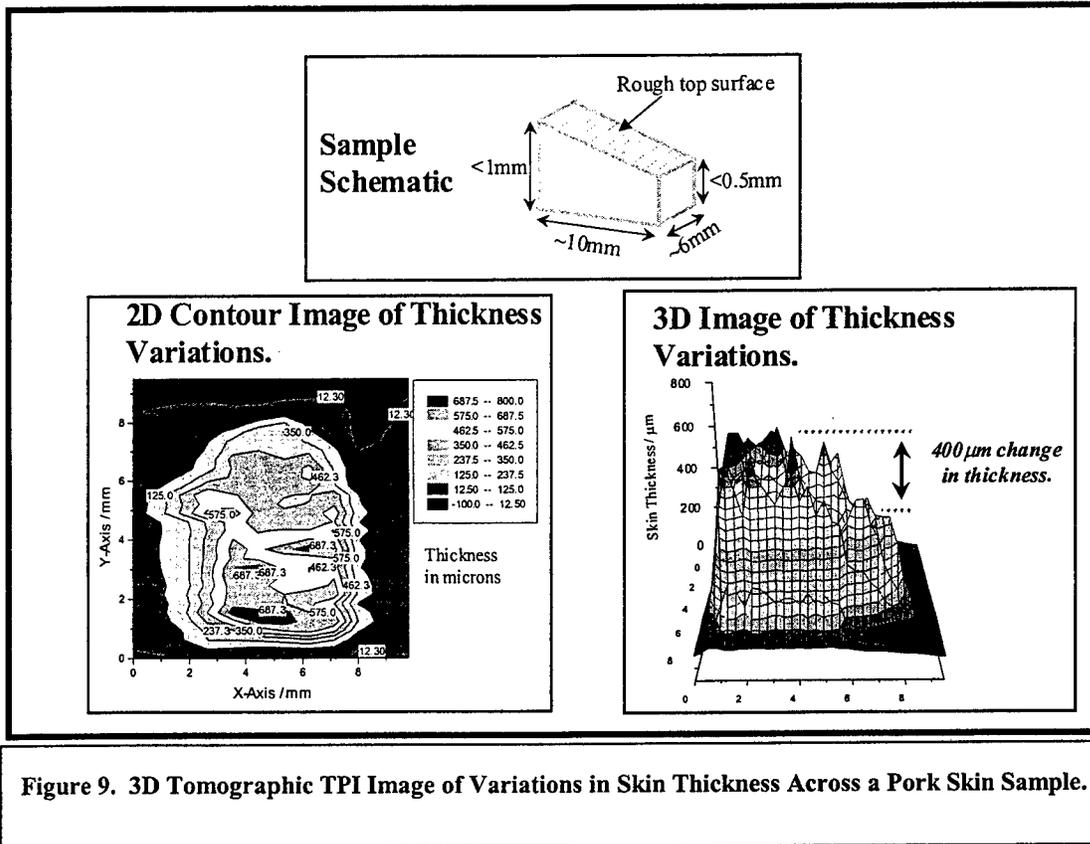
Figure 9. 3D Tomographic TPI Image of Variations in Skin Thickness Across a Pork Skin Sample.

Another set of contrast mechanisms available in TPI which further distinguishes it from some of the conventional imaging technologies is the ability to accurately determine (to within <10fs) the time of flight of the THz pulse through an object. The time of flight or delay of a THz pulse through an object of thickness d and refractive index n, relative to a reference pulse travelling through air, is given by

$$Delay = d(n-1) / c. \tag{2}$$

Hence, by measuring the delay of the THz pulse passing through an object at speed c/n relative to a reference pulse traveling at the speed of light in free space c, the thickness d can be determined to an accuracy of typically ±1μm. By plotting the thickness determined from Eq. (2) at each X-Y pixel, a 3D tomographic image of the object thickness can be easily constructed. Fig. 9 shows such an image of a 10mmx6mm area dried pork skin sample that varied in thickness from approximately 1mm at one end to <0.5mm at the other end. In Fig. 9, the sample is depicted schematically along with the 3D TPI transmission image, which faithfully reconstructs the thickness variation in the X-Y plane. Moreover, the thickness variations seen in the image were reproducible, corresponding to changes in thickness on the order of 100-200μm on a length scale of 500μm to 1mm in the X-Y plane. These reproducible variations may be due to hair follicles, but further study of the skin roughness on both faces of the sample is required for confirmation. Similar variations in thickness could be recorded using reflection techniques, which suggests that TPI may prove useful in the imaging of various skin conditions and burn diagnostics, as well as serve as a means of substantiating claims for cosmetic treatments of skin.

5. TPI OF HUMAN TISSUE: AN EXTRACTED TOOTH

The obvious, ultimate goal of any medical application of TPI is to serve as an imaging and diagnostic tool on humans. Even at this early stage of development, any data on human tissue that elucidates the advantages and disadvantages of TPI relative to conventional imaging techniques is very useful. We therefore imaged an extracted human tooth. In addition to delivering the first-ever TPI images of human tissue, this preliminary study also provided an excellent demonstration of the power of TPI. In particular, we utilised the different contrast mechanisms available in TPI to construct two very different images containing different types of medically pertinent information. Both of these images were constructed from the same data set.
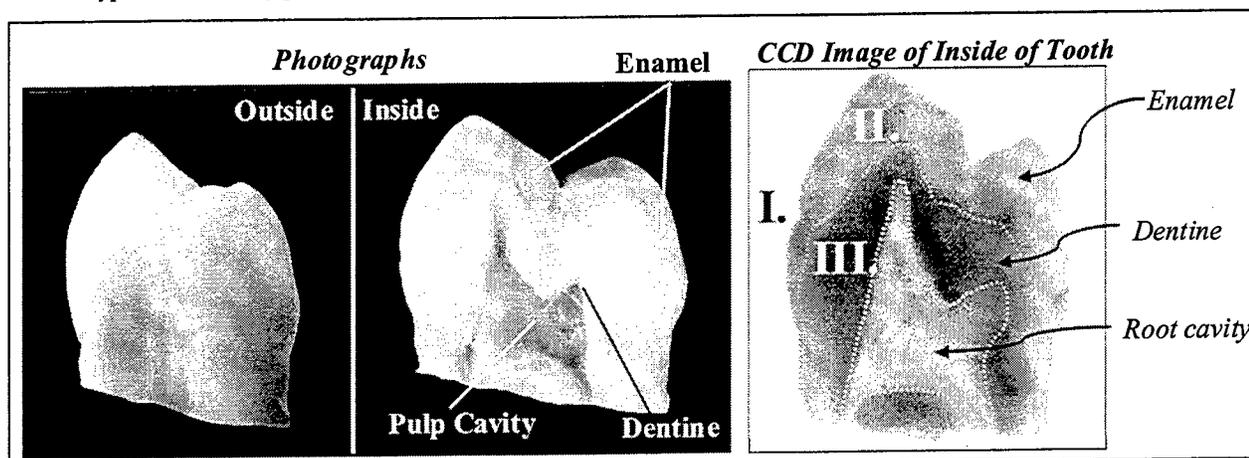
Figure 10. Visible Photographs of Outside and Inside of the Tooth, Along With Inside View Taken on a CCD Camera to Illustrate Enamel, Dentine, and Root Cavity. Images Inside Were Taken With The Tooth Cut in Half. Regions I., II., and III. are Discussed in the Text.

The tooth was an extracted premolar. At a frequency of 0.7THz, the absorption coefficient was estimated as 8cm^{-1} from a tooth that was roughly 9mm thick. In order to visibly examine the root canal, dentine, and enamel of the tooth, as well as to reduce the data acquisition time of the image, the tooth was cut in half and imaged. Fig. 10 shows external and internal photographs of the tooth, along with a view of the inside of the tooth taken by a CCD camera. The pulp cavity, enamel, and dentine can be seen on the inside photograph, but the CCD image provides even better contrast between these regions. The thickness of the tooth in the X-Y image plane varied from 1mm at one end to 4 mm at the other end.

5.1 Diagnostic Information on Enamel Thickness and Dentine: Refractive Index Imaging Using Time-of-Flight Data

Eq. (2) suggests that the changes in the refractive index from one type of tissue to another can result in large changes in the delay or time of flight of the THz pulse through the object under study. This delay or difference in the time of flight can in turn be used to construct an image of the object. To assess whether such a contrast mechanism might be utilised in dental imaging, time domain traces of the THz pulse were recorded in three different regions: I. outside the tooth, II. in the enamel region, and III. in a region covered by both enamel and dentine (see Fig. 10). Moving from outside the tooth (I) to inside the enamel region (II), a large delay (10ps) occurs as the pulse travels through the tooth enamel. As the pulse moves from the enamel region (II) into the immediately adjacent enamel and dentine region (III), a large decrease in the delay is observed (reduction to 5ps) in spite of a very small change in overall tooth thickness. This data suggests a relatively large change in refractive index at THz frequencies between the enamel and dentine. Such a change might be expected. First of all, enamel is harder and therefore is more likely to be denser than dentine, which would increase the refractive index. Accompanying this are important structural differences between enamel and dentine. Moreover, the chemical composition of the two tissues is likely to be different and also result in different indices. Enamel is ~99% mineral, whereas dentine is ~70% mineral. Such different chemical compositions are supported by the different shapes of the pulses, which show that the absorption spectra are very different in between the dentine and enamel in the THz range.

Visible image
of human tooth

Terahertz image
of human tooth

Enamel
only

Enamel
& Dentine

Image composed from
time-of-flight data
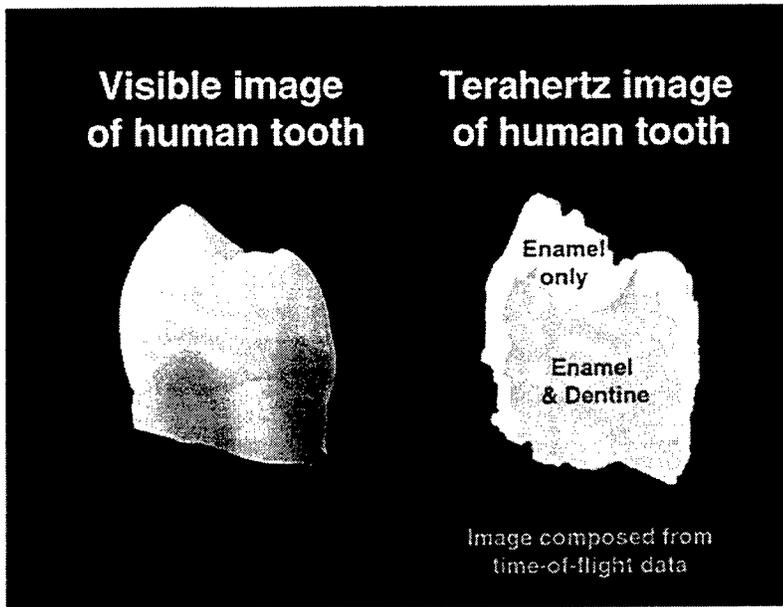
Figure 11. 2D Contour Plot of THz
Pulse Time Delay Data in Figure 14
at Different Pixels (X,Y), Along
With Photograph of Tooth.

All of the time-of-flight data is summarised in Fig.. 11, which shows a 2D contour plot of the data at each pixel. Time-of-flight data in TPI is therefore a convenient means of mapping out regions of enamel, and enamel plus dentine, as well as accurately determining the thickness of these different regions. Additional diagnostic information might be contained in the THz spectra corresponding to the various time domain traces in these different regions.

5.2 Diagnostic Information on Pulp Cavity: Panchromatic Absorption Imaging

The same THz data set used to construct the enamel and dentine images above may be manipulated in a different fashion to produce an image of the pulp cavity. Plotting the peak THz electric field of the transmitted pulse (Fig. 12) at each pixel allows us to peer into the pulp cavity. In particular, we note strong absorption in the pulp cavity (Fig. 12) which appears to reflect the build up of additional material in this area. For an empty cavity in an extracted tooth, one would expect the absorption to decrease in the cavity due to an absence of tissue. This preliminary result therefore suggests that the panchromatic absorption contrast mechanism in TPI may provide important diagnostic information about the state of the pulp cavity.

Visible image
of human tooth

Terahertz image of
cavity in human tooth

Cavity

Image composed from
absorption data
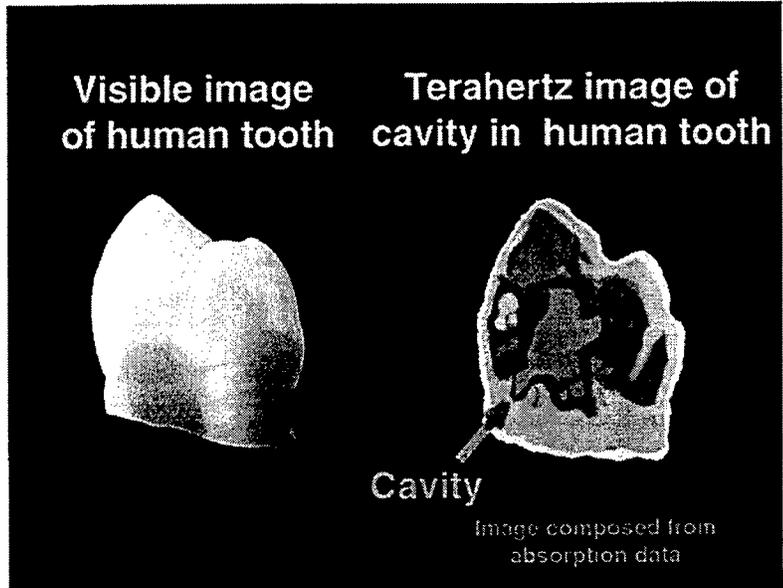
Figure 12. 2D Contour Plot of THz
Transmission Data at Different
Pixels (X,Y), Along With
Photograph of Tooth.

Figs. 11 and 12 illustrate the power of TPI; two very different images providing different information about the tooth can be constructed from the same THz data set.

217

6. FUTURE PROSPECTS FOR TPI IN MEDICAL IMAGING

6.1 Advantages Over Other Imaging Modalities

The preliminary studies of the different types of soft and hard tissue discussed above suggest that TPI may have a bright future in very specific areas of medical imaging. Relative to many conventional techniques, TPI represents a safe, non-invasive, and inexpensive clinical imaging modality with possible added diagnostic abilities. Although conventional imaging techniques such as X-Ray, X-Ray CT, MRI, ultrasound, or radioisotope imaging are currently available and yield impressive results, each has its shortcomings. These can include 1) high cost, 2) low spatial resolution, 3) safety concerns, and 4) limited or non-existent diagnostic capabilities due to lack of specificity to the chemical make-up of tissue. TPI may address some or all of these limitations: 1) lack of magnetic field and expensive X-Ray tubes imply relatively low cost, 2) spatial resolution of 200-500µm is typical for thin (<5mm) tissue, 3) THz radiation is non-ionising and the average power levels currently in use are comparable to the natural background, and the 4) spectral information inherent in TPI (extendable to down into the microwave region and up into the mid-infrared) may relay important pathological and diagnostic information.

TPI also has an important advantage relative to other laser-based imaging techniques such as fluorescence imaging and optical coherence tomography that operate in the near-infrared and visible regions of the spectrum. The development of optical-based imaging modalities has traditionally been hindered by the scattering of light in the tissue at the relatively short wavelengths used in the near-infrared and visible (e.g. λ=400nm-1300nm). The result of this scattering is attenuation of light as well as image blurring. Scattering can significantly alter the directionality, intensity, coherence, polarisation, and pulse width of the radiation probing an object. Whilst recent advances[4] have sought to redress the effects of scattering at these short wavelengths using techniques which manipulate time resolved luminescence or ballistic and snake photons, scattering remains a considerable obstacle in most biomedical applications. For highly scattering or thick media, image bearing light such as ballistic or snake photons become weak. Complicated light patterns around the object must then be measured, and this data modeled with complex computer analysis to reconstruct the image[5]. THz light, by contrast, has very long wavelengths (e.g. λ=15µm-3mm). Because the scattering probability is inversely proportional the fourth power of wavelength, $1/\lambda^4$, significant improvements are expected to rapidly occur in image quality and signal-to-noise ratios as one increases the wavelength. For example, using typical wavelengths of λ_{vis} =800nm for optical imaging and λ_{THz}=150µm for TPI, scattering should be reduced by a factor of over a billion (1.2×10^9) in THz imaging and spectroscopy of tissue. This should lead to paradigm shift in the quality of optical images at THz frequencies. Our preliminary work on the human tooth using TPI suggests that this is the case; spatial resolution on the order of 200µm was achieved with no evidence of significant scattering of the THz beam.

6.2 Prospects for Overcoming the Limitation on Penetration Depth

TPI really suffers from only one significant disadvantage relative to conventional and visible/near-infrared imaging techniques that must be overcome before imaging deep inside the body is feasible. Water has strong and broad librational (19.5THz) and stretching (6THz) absorption modes in the THz range[6]. Absorption is particularly acute toward the high frequency end of the THz region (Fig. 13). Using the 0.3THz-2.7THz bandwidth, 1µW average power, and fJ pulse energies available from our current TPI system, 2-3mm of moist dermal tissue can be penetrated, similar to typical penetration depths for ballistic photons used in visible and near-infrared imaging. However, the penetration depth for THz can be considerably improved by increasing THz power. Ultimately, the signal-to-noise ratio of a TPI system will determine the useful penetration depth in image acquisition, and therefore any improvement in incident THz power will allow thicker tissue to be examined. For example, preliminary work suggests that increasing the average THz power to the 1mW level will allow up to 8mm of skin to be imaged in the

Figure 13. Water Absorption Coefficient in Millimetre Wave, THz, and Mid-Infrared.

present bandwidth range. Very recent innovations at TREL have further increased the visible to THz conversion efficiency of the semiconductor crystal and allowed us to reach such power levels using conventional, unamplified ultrafast laser

oscillators. These power levels may also be achieved using photoconductive converters, and/or ultrafast regenerative laser amplifiers to boost the visible pulse energy available to pump the semiconductor. Thus, substantial gains in penetration depth will be achieved as THz power levels rise due to advanced engineering of semiconductors for greater visible to THz conversion efficiency, as well as the use of more compact, affordable, and powerful laser regenerative amplifiers.

Fig. 13 also shows that moving down or significantly up in frequency away from our current range (0.3THz-2.7THz) will be beneficial due to reduced water absorption. For example, with our current modest signal to noise ratio of 500:1, approximately 335μm of water can be studied in transmission measurements given our current bandwidth which peaks near 2.0THz. Shifting our coverage down to even 0.3THz would allow penetration through approximately 1mm of water. Similarly, water absorption decreases in the mid-infrared between 30THz and 45THz, as well as 54THz to 90THz, but this absorption is still larger than in the visible and near-infrared between 700nm and 1300nm. EOS detection as described in Section 2.1 has been used to extend coverage to the entire frequency range from 100GHz up to 70THz in a single THz pulse[7]. Combining such techniques with higher powers may provide one possible route to imaging much deeper into the body.

Most importantly, it should be noted that the preliminary indications of our studies suggest that water may not necessarily be as limiting a factor on tissue penetration depth as one might assume. Studies on the moist model human dermis in Section 3.2 suggest that at 2.0THz, the absorption coefficient for a sample is $\alpha \sim 35 cm^{-1}$, implying a penetration depth of 1.8mm for our modest signal-to-noise ratio of 500:1. This agrees well with experiment, where we comfortably went through 1.5mm of dermis without significant noise limitations. By contrast, the absorption coefficient for water near 2.0THz is $\alpha \sim 185 cm^{-1}$, over 5 times larger than that of the dermis. Thus, an analysis based solely on water content would imply that only 334μm of dermis could be penetrated, over 5 times less than found in practice. The limited contribution of water to the absorption coefficient is also demonstrated by the fact that a 2.0THz, $\alpha \sim 35 cm^{-1}$ for moist dermis whereas $\alpha \sim 29 cm^{-1}$ for dry dermis. The 1mW average power levels that are now achievable suggest that ~ 4mm of moist dermis could be probed. Our results in Figs. 5 and 6 (Section 3.1) on animal tissue imply that other tissue types such as fat and cartilage may have even smaller values of α and hence much larger penetration depths. By way of example, tissue with $\alpha = 25 cm^{-1}$ could be probed to depths of 5mm, whereas $\alpha = 3 cm^{-1}$ would allow tissue thickness in excess of 4cm to be imaged. This information points strongly to the need for more comprehensive, systematic, and accurate characterisation of the absorption coefficient α and the refractive index n of a variety of different tissue types at THz frequencies. Such a development programme is needed to pinpoint the areas of medical imaging where TPI will and will not be effective for imaging requiring deep penetration. Married with such efforts should be a continued programme to improve signal-to-noise ratios through more powerful sources and sensitive detectors. Lastly, effort is concentrated on the development of an innovative system for *in-vivo* TPI.

[1] B.B. Hu and M.C. Nuss, *Optics Letters* **20** 1716-1718 (1995).

[2] Q. Wu, T.D. Hewitt, and X.-C. Zhang, *Applied Physics Letters* **69** 1026-1028 (1996).

[3] A model dermis is formed by growing a collagen disk that has in it human fibroblasts that have caused the collagen to cross link and hence condense to form into a disc. The collagen comes from rats, and all growth is carried out in an incubator. The samples are stored in an incubator up to several hours before the experiment in an attempt to keep them 'alive' during the experiment.

[4] P. French, *Physics World* **69** 41-46 (June 1999).

[5] S.K. Gayen and R.R. Alfano, *Optics Express* **4** 475-480 (1999).

[6] L. Thrane, R.H. Jacobsen, P. Uhd Jepsen, and S.R. Keiding, *Chemical Physics Letters* **240** 330-333 (1995).

[7] A. Leitenstorfer, S. Hunsche, J. Shah, M.C. Nuss, and W.H. Knox, *Applied Physics Letters* **74** 1516-1518 (1999).

Subpicosecond time-resolved terahertz time-domain spectroscopy of transient carrier dynamics in semiconductors

Michael Schall, Markus Walther, Carsten Winnewisser, Hanspeter Helm, and Peter Uhd Jepsen[*]

Department of Molecular and Optical Physics, University of Freiburg

Hermann-Herder-Str. 3, D-79104 Freiburg, Germany

ABSTRACT

We have applied a newly developed transient terahertz time-domain spectrometer to study the temporal development of the dynamics of photogenerated carriers in semiconductor materials. The study presented here include semi-insulating (SI) and low-temperature-grown (LT) GaAs. By measuring the detailed shape of a subpicosecond electrical field pulse (THz pulse) transmitted through the sample at a time T after excitation with a femtosecond laser pulse, the absorption coefficient and refractive index in the region between 0.1 THz and 3 THz can be measured with high accuracy. By varying the time T, the transient absorption and index spectra can be measured with subpicosecond time resolution. Temporal and spectral behaviour of the carrier dynamics in SI and LT GaAs, in dependence of intensity and wavelength of the excitation pulse, is measured. We directly observe carrier scattering to the sidevalleys and the subsequent return of the carriers to the central valley. The experimental data strongly suggest that the transmission of the THz pulse through the photoconducting surface layer of the semiconductor can be described as instantaneous tunneling of the electric field through a metal-like barrier.

Keywords: Time-resolved spectroscopy, pump-probe, transient carrier dynamics, THz time-domain spectroscopy

1. INTRODUCTION

Terahertz time-domain spectroscopy (THz-TDS) is by now a proven and reliable technique to measure the complex dielectric function (i.e the absorption coefficient and the refractive index) of samples in the THz region of the electromagnetic spectrum with very high accuracy.[1-5] THz-TDS is based on the generation and detection of a freely propagating subpicosecond electrical field pulse with a large bandwidth compared to the center frequency. Typical characteristics of a THz pulse is a central frequency of 1 THz, with a useful spectrum extending from a few tens of GHz to 3-4 THz. The conventional THz-TDS system relies on the large bandwidth of the THz pulse, and make no explicit use of the potential time resolution offered by the short pulses.

In this paper we present results obtained with a THz-TDS system capable of measuring the complex dielectric function of a sample with subpicosecond time resolution in the spectral region between 0.1 THz and 3 THz. We have investigated the transient absorption and index spectra of semi-insulating (SI) GaAs, subsequent to excitation with a 800 nm or 400 nm visible laser pulse. THz pulses are versatile probes of charge carrier relaxation dynamics in semiconductors. Excited carriers absorp THz radiation in dependence of the instantaneous mobility, which is highest at the minimum of the conduction band of the semiconductor. Therefore, the absorption coefficient of a photoexcited semiconductor in the THz region is proportional to the carrier density near the conduction band minimum. As will be demonstrated in this paper, the transient absorption in the THz region directly shows important aspects of relaxation of carriers from a hot state with excess energies of 120 meV and 1.67 eV (800 nm and 400 nm excitation, respectively). At 800 nm excitation wavelength, the only relaxation path is energy exchange with LO phonons within the central Γ valley. At 400 nm excitation wavelength, scattering of carriers to the L and X side valleys dominates the first picoseconds of the transient absorption curves.

We also applied the transient THz spectrometer to the investigation of carrier dynamics in LT GaAs after excitation with 800 nm and 400 nm optical pulses. LT GaAs grown by molecular beam epitaxy has a short carrier lifetime and a relatively high carrier mobility, making it potentially interesting for ultrafast optoelectronic switching applications. The measurements presented here show the influence of substrate temperature and arsenic pressure during growth on carrier dynamics in the material. The sample series represent an almost complete transition from SI characteristics to LT characteristics.

---

[*]email address: jepsen@uni-freiburg.de

220

Part of the EUROPTO Conference on Terahertz Spectroscopy and Applications II
Munich, Germany • June 1999 SPIE Vol. 3828 • 0277-786X/99/$10.00

Carrier dynamics in semiconductors is a very intensely studied topic. For an overview of results and experimental techniques over the last 2 decades, see e.g. Ref. 6 and references therein.

Results of a few other experiments on transient THz-TDS have been published. In 1994, Groeneveld and Grischkowsky measured relaxation dynamics of carriers and excitons in GaAs-based quantum wells.[7] In 1996, Zielbauer and Wegener investigated dynamics of photoexcited carriers in silicon.[8] Recently, McElroy and Wynne used transient THz-TDS to investigate solvation dynamics of dyes in polar solution.[9]

2. EXPERIMENTAL SETUP

The experimental setup used in this work is schematically illustrated in Fig. (1). The setup is driven by laser pulses
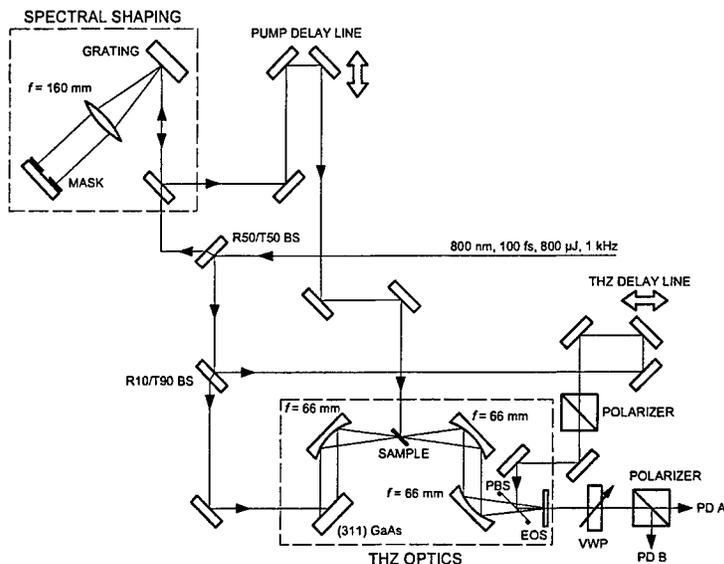
Figure 1. Experimental setup. BS = beamsplitter, PBS = pellicle beam splitter, EOS = electro-optic sampling element, VWP = variable wave plate, PD = photodiode.

from a regeneratively amplified Ti:sapphire oscillator (Clark-MXR CPA-1000). The pulses arrive at the setup with a tunable central wavelength of 790-820 nm, bandwidth of 15 nm, pulse duration of 100 fs, and pulse energy of 800 μJ. The repetition rate is 1000 Hz. The setup consists of two parts, the THz spectrometer and the pump beam arrangement, which will be described in the following.

2.1. THz spectrometer

The THz beam is generated at a (311) GaAs surface by optical rectification of the excitation pulse (energy 50 μJ). The excitation beam is unfocused with a diameter of 1.5 cm. The resulting train of THz pulses is emitted in a nearly parallel beam, and is guided by three off-axis paraboloidal mirrors in a $f - 2f - f$ geometry to the detector. The THz beam is focused to a diffraction-limited spot between the two first mirrors and at the detector surface. The sample under investigation is placed at the focal point of the first mirror.

The temporal shape of the THz pulse is measured by free-space electro-optic sampling.[10,11] Briefly, the THz pulse and a 800 nm probe pulse (linearly polarized at 45° with respect to the polarization of the THz beam) is propagating collinearly inside an electro-optic crystal. After the crystal the phase between the two polarization components of the probe beam has been retarded in proportion to the instantaneous electrical field of the THz pulse. This phase retardation is measured by a set of balanced photodiodes after a second polarizer, biased to the quarter-wave point by a variable waveplate. This setup assures a linear relation between the difference voltage of the photodiodes and the electric field of the THz pulse. By gradually changing the delay between the THz pulse and the probe pulse while monitoring the photodiode signal, the temporal shape of the THz pulse is measured. A mechanical chopper, locked to the 8th subharmonic (125 Hz) of the laser repetition rate, is placed in the beam exciting the THz emitter, and the photodiode difference signal is measured with a lock-in amplifier.

2.2. Pump beam arrangement

The pulses in the pump beam have an energy of 500 μJ. The pump beam is sent through a variable delay line, which controls the arrival time of the pump pulse at the sample surface with respect to the arrival time of the THz probe pulse. The bandwidth and central wavelength of the pump pulse is controlled in a pulse shaper, inserted in the pump beam path. The bandwidth of the shaped pulse can be adjusted from a fraction of a nm to the full bandwidth of the unshaped pulse (approx. 15 nm). The experiments presented in this paper are all performed using the full spectrum of the pump pulse. The sample is oriented at 45° with respect to both the THz beam and the pump beam, and is illuminated by the pump beam on the back surface with respect to the THz beam. With this pump geometry there are no optical components in the THz beam path while the high time resolution is maintained, assuming that only the surface of the sample is excited by the pump beam. In GaAs, the absorption depth is less than 1 μm for 800 nm photons and a few hundred nm for 400 nm photons.

3. RESULTS AND DISCUSSION

In Fig. (2) a typical THz pulse shape and the corresponding frequency spectrum is shown. The pulse has a usable
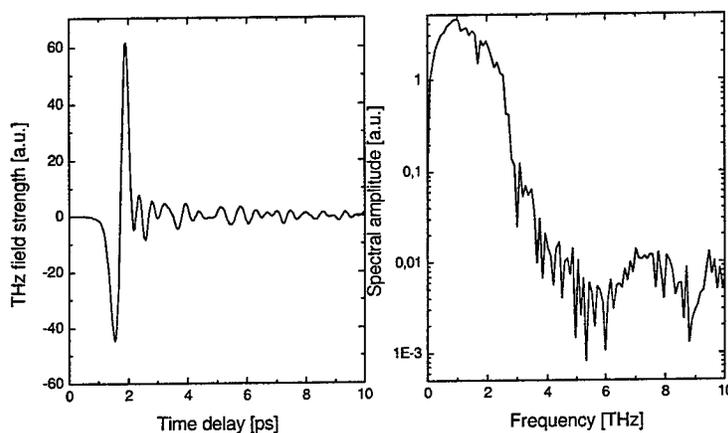
Figure 2. THz pulse shape and corresponding frequency spectrum.

spectrum extending from below 0.1 THz to 3 THz. The spectral cut-off above 3 THz is caused in part by closely spaced rotational absorption lines from residual water vapor in the THz beam path, and in part by the 5.3 THz phonon absorption band in the ZnTe detector crystal. We observe a weak, but significant, recovery of the spectrum at 7-8 THz. The spectral dip seen at 9 THz could originate from the TO phonon absorption in the GaAs emitter.

In this paper we perform two types of transient measurements, described below.

3.1. Frequency-resolved transient absorption

By measuring the pulse shape of the THz pulse transmitted through the sample with and without pumping, the transient absorption- and index spectrum within the useful bandwidth of the THz pulse can be found. If the delay between the THz probe pulse and the visible pump pulse is T, the frequency-dependent transient absorption and refractive index can be found by

$$\frac{E(\nu,T)}{E(\nu,T<0)} = \frac{\mathcal{F}(E(t,T))}{\mathcal{F}(E(t,T<0))} = \exp(-\Delta\alpha(\nu)d)\exp(i2\pi\nu\Delta n(\nu)d/c) \qquad (1)$$

where $\mathcal{F}(E)$ is the Fourier transform of the temporal THz field shape, $\Delta\alpha$ is the transient field absorption coefficient, Δn is the transient index change, and d is the effective thickness of the layer excited by the pump pulse, defined by the absorption depth of the pump light. Hence, by measuring the temporal shape of the THz pulse transmitted through the sample at different times with respect to the pump pulse, the transient absorption and index spectra can be extracted.

3.2. Frequency-integrated transient absorption

The temporal shape of the THz pulse is determined by the phase relation between all frequency components within the bandwidth of the pulse. At $t = 0$ all frequency components add up constructively to form the central subpicosecond peak of the THz pulse. This means that the change of the peak THz field strength caused by absorption in the sample is directly proportional to the sample absorption, integrated over the bandwidth of the pulse.

$$E_{THz,peak} \quad \propto \quad \exp(-\overline{\alpha}d) \tag{2}$$

$$\overline{\alpha} \quad = \quad \frac{1}{\nu_{max}} \int_0^{\nu_{max}} \alpha(\nu)d\nu \tag{3}$$

In many situations the integrated absorption change gives valuable information about carrier dynamics in the sample. Furthermore, from an experimental point of view this technique is much faster than the aquisition of the full transient absorption- and index spectra.

3.3. Semi-insulating GaAs

We have measured the transient absorption and refractive index of SI GaAs (resistivity $> 10^7 \Omega$ cm, band gap 1.43 eV at 300 K), pumped by optical pulses with wavelengths of 800 nm and 400 nm. The pulse energy in both cases were approx. 1 μJ, corresponding to an initial carrier density of approx. 10^{17} cm^{-3}. In Fig. (3) experimental data for 800 nm pump wavelength are shown. Fig. (3a) shows the transient frequency-integrated absorption of the THz
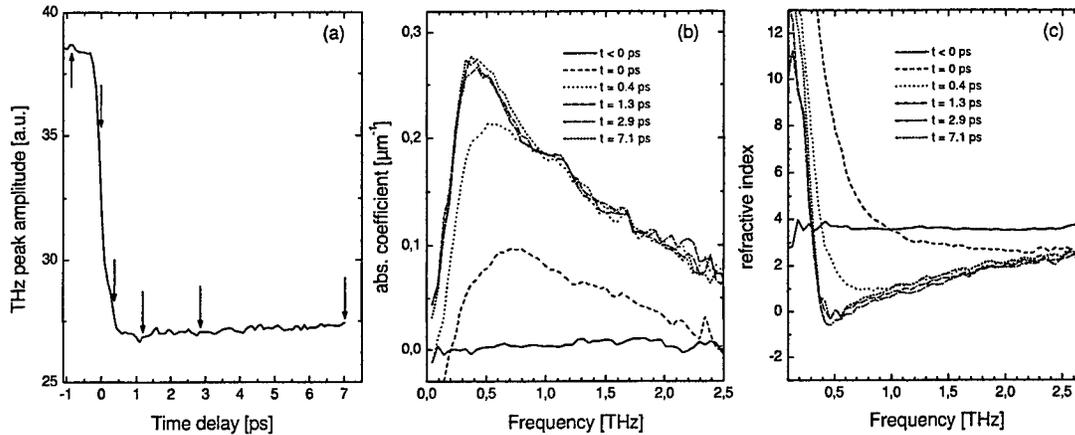
Figure 3. (a) Temporal development of transmitted peak THz field strength. (b) Transient absorption spectra. (c) Transient refractive index spectra.

pulse after transmission through the sample. The arrows indicate the points at which transient absorption and index spectra are measured. In Fig. (3b) the transient absorption spectrum is shown for at $t < 0$ ps, $t = 0$ ps, $t = 0.4$ ps, $t = 1.3$ ps, $t = 2.9$ ps, and $t = 7.1$ ps. In Fig. (3c) the transient refractive index spectrum is shown. The absorption coefficient and the index is calculated by assuming that the excited layer has a thickness of 5 μm. We notice that this is approximately 10 times larger than the expected absorption depth of 800 nm photons in GaAs.

The absorption coefficient and the refractive index changes from the dielectric behaviour of semi-insulating GaAs to a metal-like behaviour within less than one picosecond. We interpret this as the relaxation of the electrons from the initial excess energy of 120 meV to the minimum of the Γ valley. Once the electrons are thermalized they recombine with the holes in the valence band with a recombination time of several hundred ps, much slower than the time scales investigated here. The shape of the absorption and index spectra of the thermalized carriers agrees qualitatively with the behaviour of carriers as predicted by the Drude model of conduction.[3] The connection between the absorption and index spectra ($\alpha(\omega)$ and $n(\omega)$, respectively) and the Drude model is

$$\hat{\epsilon}(\omega) = \epsilon_\infty - \frac{\omega_p^2}{\omega(\omega + i\Gamma)} = \hat{n}^2 = (n(\omega) + i\alpha(\omega)c/\omega)^2 \tag{4}$$

223

where $\hat{\epsilon}$ is the complex frequency-dependent permittivity, ϵ_∞ is the permittivity at optical frequencies, ω_p is the plasma angular frequency, and Γ is the damping rate (inverse collision time) of the carriers.

The same experiment was performed with 400 nm pump wavelength, corresponding to an excess energy of the carriers of 1.67 eV. The results are presented in Fig. (4). The frequency-integrated absorption (Fig. (4a)) shows
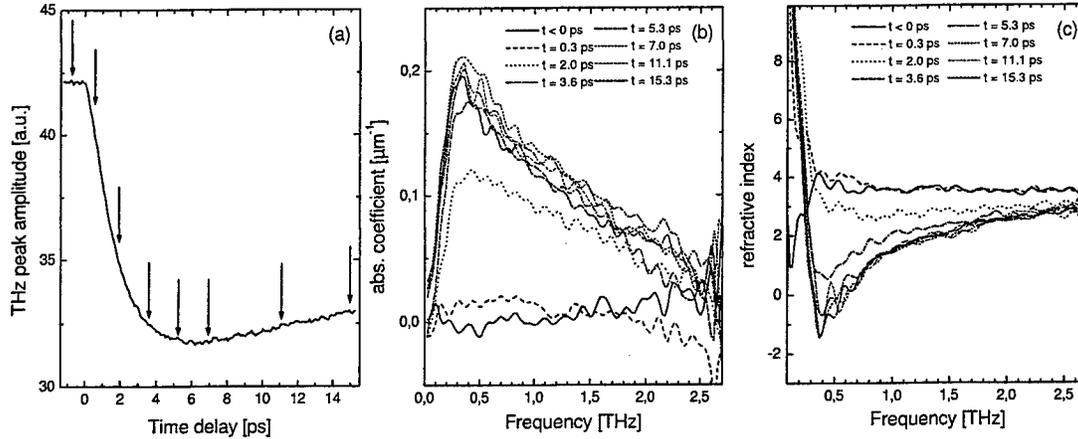
Figure 4. (a) Temporal development of transmitted peak THz field strength. (b) Transient absorption spectra. (c) Transient refractive index spectra.

a completely different behaviour. The maximum absorption is reached after 6 ps, and the subsequent decrease in absorption is much faster than in the case of 800 nm excitation. The slower rise time of the absorption we attribute to initial fast scattering to the side valleys followed by a slower scattering and relaxation back to the minimum of the Γ valley. The transient absorption and index spectra shows the same behaviour as seen in Fig. (3), except that the carriers are thermalized much slower. The absolute absorption coefficient and index after 6 ps is the same as with 800 nm excitation, showing that after the thermalization, the carrier dynamics is independent of the initial carrier distribution.

The detailed analysis of the absorption and index spectra, including a quantitative comparison with the Drude model, is in preparation.[14]

3.4. Low-temperature-grown GaAs

We have measured the frequency-integrated absorption of a series of LT GaAs samples, grown by molecular beam epitaxy with growth parameters indicated in Table (1).[12] It is expected that a low growth temperature, combined

Sample	Growth temperature	As$_4$ pressure	[As$_4$] : [Ga]	As antisite concentration
III-305	200° C	$15 \cdot 10^{-6}$ Torr	18	$15 \cdot 10^{19}$ cm^{-3}
III-306	200° C	$8 \cdot 10^{-6}$ Torr	9	$11 \cdot 10^{19}$ cm^{-3}
III-307	300° C	$15 \cdot 10^{-6}$ Torr	18	$6.4 \cdot 10^{19}$ cm^{-3}
III-308	300° C	$9 \cdot 10^{-6}$ Torr	11	$6.2 \cdot 10^{19}$ cm^{-3}
III-309	300° C	$7 \cdot 10^{-6}$ Torr	8	$4.8 \cdot 10^{19}$ cm^{-3}

Table 1. Growth parameters for the LT GaAs samples studied in this work. All samples are grown to 2 μm thickness on a SI GaAs substrate.

with a high As concentration during growth, and subsequent annealing at 500-600 degrees leads to the shortest response time of the sample. In the following we show that this agrees well with the interpretation of transient THz absorption curves of the samples. In Fig. (5) the different samples have been excited by 800 nm pulses with an energy of 80 μJ, corresponding to an initial carrier density of 10^{18} cm^{-3} to 10^{19} cm^{-3}. In part (a) of the figure the product of the absorption coefficient and the thickness of the photoconductive layer is plotted as function of
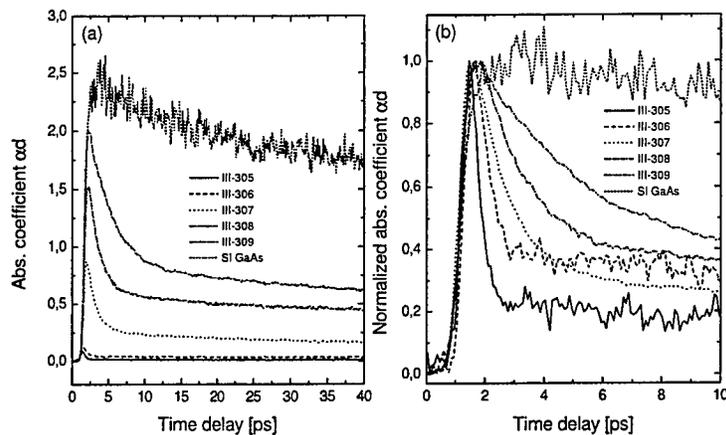
Figure 5. Transient absorption of different LT GaAs samples, pumped at 800 nm.

time. In part (b) of the figure, the absorption coefficients are normalized for direct comparison of the decay time of the signals. The transient absorption coefficient for SI GaAs, pumped with 10 μJ energy, is also included in the figure. Fig. (5) shows that the transient absorption signal is fastest for the sample grown at 200° with a high As pressure. With increasing growth temperature and decreasing As pressure, the transient absorption signal is slower, approaching that of SI GaAs. The rise time of the transient absorption coefficient is the same for all the samples. The slow tail of the transient absorption coefficient is believed to be a bulk effect. The LT GaAs layer is two microns thick, allowing a small fraction of the 800 nm photons to penetrate into the highly responsive substrate. Therefore the total absorption will be a superposition of a fast component from the LT layer and a slow component from the SI substrate.

The development of the transient absorption coefficient of the samples grown at 300°, pumped with 400 nm pulses with an energy of 15 μJ, is illustrated in Fig. (6). We only found significant absorption in the samples grown at 300°.
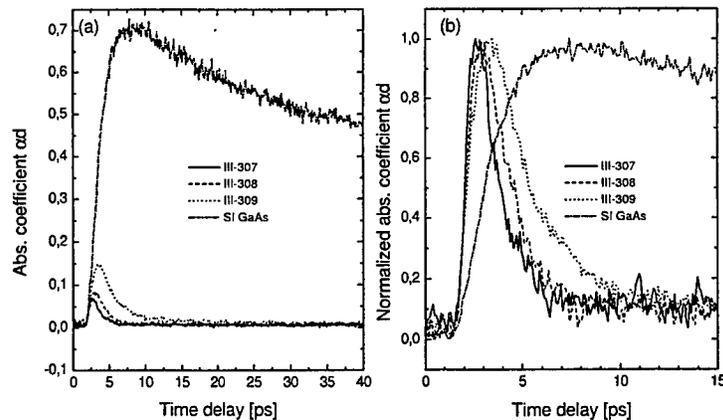
Figure 6. Transient absorption of different LT GaAs samples, pumped at 400 nm.

With 400 nm pump we observe that the falling edge of the absorption coefficient shows the same behaviour as when the samples are pumped with 800 nm pulses. Additionally, we notice that the rising edge of the absorption curve is much faster than observed in SI GaAs. The set of data in Fig. (7) illustrates the development of the absorption coefficient of a particular sample (III-308) in dependence of the pump power at 800 nm wavelength. The pump power is increased from 2.3 μJ to 80 μJ, corresponding to initial carrier densities from 10^{17} cm^{-3} to 10^{19} cm^{-3}. The rising edge of the absorption signal shows no intensity dependence, whereas the falling edge of the signal is slower at high

225
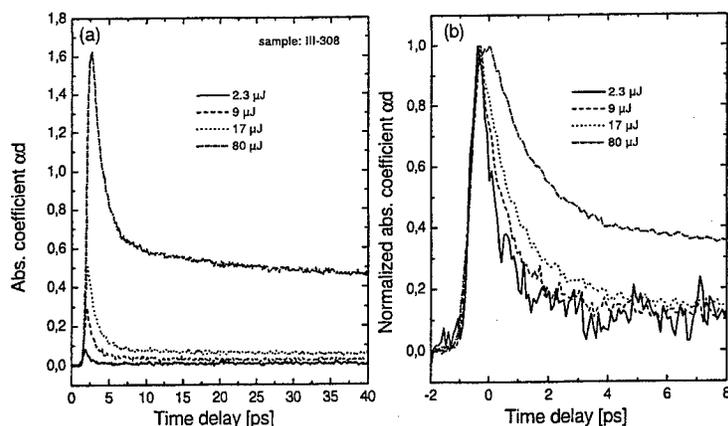
Figure 7. Transient absorption of LT GaAs, pumped at 800 nm with different intensities. The time constant of the initial decay increases from 0.8 ps to 6 ps.

pump intensities. Similar behaviour was observed by Sosnowski et al.[13]

The differences between the transient absorption in SI GaAs and LT GaAs are attributed to the presence of midband states in LT GaAs, caused by excess As.[6,13] Carriers are easily de-excited to the midband states, which therefore act as a highly effective carrier drain, with a resulting ultrafast response time. A relatively simple set of rate equations, taking the different scattering mechanisms into account, reproduces the transient absorption data quite well, and is the topic of a forthcoming publication.[15]

3.5. THz tunneling

One peculiar observation is that the THz pulse seems to arrive earlier at the detector when it is transmitted through the excited surface layer than if it is transmitted through the normal surface layer. This is caused by the huge index change of the surface layer, obvious from Fig. (3) and Fig. (4). The time difference is illustrated in Fig. (8). The time difference between the two pulses is 42 fs. With the refractive index of SI GaAs of 3.5, this corresponds
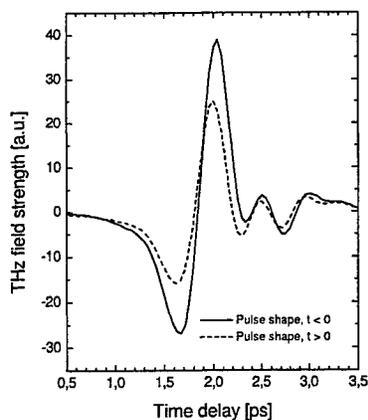
Figure 8. The THz pulse arrives 42 fs earlier at the detector when the GaAs surface is excited by the pump beam.

to a distance $\Delta x = c\Delta t/n = 3.6\mu m$, which has been traversed instantaneously. This instantaneous propagation of the field is highly reproducible, and is observed at both 400 nm and 800 nm pump wavelengths. The effect will be discussed in detail in a forthcoming publication.[16]

4. CONCLUSION

We have demonstrated the operation of a transient THz time-domain spectrometer with subpicosecond time resolution by probing transient carrier dynamics in GaAs. SI GaAs was optically pumped with femtosecond pulses at 800 nm and 400 nm, and the subsequent development of the absorption and refractive index spectrum was measured. At 800 nm, energy relaxation of the carriers occurs on a time scale faster than 1 ps. At 400 nm pump wavelength the electrons are created in a highly excited state where scattering to the X and L side valleys and rescattering to the minimum of the central Γ valley dominates the development of the absorption and index spectra.

ACKNOWLEDGMENTS

REFERENCES

1. D. Grischkowsky, S. Keiding, M. van Exter, and C. Fattinger, "Far-infrared time-domain spectroscopy with terahertz beams of dielectrics and semiconductors", *J. Opt. Soc. Am. B* **7** (10) 2006-2015 (1990)

2. M. van Exter and D. Grischkowsky, "Carrier dynamics of electrons and holes in moderately doped silicon", *Physical Review B* **41** (17) 12140-12149 (1990)

3. T.-I. Jeon and D. Grischkowsky, "Nature of conduction in doped silicon", *Phys. Rev. Lett.* **78** (6) 1106-1109 (1997)

4. T.-I. Jeon and D. Grischkowsky, "Observation of a Cole-Davidson type complex conductivity in the limit of very low carrier densities in doped silicon", *Appl. Phys. Lett.* **72** (18) 2259-2261 (1998)

5. R. A. Cheville and D. Grischkowsky, "Far-infrared foreign and self-broadened rotational linewidths of high-temperature water vapor", *J. Opt. Soc. Am. B* **16** (2) 317-322 (1999)

6. A. Othonos, "Probing ultrafast carrier and phonon dynamics in semiconductors", *J. Appl. Phys.* **83** (4) 1789-1830 (1998)

7. R. H. M. Groeneveld and D. Grischkowsky, "Picosecond time-resolved far-infrared experiments on carriers and excitons in GaAs-AlGaAs multiple quantum wells", *J. Opt. Soc. Am. B* **11** (12) 2502-2507 (1994)

8. J. Zielbauer and M. Wegener, "Ultrafast optical pump THz-probe spectroscopy on silicon", *Appl. Phys. Lett.* **68** (9) 1223-1225 (1996)

9. R. McElroy and K. Wynne, "Ultrafast dipole solvation measured in the far infrared", *Phys. Rev. Lett.* **79** (16) 3078-3081 (1997)

10. Q. Wu and X.-C. Zhang, "Free-space electro-optic sampling of terahertz beams", *Appl. Phys. Lett.* **67** (24) 3523-3525 (1995)

11. P. Uhd Jepsen, C. Winnewisser, M. Schall, V. Schyja, S. R. Keiding, and H. Helm, "Detection of THz pulses by phase retardation in lithium tantalate", *Phys. Rev. E* **53** (4) R3052-R3054 (1996)

12. A. Lohner, J. Vetterhöffer, J. Weber, W. W. Rühle, and K. Köhler, "Carrier lifetime in low temperature grown GaAs", unpublished.

13. T. S. Sosnowski, T. B. Norris, H. H. Wang, P. Grenier, J. F. Whitaker, and C. Y. Sung, "High-carrier-density electron dynamics in low-temperature-grown GaAs", *Appl. Phys. Lett.* **70** (24) 3245-3247 (1997)

14. M. Schall and P. Uhd Jepsen, "Direct observation of transient Drude conductivity in GaAs", in preparation.

15. M. Schall and P. Uhd Jepsen, "Carrier dynamics in LT GaAs studied by transient THz time domain spectroscopy", in preparation.

16. M. Schall and P. Uhd Jepsen, "Direct evidence of instantaneous tunneling of a terahertz pulse", in preparation.

Pulsed optical THz technology --- generation and amplification of coherent THz radiation

Peter Haring Bolivar, Rainer Martini, and Heinrich Kurz

Institut für Halbleitertechnik II, RWTH Aachen, D-52056 Aachen, Germany
haring@iht-ii.rwth-aachen.de

ABSTRACT

State-of-the-art coherent THz radiation sources are reviewed and inversion-less amplification mechanisms are presented, which are applicable to a wide variety of optically impulsively excited THz emitters. The amplification schemes will be experimentally demonstrated and fundamental limitations and prerequisites discussed, stressing analogies and differences to standard amplification by stimulated emission.

Keywords: Coherent THz sources, amplification without inversion, femtosecond laser technology

1. INTRODUCTION

Terahertz radiation (1 THz = 10^{12} Hz), localized between the infrared and the microwave frequencies, has an ample application potential for the spectroscopy of gases, liquids and condensed matter. As an example, distinctive rotational transitions of molecules lie in this spectral range, permitting the direct quantitative detection and chemical analysis of gases, which is important in view of environmental monitoring or control of combustion processes [1]. Also, important semiconductor properties, like carrier concentration and mobility lead to resonances in this spectral range, which enables one to derive such information directly from THz transmission experiments [2] (examples of such applications are shown in Fig. 1). THz spectroscopy constitutes, therefore an important analytic tool, which complements standard characterization methods and opens up a manifold of new interesting applications. Impulsive optical (or *time-domain*) THz techniques [2,3] with femtosecond laser systems have achieved impressive capabilities, with an unsurpassed bandwidth, exceptional sensitivity, dynamic measurement capabilities, the ability to detect coherent THz fields directly in amplitude and phase, and even real-time THz imaging systems have been demonstrated [4]. For an overview of the developed techniques see e.g. [5].
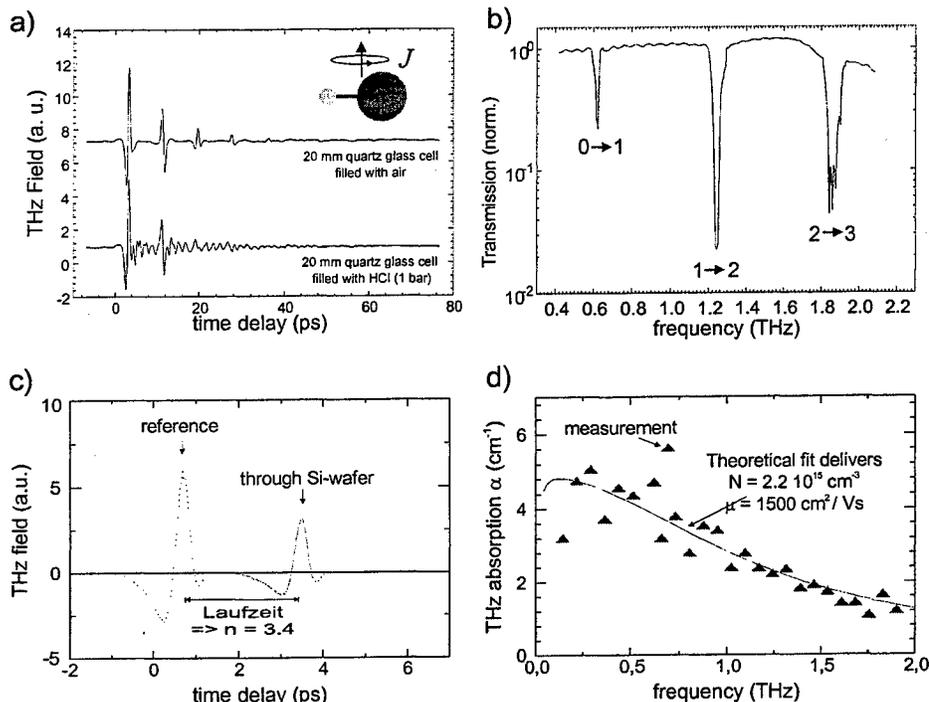
Fig. 1 Application examples for time-domain THz spectroscopy: the upper plots illustrate transients (a) and fourier spectra (b) of the THz transmission through a gas cell, which clearly illustrate the sharp rotational transitions of HCl. The lower transients (c) and spectra (d) illustrate the contact-less measurement of carrier concentration and mobility of a silicon wafer.

A key component of THz spectroscopy systems are the THz sources. In the time-domain approach most THz sources rely on the photoexcitation of coherent charge carrier distributions in appropriate semiconductor structures with femtosecond laser pulses. The dominant radiation process is then given by the acceleration of the coherent carrier ensemble, according to

228

Part of the EUROPTO Conference on Terahertz Spectroscopy and Applications II
Munich, Germany • June 1999 SPIE Vol. 3828 • 0277-786X/99/$10.00

Faraday's law of induction. Due to the coherent motion and close spacing of the ensemble of carriers, the coherent electromagnetic THz radiation is emitted in a cooperative manner. Up to now many different kinds of broadband [6-8] or tunable [9-10] emission processes have been demonstrated, and the attractive properties of time resolved techniques have raised attractive applications [5]. Nevertheless, a widespread application of the time-domain techniques is hindered by the lack of powerful and efficient THz generation processes. Although the precise efficiency of THz

emitter	$P_{THz}(nW)$	$\eta (10^{-5})$
LT-GaAs-antennas (160 kW/cm^2)		
at max. field (120 kV/cm)	720	72
at normal fields (50 kV/cm)	180	18
ID-SOS-antennas (160 kW/cm^2)		
comparison to LT-GaAs (50 kV/cm)	9	0.9
at normal fields (16 kV/cm)	0.6	0.06
In$_{0.53}$Ga$_{0.47}$As (380 W/cm^2)	180	3.2
InP (380 W/cm^2)	22	0.4
GaAs-Schottky-diodes (1100 W/cm^2, 500 kV/cm)	38	1.1
DAST (360 W/cm^2)	29	1.4
Bloch oscillations (10 kV/cm)	1.75	0.3

Fig. 2   Overview of the typical emission power levels and power conversion efficiencies of a selection of THz emitters.

emitters is strongly dependent on the exact experimental conditions, an overview containing the typical efficiency of selected THz sources pumped by a Ti:sapphire laser system is contained in Fig. 2. The power conversion efficiency is clearly extremely low (a power conversion efficiency of 10^{-6} is equivalent to a quantum efficiency of $4*10^{-4}$). An important focus of our work is thus the development of more efficient sources of coherent THz radiation. One of the main reasons restricting the efficiency of impulsively excited THz emitters is the fast loss of coherence of the photoexcited ensemble. Typically the coherence in the emitter system is destroyed by ultrafast scattering processes, restricting the cooperative motion and therefore the coherent emission time τ_{coh} to a small fraction of the radiative lifetime τ_{rad} [9]. Consequently, only a small portion of the available energy in the system is emitted coherently and the corresponding quantum efficiency $\eta = \tau_{coh} / \tau_{rad}$ is very low (typically below 10^{-3}). An efficiency enhancement can be obtained if the emission power is increased so that more energy is emitted coherently before dephasing occurs. One possibility to accomplish this power increase is the superlinear power dependence on carrier density according to the superradiant characteristics of the cooperative emission process [11]. Such an efficiency enhancement was already shown for the surface-field THz emitter InP [12] and for Bloch oscillations in GaAs / AlGaAs superlattices [13] by increasing the optical excitation intensity. But as excitation density dependent dephasing and screening effects reduce τ_{coh} for high excitation densities, only a limited efficiency enhancement can be achieved by this process. In this paper we present a method to amplify the coherent emission power by phasematched superposition with a coherent background radiation during the emission process. In contrast to former approaches the optical excitation conditions and therefore τ_{coh} remains constant during this process, avoiding a saturation of the efficiency enhancement effect. In principle the emission power can thus be enhanced until all available energy is emitted completely during τ_{coh}, e.g. the quantum efficiency can be raised to unity. This paper is organized as follows: In the first part, the principle of the amplification process is discussed, stressing analogies and differences to stimulated emission. Afterwards, the proposed properties are confirmed experimentally in a specially designed DFT setup allowing the detailed investigation of the amplification process in a single-pass configuration. The feasibility of repetitive amplification in a ring-resonator is demonstrated afterwards. The paper closes with a brief summary.

2. AMPLIFICATION PRINCIPLE

The basic amplification process is based on the superposition of a coherent background radiation during the THz emission process. If the propagating direction and the temporal shape of both the background and the newly generated THz fields are chosen identically, the electric field of the background field will interfere with the coherent intraband polarization within the THz emitter and stimulate an emission. Detailed microscopic calculations of this effect will be presented elsewhere [14], but to the external observer, the amplitudes of the background and newly generated fields just appear to up. This already turns out to be an amplification mechanism: As radiation power P scales quadratically with field amplitude, the summation of the fields leads to an overall power increase compared to an uncorrelated emission process. Consequently more energy is emitted coherently in the short time τ_{coh} before dephasing sets in. As a simple example, consider the coherent superposition of a background field (amplitude E_{BG}) with a second field (amplitude E_0) during its generation process. As the field amplitudes add up, the radiation power is raised by ΔP $(E_0 + E_{BG})^2 - (E_0^2 + E_{BG}^2) = 2E_0 E_{BG}$. The power of the background radiation is constant. Hence, the enhancement ΔP has to be attributed exclusively to the generation process of the source which is irradiated by the THz background field. The emission power of the second source has been raised by a factor of $V = 1 + 2E_{BG} / E_0$. It should be stressed that this amplification process differs from stimulated emission as e.g. V depends linearly on the background electric field amplitude and not on its power level (E_{BG}^2) as it would for stimulated emission. In the special case

229
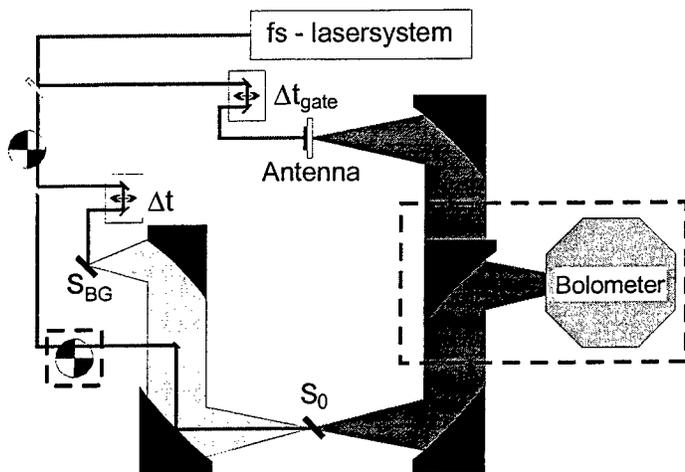
Fig. 3 Modified diffraction Fourier transforma setup used to study the amplification process. The investigated THz emission is produced from S_0 under irradiation by an independently controlled (Δt_{gen}) background emitter (S_{BG}) The combined electric field is detected and time-resolved with photoconductive antennas. Alternatively a bolometer is used to measure the time-integrated intensity in the same setup (dashed area).

of similar amplitudes ($E_0 \approx E_{BG}$) a three times stronger emission is achieved. Obviously a further increase of the background field enhances the amplification factor. A fundamental limit is only achieved when all available energy is emitted during the amplified emission process and the quantum efficiency reaches unity. It is therefore sensible to use this amplification process repetitively in a resonator setup, where the emitted radiation is coupled back and is used as background radiation driving and enhancing the next THz generation process. Each time THz radiation is emitted in phasematched superposition with the backcoupled field the total amplitude of the electric field in the resonator will be raised by the amount of E_0 yielding a quadratic growth of the radiation power. A first estimation of the maximum amplification in a resonator with a round-trip reflectivity R can thus be estimated by the formula ($E_0 /$ $(1-\sqrt{R})^2$ when stimulated emission and absorption are neglected. Considering typical resonators with $R \approx 0.9$ as an example, the power of the THz radiation can be amplified by a factor of about 380 by this coherent superposition process. Again significant differences from amplification by stimulated emission can be perceived: in our case, the power level in the resonator scales quadratically with the round-trip number instead of the exponential increase known from stimulated emission. Furthermore coherence between the backcoupled and the newly emitted radiation has to be guaranteed for amplification by coherent superposition, whereas the stimulated emitted radiation is coherent to the 'background' by nature. On the other hand no population inversion is needed for the presented amplification process. As population inversion is extremely difficult to achieve in the THz regime, this fact hence allows to apply this process to much wider group of impulsively photoexcited THz-emitters. Another point of view shows the amplification character of this process more clearly: the background radiation transmitting the emitter during the synchronously excited THz generation process can be regarded as being amplified as the coherent superposition increases its field amplitude by the amount E_0.

3. STUDY OF THE SINGLE-PASS AMPLIFICATION PROCESS

The single-pass amplification process is investigated in a modified diffracting Fourier transform setup [15] using two surface-field THz emitters made from epitaxially grown InGaAs on InP. The samples are excited with 100 fs laser pulses from a commercial Ti:sapphire laser. Figure 3 shows the setup including two complementary detection schemes for time-resolved field and time-integrated power measurements. The optically excited THz emission from the main emitter (S_0) is observed under collinear transmission of an identical THz background field produced by a second independently controlled emitter (S_{BG}). Tuning their respective generation time delay by Δt_{gen}, the temporal overlap can be adjusted in order to achieve an exact temporal overlap and thus the coherent superposition. It should be stressed that due to the temporal and spatial separation of the two emitters only the THz generation in the main emitter can be influenced by the background radiation and not vice versa – i.e. the radiated power of the background emitter remains constant. Consequently any power increase has to be attributed exclusively to an amplified THz generation process of the main emitter S_0. In the first detection scheme the combined electric field is detected with photoconductive dipole antennas gated by a third optical beam. Tuning the time-delay (Δt) of the gating pulse enables the time-resolved detection of the electric field amplitude of the combined THz radiation. Fig. 4 shows transients observed for the single (dashed lines) or combined excitation of both emitters for full temporal overlap of the two THz pulses ($\Delta t_{gen} = 0$ ps). Obviously the electric fields add, as expected for pure constructive interference. Considering that the power of the combined radiation is proportional to the square of the field amplitude, this already demonstrates an amplification of the emission of the main emitter by a factor of about three. It should be pointed out, that the temporal shape is not altered yielding two consequences: first, as the excitation density has not changed, the coherent emission time τ_{coh} has remained constant and a overall efficiency enhancement is achieved in contrast to an amplification based on superradiance. Second, the broad bandwidth of the THz radiation has not been lowered, proving the ability to amplify extreme broadband radiation. A power FFT performed on the measured signals demonstrates that the original signal bandwidth of 750 GHz (central frequency 1 THz) is only minimally lowered to 730 GHz during the amplification process.

Fig. 4 Detected field transients of the THz emission from the background and the main emitter, if only one is excited (dashed lines) and for combined excitation in full temporal overlap (solid curve). The emitted THz fields add up yielding an enhanced radiation power of the irradiated emitter.

Fig. 5 Detected pulse energy of the THz radiation from the main emitter normalized to the emission without the background field. For $\Delta t_{gen}= 0$ ps an increase by a factor of 2.7 is observed due to the amplification by the THz background radiation. This is in good agreement with the numerical results shown as dashed curve.

Such a broadband amplification could be hardly achieved by stimulated emission due to mode competition effects and the difficulty to achieve gain over such a broad spectral range.

To demonstrate the amplification effect more clearly a bolometer is used to detect the time-integrated emission power of the main emitter, i.e. the emitted energy is measured directly. The dashed area in Fig. 3 marks the modification in the setup needed to detect only the emission form the main emitter (S_0) using standard lock-in technique. Fig. 5 shows the observed signal normalized to the unamplified value in dependence of the temporal overlap of the two pulses. For $\Delta t_{gen}= 0$ ps an increase of the signal by a factor of 2.7 is observed, corresponding to the coherent field addition already seen in the time-resolved field detection experiment. As only the radiation energy emitted from the main emitter (S_0) is detected, this proves directly the amplification of the emission of S_0. This observation is confirmed by comparison of the detected signal with the one calculated from the cross-correlation of the time resolved signals, shown in figure 4. The result of this calculation is plotted in figure 5 as a dashed line. The amplitude of the amplification is reproduced well. The slight modification in the signal form is attributed to the restricted bandwidth of the time resolved detection using dipole antennas. In conclusion, this experiment demonstrates, that it is possible to amplify THz radiation by phasematched coherent superposition even over a broad spectral range. This result gains more importance, as this measurement can additionally be interpreted as an analysis of the first round-trip of the amplification in a resonator, indicating its potential as a self-supporting coherent amplification mechanism.

4. AMPLIFICATION IN A THZ RESONATOR

We finally demonstrate the feasibility of repetitive amplification by coherent superposition in a resonator setup. In this approach, the resonator couples the emitted radiation back and makes use of it as the background radiation which amplifies the next THz generation process. Fig. 6 shows the ring resonator setup used for our experiment. Gold coated mirrors are used in order to guarantee a high reflectivity of the resonator. The whole system is flushed with nitrogen to reduce the strong water absorption in the 4m resonator pathway. The THz radiation in the resonator is probed and analyzed in a time-resolved extracavity detection scheme using photoconductive dipole antennas. The radiation is extracted using a 10% output coupler. To ensure a phasematched superposition under synchronous pumping, the roundtrip-time of the THz resonator has to be adjusted exactly to the repetition rate τ_{rep} of the optical laser exciting the THz emitter. The detuned situation (not shown) allows nevertheless to detect separately the single round-trips allowing to estimate the losses of the resonator. In our case, about 50% of the amplitude is lost during a roundtrip, which limits the amplification factor in this resonator setup to about seven. Figure 6 shows the detected field transients under resonance for the normal (dashed line) and amplified emission (solid curve). Obviously the field amplitude has increased by more than a factor of two showing a more than sixfold enhancement of the THz radiation power. Currently, the amplification is limited by the high resonator losses, but this data should be regarded more as a proof of principle, than as a record value for the amplification effect. To estimate the bandwidth of the amplification process the power spectrum is calculated from the observed signals using FFT-procedures. Figure 7

shows the values for the normal (μ) and the amplified emission (ν). As guide to the eye gauss curves are fitted to the data allowing to estimate the amplification characteristics out of the fitting parameters. The bandwidth of about 600 GHz as well as the central frequency around 600 GHz is not altered by the amplification process at all. On average, the power of the radiation has been increased by a factor of about 5, whereas peak amplification factors above 6 are reached. Summarizing, the presented analysis demonstrates the possibility for the broadband self-supporting amplification of coherent THz radiation by coherent superposition in a synchronously pumped ring-resonator. Currently the amplification factor is only limited by the resonator losses, which are on the order of 60% per round trip.

5. CONCLUSIONS

In this presentation we present a new method to amplify the THz emission power by a phasematched superposition with a coherent background THz radiation during the emission process. This new parametric amplification scheme can be applied to most impulsively excited THz emitters, as no population inversion is required. The amplification is experimentally proven by performing single-pass

Fig. 6 Ring-resonator setup with extracavity detection to demonstrate the repetitive amplification of the THz emission. The round trip time has to be adjusted to the repetition rate (τ_{rep}) of the laser to ensure coherent superposition.

amplification experiments detecting both time-resolved field amplitudes as well as the time-integrated power corresponding to the THz energy. The performed single-pass experiments demonstrate an emission power increase which scales with the amplitude of the THz background field. The repetitive THz amplification is then experimentally demonstrated in a THz ring-resonator. The presented experiments demonstrate the feasibility of using this process as an alternative to stimulated emission in order to develop flexible efficient sources of coherent THz radiation. This new amplification process can now be applied to a wide class of THz emitters, fomenting the broad application of time-domain THz technologies.

6. ACKNOWLEDGEMENTS

Fig. 7 Electric field amplitude for the direct (dashed curve) and the amplified (full line) emission (left). The amplitude is enhanced by more than a factor of two, yielding approximatedly a sixfold power increase. The right figure depicts the corresponding power FFT for the amplified (ν) and the normal (μ) emission. A Gauss curve is fitted to experimental data to demonstrate the high bandwidth of the THz amplification process (around 650 GHz, limited by the bandwidth of the original signal). An average amplification factor of about 5 is observed.

TMR project *Interact.*

1. H. Harde and D. Grischkowsky, 1991, J. Opt. Soc. Am. B **8**, 1642 (1991).
2. M. van Exter and D. Grischkowsky, Phys. Rev. B **41**, 12140 (1990).
3. P. R. Smith, D. H. Auston and M. C. Nuss, IEEE J. of Quant. Electr. **24**, 255 (1988).
4. B. B. Hu and M. C. Nuss, Optic Lett. **20**, 1716 (1995).
5. M. C. Nuss and J. Orenstein, ``THz time-domain spectroscopy'' in *Millimeter and Sub-Millimeter Wave Spectroscopy of Solids*, ed. by G. Grüner (Springer-Verlag, Heidelberg, 1998).
6. P. R. Smith, D. H. Auston, and M.C. Nuss, IEEE J. Quantum Electron. QE-**24**, 255 (1988).
7. Ch. Fattinger and D. Grischkowsky, Appl. Phys. Lett. **54**, 490 (1989).
8. X.-C. Zhang, B.B. Hu, J. T. Darrow, and D. H. Auston, Appl. Phys. Lett. **55**, 337 (1990).
9. H.G. Roskos, M.C. Nuss, J. Shah, K. Leo, and D.A.B. Miller, Phys. Rev. Lett. **68**, 2216 (1992).
10. C. Waschke, H. G. Roskos, R. Schwedler, K. Leo, H. Kurz, and K. Köhler, Phys. Rev. Lett. **70**, 3319 (1993).
11. K. Victor, H.G. Roskos, and C. Waschke, J. Opt. Soc. Am. B **11**, 2470 (1994).
12. B. I. Greene, J. F. Federici, D. R. Dykaar, R. R. Jones, and P. H. Bucksbaum, Appl. Phys. Lett. **59**, 893 (1991).
13. R. Martini, G. Klose, H.G. Roskos, H. Kurz, H. T. Grahn, and R. Hey, Phys. Rev. B **54**, R14325 (1996).
14. P. Haring Bolivar, R. Martini and H. Kurz, in preparation for Phys. Rev. B.
15. A. Bonvalet, J. Nagle, V. Berger, A. Migus, J. L. Martin, and M. Joffre, Phys. Rev. Lett. **76**, 4392 (1996).

Advances in continuous-wave THz generation

Karsten Siebert, Frank Siebe, Mark Thomson, Jalil Zare Baghbidi, Rainer Leonhardt[a],
Hartmut G. Roskos

Physikalisches Institut der Johann Wolfgang Goethe-Universität Frankfurt (M),
Robert-Mayer-Str. 2-4, D-60054 Frankfurt (M), Germany
[a]On leave from: University of Auckland, Private Bag 92019, Auckland, New Zealand

ABSTRACT

We introduce two modifications of the technology of optoelectronic continous-wave (cw) THz spectroscopy. The first relates to the optoelectronic generation of cw THz radiation by heterodyne downconversion (photomixing) of two laser beams. We present a cw Ti:Sapphire laser with a simultaneous output at two independently tunable colors which are used for the mixing process. Two alternative cavity designs, a linear α-shaped cavity and a ring cavity, have been realised. A comparison with respect to tunability, bandwidth, stability and experimental handling will be given. The second improvement relates to the detection of cw THz radiation. We discuss detection schemes which are based on the electro–optic effect in nonlinear media and employ the concept of quasi-phasematching for the enhancement of the sensitivity.

Keywords: THz generation, photomixing, electrooptic detection

1. INTRODUCTION

During the last ten years the THz (far–infrared) region of the electromagnetic spectrum has regained the interest of spectroscopic research. On these grounds applications in imaging and inspection have recently been identified to be realistic goals of research.[1,2] The switching of photoconductive antennae by optical femtosecond (fs) pulses has been established as a successful way for the generation of pulsed, broadband and coherent THz radiation. Optically gated photoconductive and electro-optic detection enables the sensitive measurement of the amplitude and phase of the electric THz field.

In spite of the success of fs-laser-based THz spectroscopy, continous–wave (cw) THz systems exhibit numerous advantages. They have higher average power at every single frequency they are tuned to. Their size and costs will be much smaller due to the lack of a complex optical fs source. While the spectral resolution of pulsed THz systems is limited by the time delay between the gating pulses of the emitter and the detector, the frequency resolution of a cw system is limited only by the bandwidth of the emitted THz radiation.

While in the past much more work has been devoted to femtosecond–laser–based systems, cw techniques have increasingly gained more attention. Heterodyne downconversion, or photomixing, of two cw laser beams has proven to be a successful way to generate narrow–band radiation in the terahertz spectral region. The first demonstration of efficient and frequency–tunable photomixing in a low–temperature–grown (LT) GaAs antenna by Brown et al.[3,4] has induced intense activities centering mainly on the selection of suitable laser sources for the mixing process. In their ground–breaking work, Brown et al. mixed the radiation from two independent Ti:sapphire lasers. Subsequently, a multitude of concepts based on semiconductor diode lasers has been proposed and investigated, the dual–beam sources being either two independently running lasers,[5,6] pairs of actively frequency–locked lasers,[7] individual lasers with dual–[8] or multi–mode emission[9,10] or coupled–cavity diode lasers.[11,12]

Although diode lasers, for obvious reasons, will be the sources of choice for future technological appplications, it is not to be forgotten that Ti:sapphire sources offer a reliable alternative for terahertz spectroscopy in the laboratory and for the exploration of new application areas of terahertz radiation because they exhibit continuous tunability over a large frequency range, high output power, excellent frequency stability and operational robustness. Instead of two independent Ti:sapphire lasers, however, as in the pioneering work of Brown et al.,[3] one would prefer to run

---

Please find further contact information on our web page:
http://www.physik.uni-frankfurt.de

234

Part of the EUROPTO Conference on Terahertz Spectroscopy and Applications II
Munich, Germany • June 1999 SPIE Vol. 3828 • 0277-786X/99/$10.00

a single laser with two–color output. Indeed, the literature discusses Ti:sapphire lasers with dual–beam emission, mainly as mode–locked lasers for fs spectroscopic applications,[13–18] but also, less frequently, as cw sources.[19,20]

In the latter case, following the concept of Ref. 19, a linear α–shaped cavity was developed for lidar and second-harmonic applications and does not allow a wavelength separation of the two colors of less than 10 nm (corresponding to a frequency difference of not less than 5 THz), a severe limitation for THz spectroscopy. The linear– and ring-cavity systems with self–injection tuning reported in Ref. 20, on the other hand, provide only limited bandwidth control which may not be sufficient to suppress wavelength fluctuations of the beams and which do not allow fully independent tuning.

The laser features desired for general terahertz spectroscopic applications are dual–wavelength emission with (i) as narrow a bandwidth of each beams as possible, (ii) an unrestricted wavelength tunability of both beams, and (iii) a high output power of the beams. Furthermore, for photomixing in a photoconductive antenna one can accept a total output power of both beams only on the order of 100 mW as more power is not usable because of the danger of damaging the photoconductive antenna.[4]

The requirements for photomixing purposes but also for more general terahertz spectroscopic applications can be fulfilled with modifications of the laser designs of Ref. 19 and Ref. 20. The lasers, to be described below, are pumped by a single pump beam and provide two fully tunable, narrow–bandwidth output beams. In the following, we discuss two different layouts, a α–shaped cavity with parallel–beam output[21] and a ring–cavity with collinear emission. The performance characteristics are discussed with an emphasis on the tuning properties and the achievable bandwidth control.

Until recently the detection of cw THz radiation was always carried out with bolometers. Last year, however, Verghese et al.[22] showed that it is possible to perform optoelectronic detection of cw THz radiation with a photoconductive antenna. This method allows determination of both the amplitude *and* phase of the THz wave. An alternative way to detect THz radiation is to utilize the electro–optic (EO) effect which is induced by the THz beam in a nonlinear crystal. Up to now this approach has only been implemented in fs–laser–based THz systems where it was first demonstrated by Zhang et al.[23] in 1995. Since then great progress has been made and the detection sensitivity has been increased to a level on the order of $\Delta I/I = 10^{-8}/\sqrt{Hz}$.[24] Thus the detectivity is comparable to that of antennae if not better. We investigate the possibility to realise an EO detection scheme for cw THz radiation. As the absolute THz power in the cw case is lower than in the pulsed systems, efforts have to be made to further increase the sensitivity. A promising concept is that of quasi–phase–matching. We present proposals for practical experimental setups and discuss modifications of these schemes which would also allow cw THz generation by difference frequency mixing in EO media.

2. DUAL-COLOR LASERS

We now focus on the description of the dual–color laser systems. Figure 1 displays the layout of the laser cavities. Figure 1 (a) showing the linear, α–shaped resonator with a round–trip length of 1.36 m (spacing of the longitudinal modes: 0.47 pm, or 219.5 MHz), whereas part (b) presents the ring resonator with a passive feedback.

Both lasers are pumped by all lines of a Coherent argon–ion laser with an output power of 6 W. The Ti:Sapphire crystal, bought from Casix, is doped with Ti^{3+} ions at a relative concentration of 0.1 %, the figure of merit (FOM) of the crystal is specified as >200. The 15–mm–long Brewster–cut crystal absorbs 96 % of the pump–laser radiation. For proper laser operation it is crucial to carefully align the optical axis of the crystal in such a way that the crystal does not act as a birefringent filter inside the cavity.

2.1. Experimental setup

The spectral characteristics of the laser radiation is analyzed with a TEK 1.25–m monochromator equipped with a 2048–element CCD sensor at the place of the exit slit. The system covers a spectral range of 28.6 nm with a nominal pixel resolution of 0.014 nm. The actual resolvable bandwidth of the spectrometer is determined with a HeNe laser to be 2.5–3.5 pixels corresponding to a wavelength (frequency) resolution of 0.035–0.05 nm (16-24 GHz).

In addition, we investigate the temporal coherence of the radiation of each beam for the α-cavity with a Michelson interferometer with unequal lenths of the two arms. We select a fixed path difference of 2 m. If an interference pattern is observed with good visibility, the linewidth of the radiation has an upper limit of 150 MHz.
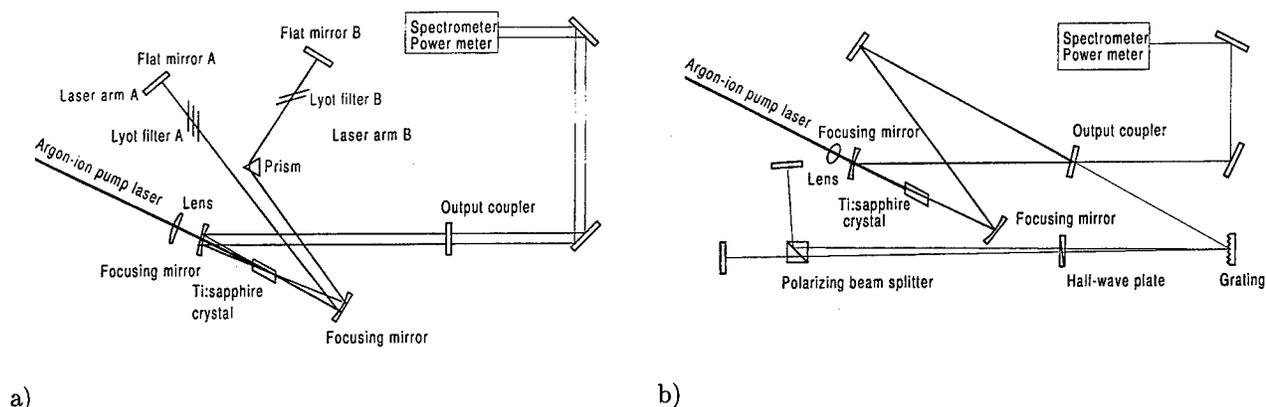
Figure 1. Schematics of the resonator designs of a) the linear α–cavity, b) the ring cavity.

The noise and mode properties of the laser with the α–cavity are studied with the help of an electronic frequency analyzer model Tektronix 494P. The spectrum analyzer allows us to determine whether laser emission occurs on individual longitudinal modes or on an ensemble of these.

2.1.1. α–cavity

The α–shaped linear cavity consists of five mirrors, three of them being shared by both beams while two mirrors in the wavelength–selection segment are used by either beam only. The dielectric coating of the mirrors is centered at 800 nm spanning a high–reflectivity range of 100 nm. The radius of curvature of the focusing mirrors is 10 cm. Through one of these mirrors, the argon–laser pump beam is focused onto the crystal with a lens of 5 cm focal length. The focusing mirrors are tilted (angle between incoming and reflected beams: 27°) in order to compensate for the astigmatism induced by the laser crystal.[25] Under all operation conditions to be discussed, for single–and double–beam emission, laser action with a circular TEM_{00} Gaussian mode showing no sign of astigmatism is achieved.

The alignment procedure of the laser is as follows. The resonator is first adjusted as a single–beam cavity in such a way that it is possible to move the laser beam horizontally on the output–coupling mirror by rotation of the flat high–reflecting mirror denoted by A. A birefringent filter (Lyot filter) operated under Brewster's angle serves as a wavelength–tuning element. It consists of three quartz plates with a thickness ratio of 1:4:16 and a thickness of the thinnest plate of 0.013 inches. The optical axes of the plates are parallel to the surfaces of the plates. Upon optimum alignment, the laser output power at the gain maximum is 750 mW for an output–coupler transmission of 2%. Subsequently, the two–beam option is implemented by inserting a 60°–flint–glass prism at Brewster's angle, a second Lyot filter and a second high–reflecting mirror denoted by B as shown in Fig. 1 (a). The two beams are parallel at the output coupler with a separation of approximately 4 mm from each other. Their relative power is adjusted by control of the horizontal position of the output coupler. The total power for both beams together is on the order of 250 mW.

The overall loss in output power in the two–beam configuration compared to the single–beam setup results from the fact that the gain for both beams is provided by a single pump beam. Under these conditions, it is impossible to achieve optimum mode overlap between the pump beam and the two laser beams. Interestingly, the laser beams do not exhibit a tendency to run at higher lateral modes simultaneously with the fundamental TEM_{00} Gaussian modes. Upon misalignment of the respective cavity, the fundamental mode disapears completely and is replaced by higher–order modes. When the cavities are properly aligned, no measures are required to suppress higher–order modes. For that reason, we operate the laser without apertures in the cavities.

2.1.2. Ring cavity

The ring resonator (Fig. 1 (b)) can be obtained from the α–cavity by positioning one of the high–reflectors and the output coupler in a way that a figure–of–eight–like resonator is formed. The scheme which is used to tune the ring laser, so–called passive self–injection, has been described by Gorris-Neveux et al.[20] The concept is as follows. The two waves travelling in the clockwise and anti-clockwise direction allow to couple out two beams at the 2–% output

coupler. One is extracted and steered to the experiment, the other provides feedback to the laser. In the feedback arm a grating combined with one of the feedback mirrors selects only one color to be reflected back into the cavity. In order to run the laser at two colors, a polarizing beam splitter together with a second mirror couples a second color back into the cavity. The half-wave plate in front of the beam splitter allows to balance the intensity of the two feedback beams. Upon optimum alignment a total output power of 800 mW for single color operation can be obtained. For two-color operation an ouput power of 700 mW equally split into the two colors is achieved.

It should be noted that the main resonator does not contain any frequency–filtering element, frequency selection occurs only in the secondary feedback cavity. The tuning scheme thus relies on the fact that the Ti:sapphire crystal is a predominantly homogenously broadened laser medium where mode competition determines the lasing frequencies.

2.2. Laser characteristics for single–beam operation

It is instructive to investigate the spectral characteristics of each beam individually while the other beam is blocked. We point out, however, that the spectral characteristics for dual–beam lasing are found to be the same as those to be presented now for single–beam lasing.

2.2.1. α–cavity

We first discuss the lasing properties of the α–cavity. The measurements are made for beam A where wavelength tuning is performed with a three–plate Lyot filter. Figure 2 (a) shows the spectrum of the laser beam monitored with the spectrometer.
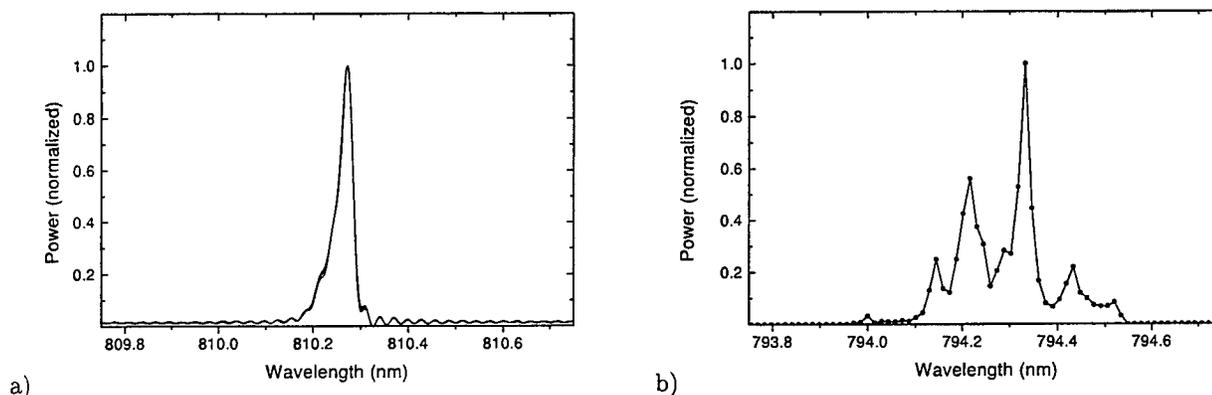
Figure 2. Emission spectra for single–color operation of a) the α–cavity, b) the ring cavity.

A resolution–limited emission profile is obtained. The graph consists actually of five camera shots each taken a few seconds after the other. The profiles overlap nearly perfectly. No changes of the line position and the line shape are observed for repeated shots indicating good bandwidth control over the spectral range as resolved by the spectrometer.

In order to obtain more information on the modal characteristics, HF measurements with the electronic spectrum analyzer are performed. The spectrum, not shown here, consists of a series of lines separated by 219.5 MHz which correspond to an interference of adjacent longitudinal cavity modes. The first five interference lines appear sporadically, only the 6th line at 1.3174 GHz is present permanently. Modes even further apart are not resolved by the spectrum analyzer. This behavior is quite independent of the chosen laser wavelength.

These data suggest that the laser runs predominantly on two longitudinal modes simultaneously. Operation at adjacent longitudinal modes is less favorable than operation at modes with a larger frequency separation (one mode plus a mode with six times the cavity mode spacing). Adjacent longitudinal modes can only be excited strongly when lasing is disturbed, e.g. by externally induced mechanical vibrations or by vigorously blowing air through the resonator.

In order to distinguish the relative strengths of the two running longitudinal modes, additional measurements are performed with the Michelson interferometer. We observe well–resolved interference fringes. Typically, the fringe pattern is stable for seconds at a time before instabilities blur the pattern briefly.

Upon visual inspection, we do not discern a superstructure on top of the fringe structure as expected when the pattern is determined by two modes of similar strength. The 6th–higher mode hence is either much weaker than the 1st mode or it does not run permanently (although it must appear often on the time scale of the integration time of the spectrum analyzer).

In summary, the clear visibility of the single–mode interference pattern in the measurements with the Michelson interferometer indicates that the laser has a tendency to run on a single longitudinal mode. The coherence length of the radiation is at least 2 m corresponding to an upper limit of the linewidth of 150 MHz. The bandwidth restriction by the Lyot filter is, however, not strong enough to prevent lasing on additional modes but these run at much lower average power.

For lasing along beam path B, where frequency selection occurs with the help of a two–plate Lyot filter and a prism, equivalent results for the bandwidth are obtained.

2.2.2. Ring cavity

Figure 2 (b) displays a single–shot spectrum of the laser radiation emitted from the ring cavity during single–color operation. The spectrum consists of a multitude of lines covering a wavelength range of about 0.4 nm bandwidth. The emission spectrum is much broader than that of the α–cavity described above. We could not confirm the results of Gorris-Neveux et al.[20] who report the emission of a single longitudinal mode from a ring cavity. We observe strong fluctuations of the spectrum indicating insufficient bandwidth control. The application of Fabry-Perot interference filters in the feedback arm of Gorris-Neveux et al. may have provided a stronger bandwidth restriction not reached with the grating in our setup. It is pointed out, however, that the addition of Lyot filters into the feedback arm did not improve the spectral characterstics of the laser spectra. This matter certainly requires further investigation.

2.3. Two-color operation

In the following, laser operation in the dual–mode configuration is investigated. The spectral characteristics of the single–beam operation discussed before are found reproduced in the dual–beam case for both cavity designs. Therefore, we will not address the modal characteristics again in this section, but rather focus on the tuning characteristics for stable two–color operation of the laser.

2.3.1. α–cavity

Independent tuning of both beams First the α–resonator will be discussed. Beam A is tuned with a three–plate Lyot filter, beam B with a two–plate filter and the prism. It is emphasized that both beams can be tuned independently from each other, with the maximum tuning range limited only by the reflectivity of the resonator mirros. Stable two–color laser operation is achieved for both output powers being balanced. Even if the output powers of the two beams differ by as much as a factor of ten a stable operation is possible because of vastly different laser gain at the operation wavelengths.

For applications in a tunable THz source, it is also desirable to reach very low difference frequencies. Wavelength differences of the two beams corresponding to the resolution limit of the spectrometer of about 20 GHz could be observed. There is no indication for a loss in lasing stability when the wavelengths are so close together. In fact, the wavelength difference can even be reduced further without problems.

The solid line of Fig. 3 (a) presents the wavelength dependence of the output power of beam A when beam B (the arm with prism and Lyot filter) is held fixed at a wavelength of 799 nm. At each wavelength setting of Fig. 3 (a), the beams are adjusted to the same power level as one would choose to do for photomixing of the beams in a photoconductive antenna in order to achieve full modulation of the mixing signal. In the region of maximum gain, an output power of 125 mW per beam is reached. The slight modulation on the curve is likely to be a consequence of a residual misalignment of the optical axis of the Ti:sapphire laser crystal leading to a frequency dependence of its transmissivity because of uncompensated birefringence. For other wavelengths of beam B, away from the gain maximum, similar tuning curves of beam A are obtained, however at reduced output powers which reflects the lower gain for beam B. Both lines can be independently tuned over a range of 100 nm which corresponds to a difference frequency of 50 THz.

It is pointed out that one can achieve even higher output powers with a different output–coupler transmissivity. Replacing the 2-% output coupler for a 4-% coupler allows us to reach an output power of 150 mW (instead of 125 mW) per beam at the gain maximum without a degradation of the laser performance.

Tuning with a fixed frequency difference The dashed line of Fig. 3 (a) displays the tuning characteristics of the dual–color laser when both colors are tuned simultaneously with a constant relative wavelength separation of 7 nm (frequency separation: from 2.95 THz at 840 nm to 3.8 THz at 740 nm). The overall tuning range as well as the absolute values of the output power differ little from the results obtained for single–beam tuning (solid line).
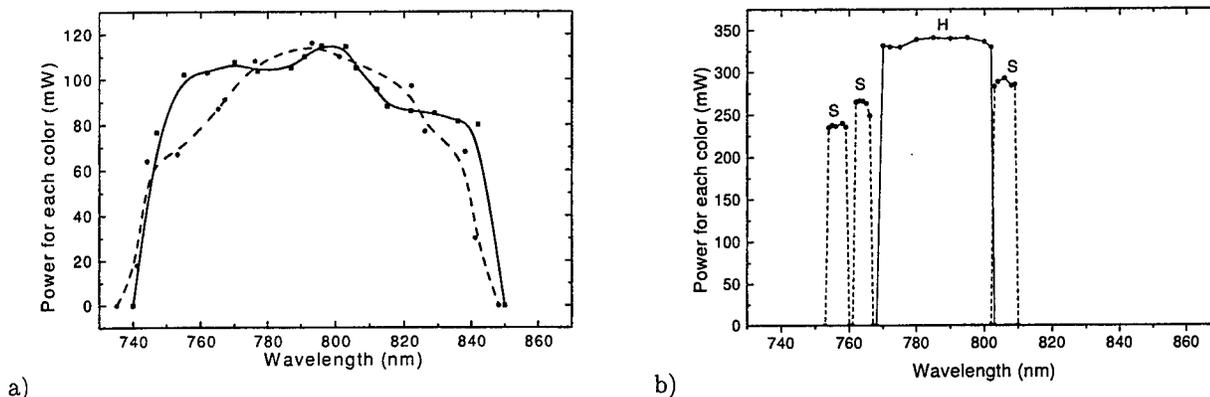
Figure 3. Tuning range for a) the linear α–cavity, b) the ring cavity.

The mode of operation discussed so far produces two parallel but non–collinear output beams at different colors. As a remark, we point out that the resonator can be converted into a laser emitting two collinear beams which can be tuned together at a fixed wavelength difference. For that purpose, one removes beam A, converts the Lyot filter in the original beam path B to a single–plate filter (retaining only the thinnest of the three plates), and rotates the optical axis of the Ti:sapphire crystal. The laser crystal itself now acts as a birefringent filter that determines the wavelength separation of the laser modes. The Lyot filter and the prism in the original beam path B allow to select wavelength pairs within a large part of the tuning range of the laser. We have tested this mode of operation with a 5.2–nm wavelength separation resulting from the rotation of the optical axis of the Ti:sapphire crystal by just a few degrees. Without the Lyot filter and the prism in the original beam path B, the laser runs at a comb of wavelengths. With these additional filter elements, however, lasing occurs only at two wavelengths that can be shifted in unison. The emission at the two colors is collinear.

2.3.2. Ring cavity

Figure 3 (b) displays the tuning range of the laser with the ring resonator. The solid curve H shows the tuning range observed with the setup as given in Fig. 1 (b). We obtain a bandwidth of 30 nm around the natural gain maximum of the laser at 785 nm, where both colors can be tuned independently. This corresponds to a relative frequency difference of the two colors between approximately 20 GHz and 13 THz. Over the whole frequency range both colors emit at equal powers of about 330 mW per beam.

For electro-optic detection schemes it is desirable to tune the optical frequency to a position above or below the featured bandwidth. This can be achieved by inserting a one–plate Lyot filter into the main resonator. Typical spectra measured in this configuration are given by the graphs plotted with dotted lines and denoted by S in Fig. 3 (b). Each of the curves represents a different frequency setting of the lyot filter. The tuning range and the output power are further reduced, but the center frequency can now be shifted freely. The observed effect can be explained as a shift of the system's gain curve by the Lyot filter. Due to the relatively broad bandwidth of the one-plate Lyot filter two colors can still be emitted simultaneously.

2.4. Comparison between the two laser configurations

The two cavity designs have to be thoroughly compared with respect to their application in tunable cw THz-signal generation. If a wide tunability up to THz frequencies as high as 50 THz is required again the α–cavity will be the system of choice as the ring cavity is restricted to frequencies up to 13 THz. On the downside one has to consider two shortcomings of the α–cavity. The first is its relatively low output power and the second the non-collinearity of the emitted colors. The latter disadvantage makes the alignment of the photomixer more complicated than for the collinear colors emitted from the ring cavity. The first disadvantage is uncritical as long as the power which can be used for photomixing is limited by the damage threshold of the photomixers. The power is sufficient for photoconductive generation and detection of THz radiation.

In conclusion, it is obvious that the α–cavity is much more favourable for THz photomixing applications than the ring cavity at least in its present form. What makes the ring cavity attractive are its high output power (resulting from the fact that the main cavity contains only the gain medium and no filter element) and the quasi-unidirectional laser operation obtained with optical feedback (see Ref. 20) which prevents the formation of longitudinal modes and thus beating between such modes. Before these inherent advantages can be exploited, however, it requires much improvement of the stability of the laser emission.

3. QUASI-PHASE MATCHED ELECTRO-OPTIC THZ GENERATION AND DETECTION

The use of electrooptic (EO) crystals for pulsed-THz generation and detection has been widely researched in recent years,[23,24,26-28] and is often the method of choice in terms of sensitivity, tolerable power threshold, ultrafast time response and ease of implementation. However, the use of such techniques has not yet been reported in the case of cw-THz, even though with the intensity modulation of an intense two color cw optical source and the improved EO materials available, cw-THz generation and detection has become a realisable goal. As the second order non-linear processes involved are inherently weaker for cw waves than in the pulsed case, attempts to increase the efficiency of EO-THz processes are important.

Common to all non-linear optical processes, the most fundamental limitations on the efficiency of THz generation and detection in electrooptic (EO) media are absorption, non-linear phase matching (dispersion) and beam divergence (diffraction), which limit the interaction length of the process. Once an EO medium has been selected that is sufficiently transparent at both the desired THz frequency (Ω) and available optical wavelength ($\lambda = 2\pi c/\omega$), and that possesses an appreciable second order non-linear susceptibility (χ^2 or d), one must turn to the problem of phase matching the temporal interaction between the pump and signal waves.

In general, both EO-THz generation (optical rectification) and detection (dynamic polarisation rotation) processes are formally equivalent to a combination of sum- and difference- frequency mixing, which involves the energy transfer from two pump fields, E_1 (optical) and E_2 (optical, THz), into a signal field, E_3 (THz, optical), each of which can be expressed as,

$$E_j(z,t) = E_j(z)\exp(i\varphi_j) \qquad j = 1..3, \tag{1}$$

with $\omega_1 \pm \omega_2 = \omega_3$.[29] Analogous to second harmonic generation (SHG), the rate of energy transfer (gain) into the signal wave at during copropagation in an EO crystal is governed by the overall phase of the processes

$$\varphi_z = \varphi_1 \pm \varphi_2 - \varphi_3 = \Delta k z, \tag{2}$$

(where $\Delta k = k_1 \pm k_2 - k_3$ is the wavevector mismatch), such that the instantaneous gain, $g(z) \propto \exp(i\varphi)$. Integration of $g(z)$ over a crystal of length L yields the net intensity gain $G \propto \sin^2(\Delta k L/2)/(\Delta k)^2$ at ω_3, so that the maximum useful crystal length is limited to $l_C = \pi/|\Delta k|$, the well-known *coherence length*. In the case of moderate THz frequencies ($\lesssim 5$ THz), this can be written as $l_C \approx \pi/\Omega|n(\Omega) - n_g(\omega)|$ where $n_g(\omega) = n(\omega) + \omega \partial n/\partial \omega$ is the optical group refractive index. If it is possible to realise an optical wavelength where $n(\Omega) \approx n_g(\omega)$ then the process is phase matched and other factors determine the maximum usable crystal length.

However, in general the condition for phase matching cannot be met, especially in the case of broadband (pulsed) THz radiation, where $n(\Omega)$ varies significantly over the bandwidth, or when a widely-tunable laser source is not available. In such a case, one is confined to use a crystal length $L \leq l_C$, although often this can limit the strength of the generated signal to below useful or detectable levels. However, if after each propagation distance l_C one can

restore the process phase φ back to $m2\pi$, $m = 1, 2, ...$ then the process can be quasi-phase matched,[30] and the usable propagation length and efficiency can approach that of the phase matched case. To illustrate the domain of applicability of such techniques, Fig. 3 shows a plot of the condition $l_A > l_C$ (where l_A is a measure of the absorption length, defined here as $l_A = (\alpha(\omega) + \frac{1}{2}\alpha(\Omega))^{-1}$) for GaP over a range of THz and optical frequencies.[31] This plot clearly shows that apart from regions of high THz or optical absorption and the narrow region below 10 THz where phase matching can be achieved (with a tunable optical source), the coherence length is the limiting factor for the usable crystal length. Hence it is highly desirable that techniques are available that allow for quasi-phase matching.
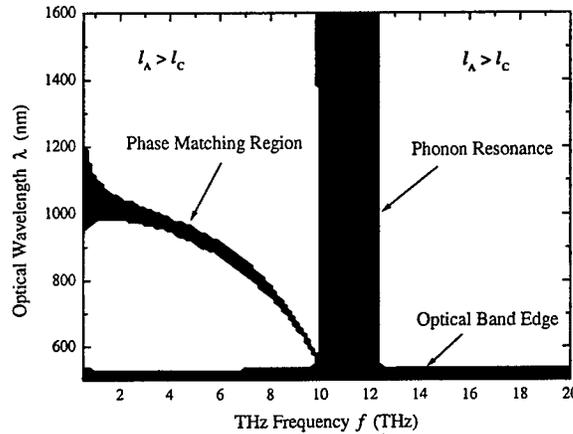
Figure 4. Domain of applicability for quasi-phase matching (white regions) in GaP represented by the condition , (and $l_A \geq 100$ μm) i.e. coherence length limited propagation. Dark regions correspond to the natural phase matched tuning range of GaP and regions of high THz and optical absorption (absorption limited propagation).

Figure 3 shows a general schematic for quasi-phase matched EO generation and detection. After the pump and signal fields have propagated a distance $L \leq l_C$ (i.e. $\varphi = \Delta\varphi_N \leq \pi/2$), the fields propagate some *linear* optical system where the process phase undergoes a shift of $\Delta\varphi_R = -\Delta\varphi_N + m2\pi$) , which may be a discrete system (as in the case of a reflection) or propagation in a second "phase correction" material. In the latter case, one requires good lattice and index matching between the EO active and passive materials in order to reduce backward reflections and other interface effects. However, this is not a requirement in the case of a dispersive reflection, where the fields always remain in the EO material.

One possible scheme for realizing a corrective phase shift by dispersive reflection is shown in Fig. 3(b), which outlines the scheme in the case of THz detection. As shown, the THz and optical pump beams with parallel polarization are launched into the EO material via a high–resistivity silicon (Si) prism and copropagate at $\theta = 45°$ in a non-birefringent <100> zinc blende crystal (e.g. GaP or ZnTe) with thickness $d \leq l_C/\cos(\theta) = \sqrt{2}l_C$. From consideration of the form of the χ^2 tensor in such crystals, this choice of propagation (e.g [110]) and polarization (e.g. [1$\bar{1}$1], TE) directions leads to the generation of the copropagating "signal" (sum and difference frequency) fields polarised in the [001] (TM) direction. In the case shown, after traversing the crystal, the fields are total internally reflected (TIR), the process phase undergoing a phase shift of,

$$\Delta\varphi_R(\theta) = \varphi_{TE}(\omega, \theta) \pm \varphi_{TE}(\Omega, \theta) - \varphi_{TM}(\omega \pm \Omega, \theta) \tag{3}$$

with the system parameters chosen such that $\Delta\varphi_R(\theta) = -\Delta kd/\cos(\theta) + m2\pi$. Hence the fields begin the next traversal of the crystal with the process phase restored to that of constructive amplification, so that after N traversals the signal intensity gain is N^2 times greater than from traversal of a single crystal, being limited only by absorption, and divergence of the THz beam.

There are several details that warrant additional comment here. The use of the Si prisms is to reduce reflective input losses and to couple out the optical beam after traversing the system. The use of TIR can be replaced by metallization of the crystal faces, which also allows for engineering of the reflection phases through the choice
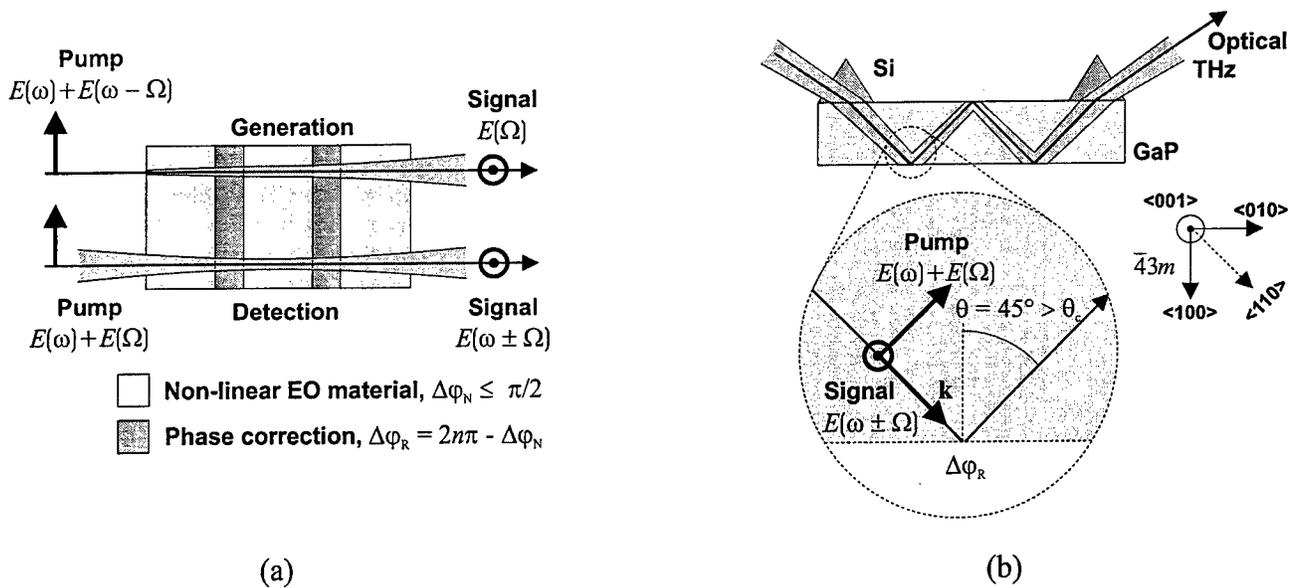
Figure 5. (a) Generic representation of quasi-phase matched THz generation and detection. (b) Realization of such a scheme in the case of THz detection in <100> zinc–blende crystals using dispersive phase reflections to restore the non-linear process phase.

of different metals. The thickness of the crystal can be chosen (as far as wave interference effects are negligible) to match the particular coherence length of the THz and optical fields employed. Also, the choice of a $\theta = 45°$ propagation geometry is not imperative; other propagation and polarisation angles can be chosen which still lead to the amplification of copropagating signal fields, although the complexity of the alignment increases. However, the case where θ is not fixed opens up a useful degree of freedom in the system, because both the propagation ($\Delta\varphi_N$) and reflection ($\Delta\varphi_R$) phase shifts can be tuned for quasi-phase matching over a range of THz and optical frequencies. The exact details of system design and applicability are to be reported elsewhere.

This novel realization of a quasi-phase matched THz generation and detection scheme is amongst several under investigation, and we anticipate that such methods will play an important role in improving the scope of lower peak power THz applications.

REFERENCES

1. B. B. Hu and M. C. Nuss, "Imaging with terahertz waves," *Optics Lett.* **20**, pp. 1716–1718, Aug. 1995.
2. R. H. Jacobsen, D. M. Mittleman, and M. C. Nuss, "Chemical recognition of gass and gas mixtures with terahertz waves," *Optics Lett.* **21**, pp. 2011–2013, Dec. 1996.
3. E. R. Brown, K. A. McIntosh, K. B. Nichols, and C. L. Dennis, "Photomixing up to 3.8 THz in low-temperature-grown GaAs," *Appl. Phys. Lett.* **66**, pp. 285–287, Jan. 1995.
4. S. Verghese, K. A. McIntosh, and E. R. Brown, "Optical and terahertz power limits in the low-temperature-grown GaAs photomixers," *Appl. Phys. Lett.* **71**, pp. 2743–2745, Nov. 1995.
5. K. A. McIntosh, E. R. Brown, K. B. Nichols, O. B. McMahon, W. F. DiNatale, and T. M. Lyszczarz, "Terahertz photomixing with diode lasers in low-temperature-grown GaAs," *Appl. Phys. Lett.* **67**, pp. 3844–3846, Dec. 1995.
6. S. Matsuura, M. Tani, and K. Sakai, "Generation of coherent terahertz radiation by photomixing in dipole photoconductive antennas," *Appl. Phys. Lett.* **70**, pp. 559–561, Febr. 1997.
7. P. Chen, G. A. Blake, M. C. Gaidis, E. R. Brown, K. A. McIntosh, S. Y. Chou, M. I. Nathan, and F. Williamson, "Spectroscopic applications and frequency locking of THz photomixing with distributed-Bragg-reflector diode lasers in low-temperature-grown GaAs," *Appl. Phys. Lett.* **71**, pp. 1601–1603, Sept. 1997.

8. M. Hyodo, M. Tani, S. Matsuura, N. Onodera, and K. Sakai, "Generation of milimeter-wave radiation using a dual-longitudinal-mode microchip laser," *Electron. Lett.* **32**, pp. 1589–1591, 1996.

9. M. D. Pelusi, H. F. Liu, D. Novak, and Y. Ogawa, "THz optical beat frequency generation from a single mode locked semiconductor laser," *Appl. Phys. Lett.* **71**, pp. 449–451, July 1997.

10. M. Tani, S. Matsuura, K. Sakai, and M. Hangyo, "Multiple-requency generation of sub-terahertz radiation by multimode LD excitation of photoconductive antenna," *IEEE Microwave and Guided Wave Lett.* **7**, pp. 1–3, Sept. 1997.

11. C.-L. Pan and C.-L. Wang, "A novel tunable dual-wavelength external-cavity laser diode array and its applications," *Opt. Quantum Electron.* **28**, pp. 1239–1257, 1996.

12. T. Hidaka, S. Matsuura, M. Tani, and S. Sakai, "CW terahertz wave generation by photomixing using a two-longitudinal-mode laser diode," *Electron. Lett.* **33**, pp. 2039–2040, Nov. 1997.

13. M. Nenchev, A. Deleva, E. Stoykova, Z. Peshev, T. Patrikov, and G. Gizbrekht, "Controlled time-delayed-pulses operation of a two-wavelength combined dye-Ti:Al$_2$O$_3$ laser," *Optics Commun.* **86**, pp. 405–408, Dec. 1991.

14. M. R. X. Barros and P. C. Becker, "Two-color synchronously mode-locked femtosecond Ti:sapphire laser," *Optics Lett.* **18**, pp. 831–833, April 1993.

15. J. M. Evans, D. E. Spence, D. Burns, and W. Sibbett, "Dual-wavelength self-mode-locked Ti:sapphire laser," *Optics Lett.* **18**, pp. 1074–1076, July 1993.

16. D. R. Dykaar, S. R. Darack, and W. H. Knox, "Cross-locking dynamics in a two-color mode-locked Ti:sapphire laser," *Optics Lett.* , pp. 1058–1060, April 1994.

17. A. Leitensdorfer, C. Fürst, and A. Laubereau, "Widely tunable two-color mode-locked Ti:sapphire laser with pulse jitter of less than 2 fs," *Optics Lett.* **20**, pp. 916–918, Sept. 1995.

18. C. Fürst, A. Leitensdorfer, and A. Laubereau, "Mechanism for self-synchronization of femtosecond pulses in a two-color Ti:sapphire laser," *IEEE J. Selected Topics in Quantum Electron.* **2**, pp. 473–479, Sept. 1996.

19. R. Scheps and J. F. Myers, "Doubly resonant Ti:sapphire laser," *IEEE Photon. Technol. Lett.* **4**, pp. 1–3, Jan. 1992.

20. M.-Gorris-Neveux, M. Nenchev, R. Barbe, and J.-C. Keller, "A two-wavelength, passively self-injection locked, cw Ti^{3+}: Al$_2$O$_3$ laser," *IEEE J. Quantum Electron.* **QE-31**, pp. 1253–1260, Aug. 1995.

21. F. Siebe, K. Siebert, R. Leonhardt, and H. G. Roskos, "A fully dual-color Ti:Al$_2$O$_3$ laser," *to be published in IEEE Journ. Quantum. Electr.* .

22. S. Verghese, K. A. McIntosh, S. Calawa, W. F. Dinatale, E. K. Duerr, and K. A. Molvar, "Generation and detection of coherent terahertz waves using two photomixers," *Appl. Phys. Lett.* **73**, pp. 3824–3826, Dec. 1998.

23. Q. Wu and X.-C. Zhang, "Free-space electro-optic sampling of terahertz beams," *Appl. Phys. Lett.* **67**, pp. 3523–3525, Dec. 1995.

24. Q. Wu and X.-C. Zhang, "7 terahertz broadband GaP electro-optic sensor," *Appl. Phys. Lett.* **70**, pp. 1784–1786, April 1997.

25. H. Kohelnik, E. Ippen, A. Dienes, and C. Shank, "Astigmatically compensated cavities for cw dye lasers," *IEEE J. Quantum Electron.* **QE-8**, pp. 373–379, March 1972.

26. A. Nahata, A. S. Weling, and T. F. Heinz, "A wideband coherent terahertz spectroscopy system using optical rectification and electro–optic sampling," *Appl. Phys. Lett.* **69**, pp. 2321–2323, Oct. 1996.

27. S.-G. Park, M. R. Melloch, and A. M. Weiner, "Comparison of terahertz waveforms measured by electro-optic and photoconductive sampling," *Appl. Phys. Lett.* **73**, pp. 3184–3186, Nov. 1998.

28. A. Leitensdorfer, S. Hunsche, J. Shan, M. C. Nuss, and W. H. Knox, "Detectors and sources for ultrabroadband electro-optic sampling: Experiment and theory," *Appl. Phys. Lett.* **74**, pp. 1516–1518, March 1999.

29. A. Yariv, *Quantum Electronics*, John Wiley & Sons, New York, 3rd ed., 1988.

30. C. J. van der Poel, J. B. B. J. D. Bierlein, and S. Colak, "Efficient type I blue second-harmonic generation in periodically segmented KTiOPO$_4$ waveguides," *Appl. Phys. Lett.* **57**, pp. 2074–2076, Nov. 1990.

31. E. D. Palik, ed., *Handbook of optical Constants of Solids*, vol. II, Academic Press, San Diego, 1991.

Mechanism of THz emission from asymmetric double quantum wells

S. R. Andrews[a,*], P. G. Huggard[a], C. J. Shaw[a], J. A. Cluff[a] and R. Grey[b]

[a]Department of Physics, University of Bath, Bath BA2 7AY, UK

[b]Department of Electronic and Electrical Engineering, The University of Sheffield, Mappin St, Sheffield S1 3JD, UK

ABSTRACT

Impulsive optical excitation of the lowest two conduction or valence subbands of a GaAs/AlGaAs double quantum well can lead to coherent THz emission associated with quantum beating of subband states. We find that in the conduction band the emission arises from a time varying intersubband polarisation generally dominated by the beating of continuum rather than bound exciton states. This is apparent in the electric field and excitation energy dependence of the frequency and amplitude of the THz radiation. Wavepackets made up of these continuum excitons have dephasing times of several picoseconds even for excitation an optical phonon energy above the lowest subband edge. The long lived coherence is partly attributed to the small energy difference between the eigenstates, which substantially reduces the number of relevant scattering events, and partly to the very similar dispersion of the subbands which restricts dephasing by interference. The effect of interference is revealed in systems with significant dispersion of the intersubband gap. Two examples are presented: the valence band of a double well and the conduction band in the presence of an in-plane magnetic field.

Keywords: semiconductor, quantum well, optical, coherence, terahertz radiation, scattering, ultrafast

1.INTRODUCTION

The dynamics of coherently excited excitonic and continuum wavepackets in semiconductors has been the subject of many experimental studies following the development of femtosecond laser sources[1]. A model system for the study of both interband and intersubband optical coherence is the asymmetric double quantum well (ADQW)[1-4]. This system is interesting because it is possible to tune the gap between the lowest energy pair of conduction or valence band states through an experimentally convenient range of energies by application of an electric field. Femtosecond interband excitation with sufficient bandwidth allows the creation of a macroscopically coherent superposition of two or more subband states. The component eigenstates of a wavepacket so created evolve at different rates leading to a spatially oscillating charge density and electric dipole moment perpendicular to the plane of the quantum wells[2-4]. Such quantum beats remain macroscopically coherent until the relative phase of the states is randomized by scattering or until the amplitude is suppressed by interference in the case that an ensemble of oscillators with significantly different frequencies is created. The interesting question which we address in this paper is whether the eigenstates involved in the intersubband polarization are predominantly bound excitons or free carriers. By free carriers or continuum states we actually mean ionized excitons because the Coulomb correlation between electrons and holes cannot be neglected.

The intersubband polarization, which mainly involves the coherence of carriers of a single type and oscillates in the far infrared, has been indirectly studied by time resolved pump-probe transmission[2,3] and directly by detection of THz emission (TE)[4]. In the latter studies it was assumed that the intersubband coherence of continuum states is short lived, as found for the *interband* case[5], and that the TE would be associated with bound exciton states. The short interband coherence lifetime of continuum states is primarily due to the different dispersion of electron and hole bands which leads to the creation of a macroscopic polarization comprised of an ensemble of oscillators with a frequency spread comparable with the laser bandwidth[6]. Dephasing by interference is consequently a very rapid process even in the absence of scattering thus leading to the situation where even a relatively small exciton population dominates the coherent behaviour on ps time scales[5]. It is therefore apparent that wavepackets made up of continuum states should not necessarily be expected to have substantially different *intersubband* dephasing times to those made up of bound excitons. In the intersubband case, the small dispersion of the gap leads to the creation of an ensemble of continuum oscillators with the same frequency in the absence of sample inhomogeneities so that dephasing predominantly occurs by scattering and both continuum and bound exciton states can separately contribute to the macroscopic polarization on ps time scales.

244

Part of the EUROPTO Conference on Terahertz Spectroscopy and Applications II
Munich, Germany • June 1999 SPIE Vol. 3828 • 0277-786X/99/$10.00

In this paper we describe TE measurements on ADQWs which reveal for the first time that wavepackets made up of continuum states can indeed make an important contribution to the long lived part of the macroscopic polarization. They tend to dominate the TE from conduction band charge oscillations except when resonantly exciting the lowest bound exciton transitions. We additionally find that the relative phase of the wavepacket component states is only weakly affected by scattering as evidenced by the wide excitation energy and density ranges over which TE of several ps duration is observed. In contrast, we find that wavepackets made up of exciton states dominate the TE from charge oscillations in the valence band. We attribute this difference to the interference of intersubband continuum oscillators in the valence band. We also show that this effect can be imitated in the conduction band by the application of an in-plane magnetic field[7].

2. EXPERIMENTAL DETAILS

The TE experiments used a mode locked Ti:sapphire laser which produces 65 fs or longer duration pulses at the sample with the aid of extra-cavity dispersion compensation. The output of the laser was split into a 300 mW pump beam and a 20 mW probe beam. The p-polarized pump beam was typically focused to illuminate ~ 1.5 mm^2 of the sample at an angle of 45° to the surface normal. Samples were mounted in the variable temperature insert of a split coil superconducting magnet and maintained at 5 K in a helium atmosphere. The magnet has fused silica windows transverse to the bore and Mylar and high resistivity silicon windows along the bore thus allowing the introduction of visible radiation and the extraction of THz radiation with low loss and dispersion. Mirrors placed within the bore allow experiments with magnetic field parallel ($B_{//}$) and perpendicular ($B_\perp$) to the plane of the quantum wells. The THz beam emitted from the sample in the specular direction was coupled by off-axis parabolic mirrors and a hyper hemi-spherical lens to a 2 THz bandwidth photoconducting receiver as shown in Fig. 1a. The receiver was fabricated from ion implanted silicon and produces a current proportional to the electric field component of an electromagnetic transient when gated by the time delayed probe beam. A good signal to noise ratio was achieved by measuring the receiver current synchronously with 8 kHz modulation of the pump beam and by averaging with the aid of a repetitively scanned delay line, yielding ~ 20 aW detection sensitivity. Details of the MBE grown samples are given in sections 3 and 8.
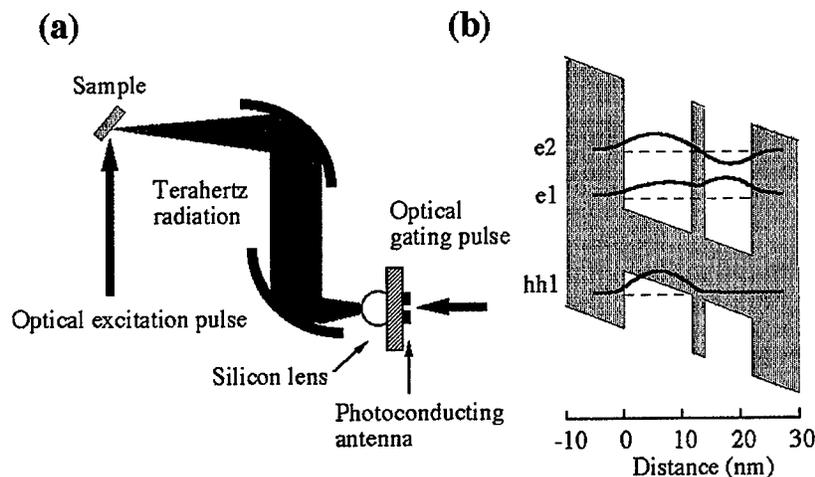
Fig.1: Schematics of (a) experimental arrangement for THz emission measurements and (b) band diagram of double quantum well used to investigate charge oscillations in the conduction band.

3. CONDUCTION BAND CHARGE OSCILLATIONS IN AN ADQW

The nominally undoped ADQW sample used to study charge oscillations in the conduction band consists of ten pairs of GaAs wells with widths of 8.5 nm and 13 nm, separated by a 3 nm thick $Al_{.21}Ga_{.79}As$ barrier. Each pair is spaced from its neighbours by 20 nm of $Al_{.21}Ga_{.79}As$. The repeat unit and schematic diagram are shown in Fig. 1. The structural parameters were verified by photoluminescence excitation (PLE) spectroscopy, electron microscopy and x-ray diffraction. The energy gap between the lowest two conduction band states (e1, e2) can be tuned by an electric field applied between a

semi-transparent NiCr surface contact and a heavily doped layer under the quantum wells. The gap goes through a minimum, T, as the levels anti-cross at a 'resonant' electric field F_O. The energies of the bound excitons, determined by PLE measurements, are shown in Fig. 1a. The different binding energies of spatially direct and indirect excitons lead to different anti-crossing fields of 12 kVcm^{-1} and 5 kVcm^{-1} for the e1-hh1, e2-hh1 wide well (WW) and e2-hh1, e2-hh2 narrow well (NW) excitons respectively. In our notation e1, hh1, lh1 denote the lowest energy electron, heavy hole and light hole states in the double well respectively.
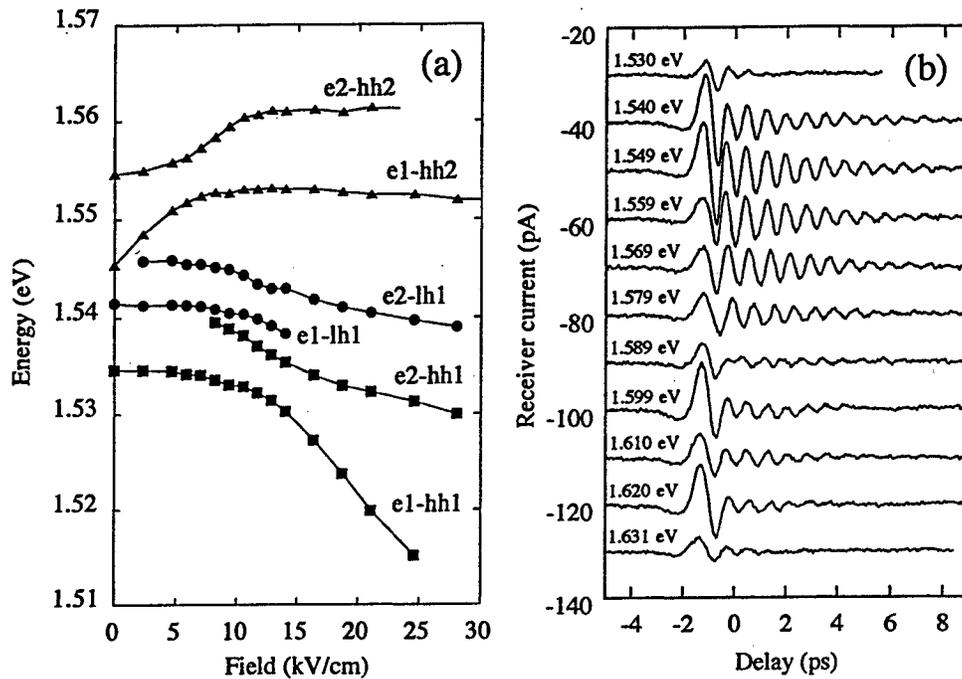
Fig.2: (a) Measured variation of exciton frequencies with electric field. (b) TE signals obtained at an electric field of 10 kVcm^{-1} the centre excitation energies indicated. The time axis has not been corrected for propagation delay.

Data showing the development of the electric field radiated by the sample with increasing delay for different excitation energies are shown in Fig. 2b. An excitation bandwidth of 8 meV was used for the experiments described in this and the following section. The sample was biased so as to produce an internal electric field of 10 kVcm^{-1}. Ringing arising from charge oscillations in the two lowest conduction subbands[4,7] is seen following an initial transient arising from a polarization 'instantaneously' created in the wells and associated with a net average electron-hole separation[11]. Charge oscillations in the valence band are suppressed by strong localization of holes in the wider well at the electric fields of interest[12]. TE measurements were generally made with a photoexcited electron-hole pair density $n_s = 4(\pm1)\times10^9$ cm^{-2} per double well per pulse, which places our experiments in the low density limit $n_s a_o^2 \sim 0.01$ where a_o is the 1s exciton radius. The excitation density dependence is discussed in section 5.

4.ELECTRIC FIELD DEPENDENCE

Values for the frequency, dephasing time and oscillation amplitude of the TE were generally obtained by fitting an exponentially damped cosine function to the data, excluding the transient due to the instantaneous polarization. Fourier analysis was used where simple harmonic decay was not observed. Figs. 3a,b shows the variation of TE frequency with electric field for three different excitation energies. The behaviour is different for excitation resonant and non-resonant with the lowest energy WW and NW bound 1s excitons. We use the term resonant to mean within ± 2 meV of the anti-crossing energy. The non-resonant behaviour is typified by 1.549 eV excitation which lies in the continua of the e1-hh1, e2-hh1 excitons (Fig. 2a). Similar behaviour was observed over most but not all of the energy range 1.54 eV to 1.62 eV. An

approximately parabolic dependence of the TE frequency on field, centred around a 'resonant' field $F_0 \sim 10$ kVcm^{-1}, is observed. The solid curve in Fig. 3a is a fit to the equation

$$f = \sqrt{\beta^2 (F - F_0)^2 + T^2} \qquad (1)$$

appropriate for uncorrelated electrons and small detuning[2]. β is the constant of proportionality between the frequency separation of the uncoupled electron states and the electric field F. The differences between exciton frequencies extracted from PLE spectra taken from the same part of the sample are shown by the broken curves in Fig. 3a. The values of T and F_0 observed in TE are consistent with calculations[12] for the beating of continuum states shown in Fig. 3c but inconsistent with that expected for bound excitons (PLE data and calculation). The difference between TE and PLE measurements is even larger for the lowest energy light hole excitons (not shown in Fig. 3a). Our results differ from a previous study[4] where no distinct variation in the TE frequency was observed, perhaps because of differences in sample homogeneity or experimental conditions.

Fig.3: (a) Electric field dependence of differences between e1-hh1, e2-hh1 (WW) and e1-hh2, e2-hh2 (NW) exciton frequencies obtained from PLE data at excitation densities of 2.10^6 cm^{-2} (dashes) and 5.10^9 cm^{-2} (dots). Circles show TE frequency obtained with excitation energy of 1.549 eV and $n_s = 4.10^9$ cm^{-2}. Solid curve is a fit of Eqn. 1 to TE (b) TE frequency obtained with an excitation energies of 1.553 eV (squares, WW) and 1.534 eV (triangles, NW). (c) Calculated 1s bound exciton (dashed curves) and exciton continuum edge (solid curve) beat frequencies.

TE traces obtained for excitation resonant with the lowest energy bound excitons in the NW and WW (Fig. 3b) exhibit significantly different frequency spectra to those observed for non-resonant excitation. This is particularly clear for resonant excitation of the NW at 1.553 eV where most of the spectral amplitude for fields near 5 kVcm^{-1} is at a frequency similar to

that expected for beating of NW excitons as deduced from the PLE measurements. A dephasing time of ~ 0.6 ps observed near 5 kVcm^{-1} which is significantly shorter than the ~2 ps observed at 10 kVcm^{-1}. For resonant excitation of the WW at 1.534 eV a non-harmonic decay was observed for fields near 14 kVcm^{-1} with spectral components at two frequencies consistent with simultaneous bound and continuum state beating. The dephasing times of the two components were similar to each other and to that obtained for non-resonant excitation but the amplitude of the continuum oscillations was much larger. Details of the spectral content of the TE traces will be presented in more detail in a future publication.
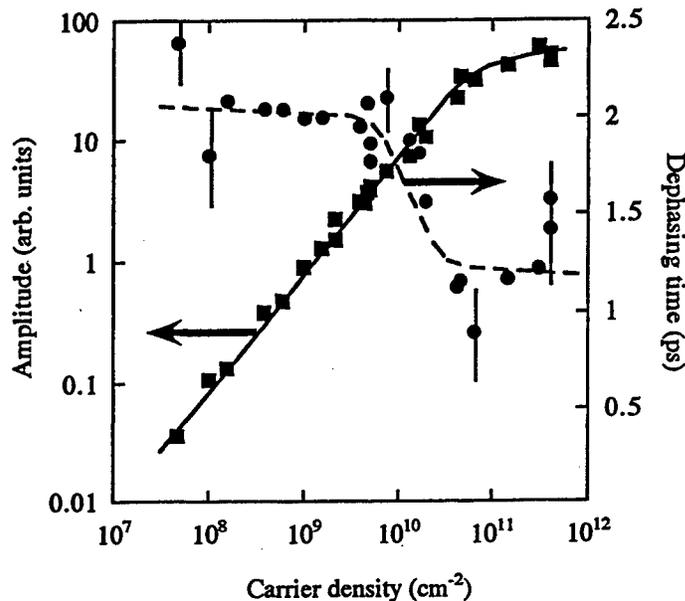
Fig.4: Variation of dephasing time (circles) and emission amplitude (squares) with excitation density n_s for centre excitation energy of 1.549 eV. The electric field is adjusted for minimum emission frequency at each n_S. Lines are guides to the eye.

5.EXCITATION DENSITY DEPENDENCE

To confirm that exciton and electric field screening by the photoexcited plasma are not responsible for the differences between subband splittings inferred from PLE and TE, PLE spectra were obtained at a similar excitation density to that used in the TE measurements (5.10^9 cm^{-2}) and at a much lower density ($n_s = 2.10^6$ cm^{-2}). At the higher of the two carrier densities both F_0 and the energy separation between e1-hh1 and e2-hh1 excitons are only 5% larger than at the lower density (Fig. 3a). These differences are too small to account for the different tunnel gaps and resonant electric fields apparent in the TE and PLE measurements. Fig. 4 shows the effect of varying n_S on the amplitude and dephasing time of the TE and tends to confirm the fact that the experiments are performed in the low density limit suggested by the PLE measurements. The non-linear variation of initial TE amplitude with n_s above ~3.10^{10} cm^{-2} can be qualitatively explained by Coulomb renormalisation of the tunnel gap[14]. The reduction in dephasing time above 10^{10} cm^{-2} is consistent with estimated electron-electron scattering and radiation damping rates[14,15,16]. For non-resonant excitation, the dephasing time is limited by sample and field inhomogeneity for temperatures below 80 K and carrier densities below a few times 10^{10} cm^{-2}.

6.EXCITATION ENERGY DEPENDENCE

Further evidence for the important role of continuum exciton states comes from the behaviour of the TE as a function of excitation energy at a fixed electric field of 10 kVcm^{-1} (Fig. 2b). The initial amplitude of the TE is not strongly resonant with the lowest energy exciton transitions as found in four wave mixing studies of the third order interband polarisation[2]. Coherent charge oscillations are observed for excitation over a range extending from the band edge to more than 100 meV

above. The TE frequency and dephasing time are approximately independent of excitation energy in this range (Fig.5). Similarly, the resonant electric field changes by less than 0.5 kVcm[-1]. This behaviour is consistent with the excitation of higher lying e1, e2-hhn and e1, e2-lhm continuum states (n,m denote subband indices) but inconsistent with the dominant involvement of bound excitons. If bound excitons were involved then the frequencies and resonant fields should vary with excitation conditions as can be seen with reference to Fig. 2a. Carriers with sufficiently large excess energies (those excited above ~ 1.59 eV) can lose energy by longitudinal optical (LO) phonon emission in a few hundred fs[17]. Intraband carrier thermalisation via inelastic electron-electron scattering also proceeds on a few hundred fs time scale for $n_s \sim 10^{10}$ cm[-2] [19]. Such carriers can only contribute to the long lived TE if the macroscopic phase of the intersubband polarization is at least partially preserved during energy relaxation. The idea that the relative phase of eigenstates can be insensitive to many body interactions has previously been invoked to explain the existence of TE from Bloch oscillations in superlattices excited well above the miniband edges[10,18].
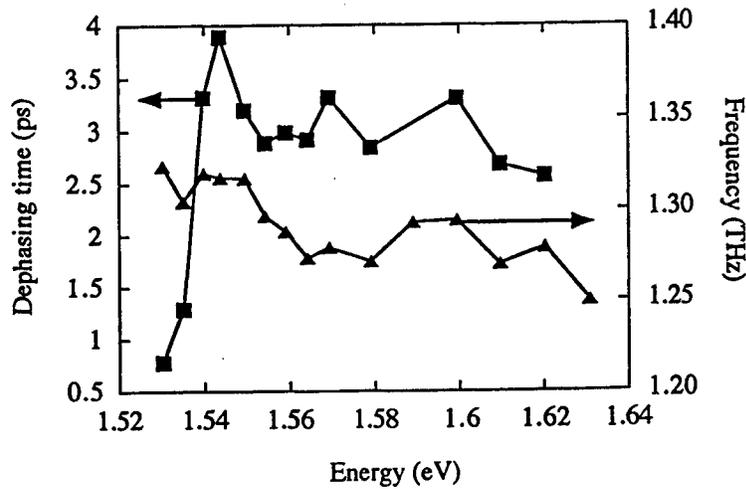
Fig.5:Variation of TE dephasing time and frequency with excitation energy at an electric field of approximately 10 kVcm[-1].

7.MAGNETIC FIELD DEPENDENCE

The experiments in magnetic field[7] were performed at an electric field where the amplitude was a maximum but the dephasing time had a somewhat smaller than maximum value of 1.75 ps. The excitation energy was 1.549 eV and the laser bandwidth 20 meV. The variation in dephasing time deduced from fitting the data to a damped cosine function is shown in Fig. 6. The variation of emission frequency with electric field was checked at several values of magnetic field to verify that the resonant electric field did not vary significantly with magnetic field. The effect of $B_{//}$ is to decrease the dephasing time by a factor of ~ 2 over the range 0 to 2 T. The oscillation frequency increases by about 0.05 THz over the same range. In this field configuration the motion of the electrons is deflected as they tunnel thus driving the coupled states out of resonance so that coherent phenomena are suppressed. Raichev[20] has developed a simple theory for the charge oscillations in a parallel magnetic field which neglects Coulomb interactions and scattering. The important feature is that the intersubband gap δE depends on the in-plane component of momentum, $p_{//}$, of the optically injected carriers:

$$\delta E = \sqrt{T^2 + (\Delta - eB_{//}sp_{//}/m)^2} \qquad (2)$$

Eqn. 2 reflects the momentum change $\delta p_{//} = eB_{//}s$ experienced by an electron tunneling a distance s between well centres. Significant suppression of the TE by interference is predicted when the energy shift $p_{//}\delta p_{//}/m$ is comparable with T which requires $B_{//} \sim 1.5$ T, in qualitative agreement with experiment. In contrast, no significant change in dephasing rate is expected or observed for $B_\perp$.
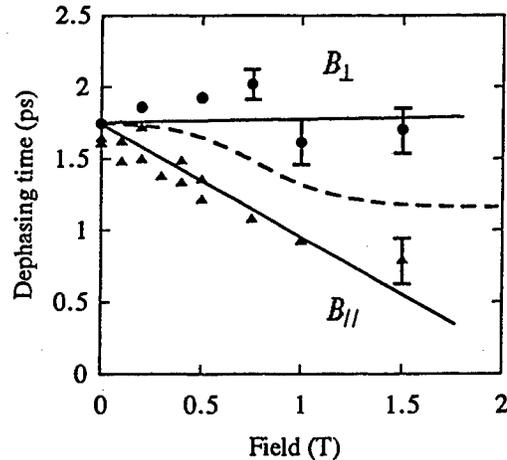
Fig.6: Measured dephasing time of TE as a function of perpendicular (circles) and parallel (triangles) magnetic field. Continuous lines are guides to the eye, dashed line is a theoretical prediction described in ref. 7.
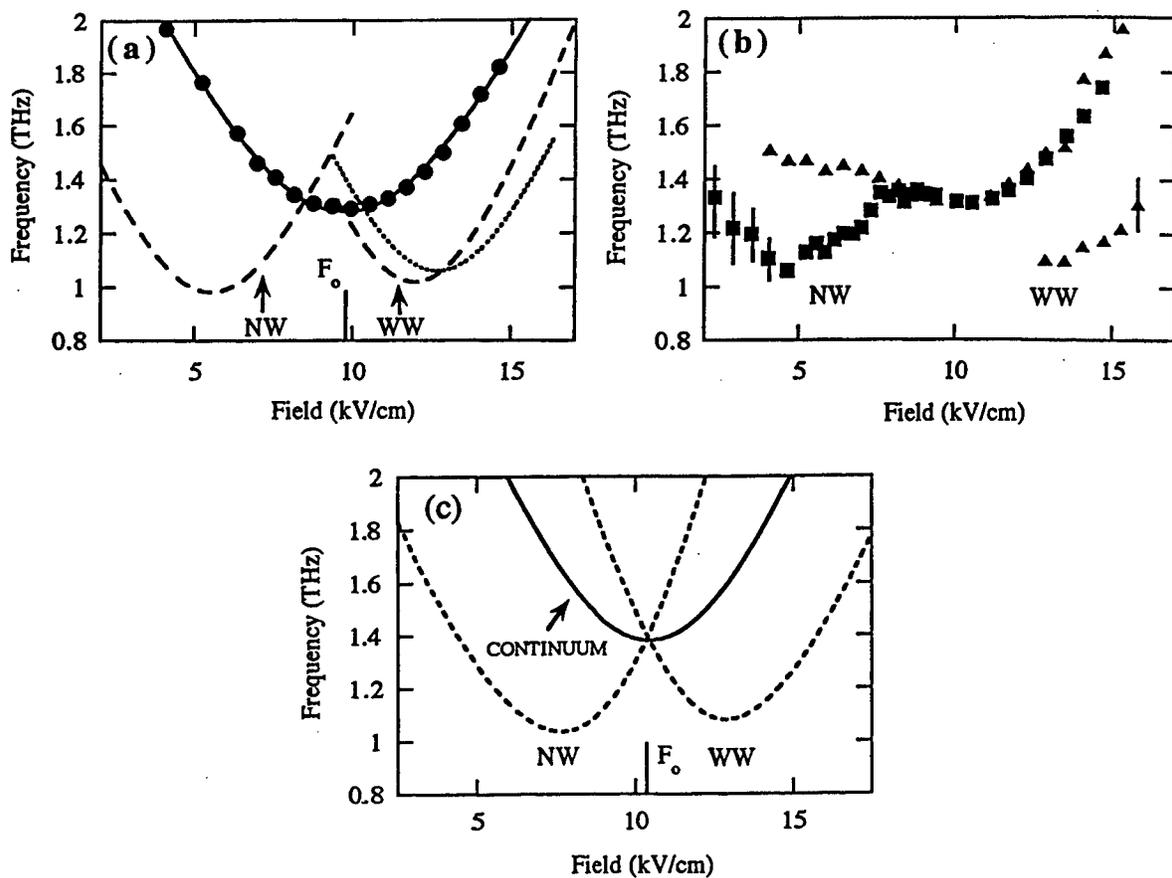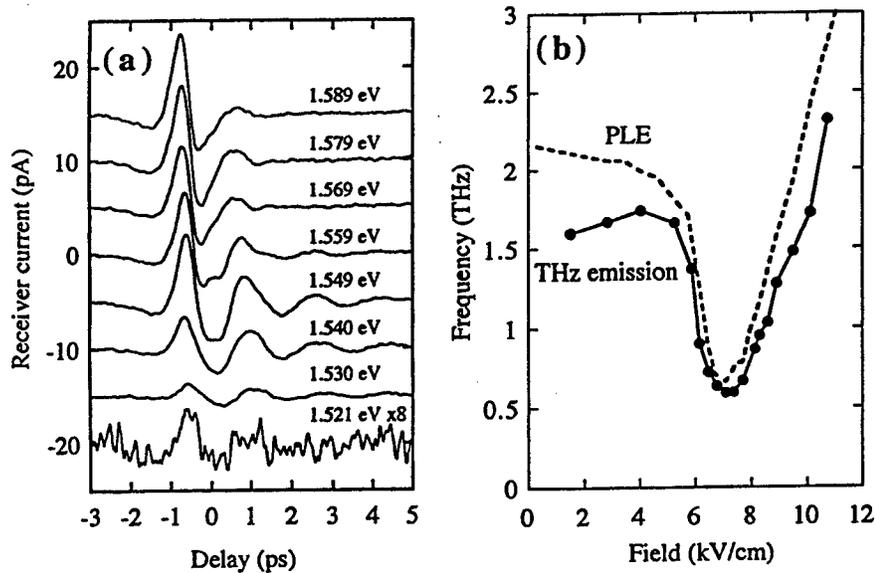

Fig.7: (a) TE traces obtained at 7 kVcm^{-1} for different excitation energies. (b) Electric field dependence of differences between e1-hh1, e1-hh2 exciton frequencies obtained from PLE data (dashed curve) and THz emission frequency (solid curve).

8. VALENCE BAND CHARGE OSCILLATIONS IN AN ADQW

An asymmetric double well having well widths of 10 nm and 6 nm separated by a 1.25 nm barrier but otherwise similar to that discussed above was also investigated in order to compare the behaviour of optically excited charge oscillations in the valence band with that in the conduction band. This structure was grown with the ordering of wide and narrow wells reversed so as to allow the lowest energy heavy hole states to be tuned through resonance by the application of a reverse bias. Fig. 7a shows TE traces obtained at various excitation energies near resonance with the lowest energy exciton transitions. Unlike previous studies[21] of TE from valence band charge oscillations in single quantum wells, which were associated with heavy hole - light hole beating, the present studies involve the lowest two heavy hole states, hh1 and hh2. Results for the THz emission frequency and the frequency separation of the e1-hh1 and e1-hh2 exciton transitions deduced

from PLE measurements are shown in Fig. 7b. There is much closer similarity between the two sets of results than found in the conduction band case described above. The TE is also strongly resonant with the e1-hh1, e1-hh2 transitions. We attribute the different behaviour to significant dispersion of the inter valence subband splitting which has been verified by band structure calculations which will be discussed in more detail elsewhere. If the dispersion is sufficiently large compared with the spectral width of the pump pulse, which is the case here, then TE from the beating of continuum hole states will be suppressed by interference thus allowing excitons to dominate.

9. CONCLUSIONS

In summary, we find that the TE from charge oscillations in the conduction band of an ADQW is dominated by the beating of continuum exciton states except under conditions where the lowest energy bound excitons are resonantly excited. In the latter case evidence of bound exciton beating is also revealed. Possible explanations for the relatively weak bound exciton signature obtained when resonantly exciting the WW are the small exciton linewidths relative to the spectrally broad excitation, the larger continuum state intersubband dipole moment[22] and dissipation[23] associated with coupling of bound excitons to continuum excitations (Fano resonance). Dissipation might also explain the short dephasing time observed for resonant excitation in the NW compared with that obtained for excitation in the continuum. In contrast to the behaviour in the conduction band, TE from charge oscillations in the valence band of an ADQW appears to be dominated by beating of exciton states. We attribute this difference to strong dispersion of the gap between the lowest two heavy hole subbands which leads to rapid dephasing of continuum wavepackets by interference.

In the conduction band, the intersubband dephasing time of continuum states created with large excess energy is very long compared with the expected ~ 100 fs energy relaxation time. We believe that the relatively small scattering rate of continuum wavepackets in the ADQW is a property of the close spacing of the energy levels; physically, the in-plane variation of eigenstates is sufficiently similar that they are almost equally affected by in-plane scattering and the relative phase is to a certain extent preserved for important 'in-plane' processes such as LO phonon emission. Although not widely appreciated, similar behaviour has previously been observed in heavy-light hole quantum beats[6,24], Bloch oscillations in superlattices[18] and in the long lived coherence of cyclotron emission optically excited well above the bandgap of GaAs[25].

10. ACKNOWLEDGMENTS

11. REFERENCES

1. J. Shah 'Ultrafast Spectroscopy of Semiconductors and Semiconductor Nanostructures', Springer Series in Solid State Sciences, 115 (1996)

2. K. Leo, J. Shah, E. O. Göbel, T. C. Damen, S. Schmitt-Rink, W. Schafer and K. Köhler 'Coherent oscillations of a wave packet in a semiconductor double-quantum-well structure', Phys. Rev. Lett. 66, 201 (1991)

3. K. Leo, J. Shah, T. C. Damen, A. Schultze, S. Schmitt-Rink, P. Thomas, E. O. Gold, S. L. Chuang, M. S. C. Luo, W. Schäfer, K. Köhler and P. Ganser 'Dissipative dynamics of an electronic wavepacket in a semiconductor double well potential', IEEE J. Q. El. 28, 2498 (1992)

4. H. G. Roskos, M. C. Nuss, J. Shah, K. Leo, D. A. B. Miller, A. M. Fox, S. Schmitt-Rink and K. Köhler 'Coherent submillimeter-wave emision from charge oscillations in a double-well potential', Phys. Rev. Lett. 68, 2216 (1992)

5. D-S. Kim, J. Shah, J. E. Cunningham, T. C. Damen, W. Schäfer, M. Hartmann and S. Schmitt-Rink 'Giant excitonic resonances in time-resolved four-wave mixing in quantum wells', Phys. Rev. Lett. 68, 1006 (1992)

6. T. Dekorsy, A. M. T. Kim, G. C. Cho, S. Hunsche, H. J. Bakker, H. Kurz, S. L. Chuang and K. Köhler 'Quantum coherence of continuum states in the valence band of GaAs quantum wells', Phys. Rev. Lett. 77, 3045 (1996)

7. S R Andrews, P. G. Huggard, C J Shaw, J A Cluff, O E Raichev and R Grey 'Magnetic field suppression of THz charge oscillations in a double quantum well', Phys. Rev. B57, R9443 (1998)

8. P. Leisching, T. Dekorsy, H. J. Bakker, H. Kurz and K. Köhler 'Exceptionally slow dephasing of electronic continuum states in a semiconductor', Phys. Rev. B51, 18015 (1995)

9. R Martini, G. Klose, H. G. Roskos, H. Kurz, H. T. Grahn and R. Hey 'Superradiant emission from Bloch oscillations in semiconductor superlattices', Phys. Rev. B54, R14325 (1996)

10. H. G. Roskos, C. Waschke, R. Schwedler, P. Leisching, Y Dhaibi, H. Kurz and K. Köhler 'Bloch oscillations in GaAs/AlGaAs superlattices after excitation well above the bandgap', Superlattices and Microstructures 15, 281 (1994)

11. P. C. M. Planken, M. C. Nuss, W. H. Knox, D. A. B. Miller and K. W. Goossen 'THz pulses from the creation of polarised electron-hole pairs in biased quantum wells', Appl. Phys. Lett. 61, 2009 (1992)

12. Weak heavy hole - light hole (hh-lh) beats with a frequency of approximately 1.65 THz can however be seen in traces at much lower and much higher electric fields, where the amplitude of the conduction band oscillations is very small, when resonantly exciting both e1-hh1 and e1-lh1 excitons.

13. A. M. Fox, D. A. B. Miller, G. Livescu, J. E. Cunningham, J. E. Henry and W. Y. Jan 'Excitons in resonant coupling of quantum wells', Phys. Rev. B42, 1841 (1990); M. Grundmann and D. Bimberg 'Anisotropy effects on excitonic properties in realistic quantum wells', Phys. Rev. B38, 13486 (1988)

14. O. E. Raichev 'Charge oscillations in double quantum wells: nonlinear effects caused by the Coulomb interaction', Phys. Rev. B51, 17713 (1995)

15. Electron-electron scattering time is estimated as 1 ps for $n_S = 10^{11}$ cm^{-2} using ref. 14. Radiation decay time is estimated as 2 ps for same n_S using the superradiance model described in ref. 16 but taking into account the refractive index of the semiconductor.

16. K. Victor, H. G. Roskos and C. Waschke 'Efficiency of submillimeter-wave generation and amplification by coherent wavepacket oscillations in semiconductor structures', J. Opt. Soc. Am. B, 11, 2470 (1994)

17. S. Hunsche, K. Leo, H. Kurz and K. Köhler 'Femtosecond intersubband relaxation in GaAs quantum wells', Phys. Rev. B50, 5791 (1994)

18. F. Wolter, H. G. Roskos, P. Haring Bolivar, G. Bartels, H. Kurz, K. Köhler, H. T. Grahn and R. Hey 'Influence of LO-phonon emission on Bloch oscillations in semiconductor superlattices', Phys. Stat. Sol. (b) 204, 83 (1987)

19. W. H. Knox, C. Hirlimann, D. A. B. Miller, J. Shah, D. S. Chemla and C. V. Shank 'Femtosecond excitation of nonthermal carrier populations in GaAs quantum wells', Phys. Rev. Lett. 56, 1191 (1986)

20. O. E. Raichev 'Suppression of the coherent charge oscillations in coupled quantum wells by an in-plane magnetic field', J. Appl. Phys. 80, 924 (1996)

21. P. C. M. Planken, M. C. Nuss, I. Brener, K, W. Goossen, M. S. C. Luo, S. L. Chuang and L. Pfeiffer 'Terahertz emission from single quantum wells after coherent optical excitation of light hole and heavy hole excitons', Phys. Rev. Lett. 69, 3800 (1992)

22. V. M. Axt, G. Bartels and A. Stahl 'Intraband dynamics in the semiconductor band edge: shortcomings of the Bloch equation method', Phys. Rev. Lett. 76, 2543 (1995)

23. We calculate $z_{12} = 5.4$ nm for the lowest heavy hole excitons and 6.7 nm for continuum states.

24. H. Wang, J. Shah, T.C. Damen and L. N. Pfeiffer 'Spontaneous emission of excitons in GaAs quantum wells: the role of momentum scattering', Phys. Rev. Lett. 74, 3061 (1995)

25. D. Some and A. V. Nurmikko 'Coherent transient cyclotron emission from photoexcited GaAs', Phys. Rev. B50, 5783 (1994)

SESSION 6

Spectroscopy and Other Applications
Using Fast Pulse Sources

Near-Field Phenomena Observed with Terahertz Pulses

Klaas Wynne[*], John Carey, Justyna Zawadzka, Dino A. Jaroszynski

Femtosecond Research Centre, University of Strathclyde, Dept. of Physics and Applied Physics, Glasgow G4 0NG, UK

ABSTRACT

Propagation of free-space femtosecond THz pulses (t rays) through and past metal structures with dimensions on the order of a wavelength has been studied. In waveguides with diameters close to one wavelength, it is found that the phase velocity can become superluminal (faster than the speed of light in vacuum) and even infinite or negative. T rays that propagate past a 100-μm metal wire are delayed when the polarization is perpendicular and advanced when it is parallel. In this case, it is also observed that the centroid velocity (related to the group velocity) can become superluminal. Many of the results do not conform to simple waveguide theory, because of multiple reflections of the evanescent waves inside the waveguide. This "Fabry-Perot" effect for evanescent waves is the cause of the negative phase velocities below the waveguide cutoff.

Keywords: Ultrafast, imaging, wave propagation, terahertz, tunneling

1. INTRODUCTION

Several successful attempts have been made to use terahertz pulses (t rays) for imaging including t-ray tomography[1] and real-time imaging,[2,3] typically with a resolution on the order of a millimeter. A near-field method for improving the spatial resolution in T-ray imaging has been reported[4] in which a metal aperture has been used to improve the resolution to 140 μm. Recently, we have demonstrated a new method of achieving sub-wavelength spatial resolution in t-ray imaging.[5,6] In this method, an optical beam is focussed to a small spot in an optical-rectification crystal and the t rays emerge in a beam, which in the near-field region has a sub-wavelength diameter. If the sample is placed directly on the generation crystal, it can be imaged in the far infrared with λ/4.3 resolution. Here it will be described how this experimental setup has been used to study the evanescent-wave propagation inside waveguides and past sub-wavelength-diameter metal wires. The near-field imaging setup allows one to couple power into waveguides with a diameter on the order of one wavelength with reasonable efficiency. It has been predicted[7,8] that waves can travel superluminally (faster than the speed of light in vacuum) in waveguides below cutoff. Experimental microwave[9,10] and femtosecond optical[11] studies have confirmed this theoretical result. However, the microwave experiments were either CW or used very long pulses and could therefore not directly observe the propagation speed of energy packets. The optical experiments do not have access to phase information as they only measure intensities rather than fields. The t-ray setup gives access to all the pertinent phase information of the pulse traveling through the waveguide while having good time-resolution. Therefore, we have been able to analyze the propagation characteristics of these evanescent waves fully for the first time. In the waveguides, it is found that the phase velocity can be superluminal and even become negative. This may result in the peak of a THz pulse emerging from a sample before entering it in apparent contradiction with the principle of causality. Theoretically, it should be possible to observe superluminal group velocities as well but a limited signal-to-noise ratio has prevented us from establishing that. However, in experiments on propagation past metal wires the unique properties of t rays could be used to prove that the group velocity exceeds that in vacuum.

Some of the superluminal propagation effects may be caused by absorptive pulse shaping in which, for example, the system preferentially transmits the front of the pulse. However, pure phase effects contribute to the superluminality too. This can be expressed using the group and loss delays. If the complex field transmission $\tilde{T}(\omega)$, these delays are given by:[12]

$$\tau_g + i\tau_L = -i\frac{\partial \ln \tilde{T}}{\partial \omega} \tag{1}$$

---

[*] KW (correspondence): email: klaas.wynne@phys.strath.ac.uk; URL: http://dutch.phys.strath.ac.uk/FRC/; Tel.: +44 (141) 548-3381; Fax: +44 (141) 552-2891. JC: email: john.carey@starth.ac.uk; Tel.: +44 (141) 548-3059. JZ: email: justyna.zwadzka@strath.ac.uk; Tel.: +44 (141) 548-3059. DAJ: email: dino@phys.strath.ac.uk; Tel.: +44 (141) 548-3057

254

Part of the EUROPTO Conference on Terahertz Spectroscopy and Applications II
Munich, Germany • June 1999 SPIE Vol. 3828 • 0277-786X/99/$10.00

The loss delay, τ_L, is related to the delay induced by absorption or reflection that affects the front of the pulse more than the back or vice versa. Some authors have concluded that the loss time (which is often causal) is "most relevant to describe the physics of tunneling"[13] but there appears to be no physical reason for this assertion.

2. EXPERIMENTAL

In our experiment,[5] t rays are generated through optical rectification of femtosecond pulses in ZnTe.[14] The laser source is a commercial Ti:sapphire oscillator and regenerative amplifier producing ~150-fs pulses at 800 nm with a 250-kHz repetition rate and 750-mW average power. About 280 mW is focussed by an f = 5 cm lens onto a 10x10 mm² aperture ZnTe crystal (Uni-Export), which has either a 1-mm or 500-µm a thickness and is cut perpendicular to the <110> crystallographic axis. The crystal is mounted on an x-y translation stage that allows translation over 25 mm in the plane perpendicular to the beam with 10-nm resolution. The t rays emitted by the ZnTe crystal are collimated and focused with two 44.5-mm diameter off-axis parabolic mirrors, which have a 38.1-mm focal length. The second off-axis parabolic mirror has a hole drilled through it, which allows an 800-nm gating beam to be overlapped with the t-ray beam in another <110> ZnTe crystal with a 500-µm thickness. The gating beam has an average power of 8 mW, is temporally delayed by a fast-scanning (6 Hz) optical delay line and focussed into the detection crystal with an f = 10 cm lens. The Pockels effect in the ZnTe detection crystal causes the ellipticity of the gate beam to change in proportion to the instantaneous electric-field strength of the terahertz pulse.[14,15] This time-delay dependent change in ellipticity is measured by sending the gate beam through a quarter-wave plate, a Glan-Thompson polarizer and balanced detection by a pair of photodiodes wired to give zero current for balanced power. The signal current is sent to a preamplifier (SR570) for amplification and filtering. This signal and a signal proportional to the instantaneous temporal delay, are digitized by a fast analog-to-digital converter (Data Translation, T112). The terahertz pulses have about three cycles and a spectrum that extends from about 5 to 100 cm⁻¹ as previously reported.[16]

To obtain the highest spatial resolution one would like to focus the 800-nm t-ray generation beam to the smallest possible spot size. As ZnTe is used as the optical-rectification crystal, the minimum spot size is determined by two-photon absorption and is approximately 200 µm. For smaller spot sizes, there is a catastrophic loss of signal intensity and green emission from the crystal. To determine the resolution of the imaging system, a knife-edge consisting of a piece of aluminum foil mounted directly on the ZnTe generation crystal, was scanned through the beam. At each position, multiple time scans over about 20 ps were taken to determine the time dependence of the terahertz pulse (*circa* one second of averaging, S/N = 300). These data are then Fourier transformed in order to obtain the position-dependent transmission spectra. The transmission is determined as $\Delta T_{field}(\omega) = E(\omega, x)/E(\omega, 0)$ where $E(\omega, 0)$ is the complex amplitude spectrum of the field at a position where the knife-edge does not absorb. The advantage of defining the transmission in this manner is that the noise has a symmetric distribution, unlike the case of an intensity ratio. The wavelength and position dependent transmission profiles have been fitted by error functions. The intensity FWHM of the t-ray beam derived from the fits to error functions, varies from 110±13 µm at 80 cm⁻¹ (λ = 125 µm), to 232 ± 85 µm at 10 cm⁻¹ (λ = 1 mm). The uncertainties given are the 1σ joint confidence intervals. At the longer wavelengths, the spatial resolution is more than 2.6 times better than the free-space diffraction limit of 0.61 λ for the intensity FWHM. As the refractive index of ZnTe is 3.1 at these wavelengths, this is not proof of a resolution enhancement due to a near-field effect. However, there appears to be no reason why the resolution could not be enhanced further using this technique with an unamplified laser and tighter focussing into the ZnTe crystal. When the ZnTe generation crystal is scanned several millimeters perpendicularly to the generation beam, little variation of the t-ray field strength (±10%) or transit time (±5 fs over short distances, see below) is observed.

Transmission and refractive-index or phase spectra are derived from the time-domain data by fast Fourier transforming (FFT). If $E(\omega)$ is the FFT of the time-domain data and $E_0(\omega)$ a reference spectrum (e.g., free space), the field transmission is given by $|E(\omega)/E_0(\omega)|$. Calculation of the accumulated phase (or the refractive index) is slightly more problematic as it involves a logarithm of a complex quantity. The method used here is that an overall refractive index, assumed constant for all frequencies, is guessed at. The accumulated phase difference with respect to free space, is then calculated from

$$\Delta\varphi(\omega) = \varphi_{guess} - i \ln\left[\frac{\tilde{E}(\omega)/\tilde{E}_0(\omega)}{\left|\tilde{E}(\omega)/\tilde{E}_0(\omega)\right|} \exp\left\{-i\left(\varphi_{guess} - \frac{\omega}{c}L\right)\right\} \right] \tag{2}$$
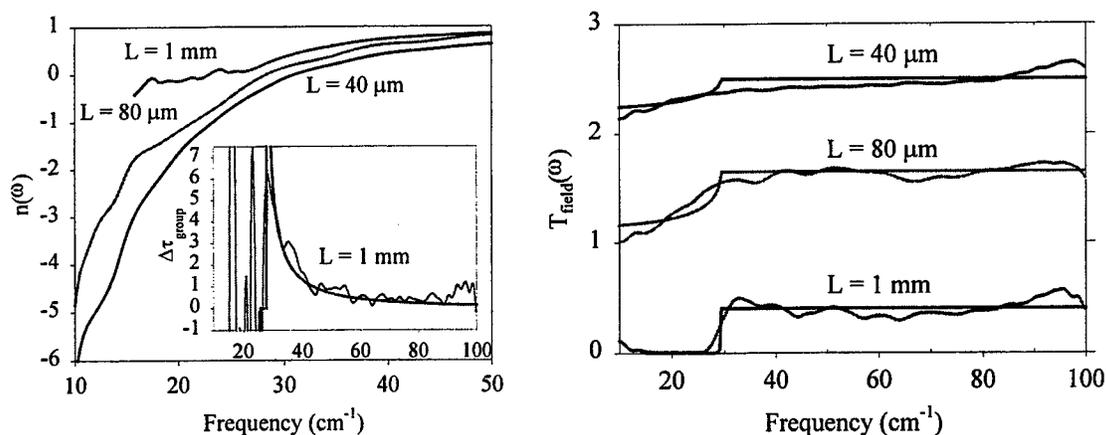
FIG. 1. Transmission through 200-μm diameter pinholes with varying length. (Left) The effective refractive index calculated from the accumulated phase. Inset: The difference from the vacuum group delay calculated from the phase. (Right) Experimental field transmission and comparison with transmission calculated from simple waveguide theory. The curves have been offset vertically for clarity.

where L is the sample length and $\varphi_{guess} = \omega\, L\, n_{guess}\, / c$ is the guess for the phase. In the data discussed here, it is a reasonable assumption that the refractive index tends to 1 at high frequencies and using $n_{guess} = 1$ is consistent with all the data. However, in the thicker samples or samples with strong dispersion, this method may lead to 2π phase jumps, which have to be corrected by hand. This (corrected) phase is then used to calculate the refractive index from

$$n = 1 + c\,\Delta\varphi\, / \left(\omega\, L\right) \tag{3}$$

and the group delay difference

$$\Delta\tau_{group} = \partial\left(\Delta\varphi\right)/\partial\omega \tag{4}$$

To investigate the evanescent-wave properties inside waveguides, several metal cylindrical pinholes were used. A set of nickel pinholes (Coherent-Ealing) with a 40-μm thickness and diameters of 50, 100, 200 and 400 μm were used. To obtain longer waveguides, sheet metal has been used and holes were drilled though them mechanically. A 1-mm thickness aluminum plate has been used to make 200 and 400-μm wide waveguides. Two 80 and 250-μm thickness brass plates were used to drill 150 and 200-μm diameter waveguides. The mechanical drilling may have resulted in some irregularities in these
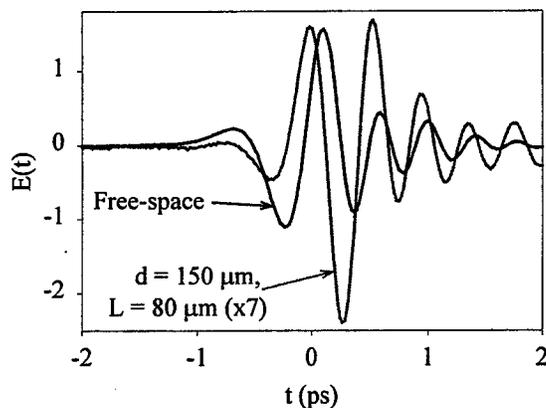
FIG 2. Comparison between a terahertz pulse traveling though free space vs. one transmitted through a 150-μm diameter, 80-μm length waveguide. It can be seen that the peak of the latter is advanced in time.

256

waveguides, which may have affected the results to some extent.

In a perfectly conducting cylindrical waveguide, the electromagnetic waves accumulate a phase, which for TE-modes is given by[17]

$$\varphi = \frac{\omega_c L}{c} \sqrt{\left(\frac{\omega}{\omega_c}\right)^2 - 1} \ , \quad \omega_c = \frac{2xc}{d} \tag{5}$$

where ω_c is the cutoff frequency, d is the waveguide diameter and L its length. For the lowest order mode, TE_{11}, the parameter x has the value[17] 1.841. It can be seen from Eq. (5) that above the cutoff frequency, the transmission is unity but the waveguide is very dispersive. Below cutoff, transmission is less than unity and the accumulated (real) phase is zero. As the phase delay is φ/c, it can be seen that the phase velocity tends to infinity as cutoff is approached. The group delay derived from Eq. (5) is

$$\tau_{group} = \frac{\partial \varphi}{\partial \omega} = \frac{\omega L}{c} \frac{1}{\sqrt{\omega^2 - \omega_c^2}} \ . \tag{6}$$

Therefore, as cutoff is approached the group velocity tends to zero. Below cutoff, however, the group delay becomes imaginary, which has been interpreted to imply an infinite group velocity. Microwave experiments by Nimtz et al. in the time[10] and frequency domain[9] appear to confirm this bizarre result. If taken to its extreme, it would appear to imply that it is possible to receive signals before they are sent.

In the initial experiments, relatively large diameter (150 to 400 μm) waveguides were studied, in order to have the cutoff frequency more or less in the middle of the accessible frequency range. FIG. 1 shows a typical case of 200-μm diameter waveguides with various lengths (TE_{11} mode cutoff frequency from Eq.(5): 29.3 cm⁻¹). The 1-mm length waveguide shows a very sharp cutoff in transmission as expected. As a 12-ps window had to be applied in the analysis of the time-domain data, the cutoff is slightly smoother than predicted by theory. The phase properties in the 1-mm case are also as expected: The effective refractive index, $n = \varphi/(k_0 L)$ with k_0 the vacuum wavevector, varies from 1 at high frequencies to 0 at the cutoff frequency. The group delay is seen to diverge at the cutoff as expected. However, for the shorter waveguides (40 and 80 μm), the transmission cutoff all but disappears and the refractive index becomes negative below the cutoff frequency. The group delay stays at a finite positive value. In some of the medium-sized waveguides, it is found that the peak of the terahertz pulse travels at superluminal velocity corresponding to a superluminal phase velocity. For example, in a 150-μm diameter, 80-μm length waveguide (FIG. 2), the peak advances by 0.1 ps. However, the center of gravity of the pulse is
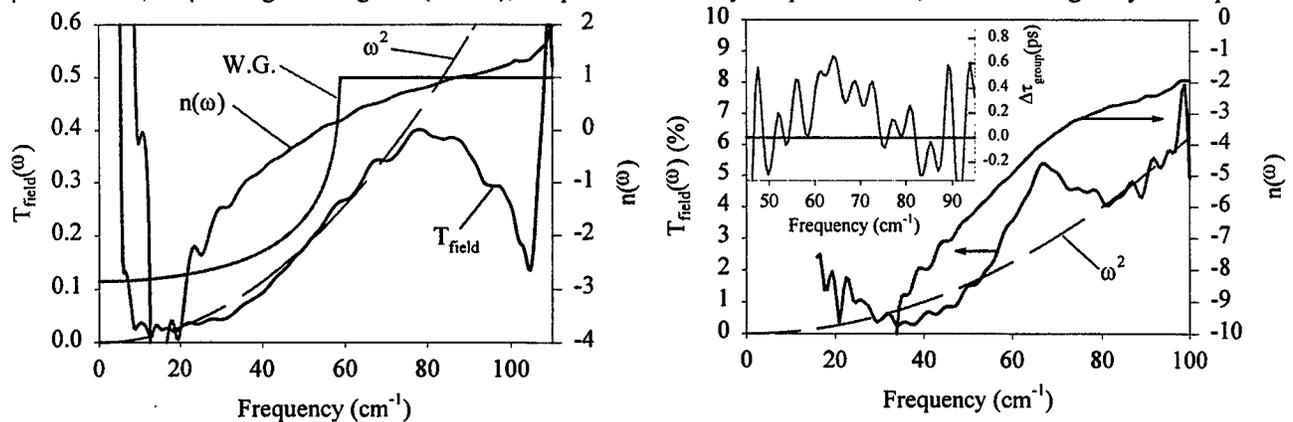
FIG. 3. (Left) Transmission through a d = 100 μm, L = 40 μm, nickel waveguide. Shown are the field transmission, the refractive index, the (simple) theoretical waveguide transmission (W.G.) and a curve proportional to the frequency squared (ω²). (Right) . Transmission of evanescent waves through a 50-μm diameter 40-μm length nickel waveguide. Shown is the electric-field transmission and the effective refractive index. The dashed line is a fit to an ω²-dependence and the inset shows the group delay relative to free-space derived from the experimental phase.
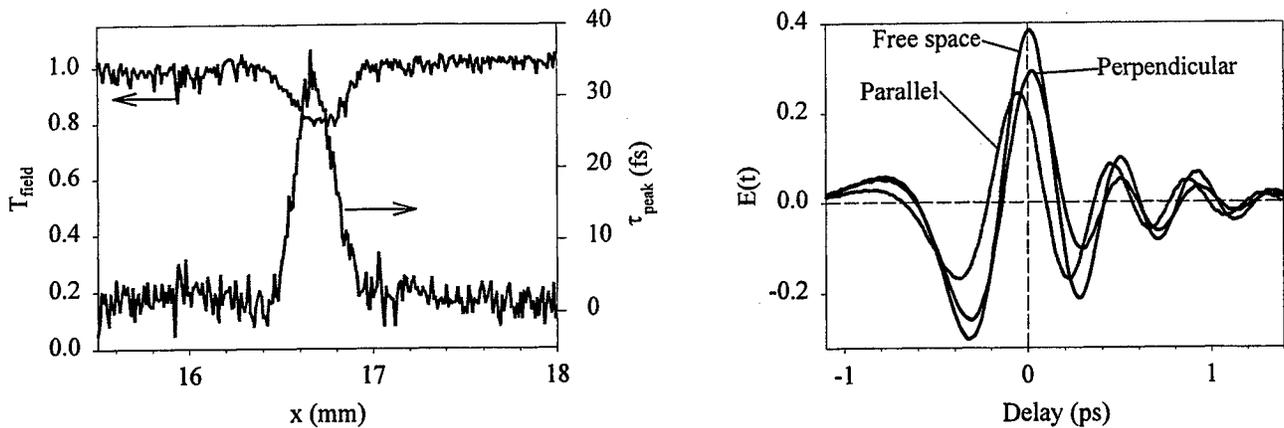
FIG. 4.(Left) T-ray image of a 100-μm diameter tinned-copper wire with the t-ray polarization perpendicular to the wire. It can be seen that the peak of the terahertz pulse is delayed on propagating close to the wire. (Right) Time domain traces for propagation past a wire with parallel and perpendicular polarization of the t rays. It can be seen that the pulse is delayed in the perpendicular case and advanced in the parallel case. However, the behavior of the centroid delay is opposite.

delayed, consistent with a subluminal group velocity.

In experiments in d = 50 μm and 100 μm (FIG. 3) waveguides, (nearly) all the transmitted light is in evanescent waves as the cutoff frequencies are at 117 and 59 cm^{-1}. In these cases, there is a complete breakdown of simple waveguide theory. It has been predicted[18] that the field transmission through sub-wavelength holes should follow an ω^2-dependence. Approximate fits to such a dependence are shown in FIG. 3 but do not fit the data very well. Particularly in the data in the 50-μm waveguide, it appears that there is a reproducible resonance. This is unexpected for the 50-μm waveguide, as the exponentially decaying evanescent waves cannot interfere and therefore should not give rise to any resonances. Again, superluminal group velocities could not be observed in these waveguides and instead negative phase velocities are observed.

Superluminal propagation has also been observed when the terahertz pulses propagate past metal wires that have a diameter smaller than that of the beam and on the order of one wavelength. FIG. 4 shows a scan through a 100-μm diameter tinned copper wire with the t-ray polarization perpendicular to the wire. In the case of perpendicular polarization, it is seen that the transmission minimizes when the beam is centered on the wire and at the same time, the terahertz pulse is delayed. In the case of parallel polarization, the transmission minimum is twice as low (four times less power transmitted) and the pulse delay is negative exhibiting a peak on either side of the wire. From the spectra taken at the delay maximum/minimum, it is found that the phase velocity varies between c and 0.87 c in the case of perpendicular polarization, and between 1.05 c and 1.43 c in the case of parallel polarization (assuming the effect is constant over a 100-μm path).

To investigate whether there are any superluminal group velocities involved, we made use of one of the unique properties of the pulses used. As the terahertz pulses are very short (their spatial extend is about one wavelength), it is straightforward to determine whether the average energy-arrival time is delayed or advanced. To this end a new delay is proposed, the centroid delay, defined by:

$$\tau_c = \frac{\int_{-\infty}^{\infty} dt\, t\, I(t)}{\int_{-\infty}^{\infty} dt\, I(t)} \tag{7}$$

where $I(t) \propto E(t)^2$ is the instantaneous intensity, which is proportional to energy. Thus, $I(t)$ is **not** a pulse envelope as the slowly-varying envelope approximation[19] breaks down for a single-cycle pulse and an envelope is not defined. It can be shown that when the slowly varying envelope approximation does hold, the definition of the centroid delay becomes identical to that of the group delay.

When the centroid delay is calculated for the data shown in FIG. 4, it is found that in the case of parallel polarization the centroid delay is positive ($\tau_c = +9.8$ fs) and in the case of perpendicular polarization it is negative ($\tau_c = -46.5$ fs). Thus, the
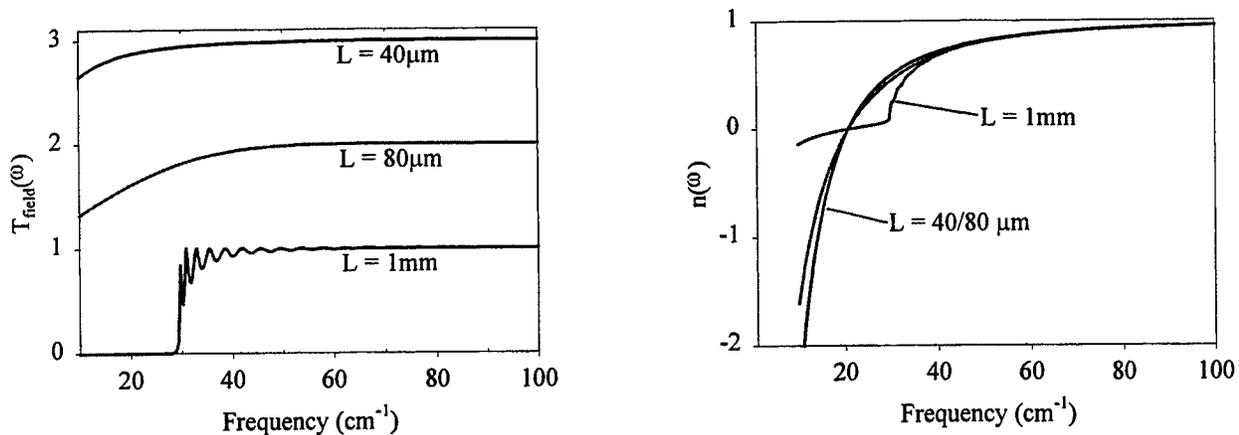
FIG. 5. Theoretical calculation of the waveguide transmission and effective index by including multiple reflections. (Left) Transmission through the waveguide for waveguide length L = 40, 80 and 1000 μm. In the 1-mm case, one can clearly see oscillations in the transmission due to the etalon effect. (Right) Idem, effective refractive index.

centroid delay has the opposite sign as the phase delay. In addition, it follows that the average arrival time of the energy can be advanced as compared to propagation through vacuum.

3. (MORE) THEORY

From the theoretical expression for the phase accumulated by an electromagnetic wave traveling through a waveguide, Eq.(5) , one can derive the effective waveguide index as $n = c\varphi / \omega L$, which results in:

$$n(\omega) = \omega_c \sqrt{\frac{1}{\omega_c^2} - \frac{1}{\omega^2}} \tag{8}$$

Thus, when the frequency approaches cutoff, the refractive index is close to zero. As the waveguide is embedded in air, which has a refractive index of approximately 1, the interfaces at the waveguide entrance and exit will act as very efficient mirrors. Of course, evanescent waves cannot interfere as they exponentially decay with distance. However, each reflection off an interface results in a phase shift, which can masquerade as a time shift. As these phase shift accumulate on multiple reflections inside the waveguide, this may lead to a significant change in the properties of the transmitted field. One can model the waveguide as a medium with a refractive index given by Eq. (8) surrounded by two semi-infinite media with refractive index equal to 1. Using Fresnel coefficients for reflection and transmission[20] and including the effects of multiple reflections in the waveguide, one can derive the frequency-dependent transmission function

$$\tilde{T}(\omega) = \frac{\alpha(\omega)e^{ikL}}{1 + \beta(\omega)e^{i2kL}} \tag{9}$$

where

$$\alpha(\omega) = \frac{4n(\omega)}{(1 + n(\omega))^2}, \quad \beta(\omega) = -\frac{(1 - n(\omega))^2}{(1 + n(\omega))^2} \tag{10}$$

and $k = \omega\, n(\omega)/c$ is the wavenumber in the waveguide.

FIG. 5 shows the field transmission and effective index calculated using Eq. (9) for waveguides with a 200-μm diameter. In the case of a waveguide with a 1-mm length, one can clearly see oscillations in the transmission just above the cutoff frequency. This is a Fabry-Perot effect in which non-evanescent waves become standing waves inside the waveguide. Although a proper Fabry-Perot effect cannot occur with evanescent waves, the multiple reflections inside the waveguide

259
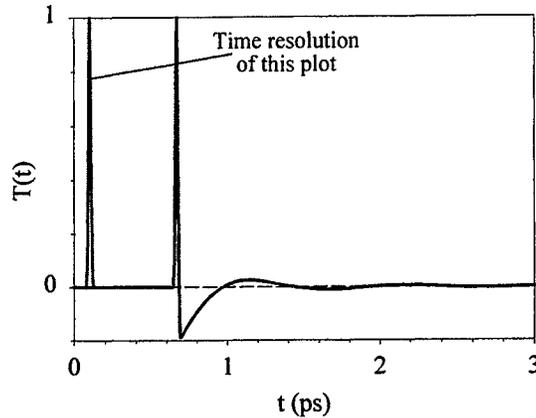
Figure 6. Time-response function for tunneling through a waveguide. This curve was calculated by numerically Fourier transforming the theoretical transmission function including multiple reflection inside the waveguide. The waveguide parameters are d = L = 200 μm.

nevertheless have a significant effect on the total transmission. Most importantly, the theory can reproduce an effective index that becomes negative at low frequencies. A strongly negative index implies a wave that emerges from the waveguide before entering it. This bizarre effect, which has been observed by us in a very short waveguide[5] is the result of phase shifts occurring on the boundary between the waveguide and air. Superluminal group velocities will only be observed when the waveguide is sufficiently long that the Fabry-Perot effect for evanescent waves can be ignored.

4. CONCLUSION

Is it possible to transmit signals faster than the speed of light in vacuum? Is it possible to receive a signal before it is sent? To attempt an answer to these questions one should first consider causality. If the device response is causal then if its length is x, the output electric field is related to the input field by

$$E_{out}(t) = \int_{-\infty}^{\infty} d\tau \, E_{in}(t-\tau) \, r(\tau - x/c) \qquad (11)$$

and the response function $r(t)$ is zero for negative argument. Any signals transmitted at times $t < x/c$ would violate causality in some Lorentz reference frames. In the case of free-space propagation, the response function is the Dirac delta function. In the present case of propagation through a waveguide, the time-response function is found from the Fourier transform

$$T(t) = \frac{1}{2\pi} \int_{-\infty}^{\infty} \frac{\alpha e^{ikL - i\omega t}}{1 + \beta e^{i2kL}} d\omega \qquad (12)$$

The effective index of the waveguide, Eq.(8), tends to 1 as the absolute value of the complex frequency tends to infinity. Therefore, this Fourier transform can be performed by complex contour integration by closing the contour in the upper-half plane (UHP) if $t - L/c < 0$. Therefore, the waveguide response is causal if there are no poles in the UHP of the integrand of Eq.(12).[21] We have not been able to find an analytical expression for the position of the poles. However, a numerical search only resulted in poles in the LHP suggesting that the response is indeed causal.

As a further causality proof, the Fourier transform of Eq. (12) was performed numerically, an example of which is shown in FIG. 6. This figure shows the time-response function of a waveguide with d = L = 200 μm, that has been calculated by evaluating the frequency-response function up to 80 THz with a 10-GHz step size and applying a Gaussian filter with a 20-THz standard deviation. The figure also shows a "delta function" to indicate the time-resolution of this graph. The first response of the system is a Dirac delta function arriving at 669 fs, corresponding to L/c. Thus, the electromagnetic-wave transmission through a waveguide is causal even when one includes the effect of multiple evanescent-wave reflections.
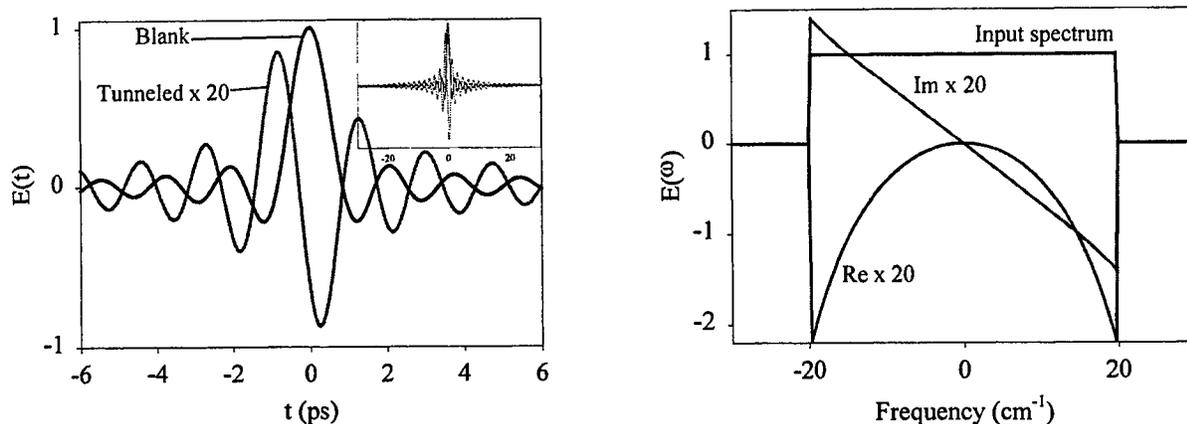
FIG. 7. Propagation of a bandwidth limited pulse through a 200-μm diameter and length waveguide. (Left) The input pulse is has a sinc(t) shape and is advanced and attenuated on propagation through the waveguide. The inset shows the sample pair of pulses on a scale from −30 to +30 ps. (Right) The (real) input spectrum is bandwidth limited to ±20 cm⁻¹. The output spectrum is attenuated and imaginary. The symmetry of the spectrum ensures that the electric field in the time domain remains real.

The causality of electromagnetic-wave propagation through a waveguide can be seen as proof that superluminal communication is impossible. In some cases, such as an evanescent wave traveling through a waveguide below cutoff, the response function has such a form that it appears as if signals are traveling superluminally. However, the tunneling device in effect performs an extrapolation into the future.[8,22] Such an extrapolation could be performed even for a pulse traveling through free space. Analysis (for example, through a Taylor expansion) of the wing of a pulse arriving before the peak could be used to predict the arrival time of the peak. This extrapolation effect has been demonstrated very beautifully in an experiment using resonant amplifiers.[23] Thus, genuinely new information is contained in discontinuities (as extrapolation through a discontinuity is impossible) and these appear always to travel at less than the speed of light in vacuum.[7] Physically, this can be understood as arising from the fact that discontinuities have Fourier components at infinite frequency and in a waveguide, these infinite frequency components would be above cutoff. A more general argument shows[21] that discontinuities of any derivative order must travel subluminally if the response function is causal.

Of course, practical communication devices do not have an infinite bandwidth and could never produce a discontinuity or a Dirac delta-function pulse. Therefore, following the above argument, practical communication devices could therefore never transmit "genuinely new" information. FIG. 7 shows a theoretical analysis of the propagation of a 20-cm⁻¹ bandwidth-limited pulse through a waveguide with a 200-μm length and diameter. Because of the bandwidth limitation, the pulse has wings in the time domain that extend to $t = \pm\infty$. The peak of the pulse is advanced by almost a picosecond and thus exits the waveguide before entering it. However, this is hardly surprising given the long tails of the input pulse. Even if this bandwidth-limited pulse had traveled through empty space, one could have predicted the entire pulse shape from a Taylor expansion of any point in the tail. However, what would happen if the signal in the tail were so weak that it would be at the level of single photons? In that case, the detector may have to wait until the arrival of the main peak and superluminal propagation of this peak in, for example, a waveguide below cutoff would appear to result in superluminal propagation of the signal. Clearly, a better definition of the concept of a signal is required.

5. ACKNOWLEDGEMENTS

6. REFERENCES

1. Mittleman, D. M., Hunsche, S., Boivin, L. & Nuss, M. C. T-Ray Tomography. *Opt. Lett.* **22**, 904-906 (1997).
2. Mittleman, D. M., Jacobsen, R. H. & Nuss, M. C. T-Ray Imaging. *IEEE J. Selected Topics Quantum Electron.* **2**, 679-692 (1996).

3. Mittleman, D. M., Cunningham, J., Nuss, M. C. & Geva, M. Noncontact Semiconductor Wafer Characterization with the Terahertz Hall Effect. *Appl. Phys. Lett.* **71**, 16-18 (1997).

4. Hunsche, S., Koch, M., Brener, I. & Nuss, M. C. THz near-field imaging. *Optics Communications* **150**, 22-26 (1998).

5. Wynne, K. & Jaroszynski, D. A. Superluminal terahertz pulses. *Opt. Lett.* **24**, 25-27 (1999).

6. Wynne, K. & Jaroszynski, D. A. in *23rd International Conference on Infrared and Millimeter Waves* (eds. Parker, T. J. & Smith, S. R. P.) 386-387 (Colchester, University of Essex, 1998).

7. Brillouin, L. *Wave Propagation and Group Velocity* (Academic Press, New York, 1960).

8. Chiao, R. Y. & Steinberg, A. M. Tunnelling Times and Superluminality. *Prog. Opt.* **37**, 345-405 (1997).

9. Brodowsky, H. M., Heitmann, W. & Nimtz, G. Comparison of Experimental Microwave Tunneling Data with Calculations Based on Maxwell's Equations. *Phys. Lett. A* **222**, 125-129 (1996).

10. Enders, A. & Nimtz, G. Zero-Time Tunneling of Evanescent Mode Packets. *J. Phys.* **3**, 1089-1092 (1993).

11. Spielmann, C., Szipöcs, R., Stingl, A. & Krausz, F. Tunneling of Optical Pulses through Photonic Band Gaps. *Phys. Rev. Lett.* **73**, 2308-2311 (1994).

12. Pollak, E. & Miller, W. H. ?? *Phys. Rev. Lett.* **53**, 115 (1984).

13. Balcou, P. & Dutriaux, L. Dual Optical Tunneling Times in Frustrated Total Internal Reflection. *Phys. Rev. Lett.* **78**, 851-854 (1997).

14. Nahata, A., Weling, A. S. & Heinz, T. F. A Wideband Coherent Terahertz Spectroscopy System Using Optical Rectification and Electro-Optic Sampling. *Appl. Phys. Lett.* **69**, 2321-2323 (1996).

15. Wu, Q. & Zhang, X. C. Free-Space Electro-Optic Sampling of Mid-Infrared Pulses. *Appl. Phys. Lett.* **71**, 1285-1286 (1997).

16. McElroy, R. & Wynne, K. Ultrafast Dipole Solvation Measured in the Far-Infrared. *Phys. Rev. Lett.* **79**, 3078-3081 (1997).

17. Liao, S. Y. *Microwave Circuit Analysis and Amplifier Design* (Prentice-Hall, Englewood Cliffs, 1987).

18. Bethe, H. A. Theory of Diffraction by Small Holes. *Phys. Rev.* **66**, 163-182 (1944).

19. Shen, Y. R. *The Principles of Nonlinear Optics* (Wiley, New York, 1986).

20. Born, M. & Wolf, E. *Principles of Optics* (Pergamon Press, Oxford, 1993).

21. Jackson, J. D. *Classical Electrodynamics* (Wiley, New York, 1975).

22. Steinberg, A. M. *et al.* An Atom Optics Experiment to Investigate Faster-Than-Light Tunneling. *Ann. Phys. (Leipzig)* **7**, 593 (1998).

23. Mitchell, M. W. & Chiao, R. Y. Negative Group Delays and "Fronts" in a Causal System: An Experiment with Very Low Frequency Bandpass Filters. *Phys. Lett. A* **230**, 133-138 (1997).

Spatially resolved optical measurements of electric terahertz signals on passive devices

M. Nagel, T. Dekorsy and H. Kurz

Institut für Halbleitertechnik II, Rheinisch-Westfälische Technische Hochschule (RWTH) Aachen, Sommerfeldstraße 24, D-52074 Aachen, Germany

ABSTRACT

Monolithic mm-wave integrated circuits (MMICs) have experienced strong improvements in operation frequencies in the last years. However, reports of III-V semiconductor transistors to have maximum frequencies as high as 400 GHz often stem from extrapolated measurements made at lower frequencies, due to bandwidth-limitations of the electronic equipment. The extrapolation of measurements at lower frequencies is insufficient for an accurate determination of the characteristics of passive or active elements in this frequency range. Another frequent restriction of conventional measurement techniques is that the signal can only be probed at specially designed interfaces. Optical sampling techniques allow the detection of electric fields with a high temporal and spatial resolution of 150 fs and 10 μm, respectively, at any point within or outside the device.[1] In addition to S-parameter measurements at passive devices we demonstrate the spatial field distribution of an ultra-short electric pulse propagating through a band-stop filter with a broad stop-band probed via electrooptic (EO) sampling. To demonstrate the potentially high bandwidth of the measurement system the geometry of the stubs has been designed to show significant attenuation around a frequency $f_0 = 350$ GHz.

Keywords: electrooptic sampling, high-frequency devices, ultra-fast optical measurement techniques, band-stop filter

1. THE MEASUREMENT SYSTEM

Band-stop filters are used in order to suppress specific unwanted frequencies. The applied thin-film microstrip (TFMS) band-stop filter design uses 6 pairs of open-circuited resonator stubs with a length and spacing of $\lambda_0/4 = 150$ μm with λ_0 being the wavelength of the center frequency of the stop-band. The fabrication steps comply to the Cyclotene-based TFMS lines with a polymer thickness $h = 6$ μm and a signal conductor width $w = 14$ μm.[2] For the purpose of demonstration the geometry of the stubs has been designed to produce significant attenuation around a frequency $f_0 = 350$ GHz and any odd multiple.[3] The stubs have a quasi-static characteristic impedance of $Z_i = 76$ Ω and the connecting line impedances are $Z_{i,i+1} = 70$ Ω. The filter is terminated with 50-Ω-TFMS lines. A scheme of the filter and the TFMS lines is shown in Figure 1. Both, ground and signal conductor are fabricated as Ti/Au-layer with a thickness of $t = 0.7$ μm.

All measurements are performed with a mode-locked Ti:sapphire laser emitting 150 fs optical pulses with a repetition rate of 75.6 MHz. The setup is based on a pump/probe scheme, where one pump pulse (3 mW average power) excites a 9V-biased photoconductive (PC) switch interconnected to the filter by a TFMS line with a length of 3.9 mm. An optical fiber is attached to the PC-switch in order to provide stable conditions for the raster-scanning of the device under test (DUT). The propagating electric field is detected by a temporarily delayed probe pulse with an EO transducer. We apply Lithium Tantalate (LiTaO$_3$) and Bismuth Silicate (BSO) crystals as probes for the external transversal and longitudinal field components, respectively. The probe beam is reflected within the crystal by total internal reflection in order to keep any light out of the device and to provide a sample constellation that is unaffected by the reflectivity of the DUT. Alternatively we are able to probe the internal field in the unpoled polymer

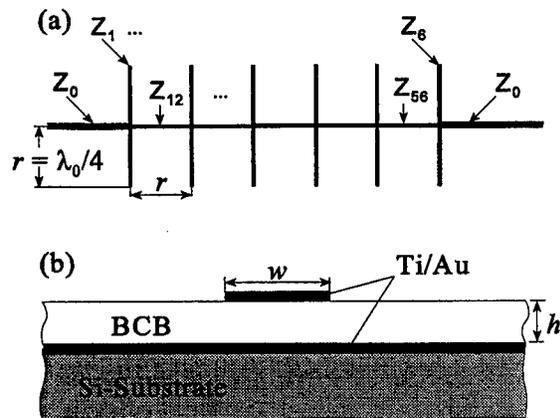**Fig. 1:** (a) Topview of the band-stop filter and (b) cross-section of the terminating thin-film microstriplines.

Part of the EUROPTO Conference on Terahertz Spectroscopy and Applications II
Munich, Germany • June 1999 SPIE Vol. 3828 • 0277-786X/99/$10.00

263

via non-invasive electric field-induced second-harmonic (EFISH) generation.[4] During the measurements the DUT and the applied PC-switch is moved by a x-y-translation stage while all other optical components stay in a fixed position.

2. TIME-DOMAIN MEASUREMENTS AND FILTER CHARACTERIZATION
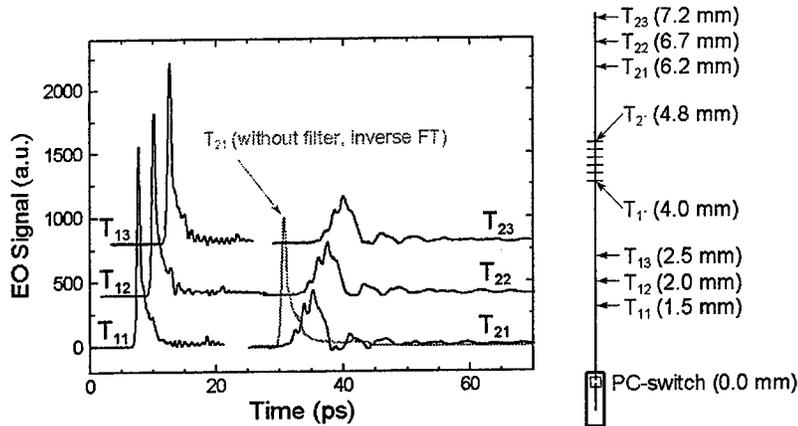
Fig. 2: Time-resolved measurements of the transversal field-amplitude of the propagating electric signal at different points on the terminating lines discribed by the scheme on the right.

Fig. 2 shows time-resolved measurements of the electric transients probed at different points on the interconnecting TFMS lines before and after the filter. From Fourier-analysis of the time-domain data, we can evaluate the frequency dependent propagation characteristics of the terminating lines in terms of attenuation and relative effective permittivity. We use this data to correct the S-parameter measurements of the filter for the contribution of the interconnects.

Probing at a distance of 2 mm in front of the filter provides a separation of the incoming signal from the reflected signal by more than 20 ps on a time scale. The temporal width of the transient measured at a distance of 1.5 mm to the PC-switch is only 640 fs. With this spectrally broad signal a phonon-polariton-resonance at 1.2 THz, corresponding to the ringing in the decaying part of the transients in front of the filter, is also generated within the $LiTaO_3$-crystal.[5] This resonance is conterminous with an upper limit of the systems measuring bandwidth. The lower limit is given by the sampled time scope corresponding to 33 GHz in this case. The minimum detectable voltage with the $LiTaO_3$-probe tip in contact to the 50 Ω-lines can be specified as ca. 1 mV. After the filter we observe a significantly attenuated signal with some typical features of a dirac-pulse with a masked frequency band. Taking into account the evaluated propagation constants of the terminations and the time-resolved data of the initial signal at T_{11} we have simulated the signal for a continuous TFMS line as the used terminations without a filter by inverse fourier-transformation. In Figure 2 we compare the simulated signal at T_{21} (gray line) with the measured signal. The peak amplitude of the filtered signal amounts to 43 % of the simulated unfiltered signal at the same point. The rising part of the filtered signal contains an oscillation of 715 GHz that corresponds to the middle of the pass-band (see Figure 3). The filter causes a time-delay of 4.6 ps to the signal.

Figure 3 shows the measured attenuation of the filter with (dashed line) and without an attenuation due to the interconnects (continuous line) from 35 to 1000 GHz. The plot exhibits a broad first stop-band with more than 10 dB attenuation between 225 GHz and 508 GHz. We can also see the beginning of the second stop-band around $3f_0$ at 908 GHz. The attenuation within the pass-bands is still high between 2 dB and 7 dB. This may be due to the use of a relative high number of resonator stubs and a resistance mismatch at the line nodes.

3. SPATIALLY RESOLVED TRANSIENT FIELD MAPPING

The spatially resolved measurements in Figure 4 are all performed with a BSO crystal sensitive to field components in normal direction to the device surface. A longitudinal probe tip has the ability to trace the field from planar waveguides along corners. The sensitivity vanishes if the field is in normal direction to the optical axis of the crystal. As a result a transversal probe, however, will have no field-response from lines in normal direction to the c-axis, what might reduce the
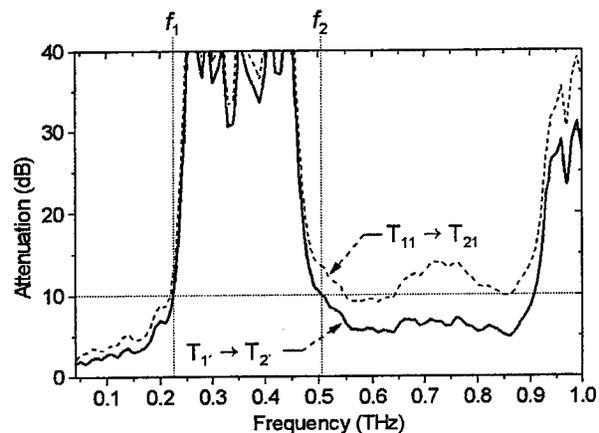
Fig. 3: Frequency dependend attenuation of the band-stop filter with and without interconnections. The labels relate to the scheme in Fig. 3.
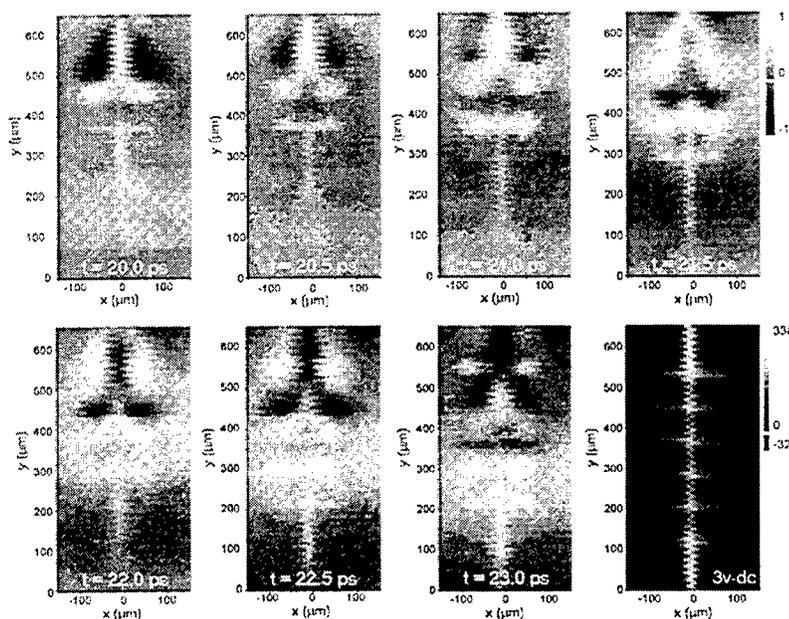
Fig. 4: Spatially resolved mappings at the band-stop filter: longitudinal electric field component of an ultra-fast transient signal at different times and electrostatic field response (downright).

readability of a corresponding field-mapping. All mappings have been made with the crystal lifted 5 μm from the DUT. This distance has reduced considerably the invasiveness of the measurement system due to dielectric load for coplanar waveguides.[6] In this case the impact is even smaller, because the biggest contingent of the electric field is enclosed within the polymer between the electrodes. The dc-mapping in Figure 4 exhibits a maximum of the normal field amplitude over the signal conductor. A small field reverse in sign can be detected beside the structure. There is a qualitative identical response from the orthogonally orientated lines as a benefit of the longitudinal probe. The stubs and there interconnects show a smaller response due to a decreased line width. This filter contains a break in one stub at y = 120 μm and x = 75 μm due to a fabrication fault, which is also apparent in the measured data. The area of the dc-mapping is equal to the area of the seven time-mappings, that exhibit snap-shots of an electric pulse with 2 ps duration (FWHM) propagating through the filter at different times. All time-mappings are normalized to the color-scale shown in the upper right of Figure 4. White or black areas stem from positive or negative field amplitudes, respectively. In this setup the pulse is sent in negative y-direction trough the DUT. We have measured a signal velocity reduction from 203 μm/ps on the interconnects to appr. 100 μm/ps within the filter what is in good agreement with the formerly shown time-resolved simulation. Hence, the minimum frequency of the first higher mode is 3.3 THz for this structure the probed waveforms are exclusive of HE_0-type. In the leading area of the signal we can observe that the pairs of resonator stubs initially carry a field with a shape similar to the dc-mapping. With further progression the stubs exhibit a spatial field response with changes in sign in symmetry to the center line. This may be due to the generation of standing waves on the resonators.

4. ACKNOWLEDGEMENTS

5. REFERENCES

1. T. Pfeifer, H.-M. Heiliger, T. Löffler, C. Ohlhoff, C. Meyer, G. Lüpke, H. G. Roskos, and H. Kurz, "Optoelectronic On-Chip Characterization of Ultrafast Electric Devices: Measurement Techniques and Applications", IEEE Jour. Sel. T. Quant. Elect., **2**, 3, 586 - 604, 1996.
2. H.-M. Heiliger, M. Nagel, H. G. Roskos, and H. Kurz, F. Schnieder and W. Heinrich, R. Hey and K. Ploog,"Low-dispersion thin-film microstrip lines with cyclotene (benzocyclobutene) as dielectric medium", Appl. Phys. Lett. **70**, 17, 2233 - 2235, 1997.
3. G. Matthaei, L. Young, E. M. T. Jones, *Microwave filters, impedance matching networks, and coupling structures*, Dedham, MA: Artech House, 1980.
4. M. Nagel, C. Meyer, H.-M. Heiliger, T. Dekorsy, and H. Kurz, R. Hey and K. Ploog, "Optical second-harmonic probe for ultra-high frequenzy on-chip interconnects with benzocyclobutene", Appl. Phys. Lett. **70**, 9, 1018 - 1020, 1998.
5. O. Hollricher, "Electrooptic high-frequency investigations at superconductors and semiconductors", Ph.D. Thesis, University of Cologne, 1993
6. W. Mertin, C. Roths, F. Taenzler, and E. Kubalek, "Probe tip invasiveness at electro-optic sampling of MMIC", *IEEE MTT-S Digest*, 1351, Atlanta, June 1993.

THz Time Domain Spectroscopy of Liquids

C. Rønne[a], K. Jensby[a], G. K. H. Madsen[a], O. F. Nielsen[b], and S. R. Keiding[a,*]

[a]Department of Chemistry, University of Aarhus, DK-8000 Aarhus C, Denmark
[b]Department of Chemistry, University of Copenhagen, DK-2100 Copenhagen, Denmark

ABSTRACT

The communication among molecules in a liquid takes place through intermolecular interactions. Molecules talk to each other through dipole moments, quadrupole moments, etc. or sometimes more directly through weak intermolecular bonds, for example hydrogen bonds. Understanding the structure and dynamics of these intermolecular interactions have proven to be crucial in the quest to obtain a better molecular description of chemical reactivity. If for example a molecule is vibrationally excited, either as a consequence of a chemical transformation or excitation by a laser, then the molecule will initially relax by intramolecular vibrational relaxation (IVR) where predominantly the low frequency vibrations are excited. Subsequently these low frequency modes relax by coupling to the low frequency intermolecular solvent modes. The time scale for these intermolecular interactions is in the range from 0.1 to 10 ps, corresponding to a maximum spectral density at a few THz, thus matching the spectral coverage of THz-time domain spectrometers. This paper will describe recent THz-TDS results on both polar and non-dipolar liquids, in particular emphasizing the relation between results obtained with THz-TDS, depolarized Raman scattering, and OHD-RIKES, and the study of hydrogen bonds in polar liquids and crystals.

Keywords: Far-infrared spectroscopy, THz-pulses, intermolecular vibrations, hydrogen bonds,

1. INTRODUCTION

The last decade has witnessed a growing interest in the low frequency properties of liquids[1,2,3]. The low frequency spectrum of a liquid is dominated by diffusive reorientation of single molecules and intermolecular librational motion[2,3,4]. The reason for this interest is the role played by these low frequency modes during a chemical reaction[5]. Many experimental and theoretical investigations have shown how solvation and relaxation takes place through coupling of the excited solute molecules with the low frequency inter- and intramolecular modes of the solvent. The communication between solvent and solute molecules primarily takes place through the low frequency vibrations of the solute.[6] Another reason for the interest in low frequency modes is the development of many new experimental femtosecond laser techniques that probes the low frequency part of spectrum. TeraHertz time domain spectroscopy (THz-TDS)[7,8,9,10], the Raman induced Kerr effect (OHD-RIKES)[11,12,13,14,15] and transient grating or four wave mixing techniques[14,16,17] are all examples of experimental techniques, based on femtosecond lasers, sensitive to the far-infrared, or low frequency spectrum of liquids. In addition to these new femtosecond techniques the classical low-frequency techniques; Inelastic neutron scattering (INS)[1], Depolarized Raman Spectroscopy (DRS)[2,3] and Fourier transform far-infrared spectroscopy (FT-FIR)[1], still provide high quality experimental data.

Parallel to these experimental developments, the theoretical description of low frequency liquid modes has advanced likewise. In particular the combination of Molecular Dynamics (MD) simulations with the theory of instantaneous normal modes (INM) seems like a very fruitful development[5]. Another trend, inspired by the time domain techniques, emphasizes the time domain description of low frequency modes in the form of time correlation functions of either dipole moments or polarizability tensors.[18,19,20,21,22] Models based on Brownian oscillators have proven successful in disentangling the inter and intramolecular contributions to the low frequency dynamics of liquids[23].

---

* Email: keiding@kemi.aau.dk

With the introduction of all these new theoretical and experimental tools an important issue is the relationship between the results obtained using different tools. Several papers address these questions from a theoretical viewpoint, but only a few papers directly compares the experimental results obtained for the low frequency modes of liquids using different experimental techniques[2,23,24,25,26,27]. The most extensive work is the comparison, based on the time correlation function formalism, recently published by Castner and Maroncelli.[21]

In the first part of this work we compare the low frequency spectrum of a series of fluorinated benzenes obtained using two of the femtosecond techniques, THz-TDS and OHD-RIKES together with depolarized Raman scattering (DRS). In particular we emphasize how similarities and differences in the measured spectral densities can be used to disentangle the different, diffusive and librational, contributions to the otherwise broad and featureless far-infrared absorption profile. The similarities also suggest that the different data fitting and representation procedures traditionally used in the different techniques are sound and healthy procedures that do not distort or misrepresent the actual molecular properties measured.
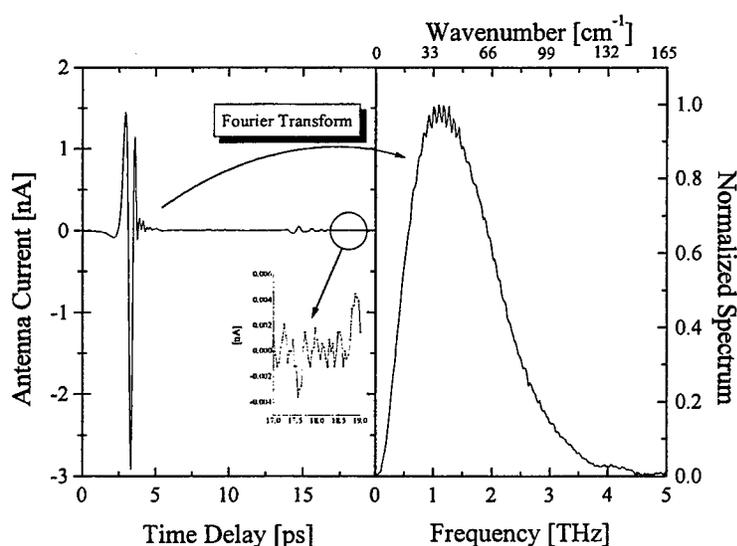
Figure 1. THz-pulse used in the THz-time domain spectrometer. The inset demonstrates the excellent signal to noise ratio obtainable. The weak oscillations are due to trace amounts of water vapor. The spectrum covers the region from 200 GHz to 4 THz where the spectral amplitude is more than 10% of the maximum value.

The technique TeraHertz time domain spectroscopy is a well-established experimental technique utilizing ultrashort electromagnetic transients[7]. The short transients are generated by driving either a non-linear optical crystal or a photoconductive antenna with a femtosecond optical pulse. The resulting transient, show in figure 1, is detected by optical sampling, either in a non-linear ($\chi^{(2)}$) crystal[28] or a photoconductive antenna. Due to the high duty-cycle of the sampling technique, a very high signal to noise ratio is obtainable in the far-infrared spectral range below 150 cm^{-1}, corresponding to wavelengths longer than 66 μm. In the THz-time domain spectrometer, the linear optical response of the sample is obtained by comparing two pulses, one that propagated through the liquid sample, and one that propagated in a reference material, typically dry air. Since the THz-TDS technique is phase sensitive, one can obtain both the absorption coefficient **and** the index of refraction of the sample. In the present THz-TDS setup we are able to extract the optical coefficients up to around 4 THz, depending on the sample. With the recent combination of very thin electro-optic detectors and sub-10 fs Ti:Sapphire lasers, the spectroscopically useful bandwidth of THz-spectrometers is expected to increase considerably[29].

2. NON-DIPOLAR LIQUIDS: COMPARISON AMONG DIFFERENT TECHNIQUES

In the following we briefly outline the theoretical expression for the experimental signals obtained using the three different techniques, THz-TDS, OHD-RIKES and Depolarized Raman Scattering. We use $\bar{M}$ the total dipole moment of the sample and $\bar{\Pi}$ for the total polarizability of the sample. These macroscopic variables are then in turn composed of single molecule properties and interaction induced moments. By comparing the different experimental techniques, one of the goals is to be

able, in more detail, to describe the molecular motions responsible for the broad and featureless absorption profile observed for most liquids in the far-infrared.

THz-TDS: Theoretically this is the simplest technique, as it just directly measured the linear absorption of the liquid, as expressed by the macroscopic total dipole moment of the sample. Using the correlation function formalism, the absorption coefficient can be expressed as [22,30]

$$\alpha(\omega) = \frac{4\pi^2}{3\hbar cV} \frac{I_M(\omega)}{n(\omega)D(\omega)} \times \omega \left(1 - exp\left[-\frac{\hbar\omega}{kT}\right]\right)$$ [1]

where V is the volume of the sample, $n(\omega)$ is the frequency dependent refractive index and $D(\omega)$ is the local field correction. The spectral density $I_M(\omega)$ is the Fourier transform of the time correlation function of the total dipole moment of the sample[31,32]

$$I_M(\omega) = \frac{1}{2\pi} \int_{-\infty}^{\infty} dt\, exp(-i\omega t) C_M(t)$$

$$= \frac{1}{2\pi} \int_{-\infty}^{\infty} dt\, exp(-i\omega t) \langle \vec{M}(t) \cdot \vec{M}(0) \rangle$$ [2]

The absorption is thus a direct consequence of the fluctuations of the total dipole moment $\vec{M}$. The total dipole moment of the sample can be expressed by the permanent single molecule dipole moments and the additional dipole moments induced by the intermolecular interactions. For a non-dipolar molecule, assuming only-pair wise interactions and the leading quadrupole-polarizability term in the expansion of the total dipole moment we obtain

$$\vec{M} = \sum_{i,j\neq i} \Delta\vec{\mu}_{ij}$$

$$= \sum_{i,j\neq i} \pi_i \vec{E}_{ij}(t)$$ [3]

$$= \frac{1}{3}\sum_{i,j\neq i} \pi_i \cdot T_{ij}^{(3)} : Q_j$$

$\Delta\vec{\mu}_{ij}$ is the interaction induced dipole moment on molecule i induced by molecule j given by the electric field $\vec{E}_{ij}$ at molecule i caused by the quadrupole moment, Q_j of molecule j and the polarizability, π of molecule i. The value of the induced dipole moment depends on the intermolecular separation through the 3. order propagator $T_{ij}^{(3)} = \nabla^3\left(1/|r_{ij}|\right)$. The polarizability is also composed of a permanent, α_i, and an induced part $\Delta\pi_{ij}$. For a non-dipolar molecule, and only retaining the leading terms, we obtain

$$\pi_i = \alpha_i + \sum_k \Delta\pi_{ik}$$

$$= \alpha_i + \sum_k \alpha_i T_{ik}^{(2)} \alpha_k$$ [4]

where $T_{ik}^{(2)} = \dfrac{3r_{ik}r_{ik} - 1}{r_{ik}^3}$. If we insert equation 4 into equation 3 we obtain an expression for the total dipole moment of the sample

$$\vec{M} = \frac{1}{3}\sum_{i,j\neq i} \alpha_i \cdot T_{ij}^{(3)} : Q_j + \frac{1}{3}\sum_{i,j,k} \alpha_i T_{ij}^{(2)}\alpha_j \cdot T_{ik}^{(3)} : Q_k$$ [5]

Another important feature of the far-infrared absorption is the presence of the factor[18]

$$\omega\left(1 - exp\left[\frac{-\hbar\omega}{kT}\right]\right) \qquad [6]$$

in equation 1. In the low frequency range, typically when $\hbar\omega < kT$, where $kT \sim 200 cm^{-1}$ at room temperature, in addition to stimulated absorption from initial to final state, one also has to take into account the stimulated emission from final to initial state. Taking this into account in the thermal averaging of the transition moments between initial and final states gives rise to the factor in the parenthesis, corresponding to the difference between the number emitted and absorbed photons. Multiplying with frequency gives the power absorbed in the sample.

The intensity of the depolarized Raman scattered light can also be conveniently expressed using the time correlation function formalism[13,18,19,20]

$$I_{DRS}(\omega) = \frac{1}{2\pi} \int_{-\infty}^{\infty} dt\, exp(-i\omega t) C_\Pi(t)$$

$$= \frac{1}{2\pi} \int_{-\infty}^{\infty} dt\, exp(-i\omega t) \langle \vec{\Pi}_2(0) : \vec{\Pi}_2(t) \rangle \qquad [7]$$

The function, C_Π represent the correlation function of the anisotropic part of the total polarizability tensor of the sample, Π_2. The scattering intensity is similarly caused by fluctuations in the total polarizability tensor of the sample. This can again be expressed using the molecular polarizability given in equation 4.

$$\Pi_2 = \sum_i \pi_i = \sum_i \left[\alpha_i + \sum_j \Delta\pi_{ij} \right] = \sum_i \alpha_i + \sum_{i,j\neq i} \alpha_i T_{ij}^2 \alpha_j \qquad [8]$$

The leading terms in both the total dipole moment and in the total polarizability thus depend on the dynamics of the molecular polarizability. When comparing DRS data with THz-TDS data we must take into account the thermal population of initial and final states. In a scattering experiment the scattering from initial to final state is represented by the Stokes part of the Raman spectrum, whereas the scattering from final to initial state is the anti-Stokes part. We must, thus multiply the DRS spectrum with the factor given in eq. 6 and we then obtain the so-called R(v) or R(ω) representation of the DRS-spectrum[18,19].

$$R_{DRS}(\omega) = \omega\left(1 - exp\left[\frac{-\hbar\omega}{kT}\right]\right) \times \frac{1}{2\pi} \int_{-\infty}^{\infty} dt\, exp(-i\omega t) \langle \vec{\Pi}_2(0) : \vec{\Pi}_2(t) \rangle \qquad [9]$$

When comparing the DRS spectrum with the results obtain from OHD-RIKES, the spectral density observed in DRS is often expressed using time dependent susceptibilities or response functions rather than correlation functions of the polarizability[25]. Following Cho et al[23] the DRS spectrum is given as

$$I_{DRS}(\omega)\left[1 - exp\left(\frac{-\hbar\omega}{kT}\right)\right] = 2\hbar^2\, Im[\tilde{\chi}_{YZYZ}(\omega)] \qquad [10]$$

where the frequency dependent third order non-linear susceptibility is the Fourier transform of the time dependent response function

$$\tilde{\chi}_{ijkl}(\omega) = \int_{-\infty}^{\infty} dt\, exp(-i\omega t) \chi_{ijkl}(t) \qquad [11]$$

and the time dependent response function is again equal to the correlation function of the polarizability

$$\chi_{ijkl}(t) = \left\langle \frac{i}{\hbar}\Pi_{ij}(t)\Pi_{kl}(0)\right\rangle - \left\langle \frac{i}{\hbar}\Pi_{kl}(0)\Pi_{kl}(t)\right\rangle \qquad [12]$$

The signal observed in an OHD-RIKES experiment can be expressed as a convolution between the material response function of the sample and the intensity autocorrelation function of the laser pulse, $G^2(t)$, and an instantaneous electronic term, σ.

$$S_{OHD-RIKES}(\tau) = \int_{-\infty}^{\infty}\left[\chi_{ijkl}(t)G_{ijkl}^2(t-\tau) + \sigma_{ijkl}\delta(t)\right]dt \qquad [13]$$

By Fourier transforming equation 13, the imaginary part contains the spectral density, directly comparable to the DRS spectral density given in equation 10

$$Im\,\widetilde{S}_{OHD-RIKES}(\omega) = Im\,\widetilde{\chi}_{ijkl}(\omega)Re\,\widetilde{G}_{ijkl}^2(\omega) \qquad [14]$$

Comparing equations 9, 10 and 14 we thus see that the spectral density measured in DRS, given in the $R(\omega)$ representation is equal to the spectral density measured in an OHD-RIKES experiment, when the OHD-RIKES spectral density is multiplied by frequency.

$$R_{DRS}(\omega) = \omega \times Im\,\widetilde{S}_{OHD-RIKES}(\omega) \qquad [15]$$

The relationship given Eq. 15 between the OHD-RIKES and the DRS data has previously been demonstrated in references 23,24, and 25.

In the OHD-RIKES experimental data it is often possible to separate the fast librational motion of the liquid molecules from the slower rotational reorientation of the molecules. The rotational diffusion time is several picoseconds, and thus typically an order of magnitude slower than the librational motion in the liquid. When the slow diffusive reorientational motion is subtracted from the OHD-RIKES data, one obtains the reduced spectral density of the OHD-RIKES data[13], i.e. the spectrum without the contribution from rotational diffusion. We will use the reduced spectral density of the OHD-RIKES data when comparing with the THz-TDS data. Descriptions of the experimental setups for the THz-TDS, DRS, and OHD-RIKES can be found in the original publications.[7,33,34,35,36] Figure 2 shows the spectra obtained for benzene, 1,3,5 trifluorobenzene, and hexafluorobenzene[37]. Due to the limited bandwidth of our THz system, the present data only extends to ~100 cm^{-1}, corresponding to 3 THz. THz-TDS is the only technique of the three where the measurements are given on an absolute scale; the power absorption coefficient in Neper/cm. In addition the refractive index, not shown, is also obtained using THz-TDS.[36] It is evident from figure 2, that there is, within the experimental uncertainty, very good agreements between the spectral response observed using the different experimental techniques. The main discrepancy is caused by the diffusive component observable at the lowest frequencies. The comparison indicates that the
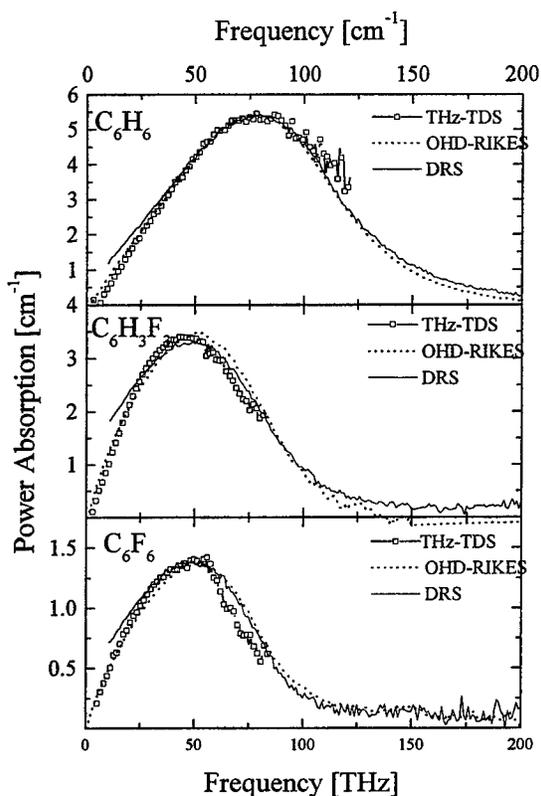

Figure 2. The spectral densities for C_6H_6, $C_6H_3F_3$, and C_6F_6 obtained using OHD-RIKES and DRS shown together with the absorption coefficient obtained using THz-TDS. The OHD-RIKES and DRS data are arbitrarily scaled to fit the THz-TDS data. However the scattering intensity observed in DRS closely follows the magnitude of the absorption coefficient observed in THz-TDS.

diffusive component is absent from the THz-TDS data. The DRS and OHD-RIKES data, including the diffusive component are in full agreement, and the THz-TDS data and the OHD-RIKES data without the diffusive component also agree. From figure 2 it is, however, evident that the DRS and THZ-TDS or the reduced OHD-RIKES spectra are different beyond the experimental uncertainty for the lowest frequencies. The diffusive reorientation of the polarizability is a single molecule property and thus not observable in the THz-TDS spectrum for non-dipolar liquids, where only collision, or interaction induced moments contributes. Another indication of the purely librational response of the non-dipolar liquids is found in the temperature dependence of the absorption coefficient. The amplitude of the interaction-induced spectrum depends on the collision rate and is thus expected to drop as the density decreases with increasing temperature. For a diffusive process the reorientation is activated and the absorption increases as the temperature is increased. The temperature dependence of the far-infrared absorption might be a sensitive probe of the character of the absorption[38]. This is illustrated in figure 3 where the far-infrared absorption is shown for three molecules, benzene, bromoform and water. For benzene the absorption drops as expected for a non-dipolar molecule where the absorption is due to collision induced processes. For the polar water molecules, however, the absorption increases with temperature[39,40], due to the activated reorientation of the permanent dipoles in liquid water. For bromoform, a polar molecule with a dipole moment of 0.99 Debye, the absorption decreases with increasing temperature indicating that induced processes and **not** diffusive reorientation of the permanent dipole moments are the main contributors to the absorption. Work is in progress to study the temperature dependent far-infrared absorption for a range of polar and non-dipolar liquids with varying dipole-, quadrupole moment and polarizability.

Figure 3. The temperature dependent far-infrared absorption for 2 dipolar, H_2O and $CHBr_3$ and 1 non-dipolar, C_6H_6 liquid. The decreasing absorption observed for bromoform indicates that induced processes are the main contributors to the absorption signal observed.

3. POLAR LIQUIDS: INTER- AND INTRAMOLECULAR HYDROGEN BONDS.

Due to the central role played by liquid water in numerous chemical and biological systems, the far-infrared response of liquid water has been extensively studied using THz-TDS[41,42,43] and a wealth of other experimental techniques[2,3,44]. In this paper we will briefly describe the results from the Aarhus laboratory and a recent attempt to find simple model systems for the $O \cdots H - O$ hydrogen bonds. Due to the strong absorption of liquid water in the far-infrared spectral range, transmission measurements are difficult, as very thin samples, $d \leq 100\mu m$, are required. In particular for temperature and index dependent measurements the use of very thin samples becomes troublesome. We have instead proposed and demonstrated THz-TDS in the reflection mode, where the optical constant are obtained from an analysis of two THz-pulses. The first (reference pulse) is from a well-known interface, for example air to silicon and the second (sample pulse) is the silicon to water interface. Using a 1.9 mm thick window of high purity silicon to the liquid cell, the sample and reference pulses are simultaneously obtained from a single scan as the front and back surface reflections from the window. At normal incidence the Fresnel coefficients can be inverted analytically and the index and absorption for the highly absorbing liquid is obtained.
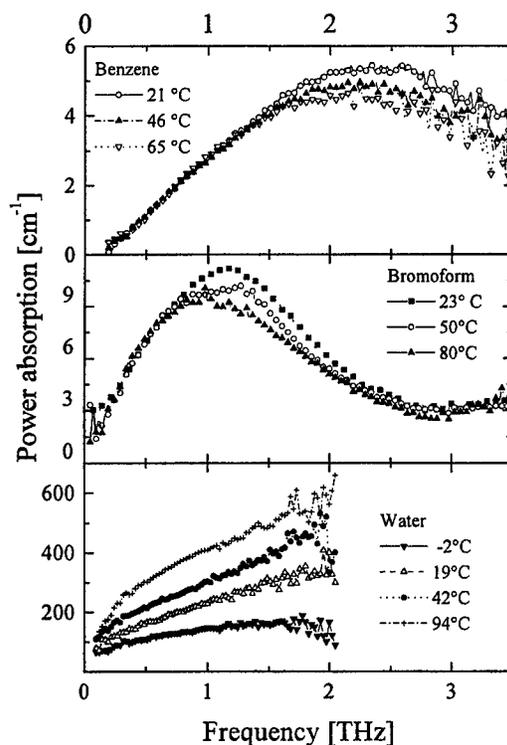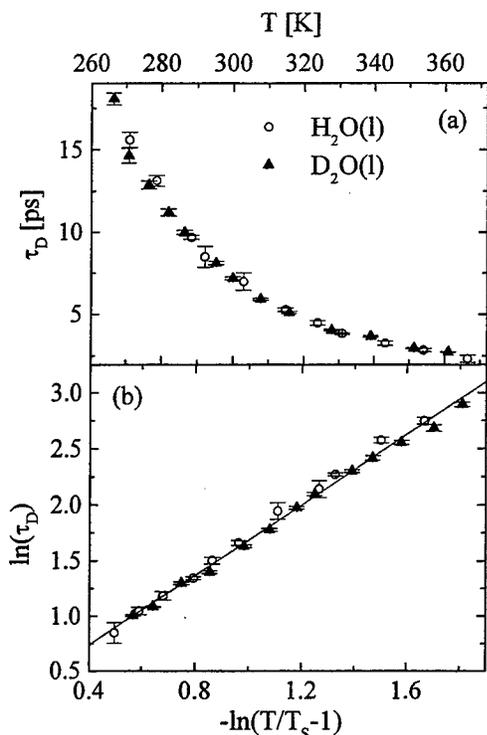
Figure 4. The upper part of the figure show the relaxation times for H_2O together with the D_2O data shifted by 7.2 K. In the lower part the relaxation times for both H_2O and D_2O are plotted versus $-\ln(T/T_S-1)$. The slope, γ, is 1.57 for both H_2O and D_2O.

The method relies on phase shift imposed on the reflected pulse by the large absorption coefficient and is, consequently not applicable in the study of non-dipolar liquid or dipolar liquids with limited far-infrared absorption.

Due to the small moment of inertia of water, the diffusional reorientation of water molecules is observed in the THz-range at room temperature, as opposed to for example larger molecules where these processes give rise to absorption typically below 0.250 THz. The dynamics of liquid water is accurately described by a simple extension of the classical Debye model.

By assuming two Debye relaxation times, a fast τ_2 and a slow τ_D, the complex dielectric constant is reproduced from 0.1-2 THz in the temperature range from -4 to 93 °C

$$\hat{\varepsilon}(\omega) = \varepsilon_\infty + \frac{\varepsilon_S - \varepsilon_1}{1 + i\omega\tau_D} + \frac{\varepsilon_1 - \varepsilon_\infty}{1 + i\omega\tau_2} \qquad [1]$$

In terms of the dipole correlation function formalism[9], this dielectric function corresponds to a double exponential decay with time constants τ_D and τ_2 and amplitudes $(\varepsilon_S-\varepsilon_2)$ and $(\varepsilon_1-\varepsilon_\infty)$. The temperature of the slow, τ_D, relaxation time is show in figure 4. For a simple activated process, one can infer the temperature independent activation energy from the slope of the plot of τ_D versus $1/T$. However, for liquid water the activation energy is also a function of temperature, indicating that temperature dependent structural changes in liquid water changes the reorientation barrier for the water dipoles.

Currently, there is a huge interest in exploring the phase diagram of water at low temperatures. A very interesting hypothesis suggest that a structural transition occur between two amorphous water structures; a strongly hydrogen bonded liquid with low density (LDL) and a weakly hydrogen bonded liquid with high density (HDL)[45]. The temperature dependent activation enthalpy for the dipolar reorientation observed in our experiment can thus naturally be explained as a temperature dependent change in the partition between LDL-water and HDL-water[46,47]. In order to clarify the structural origin of the dipole relaxation process we have performed temperature dependent studies of the relaxation times for both H_2O and D_2O, and we found that by shifting the temperature scale for D_2O by 7.2 K the slow relaxation times for H_2O and D_2O becomes equal as indicated in figure 4. This indicates that the singular point of the LDL-HDL transition for D_2O is found at a temperature 7.2 K higher than that of H_2O. A singular point in the deep supercooled region of the phase diagram will give rise to a power law dependence[48] of the relaxation times,

$\tau_D \propto \left| T - T_s \right|^{-\gamma}$, where T_S is the temperature of the singular point for H_2O and D_2O.

The straight line observed, when both H_2O and D_2O are plotted versus $-\ln(T/T_S-1)$, with $T_S = 228$ K for H_2O and $T_S=235.2$ for D_2O supports the LDL-HDL model for liquid water. Several other experimental and theoretical observations are in favor of this view of two types of water, or more correctly two types of hydrogen bonds, strong and weak.[49,50,51]

Not only in water, but also in large bio-molecules are the hydrogen bonds the key element in understanding the structure and dynamics, and thus the functionality of these vital molecules[52,53]. Consequently, studying the "Nature of the Hydrogen Bond" is presently a field of intense activity[54]. In an attempt to find a simple model system
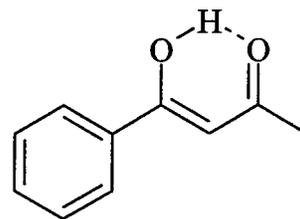

Figure 5. 1-phenyl-1,3-butanedione.

for the $O \cdots H - O$ hydrogen bond, we have recently used THz-TDS to study intramolecular hydrogen bond in 1-phenyl-1,3-butanedione shown in figure 5. This molecule belongs to a class of molecules with very strong hydrogen bonds. The strengths of the hydrogen bond is sufficient to cause the oxygen-oxygen distance (≈ 2.5Å)[55] to be considerably shorter than the normal conjugated O-O distance. Since 1-phenyl-1,3-butanedione crystals were only available in dimensions of the order of a few millimeter, i.e. comparable to the wavelength of the THz-pulses, great care must be taken in order to avoid diffractive effects. Using a THz-system with an additional focus[56] the spot-size of the THz-beam is (independent of the wavelength) of the order of 2 mm. In addition small pinholes were used to remove edge effects. Initially, we

Figure 6. The far-infrared spectrum of a 0.7 mm single crystal of 1-phenyl-1,3-butanedione. The crystal is rotated with respect to the polarized THz-pulse. due to the strong absorption data above 2 THz are uncertain.

studied small single crystals of 1-phenyl-1,3-butanedione. The far-infrared spectrum, shown in figure 6, is surprisingly rich with several sharp resonances below 2 THz. For frequencies higher than 2.0 THz the strong absorption prevents radiation from passing through our 0.7 mm thick crystals. The crystalline sample is dichroic showing a strong dependence on the orientation of the crystal. This is expected to facilitate the assignment of the observed resonances to the vibrational modes of the molecular hydrogen bonded molecule. To investigate the inter- or intramolecular character of the absorption, we have also investigated 1-phenyl-1,3-butanedione molecules dissolved in paraffin. Paraffin was simply heated above its melting point at 60 °C and the 1-phenyl-1,3-butanedione molecules (melting point 60 °C) are dissolved in the melted paraffin. The liquid solution is then poured into a preform and allowed to cool slowly. Paraffin has a very weak far-infrared absorption[57] and is consequently an ideal far-infrared host material. Furthermore, at the long wavelengths the scattering from paraffin is also negligible. In figure 7 we show a spectrum of 1-phenyl-1,3-butanedione in paraffin. Due to the lower concentration of absorbers, the strong resonance at 2.78 THz is now resolved. We have also performed measurements on the single crystal as function of temperature and observed an increase in the resonance frequencies, and narrower linewidths as temperature decreases. At this stage it is not possible to rule out the presence of intermolecular bonding in the 1-phenyl-1,3-butanedione, but the result clearly indicate that THz-TDS is a powerful experimental technique for investigating of the characteristic properties of inter- and intramolecular low frequency vibrations
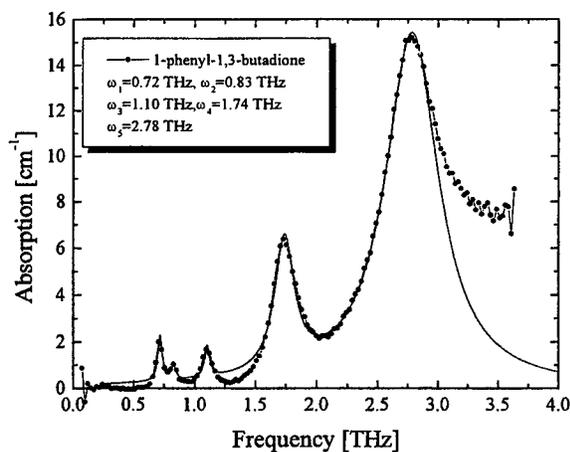
Figure 7. Far-infrared spectrum of 1-phenyl-1,3-butanedione dissolved in paraffin. The full line is a Lorentzian fit to the 5 resonances observed.

of the $O \cdots H - O$ unit. The natural extension of this work is to study bio-molecular crystals directly. Work is presently underway to study bio-molecular crystals with TeraHertz time domain spectroscopy

4.   ACKNOWLEDGMENTS

5.   REFERENCES

[1] Studies in Physical and Theoretical Chemistry 74: "Spectroscopy and Relaxation of Molecular Liquids", eds. D. Steel and J. Yarwood, Elsevier (Amsterdam, NL 1991)

[2] O. F. Nielsen, Annu. Rep. Prog. Chem., Sect. C, Phys. Chem., **90**, 3-44 (1993)

[3] O. F. Nielsen, Annu. Rep. Prog. Chem., Sect. C, Phys. Chem., **93**, 57-99 (1997)

[4] F. Guillaume, J. Yarwood, and A. H. Price, Mol. Phys., **62**, 1307 (1987)

[5] R. Stratt and M. Maroncelli, J. Phys. Chem. A, **100**, 12981 (1996)

[6] J. C. Deak, L. K. Iwaki, and D. D. Dlott, J. Phys. Chem. A, **103**, 971-979 (1999)

[7] D. R. Grischkowsky, S. R. Keiding, M. van Exter, and Ch. Fattinger, J. Am. Opt. Soc. B, **7**, 2006 (1990)

[8] J. E. Pedersen and S. R. Keiding, IEEE J. Ouant. Elec. **vol 28**, 2518 (1992)

[9] B. N. Flanders, R. A. Cheville, D. R. Grischkowsky, and N. F. Scherer, J. Phys. Chem., **100**, 11824 (1996)

[10] J. T. Kindt and C. H. Schmuttenmaer, J. Phys. Chem.,**100**, 10373 (1996)

[11] E. P. Ippen and C. V. Shank, Appl. Phys. Lett., **26**, 92 (1975)

[12] W. T. Lotshaw, D. McMorrow, C. Kalpouzos, and G. A. Kenney-Wallace, Chem. Phys. Lett., **136**, 323 (1987)

[13] Y. J. Chang and E. W. Castner, Jr. J. Phys. Chem. **100**, 3330 (1996)

[14] P. Vöhringer and N. F. Scherer, J. Phys. Chem., **99**, 2684 (1995)

[15] M. Neelakandan, D. Pant, E. L. Quitevis, Chem. Phys. Lett., **265**, 283 (1997)

[16] R. J. D. Miller, R. Casalegno, K. A. Nelson, and M. D. Fayer, Chem. Phys., **72**, 371 (1982)

[17] M. S. Pshenichnikov, K. Duppen, and D. A. Wiersma, Phys. Rev. Lett. **74**, 674 81995)

[18] O. F. Nielsen, D. H. Christensen, P.-A. Lund, and E. Præstgaard, *"Proc. 6th Intern. Conf. Raman Spec"*, ed. E. D. Schmid, R. S. Krishnan, W. Kiefer, and H. W. Schrötter, Heyden, London-Philadelphia-Rheine, 1978, Vol2, p. 208.

[19] P.-A. Lund, O. F. Nielsen, E. Præstgaard, Chem. Phys. ,**28**, 167-173 (1978)

[20] H. Stassen, Th. Dorfmüller, and B. M. Ladanyi, J. Chem. Phys. **100**, 6318 (1994)

[21] E. W. Castner, Jr. and M. Maroncelli, J. Mol. Liquids, **77**, 1-36 (1998)

[22] B. M. Landanyi, "Molecular Dynamics Simulations", chapter 10 in reference 1.

[23] M. Cho, M. Du, N. F. Scherer, G. R. Flemming, and S. Mukamel, J. Chem. Phys., **99**, 2410 (1993)

[24] *"Handbook og Raman Spectroscopy"*, eds. Lewis and Edwards (Marcel Dekker Inc.) To be published in 1999

[25] S. Kinoshita, Y. Kai, M. Yamaguchi, and T. Yagi, Phys. Rev. Lett.,**75**, 148 (1995)

[26] T. S. Perova, J. K. Vij, D. H. Christensen, and O. F. Nielsen, accepted for publication in J. Mol. Structure (1999)

[27] T. S. Perova, D. H. Christensen, U. Rasmussen, J. K. Vij, , and O. F. Nielsen, Vibrational Spectroscopy, **18**, 149 (1998)

[28] C. J. Wu and X. -C. Zhang, Appl. Phys. Lett.,67, 3523-3525 (1995)

[29] P.Y. Han, and X. C. Zhang, App. Phys. Lett. **73**, 3049 (1998)

[30] J. R. Birch and J. Yarwood, "Microwave and Far-Infrared Spectroscopy", Chapter 5 in reference 1.

[31] M. Besnard, Y. Danten, and T. Tassing, in "Collision- and Interaction-Induced Spectroscopy", 201-213, G. C. Tabisz and M. N. Neuman (eds.), Klüwer Academic Publishers (Amsterdam 1995)

[32] D. A. McQuarrie, "Statistical Mechanics", (Harper and Row, New York 1976)

[33] R. A. Farrer, B. J. Loughnane, L. A. Deschenes, and J. T. Fourkas, J. Chem. Phys., **106**, 6901 (1997)

[34] B. J. Loughnane, J. T. Fourkas, J. Phys. Chem. B, **102**, 10288 (1998)

[35] O. F. Nielsen, J. Raman Spec. **20**, 221 (1989)

[36] S. R. Keiding, J. Phys. Chem., **101**, 5250 (1997)

[37] The OHD-RIKES data are unpublished results from B. J. Loughnane and J. T. Fourkas.

[38] F. Guillaume, J. Yarwood, and A. H. Price, Mol. Phys.,**62**, 1307 (1987)

[39] Cecile Rønne, L. Thrane, P.- O. Åstrand, A. Wallqvist, K. V. Mikkelsen, and S. R. Keiding, J. Chem.Phys., **107**, 5319 (1997)

[40] Cecile Rønne, P.- O. Åstrand, and S. R. Keiding, Phys. Rev. Lett., **82**, 2888 (1999)

[41] J. T. Kindt and C. A. Schmuttenmaer, J. Phys. Chem., **100**, 10373-10379 (1996)

[42] L. Thrane, R. H. jacobsen, P. U. Jepsen, and S. R. Keiding, Chem. Phys. Lett. **240**, 330 (1995)

[43] D. M. Mittleman, M. C. Nuss, and V. L. Colvin, Chem. Phys. Lett., **275**, 332 (1997)

[44] *Water: A comprehensive Treatise*, edited by F. Franks (Plenum Press, New York, 1972-81), Vols. 1-7

[45] P. H. Poole, F. Sciortino, U. Essmann, and H. E. Stanley, Nature (London) **380**, 328 (1996)

[46] C. A. Jeffery and P. H. Austin, J. Chem. Phys., **110**, 484 (1999)

[47] E. Walrafen, M. R. Fisher, M. S. Hokmabadi, and W.-H. Yang, J. Chem. Phys., **85**, 6970-6982 (1986)

[48] R. J. Speedy and C. A. Angell, *J. Chem. Phys.*, **65**, 851 (1976)

[49] S. Woutersen, U. Emmerichs, and H. J. Bakker, Science **278**, 658 (1997)

[50] H. Tanaka, Nature, **380**, 328-330 (1996)

[51] Vedamuthu, S. Singh, and G. W. Robinson, J. Phys. Chem., **100**, 3825-3827 (1996)

[52] B. Schiøtt, B. B. Iversen, G. K. H. Madsen, F. K. Larsen, and T. C. Bruice, Proc. Natl. Acad. Sci. USA, **95**, 12799 (1998)

[53] G. A. Jeffrey and W. Saenger, *Hydrogen Bonding in Biological Structures* (Springer, Berlin 1991)

[54] O. F. Nielsen, A. Mortensen, J. Yarwood, and V. Shelley, J. Mol. Structure, **378**, 1 (1996)

[55] G. K. H. Madsen, B. B. Iversen, F. K. Larsen, M. Kapon, G. M. Reisner, and F. H. Herbstein, J. Am. Chem. Soc. **120**,10040 (1998)

[56] M. Schall, H. Helm, and S. R. Keiding, Int. J. of Infrared and Millimeter Waves, **20**, 595 (1999)

[57] A weak resonance at 2.16 THz is observed.

Spectroscopy with electronic terahertz techniques

D.W. van der Weide[a], J. Murakowski, and F. Keilmann[b]

[a]University of Delaware, Dept. of Electrical & Computer Engineering, Newark DE 19716 USA
[b]Max-Planck-Institut für Biochemie, Abt. Molekulare Strukturbiologie, 82152 Martinsried Germany

ABSTRACT

We report gas absorption spectra and energetic material reflection spectra measured with an all-electronic terahertz (THz) spectrometer. This instrument uses phase-locked microwave sources to drive picosecond GaAs nonlinear transmission lines, enabling measurement of both broadband spectra and single lines with hertz-level precision, a new mode of operation not readily available with optoelectronic THz techniques. We take two approaches to coherent measurements: (1) spatially combining the freely propagating beams from two coherent picosecond pulse generators (which have discrete spectra ranging from ~ 6 to > 500 GHz), or (2) using a more conventional coherent source/detector arrangement with sampling detectors. The first method employs a dual-source interferometer (DSI) modulating each harmonic of one source with a precisely-offset harmonic from the other source—both sources being driven with stable phase-locked synthesizers—the resultant beat frequency can be low enough for detection by a standard composite bolometer. Room-temperature detection possibilities for the DSI include antenna-coupled Schottky diodes. Finally, we have recently introduced a reflectometer based on serrodyne modulation of a linearized delay line, using a technique that is process-compatible with pulse generator circuits.

Keywords: electronic terahertz techniques, gas spectroscopy, reflection spectroscopy, nonlinear transmission lines, samplers, coherent measurements, dual source interferometer

1. INTRODUCTION

There is a strong need for integrated circuit (IC) sensors in the THz regime. Applications include multi-species gas sensing to monitor automotive and factory emissions, particularly in the presence of particulates (e.g. soot from diesels) that scatter near-infrared radiation used in today's near-infrared (NIR) gas sensors. Other applications might include measuring reflections with portable, inexpensive equipment for security and location of buried objects. Finally, all of these electronic techniques would benefit from IC-compatible coherent measurement capabilities.

For wavelengths longer than the NIR, Fourier-transform infrared (FTIR) spectroscopy is the dominant method for measuring absorption spectra[1]. While FTIR has been used in the millimeter-wave regime with specialized equipment[2], the relative weakness of the blackbody source below 10 cm^{-1} (300 GHz) requires prohibitively long scans and averaging times.

As an alternative, we employ a dual-source interferometer (DSI) that is not only compact but also free of the need for a coherent detector so that an incoherent (e.g. photoconductive or bolometric) detection mechanism can be used[3,4]. This eliminates the noise inherent in a sampling detector and establishes a baseline for future fully integrated implementations that would use sampling detectors. In the first section of this paper we describe and analyze the DSI, and demonstrate its use in measuring gas absorption spectra.

We then briefly discuss measurements of reflection spectra of energetic materials using a more conventional sampling detector, and finally review a new means of generating coherent signals from a single source. This approach may play a role in future handheld electronic THz systems.

To generate broadband (discrete) spectral energy in the 1-1000 GHz regime, we use nonlinear transmission line (NLTL) pulse generators coupled to broadband planar antennas[5-8]. The GaAs IC NLTLs used in this work consist of series inductors

---

For further author information –
D.v.d.W. (correspondence): email: dan@ee.udel.edu; WWW: http://www.ee.udel.edu/~dan
Telephone: (302) 831-8784; Fax: (302) 831-1218
J.M.: email: jam@udel.edu
F.K: email: keilmann@alf.biochem.mpg.de

276

Part of the EUROPTO Conference on Terahertz Spectroscopy and Applications II
Munich, Germany • June 1999 SPIE Vol. 3828 • 0277-786X/99/$10.00

(or sections of high-impedance transmission line) with varactor diodes periodically placed as shunt elements. On this structure at room temperature a fast (~ 1-2 ps) voltage step develops from a sinusoidal input because the propagation velocity u is modulated by the diode capacitance, $u(V) = 1/\sqrt{LC(V)}$, where L is the line inductance and $C(V)$ the sum of the diode and parasitic line capacitance[9,10]. Limitations of the NLTL arise from its periodic cutoff frequency, waveguide dispersion, interconnect metallization losses, and diode resistive losses. Improvements in NLTL design have resulted in sub-picosecond pulses at room temperature[11].

2. DUAL-SOURCE INTERFEROMETER

In this spectrometer we spatially combine the freely propagating beams from two coherent NLTL pulse generators, resulting in a compact, reliable, and easy-to-implement micro- and millimeter-wave source for spectroscopy. Because the DSI modulates each harmonic of one source with a precisely-offset harmonic from the other source—both sources being driven with stable phase-locked synthesizers—the resultant beat frequency can be low enough for detection by a standard composite bolometer. Room-temperature detection possibilities for the DSI include antenna-coupled Schottky diodes, which we have under development.

1. Description of DSI
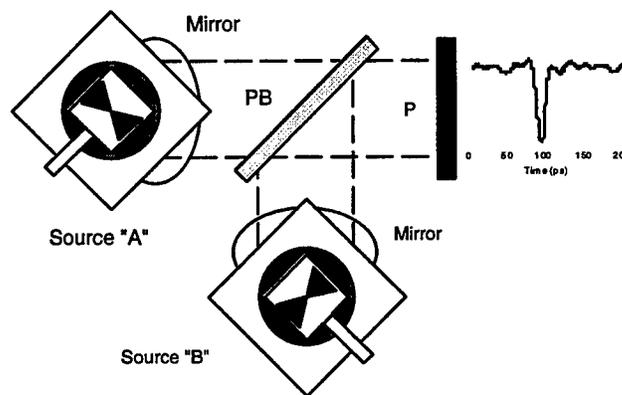
Fig. 1. Dual-source interferometer configuration. Each source/antenna combination is at the focus of a paraboloidal mirror and radiates a polarized beam, which is transmitted ("A") or reflected ("B") by the polarizing beamsplitter (PB). The output polarizer (P) selects half the power of each beam. The output waveform is that detected by a bolometer [3].

In the dual-source interferometer, the output of each NLTL feeds an integrated bow-tie antenna (Fig. 1) mounted at the focus of a hyperhemispherical high-resistivity silicon lens[12]. These lenses in turn are mounted at the foci of off-axis paraboloidal mirrors. The beams collimated by the mirrors are either transmitted (Source "A") or reflected (Source "B") by a wire-grid polarizing beamsplitter. Each beam then contributes equally to the final, linearly polarized beam by arrangement of a final wire-grid polarizer mounted at 45° to the beamsplitter. Note that, while the prototype construction is already small (~ 170 mm long, 120 mm wide, and 80 mm high), it would be possible to fabricate two antennas and their circuitry on the same substrate, making the whole system extremely compact[4]. We also note that other workers have described similar ideas using laser-triggered photoconductive switches[13-15], but one advantage of the current system is its all-electronic approach, which offers precise amplitude (0.01 dB) and frequency (1 Hz) control of the fundamental excitation.

Each source is fed by a 100-900 mW sinewave generated by one of two microwave synthesizers, both of which share a common 10 MHz timebase. The output of one synthesizer is offset by $\Delta f \ll f_0$ ($\Delta f \sim 100$ Hz; $f_0 = 3$-10 GHz), and this offset is used as a trigger for a Fast Fourier Transform (FFT) spectrum analyzer or digital lock-in amplifier. While the synthesizers and broadband power amplifiers used in the present demonstration are expensive, they could be replaced by an inexpensive single source combined with a new NLTL-based frequency translator[16,17].

2. Analysis of DSI

Here we analyze the viability of a detection method based on combining two waveforms of slightly offset frequencies at a power sensor such as a bolometer. Assume first that we have two periodic waveforms $v(t)$ and $w(t)$ of the same frequency $f = 1/T$, so that

$$v(t+T) = v(t),$$

$$w(t+T) = w(t).$$

We combine them and excite a detector with the result. The detector is slow enough that it can only measure the average power of the radiation that impinges upon it. If one of the waveforms is shifted with respect to the other by a we obtain

$$P(a) = \frac{1}{T}\int_0^T [v(t) + w(t+a)]^2 dt = \frac{1}{T}\int_0^T v^2(t)dt + \frac{1}{T}\int_0^T w^2(t+a)dt + \frac{2}{T}\int_0^T v(t)w(t+a)dt$$

$$= \frac{1}{T}\int_0^T [v^2(t) + w^2(t)]dt + \frac{2}{T}\int_0^T v(t)w(t+a)dt$$

as the detected power. Clearly, only the last term of the above formula is dependent on the amount of the relative shift a between the two waveforms; the first term is merely a DC offset. In the subsequent calculations we will focus only on the shift-dependent term which we will call $2\tilde{P}(a)$. Since the waveforms $v(t)$ and $w(t)$ are real functions, we have

$$\tilde{P}(a) = \frac{1}{T}\int_0^T v(t)w(t+a)dt = \frac{1}{T}\int_0^T v^*(t)w(t+a)dt,$$

where the "*" denotes complex conjugation. Since $v(t)$ and $w(t)$ are periodic, we can write them as Fourier series

$$v(t) = \sum_{m=-\infty}^{\infty} v_m \exp\left(\frac{2\pi im}{T}t\right)$$

$$w(t) = \sum_{n=-\infty}^{\infty} w_n \exp\left(\frac{2\pi in}{T}t\right)$$

yielding

$$\int_0^T v^*(t)w(t+a)dt = \int_0^T \sum_{m=-\infty}^{\infty} v_m^* \exp\left(-\frac{2\pi im}{T}t\right) \sum_{n=-\infty}^{\infty} w_n \exp\left(\frac{2\pi in}{T}(t+a)\right)dt$$

$$= \sum_{m=-\infty}^{\infty} v_m^* \sum_{n=-\infty}^{\infty} w_n \int_0^T \exp\left(-\frac{2\pi im}{T}t\right)\exp\left(\frac{2\pi in}{T}(t+a)\right)dt$$

$$= \sum_{m=-\infty}^{\infty} \sum_{n=-\infty}^{\infty} v_m^* w_n 2\pi T \delta_{mn} \exp\left(\frac{2\pi in}{T}a\right)$$

$$= 2\pi T \sum_{n=-\infty}^{\infty} v_n^* w_n \exp\left(\frac{2\pi in}{T}a\right) = 2\pi T \sum_{n=-\infty}^{\infty} v_n^* w_n \exp\left(\frac{2\pi in}{T}a\right)$$

or

$$\tilde{P}(a) = \frac{1}{T}\int_0^T v(t)w(t+a)dt = \frac{1}{T}\int_0^T v^*(t)w(t+a)dt = 2\pi \sum_{n=-\infty}^{\infty} v_n^* w_n \exp\left(\frac{2\pi in}{T}a\right).$$

If the relative shift a between the two waveforms is varied (slowly compared to the frequency $f = 1/T$), the detected average power will vary as well, according to the above equation. In particular, if $a = Tf't$, where $f' \ll f$ is the offset frequency, then

$$\tilde{P}(t) = 2\pi \sum_{n=-\infty}^{\infty} v_n^* w_n \exp(2\pi i f' n t) = \sum_{n=-\infty}^{\infty} \tilde{P}_n \exp(2\pi i f' n t).$$

That is, the detected power $\tilde{P}(t)$ varies in time with frequency f', $\tilde{P}(t + 1/f') = \tilde{P}(t)$, and the harmonics of the original waveforms $v(t)$ and $w(t)$ are encoded in its spectral composition as in the above formula. The attenuation of the n-th

harmonic, $\left| v'_n \Big/ v_n \right| = \left| w'_n \Big/ w_n \right|$, where v'_n (v_n) is the amplitude of the signal with (without) the sample present in the beam

path, can be easily recovered from the spectral analysis of the detected power,

$$\left| \frac{v'_n}{v_n} \right| = \left| \frac{w'_n}{w_n} \right| = \sqrt{\left| \frac{\tilde{P}'_n}{\tilde{P}_n} \right|} = \sqrt{\left| \frac{P'_n}{P_n} \right|},$$

where P'_n (P_n) is the n-th harmonic of the detected power signal with (without) the sample in the beam path.

3. DSI Results

As shown in Fig. 2, the DSI can illuminate a single-pass absorption cell using off-axis paraboloidal mirrors to collimate the radiation and collect it for detection by a bolometer. Using a digital lock-in amplifier, we could measure a single harmonic of the DSI, in this case at 133.785980 GHz, the 20th harmonic of the fundamental of 6.689299 GHz. To measure the data shown, we used a third synthesizer to provide the 10 MHz timebase for the microwave synthesizers then varied this 10 MHz signal to continuously sweep the harmonics of the DSI. This enabled the extremely narrow linewidth of 0.1 torr OCS to be resolved, with an equivalent Q ($f_0/\Delta f$) of $> 8 \times 10^9$. In Fig. 3 we show the effect of pressure broadening on this line.
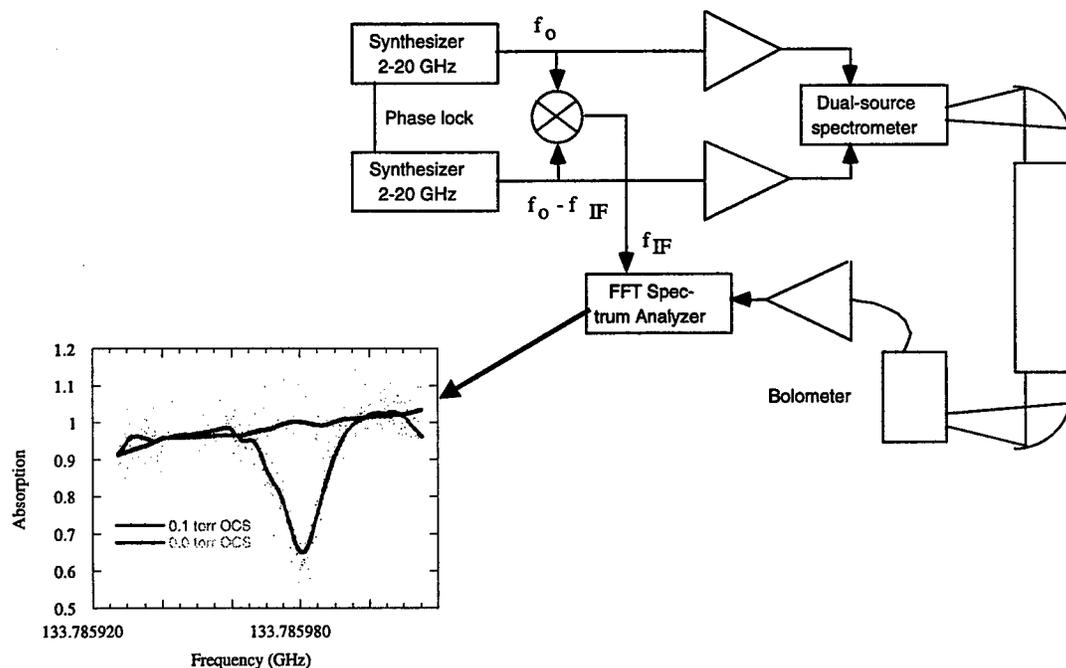

Fig. 2. Dual-source spectrometer system configured for gas absorption measurements. Inset shows raw and smoothed data from 0.1 torr OCS vs. vacuum from a 76 cm long cell, uncorrected for background power slope. Horizontal scale is 20 kHz per large division.
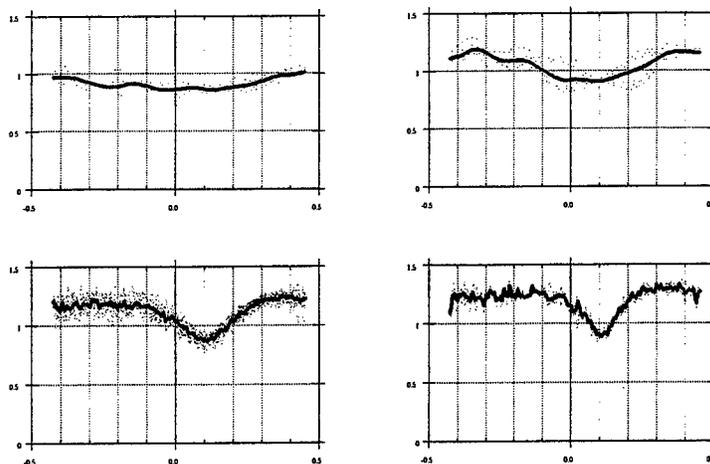
Fig. 3. Pressure broadening of OCS line measured by DSI. Center frequency 133.78597 GHz (20th harmonic of 6.6893 GHz), sweep width 11.8 MHz. Pressure, from left to right, top to bottom: 0.5, 0.3, 0.2 and 0.1 torr.

3. REFLECTION SPECTROSCOPY

Increasingly sophisticated weapons and explosives require increasingly sophisticated detection technologies. Non-metallic varieties of these threats are especially important because they elude familiar metal-detecting portals, so they have motivated development of a multi-pronged approach to detection, including residue sniffing and computerized tomography. These techniques, however, have significant drawbacks, suffering from invasiveness, slowness, unfamiliarity to the public, and significant potential for false negatives[18].

Threats like these, however, appear to be readily detectable and even identifiable using a broadband of signals in the sub-THz regime (1-500 GHz), based on experiments reported here. Traditional equipment for generating and detecting these frequencies has, however, been difficult, bulky and expensive. The objectives of this work are to develop and apply all-electronic and monolithically integrated technology for generating and detecting these broadband signals to the problem of imaging the reflection spectra of plastic weapons and explosives on human subjects.

Many of the concepts we employ here are being pursued at lower frequencies for target detection at higher resolutions than traditional narrowband radar allows. This ultrawideband (UWB), carrier-free, impulse, or baseband radar has been rapidly gaining popularity in applications where complex and elusive targets are the norm[19]. UWB radar has benefited from very recent advances in semiconductor technology enabling the production of sub-nanosecond pulses with peak powers of over 1 megawatt but having average powers in the milliwatt regime.

By contrast, the technology we employ—the integrated-circuit nonlinear transmission line (NLTL)—essentially trades power for speed, producing pico- or even sub-picosecond pulses with peak powers less than one watt and average powers in the low microwatt regime. These power levels are non-ionizing and biologically inconsequential, but because we can employ coherent detection, rejecting noise outside the frequencies of interest, we can still measure useful spectra with them.

Baseband pico- and sub-picosecond pulses of freely propagating radiation, usually generated and coherently detected with photoconductive switches and ultrafast lasers[20-22], have been useful for broadband coherent spectroscopy of materials, liquids, and gasses in the THz regime. Such systems have even been used for what could be called scale-model UWB radar[23]. These highly versatile beams of ultra-short electromagnetic pulses can be treated quasi-optically: They are diffracted and focused with mirrors and lenses, and the resultant effects can be readily observed in the time-domain waveform at the detector. Consequently, such beams are singularly useful for spectroscopy in a difficult-to-access spectral regime, and recent reports of spectroscopic imaging with these optoelectronic systems have generated much interest[24].

Using system concepts identical to the optoelectronic THz systems but with electronic components (Fig. 4), we have configured an NLTL-antenna generator and coherent sampling detector in a focused reflection spectroscopy system using off-axis ellipsoidal mirrors.
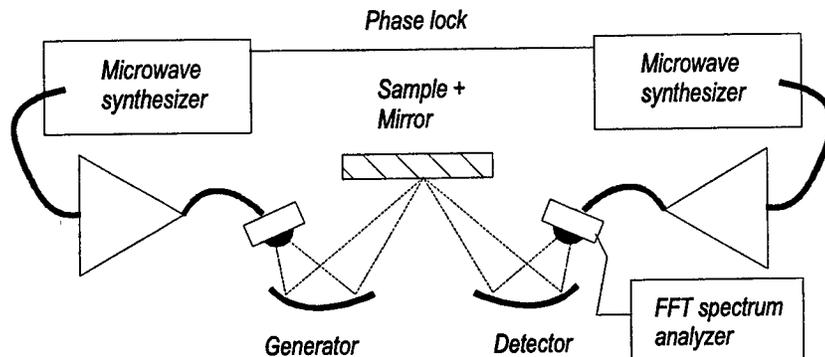
Fig. 4. System diagram for electronic THz reflection spectroscopy.

Broadband (as opposed to single-wavelength) imaging has the chief advantage of flexibility: if weapons change composition over the years, a single-wavelength or narrowband source may no longer detect the new composition, but having a broad range of frequencies maximizes the opportunity to detect the new threat's signature.

One example of this advantage is shown in the data we present here. C-4 is primarily RDX with a plasticizing binder. As shown in Fig. 5, the broadband reflection spectra out to 450 GHz show clear similarity between C-4 and RDX; both are distinct from HMX, demonstrating specificity in the dielectric response of these targets. The contrast we measure is not fully explained, but probably arises from the granularity of the materials, their dielectric constants and orientation of the sample, as distinct from rotational absorption of chemical bonds.
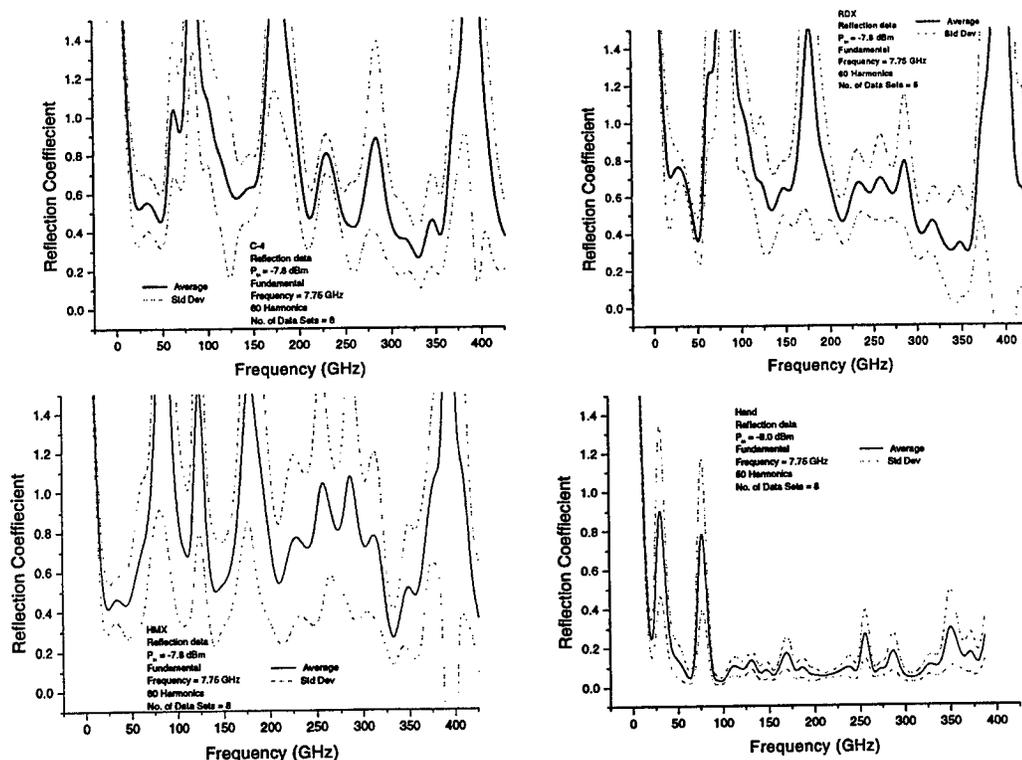
Figure 5. Measured reflection spectra of various energetic materials compared to a human hand (lower left).

These spectra each show the average and standard deviation of 8 data sets using 50 harmonics of a 7.75 GHz fundamental with the sample occasionally repositioned to simulate a security screening application. The presence of standing waves in the highly reflective arrangement resulted in sample-to-background ratios exceeding unity at some frequencies.

We have measured reflection spectra from several potential threats, such as HMX, RDX, C-4, TNT, napthalene (with a similar chemical structure to some explosives), ammonium nitrate solids and slurries, and gasoline, as well as common objects like keys, metals, wallets, credit cards, and notebooks. All show unique and repeatable signatures.

The new information gained from these results can enable progress toward developing multi-pixel arrays of these sources and detectors for a new screening technology. Our current focus is on building inexpensive "single pixel" screening technology by pursuing advances in microfabrication of these devices, integrating more functions on a chip, and reducing the cost of these systems.

4. COHERENT SIGNAL GENERATION WITH SCANNED DELAY LINES

In this final section, we briefly review a new frequency translator based on a nonlinear transmission line (NLTL) phase shifter. Rather than forming shock waves on the NLTL with large signal excitation, we use its voltage-variable delay together with both amplitude and phase linearization to modulate the phase of a small 0.5-3.0 GHz microwave signal, performance that can be scaled with integration of the circuit. The resultant single sideband modulator exhibits > 45 dBc carrier and spurious suppression. This new approach has significant applications in both instrumentation and sensing, particularly because it offers a clear path toward complete integration of a coherent measurement system.

This is a new solution that can enable complete integration of wideband network analyzers, directly addressing the need for instruments to characterize 100 GHz devices, circuits, and systems, as well as the growing opportunities for sensors in this regime. Combining a NLTL phase shifter with serrodyne (sawtooth) modulation results in a frequency translator that can use an inexpensive–ultimately integrated–microwave source to coherently convert a wideband microwave signal directly to baseband. This invention, coupled with improved directional sampling circuits[25], could enable high-performance, inexpensive, and field-capable 100 GHz vector network analysis, as well as several other new military and commercial applications which benefit from a monolithic coherent generation/ detection system.
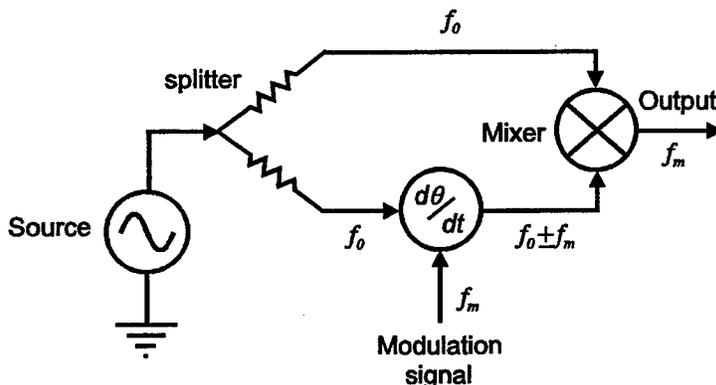
Fig. 6. Block diagram of frequency translator application. Phase shifter is serrodyne modulated at f_m and output of mixer (right) is a sinusoid at frequency f_m.

As shown in Fig. 6, a coherent electronic measurement system need not rely on phase-locked sources, but instead could use a modulated delay line to impart a (single sideband) frequency shift onto one arm of an interferometer. By serrodyne-modulating the delay line, additional sidebands are generated due to the flyback transient; these can be minimized by sufficiently short flyback times or triangle-wave modulation with appropriate Fourier transform reversals at baseband.

We built a demonstration phase shifter on a brass block with 30 abrupt junction diodes ($C_{j0} = 2$ pF) with 4.6 mm interval spacing for the first section and 20 abrupt junction diodes ($C_{j0} = 0.8$ pF) with 0.6 mm spacing for the second. This circuit was able to achieve > 2 ns delay, yet was usable beyond 3 GHz. For comparison, single GaAs IC NLTLs can achieve ~ 160 ps delays[11] with higher usable frequencies; they can also be cascaded for additional delay.

We implemented a phase linearization and amplitude compensation scheme using a gain-controlled amplifier (HP IVA 14208) for amplitude and a 12-bit D/A for phase. We measured the beat note between the original microwave signal and its frequency shifted version using both serrodyne and triangle wave modulation. Both methods gave nearly pure sinusoidal results, but the serrodyne version exhibited a flyback transient, while we could reconstruct the output sinusoid without this transient by using triangle-wave modulation by time-reversing each second cycle of the output.

In spite of the cleaner time-domain appearance of the triangle-wave modulated output, when driven at 0 dBm the serrodyne version exhibited > 45 dB of carrier and harmonic suppression compared to ~ 35 dB for the triangle wave. Fig. 7 shows the downconverted spectrum. In the future, we can address the shortfall of the triangle wave modulation with more careful waveform reconstruction.
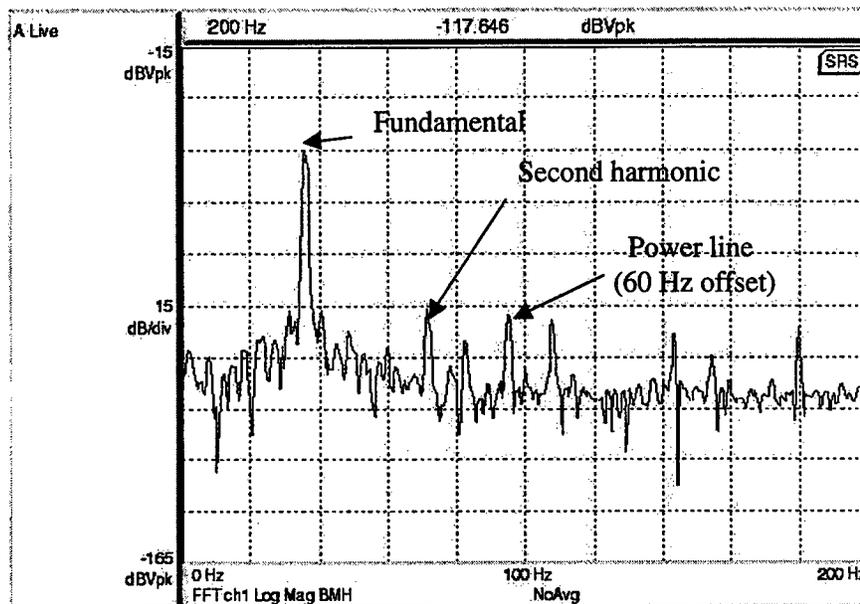
Fig. 7. Downconverted spectrum of single-sideband modulator shown in Fig. 6. Harmonics and spurious due to the line frequency and the sawtooth retrace transient are evident.

We have shown that modulated NLTL frequency translators are ultimately candidates for integration with NLTL pulse generators and diode sampling bridges, enabling for the first time the foundation of a complete monolithic electronic THz system. We extended this approach to building a 1-3 GHz reflectometer with performance comparable to a commercial network analyzer[16,17].

5. CONCLUSIONS

We have described and demonstrated a new technique for gas absorption spectroscopy using a new all-electronic THz interferometer having no moving parts but rather one whose phase is controlled electronically via a frequency offset between its two identical sources. We have also shown a more conventional coherent source/detector arrangement, but used for reflection spectroscopy of energetic materials. Finally, we presented a new means for eliminating these precision sources for a very compact and low cost approach. While this technique lays a promising foundation for inexpensive coherent microwave instrumentation, it can be further extended to other micro- and millimeter-wave sensors, such as handheld reflectometers operating in the THz regime for applications such as demining as well as sensing gasses, nonmetallic weapons and explosives.

6. ACKNOWLEDGMENTS

7. REFERENCES

1 G. W. Chantry, *Long-wave optics*, Vol. 1 (Academic Press, London, 1984).

2 M. N. Afsar, IEEE Transactions on Microwave Theory and Techniques **32,** 1598-1609 (1984).

3 D. W. van der Weide and F. Keilmann, in *1996 IEEE MTT-S International Microwave Symposium Digest*; *Vol. 3* (IEEE, New York, NY, USA, 1996), p. 1731-1734.

4 D. W. van der Weide and F. Keilmann, United States Patent 5,748,309 (1998).

5 D. W. van der Weide, J. S. Bostak, B. A. Auld, and D. M. Bloom, Electronics Letters **27,** 1412-1413 (1991).

6 D. W. van der Weide, J. S. Bostak, B. A. Auld, and D. M. Bloom, Applied Physics Letters **62,** 22-24 (1993).

7 J. S. Bostak, D. W. van der Weide, D. M. Bloom, B. A. Auld, and E. Özbay, Journal of the Optical Society of America B **11,** 2561-2565 (1994).

8 J. S. Bostak, Ph. D. Thesis, Stanford University, 1994.

9 M. J. W. Rodwell, M. Kamegawa, R. Yu, M. Case, E. Carman, and K. S. Giboney, IEEE Transactions on Microwave Theory and Techniques **39,** 1194-204 (1991).

10 M. J. W. Rodwell, S. T. Allen, R. Y. Yu, M. G. Case, U. Bhattacharya, M. Reddy, E. Carman, M. Kamegawa, Y. Konishi, J. Pusl, R. Pullela, and J. Esch, Proceedings of the IEEE **82,** 1035-59 (1994).

11 D. W. van der Weide, Applied Physics Letters **65,** 881-883 (1994).

12 D. W. van der Weide, Journal of the Optical Society of America B **11,** 2553-2560 (1994).

13 B. I. Greene, J. F. Federici, D. R. Dykaar, R. R. Jones, and P. H. Bucksbaum, Applied Physics Letters **59,** 893-895 (1991).

14 S. E. Ralph and D. Grischkowsky, Applied Physics Letters **60,** 1070-1072 (1992).

15 C. Karadi, S. Jauhar, L. P. Kouwenhoven, K. Wald, J. Orenstein, and P. L. McEuen, Journal of the Optical Society of America B **11,** 2566-2571 (1994).

16 P. Akkaraekthalin, S. Kee, and D. W. van der Weide, in *1998 IEEE MTT-S International Microwave Symposium Digest*; *Vol. 3* (IEEE, New York, NY, USA, 1998), p. 1431-1434.

17 P. Akkaraekthalin, S. Kee, and D. W. van der Weide, IEEE Transactions on Microwave Theory and Techniques **46,** 2244-2250 (1998).

18 P. Mann, in *Aviation Week & Space Technology* (1996), p. 23-27.

19 D. Herskovitz, Microwave Journal **38,** 26-40 (1995).

20 M. v. Exeter, Optics Letters **14,** 1128-1130 (1989).

21 D. Grischkowsky, S. Keiding, M. v. Exeter, and C. Fattinger, Journal of the Optical Society of America B **7,** 2006-2015 (1990).

22 M. C. Nuss, K. W. Goossen, J. P. Gordon, P. M. Mankiewich, M. L. O'Malley, and M. Bhusan, Journal of Applied Physics **70,** 2238-2241 (1991).

23 R. A. Cheville and D. Grischkowsky, Applied Physics Letters **67,** 1960-1962 (1995).

24 B. B. Hu and M. C. Nuss, Optics Letters **20,** 1716-18 (1995).

25 R. A. Marsland, Ph. D. Thesis, Stanford University, 1990.

SESSION 7

Poster Session

Cyclotron resonance light holes amplification in optically pumped semiconductors

Dmitry Veksler, Andrej V. Muravjov, Valery N. Shastin

IPM RAS, Nizhny Novgorod, Russia

ABSTRACT

Effect of amplification of far-infrared radiation on light hole cyclotron resonance in Ge and InSb under the optical pumping by CO_2 laser radiation has been calculated using the quantum mechanical model of valence band states in strong magnetic field. The model is based on 6x6 Luttinger Hamiltonian for valence band including split-off hole subband. We have found strong resonant dependence of pumping efficiency on magnetic field that is explained by quantum resonance of intersubband absorption of CO_2 laser radiation. It was shown that at the optimal magnetic fields the cross-section of the gain can reach $2 \cdot 10^{-14}$ cm^2 for pumping power density $2 \div 4$ MW / cm^2.

Keywords: cyclotron resonance, optical phonon, Luttinger Hamiltonian, CO_2 laser pumping, degenerated valence band.

1. INTRODUCTION

Semiconductor sources of submillimeter and far infrared (FIR) wavelength radiation based on cyclotron resonance (CR) transitions in Ge and InSb were discussed for the first time by B.Lax [1] and P.A.Wolf [2]. Further theoretical and experimental investigations have led to the invention of several mechanisms of stimulated emission on intraband optical transitions of hot holes in germanium (Ge), when carriers are ballisticaly heated by electric field and scattered on spontaneously emitted optical phonons. The building up of the inversion population in the valence band of Ge has been found on the light hole Landau states transitions in crossed ($\overline{\bullet} \perp \overline{\bullet}$) [3] and on heavy hole Landau state transitions in longitudinal ($\overline{\bullet} \bullet\bullet \overline{\bullet}$) [4] electrical and magnetic fields.

The common disadvantage of these mechanisms is small gain ($\alpha < 0.1$ cm^{-1}) and low efficiency ($10^{-3} \div 10^{-4}$). Because of the fast overheating of the active sample during the pumping and cryogenic operating temperatures $T < 20$K required for the gain, such lasers operate in a pulse mode only, that limits their applications.

These disadvantage can be eliminated partially using the laser on the light hole cyclotron resonance with intersubband optical CO_2 laser ($\lambda \approx 9 \div 11$ microns) excitation discussed here. The mechanism of inversion population has been discussed and analyzed in quasi-classical approach [5]. According to these classical estimations the gain appears at magnetic fields $B > 9$ T and rather high temperatures $T \approx 80$ K. The small signal gain can reach value $\alpha \approx 10$ cm^{-1}. The broadening of Landau levels caused by spontaneous emission of optical phonons ($\tau \approx 10^{-12}$ c) suppresses the effect of amplification in smaller magnetic fields.

In this paper we investigated this effect in the frame quantum mechanical model of hole states, which is more adequate in magnetic fields $B \geq 5$ T, since $\omega_c^l \geq k_b T_e$ (ω_c^l - cyclotron frequency of light hole, T_e - effective temperature of charge carriers)

2. MODEL OF CALCULATIONS

The spectrum of Landau states of holes in degenerated valence band of Ge was calculated in Luttinger Hamiltonian approach (see (1)) including terms of spin-splitted hole subband (with parameters: $\gamma_1 = 13.38$; $\gamma_2 = 4.24$; $\gamma_3 = 5.69$; $k=3.41$; $q=0.06$; $\Delta = 0.29$eV [6-7] for Ge). The magnetic field was oriented along the crystal axis z || [111].

For further author information -
D.V.: Email: veksler@ipm.sci.nnov.ru

286

Part of the EUROPTO Conference on Terahertz Spectroscopy and Applications II
Munich, Germany • June 1999 SPIE Vol. 3828 • 0277-786X/99/$10.00

$$\hat{H}_0 = \hbar\omega_0^c \begin{Bmatrix} \hat{H}_{11} & \hat{H}_{12} & \hat{H}_{13} & \hat{H}_{14} & \hat{H}_{15} & \hat{H}_{16} \\ \hat{H}_{12}{}^+ & \hat{H}_{22} & 0 & \hat{H}_{24} & \hat{H}_{25} & \hat{H}_{26} \\ \hat{H}_{13}{}^+ & 0 & \hat{H}_{33} & \hat{H}_{34} & \hat{H}_{35} & \hat{H}_{36} \\ \hat{H}_{14}{}^+ & \hat{H}_{24}{}^+ & \hat{H}_{34}{}^+ & \hat{H}_{44} & \hat{H}_{45} & \hat{H}_{46} \\ \hat{H}_{15}{}^+ & \hat{H}_{25}{}^+ & \hat{H}_{35}{}^+ & \hat{H}_{45}{}^+ & \hat{H}_{55} & 0 \\ \hat{H}_{16}{}^+ & \hat{H}_{26}{}^+ & \hat{H}_{36}{}^+ & \hat{H}_{46}{}^+ & 0 & \hat{H}_{66} \end{Bmatrix} \tag{1}$$

$$\hat{H}_{11} = (\gamma_1 + \gamma_3)(n + \tfrac{1}{2}) + \tfrac{3}{2}k + \tfrac{23}{8}q + (\gamma_1 - 2\gamma_3)\zeta^2 \qquad \hat{H}_{22} = (\gamma_1 - \gamma_3)(n + \tfrac{1}{2}) + \tfrac{1}{2}k + \tfrac{13}{8}q + (\gamma_1 + 2\gamma_3)\zeta^2$$

$$\hat{H}_{33} = (\gamma_1 - \gamma_3)(n + \tfrac{1}{2}) - \tfrac{1}{2}k - \tfrac{13}{8}q + (\gamma_1 + 2\gamma_3)\zeta^2 \qquad \hat{H}_{44} = (\gamma_1 + \gamma_3)(n + \tfrac{1}{2}) - \tfrac{3}{2}k - \tfrac{23}{8}q + (\gamma_1 - 2\gamma_3)\zeta^2$$

$$\hat{H}_{55} = \lambda + \gamma_1(n + \tfrac{1}{2} + \tfrac{1}{2}\zeta^2) + k + \tfrac{1}{2} \qquad \hat{H}_{66} = \lambda + \gamma_1(n + \tfrac{1}{2} + \tfrac{1}{2}\zeta^2) - k - \tfrac{1}{2}$$

$$\hat{H}_{12} = -\hat{H}_{34} = \sqrt{\tfrac{2}{3}}[(\gamma_2 - \gamma_3)\hat{a}^{+2} - (2\gamma_2 + \gamma_3)\zeta\hat{a}] \qquad \hat{H}_{13} = \hat{H}_{24} = \sqrt{\tfrac{1}{3}}[2(\gamma_2 - \gamma_3)\hat{a}^+\zeta - (\gamma_2 + 2\gamma_3)\hat{a}^2]$$

$$\hat{H}_{14} = \hat{H}_{41} = -\frac{q}{\sqrt{2}}$$

$$\hat{H}_{15} = \hat{H}_{46}{}^+ = \sqrt{\tfrac{1}{3}}[(2\gamma_2 + \gamma_3)\hat{a}\zeta - (\gamma_2 - \gamma_3)\hat{a}^{+2}] \qquad \hat{H}_{16} = -\hat{H}_{45}{}^+ = \sqrt{\tfrac{2}{3}}[(\gamma_2 + 2\gamma_3)\hat{a}^2 - 2(\gamma_2 - \gamma_3)\hat{a}^+\zeta]$$

$$\hat{H}_{25} = -\hat{H}_{36} = \sqrt{2}[\gamma_3(n + \tfrac{1}{2} - \zeta^2) + \tfrac{1}{2}k + \tfrac{1}{2}] \qquad \hat{H}_{26} = \hat{H}_{35}{}^+ = (\gamma_2 - \gamma_3)\hat{a}^{+2} - (2\gamma_2 + \gamma_3)\zeta\hat{a}$$

The following notations are used: $n = \hat{a}^+\hat{a}$, $\zeta = k_B\sqrt{\hbar c/eB}$, $\lambda = \Delta/\hbar\omega_c^0$.

Corresponding vectors of envelope wave-functions F_j, is :

$$\vec{\psi} = \{F_{3/2,3/2}; F_{3/2,1/2}; F_{3/2,-1/2}; F_{3/2,-3/2}; F_{1/2,1/2}; F_{1/2,-1/2}\}.$$

These six components F_j, $j=1..6$ correspond to quantum numbers $(J, Mj) = (3/2,3/2; 3/2,1/2; 3/2,-1/2; 3/2,-3/2; 1/2,1/2; 1/2,-1/2)$ respectively.

The expansion of F_j into a series of harmonic oscillator eigenfunctions •.

$$F_j = \sum_{n=0}^{n_{max}} c_{j,n} f_n \tag{2}$$

allows to reduce a problem to quasi-infinite system of the algebraic equations:

$$\sum_{n=0}^{n_{max}} \sum_{j=1}^{6} (D_{i,m,j,n} - \varepsilon\delta_{ij}\delta_{mn})c_{j,n} = 0, \ i = 1,2,..,6; \ m = 0,1,..,n_{max} ., \ D_{i,m,j,n} = \int_{-\infty}^{\infty} f_n \hat{H}_{i,j} f_m^* dx dy \tag{3}$$

The limited number of term (n_{max}), required for convergence of the procedure depends on the energy of the highest Landau level to be calculated, that in our calculation was $n_{max}=600$.

Equations (3) are solved by a diagonalization of the matrix $D_{i,m,j,n}$ using the method Jacobi, which give spectrum of eigen energies ε^k and corresponding eigen vectors $c_{j,n}{}^k$.

To estimate a lifetime of hole on certain state ε^k we used quasi-classical approach. The lifetime of the hole at the lattice temperature $T_1 = 77$ K -120 K is determined by spontaneous emission of optical phonons by holes with energy $\varepsilon > \omega_0$ (where $\omega_0 = 37$ meV is an optical phonon energy in Ge) and absorption and emission of acoustic phonons.

$$\frac{1}{\tau_a} = \nu_a(\varepsilon) = \frac{\sqrt{2}E_1^2 m_h^{3/2} k_b T_1}{\pi\hbar^4 \rho u_1^2}\sqrt{\varepsilon}, \ \frac{1}{\tau_{opt}} = \nu_{opt}(\varepsilon) = 2\nu_0\sqrt{\varepsilon/\hbar\omega_0 - 1},$$

$E_1 = 4.6$ eV is the deformation potential constant, $\rho = 5.32$ g/cm^3 is the density of the material, $u_l = 5.4\cdot10^5$ cm/c is the velocity of longitudinal sound, $m_h = 0.35m_0$ is the effective mass of a heavy hole, $\nu_0 = 0.92\cdot10^{12}$ c^{-1} is the characteristic frequency of holes scattering by optical phonons [8] in Ge.

To calculate the absorption spectrum on optical transitions we used the perturbation:

$$\hat{U} = \frac{d\hat{H}}{d\vec{p}}\delta\vec{p} = \hat{V}\delta\vec{p}, \ \delta\vec{p} = \frac{e}{c}\vec{A} = \frac{eE_0\vec{e}}{2\omega}\{\exp(i(\omega t - \vec{k}\vec{r})) + \exp(-i(\omega t - \vec{k}\vec{r}))\}.$$

Matrix element of intraband transition between stationary states s and t under the monochromatic radiation with frequency ω in the dipole approach is given by:

$$U_{st}^0 = \iiint \psi^s \frac{eE_0(\hat{e}\hat{V})}{2\omega} \psi^{t*} d^3\bar{r} = \iiint \frac{eE_0\omega_{st}}{2\omega} \psi^s(\hat{r}\bar{e})\psi^{t*} d^3\bar{r} , \tag{4}$$

where $\ast$ is a vector of polarization, E_0 is an electric field strength in the electromagnetic wave, $\omega_{\ast\ast} = \frac{\varepsilon_\ast - \varepsilon_\ast}{\hbar}$, e is a charge of the hole, $(\hat{\bar{r}e})$ is the dipole moment operator. For a linearly polarized wave $(\hat{\bar{r}e}) = \hat{X}$ in the Faraday configuration. Taking into account that $\hat{X} = \lambda_B \frac{\hat{a} + \hat{a}^+}{\sqrt{2}}$, and formula (2), we have:

$$U_{st}^0 = eE_0 \frac{\omega_{st}}{2\omega} \sum_{i,j} \sum_{m,n} c_{n,i}^s c_{m,j}^t \iiint f_n \hat{X} f_m d^3\bar{r} \delta_{i,j} =$$

$$e\lambda_B E_0 \frac{\omega_{st}}{2\sqrt{2}\omega} \sum_{i,j} \sum_{m,n} c_{n,i}^s c_{m,j}^t \delta_{i,j} (\sqrt{m} \cdot \delta_{n,m-1} + \sqrt{m+1} \cdot \delta_{n,m+1}) \tag{5}$$
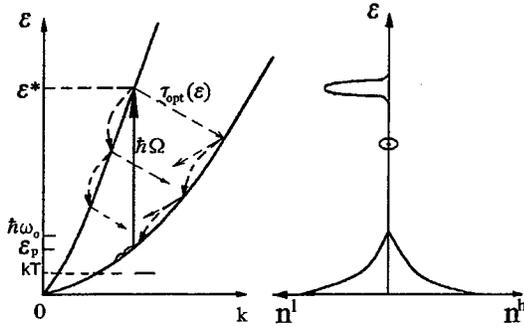

Fig. 1: The mechanism of population inversion. n^l and n^h are populations of light and heavy holes states.

The hole excitation is as follows (fig.1): heavy holes with energy $\varepsilon \approx m_l/m_h \, \Omega$ (Ω is the energy of pumping quantum) are excited to states of the light holes subband.. The spectral width of the initial states is defined by homogeneous broadening of Landau levels and the anisotropy.

At considered doping level of acceptors $10^{15} \div 10^{16}$ cm^{-3} and lattice temperature 77 K hole - hole scattering reduce holes termalization times [9]. Therefore we can expect the Maxwell-Boltsman distribution for holes at $\varepsilon < \omega_0$. The energy relaxation of hot holes is determined by optical phonon emission. It makes the indispensable inverse population of light holes states at $\varepsilon^* > \omega_0$.

The probability of optical transitions from the state t to the state s is defined by formula:

$$P(\omega)_{t\to s} = \frac{2\pi}{\hbar} |U_{st}^0|^2 g(\varepsilon_t - \varepsilon_s - \hbar\omega) . \tag{6}$$

Here $g = \frac{1}{2\pi} \frac{\Delta\varepsilon_L}{(\varepsilon_t - \varepsilon_s - \hbar\omega)^2 + (\Delta\varepsilon_L/2)^2}$, $\Delta\varepsilon_L = \frac{\hbar}{\tau_{st}}$, $\frac{1}{\tau_{st}} = \frac{1}{\tau_s} + \frac{1}{\tau_t}$ - the form-factor, which takes into account a homogeneous broadening of CR-line.

The substitution of (4) into (6) and taking into account the relation between the electric field and intensity: $J = \frac{\chi_0 cE_0^2}{8\pi}$ gives:

$$P(\omega,J)_{t\to s} = \frac{4\pi^2 e^2}{\hbar c\chi_0} \cdot \frac{\omega_{ts}^2}{\omega^2 8\pi} \cdot J \cdot |\langle t|\hat{\bar{r}e}|s\rangle|^2 g(\hbar\omega_{st} - \hbar\omega) . \tag{7}$$

Here χ_0 - the index of refraction (in Ge $\chi_0 = 4$), $\omega_{st} = \omega_t - \omega_s$.

Then distribution function of excited carriers can be found from the kinetic equation:

$$\frac{dn_s}{dt} = \sum_t n_t P(\Omega, J_p)_{t\to s} + \sum_t n_s P(\Omega, J_p)_{s\to t} - \frac{n_s - n_s^0}{\tau_s} . \tag{8}$$

Here n_s and n_t are populations of initial and final states, $P(\Omega,J_p)_{t\to s}$ is the probability of transition from the state t to the state s under the pumping, τ_s is the relaxation time of holes at the level ε_s.

The solution of equation (8) is $n_s = n_s^0 + n_s^1$, where $n_s^1 << n_s^0 \cdot (\varepsilon = m_l/m_h \, \Omega)$, $n_s^0 = N_v \exp\{-\varepsilon_s(k_z)/k_b T\}$. The n_s^1 is:

$$n_s^l = \frac{\sum_t n_t^0 P(\Omega, J_p)_{t \to s}}{\sum_t P(\Omega, J_p)_{s \to t} + \tau_s^{-1}} \qquad (9)$$

The population of the j-th state n_j is subjected to the normalization condition:

$$\sum_{j=1}^{\infty} \frac{1}{2\pi} \int_{-k_{br}}^{k_{br}} n_j(k_z) dk_z = 1 .$$

The constant N_v is found by this requirement. The number of quantum absorbed by one hole is:

$$Q = \sum_{k_z,s,t}^{t>s} P_{t \to s}(n_t - n_s) = \frac{1}{2\pi} \int_{-k_{br}}^{k_{br}} dk_z \sum_{s,t}^{t>s} P_{t \to s}(n_t - n_s) .$$

The cross-section is:

$$\sigma(\omega) = \frac{Q}{J/\hbar\omega} = \frac{2\pi \mathring{a}^2}{c} \frac{1}{\chi_0} \cdot \sum_{t,s}^{t>s} \int_{-k_b}^{k_b} dk_B \frac{\omega_{st}^2}{\omega} |\langle t|\hat{r}e|s \rangle|^2 (n_s(k_z) - n_t(k_z)) \cdot g(\Delta\varepsilon_{st} - \hbar\omega) \quad (10)$$

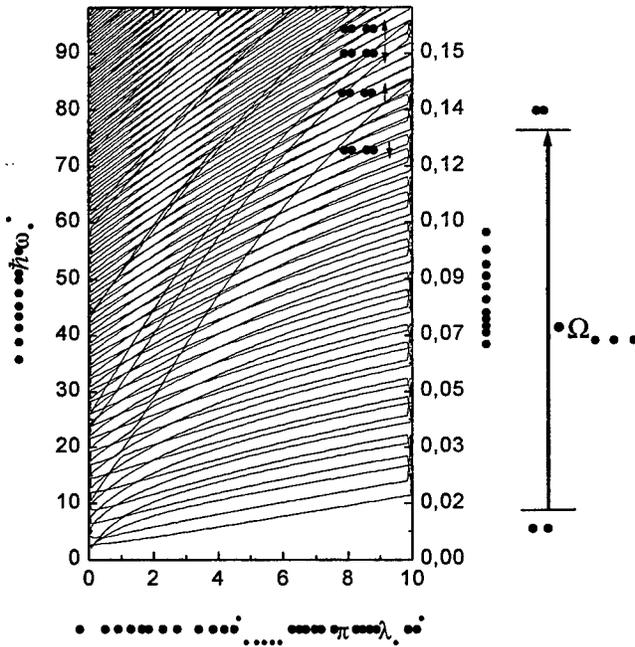## 3. RESULTS OF CALCULATIONS

Fig.2: Landau levels in valence band of Ge vs. the square of the normalized longitudinal wave-vector. $B = 15$ T, $B \parallel [111]$. Numbers of the light holes Landau levels and the total spin direction are designated.

The calculated energy spectrum of Landau levels in the valence band of Ge is shown in fig.2. It is possible to distinguish two groups of energy levels relevant to light and heavy holes, which is indicated in particular by the character of oscillating wave functions. The Landau levels of light holes are spaced less towards high energies, which is caused by interaction with the split-off-subband. Under certain conditions this non-equidistance of Landau levels allows to separate the absorption and emission spectra on light hole CR transitions and to obtain the effect of the CR amplification on inverted light holes with energy ε^* (fig.1). The Landau states of light and heavy holes are strongly intermixed at energies $\varepsilon < \omega_c^l$, which can be seen in fig.2. This mixing violates the selection rules for optical transition $\Delta n = \pm 1$ and gives rise to hybrid resonances near the classic CR of l-holes in the absorption spectrum (fig. 3a). (Note that the cross-section estimation error due to discreteness of integration over k_z causes narrow spikes between the heavy/light holes resonances, which are not of physical nature and which disappear with a decreasing integration step. However, the integration step quantity, chosen by us, is enough for a good averaging in the range of light holes absorption, which is interesting for us, because the absorption lines here are by an order wider, than in the range of heavy holes absorption and they are overlapped.) Also, the hybridization of small energy states gives an increase in the absorption on h-l transitions at frequencies close to harmonics of the l- holes CR. Therefore, pumping efficiency and effect of light hole CR amplification strongly depends on the magnetic field and on the pumping frequency.

The analysis of matrix elements has shown, that the maxima of absorption correspond to transitions from the Landau levels of heavy holes positioned below the zero Landau level of light holes. The first such maximum in the absorption spectrum is close to the second CR harmonic of light holes. We shall denote it as «1», and so on. The ladder of Landau levels of l-holes with an effective spin ↑ remains practically uninvolved, since the h-l transitions to it go, the main, from the states not occupied by carriers at the temperature of $T \approx 80$ K.

Fig.3b shows the small signal absorption cross-section calculated at the excitation of the hole system by pumping to level «3↓» (at frequency of the h-l resonance «2», close to a CR triple-frequency harmonic of light holes). It is seen from the figure that a little bit to the right from the resonance absorption by the termalized light holes there is a resonance of absorption by excited holes (energy range 20 ÷ 26 meV), and in the interval 26 ÷ 32 meV there is a negative peak related to amplification on CR of light holes. At the excitation of holes to the next Landau level of a light subband, the effect of amplification will take place at a lower frequency, which reflects the non-parabolicity of the light hole subband. It is important, that the density of states behaves as $\propto 1/k_z$, and the population of the low Landau states is follow down with k_z. Therefore the main body of the integral in formula (10) is obtained at small k_z, and the non-uniform broadening of the line of CR amplification, caused by emission transitions between different excited Landau levels, is inessential.

From matching fig. 3a and fig. 3b one can see noticeably decrease of the resonant photoabsorption at the pumping frequency. It is the effect of saturation of optical transition and it restricts the usable pumping power. The calculations have shown, that the intensity Jp = 4 MW / cm^2 is close to saturating, and the further increasing of pumping intensity do not give an increase of small signal gain.
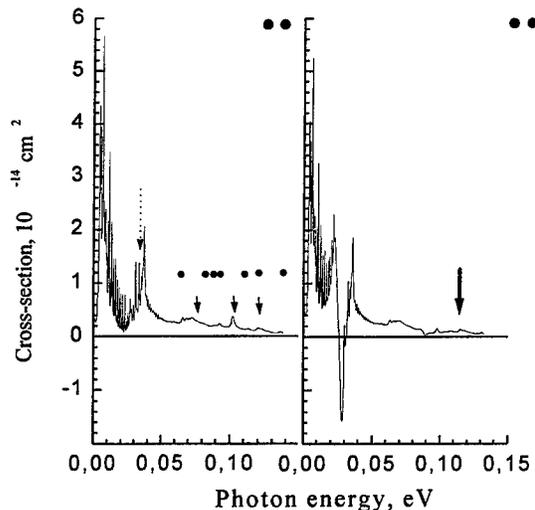
Fig.3: Absorption cross-section for the circular polarized FIR radiation in the Faraday configuration by a) termalized and b) photoexcited holes. (Jp=4 MW/cm^2) in Ge $B = 15$ T, $T_e = 77$K.

The dotted arrow in fig a) indicates a point of quasi-classical light hole CR, the short arrows indicates positions of maxima of absorption on the h-l resonances. The arrow in fig. b) indicates the energy of pumping quantum.

Fig.4: Pumping efficiency and appropriate amplification cross-section vs. pumping frequency. Polarization is circular. a) $B = 15$ T b) $B = 18$ T.

In spite of the fact that the maximum number of excited holes is reached at the pumping of the 1-st **h-l** resonance, the effect of amplification is approximately identical at pumping in both the 1-st and the 2-nd resonances (see fig.4). It happens because the matrix elements of cyclotron resonance transitions are proportional to the Landau level number. For Landau levels with the small numbers (for example, 2 and 3-rd) the ratio of probabilities of CR transition can be quite high. With increasing magnetic field the maximum of amplification cross-section diminishes. It is related, apparently, to the nonparabolicity of the valence band, as cyclotron mass enters the denominator of formula (10). The rise in temperature of the carriers from 77 K up to 120 K in a field $B = 18$ T causes a decrease in the magnitude of optimum amplification, which does not correlate with quasi-classical estimates that predict for Ge an increase in the amplification in this temperature range. Another relevant feature of quantization, contradicting the quasi-classical approach, is the existence of pump frequency regions in which amplification is absent.

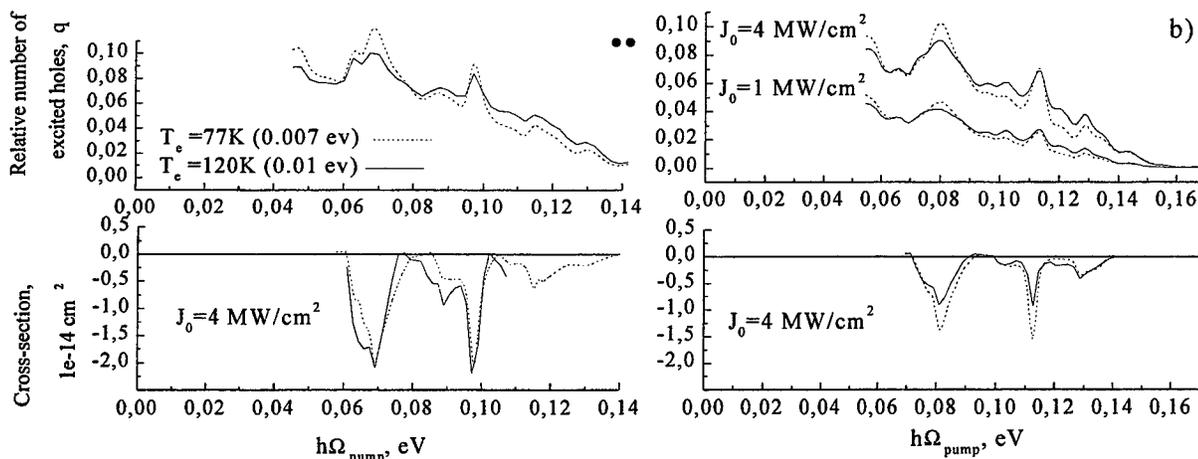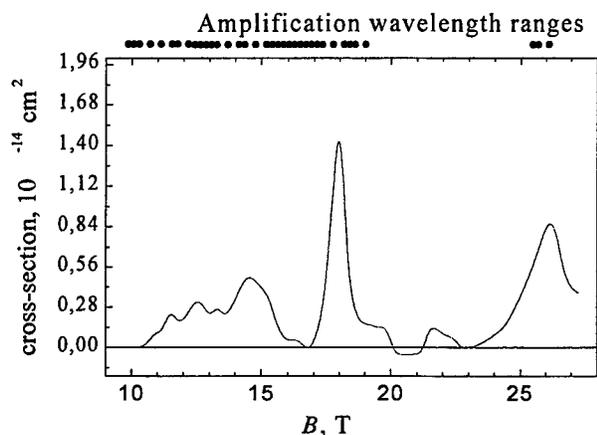**Fig.5:** Light hole CR amplification cross-section in Ge vs. the magnetic field at CO_2 laser pumping ($\Omega_{CO2} = 117$ meV). $T = 77$ K.

The dependence of amplification cross-section on the magnetic field at the fixed pumping frequency is given in fig.5. The amplification begins in magnetic fields more than 10 T (which corresponds to quasi-classical estimations). In the interval of fields $B = 10.5 \div 27$ T the magnitude of the amplification cross-section has resonant character and reaches a maximum. Amplification vanishes with a further increase of a magnetic field. The results of quantum calculations have confirmed a possibility of amplification on light holes CR in conditions of optical pumping. The maximal cross-section of amplification is in $2 \div 4$ times large than that predicted by the classical estimates.

4. ESTIMATES FOR InSb

InSb. is a direct band material with a narrow gap. It has smaller than Ge anisotropy of the energy spectrum. Parameters of InSb are: $m_c = 0.013m_0$, $m_l = 0.015m_0$, $m_h = 0.35m_0$, $\Delta = 0.9$ eV, $\varepsilon_g = 0.23$ eV. The mass of light hole in InSb is 3 times less than in Ge, and the non-equidistance here is as strong as in Ge because of the conduction band. The order of the scattering rate is the same.
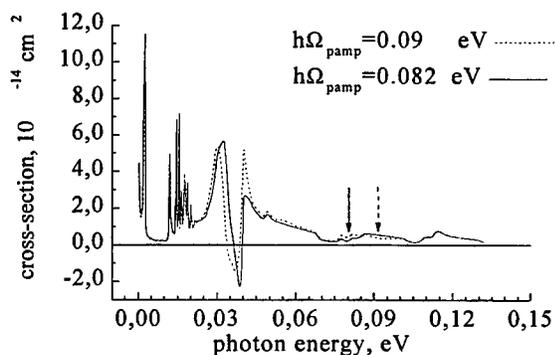
Fig.6: Absorption cross-section vs. the photon energy at different pumping frequencies in InSb. Here $B = 5$ T, $J_p = 2$ MW/cm^2, $T = 77$ K. The arrows indicate positions of pumping.

Therefore, smaller magnetic field is enough for a frequency separation of the absorption and the amplification lines. In fig.6 the result of calculation of amplification in $B = 5$ T is shown (such magnetic field corresponds to the amplification frequency near the upper edge of strong lattice absorption). The magnetic field $B \leq 1.5$ T. corresponds to the lower edge; however, CR - amplification is impossible in such small fields at such conditions as in fig.6. At $B = 5$ T the effect of amplification can be expected at wavelengths $\lambda \approx 40$ μm. The lattice absorption is about 3 cm^{-1} at this wavelength. From fig.6 it is seen, that the hybrid resonances in the absorption spectrum of InSb are less pronounced. The mixing of light and heavy hole states can be less essential because of a greater difference of their masses, than in Ge. But intersubband optical transitions (h-l resonances) are still strongly expressed. They are inhomogeneously broadened, which is indicated in particular by the character of saturation of them at various pumping frequencies.

5. CONCLUSION

The quantum mechanical calculations of far-infrared absorption spectrum of p-Ge in strong magnetic filed under CO_2 laser optical excitation, performed here confirm and specify the idea of the amplification on light hole cyclotron resonance originally based on quasi-classical considerations.

It has been found that in magnetic fields $B = 9 \div 20$ T, required for amplification effect, intersubband absorption on the frequency of pumping CO_2 laser has resonant dependence on magnetic field, that remarkably influence on the efficiency of the gain mechanism. The observed resonance maxima in the absorption spectrum near the pumping frequencies is a result of quantization of density of states on direct optical heavy-to-light hole transitions. Thus, a sufficient inversion population of excited light holes can be reach at a moderate power of CO_2 laser pumping radiation only at the certain resonance frequencies of the pumping laser, or in the case of fixed pumping frequency, as for CO_2 laser at the resonance values of magnetic field.

In spite of the gain mechanism requires high threshold pumping power density (few MW/cm^2), liquid nitrogen working temperatures and relatively high level of small signal gain ($10 \div 100$ cm^{-1}) make optically pumped p-Ge and p-InSb perspective active media for pulsed Terahertz frequencies tunable sources. The comparatively small light hole effective mass of InSb determines the preferential use of this semiconductor for the generation of radiation with frequency $f > 6$ THz (the upper frequency limit is determined by the reasonable values of magnetic fields used). Due to the greater light hole mass the p-Ge has advantage for the frequencies $3 < f < 10$ THz.

Another perspective active media for light hole CR amplification under optical pumping can be Ge/GeSi heterostructure with quantum wells, there non-equidistance of light hole Landau levels should be higher.

6. ACKNOWLEDGEMENTS

7. REFERENCES

1. B.Lax, Cyclotron resonance and impurity levels in semiconductors, In: Quantum Electronics Symposium. N.Y.: Columb. Univ. Press, 1959, p.428-447
2. P.A.Wolff, Proposal for a cyclotron resonance maser in InSb, Physics, 1, 147-157 (1964).
3. Y.L.Ivanov, Generation of cyclotron radiation by light holes in germanium, Optical and Quantum Electronics, 23.2, (1981)
4. V.I.Gavrilenko, Z.F.Krasil'nik, Negative mass cyclotron resonance maser, Optical and Quantum Electronics, 23.2, (1981)
5. V.N. Shastin, The possibility of the submillimeter waves amplification on the light hole cyclotron resonance at the intravalenceband optical excitation of p-Ge, Sov. Fizika Tehn. Poluprov, 15, 1641 (1981).
6. M.V. Jakunin, Magnetophonon resonance on holes in Ge. Sov. Fizika Tehn. Poluprov FTP, 18.6, 969-976 (1981).
7. Luttinger J.M., Phis. Rev., v.102,4, p. 1030-1041 (1956)
8. M. Costato, L.Reggiani, Scattering probabilities for holes, Phys.Sr.Sol(b), 58.2, 471-482 (1973)
9. E.V.Beregulin, P.M.Valov, I.D.Yaroshecky, The Investigations of carriers cooling and heating by light in the semiconductors, FTP, 12,1, 109-116 (1978).

3D Photonic crystals: Low cost,
High quality filters for THz applications

S. Rowson[a], A. Chelnokov[a], J.-M. Lourtioz[a] and L. Duvillaret[b], J.-L. Coutaz[b]

[a]Institut d'Electronique Fondamentale, UMR 8822 du CNRS,
Université Paris-Sud, Bât. 220, 91405 Orsay Cedex, France

[b]Laboratoire d'Hyperfréquences et Caractérisation,
Université de Savoie, 73376 Le Bourget-du-Lac, France

ABSTRACT

We report a low cost and material independent fabrication technique to produce sub-millimeter three-dimensional photonic crystals. The crystal is made by stacking mechanically machined dielectric substrates. Interstitial defects can be introduced in the structures. This technique is illustrated by experimental studies with highly resistive silicon based crystals with and without defects. A terahertz time-domain spectroscopy set-up is used for broad band transmission characterization of the crystals. Systematic measurements of the transmission characteristics for different crystal thicknesses (number of lattice periods) and incident angles were performed. A wide complete photonic band gap centered at 265 GHz with a 19% band-gap to mid-gap frequency ratio, and excellent filtering properties (2.2 dB/GHz slope at 240 GHz) are observed with only six crystal periods. The influence of the defects was experimentally studied and an external control of their mode's transmission coefficients is demonstrated. The transmission coefficient of the defect modes is controlled by illuminating the interstitial silicon defects with a 330 mW laser beam. Numerical simulations reproduce this behavior by modeling the illumination as an increase of the defect absorption.

Keywords: Photonic crystal, defect, control.

INTRODUCTION

The interest brought to photonic crystals has not ceased to increase since the first demonstration of a photonic band gap about ten years ago.[1] Many application possibilities[2,3] (wave guides, filters, antenna substrates...) are foreseen for these periodically arranged dielectric or metallic structures. Moreover, the insertion of defects in a photonic crystal leads to a strong localization of the electromagnetic field for certain frequencies within the photonic bandgap (PBG).[3] At these frequencies, the defects behave as high-quality resonators with sharp transmission peaks. This suggests that photonic crystals with defects could then be used as narrow-band transmission filters with the advantage of being effective in all the directions of wave propagation. Meanwhile, efficient external coupling to these defect modes as well as the interaction between several defects demands further exploration. A further step towards active filters and, more generally, adaptable photonic crystals would require to command either the frequency position or the transmission level of the defect modes. To vary the frequency positions of transmission resonance deformable metallic-wire PBG structures have been proposed at microwave frequencies.[4] The transmission level of defect modes can be modulated by for example changing the absorption of the material creating the deect.[5]

The first photonic crystal was demonstrated in 1991 with a face-centered-cubic (FCC) crystal symmetry obtained by drilling holes in a bulk dielectric material. A layer-by-layer photonic crystal (later referred to as the wood-pile structure) was introduced in 1993 as an alternative structure much easier to fabricate and thus preferred for smaller dimensions. The wood-pile structure obtained by stacking layers of rods[6] has the same FCC crystal symmetry but with a different orientation. Figure 1 illustrates the wood-pile structure. Four layers of rods are stacked to build one period of crystal. Each layer consists of equally spaced parallel rods. The rods of two consecutive layers are perpendicular The first experimental results validating theoretical predictions for microwave frequencies (12-15 GHz) were obtained in 1994 with a crystal of alumina rods.[7] To reduce the size of the structures the authors used anisotropic etching techniques for silicon. The first technique[8]

Part of the EUROPTO Conference on Terahertz Spectroscopy and Applications II
Munich, Germany • June 1999 SPIE Vol. 3828 • 0277-786X/99/$10.00

293

consisted of etching grooves through silicon wafers to obtain parallel rods. Stacking the wafers gave the desired structure. With the second technique[9] parallel grooves were etched, at least half a wafer deep, on both sides of the wafers. This technique gave a half period of crystal with just one wafer thus gaining a factor of 2 on the size. A photonic band gap was obtained around 350 GHz. However, the <111> silicon planes used for the anisotropic etching imposed a 70.5° angle in-between the front and back side grooves, thus giving a distorted wood-pile structure. The wood-pile structure was recently used by Fleming et al. to obtain the first three dimensional photonic crystal with a PBG around 1.55 µm wavelength.[10]
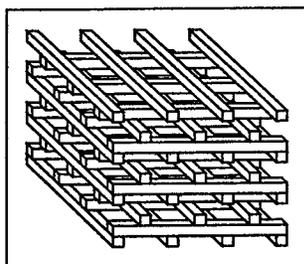
Figure 1: Schematic layer-by-layer photonic crystal
(wood-pile structure)

In this paper we report a combined experimental and numerical study of sub-millimeter wood-pile photonic crystals obtained by a low cost and material independent fabrication technique. The crystal is made by stacking mechanically machined[11] substrates and enables interstitial defects to be inserted in the structures. A terahertz time-domain spectroscopy set-up is used for broad band transmission characterization of the crystals. This technique is demonstrated with highly resistive silicon based crystals with and without defects. In the first section, the fabrication and characterization methods will be described. In the second section systematic measurements of the transmission characteristics for different crystal thicknesses (number of lattice periods) and incident angles will be presented. In the third section the influence of the defects is studied. In the fourth section an external control of the defects transmission coefficients is demonstrated.

1. CRYSTAL FABRICATION AND CHARACTERIZATION

The structures are mechanically machined with a dicing saw used for cutting electronic chips from wafers. A series of grooves half a wafer deep are cut across the silicon wafer leaving parallel square section rods on the surface. The wafer is

Figure 2: Fabrication process

turned over and rotated by 90°. The same grooves are cut on the back side of the wafer. The square grid obtained where t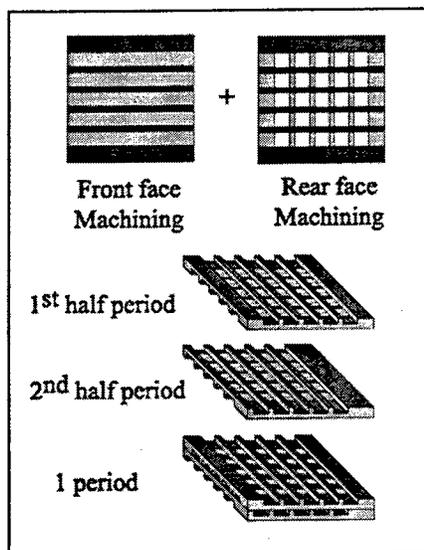he grooves from both sides of the wafer overlap gives a half period of the wood-pile structure. It is a self supported structure with the same mechanical properties as those given by double etching technique,[9] without the problem of imposed angles. For extra strength and assembling purposes the grid is surrounded by a square of bulk material. Two grid/square configurations are used to construct one crystal period. In one case the grid is centered in the square, in the second case the grid is shifted half a period from the center of the square. Stacking alternately the two different grids and aligning them with the edge of the bulk material gives the wood-pile structure. This process is illustrated in figure 2.

We use silicon wafers 270 μm thick with a resistivity greater than 1 kΩ.cm. The grooves are 360 μm wide and separated by 135 μm resulting in rods of 135 μm^2 cross section. Each grid is formed by 25 rods in both directions surrounded by 3mm of bulk silicon. Up to twelve grids are used giving 6 periods of crystal and an overall dimension of 20x20x3 mm^3. Figure 3, presents a photograph of a six period structure. The Load Point dicing saw is entirely programmable and has a precision better than 2 μm. The Sementic diamond coated dicing wheel used gives a near to optical polish surface quality to the rods. The grids are assembled and maintained together by their sides with a coat of acetone solvent type glue.

We used a terahertz time-domain spectroscopy setup[12] to measure the complex refractive index of the photonic crystal. In the setup, picosecond electrical pulses are emitted and detected using two identical low-temperature-grown GaAs photoconductive switches as antennas. The spectrum of the pulses extended from 80 GHz to over 1 THz. A nearly parallel incident beam was obtained by collimating the emitted electromagnetic (EM) impulsion with a high-resistivity silicon hemispherical lens. An iris diaphragm of 8 mm diameter was placed in front of the crystal to prevent the incident beam (10 mm diameter) from passing through the bulk material surrounding the crystal. The beam was linearly polarized with a ratio of 20 dB. The transmitted beam was focused onto the detecting antenna with a lens identical to the one used for collimating. Both the emitting and the receiving switches were strobed with 110 fs optical pulses from a self-modelocked Ti:Saphire laser. The temporal shape of the received signal was obtained by varying the relative delay between the optical pulses that strobe the emitting and the receiving switches. The transmission spectrum of the sample was then determined by dividing the Fourier-transformed temporal signals obtained with and without the sample.
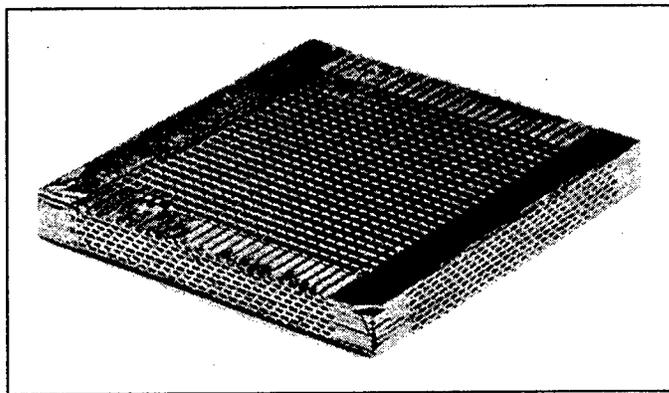
Figure 3: Photograph of a realized wood-pile photonic crystal. Twelve mechanically machined
silicon substrates are stacked to obtain six crystal periods. The overall dimension is 20x20x3

For numerical simulations we use a commercial three-dimensional finite elements electromagnetic wave propagation simulator (HFSS) to calculate the transmission spectra of the structures. This enables complete calculations with and without defects. Furthermore material losses can be modeled, ensuring accurate results.

2. COMPLETE PBG

In this section, we demonstrate the performances achieved with the structures obtained by using the mechanical machining fabrication process. Systematic measurements of the transmission characteristics for different crystal thicknesses (number of lattice periods) and incident angles are performed with a structure without defects. First the results for one and two periods will be presented followed by the demonstration of a complete PBG with a crystal six periods thick

Figure 4 shows the experimental and numerical results obtained with one crystal period on the left and two crystal periods on the right. The solid lines correspond to the measured spectrum and the lines with circles correspond to HFSS simulations. The spectra were measured at normal incidence, following the stacking direction.

Figure 4: Influence of the number of periods on the normal incidence transmission spectra.

For one crystal period a sharp resonance peak is observed. The peak is centered at 300 GHz for the measured spectra and at 310 GHz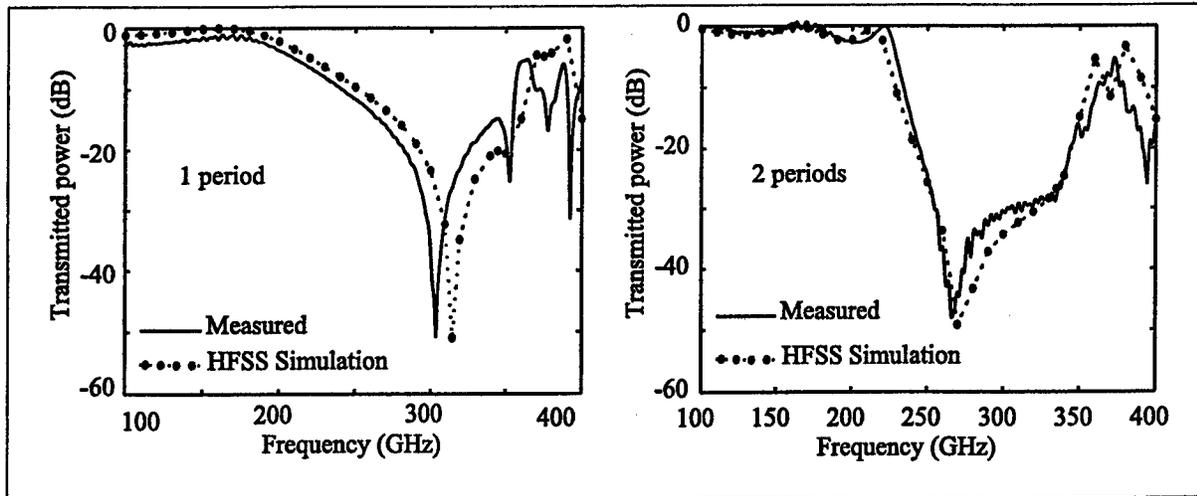 for the simulation with a 50 dB attenuation. A close to 0 dB transmission is observed for low frequencies. These excellent transmission properties are also obtained with two crystal periods along with a broad stop band between 250 GHz and 350 GHz with an average 35 dB attenuation. These results reveal the high precision and the quality of the mechanically machined structures. The good agreement between the simulations and the measurements for the width and shape of the bands as well as for the attenuation in the forbidden bands enabled us to verify that the HFSS method is valid for these types of calculations. The next step is then to demonstrate a complete PBG for these structures.

Figure 5, presents the transmission spectra measured for different incident angles with a crystal six periods thick. From top to bottom the spectra are measured following the stacking direction, at 45° and perpendicular to it, respectively. The inserts show a schematic wood-pile structure, the arrows materialize the incident probe beam. The three transmission spectra contribute to the verification of the existence of a complete photonic band gap in all three dimensions for the wood-pile structure. In our case the complete band is centered at 265 GHz and is 50 GHz wide. This gives a band-gap to mid-gap frequency ratio of 19% for the complete photonic band gap.

Higher order bands appear for the spectra measured through the top surface. The top and middle spectra in fig. 5 show a second order forbidden band gap from 400 to 420 GHz and from 360 to 400 GHz, respectively, with almost the same attenuation as the first order band. Transmission minima at higher frequencies may indicate even higher order bands. In contrast, the very low transmission at high frequencies is likely related to diffraction effects due to the small thickness of the crystal in the stacking direction. For this reason only the first order band is observable. The slightly lower signal dynamics, 35 dB, for the band in the bottom spectrum fig. 5 is explained by the use of an additional slot diaphragm (3x8 mm²) for the measurements.

Further observations of these spectra show excellent filtering properties and confirm the good quality of the mechanically machined wood-pile. The extremely steep slopes, 2.2 dB/GHz, surrounding the band gaps demonstrate the frequency selection possibilities of such structures. The high precision of the crystal's periodicity provides high transmission for the frequencies below the first band gap and a 45 dB attenuation, reaching the measurement limits, in the forbidden gap and this for only 6 periods of crystal.

In this section we have demonstrated the high quality of the crystals obtained with the mechanical machining process. A broad complete photonic band gap, centered at 265 GHz with a 19% band-gap to mid-gap frequency ratio, and promising filtering properties were observed with only six crystal periods. These results were confirmed by numerical simulations. In

the rest of the paper the same fabrication method will be used to elaborate more sophisticated structures by inserting defects.
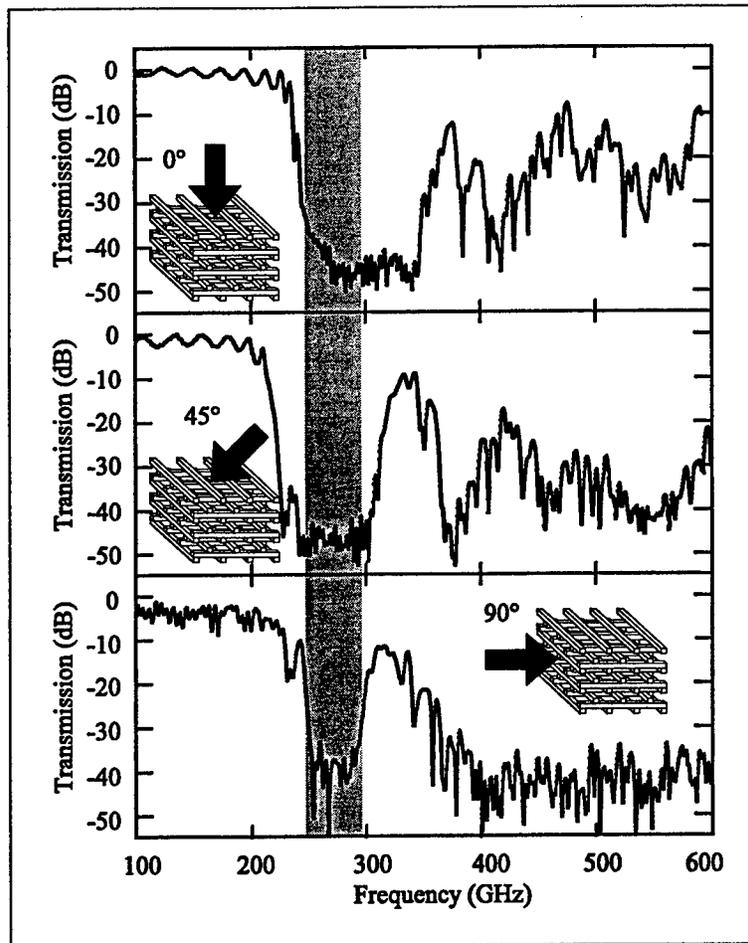
Figure 5: Complete photonic bandgap

3. DEFECTS

In this section the influence of defects on the transmission properties of the photonic crystal is studied. Transmission spectra
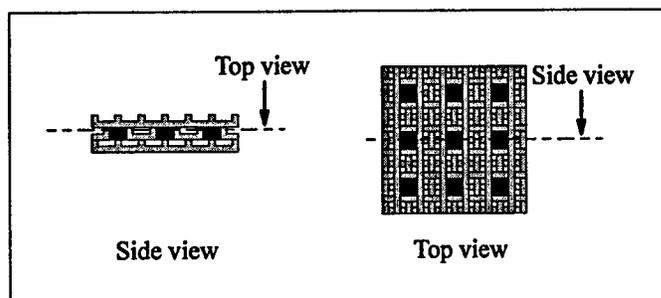
Figure 6: Position of defects

for different incident angles are experimentally measured through the crystal surface. A crystal one and a half periods thick

was fabricated using three mechanically machined grids. Defects were created by inserting silicon parallelepipeds in lattice interstitial sites as indicated in figure 6. Each parallelepiped had a square base of 360x360 μm^2 and a height of 270 μm. Nine defects were created for characterization purposes. Indeed their large number and especially their proximity enabled strong coupling possibilities that improved the detection of the defect modes. This would probably not be a good choice for applications as defect coupling induces undesirable effects. Indeed, different coupled defect modes are excited in function of the incidence angle leading to frequency shifting of the associated resonances.
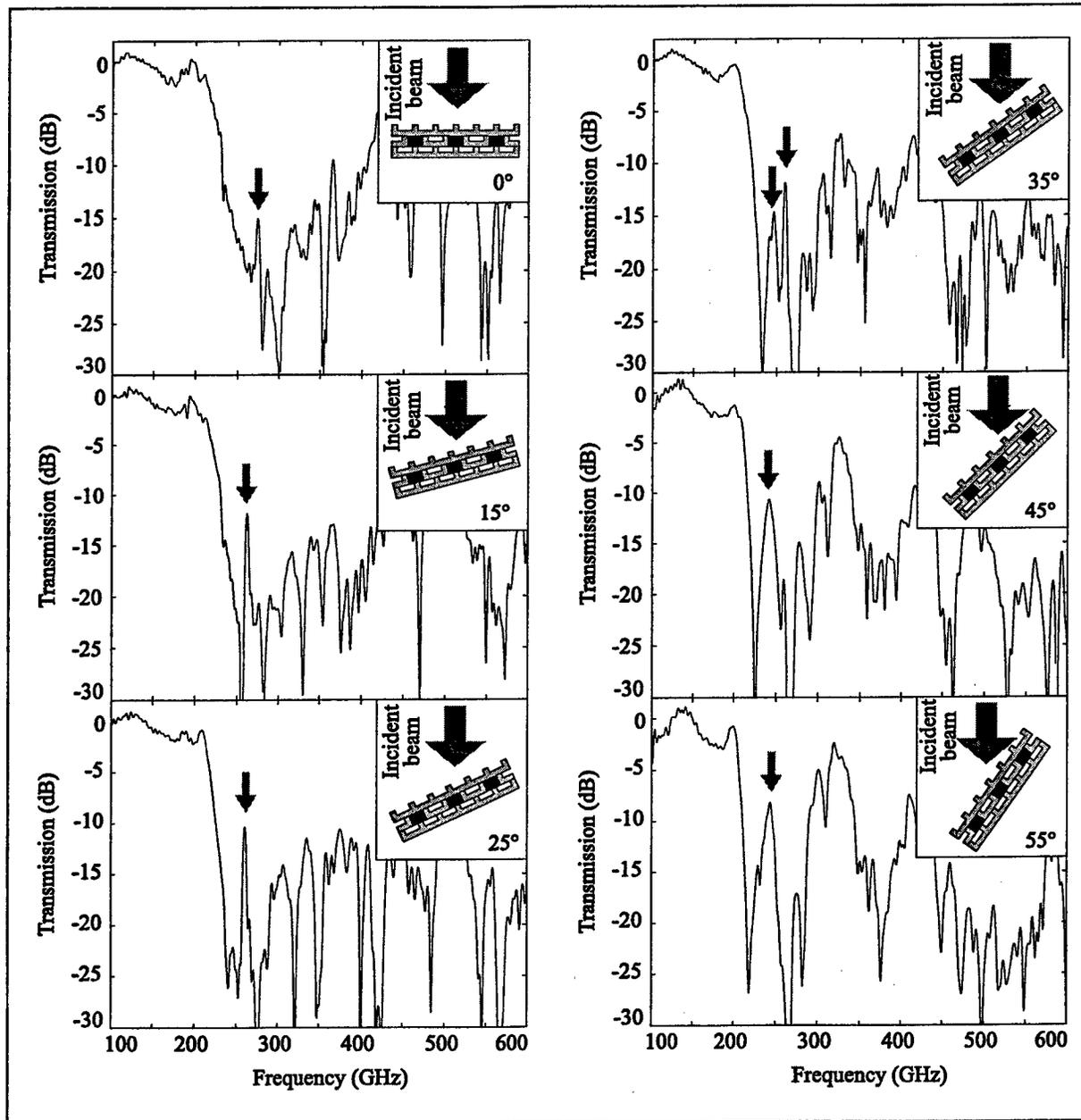
Figure 7: Influence of the incident angle on the transmission spectrum of a crystal with multiple defects (fig. 6).

The transmission spectra for incident angles varying from normal incidence (following the stacking direction) up to 55° from the stacking direction were measured and are presented in figure 7. The inserts show a schematic wood-pile structure, the arrows materialize the incident probe beam. The defects induce transmission modes inside the stop band that are pointed

out in the figure by arrows. Two different regimes can be noticed. First for the normal incidence case and for small incidence angles a narrow transmission peak is observed. This peak is centered at 254 GHz with an amplitude of -10 dB for an incident angle of 25°. In the second case for large incidence angle a broad transmission peak is observed. For an incidence angle of 55° the peak is centered at 238 GHz and 30 GHz wide with a maximum amplitude of -7 dB. For intermediate incident angles, around 35°, both peaks can be observed. We consider that these two regimes can reasonably be attributed to different coupling modes in between the defects in function of the incidence angle. Indeed for small incident angles the defects act as a plane defect in the propagation direction. For large incident angles the defects are spread out in the propagation direction and are strongly coupled in the transversal direction. This can explain the shift to lower frequencies of the defect modes as the incident angles increases.

4. DEFECT CONTROL

In this section a method to control the transmission coefficient of defect modes is demonstrated. A large size defect was created in a crystal two an a half periods thick by inserting 4 silicon parallelepipeds in lattice interstitial sites as indicated in figure 8. Each parallelepiped had a square base of 360x360 μm^2 and a height of 270 μm. The relatively large size of the defect along with the small crystal thickness were chosen to improve the detection of the defect mode. Note that the defect volume was smaller than that of a lattice cell. A further improvement was obtained by placing a metallic diaphragm of limited aperture (ϕ=3mm) in front of the crystal surface for transmission measurements.
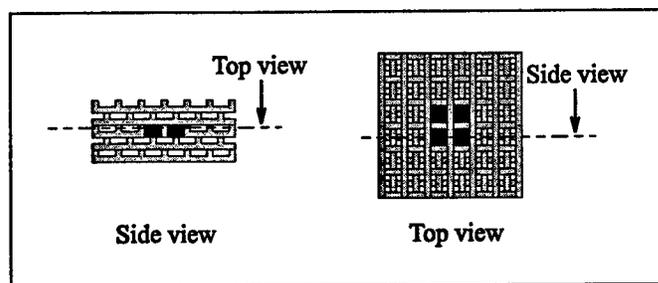

Figure 8: Large defect

Since defect modes in photonic crystals are strongly resonant, even a slight increase of the absorption may lead to a drastic change in the mode transmission level. The absorption of silicon in the THz range is mostly due to the free carrier absorption[13,14] and the concentration of free carriers in semi-insulating silicon can easily be increased by external illumination. A Ti:Saphire laser beam (λ=0.8 μm) was focused onto the defect to locally change the absorption coefficient of the defect material. The angle of the laser beam with respect to the (001) crystal direction (perpendicular to the front surface of the crystal) was close to 42.5°. In this condition, the beam passed through empty interstitial sites of the lattice before reaching the defect (fig. 9).

Fig. 10 (left) shows the transmission spectra measured in the stacking direction with and without illuminating the defect. The solid line shows the transmission spectra obtained without illuminating the defect. The first forbidden band extends from 220 to 320 GHz with a rejection ratio of -45 dB. This measured level corresponds to the noise floor of the measuring set-up. As before, high transmission levels (between -3 and -5 dB) are reached for the first transmission band (frequencies below 220 GHz). A sharp transmission peak appears at 253 GHz due to the presence of the defect. This frequency is well inside the complete band gap of the photonic structure (fig. 5). The full width at half maximum of the peak is 3.3 GHz, which actually corresponds to the frequency resolution of the measurement set-up. The transmission level of the defect mode is relatively low ($\approx$-27 dB). We explain this result by the conjugated effects of the weak coupling of the incident plane wave to the defect mode, and, in a greater extent, by the lack of resolution of the measuring set-up. The transmission spectrum in dashed lines (fig. 10, left) was measured with the defect illuminated with an external laser beam. The power of the Ti:Saphire laser beam was of 330 mW. As seen, the transmission peak of the defect mode disappears whereas the overall shape of the transmission spectrum does not change significantly.
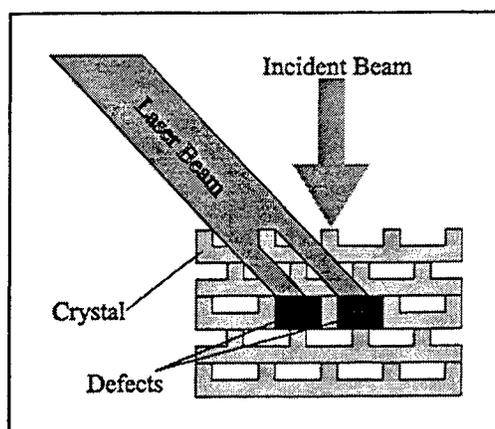
Figure 9: Defect illumination.

To confirm the experimental results, we calculated the propagation of the electromagnetic waves in the photonic crystal using the HFSS finite elements electromagnetic simulator from Hewlett-Packard. The precise simulation of the defect shown in the Fig. 8 would have required a prohibitive calculation time. Therefore we reduced the computational task by considering a defect composed of only one of the four silicon parallelepipeds inserted in the middle of the two and a half crystal periods. The thickness of this reduced defect was identical to that of the real defect. The semi-insulating silicon (1 kΩ.cm) used to build the photonic crystal and the defect was simulated as an absorbing dielectric with a frequency-independent permittivity of 11.4 and a loss tangent of 0.002.[6,7]. The calculated transmission spectra in the stacking direction
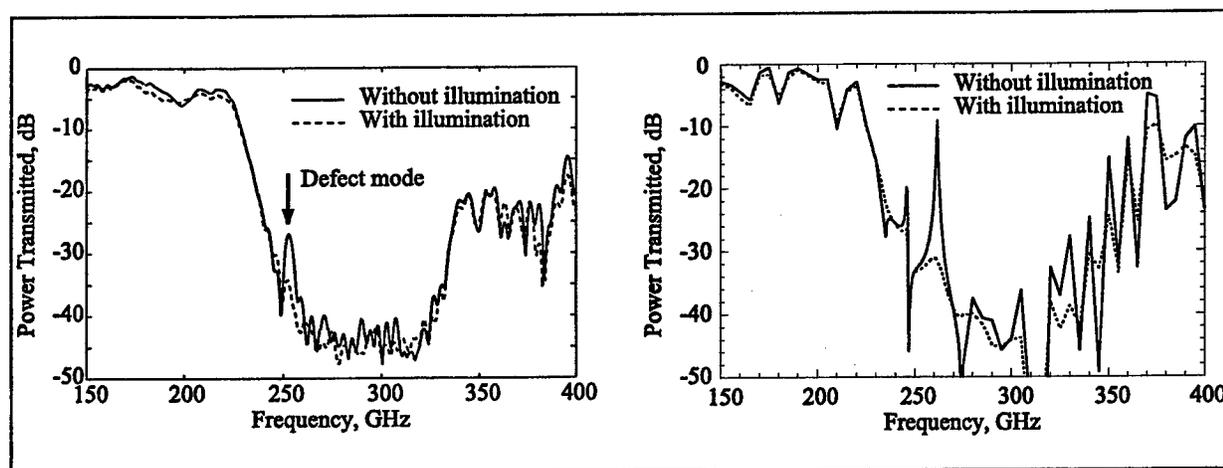
Figure 10: Measured transmission spectra with and without illumination of the defect (left).
Calculated transmission spectra with and without illumination of the defect (right)

are shown in fig. 10 (right). The position of the lower bandgap edge is at 225 GHz as in the experiments. In contrast, the central frequency of the transmission peak associated to the defect is calculated at 263 GHz instead of 253 GHz, measured experimentally. The shift to a lower frequency in the experiments suggest that coupling effects are present between the individual modes associated with the four silicon parallelepipeds : Their degeneracy is lifted, but only the symmetric mode with a lower energy is excited by the THz plane wave. In the absence of laser illumination, the calculated width of the transmission peak is 0.7 GHz (i.e., 6 times smaller than the spectral resolution of our measurement system) and the transmission maximum is -10 dB. This confirms that the relatively low transmission level measured in our experiments is more likely due to the lack of spectral resolution than to the residual losses of the semiconductor material. The illumination of the defect by the laser beam was simulated by an increase of the localized defect absorption to the value of 20 cm^{-1} (loss

tangent value of 0.1 and carrier density of $\approx 10^{15}$ cm^{-3})[15]. As seen in figure 10, the calculations are in good agreement with the experiments. Under illumination the resonant peak completely vanishes while the overall spectral shape is unchanged. The attenuation by more than 30 dB results from a fractional absorption per pass of 40% in the silicon micro-resonator.

5. CONCLUSION

We have conducted an experimental and numerical study of a sub-millimeter wood-pile photonic crystals obtained by a low cost and material independent fabrication technique. The crystal is made by stacking mechanically machined highly resistive silicon substrates. A terahertz time-domain spectroscopy set-up was used for broad band transmission characterization of the crystals. First a wide complete photonic band gap, centered at 265 GHz with a 19% band-gap to mid-gap frequency ratio, and excellent filtering properties (2.2 dB/GHz slope at 240 GHz) was demonstrated. Then, the influence of interstitial defects inserted in the structures was studied. We experimentally demonstrated the possibility of commanding the transmission level of defect modes in three-dimensional photonic crystals. The defect mode transmission level was controlled by varying the defect absorption with an external laser beam. Transmission spectra with and without laser illumination were well reproduced by numerical simulations. This study may be considered as a first step towards the development of adaptable photonic crystals and 3D active filters at sub-millimeter wavelengths.

REFERENCES

1. E. Yablonovitch, "Inhibited Sponteneous Emission in Solide-State Physics and Electronics", Phys. Rev. Lett., Vol. 58, pp. 2059, 1987.
2. Special issue on Photonic Band Structures, "Development and Applications of Materials Exhibiting Photonic Band Gaps", Journal of the Optical Society of America B, Vol. 10, No. 2, 1993.
3. J.D. Joannopoulos, R.D. Meade and J.N. Winn, *Photonic Crystals*, Princeton University Press, Princeton (1995)
4. D.F. Sievenpiper, M.E. Sickmiller and E. Yablonovitch, "3D wire mesh photonic crystals", Phys. Rev. Lett., Vol. 76, No. 4, pp. 2480-2483, 1996.
5. A. Chelnokov, S. Rowson, J.-M. Lourtioz, L. Duvillaret and J.-L. Coutaz, "Light commandable defect modes in a three dimensional photonic crystal", Electron. Lett., Vol. 34, No. 20, pp. 1965-1967, 1988.
6. K. M. Ho, C. T. Chan, C. M. Soukoulis, R. Biswas and M. Sigalas, "Photonic band gaps in three dimensions: new layer-by-layer periodic structures", Solid State Comm., Vol. 89, No 5, pp. 413-416, 1994.
7. E. Özbay, A. Abeyta, G. Tuttle, M. Tringides, R. Biswas, C. T. Chan, C. M. Soukoulis and K. M. Ho, "Measurement of three-dimensional photonic band gap in a crystal structure made of dielectric rods", Phys. Rev. B, Vol. 50, No 3, pp. 1945-1948, 1994.
8. E. Özbay, E. Michel, G. Tuttle, M. Sigalas, R. Biswas, and K. M. Ho, "Micromachined millimeter-wave photonic band-gap crystals", Appl. Phys. Lett., Vol. 64, pp. 2059, 1994.
9. E. Özbay, E. Michel, G. Tuttle, R. Biswas, K. M. Ho, J. Bostak and D. M. Bloom, "Double-etch geometry for millimeter-wave band-gap crystals", Appl. Phys. Lett., Vol. 65, No. 13, pp. 1617-1619, 1994.
10. J.G. Fleming and S.-Y. Lin, "Three-dimensional photonic crystals with a stop band from 1.35 to 1.95 μm", Optics Letters, Vol. 24, No. 1, pp. 49-51, 1999.
11. A. Chelnokov, S. Rowson, J.-M. Lourtioz, L. Duvillaret, J.-L. Coutaz, « Terahertz characterization of a novel mechanically machined 3D photonic crystal », Electron. Lett. Vol. 33, pp. 1981-1983, 1997.
12. L. Duvillaret, F. Garet and J-L. Coutaz, "A reliable method for extraction of material parameters in THz time-domain spectroscopy", IEEE Journal of Selected Topics in Quantum Electronics, Vol. 2, No 3, pp. 739-746, 1996.
13. M. Van Exter and D. Grischkowski, "Optical and electronic properties of doped silicon from 0.1 to 2 THz", Appl. Phys. Lett., Vol. 56, pp. 1694-1696, 1990.
14. M. Van Exter and D. Grischkowski, "Characterization of an Optoelectronic Terahertz Beam System", IEEE Trans. Microwave Theory Tech., Vol. 38, No. 11, pp. 1684, 1990.
15. F. Garet, L. Duvillaret, L. Noel, J.-M. Munier, J.-L. Coutaz and P. Febvre, "Characterisation of materials in the 50 GHz - 2.5 THz range by time-domain terahertz spectroscopy", ESA Workshop on Millimetre Wave Technology and Applications (Finland, 27-29 may 1998)

Parametric THz-wave generation using trapezoidal LiNbO$_3$

Akihiro Morikawa[a], Kodo Kawase[b], Jun-ichi Shikata[a], Tetsuo Taniuchi[a], and Hiromasa Ito[a,b]

[a]Research Institute of Electrical Communication, Tohoku University
2-1-1 Katahira, Sendai 980-8577, Japan

[b]Photo Dynamics Research Center, RIKEN
19-1399 Nagamachi Koeji, Sendai 980-0868, Japan

ABSTRACT

A compact tunable terahertz (THz)-wave source that operates at room temperature has been realized by introducing a novel configuration of a laser-pumped parametric oscillator using a trapezoidal LiNbO$_3$ crystal. We used total reflection for the pump and resonated idler waves under noncollinear phase-matching conditions by using a trapezoidal LiNbO$_3$ crystal, so that the interacting position was located at the THz-wave exit surface, and direct radiation could be produced without any coupling devices. Continuously tunable coherent THz-wave radiation was successfully demonstrated at wavelengths from 130-310μm (frequency: 0.9-2.3THz) with a maximum output of 45pJ/pulse (4.5mW at the peak). In addition, the THz-wave had an excellent, circular Gaussian-like beam profile with a divergence of 2.4 degrees. Our parametric method has several advantages over other methods. This easy to use compact system has wide tunability, coherency, a relatively high peak power, and a single fixed wavelength pump source. These features will be useful for a wide range of applications.

Keywords: THz-wave, parametric oscillator, nonlinear frequency conversion, trapezoidal LiNbO$_3$, reduced propagation loss, extended tunability, coupling method

1. INTRODUCTION

While optical and microwave technologies are well established, the spectral region of terahertz (THz) frequencies between light waves and microwaves still remains unexplored. Therefore, it is highly likely that new phenomena will be found in this frequency range in research in the life sciences, basic and applied physics, communication, and so forth. Over the past few years, THz-wave generation and detection have attracted much attention from both fundamental and applied perspectives. Most of the studies have utilized the ultrabroad bandwidth characteristics of THz pulses from high-speed photoconductors or electro-optic materials irradiated with a mode-locked subpicosecond laser[1-4]. In contrast, we have demonstrated continuously tunable THz-wave generation (wavelength: 140-310μm, frequency: 0.9-2.1 THz) using the laser-pumped parametric scattering from the A$_1$-symmetry polariton mode of LiNbO$_3$. New output coupling methods for the THz-wave, such as a grating or Si-prism couplers, have been introduced to substantially improve the efficiency of this method[5-11]. The THz-wave source has several advantages over other methods: it has excellent coherency, wide tunability, and a relatively high peak power. In addition, it requires only one laser pump source of a fixed wavelength, making it compact (tabletop size) and easy to handle. We have also demonstrated several applications of this tunable THz-wave source, such as THz spectroscopy without a

302

Part of the EUROPTO Conference on Terahertz Spectroscopy and Applications II
Munich, Germany • June 1999 SPIE Vol. 3828 • 0277-786X/99/$10.00

monochromator[9-11] and differential imaging[12]. In this paper, we describe the novel configuration of the THz-wave parametric oscillator (TPO) using a trapezoidal LiNbO$_3$ crystal and compare its improved performance to a conventional TPO with a rectangular crystal.

2. PRINCIPLE OF OPERATION

The generation of coherent tunable THz-waves is based on the parametric down conversion of laser light, using both second- and third-order nonlinearities (stimulated parametric scattering from the A$_1$-symmetry polariton mode of LiNbO$_3$). Stimulated polariton scattering occurs in polar crystals, such as LiNbO$_3$, LiTaO$_3$, and GaP, which are both infrared-active and Raman-active[13]. LiNbO$_3$ is one of the most suitable materials for generating THz-waves efficiently, due to its large nonlinear coefficient as well as its wide transparency in the optical wavelength range. As shown in Fig.1,
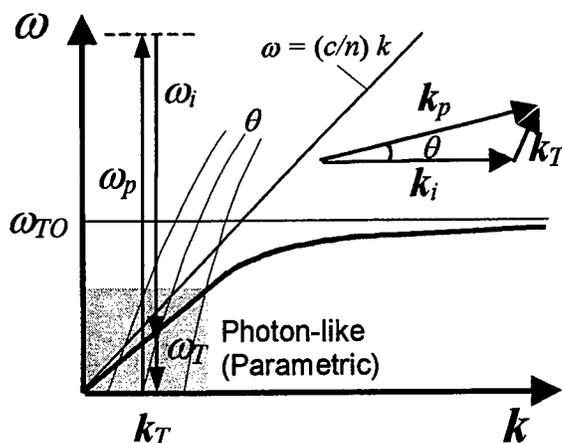
Fig.1. Dispersion relationship of a polariton, elementary excitation generated by the combination of a photon and a transverse optical phonon (ω_{TO}). A polariton in the low energy region behaves like a photon at THz frequency. A tunable THz-wave is obtained by controlling the wavevector k_T because of the phase-matching condition as well as the energy conservation law, which both hold in the stimulated parametric process.
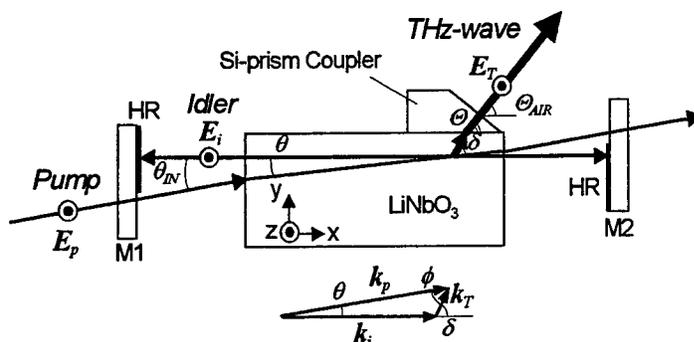
Fig.2. Conventional experimental cavity arrangement for the THz-wave parametric oscillator (TPO) using a Si-prism coupler on the y-surface of the LiNbO$_3$ crystal. The inset shows the noncollinear phase-matching condition.

polaritons exhibit photon-like behavior in the non-resonant frequency region (far from the TO-phonon frequency ω_{TO}). A signal photon at THz frequency (ω_T) and a near-infrared idler photon (ω_i) are created from a near-infrared pump photon (ω_p) parametrically, in obedience to the energy conservation law $\omega_p = \omega_T + \omega_i$ (p: pump, T: THz, i: idler). In the stimulated scattering process, the momentum conservation law $k_p = k_T + k_i$ (noncollinear phase-matching condition; see the insets of Figs.1, 2) also holds. This leads to the angle-dispersive characteristics of the idler and THz-waves generated. Thus a coherent THz-wave is generated efficiently by using an optical resonator for the idler wave as shown in Fig.2, and continuous and wide tunability is accomplished simply by changing the angle θ_{IN} between the incident pump beam and the resonator axis (angle-tuning).

3. TPO DESIGN USING A TRAPEZOIDAL LiNbO$_3$ CRYSTAL

As described above, the idler (near-infrared) and THz-waves are generated parametrically from a pump source, and three wave vectors k_p, k_i and k_T (p: pump, i: idler, T: THz) are noncollinearly phase-matched. When a Nd:YAG laser (λ=1.064μm) is used as the pump, the idler wave emerges at angle θ of 0.5-1.0 degrees (wavelength: 1.068-1.072μm), and the THz-wave is generated at angle δ of around 65 degrees inside the LiNbO$_3$ crystal (Fig.2). To avoid total reflection inside the crystal (the refractive indices at THz frequencies $\approx$5.2), an output coupling method for the THz-wave is necessary. This may be a grating coupler[5,6], a Si-prism coupler[7-11], or a cut exit (cutting a corner of the crystal perpendicular to the direction of THz-wave propagation)[14]. However, these methods result in a significant loss of THz-waves, especially at short wavelengths, because the absorption coefficient of LiNbO$_3$ at THz frequencies exceeds several tens cm^{-1} (Fig.3) and the THz-wave power drops a few orders of magnitude, even with 1mm propagation.

To achieve efficient coupling and minimize absorptive loss of the THz-wave, we designed a novel TPO configuration using a trapezoidal LiNbO$_3$ crystal (Fig.4). While the pump and idler waves are totally reflected at the top surface of the crystal, the coupled THz-wave leaves the exit surface
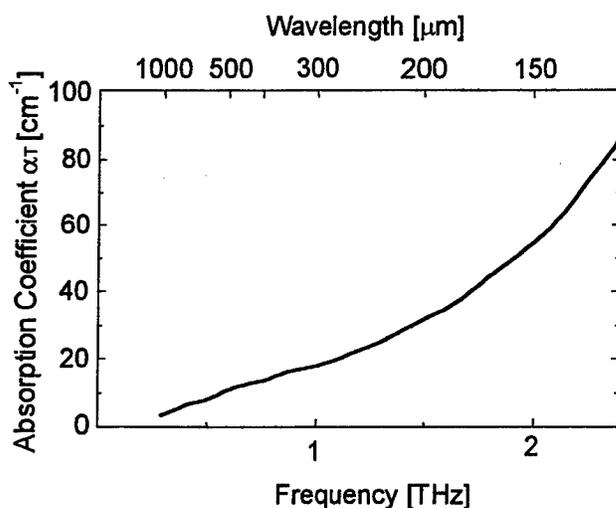
Fig.3. Absorption coefficient of LiNbO$_3$ at THz frequencies measured with a Fourier transform infrared (FTIR) spectrometer.
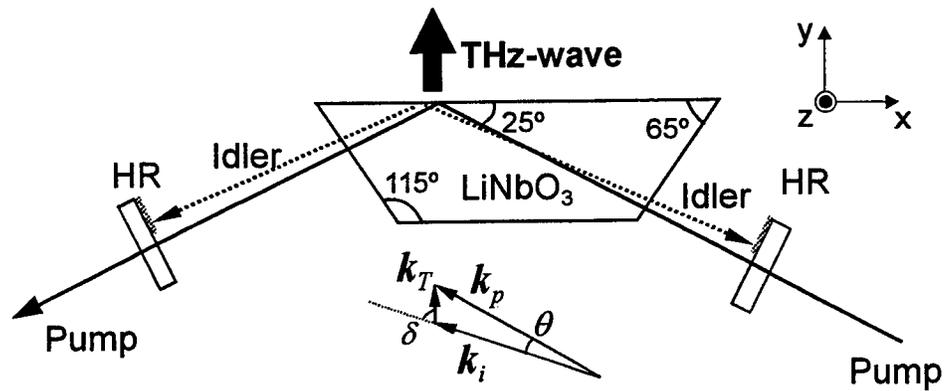
Fig.4. TPO configuration using a trapezoidal LiNbO₃ crystal. The pump and idler waves are totally reflected under noncollinear phase-matching conditions, and the THz-wave is emitted vertically from the y-surface of the crystal.

almost vertically. The absorption loss is minimized since the interaction area is located near the exit surface, and around 45% of the THz-waves generated there will pass through the surface.

4. EXPERIMENTAL SETUP

An experimental setup using the trapezoidal LiNbO₃ TPO is shown in Fig.5. The pump source used was a Q-switched Nd:YAG laser (Lotis TII LS-2136-LP, λ=1.064μm, pulse width: 25ns, repetition rate: 50Hz) polarized along the z-axis of the crystal, which produced a 1.6mm spot. The TPO consisted of a 75mm-trapezoidal LiNbO₃ crystal (lower base: 50mm) and two flat mirrors, M1 and M2, with a cavity length of 17cm. The incident and outgoing surfaces of the crystal were anti-
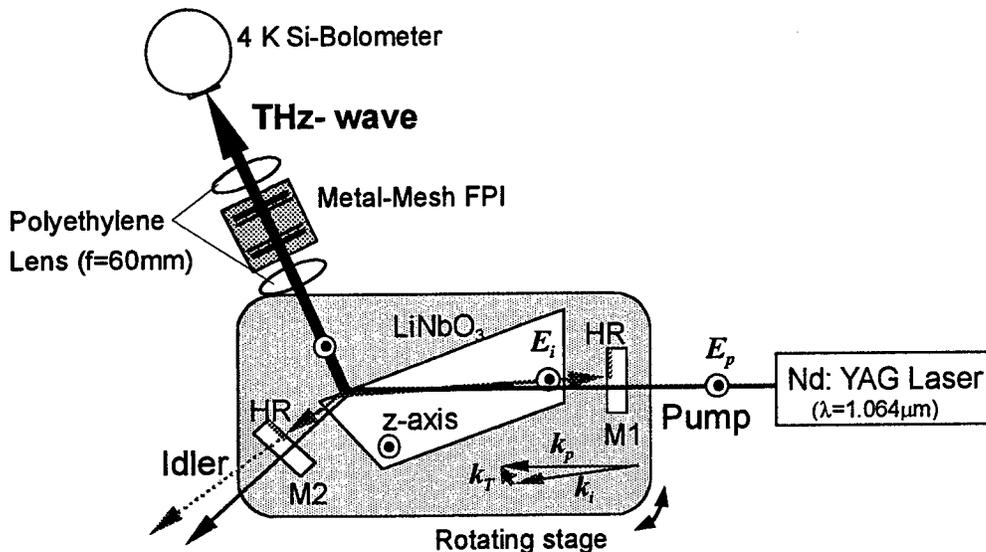
Fig.5. Experimental cavity arrangement of the TPO using a trapezoidal LiNbO₃ crystal. The crystal and the two mirrors are mounted on a rotating stage to tune the wavelength.

reflection (AR) coated for the pump and idler waves, and the mirrors were high-reflection (HR) coated for the resonated idler wave (R=98%@~1.07μm). The TPO was mounted on a computer-controlled rotating stage, which enables continuous tuning of the THz-wave. The THz-wave radiation was detected with a 4K Si-bolometer, and its spectrum was measured with a Fabry-Perot interferometer (FPI) using a Ni mesh with a 65μm grid spacing.

5. RESULTS AND DISCUSSION

The angle-tuning characteristics of the THz-wave are shown in Fig.6. The dots are the experimental results, which agreed well with the tuning curve (solid line) calculated from the noncollinear phase-matching condition[15,16]. A tunability of 310-130μm for the THz-wave (1.068-1.073μm for the idler) was obtained by varying the incident pump angle from 0.9 to 2.4 degrees. Fig.7 shows an example of
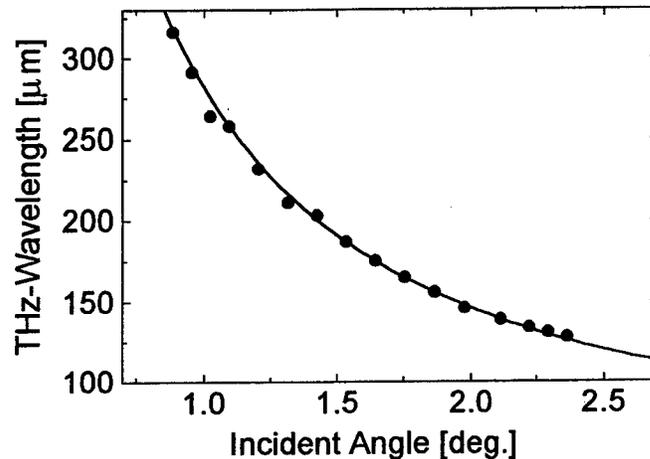
Fig.6. Angle-tuning characteristics of the THz-wave. The solid line indicates the calculated tuning curve and the dots are the experimental results.
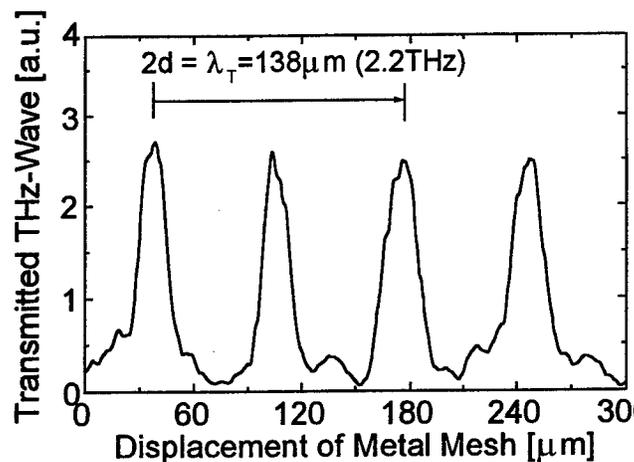
Fig.7. THz-wavelength measured with a metal-mesh Fabry-Perot interferometer.

a THz-wavelength measurement using the metal-mesh FPI (Fig.5), where the distance between two peaks corresponds to half the wavelength. A wavelength of 138μm (2.2THz) was measured successfully, while it is difficult to operate the conventional TPO (Fig.2) at wavelengths less than 150μm.
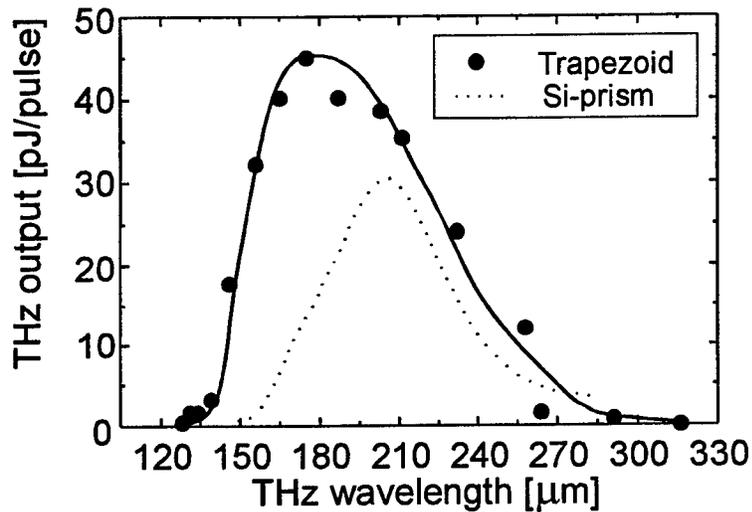
Fig.8. Measured wavelength dependence of the THz-wave output of the TPO with a trapezoidal LiNbO$_3$ crystal pumped at 38mJ/pulse. The dots are the experimental results and the solid line is the least-square fitting curve. The dotted line is the output characteristic of the conventional TPO with a Si-prism.
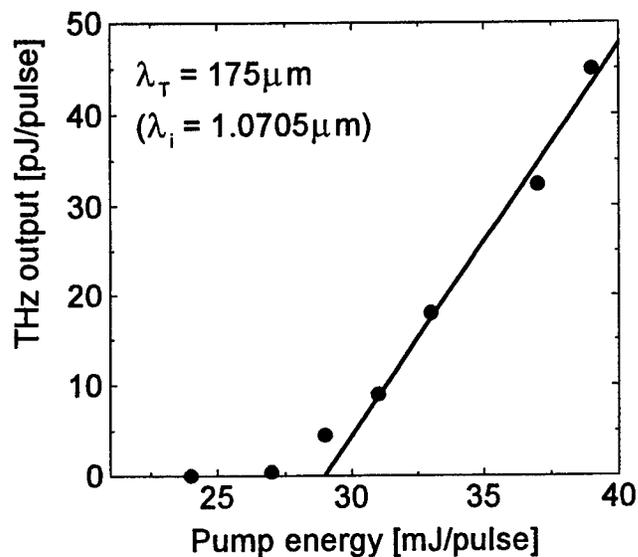
Fig.9. Input-output characteristics of THz-wave (wavelength: 175μm). The oscillation threshold was measured to be 29mJ/pulse (60MW/cm^2).

Fig.8 shows the output characteristics of the THz-wave at each wavelength for a fixed pump input of 39mJ/pulse (80MW/cm²). The maximum output of 45pJ/pulse (peak power: 4.5mW) was achieved at around 175μm, which was 1.5 times higher than that obtained from the conventional Si-prism TPO (dotted line). The enhanced THz-wave output at short wavelengths is remarkable, and this result clearly shows the effect of the minimized absorption loss inside the LiNbO₃ crystal due to the minimized propagation between the interaction area and the exit surface. Fig.9 shows the input-output characteristics of the TPO, where the idler and THz wavelengths are 1.0705μm and 175 μm, respectively. The THz-wave output increased linearly with the pump input well above the oscillation threshold, and the threshold was measured to be about 29mJ/pulse (60MW/cm²) in this experiment.

The THz-wave beam profile was also investigated at various distances from the exit surface of the crystal. The measurement was performed using a 1mm-slit and a white polyethylene lens in front of the Si-bolometer. A nearly circular Gaussian profile was obtained at every position from the exit surface, as shown in Fig.10. The beam diameter at the exit was around 1.6mm, and its divergence was around 2.4 degrees. The beam diameter at the exit agrees well with the spot size of the totally reflected pump in the XZ-plane of the crystal, thus the external THz-wave radiation originates from components generated very near to the exit surface. The characteristics of the THz-wave, such as an excellent transverse mode profile and its sharp directivity, will be useful for imaging and other applications.
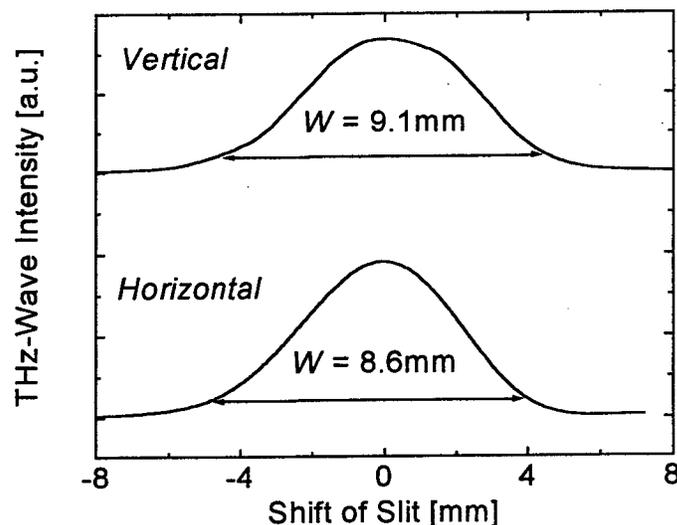
Fig.10. Transverse mode profile of THz-wave measured at 50mm from the exit surface. The upper curve is in the z-direction (vertical) and the lower is in the x-direction (horizontal).

6. CONCLUSION

In conclusion, we produced an efficient tunable THz-wave parametric oscillator using a trapezoidal LiNbO₃ crystal. We measured the tunability, output power, and beam divergence of this TPO. By virtue of the minimized absorption loss of the THz-wave, tunability was achieved in shorter

wavelength regions. Our parametric method has significant advantages over other available sources of THz-waves: it is compact, easy to use, and has wide tunability. This method has many potential applications, including spectroscopic measurements of various materials, medical and biological applications, THz imaging, monitoring different gasses, use in communication, and so forth. Further study is required to increase its efficiency, narrow the linewidth, and establish a continuous wave operation, possibly by utilizing a domain-inverted structure[17,18].

7. ACKNOWLEDGMENTS

8. REFERENCES

1. P. R. Smith, D. H. Auston, and M. C. Nuss, "Subpicosecond photo-conducting dipole antennas," IEEE J. Quantum Electron. **24**, pp.255-260, 1988.
2. M. van Exter and D. Grischkowsky, "Characterization of an optpelectronic terahertz beam systems," IEEE Trans. Microwave Theory Tech. **38**, pp.1684-1691, 1990.
3. M. C. Nuss and J. Orenstein, "Terahertz time-domain spectroscopy (THz-TDS)," in Millimeter-Wave Spectroscopy of Solids, G. Gruener ed., Heidelberg, Springer-Verlag, 1997.
4. D. M. Mittleman, R. H. Jacobsen, and M. C. Nuss, "T-ray imaging," IEEE J. Selected Topics in Quantum Electron. **2**, pp.679-691, 1996.
5. K. Kawase, M. Sato, T. Taniuchi, and H. Ito, "Coherent tunable THz-wave generation from LiNbO$_3$ with monolithic grating coupler," Appl. Phys. Lett. **68**, pp.2483-2485, 1996.
6. K. Kawase, M. Sato, T. Taniuchi, and H. Ito, "Characteristics of THz-wave radiation using a monolithic grating coupler on a LiNbO$_3$ crystal," Int. J. Infrared and Millimeter Waves **17**, pp.1839-1849, 1996.
7. K. Kawase, M. Sato, K. Nakamura, T. Taniuchi, and H. Ito, "Unidirectional radiation of widely tunable THz-wave using a prism coupler under noncollinear phase matching condition," Appl. Phys. Lett. **71**, pp.753-755, 1997.
8. T. Walther, K. R. Chapin, and J. W. Beven, "Comment on " Unidirectional radiation of widely tunable THz-wave using a prism coupler under noncollinear phase matching condition "," Appl. Phys. Lett. **73**, pp.3610-3611, 1998.
9. H. Ito, K. Kawase, and J. Shikata, "Widely tunable THz-wave generation by Nonlinear optics," IEICE Trans. Electron **E81-C**, pp.264-268, 1998.
10. K. Kawase, J. Shikata, M. Sato, T. Taniuchi, and H. Ito, "Widely tunable coherent THz-wave generation using nonlinear optical effect," Electron. Commun. in Japan (Part 2) 7, pp.10-18, 1998.
11. J. Shikata, K. Kawase, M. Sato, T. Taniuchi, and H. Ito, "Enhancement of terahertz-wave output from LiNbO$_3$ optical parametric oscillators by cryogenic cooling," Opt. Lett. **24**, pp.202-204, 1999.

12. K. Kawase, J. Shikata, T. Taniuchi and H. Ito, "Widely tunable THz-wave generation using optical parametric oscillator and its application to differential imaging," 4th International Conference on Millimeter and Submillimeter Waves and Applications, San Diego, USA (July 1998).

13. Y. R. Shen, "*The Principle of Nonlinear Optics*," John Wiley and Sons, New York., pp.169-172, 1984.

14. J. M. Yarborough, S. S. Sussman, H. E. Puthoff, R. H. Pantell, and B. C. Johnson, "Efficient tunable optical emission from $LiNbO_3$ without a resonator," Appl. Phys. Lett. **15**, pp.102-105, 1969.

15. D. R. Bosomworth, "The far infrared optical properties of $LiNbO_3$," Appl. Phys. Lett., vol.9, pp.330-331, 1966.

16. G. J. Edwards and M. Lawrence, "A temperature-dependent dispersion equation for congruently grown lithium niobate," Opt. Quant. Electron. **16**, pp.373-375, 1984.

17. K. Kawase, and H. Ito, "Submillimeter generation using periodic domain reversal," Nonlinear Optics 7, pp.225-229, 1994.

18. Y. J. Ding and J. B. Khurgin, "A new scheme for efficient generation of coherent and incoherent submillimeter to THz waves in periodically poled lithium niobate," Opt. Commun. **148**, pp.105-109, 1998.

Jun-ichi Shikata: e-mail: shikata@riec.tohoku.ac.jp
Telephone: +81-22-217-5518 Fax: +81-22-217-5521

Millimetre-wave magneto-optical determination of the anisotropic superconducting order parameter in the molecular superconductor κ-(BEDT-TTF)$_2$Cu(NCS)$_2$

J.M. Schrama[a], E. Rzepniewski[a], A. Ardavan[a], R. Edwards[a], J. Singleton[a],
M. Kurmoo[b] and P. Day[c]

[a] Clarendon Laboratory, University of Oxford, Parks Road, Oxford OX1 3PU, UK.

[b]IPCMS, 23 rue de Loess, BP 20/CR, 67037 Strasbourg, France.

[c]The Royal Institution, 21 Albemarle Street, London W1X 4BS, UK

ABSTRACT

We have used a novel millimetre-wave magneto-optical technique to study the angle-dependence of the high-frequency conductivity of the molecular superconductor κ-(BEDT-TTF)$_2$Cu(NCS)$_2$. The data strongly suggest that the superconducting gap has nodes directed along the **b** and **c** directions of the crystal, in agreement with recent theoretical predictions. This supports the idea that the superconductivity in κ-(BEDT-TTF)$_2$Cu(NCS)$_2$ is d-wave in nature, and is mediated by spin fluctuations.

Keywords: Order parameter symmetry, organic superconductors, unconventional superconductivity, millimetre-wave techniques

The family of superconducting charge-transfer salts κ-(BEDT-TTF)$_2$X, where X can, for example, be Cu(NCS)$_2$, Cu[N(CN)$_2$]Br or I$_3$, has attracted considerable recent attention. A variety of experiments have suggested that the superconducting gap function may contain nodes at certain points on the Fermi surface; e.g. the ^{13}C NMR spin-lattice relaxation rate[1] varies as T^3 and the thermal conductivity[2] is proportional to T below the superconducting critical temperature T_c. In addition, microwave penetration-depth studies[3] show a non-BCS-like behaviour of the penetration depth as a function of T and the electronic component of the specific heat[4] has an unconventional field dependence below T_c. However, Shubnikov-de Haas,[5,6] magnetic breakdown,[7] and angle-dependent magnetoresistance oscillation[8] experiments demonstrate that these salts have well-defined quasi-two-dimensional (Q2D) Fermi surfaces, indicating that the quasiparticles can be described by Fermi-liquid theory at low temperatures (the Fermi surface is shown in Figure 1). Furthermore, it has been possible to fit experimental Fermi-surface-topology data to a simplified model of the tight-binding bandstructure (the so-called effective dimer model) to a good degree of accuracy.[5,9–11]

The combination of unconventional superconductivity and a tractable analytical representation of the bandstructure makes the κ-(BEDT-TTF)$_2$X superconductors attractive for theoretical studies, and a number of authors[9,10,12,13] have explored the possibility of d-wave superconductivity mediated by spin fluctuations. Such approaches predict that the superconducting order parameter will have four, roughly perpendicular, gap nodes, the exact orientation of the nodes depending on the underlying details of the Fermi surface.[10,12] Experiments performed thus far have merely detected the probable presence of the gap nodes, without giving information about their relative orientation. In this paper, we use a millimetre-wave magneto-optical technique to determine the orientation of the gap nodes in κ-(BEDT-TTF)$_2$Cu(NCS)$_2$. The data appear to be in good qualitative agreement with the predictions of Schmalian.[10]

The experiments were carried out on a number of crystals of κ-(BEDT-TTF)$_2$Cu(NCS)$_2$, grown by conventional electrochemical means[14] and of approximate size $1 \times 0.5 \times 0.05$ mm^3. A single crystal was placed at the centre of a silver rectangular resonant cavity of dimensions $6 \times 3 \times 1.5$ mm^3, resonating in the TE$_{102}$ mode at around 70 GHz; the quality factor of the cavity is ~ 1500 when empty, falling to ~ 1000 when the cavity is loaded with the sample. The high-frequency field distribution in the cavity is very well-defined, and the sample is placed in an antinode of the oscillatory magnetic field **H**, such that **H** is parallel to the

Part of the EUROPTO Conference on Terahertz Spectroscopy and Applications II
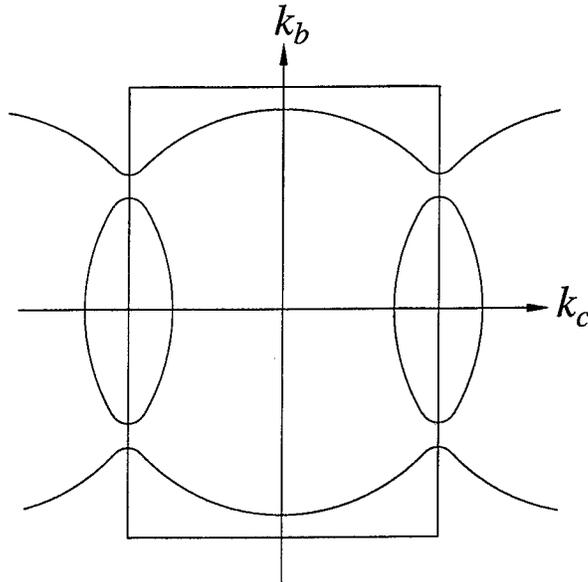Munich, Germany • June 1999 SPIE Vol. 3828 • 0277-786X/99/$10.00

311

Figure 1. The Fermi surface of κ-(BEDT-TTF)$_2$Cu(NCS)$_2$.

highly-conducting Q2D planes of the sample. Oscillatory circulating currents are induced in the plane perpendicular to **H**; hence they always have a component in the low conductivity direction (*i.e.* perpendicular to the high-conductivity planes). The skin depth in this regime is rather larger than the sample dimensions and the millimetre-wave field penetrates the sample completely.[15] The currents induced in the sample dissipate power from the cavity's millimetre-wave field, and for small changes, the change in the cavity's quality factor is proportional to the change in the sample's conductivity. The cavity system therefore allows the sample's bulk conductivity to be measured at GHz frequencies.[15]

In the current experiment, the sample was placed on a mount which allowed it to be rotated about the normal to its highly-conducting Q2D planes within the cavity; thus the orientation of **H** within the highly-conducting planes can be varied. In the discussion that follows, the orientation of **H** will be defined by the azimuthal angle of rotation ϕ; $\phi = 0$ corresponds to **H** being parallel to the **c** direction of the lattice. In such an arrangement, the induced circulating currents always have the same interplane component; however, the direction of the inplane component of the induced current can be changed by rotating the sample. The cavity was placed in a variable temperature insert within a 17 T superconductive magnet. The quasistatic magnetic induction B provided by the magnet was applied perpendicular to the sample's Q2D planes.

Figure 2(a) shows the transmission of the cavity as a function of B for several different orientations (denoted by ϕ) of the oscillatory field **H** within the sample's Q2D conducting planes. Our experimental apparatus has a background absorption[15] which may be seen at $B \approx 2$ T; this feature is present in the absence of a sample and is independent of temperature and sample orientation. At high B, the cavity transmission is dominated by the normal-state conductivity of the sample; at the lowest temperatures, Shubnikov-de Haas oscillations can be clearly observed.[15,16] At low B, the cavity transmission decreases steeply before reaching a minimum; the postion of the minimum and its depth are strongly temperature dependent. A comparison of the position of the minimum as a function of temperature with the known temperature dependence of the upper critical field of κ-(BEDT-TTF)$_2$Cu(NCS)$_2$[14] demonstrates that the minimum is associated with the superconducting to normal transition of the sample.

An number of mechanisms for millimetre-wave power dissipation are known to occur within the superconducting state.[17] The dissipation due to these mechanisms becomes larger than that due to the normal-state electrons close to the phase transition (magnetic field- or temperature-driven) to normal behaviour.[17] The data in Figure 2(a) support such a picture; the fact that a *minimum* in the cavity transmission occurs just
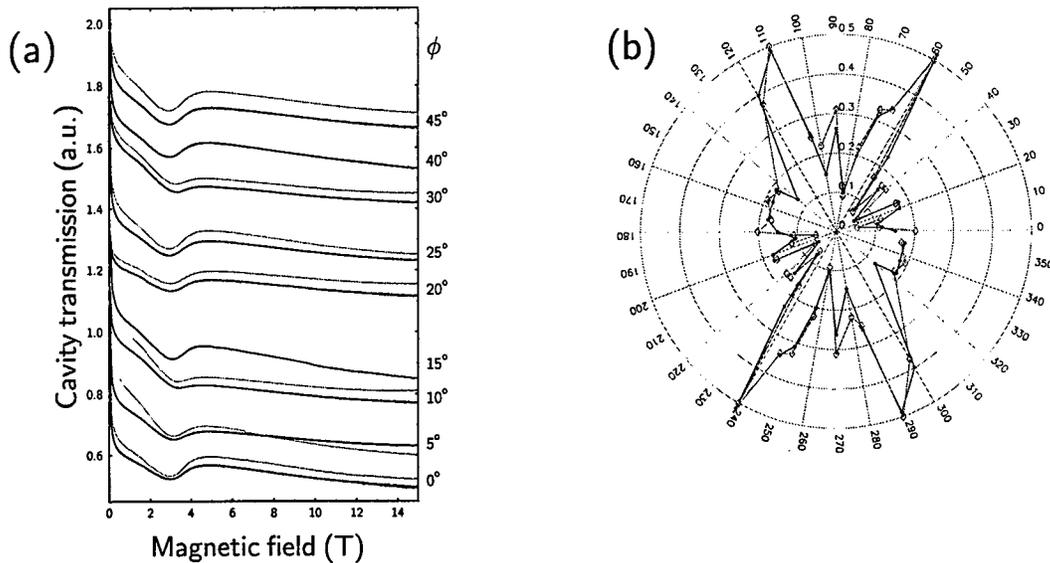
Figure 2. (a) Cavity transmission versus applied magnetic field for a range of sample orientations, ϕ. The temperature is 1.4 K and the measurement frequency is 70 GHz. (b) The normalized amplitude of the dip associated with the superconducting transition as a function of the sample orientation.

below the superconducting to normal transition shows that the dissipation in the cavity is *larger* in the superconducting state close to the upper criticial field than in the normal state.

At high B, the cavity transmission is dominated by the normal-state conductivity, which is largely ϕ independent. In contrast, the low-field cavity transmission, and in particular the depth of the minimum denoting the superconducting to normal transition, varies markedly with ϕ. As described above, the minimum occurs because of differences between the amount of dissipation in the superconducting and normal states[17]; the fact that the minimum varies with ϕ indicates that the relative strengths of the dissipative mechanisms in the superconducting and normal states depends on the direction in which the oscillatory current induced by **H** flows.

The geometry of the experiment dictates that **H** always lies perpendicular to the the interplane direction, so that the circulatory induced current must have a component flowing in the interplane direction for all ϕ. Because of the very large conductivity anisotropy of κ-(BEDT-TTF)$_2$Cu(NCS)$_2$,[14] the size of the circulating current will almost entirely be determined by the interplane conductivity, so that it will be almost ϕ independent[15]; this explains the approximate ϕ-independence of the cavity transmission in the normal state in Figure 2(a). Therefore the variation with ϕ of the dissipative mechanisms which cause the minima in Figure 2(a) must be due to the direction in which the *in-plane* component of the induced current flows.

The Fermi surface of κ-(BEDT-TTF)$_2$Cu(NCS)$_2$ is shown in the Figure 1. The flow of in-plane currents at low temperatures will be due to quasiparticles with energies within $\sim k_B T$ of the Fermi energy; as the quasiparticle velocities **v** are given by $\hbar \mathbf{v} = \nabla_\mathbf{k} E(\mathbf{k})$, these will have velocities directed perpendicular to the Fermi surface. By choosing as in-plane current direction, we are chiefly selecting quasiparticles with a particular direction of **v**, and hence probing a particular section of the Fermi surface. If there is a node in the superconducting gap at that point, the dissipative mechanisms which affect the induced current will be very similar in the superconducting and normal states (the number of normal quasiparticles involved in the current flow will be very similar in the normal and superconducting states). Hence, the depth of the minimum in the cavity dissipation close to the phase boundary will be small. On the other hand, if the superconducting gap function is large on that part of the Fermi surface, there will be a large difference in the dissipative mechanisms affecting the induced current as one moves from the superconducting state to the

normal state; hence the minimum will be deep. In this way, the ϕ dependence of the superconducting gap can be mapped out by examining the depth of the minimum.

Figure 2(b) shows the depth of the minimum below the extrapolated normal-state cavity transmission as a function of azimuthal angle ϕ. In order to remove any possible effects caused by the sample's geometry, the data have been normalised by dividing by the Fourier amplitude of the Shubnikov-de Haas oscillations at the same angle ϕ (see Figure 2(a)); in such a cavity measurement, the size of the Shubnikov-de Haas oscillations is a good absolute indication of the interplane conductivity[15] and so can be used to normalise out variations in the coupling between the sample and the millimetre-wave fields. The normalised minimum depth shows a clear "X" shape, with nodes directed along the **b** and **c** directions of the crystal. This strongly suggests that the superconducting order parameter also possesses nodes in these directions, in agreement with the fluctuation-exhange approximation calculations of Schmalian.[10]

It should also be noted that the antinodes of Figure 2(b) are of a qualitatively similar form to the predicted antinodes in the supercondcucting gap shown in Figure 3 of Schmalian[10] (in Schmalian's notation, the y and x directions correspond to the **c** and **b** crystal directions of κ-(BEDT-TTF)$_2$Cu(NCS)$_2$ respectively), although the very narrow "suppressed gap" regions are not visible in our data, possibly because of the limited angular resolution.

In summary, we have used a millimetre-wave magneto-optical technique to study the superconducting to normal transition of κ-(BEDT-TTF)$_2$Cu(NCS)$_2$. The data strongly suggest that the superconducting gap has nodes directed along the **b** and **c** directions of the crystal, in agreement with recent theoretical predictions.[10] This provides support for the idea that the superconductivity in κ-(BEDT-TTF)$_2$Cu(NCS)$_2$ and other κ-phase BEDT-TTF salts is d-wave in nature, and is at least partly mediated by spin fluctuations.

REFERENCES

1. S.M. de Soto *et al.*, Phys. Rev. B **52**, 10364 (1995); H. Mayaffre *et al.*, Phys. Rev. Lett. **75**, 4122 (1995); K. Kanoda *et al.*, Phys. Rev. B **54**, 76 (1996).
2. S. Belin, K. Behnia and A. Deluzet, Phys. Rev. Lett. **81**, 4728 (1998).
3. Stephan Friemel, Thesis, Universite Paris XI, Orsay (1997).
4. Y. Nakazawa and K. Kanoda, Phys. Rev. B **55**, R8670 (1997).
5. J.M. Caulfield *et al.*, J. Phys.: Condens. Matter **6**, 2911 (1994).
6. C.M. Mielke *et al.*, Phys. Rev. B **56**, R4309 (1997).
7. N. Harrison,*et al.*, J. Phys.: Condensed Matter, **8**, 5415 (1996).
8. M.-S. Nam, M. M. Honold, N. Harrison, C. H. Mielke, S. J. Blundell, J. Singleton, M. Kurmoo and P. Day, Synthetic Metals **103**, 1905 (1999).
9. R. Louati, S. Charfi-Kaddour, A. Ben Ali, R. Bennaceau and M. Heritier, Synthetic Metals, in press.
10. Jörg Schmalian, Phys. Rev. Lett. **81**, 4232 (1998).
11. G. Visentini *et al.*, Europhys. Lett. **42**, 467 (1998).
12. Kazuhiko Kuroki and Hideo Aoki, preprint, cond-mat/9812026.
13. Kazumi Maki, E. Puchkaryov and Hyekyung Wong, Synthetic Metals, in press.
14. T. Ishiguro, K. Yamaji and T Saito, Organic Superconductors, *Springer Verlag*, (1998).
15. A. Ardavan *et al.*, Phys. Rev. Lett. **81**, 713 (1998).
16. A. Polisski *et al.*, J. Phys.: Condens. Matter **8**, L195 (1996).
17. See *e.g.* Tinkham, "Introduction to Superconductivity", second edition, *McGraw Hill* (1996), Section 2.5.2.

Time resolved detection of far-field THz-radiation patterns - spatially restricted coherence of surface field THz emitters

F. Hilbk-Kortenbruck, P. Haring Bolivar, R. Martini, H.P.M. Pellemans, and H. Kurz

Institut für Halbleitertechnik II, RWTH Aachen, D-52056 Aachen
haring@iht-ii.rwth-aachen.de

ABSTRACT

The measurement of the spatial coherence of a macroscopic ensemble of carriers excited coherently by femtosecond laser pulses is presented. The spatial coherence of the excited ensemble is derived from time- and spatially resolved measurements of the far-field THz-emission pattern. The analysis concentrates on surface field emitters, which are widespread broadband sources of coherent THz-radiation. We find that these emitters are fully spatially coherent for emission frequencies up to 1.6 THz, above which frequency the spatial coherence starts to decrease. For frequencies above 2.5 THz the spatial coherence of the emitter is limited to one THz wavelength.

Keywords: Time-resolved THz spectroscopy, spatial THz emission pattern, femtosecond technology, surface-field emitters

1. INTRODUCTION

Optically excited surface-field emitters are widespread broadband sources of coherent THz radiation. These are attractive for the use in THz-transient spectroscopy setups because of their simplicity, reliability, and relatively easy alignment. Their operation is based on the acceleration of photo-injected carriers in the large 'built-in' electric field normal to the surface of a semiconductor, which results from the band-bending near a semiconductor surface. The simplest possible picture for the emission process treats the accelerated carriers as an ensemble of dipoles, oscillating in a direction normal to the surface of the semiconductor. Basic antenna theory states that the emission pattern of such an ensemble is that of the distribution function of individual oscillators, multiplied by the radiation pattern of an individual dipole [1]. The carrier distribution is given by the Gaussian spatial profile of the optical excitation pulse, and gives a Gaussian emission pattern. The dipole contribution is proportional to $\sin(\theta)$, where θ is the angle from the surface normal. The use of optical pulses that are short in comparison with the THz frequencies emitted assures that the created carrier distribution is fully coherent.

2. EXPERIMENT

We adapted a standard THz-transient setup to measure the angle-dependent emission characteristics of the surface-field emitter. A self-mode-locked Ti:Sapphire laser (Coherent Mira 900) produces pulses with an fwhm width of approximately 90 fs . We use 500 mW time-averaged power to excite the surface-field emitter, an InGaAs epitaxial layer on an InP substrate. The emitted THz radiation is detected using an ID-SOS photoconductive antenna, where a Si lens (d=3mm) is used to increase the sensitivity. We use an optical fiber to couple the gating pulse to the PC antenna to allow the detector antenna to be freely positioned [2]. The gate pulse is pre-compensated for the fiber dispersion using a grating pair, and has an fwhm width of 120 fs after the fiber. A fast-scan measurement technique is used for data collection.
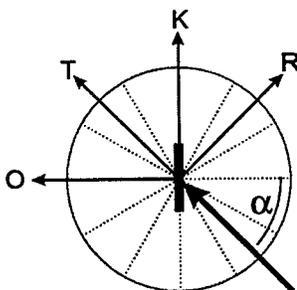
Fig. 1: Geometry of the experiments. The optical pump beam is incident on the sample with an angle α. The main THz signals are detected in the specular-reflection direction R, and the transmission direction T. In some experiments, we also see additional, distinct signals emitted from the edge of the sample (K) and emitted normal to the sample surface (O).

The sample geometry in the experiment is shown in Figure 1. The sample and the detector are mounted on individual rotation stages, so that the angle of the incident beam and the detection angle for THz emission can be varied

Part of the EUROPTO Conference on Terahertz Spectroscopy and Applications II
Munich, Germany • June 1999 SPIE Vol. 3828 • 0277-786X/99/$10.00

315

Fig. 2: Angle-dependent measurement of the emitted THz-transients for optical spotsizes of 215 μm (left) and 823 μm (right). The incidence angle of the optical beam was 315° for both measurement, where the sample surface normal is oriented at 0°. The distance behind the sample was r=11 mm.

independently. In the figure we indicate four distinct directions for the emission, corresponding to the THz beam emitted in the transmission (T) and reflection (R) direction of the optical beam, signal emitted in the plane of the sample (K), and normal to the plane of the sample (O).

We measured the emitted power as a function of excitation intensity, and found excellent agreement with calculations where the screening effect of the generated THz field is taken into account [3]. The largest emitted THz power is obtained for an incident angle α corresponding to Brewster's angle, where the power absorbed in the sample is maximized. However, for standard THz-transien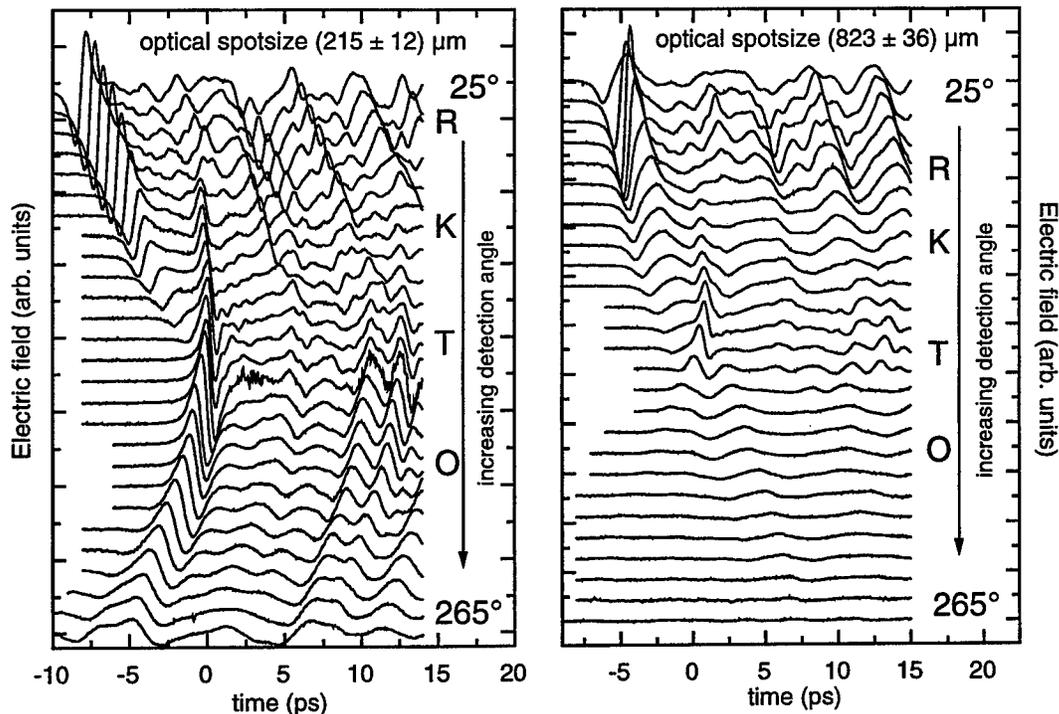t experiments it is much more convenient to use an incident angle of 45°. Since the emitted power for this incidence angle is only slightly lower, we performed all experiments with this excitation angle. The THz power falls of quadratically with the radial distance from the emitter, confirming that we are working in the far field of the emitter.

Figure 2 shows time-dependent measurements of the emitted THz-transients as a function of emission angle. Results are shown for two different spot sizes: 215±12 μm for the left figure, 823±36 μm for the right figure. For both graphs, the excitation beam falls in along the 315° direction. The smallest angle measured was limited by the physical size of the detector mount to 25°. Both scans were made at a distance r=11 mm from the sample. The oblique angle of incidence of the excitation beam results in a phase shift between the individual 'dipoles' excited at different positions. This, in turn, results in an angle shift of the emitted THz pulse in such a way, that the THz radiation is collinear with the incident (T) or reflected (R) excitation beam.
The strongest signal is observed in the reflected (R) direction. As expected, the emission angle is much broader for the smaller spotsize than for the larger spotsize. The THz signal in the transmitted (T) direction should be similar to that in the R direction, but is substantially smaller due to interference, absorption and reflection effects in the sample.
In addition to the signals seen in the reflected and transmitted directions, there is also distinct emission in directions along the plane of the sample, and perpendicular to it (K and O, respectively). Since all these contributions have quite a broad
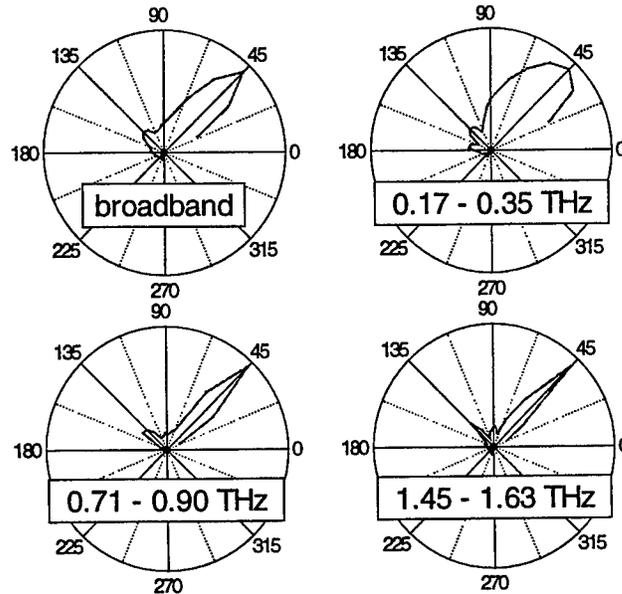
Fig. 3: Angular emission profiles for the broadband-integrated power (0.17-4.5 THz, upper left), and for three separate narrow-band frequency ranges.

angular spread, they partially overlap for certain angles. This makes it necessary to perform analysis of the results in the frequency domain [4].

We Fourier-transformed the time-domain data, and integrated the resulting spectra piecewise in bands of 165 GHz. Figure 3 shows the results in polar plots. In the broadband figure, all Fourier components from 0.17 to 4.5 THz are included. The three other figures show how the beamwidth decreases with increasing frequency, as expected for a fully coherent emitter of constant size.

We calculate the THz effective spotsize at the emitter from Gaussian fits to the far-field emission [5]. The results are shown in Figure 4, where the calculated spotsize is divided by the free-space THz wavelength. For frequencies up to 1.6 THz the
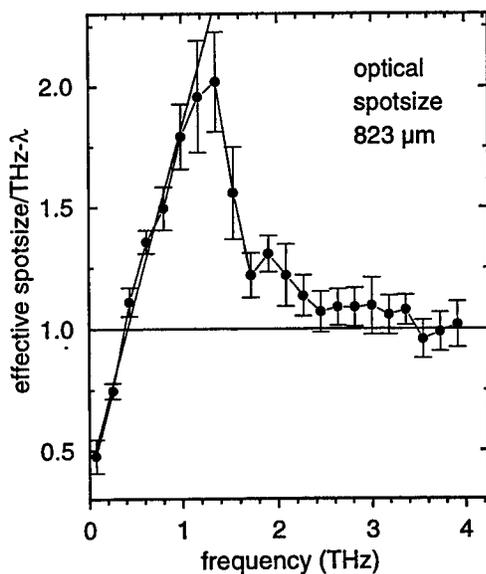
Fig. 4: Extracted effective spotsize normalized to the respective THz-wavelength as function of frequency. The effective spotsize is calculated at the position of the emitter from a Gaussian fit to the far-field THz emission pattern. The solid line is a linear fit to the low-frequency data.

317

relative spotsize increases linearly with frequency. For very low frequencies the calculated effective spotsize is larger than the optical spotsize, indicated by the fact that the straight-line fit does not go through the origin of the plot. For these low frequencies, the true emission area is much smaller than the emitted wavelength. Therefore, it is no longer possible for the ensemble to work as a Gaussian-beam emitter. Rather, the ensemble starts to approach a point source with a corresponding broad spatial-emission pattern.

Surprisingly, for frequencies above 1.6 THz the relative spotsize is seen to decrease to a value smaller than the physical spotsize. This indicates that the ensemble of emitters is no longer fully coherent. For frequencies above 2.5 THz the coherence length is reduced to approximately one wavelength.

3. DISCUSSION

The above results indicate that two assumptions of the simple interpretation of a surface-field emitter as a distribution of similar, fully coherent dipole emitters are not totally upheld in reality. First, we do not observe the elementary dipole contribution to the emission characteristics. The reflected THz beam can be described without taking this factor into account. This constitutes somewhat weak negative evidence, since for the rather large reflection angle involved the effect of the $\sin(\theta)$ factor is not large. However, the observed emission of power in a direction normal to the surface is forbidden for true dipole-emission, and therefore indicates that the acceleration of the carriers has an in-plane component. Screening effects during the excitation of the carriers result in such an in-plane component of the acceleration. A second, interesting result of our experiments is that the photo-excited semiconductor is not fully spatially coherent as a THz emitter. Possible explanations are that for high frequencies the coherence of the optically excited carriers is reduced, or that a different process with a smaller coherence length contributes to the THz emission at higher frequencies.

The large increase of the emission angle for very low frequencies is a straightforward result of the too-small emission spot for these wavelengths. This is the reason why, in a standard THz-transient setup, a surface-field emitter has a relative poor low-frequency performance in comparison with other sources, such as photo-conductively gated dipole antennas: only a small fraction of the emitted field is collected by the parabolic mirror normally used in such a setup to collimate the THz beam.

The results show that a significant part of the THz radiation is emitted in a direction along the edge of the semiconductor slab. This power is not collected in a standard THz-transient setup, and therefore represents an undesirable loss.

Some extra oscillations, for long time delays after the pulse maximum, are observed in the THz-transients. These are caused by reflections in the sample, and possible by reflections between the sample and parts of the setup.

4. CONCLUSIONS

We have performed coherent angle- and time-resolved measurements of the THz emission of optically excited surface-field emitters. Efficiency measurements show excellent agreement with calculations where the screening effect of the generated THz field is included. The radial-distance dependence of the THz power confirms that the measurements are performed in the far field of the emitter. We have obtained the effective spatial coherence of the surface-field emitter from an analysis of the emission pattern as a function of the THz frequency, and, interestingly, find that the spatial coherence of the source starts to decrease for frequencies above 1.6 THz, to reach a limiting value of approximately a single THz wavelength for all frequencies above 2.5 THz.

5. ACKNOWLEDGEMENTS

REFERENCES
1. J.D. Kraus, *Antennas*, McGraw-Hill, New York, 1950.
2. N. M. Froberg, B. B. Hu, X.-C. Zhang, and D.H. Auston, IEEE J. Quantum Electron. **28**, 2291 (1992).
3. J.T. Darrow, X.-C. Zhang, and D.H. Auston, Appl. Phys. Lett. **58**, 25 (1991); J.T. Darrow, X.-C. Zhang, D.H. Auston, and J.D. Morse, IEEE J. Quantum Electron. **28**, 1607 (1992).
4. P. U. Jepsen and S. R. Keiding, Opt. Lett. **20**, 807 (1995)
5. Here we defined the spotsize as the diameter which includes half the beam power.

THz-imaging in a Brewster-angle configuration - characterization of thin oxide coatings for fuel cell applications

M. Brucherseifer, P. Haring Bolivar, H. Klingenberg[1] and H. Kurz

Institut für Halbleitertechnik II, RWTH Aachen, D-52056 Aachen, Germany
[1]Institut für Technische Physik, DLR, D-70569 Stuttgart, Germany
brucherseifer@iht-ii.rwth-aachen.de

ABSTRACT

Time-resolved THz imaging for the incidence-angle dependent three-dimensional tomographic characterization of layered structures is presented. We illustrate the capabilities of the developed system on multi-layer ceramic samples used for solid oxide fuel cells (SOFC). Diverse methods for determining unknown refractive indices are discussed. The significant influence of the angle of incidence of a THz imaging system on the measured signal is demonstrated, which can be exploited especially in Brewster-angle configurations to enhance the capabilities of any THz tomography system.

Keywords: time-resolved THz spectroscopy, femtosecond technology, THz imaging, SOFC

1. INTRODUCTION

Despite of the great potential of radiation in the terahertz (THz) frequency range, this section of the electromagnetic spectrum remained to be hardly accessible for a long period of time. Nevertheless, since the emergence of *time-domain* (or *impulsive optical*) THz spectroscopy (for an overview see e.g. [1]), this range of the electromagnetic spectrum has now become readily accessible. Many applications of time-domain THz techniques based on ultrafast laser pulses have been demonstrated and even THz imaging systems have been developed [2-5]. THz imaging has an enormous application potential: on the one side, THz frequencies are resonant to many interesting elementary excitations. Hence, THz imaging allows the spatially resolved monitoring of many important properties of condensed matter, like e.g. electronic densities and mobilities in semiconductors [7], Cooper-pair densities in superconductors [7] or even chemical compositions in material compounds [8]. Additionally, THz radiation allows to see through many technologically relevant materials, like polymers or ceramics, which are not transparent to conventional electromagnetic radiation [2]. Hence, many attractive applications for THz imaging exist.

Diverse THz imaging techniques have been developed, based on either the spatially resolved analysis of transmitted [2] or reflected [5] optically generated THz pulses. This paper focuses on the second possibility, namely the time and spatially resolved detection of reflected THz pulses which permits the three-dimensional tomographic THz analysis of the internal structure of objects. A new THz-tomography setup is presented, which permits incidence-angle dependent analysis. It will be demonstrated, how the angle of incidence of the THz pulses has a significant influence on the observability of the internal structure of the sample under study. This dependencies can be exploited, especially in Brewster-angle configurations, to enhance the capabilities of THz tomography systems.

The characterization capabilities of the developed THz tomography setup are demonstrated on multilayered ceramic oxide structures used for solid oxide fuel cells (SOFC). These investigations include the development of different methods for measuring unknown refractive indices of the analyzed materials, as well as the THz characterization of complete SOFC samples under orthogonal and Brewster-angle incidence. In the following, we will first briefly introduce the investigated SOFC samples. The next part describes the employed THz tomography system and the following sections summarize the THz imaging characterization experiments on the SOFC samples. The last section presents briefly the employed data analysis algorithms.

2. SOLID OXIDE FUEL CELLS

Fuel cells represent a very promising clean and efficient power generation technology with an enormous application potential. Despite of many advantages, current approaches are in many cases not yet capable of competing with established technologies mainly due to cost and reliability related problems. The necessary further development of reliable and cost

Part of the EUROPTO Conference on Terahertz Spectroscopy and Applications II
Munich, Germany • June 1999 SPIE Vol. 3828 • 0277-786X/99/$10.00

319

efficient manufacturing technologies is closely related to the development of powerful, flexible and nondestructive characterization systems for quality control and online monitoring of manufacturing processes. We will demonstrate how time resolved THz tomography allows to characterize fuel cell structures, in order to support the breakthrough of these attractive technologies.
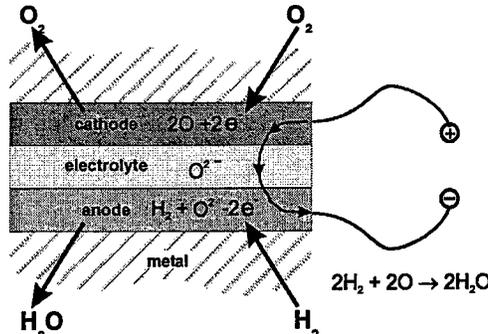

Fig. 1: Schematical cross-section of a solid oxide fuel cell embedded between two bipolar metallic plates. Several of such layered units can be stacked together to form larger power generation units

The analyzed fuel cells are SOFC, a very efficient kind of high-temperature fuel cells, intended for power plant applications [9,10]. These layered systems of ceramic oxides and metals, can nevertheless hardly be characterized by conventional means. A typical SOFC consists of a three layer system like shown in the cross-section in Fig 1: a porous cathode and a porous anode to guarantee the supply of the reaction gases, and a gas impermeable electrolyte. The diffusion of the ionized reaction gases then leads to an electrolytic reaction, which produces electrical voltage and power, and excess heat. The single cells are separated by bipolar plates through which the gases for each cell are supplied. Cells typically induce voltages of only 1 V at a working temperature of 800°C. Several of these layered cells are therefore stacked together into power generation units. The samples under investigation are either single layer or complete three layer SOFC elements [9]. They are all manufactured by the group of Dr. R. Henne at the *Institut für Technische Thermodynamik* of the DLR in Stuttgart, Germany.

3. TERAHERTZ TOMOGRAPHY

THz tomography systems are based on the time resolved measurement of THz pulses that are reflected from a sample [5]. Hence, like in a time of flight experiment, time delays of THz reflections at interfaces correlate with the depth from which the reflections originate. If the propagation constants of the THz pulse, i.e. if the refractive index profile is known one can thus measure the vertical profile of a sample. The spatial resolution along the two lateral dimensions can then either be achieved by using a focused THz pulse and sequentially measuring reflected signals at different positions by scanning the object within the focal plane of the THz tomography system [7], or by measuring in parallel the reflection of a broadened parallel THz beam [3,4]. Since the second approach is by far more demanding in terms of the necessary incident THz power levels, we adopt the first approach for our analysis.
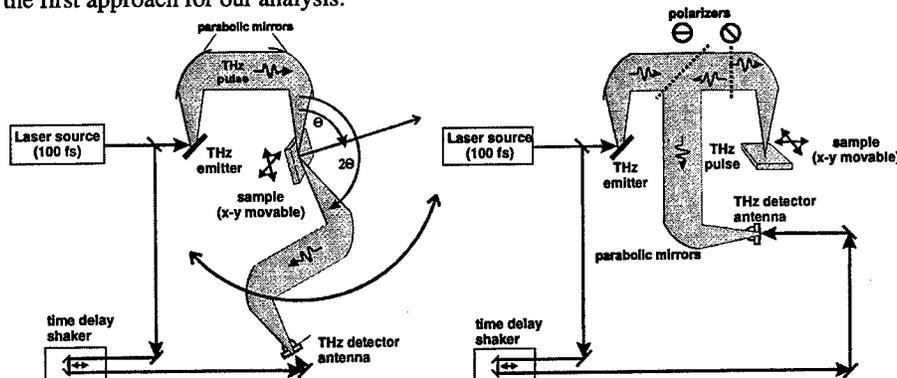

Fig 2.: Two complementary setups for THz tomography. The spatial resolution is achieved by moving the sample in the focal plane of the THz imaging system. The setup on the left allows to vary the angle of incidence of the THz radiation. The setup on the right side is especially designed for the examination of samples under normal incidence.

The employed experimental setups are depicted in Fig. 2. Femtosecond laser pulses from a commercial Ti:sapphire laser system are both used to generate THz pulses and to detect them by gating a photoconductive THz antenna. The THz pulses are focused on the sample and the reflected radiation onto the detection antenna with parabolic metallic mirrors. The analyzed object is moved in the focal plane of the setup to warrant the lateral resolution of the sample. The temporal evolution of the reflected signal is scanned with a fast shaker system. An AIX*Scan*® data acquisition system (40 MHz sampling rate) allows the rapid acquisition of complete THz transients. Integrated digital signal processors (DSP) permit the online automated analysis of the measured data.

The setup schematically represented on the left side of Fig. 2 allows for the first time the THz tomographic analysis under the variation of the angle of incidence of the THz pulses. With this setup it is however not possible to analyze samples under exact normal incidence, as the size of the employed mirrors restricts the minimal angle between incident and reflected beams. Therefore a new THz tomography approach is presented, which is shown on the right side of Fig. 2. By utilizing a pair of polarizing beamsplitters it is now possible to analyze samples under precise normal incidence. This new approach, while frequently used in far-infrared Fourier Transform Spectroscopy [11], has not been applied for time-resolved THz spectroscopy experiments previously.

1. Characterization of single layer perovskite samples

A necessary step before being able to interpret THz-tomographic images is the determination of the refractive index n, or the refractive index profile $n(z)$, of the analyzed samples. This is of special importance, as for most material systems, the properties in the THz frequency regime are unknown. For the analyzed ceramic material systems, we find that the usual calculation of the refractive index from reflection coefficients, e.g. $R = (n_1-n_2) / (n_1+n_2)$, does not yield reliable results. This approach is problematic since long time fluctuations of the laser system, or the surface and interface textures of the sample may affect the detected reflection amplitudes. In addition, unknown absorption coefficients of the involved materials also considerably influence measured amplitudes. A reliable determination of the refractive coefficient profile is therefore problematic.
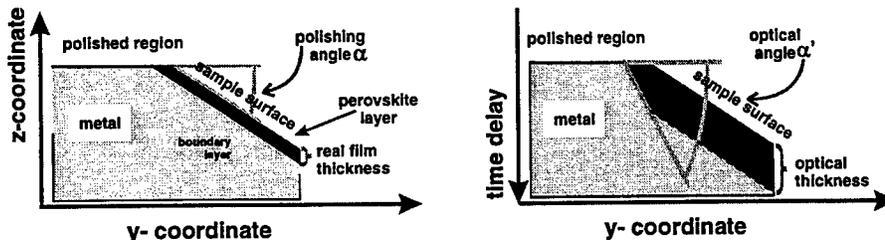

Fig 3.: Scheme of the refractive index measurements. The left figure depicts the cross-section of a layered sample polished at a defined sample, the right figure depicts the time delay (i.e. the optical thickness) the THz pulse experiences. The refractive index can thus easily be calculated from the ratio of the slopes of the polishing angle and the delay time slope of the backside reflex in the transition region.

An alternative to comparing THz reflection *amplitudes* for determination of the refractive index of a sample, is the measurement of the *time delay* of THz reflections in a sample with a well known geometry, e.g. a sample with a well known layer thickness. As in many cases dimensions are not precisely known, we developed a new approach to measure refractive indices, which can readily be applied to layered structures. The basic idea is to polish a sample under a small angle, as depicted in Fig. 3. The left part of the figure depicts a schematical cross-section of a single layer sample that was polished at a small angle from top to bottom. The right part of the figure depicts the corresponding time delay at which reflections of the different interfaces appear. THz pulses are assumed to be incident from the top of the figure. As THz pulses that are reflected from the front surface exclusively propagate through air $(n=1)$, the detected time delay exactly reproduces the shape of the surface. However, if THz pulses are transmitted through a layer, its velocity becomes slower due to the higher refractive index of the layer. It therefore needs a longer time to traverse this layer, and the layer thus appears thicker in time domain. Due to simple continuity considerations, this leads automatically to a transition region where the thickness of the layer increases. In that region the different slope of the backside reflex is given by the refractive index. It is clear that n can then be determined from the ratio of the slope in the transition region divided by the one of the front reflection. Since no further assumptions have to be made, this method for determining refractive indices is less problematic than previous approaches.
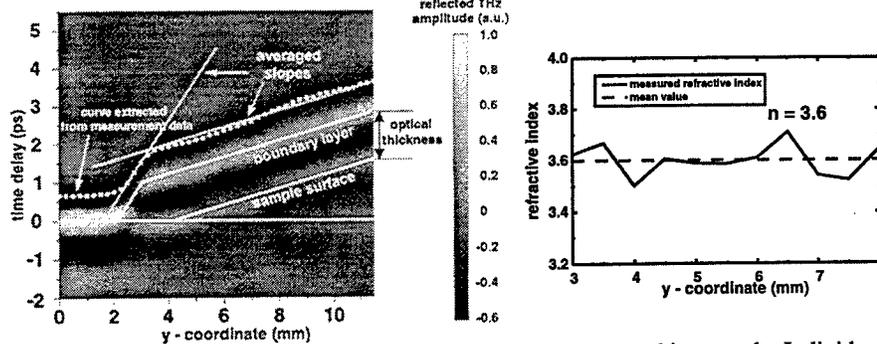
Fig 4.: The left part of the figure depicts a THz line scan of a single layer perovskite sample. Individual THz transients are taken on a line across the polished interface region (y-coordinate), as sketched in Fig. \ref{sketchslope}. The gray scale indicates the reflected THz field amplitudes at the respective time delay. The right figure depicts the refractive index extracted from several of such line scans at different positions along the interface.

Figure 4 demonstrates experimental data of such a measurement of the refractive index. The sample is an yttria stabilized zirconia film (*YSZ*) plasma—sprayed onto a metallic Ni/ZrO_2 anode. The sample is polished as described before. A THz line scan is taken across the polished interface region and the amplitude of each THz transient at any time delay taken at each y-position is depicted on a gray scale map. The measured peak positions (light areas) clearly resemble the expected positions for the interfaces, as depicted already in Fig. 4. In the region where the thickness of the layer is constant, the lines of the back- and front side reflections are parallel. In the transition region where the layer thickness increases the slope of the back reflection is steeper. The ratio of both slopes allows to determine the refractive index of the zirconia layer. Similar line scans are measured at several positions along the interface and the respective refractive indices are also calculated. These values are depicted in the right part of Fig. 4. The 5% variation of the determined values is at least partially due to real variations of the refractive index, given by an inhomogeneous porosity of the zirconia layer.
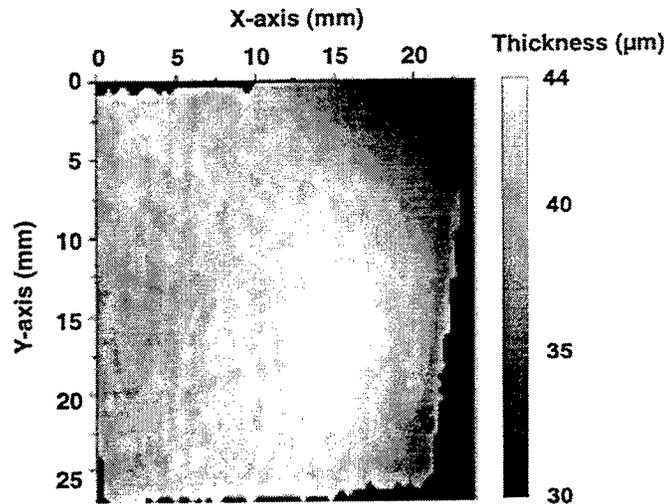
Fig. 5: THz tomographic measurement of the spatially resolved thickness of a YSZ layer. The concentric thickness variation seems to indicate a temperature gradient in the substrate during the plasma spraying of the layer.

The determined refractive index has approximately a value of 3.6. Taking this value one can now readily characterize and e.g. determine the thickness distribution of samples with such zirconia layers. Such a measurement for a complete (unpolished) layer of zirconia on a metallic substrate is presented in Fig. 5. The figure depicts a spatially resolved map of the thickness of the *YSZ* layer. One can clearly see the strong variation of the layer thickness. The observed concentric structure is probably caused by a temperature gradient during the deposition of this layer. This measurement hence exemplifies, how THz tomography can aid the manufacturing process of this type of materials for SOFC applications.

2. Characterization of multi-layer solid oxide fuel cells

A complete sample consisting of three ceramic layers on a metal substrate is now analyzed with the THz tomography setup. The anode, electrolyte and cathode consist respectively of $NiZr_2$-cermet, yttria stabilized zirconia and $LaSr$-perovskite layers. The metallic substrate is $CrFe5Y_2O_3l$. The sample is again polished at a small angle of approximately 1.5° to determine the refractive indices of the three layers. In order to obtain the best possible spatial resolution we measure first the SOFC under normal incidence with the setup depicted in the right part of Fig. 2. Like before, line scans of THz transients across the polished section are taken. Such a line scan is represented in Fig 6.
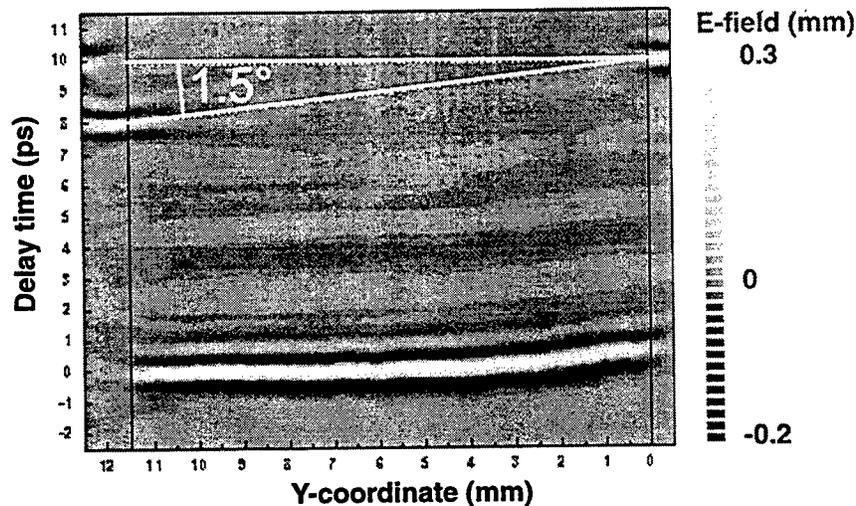

Fig. 6: THz line scan of the three layer SOFC structure, taken under normal incidence to optimize spatial resolution. Only reflections at the front interface can be observed.

Reflections from the sample surface (at delay times around 0 ps) as well as from the surrounding sample mounting (at ≈ 10 ps) can clearly be detected. The slope on the right side of the front reflection indicates the polishing angle. However no reflections from the interface layers are visible. The only slight additional THz amplitude fluctuations visible in Fig. 6 are artifacts (ghost images of the front reflex) related to residual water absorption and internal reflections of the THz source. The absence of any reflections from internal layer interfaces is mainly due to the extremely strong reflection at the surface. Only a small part of the THz pulse is coupled into the sample, and hence the small reflections from the interfaces are overshadowed by the measurement artifacts.

To decrease the surface reflection and therefore increase the coupling of the THz pulse into the sample, we therefore adopt a different reflection geometry. We vary the angle of incidence and evidently, when the incidence angle matches the Brewster angle of the front surface, the sensitivity of the detection of internal structures increases drastically. A measurement at the Brewster angle is presented in Fig. 7. As expected, reflections from the backside of all layers can now easily be identified, despite of the still present artifacts of the measurement. Comparing this measurement to the one before demonstrates how the angle of incidence of a THz imaging system has a significant influence on measured signals and that such dependencies can be exploited to enhance the capabilities of any THz tomography system to selectively detect specific structures of the analyzed objects.

From Fig. 7 one can also already see, that the refractive indices of layer 2 and 3 do not differ too much. This is evident from the similar slopes of the back reflection in the transition regions of this layers. The small refractive index change therefore explains the difficulty in detecting the respective interface. The main reason which prevented to discern the internal structure are nevertheless still the ghost artifacts. Therefore an adaptive filter was applied to be able to identify only that features from the measurement that are of further interest. In this case that are only the maximum peaks of the reflexes of
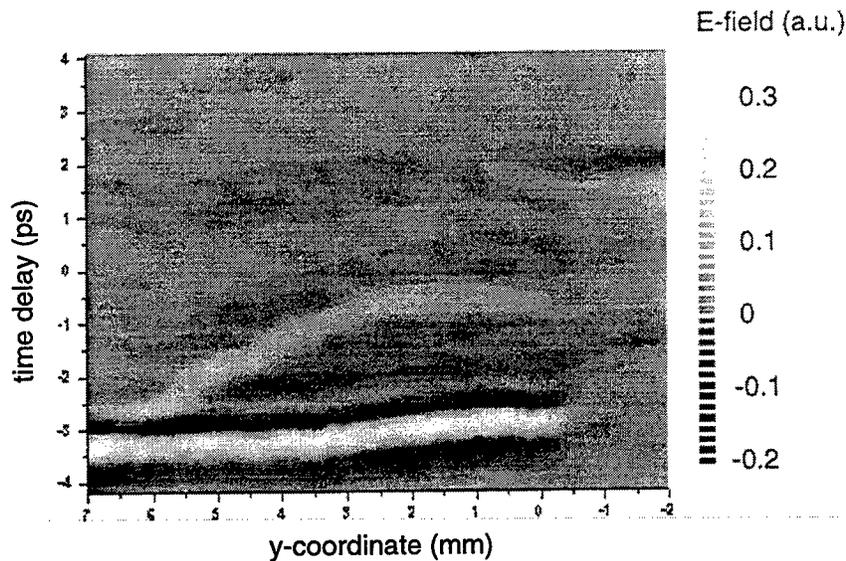
E-field (a.u.)

Fig. 7: THz tomographic line scan of the three layer SOFC structure taken at a Brewster-angle. This configuration minimizes front interface reflections and hence increase the incoupled part of the THz radiation. The reflection from the back side of all three layers are now readily observable.

the surface and the background layer. A comparison of a peak detection applied on the pure measurement data and the filtered data is shown in Fig. 8.
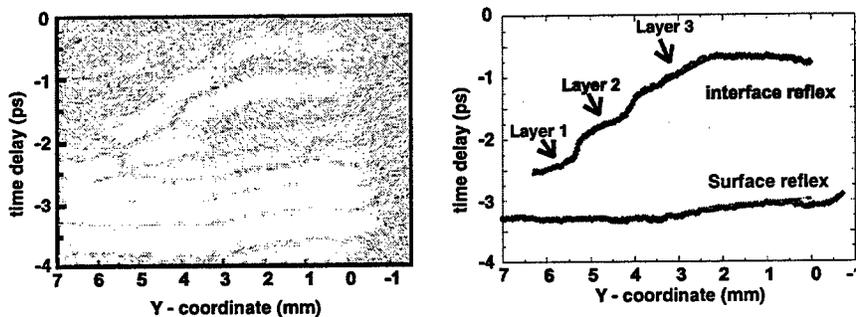
Fig. 8: Comparison of different data extraction algorithms. The left side shows a standard peak detection of the measured data. The right side shows the analysis after adaptive filtering in order to extract only the reflex from the surface and from the backside.

From that filtered data the respective slopes can be extracted which lead to the refractive indices of each layer. This application demonstrates thus the capability of THz tomography as a powerful tool for nondestructive characterization of multilayered systems.

4. SUMMARY

A time-resolved THz imaging system for three-dimensional tomographic analysis of layered structures was presented. The developed system was demonstrated on multi-layer ceramic samples used for high temperature solid oxide fuel cells (SOFC). Various means for measuring unknown refractive indices are discussed and it is shown that the angle of incidence of a THz imaging system has a significant influence on measured signals. Especially in Brewster-angle configurations this

can be exploited to enhance the capabilities of any THz tomography system. The importance of numerical postprocessing of the measured data is exemplified and discussed.

5. ACKNOWLEDGEMENT

1. M. C. Nuss and J. Orenstein, "THz time-domain spectroscopy" in *Millimeter and Sub-Millimeter Wave Spectroscopy of Solids*, ed. by G. Grüner (Springer-Verlag, Heidelberg, 1998).
2. B. B. Hu and M. C. Nuss, Optic Lett. **20**, 1716 (1995).
3. P. U. Jepsen, C. Winnewisser, M. Schall, V. Schyja, S. R. Keiding and H. Helm, Phys. Rev. B **53**, 3052 (1995).
4. Q. Wu, T. D. Hewitt, and X.-C. Zhang, Appl. Phys. Lett. **69**, 1026 (1996).
5. D. M. Mittleman, S. Hunsche, L. Boivin and M. C. Nuss, Optic Lett. **22**, 904 (1997).
6. D. M. Mittleman, J. Cunningham, M. C. Nuss and M. Geva, Appl. Phys. Lett. **71**, 16 (1997).
7. C. Jaeckel, G. Kyas, H. G. Roskos, H. Kurz, B. Kabius, D. Meertens, W. Prussseit and B. Utz, J. Appl. Phys. A **80**, 3488 (1996).
8. M. C. Nuss, IEEE Circuits and Devices **12**, 25 (1996).
9. R. Henne, E. Fendler, M. Lang, First European SOFC Forum Proceedings, Editor U. Bossel, Vol. 2, 617 (1994).
10. N. Q. Minh, J. Am. Ceram. Soc. **76**, 563 (1993).
11. D. H. Martin and E. Puplett, Infrared Phys. **10**, 105 (1970).
12. H. D. Lüke, *Signalübertragung*, (Springer Verlag, 1991).
13. D. M. Mittleman, R. H. Jacobsen, R. Neelamani, R. G. Baraniuk, M. C. Nuss, Appl. Phys. B **67**, 379 (1998).

Unconditionally stable high current density resonant tunnelling diodes

O. Dupuis, J. C. Pesant, P. Mounaix, F. Mollot, O. Vanbésien and D. Lippens

Institut d'Electronique et de Microélectronique du Nord, UMR CNRS 9929
Université des Sciences et Technologies de Lille
Avenue Poincaré, BP 69, 59652 Villeneuve d'Ascq Cedex, France

ABSTRACT

In the context of very high frequency components, where quantum well devices have already shown promise, we report, in this communication, on the optimisation, realisation and characterisation of GaAs and InP-based resonant tunnelling diodes. A fully planar technology has been achieved for a GaAs triple-well structure, with the use of ion implantation techniques, whereas mesa-etched technology together with airbridge integration have been used for the InP-based devices. In terms of performance, both material systems have shown excellent DC characteristics with a current density of 60 kA/cm^2 associated with a current contrast of 6:1 for the GaAs-based RTD. An even higher current density has been achieved for the InP-based devices with 215 kA/cm^2 while still preserving a peak-to valley current ratio of 9:1. In addition, 1µm^2-area InP-based RTD's have been found to be unconditionally stable without the necessity of a stabilising network. These anticipated properties for very small area devices, which meet the stability criteria, enables us to perform small signal characterisation over the whole range of the negative differential resistance region. Analysis of the measured scattering parameters up to 50 GHz shows an increase in the capacitance-voltage characteristics.

1. INTRODUCTION

Resonant tunnelling diodes have now shown promise at submillimeter wavelengths with the recent achievements of 28 µW at 300 GHz and in excess of 10 µW at 650 GHz by the Jet Propulsion Laboratory (JPL) [1]. One of the major concerns in connection with the use of such quantum well devices at very high frequency is the current capability of the devices which appears as a key figure of merit of the cut-off frequency and hence in the overall performance [2-3]. In this communication, we show how the electrical properties of resonant tunnelling diodes can be optimised while maintaining a high peak-to valley current ratio. In practice both GaAs and the InP-based technologies will be considered. For the former, the basic idea was to take advantage of a Double Barrier Heterostructure (DBH) with a pre-well and post-well configuration. By this means, high conduction band offset can be preserved in the vicinity of the DBH and resonant tunnelling transitions between systems of the same dimensionality can be achieved. Also from the technological side, the active region of the devices can be defined by means of ion implantation techniques. For the latter, the main advantage stems from the low effective mass of cladding layers with the associated benefits of a high quantum transparency of the DBH and very favourable transport properties. In contrast, the fabrication of the devices involves mesa etched structures which can be difficult at submicron dimensions. On the basis of these concepts, two kinds of structure have been grown by Gas Source Molecular Beam Epitaxy and fabricated with e-beam patterning, reactive ion etching and air bridge contacting techniques. For the resonant tunnelling diodes grown on Semi-Insulating substrates, ion implantation was performed with Boron (10^{13} cm^{-2}, 110 kV). The devices exhibit a current contrast of 6:1 together with a current density of 60 kA/cm^2. For the InP based material system, a much higher current density was achieved with 215 kA/cm^2 whereas a peak-to valley current ratio of 9:1 was preserved. In contrast to the excellent performance which are state-of-the art results, the technological procedures are very critical and do not seem easily extended to a monolithic integration of devices in arrays. On the other hand the devices fabricated with 1µm^2 area are found unconditionally stable without the use of a stabilising network. These properties were expected for very small area devices, thus meeting the stability criteria, enabling us to perform small signal characterisation over the whole range of the negative differential resistance region. Analysis of the measured scattering parameters up to 50 GHz demonstrates an increase in the capacitance-voltage characteristics resulting from trapping of carriers within the quantum well.

For further informations
O.D. : Email: Olivier.Dupuis@IEMN.univ-lille1.fr

326

Part of the EUROPTO Conference on Terahertz Spectroscopy and Applications II
Munich, Germany • June 1999 SPIE Vol. 3828 • 0277-786X/99/$10.00

The next section deals with the numerical procedure which was used for predicting the electrical characteristics. The devices fabricated using a GaAs-based and InP based technology will be considered in section 3. Section 4 is devoted to the rf assessment of the devices while concluding remarks are given in section 5;

2. NUMERICAL PROCEDURE FOR I-V COMPUTATION

The fabrication of high performance Resonant Tunnelling Diodes is a formidable task due the very challenging issues [4-8] not only from the epitaxial growth side but also during the fabrication of the device. In order to minimise the risk and also the cost, it is preferable, prior to any fabrication batch, to predict as accurately as possible, the expected current-voltage characteristics and to investigate the impact of a change in the device configuration and/or material parameters. To this aim, we have developed, at IEMN, a simulation code of the electrical characteristics of Heterostructures devices which has been applied successfully to resonant Tunnelling Diodes in the framework of this work. The inputs are the microstructure parameters in terms of thickness and doping concentration along the operating conditions notably applied voltage and device temperature. The outcomes of this are the capacitance-voltage characteristics and current-voltage relationship.

In practice a real structure consists of a Double Barrier Heterostructure (DBH's) sandwiched between two contact layers; which acts as electron reservoirs. In addition, these contacting layer are generally modulation doped with a High-low (and reciprocally) doping concentration. The purpose of such doping concentration is to meet the requirement of a highly doped region for low contact resistance and of a moderate doped region to minimise the diode capacitance or to preserve an injection region which is moderately degenerated. As a consequence, like in any modulation doped device, a diffusion process takes place yielding a subsequent band bending in the emitter and collector regions. Besides this, electrons accumulates in front of the DBH and form a quasi triangular electrostatic potential well by space charge effects, resulting in quantum size effects even for generic structures. The quantum region is un-doped but carriers can be also accumulated in the central quantum well which is fed by the tunnelling current. The description of these space charge effects is of prime importance to have a deep insight into resonance conditions. The outcome is thus the peak voltage corresponding to the onset of negative differential conductance (NDC) effects. Another key figure of merit is the voltage range over which NDC effects are seen. This voltage influence greatly the stability of the devices, as pointed out in the following and the output power which could be delivered by the devices used solid state sources. Simplified theories predict a sharp decrease of the current values when the device is driven in NDC region. In practice however, the fact that the structures includes cladding layer means that the voltage across the diodes is a result of a voltage drop across the DBH itself and the depleted region resulting in much broader voltage range, a welcome feature both from the stability and power limitation points of view.

Another criterion of major concern is the current density flowing through the structure. This current density is a direct consequence of the quantum transmission probabilities for any energy value available for electrons. This is one of the main difference with respect to other quantum closed system in the sense that the openness of the structure implies not only to determine the resonant energy but also the whole transmission spectrum. The input data [9-10] influences greatly the transmission probabilities since an exponential relationship can be found as a function of barrier thickness, effective mass and injection energy [11]. This great sensitivity is one of the main limitation encountered in practice where an inevitable dispersion can be foreseen notably when the barriers are grown on the nanometer scale. Also, it is problematic to use without ambiguity a conduction band edge effective mass. This parameter is a bulk figure and we make use of ultra thin layers and also electrons are tunnelling deep in the forbidden gap of wide gap materials. Despite these uncertainties, the calculations [12-14] permits one to have a reasonably clear understanding of the electrical characteristics involved except perhaps the peak-to valley current ratio. In fact, it was early recognised that a degradation of current contrast (peak-to-valley ratio) is a consequence of scattering assisted phenomena which are difficult to deal with a reverse-engineering approach. Having these assumptions in mind, the numerical procedure consists to first solve the Poisson equation in the zero current Thomas Fermi approximation. The Poisson equation reads:

$$\frac{\partial}{\partial z}\left(\epsilon(z)\frac{\partial}{\partial z}V(z)\right) = -q\left(N_D^+(z) - N_A^-(z) + p(z) - n(z)\right) \tag{1}$$

A discretized form of this equation is solved using a variable spatial discretization mesh depending on doping concentration and mobile charge. This allows us to treat simultaneously wide regions such as cladding layers as well as potential perturbations on the mono-layer scale. As boundary conditions, we use Dirichlet conditions on both sides in the emitter and collector regions which are considered as discussed above at equilibrium (Thomas-Fermi approach). The calculation procedure makes use of an (over)relaxation method to accelerate convergence.

Starting from the conduction band profile calculated under these conditions, we subsequently computed the eigenstates by solving the Schrödinger equation in the mono-electron and effective mass approximations.

$$-\frac{\hbar^2}{2}\frac{\partial}{\partial z}\left(\frac{1}{m_e^*(z)}\frac{\partial}{\partial z}\varphi(z)\right) + V(z)\varphi(z) = E_z\varphi(z) \tag{2}$$

At this stage to have further insight into the real band bending, the local carrier density can be computed accurately by assuming that the overall density $n(z)$ is given by the superposition of a two dimensional electron density (n_{2D}) and of a three-dimensional carrier density (n_{3D}). Both contributions can be computed according to the relevant 2D and 3D- densities of states using the following relations:

$$n(z) = n_{2D}(z) + n_{3D}(z) \quad \text{with}$$

$$n_{2D}(z) = \sum_i \frac{m^* kT}{\pi\hbar^2}\, Ln\left(1 + \exp\left(\frac{E_F - E_i}{kT}\right)\right)\left|\psi_i(z)\right|^2 \qquad \text{for } E \le E_b$$

and

$$n_{3D}(z) = \frac{1}{2\pi^2}\left(\frac{2m^*}{\hbar^2}\right)^{3/2} \int_{E_b}^{\infty} \frac{E - E_c(z)}{1 + \exp(\frac{E - E_F}{kT})}\, dE \qquad \text{for } E \ge E_b \tag{3}$$

where E_b is the threshold energy between 2D and 3 D densities of states

The numerical procedure can be carried out until convergence is reached. In a final step, once the potential profile and carrier concentrations are known, capacitance and current density can be computed. For the former, it is defined as the accumulated carrier density variation as a function of bias voltage (equivalent to the depleted charge density owing to electroneutrality conditons) :

$$C(V) = q\frac{\partial n_s(V)}{\partial V} \tag{4}$$

whereas the current density reads:

$$J(V) = \frac{q m_e^* k_B T}{2\pi^2\hbar^3}\int T(E,V)F(E,V)dE$$

with

$$F(E,V) = \ln\left(\frac{1 + \exp((E_F - E)/k_B T)}{1 + \exp((E_F - qV - E)/k_B T)}\right) \tag{5}$$

$T(E,V)$ is the global transmission from the emitter to the collector [12-13], which can be computed from the wavefunction in the collector and emitter regions respectively. $F(E,V)$ is the so-called supply function which describes the balance between emitter and collector carrier streams. Let us mention that this approach has the advantage to include both tunneling and thermionic current contributions

3. DESIGN OF HIGH PERFORMANCE RTD's

In the following, we will draw a contrast between the GaAs-based material system from the InP based technology

3.1 GaAs Based technology

Let us firstly consider Figure 1 which shows the growth sequence of a GaAs Resonant Tunnelling Device starting from a GaAs Semi-Insulating substrate. The active region consists of a central well grown with a tri-layered scheme. An InGaAs layer was grown in order to increase the energy shift between ground state and first excited states. This band gap engineering can be understood on the basis of simple considerations. Indeed, any narrow gap potential perturbation will mainly influence the ground state which exhibits a maximum in the probability density at the centre of the well [15]. In contrast, provided the perturbation is localized, its impact on the first excited state will be of second order. In addition, the fact to introduce a confinement in a low effective mass region (InGaAs) is favourable for a large offset between successive index eigenstates. In terms of current -voltage characteristics, this means that the spurious conduction via the second excited state will be rejected at higher energies with respect to the main tunnelling phenomena, resulting in an increase in current contrast.

Contact layer	GaAs	2.10^{18} at.cm^{-3}	1000 Å
Spacer	GaAs	1.10^{18} at.cm^{-3}	100 Å
Prewell	In$_{0.2}$Ga$_{0.8}$As	u.d	50 Å
Transition	GaAs	u.d	5 Å
Barrier	AlAs	u.d	17 Å
	GaAs	u.d	5 Å
Well	In$_{0.2}$Ga$_{0.8}$As	u.d	40 Å
	GaAs	u.d	5 Å
Barrier	AlAs	u.d	17 Å
Transition	GaAs	u.d	5 Å
Postwell	In$_{0.2}$Ga$_{0.8}$As	u.d	50 Å
Spacer	GaAs	1.10^{18} at.cm^{-3}	100 Å
Contact layer	GaAs	2.10^{18} at.cm^{-3}	1 µm

GaAs S.I. substrate

Figure 1 Epitaxial sequence for the devices fabricated from GaAs based materials systems

Turning now to the cladding layer one can note that the DBH is sandwiched between two InGaAs quantum wells. The goal of such engineering is twofold: (i) the first motivation was to induce tunnelling transitions between systems of the same dimensionality eg. 2D-systems (ii) the pre-well plays the role of an injector and one can expect higher tunnelling probabilities due to the lower effective mass. In order to illustrate such a band gap engineering with a quantitative determination of electrical characteristics, we plotted in Figure 2 the conduction band profile, whereas Figure 3 depicts the current-voltage characteristics calculated at room temperature.
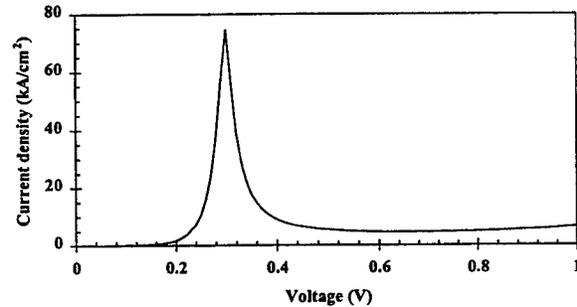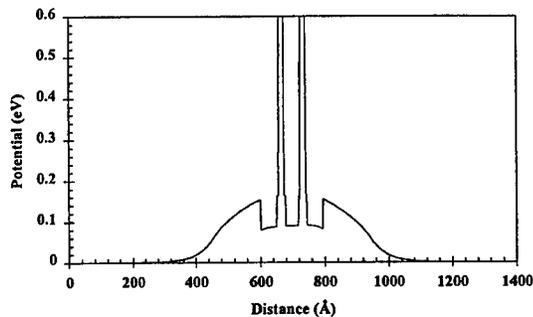

Figure 2: Calculated conduction band profile (GaAs-based)   Figure 3 Calculated current-voltage characteristics

For the sample under investigation, the barriers thickness is 1.7 nm, the InGaAs quantum wells are 5nm wide for an Indium concentration of 30 %. This Indium content was chosen to satisfy some requirements in the pseudomorphic growth of epilayers and to obtain a significant impact of quantum size effects induced by the InGaAs quantum wells. The expected current density is 60 kA/cm2 for a peak voltage of 500mV. Such a relatively high current density can be explained by the rather high doping concentration in the cladding layer (1×10^{18} cm^{-3}) and the barrier thickness limited to 1.7nm. Besides the capping and buried contact layers were doped to 2×10^{18} cm^{-3} for optimising the contact resistance.

Let us now consider the device fabrication, and first of all some of the guides lines for fabricating devices intended to operate at millimetre and submillimetre wavelengths. One of the first criteron is to fabricate small area device for the achievement of a low capacitance. Also the lateral dimension has to be shrunk in order to limit the current flowing through the active region and hence the spurious increase in heterostructure temperature. Indeed, a too high local temperature is deleterious and yields a burnout of the devices. In addition, the devices have to be planarly integrated for subsequent use in a low parasitic environment. Generally speaking, such a requirement is met by developing an air bridge technology which will be discussed later. However, in the present case the use of a GaAs technology permits one to implement a fully planar approach making use of ion implantation. Towards this goal, preliminary Computer Aided Design (T-CAD) was carried out, in a first stage, to determine the various doses and expected depth. The critical step was the definition of the active region by avoiding 'open circuit' effects in the buried conductive GaAs layer. After a parametric study, it was decided to implant with Boron species with the following parameters (10^{13} cm^{-2}, 110 kV). By this means we successfully fabricated the devices which exhibited the typical current-voltage characteristics displayed in Figure 4. The measured current density at peak voltage (500mV) was found to be 60 kA/cm2 for a peak-to valley ration of 6:1which are state-of-the art results for the considered material system.
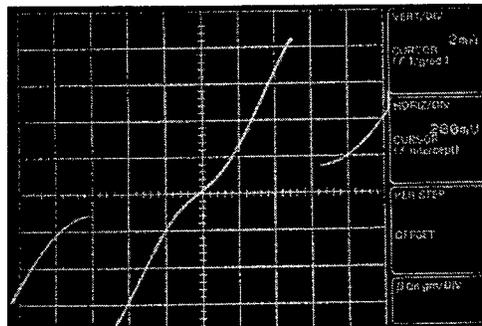

Figure4 Current-voltage characteristics for RTD's fabricated in a GaAs technology by ion implantation

3.2 InP-based technology

Figure 5 shows the epitaxial material, starting from a Semi-Insulating InP substrate by using a Gas Source Molecular Beam Epitaxy (GSMBE). All the epilayers were lattice matched to InP except a central potential InAs perturbation. The latter is highly strained and has to be grown under pseudomorphic conditions.

Contact layer	$In_{0.53}Ga_{0.47}As$	$>1 \times 10^{19}$ at.cm-3	5000 Å
Cladding layer	$In_{0.53}Ga_{0.47}As$	1×10^{18} at.cm-3	1000 Å
Spacer	$In_{0.53}Ga_{0.47}As$	n.i.d	50 Å
Barrier	AlAs	n.i.d	17Å
	$In_{0.53}Ga_{0.47}As$	n.i.d	10 Å
Well	InAs	n.i.d	25 Å
	$In_{0.53}Ga_{0.47}As$	n.i.d	10 Å
Barrier	AlAs	n.i.d	17 Å
Spacer	$In_{0.53}Ga_{0.47}As$	n.i.d	50 Å
Cladding layer	$In_{0.53}Ga_{0.47}As$	1×10^{18} at.cm-3	1000 Å
Contact layer	$In_{0.53}Ga_{0.47}As$	$>1 \times 10^{19}$ at.cm-3	5000 Å
Buried layer	InP	5×10^{18} at.cm-3	5000 Å

Fe-doped Semi-Insulating InP substrate

Figure 5 growth sequence for the InP-based devices

The basic idea of such a band gap engineering is similar to that previously described namely the fact that a central narrow gap inserted in the middle of the Double barrier heterostructure which lowers the ground state while the first excited state is unaffected by this perturbation. In case of highly degenerated layer on each side of the DBH, the anti-crossing between the emitter Fermi level and the ground sate, which corresponds to onset of strong conduction. This takes place close to equilibrium conditions. Therefore any imbalance between the current from emitter to collector and vice versa yields a huge increase in current density. At increasing voltage, the current increase in a quasi linear fashion as a consequence of the linear energy dependence of supply function, up to the peak voltage where a dramatic decrease in current value is observed. Such a extremely non linear behaviour can be calculated by means of the theoretical approach, depicted in section 2. Figure 6 shows the results of such a calculation, performed taking the parameters listed in Figure 5. The calculated threshold voltage for NDC is 0. 25 V for a peak current density of the order of 200 kA/cm^2.
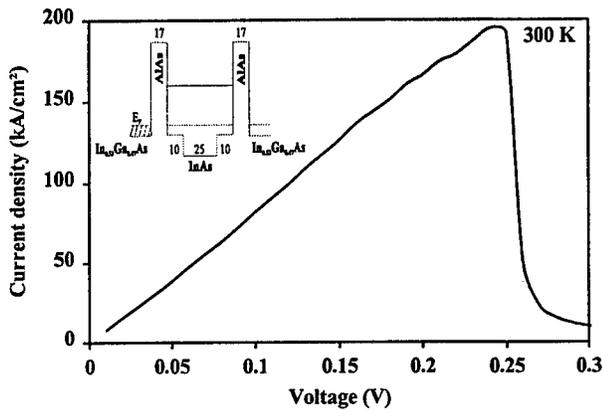

Figure 6 Calculated I-V characteristics for an InP
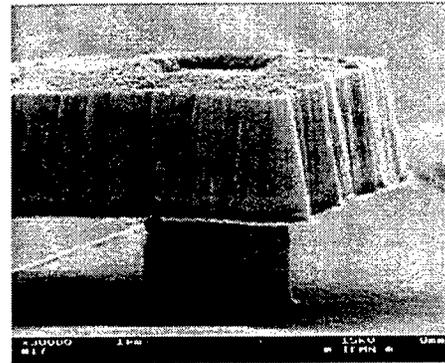Technology

Figure 7 Scanning Electron Microphotograph for a 1 μm^2
device integrated with an air bridge technology p

Let us now report on the devices fabrication which cannot make use of the fully planar ion implantation techniques due to the nature of the low gap material. In that case, we used an air bridge technique which is illustrated in Figure 7. This Figure shows the Scanning Electron Microphotograph of a 1 μm^2 devices interconnected to a Coplanar Waveguide Transmission lines for subsequent wafer probing of the devices. The anode is patterning by means of an electron beam equipment whereas the mesa was etched using Reactive Ion Etching. Let us recall that such small areas permits one to considerably limit the current in the device as seen in figure 8 which shows the current-voltage characteristic of a typical device. The peak current, reached at approximately 400mV, was in excess of 2 mA. This means that the current density flowing through the microstructure exceeds 200 kA/cm^2 in excellent agreement with calculated data. Moreover, the linear increase in the current versus voltage, before the occurrence of NDC effect, is also in accordance with predicted I-V curves. The voltage range for NDC effect is of the order of 300mV
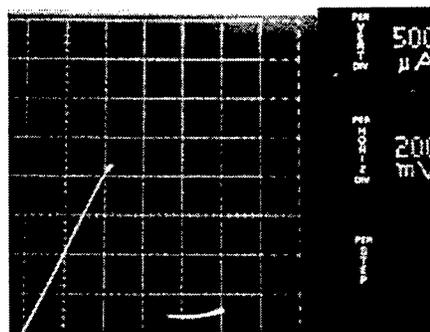

Figure 8: Current-voltage characteristics measured directly under dc probes

4. RF CHARACTERIZATION

The first stage in rf characterization was to carefully record the current-voltage characteristic under coplanar probes. Unlike dc probes available during fabrication for preliminary assessment, rf probes exhibit low parasitics so that the stability of the devices can be studied. Let us recall that the stability criteria depends on on the diode characteristics through the capacitance and conductance of the device and also on the interconnecting element mainly the series self-inductance. This key criterion reads:

$$L_s > R_s \, |R_d| \, C_d \qquad (6)$$

Where Ls is the self inductance, R_s the series resistance C_d and R_d the diode capacitance in NDC region. It can be seen from equation 6 that $R_s \cdot R_d$ scale as 1/A (A is the diode area) whereas Cd is proportional to A. It results from this that at sufficiently small area the device is found to be unconditionally stable over the NDC region. Clearly the threshold depends on the technological process through Ls and Rs but also from the current density flowing through the devices. Under these conditions, high current drivability devices are found unstable in the major part of the NDC curve. In the present case due to the drastic shrinking in device dimension the devices exhibit a continuous variation for bias points in NDC as can be shown in Figure 9 which shows the variations of current versus voltage for a 1 μm^2 area device, characterised at room temperature with picoprobes. It can be shown that the Negative differential conductance (resistance) can be continuously tracked under NDC conditions. For the device under investigation the current density is slightly lower than those reported below with Jp= 123 kA/cm^2.
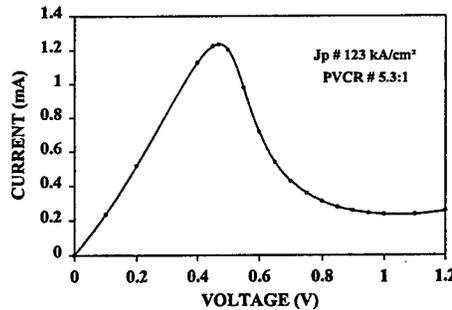

Figure 9 Current-voltage characteristics

Under such stability conditions, and without the requirement of a stabilizing network, the scattering parameters can be measured over the whole bias range including Positive Differential Conductance (PDC) and NDC regions. Thus we obtain the typical variations displayed in Figure 10 on Smith Chart. The tangent circle to the outer circle correspond to a reflection coefficient equal to one. Outside this region, the reflection coefficient is greater than one. This means that the device delivers an extra power with respect to the incident electromagnetic power delivered by the source of network analyser. At low frequency the diode conductance corresponds the values which can be deduced by derivating the I-V characteristics. This is expected from the high quality of epilayer avoiding some trapping effects with a slow response time. At increasing frequency the conductance level rolls off according to a Rc constant involving the diode resistance and the overall capacity of the devices. Therefore for certain bias points close to the valley voltage cut-off frequency, and under small signal conditions, the reflection coefficient can be directly measured (cross over of the diode reflection coefficient with the circle corresponding to a Standing Wave ratio (SWR) equal to 1).

Analysis of the small signal impedance measurements [16] can also be carried out by recording and plotting the variations of the real and imaginary intrinsic part of impedance as a function of bias voltage. Typical bias voltage variations are displayed in Figures 11 and 12 respectively. The conductance is nearly constant in PDC region while exhibiting a well defined at approximately 0.55 V. Confidence into the measurements can also be found from the capacitance variations versus voltage plotted in Figure 12 which shows an increase in capacitance in NDC. Such an increase is a direct consequence of the charge trapped within the central when the diodes is under resonant conditions.
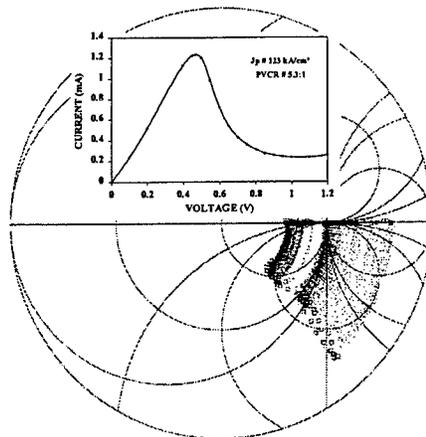
Figure 10 Variations versus frequency of the small signal impedance of the Diode under PDC and NDC conditions. Scattering parameters measurements were carried out up 50GHz . The tangent circle to the outer one corresponds to a unitary Standing Wave Ratio (SWR). Outside this delimited zone, SWR is greater than one. This means that the reflected wave is greater than the incident one. Note the excellent stability of these measurements
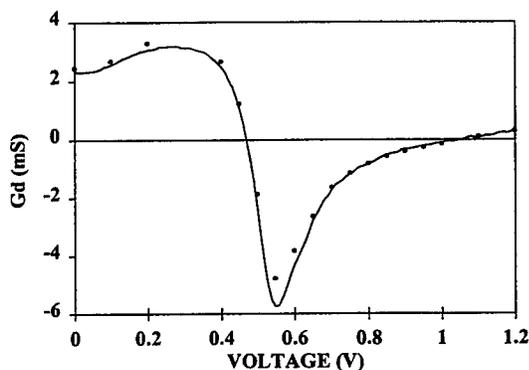

Figure 11 Voltage dependence of the small signal intrinsic conductance extracted in the whole range of bias
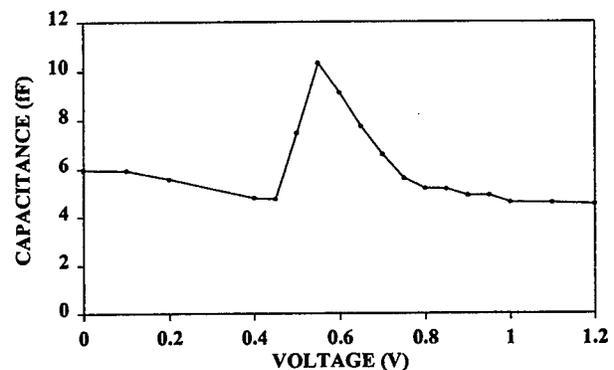
Figure 12 Capacitance variations versus bias voltage for a $1\mu m^2$ area device (InP technology)

5. CONCLUSION

In summary, high performance resonant tunnelling diodes have been successfully fabricated and rf tested over a wide frequency range. Two technologies were investigated based on InP and GaAs substrates respectively. For the former, full planar integration was achieved by means of ion implantation with current density as high as 60 kA/cm2. Due to low effective mass, higher tunnelling current density was recorded for InP-based microstructures which were air-bridge contacted with highest results in the 200 kA/cm². At such high current densities, the stability issue becomes of prime importance and has be solved by shrinking dramatically the dimension of the devices. For $1\mu m^2$ area devices they were found unconditionally stable. This permits us to fully characterised the scattering parameters of the devices up to 50 GHz. Analysis of intrinsic elements shows strong non linearity in the conductance and capacitance variation versus voltage, with an increase of the capacitance in Negative Differential Conductance region.

6. ACKNOWLEDGMENT

6. REFERENCES

1. M. Reddy at al. "Monolithic Schottky Collector Resonant Tunnelling Diodes Arrays to 650 GHz", *IEEE Electron Devices letters* , Vol. **18**, N°5, 1997

2. E. R. Brown, J. R. Söderström, C.D. Parker, L.J. Mahoney, K.M. Molvar, and T.C. Mc Gill, 'Oscillations up to 712 GHz in InAs/AlSb Resonant Tunnelling Diodes', Appl. Phys. Lett.; **58**, pp. 2291-2293, 1991

3. J. R. Södersrtöm, E. R. Brown, C. D. Parker, L. J. Mahoney, J.Y. Yao, T.G. Anderson and T.C. Mc Gill," Growth and Characterization of High current density, High speed In/AlSb Resonant tunnelling Diodes", J. Appl. Phys., **58**, pp. 275, 1991

4. T.P.E. Broekart, W. Lee, and C.G. Fonstad, "Pseudomorphic $In_{0.53}Ga_{0.47}As$/AlAs /InAs Resonant Tunnelling Diodes with peak-to-valley ratios of 30 at room temperature", Appl. Phys. Lettes, **53**, pp. 1545-1548, 1988

5. D. Z. Y. Ting, M. L. Jackson, D.H. Chow, J.R. Söderström, D. A. Collins, and T. C. Mc Gill, "X-point tunnelling in AlAs/GaAS Double Barrier Heterostructures", Solid State Electronics, **32** , pp. 1513, 1989

6. T. S. Moise, Y.C. Kao, A. J. Katz, T.P. Broekaert, and F.G. Celio, "Experimental sensitivity analysis of pseudomorphic InGaAs/AlAs Resonant Tunnelling Diodes", J. Appl. Phys. **78**, pp. 6305, 1995

7. H. Kitabayashi, T. Waho, and M. Yamamoto, "Resonant interband tunnelling current in InAs/AlSb/GaSb/InAs Double Barrier Diodes", J. Appl. Phys., **84**, pp. 1460, 1998

8. H. Kitabayashi, T. Waho, and M. Yamamoto,3'Resonant Interband Tunnelling current in InAs/AlSb/GaSb,/InAs diodes with extremely thin AlSb barrier layers", Appl. Phys. Lett., **71**, pp; 512, 1997

9. S. Adachi, 'GaAs, AlAs, and AlxGa1-x As : Material parameters for use in research and device applications , J. Appl. Phys., **58**, p. R1, 1985

10. S. Adachi, 'Material parameters of $In_{1-x}Ga_xAs_yP_{1-y}$ and related binaries", J. Appl. Phys., **53**, pp. 8775, 1982

11. B. Ricco, and M. Y. Azbel, "Physics of resonant tunnelling. The one dimensional double barrier case", Phys. Rev., **29**, pp. 1970, 1984

12. T. Fiig, and A. P. Jauho, "Self-consistent model for two-dimensional accumulation layer states in resonant tunnelling devices", Appl; Phys. Lett., **59**, pp. 2245, 1991

13. L. Burgnies, O. Vanbésien, V. Sadaune, D. Lippens, J. Nagle, and B. Vinter, "resonant Tunnelling Structures with local potential perturbations",J. App. Phys., **75**, pp. 4527, 1994

14. X. Oriols, J.J. Garcia, F. Martin, J. Suné, T. Gonzales, J. Mateos, D. Pardo, and O. Vanbésien, To be published in Semiconductor Science and Technology, June 1999

15. S. Niki, C. L. Lin, W. S.C; Chang, nad H.H. Wieder, " Band edge discontinuities of strained layer $In_xGa1-xAs$/GaAs Heterojunctions and quantum wells", Appl. Phys. Lett., **55** , pp; 1339, 1989

16 O. Dupuis et al. 'Admittance engineering for RTD's and HBV's ', Workshop on Compounds Semiconductor Devices and Integrated Circuits, May 24-27, Berlin, Proceedings pp. 128-129

Micromachining techniques at terahertz frequencies

S. Arscott[a], L. Duvillaret[b], P. Mounaix[a], F. Garet[b], J.-L. Coutaz[b] and D. Lippens[a]

[a]Institut d'Electronique et de Microélectronique du Nord (IEMN), Université des Sciences et Technologies de Lille, Avenue Poincaré BP 69, 59652 Villeneuve d'Ascq Cedex, France
[b]Laboratoire d'Hyperfréquences et de Caractérisation, Université de Savoie (LAHC), 73376 le Bourget du Lac Cedex, France.

ABSTRACT

In this paper we have characterised the refractive index and absorption coefficient of negative photoresist $NANO^{TM}$ XP SU-8 from 0.1-1.6 THz using terahertz time-domain spectroscopy. Over the measured frequency range it was found that the refractive index (n) is a relatively flat function of frequency, decreasing from 1.8 to 1.7. The value of absorption coefficient (α) is seen to increase in a linear fashion over the given frequency range, being 25 cm^{-1} at 1 THz. From this data we have extracted functions of dielectric constant (ε_r) and dielectric loss tangent ($\tan(\delta)$) versus frequency, quantities which will be of use for future terahertz circuit design. In addition to these measurements, we have demonstrated two novel applications of SU-8. Firstly, we have fabricated membrane-like features by using a multi-exposure photolithographic technique on a single layer of SU-8, and secondly we have utilised a thin layer of SU-8 (0.4 μm) as a patternable adhesion layer as part of a semiconductor epitaxial lift-off (ELO) process designed to transfer III-V semiconductor epitaxial layers onto lower loss host substrates.

Keywords: SU-8 negative photoresist, terahertz time-domain spectroscopy, micromachining, microstructuring, membrane structures, epitaxial lift-off techniques

1. INTRODUCTION

The negative photoresist $NANO^{TM}$ XP SU-8 is gaining much attention recently for applications which range from microstructures for micromachining [1] to being a potential component in ultra-high frequency microcircuits due to the manufacture of waveguide structures [2]. The high aspect ratios (>10:1) and ultra-thick layers (2000 μm) which are attainable by patterning the photoresist facilitate the manufacture of 3-D features which could be utilised in conjunction with ultra-high frequency devices, notably the heterojunction barrier varactor (HBV) [3] for the next generation of integrated circuits which are aimed at operating at THz (10^{12} Hz) frequencies. To our knowledge there have been no studies concerning the dielectric properties of SU-8 in this frequency domain. In this paper we have characterised the refractive index and absorption coefficient of SU-8 from 0.1-1.6 THz using terahertz time-domain spectroscopy.

This paper is divided into terahertz time-domain spectroscopy characterisation and applications of SU-8. Part 2 outlines the principles of terahertz time-domain spectroscopy. Part 3 presents the results of the spectroscopic technique when applied to features fabricated from the negative photoresist SU-8. In part 4, novel applications of SU-8 within in the sphere of micromachining are presented.

2. EXPERIMENTAL

2.1 Terahertz time-domain spectroscopy

Terahertz time-domain spectroscopy [4,5] is a powerful and fast technique for measuring the complex refractive index ($n_c = n_r + in_i$) of materials over a very wide range of frequencies, extending from tens of gigahertz up to terahertz frequencies. The technique is based on measuring the time dependence of the electric field of a short sub-picosecond electromagnetic pulse which is transmitted through a sample for measurement. The ratio of the Fourier transforms of the data measured *with* and *without* the presence of the sample yields the complex transmission coefficient of the sample in the frequency domain. The refractive index (n) and absorption coefficient (α) can then be extracted from this data.

For further author information-
email: stephen.arscott@IEMN.univ-lille1.fr

Part of the EUROPTO Conference on Terahertz Spectroscopy and Applications II
Munich, Germany • June 1999 SPIE Vol. 3828 • 0277-786X/99/$10.00

335

Figure 1(a) below shows a schematic diagram of the experimental set-up used to measure the refractive index and the absorption coefficient of the SU-8 samples.

Terahertz time-domain spectroscopy can accurately measure these optical parameters by utilising sub-picosecond electromagnetic pulses which can be generated by pulsed optical excitation of an LT-GaAs photoconductive switch using a self-mode-locked Ti:Sapphire laser [4]. The collimation of the terahertz signal is obtained by using a lens fashioned from high-resistivity silicon. Figure 1(b) shows the electromagnetic spectrum which is generated for measurement, demonstrating that a signal covers the bandwidth 0.1 THz to approximately 2.5 THz.
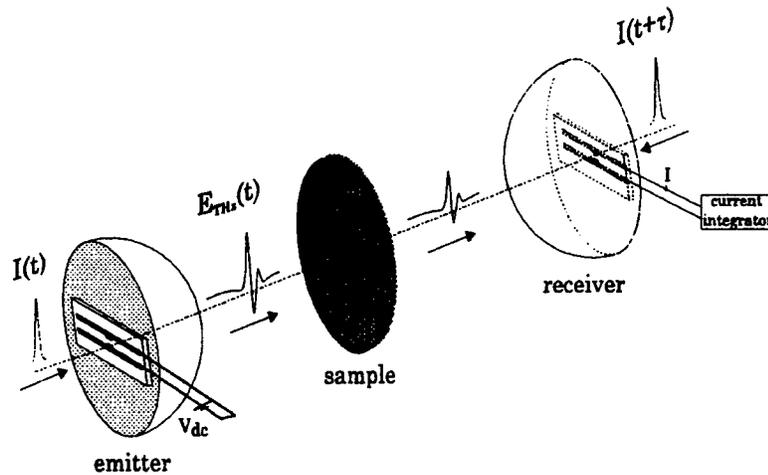

Figure 1(a): Schematic diagram of experimental set-up used to perform terahertz time-domain spectroscopy.
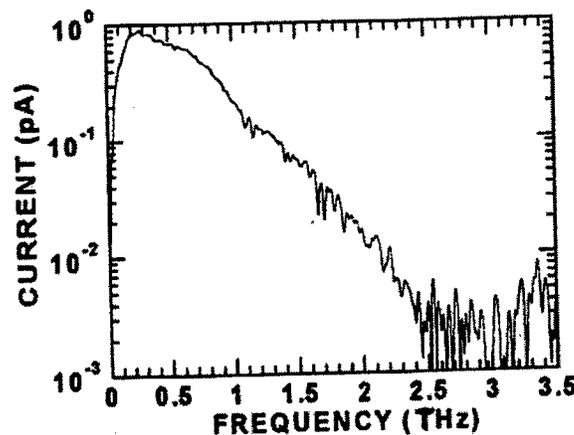

Figure 1(b): Frequency spectrum generated by terahertz time-domain spectroscopy.

2.1 Fabrication of samples

SU-8 is a three-component epoxy based negative photoresist formed by dissolving the resin (SU-8) in an organic solvent γ-butyrolactone (GBL) and finally adding a photo-initiator (triaryl sulphonium) which makes up 10% of the resin mass [6]. The resist can be easily spun using a conventional spin-coater, photolithographically patterned using standard UV equipment and finally annealed to form the resultant cross-linked polymer which is an extremely durable material [7].

In practice, the samples used for this study were fabricated using SU-8 100 resist which has an SU-8:GBL ratio equal to 73%. The host substrates which were used for the fabrication of the samples were silicon wafers having a diameter of 2 inches which had been successively cleaned in acetone, isopropanol and water and dried at 120 $^{\circ}$C for 30 minutes prior to resist deposition. Approximately 5 ml of the resist was delivered onto each wafer in order to obtain full wafer coverage. A 60-second spin was then performed at 400 rpm and 500 rpm in order to obtain two samples having a nominal thickness of 620 μm and 520 μm respectively. A pre-bake at a temperature of 100 °C for 5 hours was used to expel the organic solvents from the resist. The SU-8 layers were then photolithographically patterned into the correct size required for the terahertz time-domain spectroscopic measurements (20 mm × 20 mm). The resultant SU-8 samples were released from the silicon wafers by using a lift-off technique which involved etching the silicon completely away in a potassium hydroxide-water (KOH:H_2O) (50 g:100 ml) etch solution at a temperature of 65 $^{\circ}$C. There is an extremely high etch-selectivity between the materials since cross-linked SU-8 is inert to such hot alkaline solutions. By using this technique we have been able to produce samples with a good degree of parallelism between the front and back surfaces, an essential feature for the terahertz time-domain spectroscopic results which were to be performed.

Figures 2(a) and (b) below show SEM images of typical features which we are able to fashion in this laboratory by using the photoresist SU-8. A high aspect ratio (15:1) and high uniformity in the resist thickness across the wafer have been achieved by careful optimisation of the processing parameters.
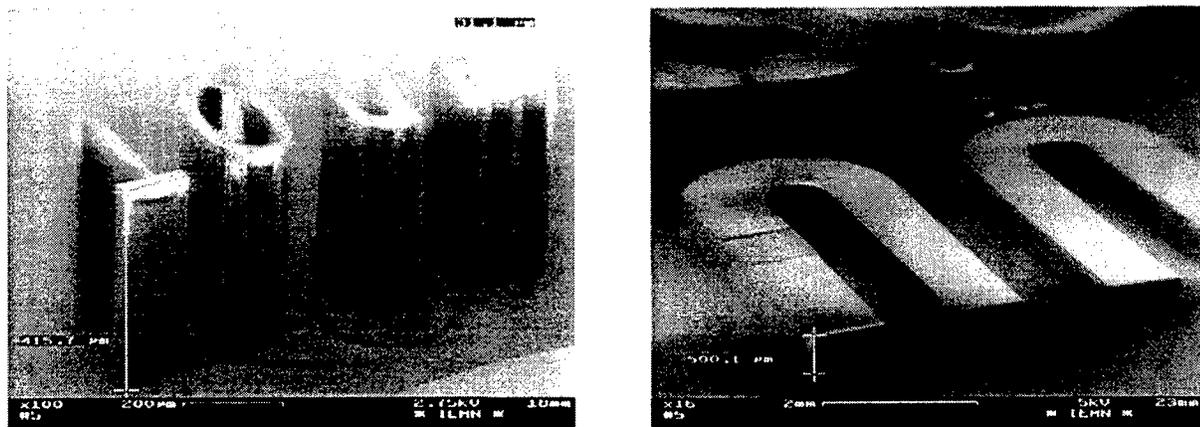
Figure 2(a) and (b) *SEM micrographs of the high aspect ratio features which are attainable using the negative photoresist SU-8.*

3 RESULTS

Figure 3(a) below shows the variations of the refractive index and the absorption coefficient of the SU-8 samples versus frequency. Over the measured frequency range, it can be seen that the refractive index of SU-8 is a relatively flat function of frequency, decreasing from 1.8 to 1.7 over a bandwidth of 0.1-1.6 THz, a variation of ~5%. The value of absorption coefficient for SU-8 is 25 cm^{-1} at 1 THz and is seen to increase with frequency over the measured range in an approximately linear fashion. The value of the absorption coefficient of SU-8 can be compared with values of absorption coefficient for other materials, e.g. SiO_2 glass has a value of 70 cm^{-1} at a measurement frequency of 1 THz [4]. A slight difference between the two samples is observed in the spectroscopic results, this can be attributed to uncertainty in the thickness of the sample [5].

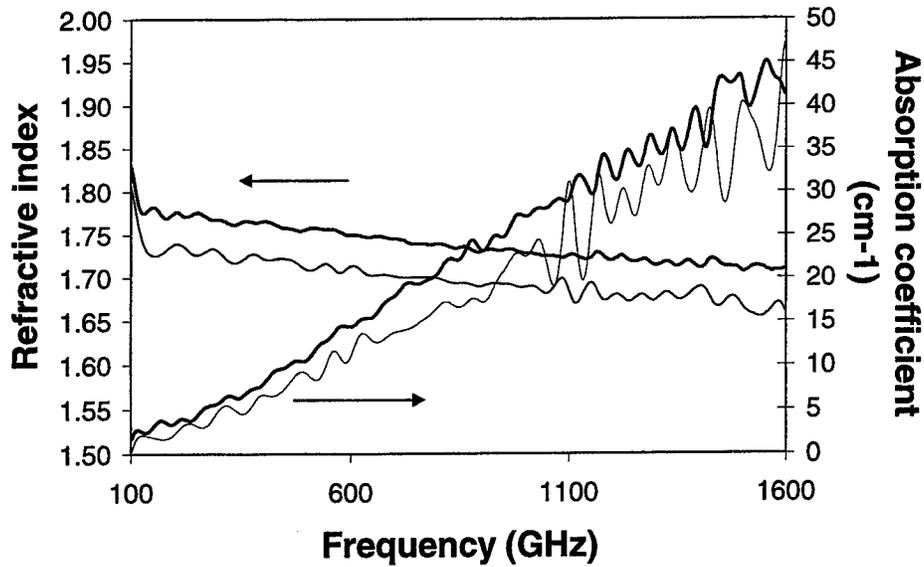**Figure 3(a):** Measured variation of the refractive index n and the absorption coefficient α of SU-8 samples versus frequency, the bold lines are for a sample thickness of 620 μm, the feint lines for 520 μm.

Functions of dielectric constant (ε_r) and dielectric loss tangent (tan(δ)) versus frequency can be extracted from these measured parameters to give meaningful data for future terahertz frequency design. The relationships between the dielectric constant, the dielectric loss tangent and the optical parameters, refractive index and the absorption coefficient, can be found in the literature [8]. The value of dielectric constant is equal to the square of the refractive index and the dielectric loss tangent is a linear function of the absorption coefficient, frequency and refractive index. Figure 3(b) below demonstrates the relationship between the dielectric constant and dielectric loss tangent of SU-8 versus frequency over the measurement range. As with the refractive index, the value of dielectric constant is seen to be rather constant over the large frequency measurement range, e.g. varying from 3.2-2.9 in the range 0.1-1.6 THz. The associated dielectric losses are seen to vary from around 0.04-0.08 over the measured frequency range.
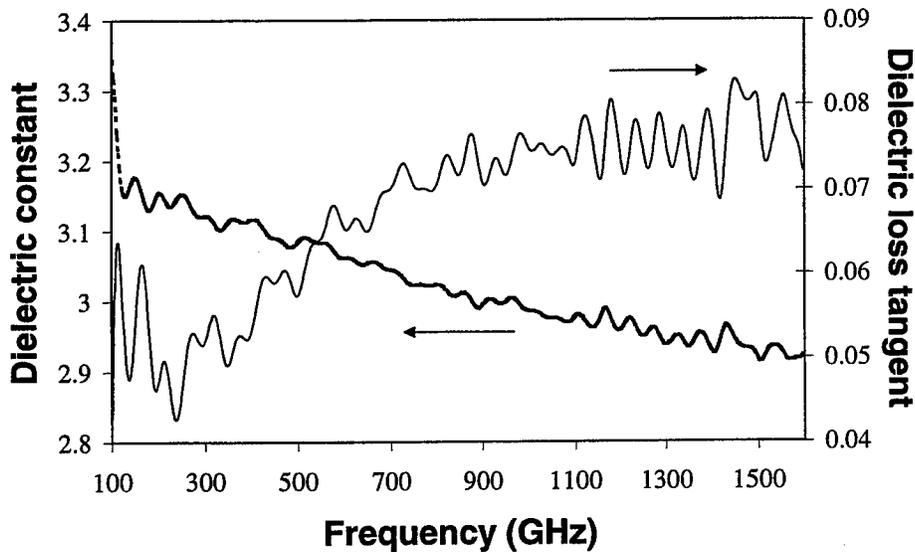

Figure 3(b): Extracted variations of the dielectric constant (ε_r) and the dielectric loss tangent (tan(δ)) of SU-8 samples versus frequency for the sample having a thickness of 620 μm.

4. APPLICATIONS

4.1 Membrane structures

Membrane structures have proved to be very powerful for micromachining applications [9]. For example, filter structures can be realised which have reduced losses due to the removal of the bulk of the underlying medium. Such structures are usually fabricated by removal of underlying semiconductor material on which has been deposited the membrane layer, usually a dielectric e.g. Si_3N_4 on GaAs or SiO_2 on Si. This method usually involves selectively etching, with a suitable etch, a via-hole from the rear surface of the wafer. Thus, membrane structures which are more convenient and less cumbersome to fabricate would be of great use in terahertz design.

Figure 4(a) below shows a novel membrane-like structure which we have been able to produce in our laboratory. The membrane has a thickness of 36 µm and is supported by side features having a thickness of 600 µm also fashioned from SU-8. A *single* deposition of SU-8 100 photoresist was used to form the structure by using a multi-exposure technique during the photolithography. This was achieved using different exposure times in sequence in order to form the side supports and the membrane. The exposure time used to produce the side supports was 1 minute in contrast to a brief 5 second exposure time used in order to form the membrane part of the structure. Such '2½D' photolithographic patterning techniques as this could prove to be very powerful in future terahertz circuit design, and a step towards true 3D patterning of features
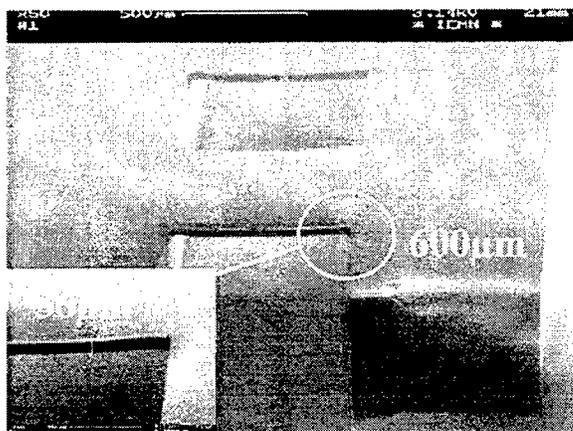

Figure 4(a): Membrane-like structure produced by a multi-exposure photolithographic technique
on a *single* layer of SU-8 photoresist.

4.2 Epitaxial lift-off and transfer techniques

In order to maximise the performance of III-V semiconductors devices at terahertz frequencies it is important to develop a reliable technique for the transfer of such devices/epitaxial layers from the parent III-V substrate onto low loss, lower dielectric constant substrate, e.g. quartz. Such techniques have been developed, usually employing an epoxy resin to bond the pre-fabricated active devices top-side down onto a new host wafer, e.g. the QUID technique [10]. Alternatively, epitaxial lift-off/transfer techniques can be used to transplant an InGaAs/InAlAs epitaxial layer onto a new host substrate prior to device processing. In a step towards this goal, we have been able to use a thin coating of SU-8 as a *photo-patterning* the adhesive layer forming part of an epitaxial layer transfer process which we are currently developing at IEMN. Figure 4(b) below shows an InGaAs/InAlAs epitaxial layer having a thickness of 1.7 µm which has been transferred to a SiO_2 glass substrate having a thickness of 2 mm. The intermediate SU-8 adhesive layer is seen to have a thickness of 4000Å. The SEM shows that the InGaAs/InAlAs epitaxial layer is free from macroscopic defects which can reduce the yield of active devices. Maintaining the quality of the epitaxial layer throughout the process is of vital importance if the resultant active devices are to have good characteristics at low and high frequencies.
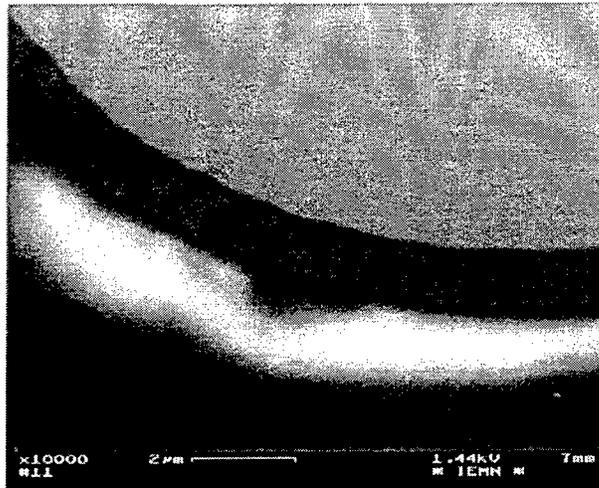
Figure 4(b): InGaAs/InAlAs (1.7μm) epitaxial layer which has been transferred to a SiO₂ host substrate by using a thin (4000Å) intermediate layer of SU-8.

The InP substrate can be totally removed by using a hydrochloric acid/water (HCL:H_2O) etch solution. Such an etch solution has a very high selectivity between InGaAs and InP, an etch rate ratio between the InGaAs and the InP as high as 500 has been observed [11]. By using the process we have been able to successfully transfer a 1 cm² InGaAs/InAlAs epitaxial layer onto a SiO₂ glass host wafer. The intermediate layer of SU-8 was seen to be totally free from defects and bubbles caused by solvent expulsion that can occur during drying. Such defects have been observed to cause damage and drastically reduce yield in the resultant transferred devices [10]. Also, we have demonstrated that by having the power to photo-pattern the SU-8 intermediate layer we have been able to produce a very planar InGaAs/InAlAs/SU-8 layer on the SiO₂ glass host substrate by elimination of resin edge-bead effects. This planarity is an essential feature if further photolithographic steps are to be performed on the epitaxial layer, especially if sub-micron features and air-bridge technology is required for active device formation. We have performed a temperature cycling experiment by using a rapid thermal annealer (RTA) and have demonstrated that the InGaAs/InAlAs/SU-8/SiO₂ system is stable up to ohmic formation temperatures, e.g. 400 °C for 40 seconds. We have also seen that this system is compatible with standard photolithographic processing. In addition to this, an important point to note is that by using phosphide based devices, we eliminate the necessity of the 'etch-stop' layer which has to be employed in order to perform epitaxial lift-off techniques when utilising gallium arsenide based technology [12].

5. CONCLUSION

We have presented the first measurements in the terahertz frequency domain on structures formed from the ultra-thick negative photoresist SU-8. Large area samples having parallel surfaces have been produced by a lift-off technique for the measurements. Terahertz time-domain spectroscopy has been utilised in order to observe the refractive index (n) and absorption coefficient (α) of the material under test in the frequency range 0.1-1.6 THz. From these measured parameters we have extracted the corresponding values of the dielectric constant (ε_r) and dielectric loss tangent (tan(δ)) of SU-8. In addition to this characterisation, we have demonstrated two novel applications of SU-8 for terahertz technology. Firstly, a membrane structure has been fabricated using a single deposition of the photoresist by utilising a multi-exposure photolithographic technique, this is a first step towards true 3D photolithographic microstructuring. Secondly, a thin layer of SU-8 has been used as a photo-patternable adhesive layer as part of an epitaxial lift-off technique. We have fabricated a highly planar InGaAs/InAlAs/SU-8/SiO₂ system which is stable up to ohmic contact formation temperatures for phosphide based devices, opening the way to further device post-processing after epitaxial layer transfer onto lower loss substrates.

6. ACKNOWLEDGEMENTS

7. REFERENCES

1. Mann, C. M.,: 'Fabrication technologies for terahertz waveguide', *Proc. IEEE 6th Int. Conf. on terahertz electronics*, Leeds UK, 1998, pp. 46-49
2. Thorpe, J.R., Steenson, D.P., and Miles, R.E.: 'High frequency transmission line using micromachined polymer dielectric', *Electron. Lett.* 1998, **34**, (12), pp. 1237-1238
3. Melique, X., Mann, C., Mounaix, Thornton, F., Vanbesian, O, J., P., Mollot, and Lippens, D.,: due for publication '5-mW and 5% efficiency 216-GHz InP-based heterostructure barrier varactor tripler', *IEEE Microwave and Guided Wave letts.*, 1998, **8**, (11)
4. Duvillaret, L., Garet, F., and Coutaz, J-L,: 'A reliable method for extraction of material parameters in terahertz time-domain spectroscopy', *IEEE J. Sel. Topics in Quant. Electron.* 1996, **2**, (3), pp. 739-746
5. Duvillaret, L., Garet, F., and Coutaz, J-L.,: 'Highly precise determination of optical constants and sample thickness in terahertz time-domain spectroscopy', Appl. Optics, **38**, (2), pp. 409-412
6. Lee, K.Y., Labianca, N., Rishton, S.A., Zolgharnain, S., Gelorme, J.D., Shaw, J., and Chang, T.H.-P.,: 'Micromachining applications of a high resolution ultra-thick photoresist', *J. Vac. Sci. Technol. B*, 1995, **13**, (6), pp. 3012-3016
7. Lorenz, H., Despont, M., Renaud, P,: 'High aspect ratio, ultra-thick, negative-tone near-UV photoresist and its applications for MEMS', *Sensors and actuators, Part A, Physical.*, 1998, **64**, (1), pp. 33-37
8. Madelung, O., and Hellwege, K.-H., *Landolt-Bornstein new series: Numerical data and functional relationships in science and technology*, 1982, **17**, pp. 10-16
9. Lubecke, M., Mizuno, K., and Rebeiz, G.M.,: 'Micromachining for terahertz applications', IEEE Trans. Microwave Theory and Techniques, **46**, (11), 1998, pp. 1821-1831
10. Basco, R., Prabhu, A., Yngvesson, K.S., and Lau, K.M.,: 'Monolithic integration of a 94 GHz AlGaAs/GaAs 2-DEG mixer on quartz substrate by epitaxial lift-off', IEEE Trans. Electron. Dev. 44, (1), 1997, pp. 11-16
11. Tong, M., Nummila, K., Ketterson, A.A., and Adesida, I.,: 'selective wet etching characteristics of InGaAs/InAlAs/InP',J. Electrochem. Soc. 139, (10), 1992, pp. L91-L93
12. Yablonovitch, E., Gmitter, T., Harbison, J.P., and Bhat. R., 'Extreme selectivity in the lift-off of epitaxial GaAs films', Appl. Phys. Lett. 51, (26), 1987, p2222-2224

Cyclotron resonance of two-dimensional holes in strained multi-quantum-well Ge/GeSi heterostructures

Vladimir Ya.Aleshkin, Vladimir L.Vaks, Dmitrii B.Veksler, Vladimir I.Gavrilenko, Irina V.Erofeeva, Oleg A.Kuznetsov, Mariya D.Moldavskaya

Institute for Physics of Microstructures, Russian Academy of Sciences
GSP-105, 603600, Nizhny Novgorod, Russia

ABSTRACT

Cyclotron resonance of two-dimensional (2D) holes in high-mobility undoped multi-quantum-well Ge/GeSi (111) heterostructure has been studied in both "classical" ($\hbar\omega_c \leq kT$) and quantizing ($\hbar\omega_c \gg kT$) magnetic fields. Effects of hole heating on 2D hole cyclotron resonance has been investigated. The calculations of 2D hole Landau levels in rectangular quantum well have been performed allowing to interpret the evolution of CR spectra in going from "classical" to "quantum" range.

Keywords: cyclotron resonance, strained heterostructure, carrier heating, Landau levels, shallow impurity

INTRODUCTION

The paper presents the results of investigation of two-dimensional (2D) hole energy spectra in strained Ge/GeSi heterostructures by cyclotron resonance technique. Two-dimensional systems based on Si and Ge are being widely investigated during last 20 years because of possibility of their device applications [1, 2]. It was shown that the built-in strain resulted from a mismatch of lattice constants of Si and Ge as well as quantum confinement open wide possibilities for band engineering in SiGe structures. Nowadays 2D electron gas realized in strained Si layers in «Si-rich» Si/SiGe(001) heterostructures is much more investigated then 2D hole gas. One of the reasons is the complicated valence band structure; another is the low mobility of 2D holes suffering from alloy scattering in SiGe quantum wells. Use of Ge/GeSi heterostructures where quantum wells for holes are realized in pure Ge layers can alleviate the last problem. The built-in deformation splits the light and heavy subbands thus providing the 2D holes of the low mass and high mobility. It makes possible to study some subtle effects such as cyclotron resonance. Cyclotron resonance of 2D holes in selectively doped Ge/Ge$_x$Si$_{1-x}$(001) heterostructure ($x = 0.7$, $\mu_{2D} \approx 1.5 \cdot 10^4$ cm^2/V·c, $p_s = (1 \div 2) \cdot 10^{12}$ cm^{-2}) has been studied in «quantum» regime by C.M.Engelhardt et al. [3]. They have observed a few cyclotron resonance lines in absorption spectra. To explain the experiment [3] R.Winkler et al. [4] have performed the calculations of hole Landau levels taking into account effects of built-in deformation and self-consistent confinement potential. These calculations have allowed to interpret the spectral lines observed as transitions between the few lowest nonequidistant hole Landau levels and to explain the magnetic field dependence of the line intensity resulted from the carrier redistribution between Landau levels with magnetic
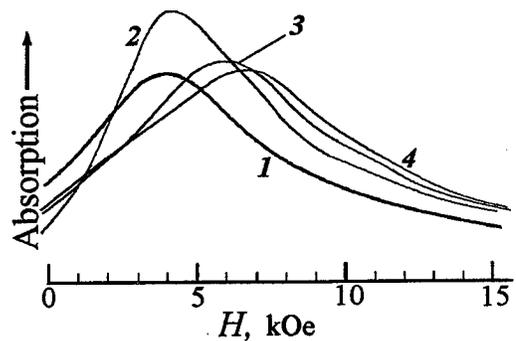
Figure 1. Cyclotron resonance absorption spectra of photoexcited holes in strained undoped Ge/Ge$_{0.88}$Si$_{0.12}$ heterostructure (d$_{Ge}$ = 200 A, d$_{GeSi}$ = 260 A, ε_{Ge} = 2,18·10^{-3}) in d.c.lateral electric fileds:
1) $E = 0$; 2) $E = 10$ V/cm,
3) $E = 16.7$ V/cm, 4) $E = 23.3$ V/cm
$f = 130$ GHz, $T = 4.2$ K.

For further author information -
M.D.M.: Email: mmold@ipm.sci-nnov.ru
        Fax: (8312) 675553

342

Part of the EUROPTO Conference on Terahertz Spectroscopy and Applications II
Munich, Germany • June 1999 SPIE Vol. 3828 • 0277-786X/99/$10.00

field. In our earlier paper [5, 6] cyclotron resonance in undoped strained $Ge/Ge_{1-x}Si_x(111)$ heterostructures ($x = 0.1$, $d_{Ge} \approx$ 200 A, $\mu_{2D} \approx 1.0 \cdot 10^5$ cm^2/V·c) has been studied at $f = 130$ GHz, i.e. in «semiclassilal» case $\hbar\omega_c \approx kT$. The spectral position of CR of 2D photoexcited holes corresponded to the small effective mass value $m = 0.07m_0$ (fig.1, bold curve). This figure is in a good agreement with the calculated mass at the bottom of the lowest hole quantum subband. Application of lateral electric field to the sample has been found to result in the remarkable shift of hole cyclotron resonance line to high magnetic fields (fig1). It has clearly demonstrated the strong nonparabolicity of the lowest hole subband predicted theoretically [7].

In this paper we present the study of «quantum» ($\hbar\omega_c \gg kT$) cyclotron resonance absorption in undoped samples that became possible due to the usage of the powerful radiation sources: backward wave tube oscillators. Investigation of hole heating effects on cyclotron resonance as well as calculations of 2D hole Landau levels in strained $Ge/Ge_{1-x}Si_x(111)$ heterostructure allowed to interpret the experimental spectra and to reveal the cyclotron resonance spectra evolution from «classical» to «quantum» regime.

2. EXPERIMENTAL

Multi-quantum-well $Ge/Ge_{1-x}Si_x$ undoped heterostructure ($x = 0,12$, $d_{Ge} = 200$ A, $d_{GeSi} = 260$ A, number of periods $N = 162$) was grown by CVD technique on Ge(111) substrate. The whole width of the structure exceeds the critical value providing stress relaxation between the substrate and the heterostructure and the elastic biaxial deformation of Ge layers $\varepsilon = 2,18 \cdot 10^{-3}$.

The cyclotron resonance absorption spectra of the heterostructure were measured in Faraday configuration at $T = 4.2$ K. The backward wave tube oscillators were used as radiation sources in frequency range $f = 350 \div 700$ GHz (i.e. corresponding to CR in quantizing magnetic fields). Radiation was guided by a quasioptical system to the sample placed in the liquid helium cryostat in the center of super conducting solenoid. The sample was oriented perpendicular to the magnetic field ($H \parallel [111]$) and to the wave vector of radiation. The holes were excited by GaAs LED illumination ($\lambda \approx 0.9$ μm) that was triggered at $f = 1$ kHz, thus all spectra were measured at modulation of photoexcitation. The excited carriers produced the modulation of microwave radiation passing through the sample that was detected by n-InSb photoresisitor. The lock-in amplifier was used for the recovering of the transmission signal. Strip ohmic contacts were deposited on the sample surface to allow lateral electric field application.

The observed cyclotron resonance absorption spectra at $f = 370$, $f = 600$ and $f = 690$ GHz are shown in fig.2 a, b, c. The lowest curves represent the spectra at zero electric field while the upper ones are obtained at some d.c. voltages applied to the sample. As it is seen there are few features in the spectra. To distinguish these features each curve was resolved into three or four Lorentzians. Their positions are marked on fig.2 a, b, c by arrows. Line 0 has the maximum near $H = 0$ and results probably from non-resonant tails of the other lines 1, 2, 3 (polarization of the radiation was nearly linear). Other lines 1, 2, 3 are evidently resonant. Note that in contrast to the cyclotron resonance in «classical limit» (fig.1) d.c. electric field does not shift the lines but changes the relative magnitudes of lines 2 and 3. The line positions in the wide frequency range $130 \div 700$ GHz are plotted in fig.3. Line 1 is seen to be extrapolated to $E = 0.85$ meV at $H = 0$; hence this line can not be attributed to cyclotron resonance of free carriers. Earlier [8] residual shallow acceptors with small binding energy $E_b \approx 3.7$ meV were revealed in quantum wells of this heterostructure. It is natural to attribute the line 1 to the transitions between excited shallow acceptor or A+-centers states [9] associated with two different Landau levels. The excited states should become populated under LED illumination. Line 2 has constant slope both in «classical» and «quantum» frequency ranges and was shown [5] to result from cyclotron resonance of 2D holes occupying the lowest Landau level. At last, the line 3 becomes discernible only at $f \geq 400$ GHz, its intensity being increased in comparison with that of the line 2 in d.c. fields. At $f = 690$ GHz the intensity of the line 3 if compared with the line 2 becomes smaller than at $f = 600$ GHz but it increases at the application of d.c. field. It indicates that the line 3 is associated with cyclotron transition of 2D hole from higher Landau level: at low frequencies the transitions 2 and 3 have nearly the same energies and are observed as one line; when frequency increases two lines become discernible but the population of the Landau level corresponding to the line 3 decreases.

3. CALCULATIONS AND COMPARISON WITH EXPERIMENT

Calculations of Landau levels of 2D holes in rectangular quantum well in strained Ge/GeSi heterostructures were performed using 4x4 k·p Hamiltonian in axial approximation including strain Hamiltonian [10]. Quantum well depth was
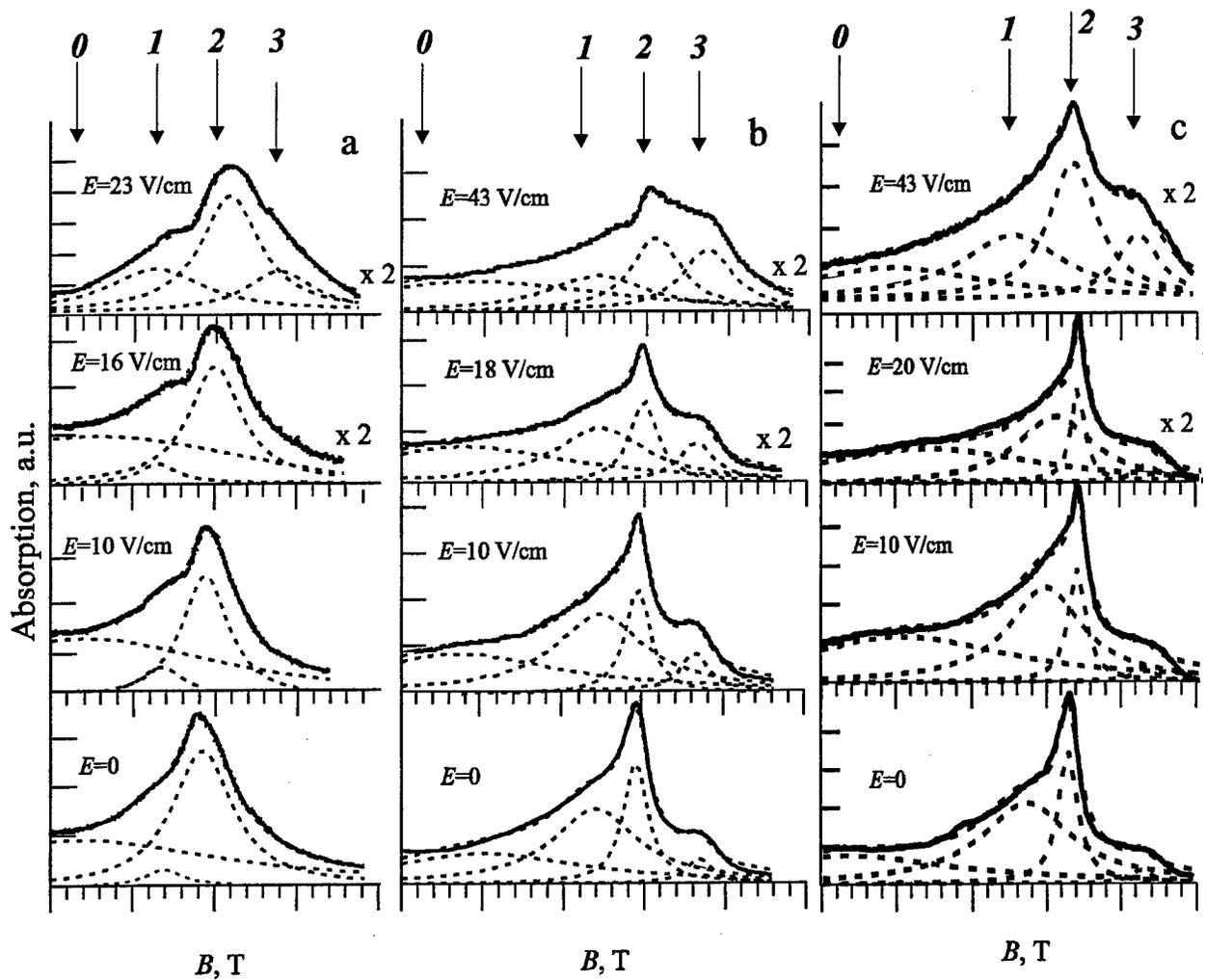
343

Figure 2. Cyclotron resonance absorption spectra of 2D photoexcited holes in Ge/Ge$_{0.88}$Si$_{0.12}$ heterostructure in d.c. lateral electric fields (solid lines). $T = 4.2$ K. a)$f = 370$ GHz, b)$f = 600$ GHz, c)$f = 690$ GHz

Each absorption curve is resolved into three or four Lorentzians (dashed lines). Lorentzians positions are marked by arrows.

obtained using the results of [11]. The symmetry results in the conservation of the total angular momentum projection on the magnetic field direction M_j and of the parity of the wave function with respect to the reflection in the plane z = 0 that goes through the quantum well center perpendicular to the magnetic field direction. Thus each state could be classified by eigenvalue $n = M_j+3/2$ ($n = 0,1,2,...$), and should be either symmetric (s) or antisymmetric (a) with respect to the plane z=0. This notation is used in Fig.4 where fan chart of lower Landau levels is plotted. The index in notation indicates the subband from which the given Landau level originates from. The correction resulted from the nondiagonal warping term in Hamiltonian was found to be 3÷5% for several lowest Landau levels. In Faraday configuration dipole transitions are allowed between two states of the same parity if $\Delta n = \pm 1$. The most of photoexcited holes in our experiments populate the lowest Landau level $0s_1$. The allowed cyclotron resonance transition $0s_1 \rightarrow 1s_1$ corresponds to the cyclotron mass $m_c = 0.064m_0$ that is a little bit less than the observed mass for the line 2 of $0.073m_0$. Similarly the calculated mass for the allowed transition from the next Landau level $3a_1 \rightarrow 4a_1$ $m_c = 0.065m_0$ is less than the observed one for the line 3 ($0.08m_0$). The 7 % discrepancy between the calculated and the observed effective mass values can not be explained by the neglecting the split-off hole subband. This correction seems to be for lowest Landau levels less than 1%. The reasonable origin of the discrepancy may nonrectangular form of the well potential due to Si profile blurring during the growth.

The evolution of the 2D hole cyclotron resonance spectrum with the frequency can be understood from the results presented in fig.4. As it is seen the lower Landau levels are weakly interacting and their energies depend linearly on the magnetic field up to 30 kOe. It explains why the mass values corresponding to the transitions 2 and 3 remain constant in "quantum" frequency range. In contrast the upper Landau levels become nonequidistant at low magnetic fields and their energies depend nonlinearly on the magnetic field. This results in the shift of the "classical" cyclotron resonance line to higher magnetic fields at hole heating when the excited levels become populated (fig.1)

Thus cyclotron resonance of 2D hole in undoped strained multi-quantum-well Ge/GeSi (111) heterostructures were investigated in wide frequency range 130÷700 GHz. Effects of built-in deformation and confinement on 2D hole energy spectra were demonstrated. Calculations of 2D hole Landau levels and investigation of hole heating allowed to interpret the observed evolution of the cyclotron resonance spectrum from "classical" to "quantum" range.
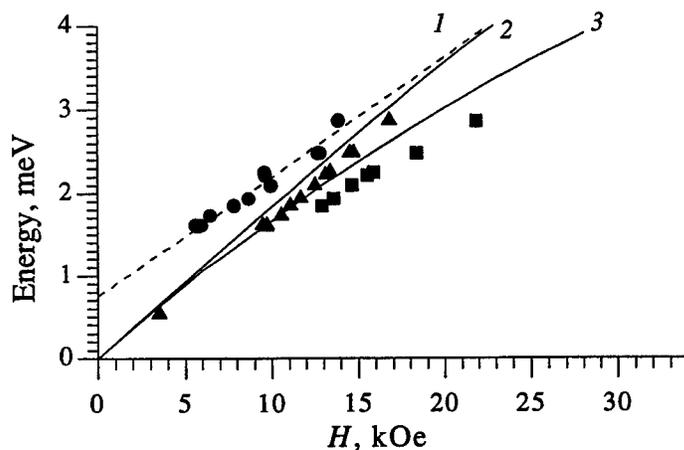
Figure3. Spectral positions of the observed absorption lines *1, 2, 3* (see Fig.2) versus magnetic field (the dots). The dashed line shows the extrapolation of the line 1 to $H = 0$. The solid lines show calculations of the hole cyclotron transitions corresponded to the observed lines *2, 3*.

Figure 4. Fan chart of calculated Landau levels in rectangular quantum well in $Ge/Ge_{0.88}Si_{0.12}$ heterostructure. Arrows *2, 3* correspond to the lines *2, 3* on fig.3.

4. ACKNOLEDGEMENTS

5. REFERENCES

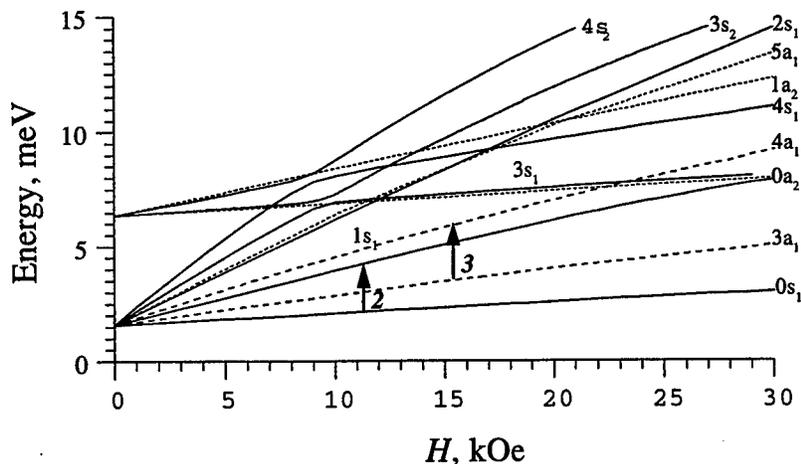1. S.C.Jain, W.Hayes. "Structure, properties and applications of GeSi strained layers and superlattices", Semicond. Sci. and Technol., **6,** pp.547-576, 1991

2. E.Kasper and F.Schaffler. "Group IV Compounds", In Semiconductors and Semimetals, Academic Press, Boston, ed. by P.Pearsell, **33,** pp.233-307, 1991

3. C.M.Engelhardt, D.Tobben, M.Ashauer et al., "High mobility 2D hole gases in strained Ge channels on Si substrates studied by magnetotransport and cyclotron resonance", Solid State Electron, **37,** pp.949-952, 1994.

4. R.Winkler, M.Merkler, T.Darnhofer and U.Rossler, "Theory for cyclotron resonance of holes in strained asymmetric Ge/SiGe quantum wells", Phys.Rev.B, **53,** pp.10858-10864, 1996

5. V.I.Gavrilenko, I.N.Kozlov, O.A.Kuznetsov et al. "Cyclotron resonance of charge carriers in strained Ge/GeSi heterostructures", JETP Lett., **59,** pp.327-330, 1994

6. V.Ya.Aleshkin, N.E.Bekin, I.V.Erofeeva et al., "Cyclotron resonance investigation of multi-quantum-well heterostructures Ge/GeSi", Extended Abstracts of the 1995 Int.Conference on Solid State Devices and Materials, Osaka, Japan, pp.917-919, 1995

7. V.Ya.Aleshkin and N.A.Bekin, "Electron and hole spectra and selection rules for optical transitions in Ge/GeSi heterostructures", Semiconductors, **31,** pp.235-245, 1997

8. V.I.Gavrilenko, I.V.Erofeeva, A.L.Korotkov et al., " Shallow accpetors in Ge/GeSi strained multilayer heterostructures with quantum wells", JETP Lett. , **65,** pp.194-198, 1997

9. S.Holmes, J.P.-Cheng, B.D.McCombe et al., "Occupancy of shallow donor impurities in quasi-two-dimensional systems: D^0 and D^- states", Phys.Rev.Lett., **69,** pp. 2571-2574, 1992

10. Bir and Pikus, "Symmetry and Strain-Induced Effects in Semiconductors",Wiley, New York, 1974

11. C.G.Van de Walle and R.M.Martin, "Theoretical calculation of heterojunction discontinuities in the Si/Ge system", Phys.Rev B, **34,** pp. 5621-5634, 1986

Beam-mode analysis of a slotted horn antenna suitable for micro-machined rectangular waveguide

Brian M. Towlson and John W. Bowen

Department of Cybernetics, The University of Reading,
Whiteknights, Reading, Berkshire, RG6 6AY, UK

ABSTRACT

This paper describes a Gauss-Hermite beam-mode analysis of the far-field radiation pattern of a sectoral horn antenna with a tapered slot in its upper broadwall. This type of antenna is suitable for integration with micro-machined rectangular waveguide, examples having been fabricated for frequencies as high as 1.6 THz. Microwave scale model radiation pattern measurements are presented. A procedure for carrying out a beam-mode analysis from the measured far-field pattern rather than the usual case of a theoretical near-field distribution is described. The beam-mode analysis technique is of general applicability to all types of antenna.

Keywords: antennas, beam-mode analysis, micro-machined waveguide, quasi-optics, terahertz

1. INTRODUCTION

One of the factors that has hampered the widespread introduction of systems operating at frequencies near 1 THz has been the lack of a relatively inexpensive and reliable technique for producing integrated subsystems. While it is still possible to use conventional machining and fabrication techniques to make hollow metal waveguide components that give good performance at these frequencies, the tolerances required make them prohibitively expensive for all but the most specialized applications. This has lead to the exploration of the use of various micro-machining techniques for waveguide manufacture which have the further advantage of allowing monolithic device integration. If such components are to be of general use, they require monolithically fabricated antennas to couple the guided radiation to beams propagating in free space. It is often necessary to couple these free space beams to quasi-optical systems, which employ reflecting or refracting optics to control the diffractive spreading of the beam. For the purpose of understanding how best to couple radiation between antennas and quasi-optical systems, it is convenient to analyse the beam launched by an antenna into a superposition of orthonormal beam-modes, each of which maintains a well-defined form as it propagates. The total field in any beam cross-section then being given by the coherent sum of the beam-mode fields in that cross-section.

This paper carries out such a beam-mode analysis for a sectoral horn antenna with a tapered slot in its upper broadwall. The antenna is suitable for monolithic integration with micro-machined waveguide and examples have been fabricated for frequencies as high as 1.6 THz. The beam-mode analysis technique described here is unusual in that its starting point is the measured far-field radiation pattern of the antenna. Beam-mode analysis has hitherto been confined to analysing the beams launched by antennas for which a theoretically known analytical expression for the field in the antenna's aperture plane exists[1,2,3,4,5]. This approach could not be taken here, as this antenna has no clearly defined aperture plane and there is no analytical expression for its near-field. In order for the technique to be successful, it is necessary to measure both the amplitude and phase far-field radiation patterns. At present, this is most easily achieved with microwave scale models of the terahertz antennas and the results presented here are based on X-band model measurements.

2. MICRO-MACHINING

The main steps in the micro-machined waveguide fabrication process[6] are illustrated in Fig. 1. After metallising the upper surface of a semiconductor wafer substrate, a layer of positive photo-resist is spun on to a thickness which defines the ultimate height of the waveguides (Fig. 1(a)). Areas of the resist are exposed to ultra-violet light through a mask and developed away to leave raised areas which define the interior walls of the waveguides (Fig. 1(b)). An even layer of metal is evaporated over the whole surface of the wafer and this is strengthened by electro-plating further metal (Fig. 1(c)). Finally, the remaining photo-resist is dissolved to leave hollow metal rectangular waveguide circuits on the surface of the wafer (Fig. 1(d)). Additional processing steps can be used to define solid-state devices in the semiconductor substrate and to grow contact pillars on them.
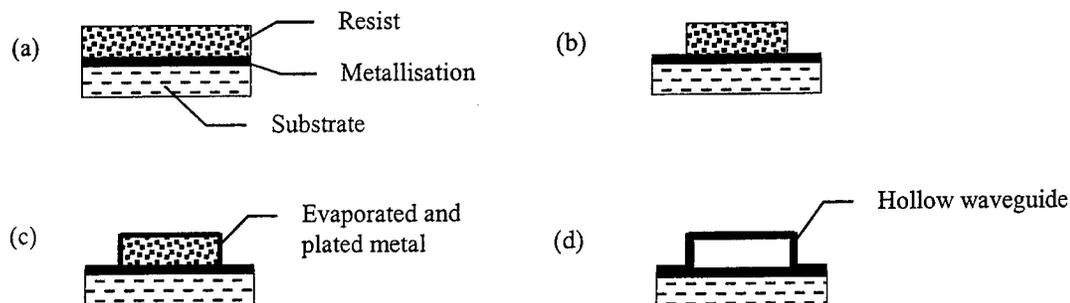
Part of the EUROPTO Conference on Terahertz Spectroscopy and Applications II
Munich, Germany • June 1999 SPIE Vol. 3828 • 0277-786X/99/$10.00

347

Figure 1. *Micro-machined waveguide fabrication process. (Transverse cross-section through waveguide).*

3. ANTENNA

The height of the waveguide structures produced by the micro-machining process is limited by the maximum photo-resist thickness that can be used. A consequence of this is that, while it is possible to taper the width of the waveguides to any desired dimension, it is not possible to taper them to increase their height. Thus, it is not possible to form a structure approximating a horn antenna which tapers in both dimensions. However, H-plane sectoral horns, just tapering in width across the substrate, can be fabricated. While such horns have an acceptable beam-width in the H-plane, the narrow confinement of the electric field in the aperture above the substrate leads to an unacceptably wide E-plane pattern. To improve on the E-plane pattern a new antenna consisting of an H-plane sectoral horn with a tapered slot in its upper broadwall was devised (Fig. 2). The slot allows the E-plane electric field at the antenna to extend to a greater height, outside the confines of the waveguide, before it is radiated. The antenna is directly compatible with the micro-machining process. The slot is formed after the metal layer has been evaporated, as in Fig. 1(c). A further layer of photo-resist is spun over the structure, exposed through a mask and developed, leaving the metal in the slot area uncovered so that it can be removed by etching. Examples of this type of antenna have been fabricated and characterised at frequencies between 180 GHz[7] and 1.6 THz[8].
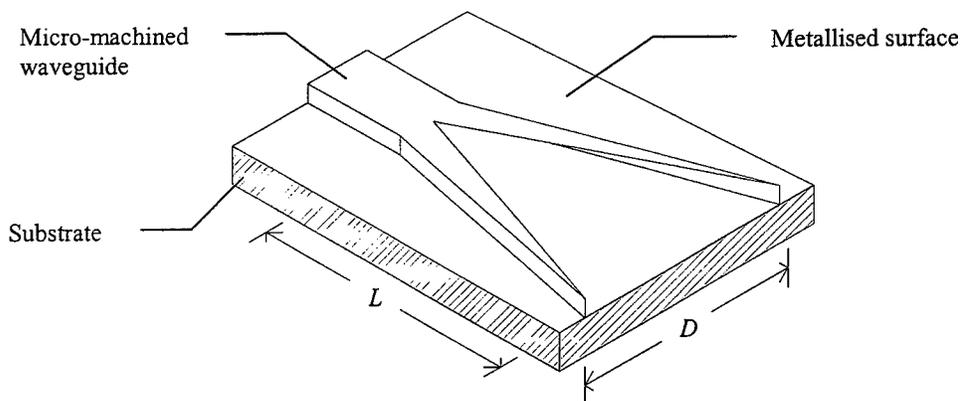
Figure 2. *Micro-machined antenna.*

4. SCALE MODEL MEASUREMENTS

The properties of the antenna were explored with the aid of an X-band scale model made from brass sheet. The dimensions, with reference to Fig. 2, were $D = 109$ mm, $L = 125$ mm, while the structure had the same height as full-height waveguide. Co- and cross-polar antenna pattern measurements were made at 8, 10 and 12 GHz for a range of phi-cuts. The E- and H-plane co-polar amplitude patterns are shown in Fig. 3. Phase patterns were also recorded. The addition of a ground plane

outside the confines of the antenna was found to have little effect. The maximum cross-polar levels were at −8 dB. The main lobe in the E-plane was found to be elevated at 20° above the substrate plane.

(a) 8GHz, H-plane

(b) 8GHz, E-plane

(c) 10GHz, H-plane

(d) 10GHz, E-plane

(e) 12GHz, H-plane
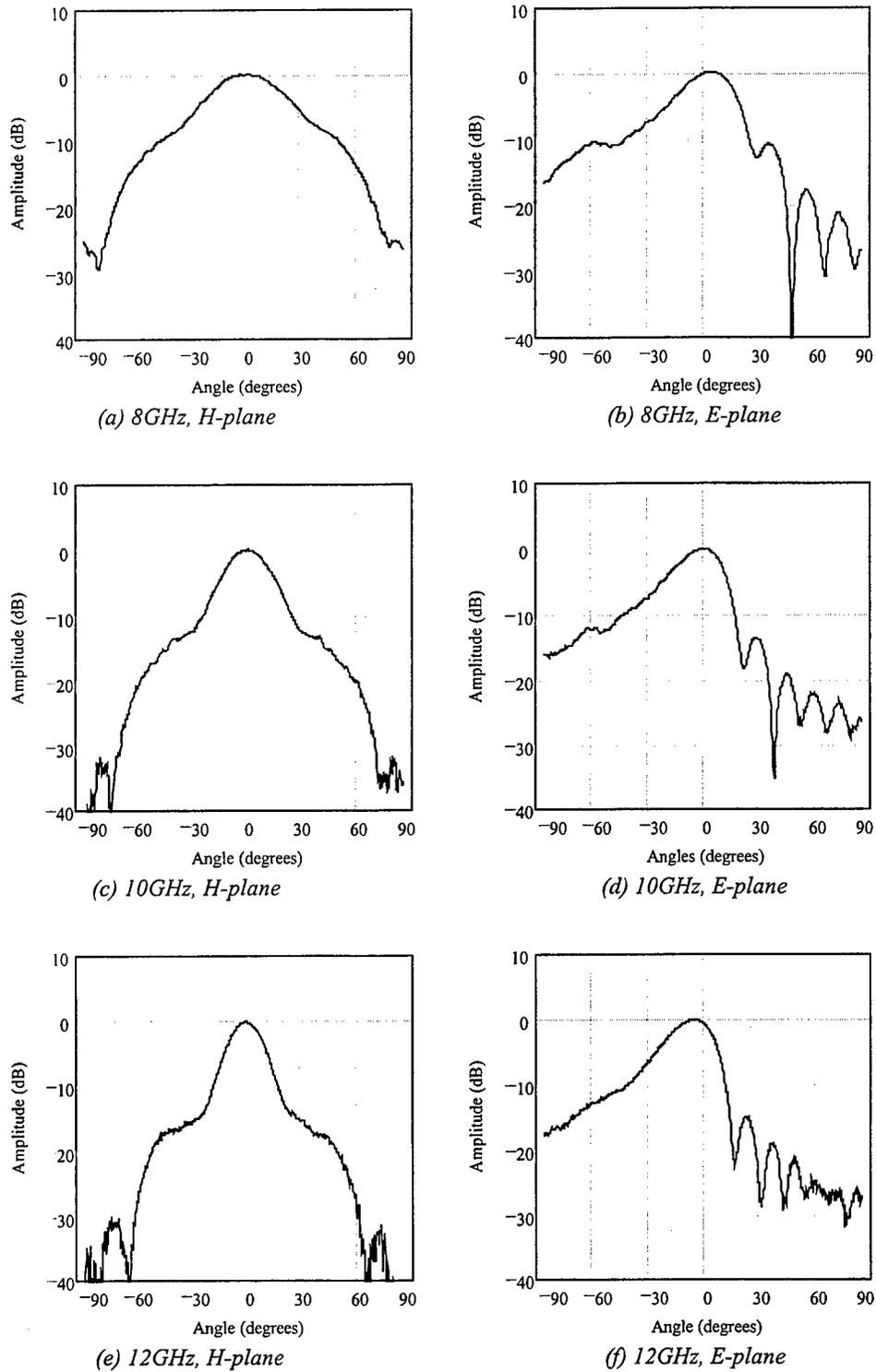
(f) 12GHz, E-plane

Figure 3. *Measured co-polar antenna patterns*

5. BEAM-MODE ANALYSIS

The field in any cross-sectional plane through the beam could be represented by a superposition of any set of orthonormal functions. However, the Gauss-Hermite functions are particularly useful, as, subject to a paraxial approximation, each gives rise to a beam-mode which retains a scaled but characteristic cross-sectional amplitude and phase distribution as it propagates[9].

The beam-field corresponding to the Gauss-Hermite beam-mode with mode numbers m and n takes the following form:

$$\psi_{mn}(x,y,z)e^{i\omega t} = u_{mn}(x,y,z)e^{-i(kz-\omega t)} \tag{1}$$

where

$$u_{mn}(x,y,z) = \left(\frac{1}{2^{m+n}m!n!}\right)^{\frac{1}{2}} \cdot H_m\left(\sqrt{2}\,\frac{x}{w_x}\right) \cdot H_n\left(\sqrt{2}\,\frac{y}{w_y}\right) \cdot \exp i\left(m\phi_x + n\phi_y\right) \cdot u_{00}(x,y,z) \tag{2}$$

and

$$u_{00}(x,y,z) = \left(\frac{2}{\pi}\right)^{\frac{1}{2}} \frac{1}{w_x^{1/2}w_y^{1/2}} \exp-\left(\frac{x^2}{w_x^2} + \frac{y^2}{w_y^2}\right) \cdot \exp-i\left(\frac{kx^2}{2R_x} + \frac{ky^2}{2R_y} - \frac{\phi_x}{2} - \frac{\phi_y}{2} - \phi_0\right) \tag{3}$$

Here, the beam is taken to be propagating along the z-axis of a Cartesian co-ordinate system, $H_N(X)$ is the Hermite polynomial of X of mode or order number N, ω is angular frequency, k is the magnitude of the wave-vector, t is time, and ϕ_0 is an arbitrary phase angle. The beam-mode is characterized by the two sets of parameters w_x, R_x, ϕ_x and w_y, R_y, ϕ_y; the z-dependence of each set being described by :

$$\hat{w}^2 = \hat{w}_0^2\left(1 + \hat{z}^2\right) \tag{4}$$

$$\hat{R} = \hat{z} + \frac{1}{\hat{z}} \tag{5}$$

$$\phi = \tan^{-1}\hat{z} = \sin^{-1}\left(1 + \hat{z}^{-2}\right)^{-\frac{1}{2}} \tag{6}$$

The cap ^ indicates division by $kw_0^2/2$ to produce a reduced, dimensionless quantity; $\hat{z}$ being referenced to the position $z = z_0$, at which the beam has its narrowest width (the beam-waist w_0), thus

$$\hat{z} = 2(z - z_0)/kw_0^2 \tag{7}$$

This description allows for astigmatic beams, each set of parameters having its corresponding beam-waist w_{0x} and w_{0y}, located at z_{0x} and z_{0y} respectively. The parameter w represents the width of the field distribution in the beam-mode, R is the radius of curvature of the spherical phase-fronts in the beam-mode, and ϕ represents an on-axis phase factor describing the slippage of the beam-mode's phase relative to a plane-wave. Equation (3) for $u_{00}(x,y,z)$ describes the fundamental Gaussian beam-mode, which has a Gaussian transverse amplitude distribution of $1/e$ amplitude half-width w.

Because the Gauss-Hermite functions form a complete orthonormal set, any arbitrary function, $u_A(x,y;z)$, such as a measured antenna beam pattern, can be described as a linear combination of these functions, $u_{mn}(x,y;z)$, thus

$$u_A(x,y;z) = \sum_{m,n} C_{mn} . u_{mn}(x,y;z) \tag{8}$$

where the weighting factors C_{mn} may be complex. Further, these functions are orthonormal to each other, hence the coefficients of each have unique values for a particular u_A, and can be determined by evaluation of the integral, over any z cross section, of the product of the conjugate of that function with the beam under consideration

$$C_{mn} = \iint u_{mn}^*(x, y; z) u_A(x, y; z) dxdy \qquad (9)$$

However, in practice, the set of beam-modes u_{mn} involves an open choice of values for the w, R, and ϕ parameters, in both the x and y directions. Though this choice does not affect the completeness and orthogonality of the set, it will affect the resulting values of C_{mn}, and so there may be a preferred choice. For example, if the beam to be fitted has an axially symmetric Gaussian distribution of amplitude, of width parameter w_G and uniform phase, it may be fitted exactly by a single fundamental mode of $w = w_G$ and $R = \infty$, for both the x and y directions. Different choices of w and R would be possible, but would require an infinity of modes for an exact fit, since Gauss-Hermite functions are not orthogonal to a Gaussian function of different parameter values.

A common choice of parameter values for the beam-mode set is one that minimizes the number of modes with coefficients of significant magnitude. This allows a good fit to u_A with a finite, and minimal, number of beam-modes, allowing clear and simple description of the field, as well as computational economy. Similarly, a choice can be made that allows a best fit to the field with a given number, say ten, of beam-modes. For coupling to quasi-optical systems (in which a single moded beam provides the usual form of input), another popular criterion is to choose parameter values that maximize the power contained within the fundamental mode. The fraction η_{00} of the total beam power carried by the fundamental Gaussian mode is given by

$$\eta_{00} = \frac{\iint C_{00}^2 u_{00}^2 . dxdy}{\iint |\psi|^2 . dxdy} \qquad (10)$$

where the denominator represents the total power contained in the beam, and both integrals are over the whole plane.

Since antenna pattern measurements are almost exclusively taken in the form of far-field angular variation of amplitude and phase, the first stage of the analysis must be to convert this to some equivalent E-field distribution over a plane in the near-field.

It can be shown that, in the far-field, the field distribution $\psi(\rho, \theta, \phi)$ expressed in polar co-ordinates approximates to[10]

$$\psi(\rho, \theta, \phi) \rightarrow i.2\pi k^2 . \cos\theta . A(\theta, \phi) \left(\frac{\exp - ik\rho}{k\rho} \right) \qquad (11)$$

where ρ is the downbeam distance, assumed to be much greater than the wavenumber k, and $A(\theta, \phi)$ is known as the angular spectrum of the beam. This latter is more usually expressed in Cartesian co-ordinates, $A(k_x, k_y)$, and describes the complex amplitude of the corresponding plane wave component of the beam with direction vectors k_x, k_y. From consideration of the wave equation, $A(k_x, k_y)$ can be seen to be related to the near-field beam distribution, $\psi(x, y; z=0)$, by

$$A(k_x, k_y) = \frac{1}{4\pi} . \iint \psi(x, y; z = 0) e^{i(k_x x + k_y y)} . dxdy \qquad (12)$$

which can be seen to be an inverse Fourier transform relationship[11]. Thus $A(k_x, k_y)$ may be considered as the spatial frequency spectrum of $\psi(x, y; z=0)$. From inverting the two above equations, therefore, an expression for the E-field distribution in the origin plane may be found, and it is on this distribution that beam-mode analysis may be performed.

For the mode analysis itself, firstly a value for the beamwidth parameter w must be chosen. As discussed previously, this choice is entirely arbitrary, so that some optimizing criterion should be applied for the results to be genuinely useful. In this

case, since the main concern is to couple to quasi-optical systems, that of maximum fundamental mode power is the most logical choice.

For this part of the procedure, the amplitude distribution of the E-field is taken, multiplied by each Gauss-Hermite mode in turn, and integrated over the whole available cross-section, thus exploiting the orthonormal property of the functions. The result of this integration is the modulus of the coefficient of that mode, with the chosen width parameter, in the E-field data. The relative power carried by each mode is then given by the square of its coefficient, and the total power of the beam by the integral of the field squared, so that the fractional power in each mode is given by the ratio of these quantities. The optimum width parameter is thus found by evaluating this ratio for the fundamental mode over a range of values of w, until a maximum is found.

Using this optimum w, the integration procedure is then repeated, but this time including both the amplitude and phase of the E-field, so that the result is the set of complex mode coefficients, C_{mn}. For clarity, these coefficients are normalized relative to the fundamental, dividing each by C_{00}.

6. RESULTS

The above procedure was used to analyse the principal planes of the 8 GHz, 10 GHz, and 12 GHz measurements described previously for modes up to $n = 20$, and the resulting coefficients for 10 GHz were used to reconstruct a theoretical far-field pattern, to check the accuracy of the analysis. The results of this reconstruction, in comparison to the original measurements, are given in Figures 5 and 6, and show that the described method is accurate out to about 60°, although some of the smaller ripples in the E-plane are not resolved. Resolution and range could be improved beyond that presently available by the use of greater range and finer resolution in the discrete Fourier transforms used, and by the correspondingly larger number of modes which it would then become feasible to consider. However, this would represent a considerable increase in the processing time and power required.
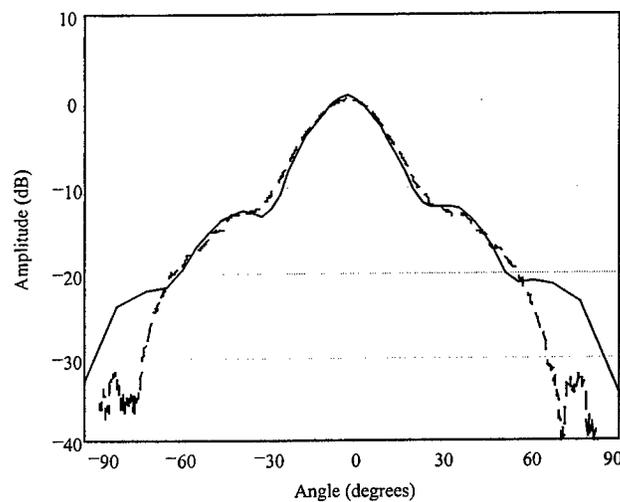

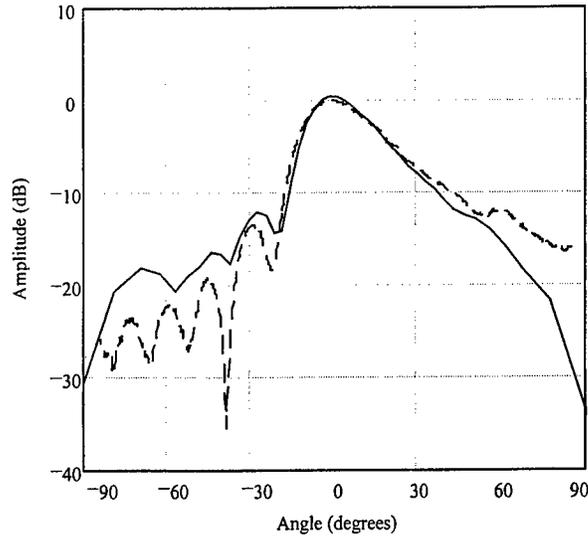Fig5. *10GHz H-plane, measured (dashed) and synthesized (solid)*

Figure 6. *10GHz E-plane, measured (dashed) and synthesized) (solid)*

A graphical summary of the results for all three frequencies is given in Fig 7, in terms of the magnitudes of the coefficients for each mode plotted on a logarithmic scale. The full results for 10 GHz, with both the magnitude and phase of the mode coefficients, are given in Table I. The optimum beamwidths chosen for each plane, and the percentage of power contained within the fundamental mode for these values, are given in Table II. Also included is the theoretical percentage of power that would be contained within a two-dimensional astigmatic fundamental mode (i.e. the u_{00} mode), calculated from the product of the E- and H-plane u_0 mode fractional powers. From these, it can be seen that at the design frequency, 10 GHz, E- and H-plane beamwidths are approximately equal, and that with increasing frequency, the optimum H-plane beamwidth increases, whilst the optimum E-plane width decreases. Note that although operation at 12 GHz appears to give a superior antenna pattern, the beam is much less Gaussian in the E-plane, leading to a lower overall fundamental mode power.
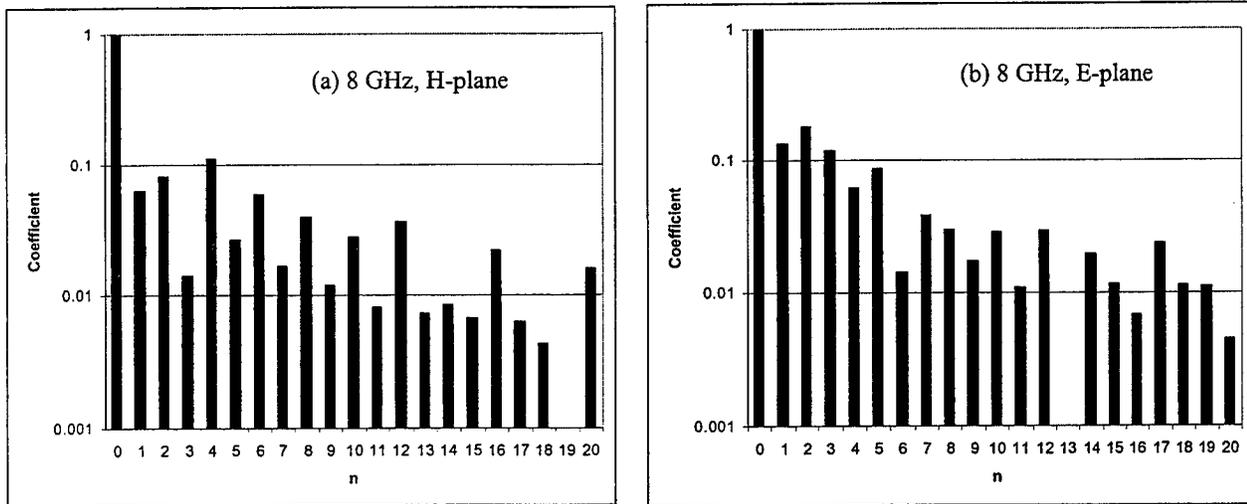

Figure 7. Magnitudes of beam-mode coefficients for mode number n (continued over page).
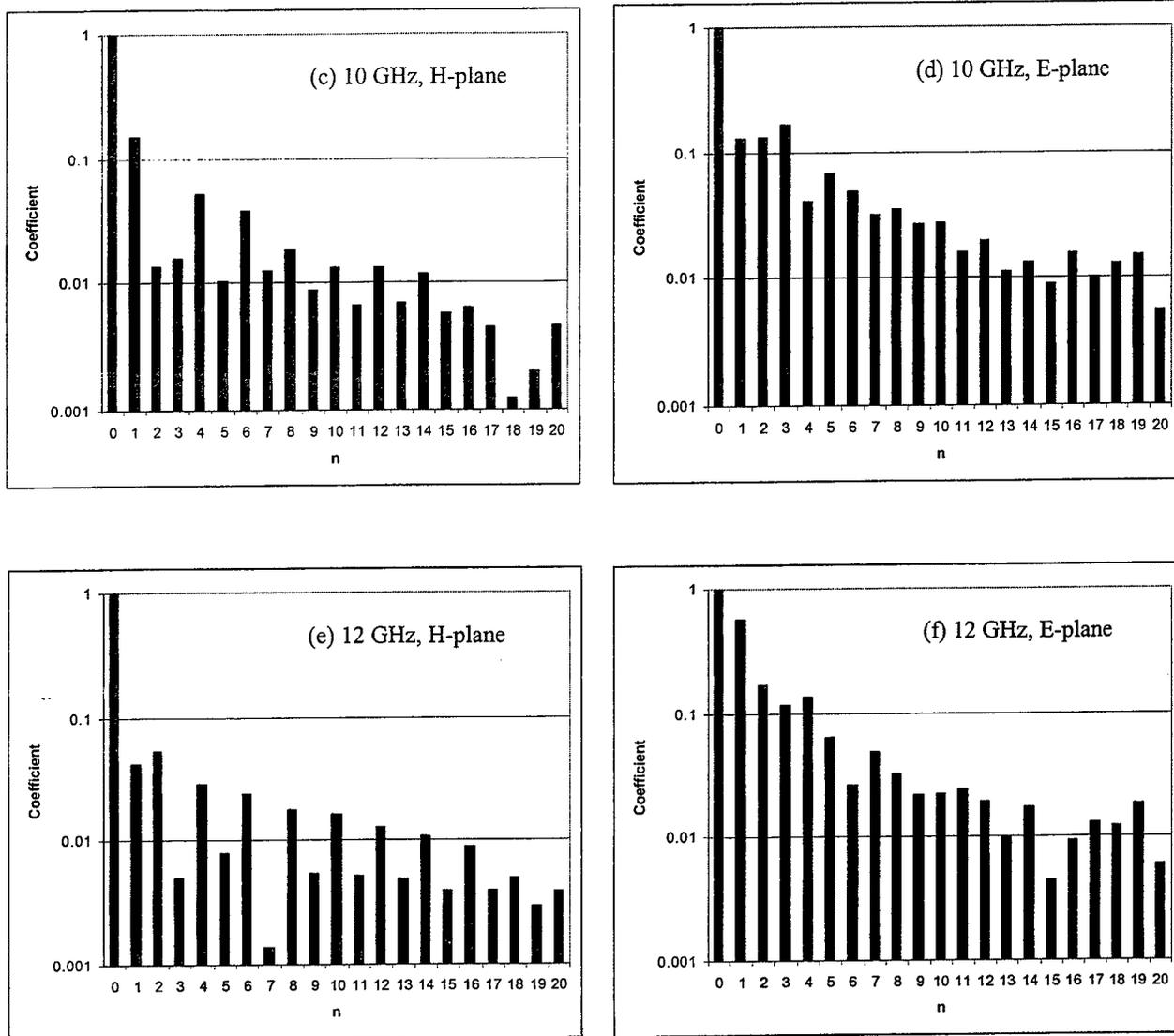
Figure 7. Magnitudes of beam-mode coefficients for mode number n (continued from previous page).

7. DISCUSSION

This paper has presented preliminary results of a beam-mode analysis of a novel antenna suitable for monolithic fabrication using micro-machining techniques. The antenna has 3 dB beam-widths of about 30° in the E- and H-planes, with sidelobes and cross-polar levels below −12 dB and −8 dB respectively. It has been shown that 83.7% of the co-polar power is in a fundamental Gaussian beam-mode. This compares favourably with the corrugated horn, in which 98% of the power is carried in a fundamental beam-mode[1], the hexagonal horn, with 86% in the fundamental mode[3], and the diagonal horn, for which the figure is 84%[4].

The beam-mode analysis technique has been developed to take measured far-field antenna patterns (both amplitude and phase are required) and return a set of constituent Gauss-Hermite beam-mode coefficient amplitudes and phases. It gives the optimum beamwidth w for maximum coupling to a fundamental Gaussian beam-mode and an estimate of the proportion of the beam power that is contained within the fundamental mode. At present the beam-mode analysis software works in one dimension only, but extension to two dimensions is possible and planned, given sufficient computing power. Future work

will be directed towards interpreting the phase term, to allow determination of the phase-front radius of curvature, and hence the distance from the origin plane (that containing the centre of rotation of the test antenna) to the beam-waist location.

E-plane			H-plane		
n	C_n/C_0	ϕ_n/radians	m	C_m/C_0	ϕ_m/radians
0	1	0.480247	0	1	0.493025
1	0.130914	2.21826	1	0.151572	-1.8745
2	0.13308	-1.37411	2	0.0135094	-1.98053
3	0.169338	-0.64896	3	0.0157304	1.92694
4	0.0406663	1.43679	4	0.0512979	1.69454
5	0.0685385	-2.85263	5	0.0102604	-0.393332
6	0.0495264	$-\pi/2$	6	0.037599	-0.332572
7	0.0313954	0.0852643	7	0.0124508	π
8	0.0347832	2.07883	8	0.0180998	-2.55819
9	0.0266603	-2.73206	9	0.00878356	1.06804
10	0.0275616	-1.17138	10	0.0131925	1.45059
11	0.0158033	1.03328	11	0.00657027	-1.0805
12	0.0196471	2.49113	12	0.0132072	-0.635746
13	0.0110288	-2.88985	13	0.00689672	-2.87263
14	0.0131154	-0.839602	14	0.0116836	-2.24627
15	0.00872837	1.32953	15	0.0056798	1.84271
16	0.0155907	2.16369	16	0.00636919	2.90613
17	0.0100894	0.586469	17	0.00439873	0.452823
18	0.012847	-0.664033	18	0.0012461	2.35634
19	0.0148933	-2.19207	19	0.00199762	-1.1969
20	0.0054728	2.35619	20	0.00452317	$-\pi/2$

Table I: *Normalized mode coefficients and relative phases for 10GHz, E- and H-planes.*

	Beamwidth/m		Fundamental mode power		
Frequency	H-plane	E-plane	H-plane	E-plane	Total
8GHz	0.01019	0.01379	96.0%	91.5%	87.8%
10GHz	0.012025	0.01220475	91.0%	92.0%	83.7%
12GHz	0.01327	0.0101	99.2%	70.5%	69.9%

Table II: *Optimum beamwidths and fundamental mode powers.*

8. ACKNOWLEDGEMENTS

9. REFERENCES

1. R.J. Wylde , "Millimetre-wave Gaussian beam-mode optics and corrugated feed horns", *IEE Proceedings – H: Microwaves, Antennas and Propagation*, **131**, pp. 258-62, 1984.

2. R.J. Wylde, and D.H. Martin, "Gaussian beam-mode analysis and phase-centers of corrugated feed horns", *IEEE Transactions on Microwave Theory and Techniques*, **41**, pp. 1691-9, 1993.

3. T. Shen, W. Dou, and Z. Sun, "Asymmetrical Gauss-Hermite beam-mode analysis of the hexagonal horn", *IEEE Transactions on Microwave Theory and Techniques*, **46**, pp. 1444-51, 1998.

4. S. Withington, and J.A. Murphy, "Analysis of diagonal horns through Gaussian-Hermite modes", *IEEE Transactions on Antennas and Propagation*, **40**, pp. 198-206, 1992.

5. J.A. Murphy, and R. Padman, "Phase centers of horn antennas using Gaussian beam mode analysis", *IEEE Transactions on Antennas and Propagation*, **38**, p1306-9, 1990.

6. C.E Collins, J.W. Digby, R.D. Pollard, R.E. Miles, G.M. Parkhurst, J.M. Chamberlain, D.P. Steenson, N.J. Cronin, L.S. Karatzas, and J.W. Bowen, "W-band measurements of 100 µm height micro-machined air-filled rectangular waveguides", *IEEE MTT-S International Microwave Symposium Digest,* Denver, Colorado, USA, pp. 1439–1442, 1997.

7. J.W. Digby, C.E. McIntosh, G.M. Parkhurst, B.M. Towlson, S. Hadjiloucas, J.M. Chamberlain, R.D. Pollard, R.E. Miles, D.P. Steenson, J.W. Bowen, L.S. Karatzas, D.A. Brown, N.J. Cronin, and S.R. Davies, "Fabrication and characterisation of micro-machined rectangular waveguide components for use at millimetre wave and terahertz frequencies", *IEEE Transactions on Microwave Theory and Techniques*, under review.

8. J.W. Bowen, S.T.G. Wootton, S. Hadjiloucas, B.M. Towlson, L.S. Karatzas, N.J. Cronin, S.R. Davies, C.E. Collins, J.M. Chamberlain, R.E. Miles, and R.D. Pollard, "Micro-machined waveguide antennas for 1.6 THz", *23rd International Conference on Infrared and Millimeter Waves*, eds. T.J. Parker and S.R.P. Smith, Colchester, UK, pp. 189–190, 1998.

9. D.H. Martin, and J.W. Bowen, "Long-wave optics", *IEEE Transactions on Microwave Theory and Techniques*, **41**, 1676–1690, 1993.

10. J.T. Foley and E. Wolf, "Note on the far field of a Gaussian beam", *Journal of the Optical Society of America*, **69**, pp. 761-4, 1979.

11. J.W.Goodman, *Introduction to Fourier Optics*, McGraw-Hill, San Fransisco and London, 1968.

Quasi-optical characterisation of waveguides at frequencies above 100 GHz.

Sillas Hadjiloucas[a], John W. Bowen[a], John W. Digby, J. Martyn Chamberlain[b], and D. Paul Steenson[c]

[a] Deptartment of Cybernetics, The University of Reading, Whiteknights, Reading, RG6 6AY, UK.
[b] Physics Deptartment, University of Nottingham, Nottingham, NG7 2RD, UK.
[c] Institute of Microwave and Photonics, Deptartment of Electrical & Electrical Engineering, The University of Leeds, Leeds, LS2 9JT, UK.

Keywords: Quasi-optics, null-balance reflectometer, vector network analyser, waveguide characterisation, de-embedding

ABSTRACT

We analyse the precision of a quasi-optical null-balance bridge reflectometer in measuring waveguide characteristic impedance and attenuation using a one-port de-embedding technique after taking into account errors due to imperfect coupling of two fundamental Gaussian beams. In order to determine the desired precision, we present in-waveguide measurements of characteristic impedance and attenuation for a WR-8 adjustable precision short in the 75-110 GHz frequency range using a Hewlett-Packard HP 8510 vector network analyser.

INTRODUCTION

This paper presents measurements of characteristic impedance and attenuation for a WR-8 waveguide adjustable precision short in the 75-110 GHz frequency range. Measurements were performed using a HP 8510 vector network analyser calibrated with a TRL (Thru-Reflect-Load) technique. We use a one-port de-embedding technique to evaluate characteristic impedance and attenuation of waveguides from a series of S_{11} measurements. The precision in the measurements indicate the levels of performance required if one is to use a quasi-optical technique to measure these parameters. In our previous analyses we have evaluated the precision of a quasi-optical null-balanced bridge reflectometer in complex reflection coefficient measurements[1], after taking into account the quantisation error in the grid angle and micrometer readings, the transmission or reflection coefficient at the surface of a planar sample, the noise equivalent power of the detector, the source power and the post-detection bandwidth. More recently we have evaluated the propagation of errors to waveguide characteristic impedance and attenuation using the same de-embedding technique[2] that was employed here. In our previous treatment we have not taken into account misalignment errors between the instrument's test port and the device under test and this is the subject of the current paper.

REPEATABILITY MEASUREMENTS ON A VECTOR NETWORK ANALYSER

In order to establish the levels of performance that would have to be achieved by a quasi-optical system, S_{11} measurements in the 75-110 GHz frequency range were performed on a commercially available WR-8 adjustable waveguide precision short with its back-short position varied between 2 to 5 mm in increments of 1 mm (Figures 1 and 2). A HP 8510 vector network analyser calibrated with a TRL (Thru-Reflect-Load) technique was used for this purpose. Measurements were repeated by moving the adjustable back-short in the other direction so that the combined error in S_{11} composed of the precision of the HP 8510 and of the error in accurately placing the back-short in the exact position could be determined (Figures 3 and 4). Performing in-waveguide measurements using the network analyser eliminate possible alignment errors that would be present if the measurements were performed with free-space propagating beams. It can be observed that the amplitude errors in the S_{11} measurements are of the order of 0.005 dB and the errors in the phase are of the order of 0.005 rad.

Part of the EUROPTO Conference on Terahertz Spectroscopy and Applications II
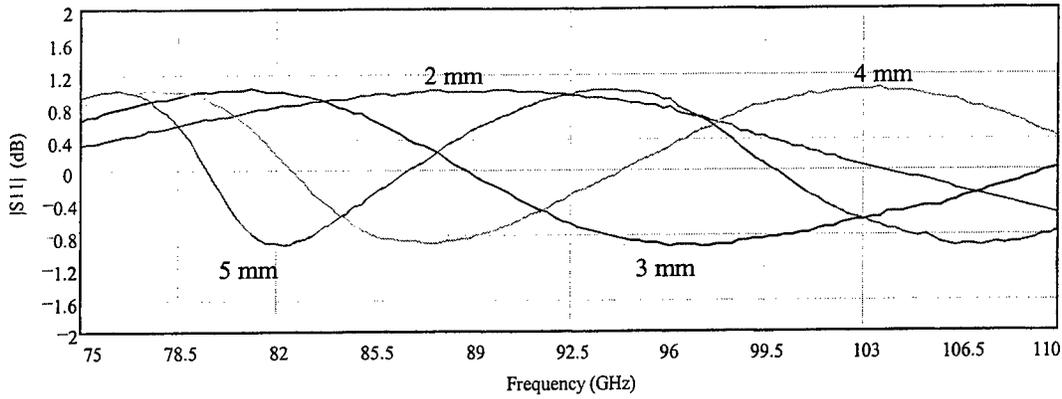Munich, Germany • June 1999 SPIE Vol. 3828 • 0277-786X/99/$10.00

357

Figure 1. In-waveguide S_{11} amplitude measurements of a precision adjustable short with the back-short position adjusted at 2, 3, 4 and 5 mm using the HP 8510 vector network analyser.

Figure 2. In-waveguide S_{11} phase measurements of a precision adjustable short with the back-short position adjusted at 2, 3, 4 and 5 mm using the HP 8510 vector network analyser.

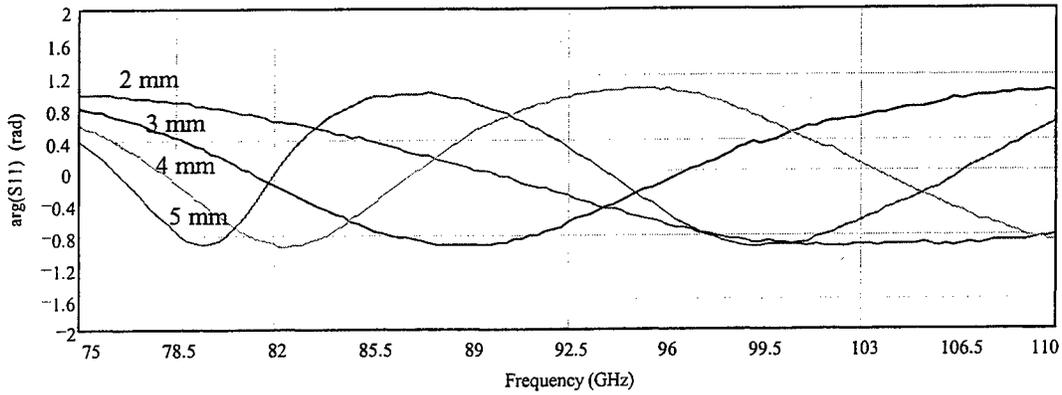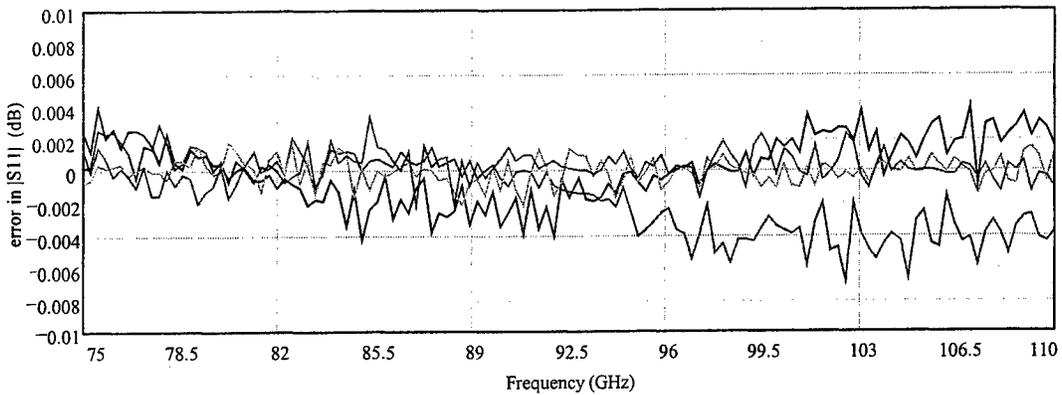Figure 3. Typical amplitude errors in S_{11} measurements of the same precision adjustable short based on repeatability measurements using the HP 8510 vector network analyser.
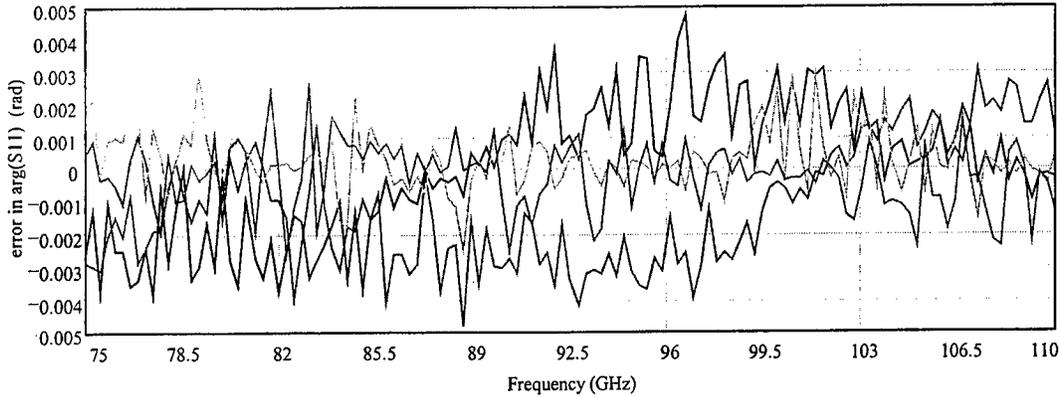
Figure 4. Typical phase errors in S_{11} measurements of the same precision adjustable short based on repeatability measurements using the HP 8510 vector network analyser.

QUASI-OPTICAL COUPLING AND DE-EMBEDDING

Figure 5 shows a null-balance quasi-optical bridge reflectometer capable of measuring complex reflection coefficients of samples in the millimetre and sub-millimetre frequency range. The system uses tungsten wire polarising grid beam splitters, reflectors and a train of lenses to control the diffractive spreading of the beams. A corrugated feed horn fitted at the source ensures Gaussicity of the beam with minimal astigmatism. Different waveguide lengths are connected to a corrugated feedhorn antenna and the antenna-waveguide structure is positioned in the test arm of the reflectometer.
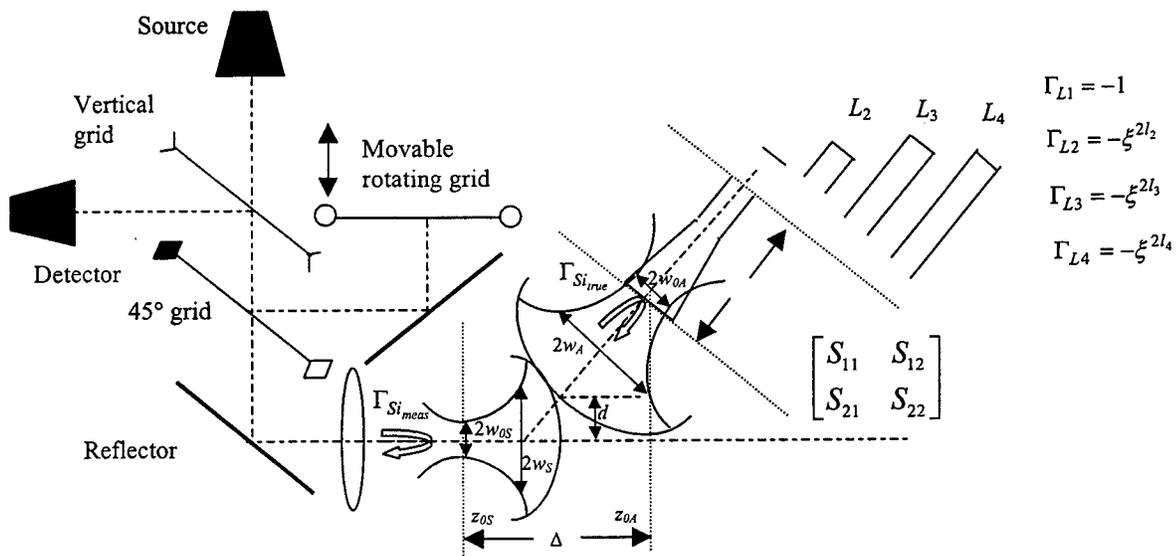

Figure 5 Projection of the coupling assuming a fundamental Gaussian beam-mode launched from a corrugated horn-lens system of a null-balance bridge reflectometer to another corrugated horn system with different waveguide lengths attached to its end.

359

For the case where both the source S and receiving antenna-waveguide system A, are fundamental Gaussian beam-modes, $U_A(x,y,z)$ and $U_S(x,y,z)$, the relative amplitude of a coherently detected signal is given[3,4,5] by the overlap or coupling integral $<U_A|U_S>$:

$$\langle U_A \mid U_S \rangle = \left| \iint_C U_A^*(x,y,z) U_S(x,y,z) dxdy \right| \qquad (1)$$

evaluated over any convenient constant z-plane, C. If U_A and U_S are both normalised to unity power, i.e. $<U_A|U_A>$ and $<U_S|U_S>$ are both equal to 1, the maximum possible value for $<U_A|U_S>$ is 1 and this value is obtained if the modes U_A and U_S are co-axial and have equal and co-incident beam-waists, otherwise $<U_A|U_S>$ will be less than 1 indicating an imperfect match of incident signal to the receiving antenna-waveguide system.

For coaxial modes with non-co-incident beam waists of different size, it can be shown that the coupling coefficient expressed in terms of the beam-waist sizes w_{0A} and w_{0S} and the separation of the beam waists $\Delta = z_{0A} - z_{0S}$, is:

$$\langle U_A \mid U_S \rangle_{axial} = (\overline{\overline{kw_0}})^2 \left[(k^2 w_0^2)^2 + (k\Delta)^2 \right]^{-1/2} \qquad (2)$$

where $\overline{\overline{w}}_0 = \sqrt{w_{0A} w_{0S}}$ and $\overline{w_0^2} = (w_{0A}^2 + w_{0S}^2)/2$. Furthermore, the corresponding phase term from the coupling integral gives a phase error term: $\phi = \tan^{-1}\left[(\Delta/\overline{kw_0^2})\right] - k\Delta$. For beams with equal beam-waists, setting $w_{0A} = w_{0S} = w_0$, equation 2 simplifies to $\langle U_A \mid U_S \rangle_{axial} = \left[1 + (k\Delta/k^2 w_0^2)^2\right]^{-1/2}$. Close observation of equation 2 shows that the larger the value of kw_0, the greater the tolerance for Δ.

For laterally displaced modes at a distance d, where U_A and U_S have parallel but not coincident axes, the coupling integral is:

$$\langle U_A \mid U_S \rangle_{lat} = \langle U_A \mid U_S \rangle_0 \exp(-d^2/d_e^2) \qquad (3)$$

where $d_e^2 = 2\left[(k^2 \overline{w_0^2})^2 + (k\Delta)^2\right]/(k^2 \overline{w_0^2})$ and $\langle U_A \mid U_S \rangle_0$ denotes the value for $d \to 0$ and is given from:

$$\langle U_A \mid U_S \rangle_0 = (\overline{\overline{kw_0}})^2 \left[(k^2 \overline{w_0^2})^2 \right]^{-1/2} \qquad (4)$$

In a similar manner, for rotationally displaced modes where U_A and U_S are inclined at a small angle θ, the coupling integral is:

$$\langle U_A \mid U_S \rangle_{rot} = \langle U_A \mid U_S \rangle_0 \exp(-\theta^2/\theta_e^2) \qquad (5)$$

where $\theta_e^2 = \left[(8\overline{w_0^2} / k^2 \overline{\overline{w}}_0^4 \right]$.

It is convenient to treat any misalignment in a uniform manner and therefore an alignment product A is defined so that:

$$A = \langle U_A | U_S \rangle_{rot} \langle U_A | U_S \rangle_{lat} \langle U_A | U_S \rangle_{axial} \qquad (6)$$

Furthermore, each 1-port test piece can be considered to be a length of waveguide terminated in a short and connected to the reflectometer by a 2-port device consisting of a further length of waveguide and the feed antenna. The situation is illustrated in Figure 5. For a perfectly coupled reciprocal 2-port device with scattering matrix S the complex reflectance Γ_{Si} is related to the load reflectance Γ_{Li} by:

$$\Gamma_{Si_{true}} = \frac{S_{11} + \Gamma_{Li}(S_{21}^2 - S_{11}S_{22})}{1 - \Gamma_{Li}S_{22}} \qquad (7)$$

The terminating reflectance Γ_{Li} depends on the complex propagation constant of the waveguide ξ and the length l_i with the waveguide lengths chosen so that $l_2 = l_3 / 2 = l_4 / 3$ and calculations performed in length units of $2l_2$. It is assumed that the shorts are loss-less. The unknown parameters in equation 7 can be found by terminating with four different load reflectances and solving the resulting set of simultaneous equations. The terminal plane is defined by the location of the short in the shortest length of waveguide. In order to take into account imperfect coupling and thus move to the terminal plane defined by the beam waist in the test port of the reflectometer equation 7 must be modified taking into account the coupling coefficient:

$$\Gamma_{Si\,meas} = \Gamma_{Si\,true} - \sigma_{\Gamma_{si}} \qquad (8)$$

where $\sigma_{\Gamma_{si}}$ is the error in the true Γ_{Si} due to coupling losses. For a given misalignment $\Gamma_{Si\,meas}$ can be written as $\Gamma_{Si\,meas} = A^2 \Gamma_{Si\,true}$ where $1 \leq A < 0$ and the squared term arises to take into account the coupling losses in the double-pass nature of the measurements. For rotationally displaced modes:

$$\sigma_{\Gamma_{Si}} = \frac{\partial \Gamma_{Si\,meas}}{\partial \theta}\sigma\theta = \frac{\partial \Gamma_{Si\,meas}}{\partial A}\frac{\partial A}{\partial \theta}\sigma\theta = \frac{\partial \left[A^2 \Gamma_{Si\,true}\right]}{\partial A}\frac{\partial A}{\partial \theta}\sigma\theta = 2A\Gamma_{Si\,true}\left(\frac{\partial A}{\partial \theta}\right)\sigma\theta \qquad (9)$$

Setting $\sigma A = \left(\dfrac{\partial A}{\partial \theta}\right)\sigma\theta$, it follows that $\sigma_{\Gamma_{Si}} = 2A\Gamma_{Si\,true}\sigma A$ so that the error in the calculated propagation constant due to rotationally displaced modes may be calculated from $\Gamma_{Si_{meas}}$ with four different waveguide lengths from:

$$\sigma_{\xi_{rot}} = \sqrt{\sum_{i=1}^4 \left(\frac{\partial \xi}{\partial \Gamma_{Si\,meas}}\right)^2 \sigma_{\Gamma_{Si}}^2} \qquad (10)$$

where explicit forms of the $\dfrac{\partial \xi}{\partial \Gamma_{S1}}, \dfrac{\partial \xi}{\partial \Gamma_{S2}}, \dfrac{\partial \xi}{\partial \Gamma_{S3}}$ and $\dfrac{\partial \xi}{\partial \Gamma_{S4}}$ terms are shown in the appendix.

Similar arguments can be made for laterally and axially displaced modes after setting $\sigma A = \left(\partial A / \partial d\right)\sigma d$ and $\sigma A = \left(\partial A / \partial \Delta\right)\sigma \Delta$ respectively, so that the total error in the propagation constant can be calculated from the sum of squares of the independent errors:

$$\sigma_{\xi_{tot}} = \sqrt{\sigma_{\xi_{axial}}^2 + \sigma_{\xi_{lat}}^2 + \sigma_{\xi_{rot}}^2} \tag{11}$$

The propagation constant ξ is related to the attenuation a and guide wavelength $\lambda_g = 2\pi / k_g$ (where k_g is the guide wavenumber) through $\xi = e^{-a} e^{-jk_g}$ and can be calculated from $\Gamma_{Si_{meas}}$ with four different waveguide lengths from:

$$\xi = \frac{1}{2} \frac{\Gamma_{S4}\Gamma_{S3} + \Gamma_{S1}\Gamma_{S2} - 2\Gamma_{S3}\Gamma_{S1} - \Gamma_{S4}\Gamma_{S2} + \Gamma_{S1}\Gamma_{S4} + \Gamma_{S2}\Gamma_{S3}}{\Gamma_{S1}\Gamma_{S3} + \Gamma_{S2}\Gamma_{S4} - \Gamma_{S1}\Gamma_{S4} - \Gamma_{S2}\Gamma_{S3}}$$
$$\pm \frac{1}{2} \frac{\sqrt{\Gamma_{S2} - \Gamma_{S4}} \sqrt{4\Gamma_{S4}\Gamma_{S3}\Gamma_{S2} + \Gamma_{S2}\Gamma_{S1}^2 - 3\Gamma_{S3}^2\Gamma_{S2} + 2\Gamma_{S1}\Gamma_{S2}\Gamma_{S3} - 4\Gamma_{S4}\Gamma_{S1}\Gamma_{S2} - 2\Gamma_{S4}\Gamma_{S3}\Gamma_{S1} - 4\Gamma_{S3}\Gamma_{S1}^2 - \Gamma_{S4}\Gamma_{S3}^2 + 4\Gamma_{S3}^2\Gamma_{S1} + 3\Gamma_{S4}\Gamma_{S1}^2}}{\Gamma_{S1}\Gamma_{S3} + \Gamma_{S2}\Gamma_{S4} - \Gamma_{S1}\Gamma_{S4} - \Gamma_{S2}\Gamma_{S3}} \tag{12}$$

Alternatively, the simultaneous equations can also be solved to give the S-parameters for the connecting 2-port:

$$S_{11} = \frac{\Gamma_{S2}\Gamma_{S3} + \xi\Gamma_{S1}\Gamma_{S2} - \xi\Gamma_{S3}\Gamma_{S1} - \Gamma_{S3}\Gamma_{S1}}{\Gamma_{S2} + \xi\Gamma_{S2} - \xi\Gamma_{S3} - \Gamma_{S1}} \tag{13}$$

$$S_{21} = \pm\sqrt{\xi^2 - 1} \sqrt{\Gamma_{S1} - \Gamma_{S3}} \frac{\sqrt{\Gamma_{S1}\Gamma_{S2} - \Gamma_{S3}\Gamma_{S1} + \Gamma_{S2}\Gamma_{S3} - \Gamma_{S2}^2}}{\sqrt{\xi}(\Gamma_{S2} + \xi\Gamma_{S2} - \xi\Gamma_{S3} - \Gamma_{S1})} \tag{14}$$

$$S_{22} = -\frac{\Gamma_{S2}\xi + \Gamma_{S2} - \xi\Gamma_{S1} - \Gamma_{S3}}{\xi(\Gamma_{S2} + \xi\Gamma_{S2} - \xi\Gamma_{S3} - \Gamma_{S1})} \tag{15}$$

The errors in the S_{11} due the coupling coefficient may be calculated after replacing equation 12 in equation 13 and using:

$$\sigma S_{11} = \sqrt{\left(\frac{\partial S_{11}}{\partial \Gamma_{S1}}\right)^2 \sigma^2\Gamma_{S1} + \left(\frac{\partial S_{11}}{\partial \Gamma_{S2}}\right)^2 \sigma^2\Gamma_{S2} + \left(\frac{\partial S_{11}}{\partial \Gamma_{S3}}\right)^2 \sigma^2\Gamma_{S3} + \left(\frac{\partial S_{11}}{\partial \Gamma_{S4}}\right)^2 \sigma^2\Gamma_{S4}} \tag{16}$$

RESULTS

In the following section we present theoretical errors in the coupling coefficient for a 100 GHz beam assuming unequal beam-waist sizes of w_{0S}=4 mm, and w_{0A}=3, 4 and 6 mm. The error in the coupling coefficient due to axial positioning error of the test piece is given from:

$$\sigma A_{rot} = (\partial A / \partial \theta)\sigma\theta = \langle U_A | U_S \rangle_0 \left[-2(\theta / \theta_e)\exp(-\theta^2 / \theta_e^2)\right]\sigma\theta \qquad (17)$$

The error in the coupling coefficient due to lateral positioning error of the test piece is given from:

$$\sigma A_{lat} = (\partial A / \partial d)\sigma d = \langle U_A | U_S \rangle_0 \left[-2(d / d_e)\exp(-d^2 / d_e^2)\right]\sigma d \qquad (18)$$

The error in the coupling coefficient due to longitudinal positioning error of the test piece is given from:

$$\sigma A_{axial} = (\partial A / \partial \Delta)\sigma\Delta = \frac{-k^4 \overline{w}_0^4 \Delta}{\left(k^4 w_0^4 + k^2 \Delta^2\right)^{3/2}} \sigma\Delta \qquad (19)$$

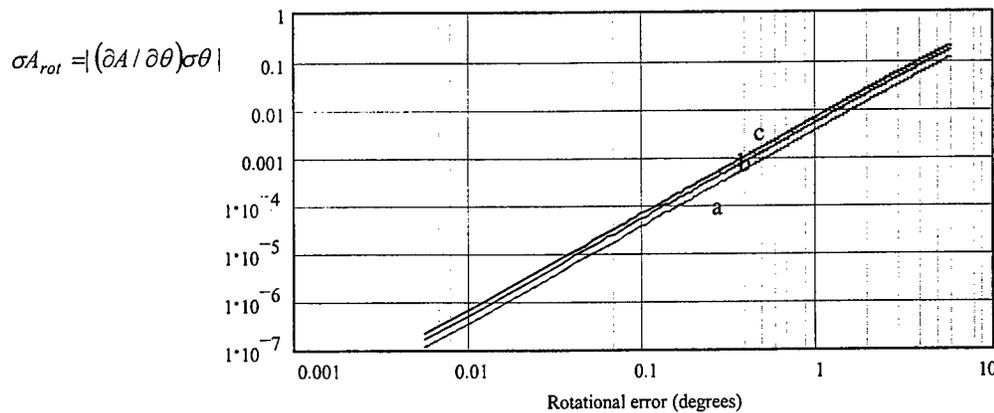$$\sigma A_{rot} = |(\partial A / \partial \theta)\sigma\theta|$$

Figure 6. Error in the coupling coefficient due to rotational error assuming w_{0S}=4 mm and a), w_{0A}=3 mm b) w_{0A}=4 mm and c) w_{0A}=6 mm.
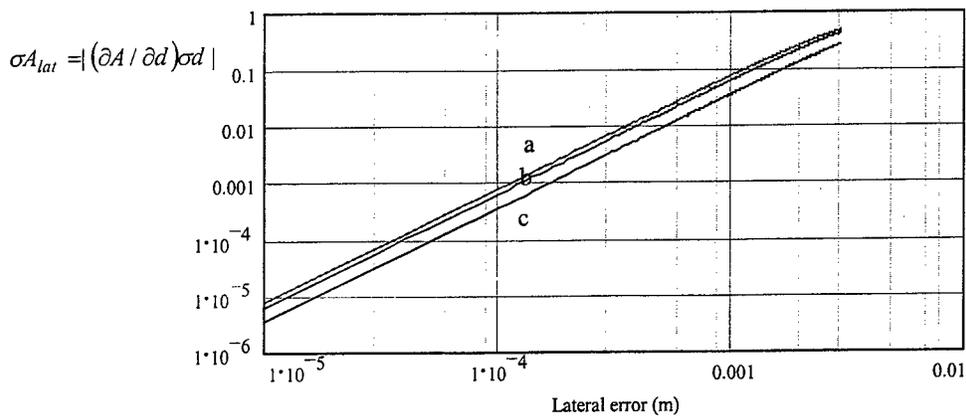
$$\sigma A_{lat} = |(\partial A / \partial d)\sigma d|$$

Figure 7. Error in the coupling coefficient due to lateral error assuming w_{0S}=4 mm and a), w_{0A}=3 mm b) w_{0A}=4 mm and c) w_{0A}=6 mm.

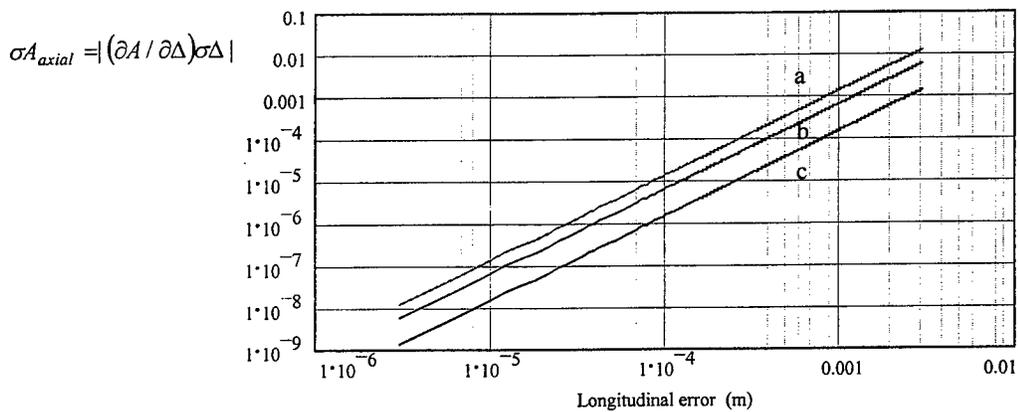$$\sigma A_{axial} = |(\partial A / \partial \Delta)\sigma \Delta|$$

Figure 8. Error in the coupling coefficient due to longitudinal (axial) error assuming w_{0S}=4 mm and a), w_{0A}=3 mm b) w_{0A}=4 mm and c) w_{0A}=6 mm.

CONCLUSIONS

Although the type of errors described in this paper apply to a quasi-optical null-balance bridge reflectometer, free-space quasi-optical measurements using the HP 8510 or the AB millimetre vector network analysers and the same de-embedding procedure would incorporate the same errors in the measured S_{11}. The propagation of the errors described in Figures 6, 7 and 8 to the calculated characteristic impedance and attenuation in waveguides will be discussed at the conference.

REFERENCES

1. S. Hadjiloucas and J.W. Bowen, "The Precision of Quasi-optical Null-Balanced Bridge Techniques for Transmission and Reflection Coefficient Measurements", Review of Scientific Instruments, **70**, pp. 213-219, 1999.

2. J.W. Bowen and S. Hadjiloucas, "A 1-Port De-embedding Technique for the Quasi-optical Characterisation of Integrated Components", IEEE Transactions on Microwave Theory and Techniques MTT, *Submitted.*

3. W.B. Joyce, and B.C. DeLoach, "Alignment of Gaussian Beams", Applied Optics, **23**, pp. 4187-4197, 1984.

4. D.H. Martin, Millimetre-wave optics, Lecture Notes, Queen Mary College, University of London, UK.

5. H. Kogelnik, "Coupling and Conversion Coefficients for Optical Modes in Quasi-Optics", Microwave Research Institute Symposia, Series 14, (Polytechnic Press, New York), pp. 333-347, 1964.

APPENDIX

The sensitivity of the propagation constant to Γ_{S1} can be calculated from:

$$\frac{\partial \xi}{\partial \Gamma_{S1}} = \frac{1}{2} \frac{\Gamma_{S2} - 2\Gamma_{S3} + \Gamma_{S4} - \frac{1}{2}\frac{\left(\sqrt{\Gamma_{S2}-\Gamma_{S4}}\right)\cdot\left[2\Gamma_{S1}\Gamma_{S2}+2\Gamma_{S2}\Gamma_{S3}-4\Gamma_{S4}\Gamma_{S2}-2\Gamma_{S4}\Gamma_{S3}-8\Gamma_{S1}\Gamma_{S3}+4(\Gamma_{S3})^2+6\Gamma_{S1}\Gamma_{S4}\right]}{P}}{\Psi} - \frac{1}{2}\frac{\left[Z - \left(\sqrt{\Gamma_{S2}-\Gamma_{S4}}\right)\cdot P\right]}{\Psi^2}(\Gamma_{S3}-\Gamma_{S4})$$

The sensitivity of the propagation constant to Γ_{S2} can be calculated from:

$$\frac{\partial \xi}{\partial \Gamma_{S2}} = \frac{1}{2} \frac{\Gamma_{S1} - 2\Gamma_{S4} + \Gamma_{S3} - \frac{1}{2\sqrt{\Gamma_{S2}-\Gamma_{S4}}}\cdot P - \frac{1}{2}\frac{\sqrt{\Gamma_{S2}-\Gamma_{S4}}}{P}\left[4\Gamma_{S4}\Gamma_{S3}+(\Gamma_{S1})^2-3(\Gamma_{S3})^2+2\Gamma_{S1}\Gamma_{S3}-4\Gamma_{S1}\Gamma_{S4}\right]}{\Psi} - \frac{1}{2}\frac{\left[Z - \left(\sqrt{\Gamma_{S2}-\Gamma_{S4}}\right)\cdot P\right]}{\Psi^2}(\Gamma_{S4}-\Gamma_{S3})$$

The sensitivity of the propagation constant to Γ_{S3} can be calculated from:

$$\frac{\partial \xi}{\partial \Gamma_{S3}} = \frac{1}{2} \frac{\Gamma_{S4} - 2\Gamma_{S1} + \Gamma_{S2} - \frac{1}{2}\frac{\left(\sqrt{\Gamma_{S2}-\Gamma_{S4}}\right)\left(4\Gamma_{S4}\Gamma_{S2}-6\Gamma_{S2}\Gamma_{S3}+2\Gamma_{S1}\Gamma_{S2}-2\Gamma_{S1}\Gamma_{S4}-4(\Gamma_{S1})^2-2\Gamma_{S4}\Gamma_{S3}+8\Gamma_{S1}\Gamma_{S3}\right)}{P}}{\Psi} - \frac{1}{2}\frac{\left[Z - \left(\sqrt{\Gamma_{S2}-\Gamma_{S4}}\right)\cdot P\right]}{\Psi^2}(\Gamma_{S1}-\Gamma_{S2})$$

The sensitivity of the propagation constant to Γ_{S4} can be calculated from:

$$\frac{\partial \xi}{\partial \Gamma_{S4}} = \frac{1}{2} \frac{\Gamma_{S3} - 2\Gamma_{S2} + \Gamma_{S1} + \frac{1}{2\left(\sqrt{\Gamma_{S2}-\Gamma_{S4}}\right)}P - \frac{1}{2}\frac{\left(\sqrt{\Gamma_{S2}-\Gamma_{S4}}\right)}{P}\left[4\Gamma_{S2}\Gamma_{S3}-4\Gamma_{S1}\Gamma_{S2}-2\Gamma_{S3}\Gamma_{S1}-(\Gamma_{S3})^2+3(\Gamma_{S1})^2\right]}{\Psi} - \frac{1}{2}\frac{\left[Z - \left(\sqrt{\Gamma_{S2}-\Gamma_{S4}}\right)\cdot P\right]}{\Psi^2}(\Gamma_{S2}-\Gamma_{S1})$$

where:

$$\Psi = \Gamma_{S1}\Gamma_{S3} + \Gamma_{S2}\Gamma_{S4} - \Gamma_{S1}\Gamma_{S4} - \Gamma_{S2}\Gamma_{S3}$$

$$P = \sqrt{4\Gamma_{S4}\Gamma_{S3}\Gamma_{S2} + \Gamma_{S2}(\Gamma_{S1})^2 - 3(\Gamma_{S3})^2\Gamma_{S2} + 2\Gamma_{S1}\Gamma_{S3}\Gamma_{S2} - 4\Gamma_{S1}\Gamma_{S4}\Gamma_{S2} - 2\Gamma_{S4}\Gamma_{S3}\Gamma_{S1} - 4\Gamma_{S3}(\Gamma_{S1})^2 - \Gamma_{S4}(\Gamma_{S3})^2 + 4(\Gamma_{S3})^2\Gamma_{S1} + 3\Gamma_{S4}(\Gamma_{S1})^2}$$

$$Z = \Gamma_{S4}\Gamma_{S3} + \Gamma_{S1}\Gamma_{S2} - 2\Gamma_{S1}\Gamma_{S3} - 2\Gamma_{S4}\Gamma_{S2} + \Gamma_{S1}\Gamma_{S4} + \Gamma_{S2}\Gamma_{S3}$$

Fermi surface traversal resonance in metals: Two theories and an experiment

A. Ardavan[a] J.M. Schrama[a], S.J. Blundell[a], J. Singleton[a], A. Semeno[a],
P. Goy[b], M. Kurmoo[c] and P. Day[d]

[a] Clarendon Laboratory, University of Oxford, Parks Road, Oxford OX1 3PU, UK.

[b]Laboratoire Kastler-Brossel, Departement de Physique de l'Ecole Normale Superieure,
CNRS-URA 18 and Paris 6 University, 24 rue Lhomond, 75231 Paris Cedex, France

[c]IPCMS, 23 rue de Loess, BP 20/CR, 67037 Strasbourg, France.

[d]The Royal Institution, 21 Albemarle Street, London W1X 4BS, UK

ABSTRACT

Fermi-surface traversal resonance (FTR) is caused by the periodic motion of carriers in a magnetic field across open sections of Fermi surface (FS). Owing to the warping of the FS, the real space velocities of the carriers oscillate, generating resonances in the high frequency conductivity which may be described by a semiclassical model. A rectangular resonant cavity, oscillating at 70 GHz, which can rotate in the external magnetic field, has been used to confirm the existence of the effect in the organic metal α-(BEDT-TTF)$_2$KHg(SCN)$_4$. The data contain a great deal of information about the FS, including the direction and anharmonicity of warping components. A quantum mechanical model is presented which predicts all of the features of FTR appearing in the semiclassical model. This confirms that FTR is a fundamental property of low-dimensional systems, existing under a very wide range of conditions.

Keywords: Fermi surface, millimetre-waves, magnetic resonance, semiclassical-quantum correspondance

1. INTRODUCTION

The Fermi-surface topologies of metals have been studied for many years[1] using techniques such as the de Haas-van Alphen (dHvA) and Shubnikov-de Haas effects (SdH),[2] and more recently, angle dependent magnetoresistance oscillations (AMRO).[3] However, much information can also be gained from high magnetic field measurements of the high frequency properties. For example, cyclotron resonance (CR) appears as a modulation of the conductivity, $\sigma(\omega)$, at the cyclotron frequency, ω_c. Interest in the measurement of CR has been stimulated by the desire to compare the carrier mass measured in CR experiments (the dynamical mass, renormalized by electron-phonon interactions) with the "bare" band mass (obtained from bandstructure calculations and including no interaction renormalizations) and the effective mass obtained from SdH and dHvA oscillations (which is renormalized by both electron-phonon and electron-electron interactions).[4]

Traditional CR arises only from closed Fermi surface orbits. The role played by open orbits in the high frequency properties has been considered by several groups and a range of effects has been suggested.[5-7] In this paper we describe a new effect responsible for resonances arising from the traversal of charge carriers across quasi-one-dimensional (Q1D) sections of Fermi-surface (FS), Fermi-surface traversal resonances (FTR). We begin, in Section 2, by describing a semiclassical model predicting FTR and its characteristics. In Section 3, we describe an experiment that employs novel millimetre-wave techniques to measure FTR in the organic molecular metal α-(BEDT-TTF)$_2$KHg(SCN)$_4$. A simple quantum-mechanical model of a system of conducting chains is used in Section 4 to provide an alternative explanation for FTR; the model is derived with reference to the semiclassical model in Section 2 as the corresponding features of FTR emerge.

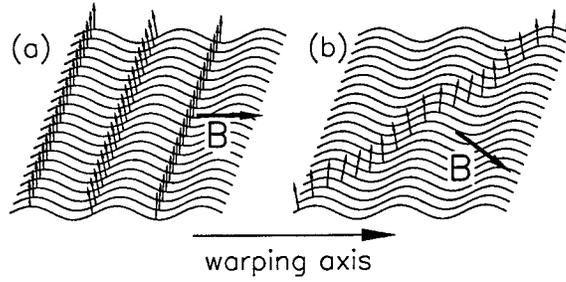Corresponding author: A. Ardavan, E-mail: arzhang.ardavan@physics.ox.ac.uk

366

Part of the EUROPTO Conference on Terahertz Spectroscopy and Applications II
Munich, Germany • June 1999 SPIE Vol. 3828 • 0277-786X/99/$10.00

Figure 1. The path taken by a carrier across a warped Q1D Fermi surface when (a) **B** is parallel to the warping axis and (b) **B** is at an angle to the warping axis. The small arrows indicate the real space velocity.

2. SEMICLASSICAL DESCRIPTION OF FTR

When a magnetic field **B** is applied to a metal, a carrier of charge q, velocity **v** and wavevector **k** experiences the Lorentz force, $\hbar\dot{\mathbf{k}} = q(\mathbf{v} \times \mathbf{B})$. The velocity, $\mathbf{v}(\mathbf{k}) = \hbar^{-1}\nabla_{\mathbf{k}}\mathcal{E}(\mathbf{k})$, is by definition perpendicular to the surfaces of constant energy. Therefore a carrier on the FS follows a path defined by the intersection of the plane perpendicular to **B** with the FS. Thus the particle's real space velocity may evolve with time in different ways depending on the orientation of **B** with respect to the FS. Using the Boltzmann transport equation, Eqn. 1, the evolution of the particle's velocity can be related to its contribution to the frequency-dependent conductivity of the metal.[3,7]

$$\sigma_{ij}(\omega) = \frac{e^2}{4\pi^3} \int d^3k \left[-\frac{\partial f_0(\mathbf{k})}{\partial \mathcal{E}(\mathbf{k})} \right] v_i(\mathbf{k}, 0) \int_{-\infty}^{0} v_j(\mathbf{k}, t) \cos(\omega t) e^{t/\tau} dt \tag{1}$$

Here, τ is the relaxation time, $v_i(\mathbf{k}, t)$ is the ith component of the velocity of a carrier with wave vector **k** at time t, $f_0(\mathbf{k}) = (e^{(\mathcal{E}(\mathbf{k})-E_F)/k_BT} + 1)^{-1}$ is the Fermi function and $\mathcal{E}(\mathbf{k})$ is the energy of the carrier.

Fig. 1 shows two possible paths followed by a charged particle across a section of a simple Q1D FS in the presence of a magnetic field, **B**, lying in the plane of the sheet. In (a), where **B** is parallel to the warping axis, the particle follows a path parallel to the corrugations. Its real space velocity is well correlated with the velocity at an earlier time; this kind of trajectory contributes to the d.c. conductivity, and there is a peak in the angle-dependent magneto-conductivity for this magnetic field orientation.[3,7] In (b), the trajectory crosses the peaks and troughs of the FS sheet and the component of the velocity parallel to the sheet oscillates. We can see the effect that this oscillatory velocity will have on the high-frequency conductivity, by considering the contribution to the conductivity of a single carrier,

$$\sigma'_{yy}(\omega) \propto v_y(0) \int_{-\infty}^{0} v_y(t) \cos(\omega t) e^{t/\tau} dt \tag{2}$$

which is the part of Eqn. 1 that is integrated over all carriers at the Fermi surface to obtain the total conductivity. If we have an oscillatory velocity component, $v_y(t) = v_0 \cos(\omega_{1D} t)$, then

$$\sigma'_{yy}(\omega) \propto \frac{v_0^2}{2\tau} \left[\frac{1}{(\omega_{1D} + \omega)^2 + \frac{1}{\tau^2}} + \frac{1}{(\omega_{1D} - \omega)^2 + \frac{1}{\tau^2}} \right]. \tag{3}$$

Thus we find that there is a resonance in the high-frequency conductivity when $\omega = \omega_{1D}$, the frequency of oscillation of the real-space velocity. The amplitude of the resonance in the conductivity is proportional to the square of the amplitude of the velocity oscillation.

The frequency, ω_{1D}, of the oscillatory component of **v** is proportional to $\sin\psi$, where ψ is the angle **B** makes with the warping axis; the velocity oscillation is induced by the component of **B** perpendicular to the warping axis. In a real experiment, the magnetic field is swept while the conductivity is measured at a

known fixed frequency (see Section 3), ω_0. Since $\dot{k}$ is proportional to B, the magnetic field at which resonance occurs, B_r, is given by

$$\frac{\omega_0}{B_r} = A \sin \psi \qquad (4)$$

where A is a constant of proportionality. This characteristic behaviour enables the resonances to be identified.

In real systems the warping will be more complicated. We can define a general Q1D FS sheet in an orthorhombic crystal (lattice parameters a, b and c), given by

$$\mathcal{E}(\mathbf{k}) = \hbar v_F(|k_x| - k_F) - \sum_{p,q} t_{pq} \cos(\mathbf{R}_{pq} \cdot \mathbf{k}_\parallel + \varphi_{pq}) \qquad (5)$$

where $\mathbf{R}_{pq} = (0, pb, qc)$ are real space vectors which define the corrugations and φ_{pq} are phase factors.[3,5] As the particle crosses this FS, each nonzero t_{pq} generates an oscillatory component in the velocity, and each oscillatory component of the velocity generates an FTR as described by Eqn. 3. By observing the resulting FTRs in the high frequency conductivity, one is measuring the Fourier components of the Q1D FS sheet. For a non-sinusoidally warped FS, there will be resonance harmonics at fields B_r given by.

$$\frac{\omega_0}{B_r} = nA \qquad (6)$$

where n is an integer. For example, if a FS is defined by R_{10} and R_{20} with $t_{10} = \alpha t_{20}$, there is a FTR harmonic at half the magnetic field of the fundamental. The amplitude of the oscillatory part of the real-space velocity is proportional to the size of the t_{pq} causing it, so the ratio of the amplitudes of the conductivity resonances is given by α^2.

Since $\dot{k} = q v_F B_\parallel / \hbar$, where v_F is the Fermi velocity, and the period of the warping in reciprocal space is $2\pi / R_{pq}$, the minimum time a particle takes to cross one warping period is

$$\frac{2\pi}{\omega_0} = \frac{2\pi\hbar}{R_{pq} q v_F B_\parallel}. \qquad (7)$$

Thus A in Eqn. 4 is related to R_{pq} by

$$A = \frac{q v_F R_{pq}}{\hbar}. \qquad (8)$$

By analogy with the definition of the carrier mass measured in CR, m^*_{CR}, given by $\omega_c = qB/m^*_{CR}$, which is a measure of how rapidly a carrier traverses a closed FS orbit, we can define a Q1D "mass", m^*_{1D}, which is a measure of how rapidly a carrier crosses a Q1D corrugation or, equivalently, how rapidly it crosses the Brillouin zone. Then, for a carrier traversing parallel to the warping axis,

$$\omega_{1D} = \frac{qB}{m^*_{1D}} \qquad (9)$$

or equivalently, $m^*_{1D} = q/A$.

3. MEASUREMENT OF FTR IN AN ORGANIC MOLECULAR METAL

Charge transfer salts of the organic molecule BEDT-TTF[8] provide a fascinating class of highly two-dimensional conducting systems. The BEDT-TTF cations form layers separated by non-conducting anion layers. The overlap of the π-orbitals of the BEDT-TTF is large in the inplane direction and small in the interplane direction; the resulting bandstructure is highly two-dimensional. Owing to the small number of molecular orbitals involved in the bandstructure formation, the FSs are usually very simple, often containing closed quasi-two-dimensional (Q2D) and open quasi-one-dimensional (Q1D) sections.[9] This underlying simplicity, combined with the wide variety of groundstates exhibited by the materials (including superconductivity, density-waves and magnetic order) and the availability of very high quality crystals[10] has lead to a great theoretical and experimental interest in BEDT-TTF-based conductors. Many recent measurements, including magnetic breakdown,[11] observation of the bulk quantum Hall effect[12] and high field de Haas-van Alphen
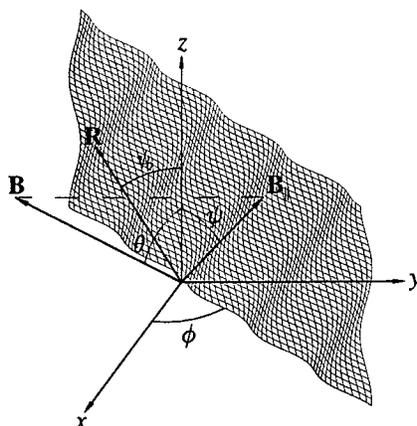
Figure 2. The definition of the angles θ, ϕ, ψ and ψ_0 in a real experiment. The axes are defined with respect to the sample.

oscillations,[13] indicate that the Q1D FS sections are vital in detemining the behaviour of the BEDT-TTF-based metals. New methods of detecting and probing these FS sections, such as measurement of FTR, are therefore of special interest to experimentalists in this field.

The d.c. and low frequency properties of the organic molecular metal α-(BEDT-TTF)$_2$KHg(SCN)$_4$ have been extensively studied. Below about 8 K, the material's FS is thought to contain very warped Q1D Fermi sheets caused by a charge- or spin-density-wave induced reconstruction.[14] Since very high quality single crystals of this material are available, it was chosen as a suitable candidate in which to look for FTRs.

The high frequency (i.e. $\geq$ 10 GHz) properties of organic molecular metals have proved difficult to measure; the single crystals are very small and the carrier densities are rather high. To address these difficulties, we have designed a very sensitive system for measuring the angle-dependent magneto-conductivity of organic molecular metals at around 70 GHz using a rectangular resonant cavity. While cylindrical cavities are simpler to manufacture, the rectangular geometry has important advantages in the measurement of organic molecular metals. The resonant modes of a rectangular cavity are separated by large intervals in frequency space[15]; the number of cylindrical modes is much larger and their relative frequencies are strongly dependent on the exact proportions of the cavity. The presence of a metallic sample can lead to mixing of the cylindrical modes, and hence uncertainties about the sample's electromagnetic environment.[15]

The cavity is of dimensions 6 mm $\times$ 3 mm $\times$ 1.5 mm, resonating in the TE_{102} mode with a quality factor of 1500 when empty and about 1000 with a sample present. The high frequency field distribution in the cavity is very well defined, and the sample is placed in an antinode of the oscillatory magnetic field, **H**, such that **H** lies parallel to the conducting planes of the sample. The induced currents then have a component in the direction of low conductivity. The skin depth in this regime is rather larger than the sample dimensions and the millimetre-wave field penetrates the sample completely. The currents induced in the sample dissipate power from the cavity's millimetre-wave field; for small changes, the change in the cavity's quality factor is proportional to the change in the sample's conductivity.[16-18] Thus the change in the amplitude cavity transmission is proportional to the change in the sample's conductivity. Since the conductivity anisotropy is very large, power dissipation is almost entirely due to interplane currents and it is the interplane conductivity which is probed by the measurement.[16-18]

To measure the angle-dependent high frequency conductivity, the sample must be rotated with respect to the steady magnetic field. However, it is important that the high frequency field rotates with the sample; if the sample moves with respect to the high frequency field, the nature of the measurement is completely changed. Thus the cavity must rotate with the sample through the steady magnetic field; this is possible in our system, in contrast to earlier resonant measurements.[17,18]

Warping component	$\phi = 20°$		$\phi = 40°$		
	A/ω_0	ψ_0	A/ω_0	ψ_0	m_{1D}^*/m_e
One	0.51	141°	0.58	146°	0.73 ± 0.05
Two	0.46	25°	0.46	27°	0.86 ± 0.01

Table 1. Parameters obtained from the fits of Eqn. 12 in Fig. 3(b)

In our experiment, the swept quasistatic magnetic field, **B**, did not in general lie in the plane of the Q1D Fermi sheets, but instead the plane of rotation of **B** made an angle ϕ with the plane of the Q1D sheets (see Fig. 2). The angle which **B** makes with the sample, θ, and the angle of rotation of the component of **B** in the plane of the Q1D sheet, ψ, are related by

$$\tan \psi = \tan \theta \cos \phi \qquad (10)$$

and the magnitude of the in-plane component of **B** is

$$B_\| = B\sqrt{\sin^2 \theta \cos^2 \phi + \cos^2 \theta} \qquad (11)$$

Using these relations, we can transform our measurement coordinates, B and θ, into the in-plane coordinates, $B_\|$ and ψ. The results can then be more easily interpreted in terms of the theory presented above.

The range of reciprocal magnetic field space in which magnetic resonances are observable is limited at the lower end by the maximum magnetic field available, 15 T, and at the upper end by the condition $\omega\tau > 1$, where ω is the frequency and τ is the scattering time. In addition, our experimental apparatus had a background absorption at a magnetic field of 2 T, which tended to obscure features due to the sample in this region of field. In this experiment, the reciprocal field range accessible was therefore from 0.07 to 0.5 T^{-1}.

The transmission of the cavity containing the sample was measured as a function of magnetic field, B, for a range of cavity angles, θ, and for two azimuthal angles, $\phi = 20°$ and 40°, corresponding to rotation of the sample inside the cavity. Figure 3(a) shows the amplitude transmission of the cavity versus B for several values of θ with $-10° < \theta < 25°$. A fall in the cavity transmission corresponds to an increase in the sample's conductivity. The temperature is 1.4 K and the measurement frequency is 70.7 GHz.

The background absorption can be seen at 2 T. This feature is present in the absence of a sample; it is independent of cavity orientation and temperature. At 2.5 T, a very sharp absorption can be seen. This is a spin resonance of the charge carriers, corresponding to a g-factor very close to 2. The field resolution of the apparatus is insufficient to study this absorption in detail, and its size is dependent on the rate at which the magnetic field is swept. At high fields, oscillations appear which are periodic in $1/B$. These are the SdH oscillations in the high frequency magnetoconductivity.[17,18]

At intermediate fields, two resonances are apparent. Their positions are strongly dependent on the cavity angle. One moves up in B and the other moves down as θ is varied; they cross each other when $\theta = 10°$. The inset in Figure 3(a) shows the positions of the resonances in reciprocal magnetic field as a function of θ. It is immediately apparent that their positions follow the form expected for the new Q1D resonances described earlier (see Eqn. 4), with each of the two 'arches' corresponding to a warping component in the Q1D Fermi sheet.

In Figure 3(b) the same resonances are plotted in terms of the in-plane coordinates, $B_\|$ and ψ, together with the resonances observed at the second azimuthal angle. The solid lines are fits to the equation

$$\frac{1}{B_\|} = \frac{A}{\omega_0} \sin(\psi + \psi_0) \qquad (12)$$

with A and ψ_0 as free parameters. In this modification of Eqn. 4, ψ_0 corresponds to the direction of the warping component generating the resonance.

Table 1 contains the values of A and ψ_0 obtained from the fits of Eqn. 12 in Figure 3(b). There is good agreement between the values obtained from each of the azimuthal angles, ϕ. These results imply that there
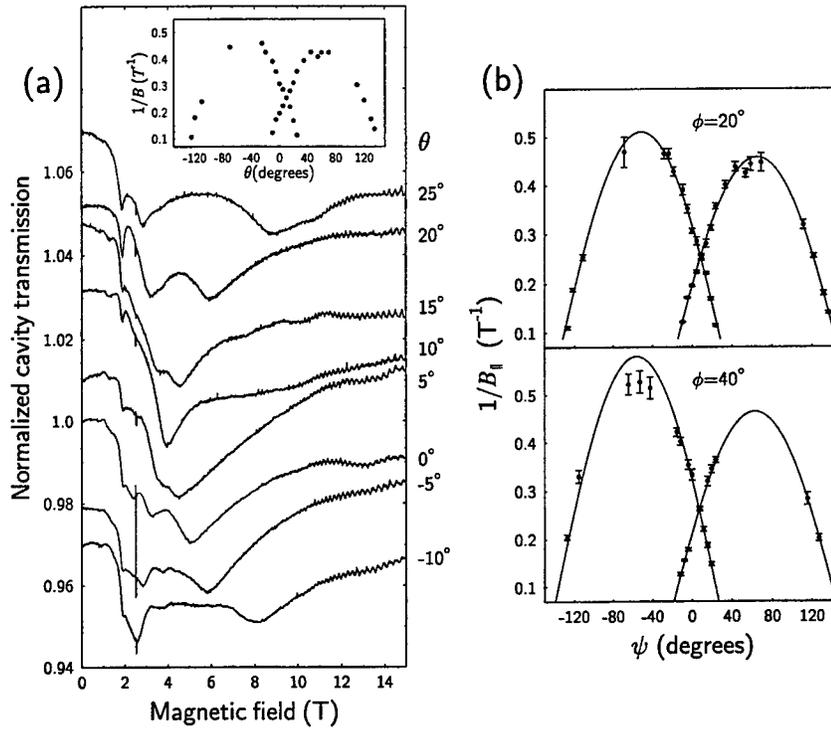
Figure 3. (a) Amplitude cavity transmission as a function of magnetic field for a range of angles, θ. The temperature is 1.4 K. ϕ is 20°. The traces are offset for clarity. The inset shows the positions of the resonances as a function of θ. (b) Resonance positions in in-plane coordinates defined in Eqns. 10 and 11, for $\phi = 20°$ and $\phi = 40°$. After Ardavan et al..[16]

are two warping components in the Q1D Fermi sheet, with axes at 143° ± 3° and 26° ± 1° to the crystal b direction (the direction of low conductivity). The values of m_{1D}^*, defined in equation 9, are 0.63 ± .05 and 0.86 ± 0.01 respectively in units of m_e, the free electron mass.[16]

4. QUANTUM MECHANICAL DESCRIPTION OF FTR

Each of the features of FTR predicted by the semiclassical description described earlier can be reproduced by a simple quantum mechanical model. In this Section, the model is derived; reference is made to previous Sections as correspondences between the semiclassical and quantum mechanical models emerge. The quantum mechanical model is an extension of the method of Yakovenko and Goan[19] and is mathematically similar to the description of the Wannier-Stark ladder.[20]

4.1. Formulation of the problem

Consider a set chains parallel to x, labelled by the index n and separated by a distance b in the y-direction, arranged in a plane (see Fig. 4); carriers move freely in the chains. In the absence of any interactions between the chains, the eigenfunctions of the system are given by the product of a plane wave along the chain and a transverse wavefunction representing the occupation of a particular chain,

$$|\psi\rangle = e^{ik_x x}|\phi_n\rangle \tag{13}$$

where the integer n is the index of the occupied chain. We use the linearized Hamiltonian,

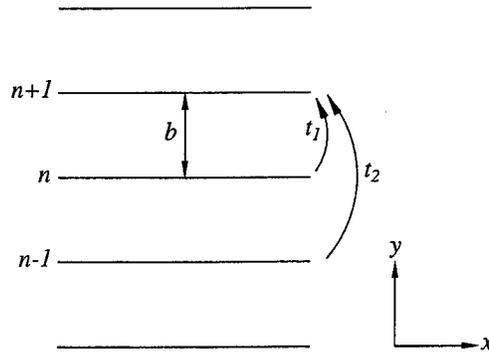$$\mathcal{H} = \hbar v_F \hat{k}_x \tag{14}$$

Figure 4. Schematic of the chains, showing the chain indices, the transitions corresponding to t_1 and t_2 and the chain separation.

since we consider only the carriers close to the Fermi surface. Since the carriers are confined to a single chain, the only contribution to the energy is from motion along the chain, and the corresponding Fermi surface is formed by the planes $k_x = \pm k_F$.

Adding hopping between the chains, the Hamiltonian becomes

$$\mathcal{H} = \hbar v_F \hat{k}_x - \sum_i t_i(c_{n+i}^\dagger c_n + c_{n-i}^\dagger c_n) \tag{15}$$

where $c_{n+i}^\dagger c_n |\phi_n\rangle = |\phi_{n+i}\rangle$ and t_i gives the strength of the transfer between chains i apart. The presence of the hopping terms modifies the eigenstates of the system; a carrier is no longer confined to a particular chain so its wavefunction is now distributed across many chains. The eigenstates become

$$|\xi_m\rangle = \sum_n a_{mn} |\phi_n\rangle \tag{16}$$

The hopping allows carriers to move in the transverse direction. This implies that the Fermi surface corresponding to the Hamiltonian in Eqn. 15 has warping components in the k_y-direction. Indeed, the t_i in Eqn. 15 are closely related to the transfer integrals used in tight-binding calculations of the bandstructure[9] and the t_{pq} defining the Fermi surface geometry in Eqn. 5. If only t_1 is non-zero, there is a single warping component and the Fermi sheets are sinusoidally warped in the k_y direction. Higher order t_i generate harmonics of the warping, and thus non-sinusoidally warped Fermi sheets.

In the semiclassical description of FTR, a magnetic field perpendicular to the warping axis causes real-space velocity oscillations of the carriers as they cross the Fermi surface. Adding a magnetic field of strength B parallel z to the current model, and choosing a gauge such that the vector potential is $\mathbf{A} = (-By, 0, 0)$, we apply the tranformation

$$\hbar \hat{k}_x \rightarrow \hbar \hat{k}_x - qA_x = \hbar \hat{k}_x - qBy = \hbar \hat{k}_x + eBnb. \tag{17}$$

Thus the Hamiltonian becomes

$$\mathcal{H} = v_F \left(-i\hbar \frac{\partial}{\partial x} + eBnb \right) - \sum_i t_i(c_{n+i}^\dagger c_n + c_{n-i}^\dagger c_n). \tag{18}$$

Operating on the states $|\phi_n\rangle$ with $\mathcal{H}$, we find that

$$\mathcal{H}|\phi_n\rangle = n\Omega |\phi_n\rangle - \sum_i t_i(|\phi_{n+i}\rangle + |\phi_{n-i}\rangle) \tag{19}$$
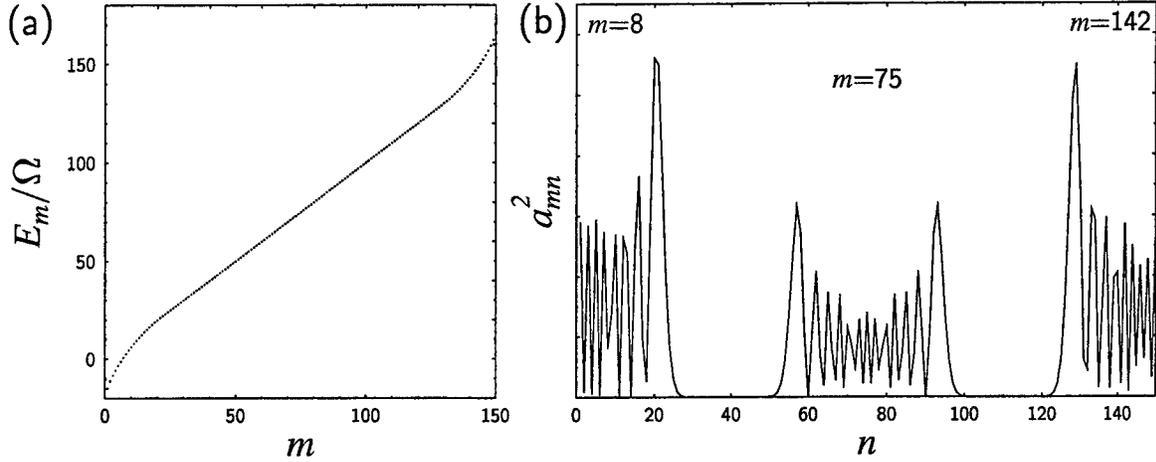
Figure 5. Results of the diagonalization of $\mathcal{H}$ for $t_1 = 10\Omega$. (a) The eigenenergies, E_n of $|\xi_n\rangle$. (b) The probability density functions of states $|\xi_8\rangle$, $|\xi_{75}\rangle$ and $|\xi_{142}\rangle$.

where $\Omega = eBbv_F$.

If we confine the carriers to only the chains $1 < n < N$, by imposing the boundary conditions $|\phi_n\rangle = 0$ for $n < 1$ and $n > N$, the Hamiltonian can be written as a finite matrix,

$$\mathcal{H} = \begin{pmatrix} \Omega & -t_1 & -t_2 & -t_3 & \cdots & -t_N \\ -t_1 & 2\Omega & -t_1 & -t_2 & \cdots & -t_{N-1} \\ -t_2 & -t_1 & 3\Omega & -t_1 & \cdots & -t_{N-2} \\ \vdots & \vdots & \ddots & \ddots & \ddots & \vdots \\ -t_{N-1} & -t_{N-2} & \cdots & -t_1 & (n_N-1)\Omega & -t_1 \\ -t_N & -t_{N-1} & \cdots & -t_2 & -t_1 & n_N\Omega \end{pmatrix}. \tag{20}$$

that can be diagonalized numerically. The mth eigenvector of this matrix is $|\xi_m\rangle$: the components of the mth eigenvector of this matrix are the a_{mn} in Eqn. 16, and the eigenvalues are the corresponding transverse-motion energy levels of the system.

4.2. The eigenstates

In the absence of any interactions between the chains, $t_i = 0$ for all i, $\mathcal{H}$ is already diagonal, and the states $|\phi_n\rangle$ form the eigenstates of the system with the corresponding eigenenergies $E_n = n\Omega$. Thus there is a magnetic field-induced ladder of states equally separated by an energy which is proportional to the strength of the z-component of the magnetic field; the photon frequency, $\Omega/\hbar$, corresponding to the energy separation, is the same as the FTR resonance frequency in Eqn. 7 (since the magnitude of R_{pq} in Eqn. 7 is b, and the charge on the carrier is e). However, these states are not connected by the dipole operator; optical transitions between these states are not possible. This is to be expected; semiclassically, this corresponds to the case where the Fermi sheet is not warped and the carrier's real-space velocity does not oscillate as it crosses the sheet. Thus it cannot cause a resonance in the high-frequency conductivity by coupling to an oscillatory electric field.

4.2.1. First order hopping

Sinusoidal warping of the Fermi sheet is introduced by making t_1 non-zero. Fig. 5(a) shows the eigenenergies of the new eigenstates $|\xi_m\rangle$, E_m/Ω, plotted against m, obtained by diagonalizing $\mathcal{H}$ for the case where $t_1 = 10\Omega$
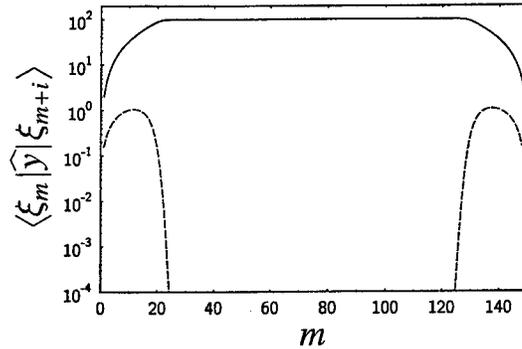
Figure 6. Transition matrix elements $\langle \xi_m | \hat{y} | \xi_{m+i} \rangle$ for $i = 1$ (solid) and $i = 2$ (dashed), calculated for $t_1 = 10\Omega$.

and $N = 150$. Again, the eigenenergies form a ladder, $E_m = m\Omega$, except near the edges; the significance of the states near the edges is discussed below. Fig. 5(b) shows a_{mn}^2 plotted against n for the three eigenstates $m = 8, 75, 142$. a_{mn}^2 is the probability that, in the mth eigenstate, the nth chain is occupied. The plots in Fig. 5(b) can therefore be thought of as real-space probability density functions for the eigenstates $|\xi_8\rangle$, $|\xi_{75}\rangle$ and $|\xi_{142}\rangle$.

$|\xi_{75}\rangle$ is a state that exists entirely within the bulk of the material; the probability density is localised within a band well away from the edges of the crystal (i.e. well away from the chains $n = 1$ and $n = 150$). Within the band, the probability density is concentrated toward the edges. Semiclassically, the particle is moving along the chain direction with a sinusoidal transverse oscillation. It spends longer near the limits of its excursion than near the centre, since the transverse velocity is smallest at the limits of the transverse motion. The states $|\xi_8\rangle$ and $|\xi_{142}\rangle$ are edge states; their probability density functions do not vanish at the edges. The corresponding semiclassical orbits are skipping orbits, with the particle executing sinusoidal motion between successive reflections from the crystal edge. The difference between the edge states and bulk states is also reflected in their eigenenergies. The energies of the bulk states still form a ladder of energies separated by Ω, but the energies of the edge states are modified by the extra confinement caused by the proximity of the crystal edge and the separation of energies increases. This is the reason for the deviation of the energies plotted in Fig. 5(a) from a straight line toward the crystal edges.

With interchain interactions in place, dipole transitions are possible between the states $|\xi_m\rangle$. In the semiclassical case, the oscillatory electric field must be polarized parallel to the direction of the oscillatory velocity if the conductivity resonance is to be detected. The corresponding selection rule in the quantum case is that the dipole operator $\hat{r}$ must be parallel to y; the transition matrix elements that follow were calculated for this case. Fig. 6 shows the first order dipole transtion matrix elements, $\langle \xi_m | \hat{y} | \xi_{m+1} \rangle$, plotted on a logarithimic scale against m (solid line). The second order transitions, $\langle \xi_m | \hat{y} | \xi_{m+2} \rangle$, are also plotted (dashed line). The first order transition matrix elements between neighbouring bulk states are uniform, with an energy Ω. These transitions correspond to the first harmonic of FTR in the semiclassical model. The transition *probability*, $|\langle \xi_m | \hat{y} | \xi_{m+1} \rangle|^2$, is proportional to the change in the *power* transmission of the cavity at the resonance field; in the experiment described in Section 3, we measure the *amplitude* transmission, which is proportional to the magnitude of the matrix element, $|\langle \xi_m | \hat{y} | \xi_{m+1} \rangle|$.

Second order transitions are not allowed between the bulk states. This is also consistent with the semiclassical description; harmonics of FTR occur when the real-space velocity of the carrier contains harmonics. It is interesting to note, however, that second and higher order transitions do occur between edge states; this is because, even in the absence of higher order t_i, the real-space velocity of the edge states, whose orbits are skipping orbits, have higher-harmonic content as a result of the skipping.

If the ratio Ω/t_1 is increased (i.e. the magnetic field strength is increased for a constant hopping interaction), it is found that the probability density functions of the states $|\xi_m\rangle$ become narrower; the effect of the
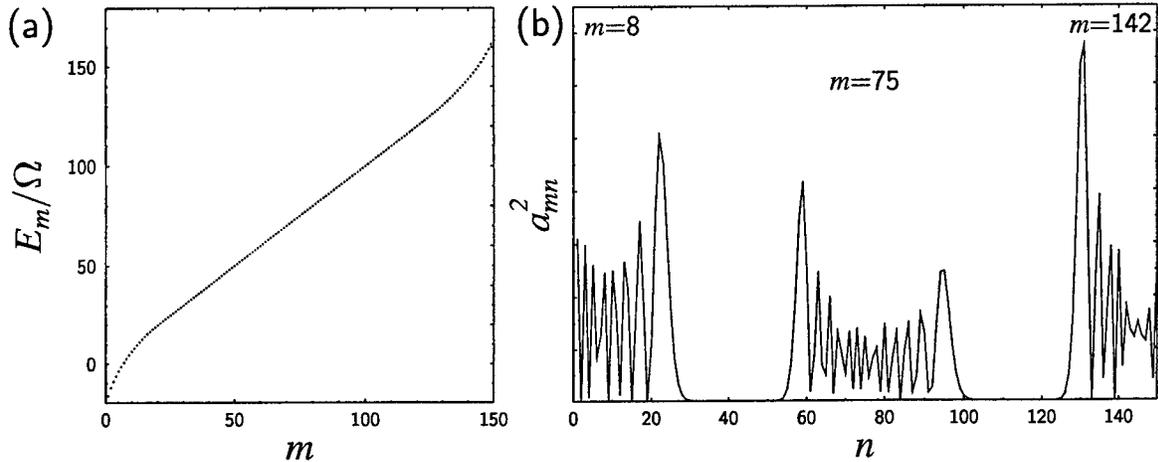
Figure 7. Results of the diagonalization of $\mathcal{H}$ for $t_1 = 10\Omega$, $t_2 = t_1/10$. (a) The eigenenergies, E_n of $|\xi_n\rangle$. (b) The probability density functions of states $|\xi_8\rangle$, $|\xi_{75}\rangle$ and $|\xi_{142}\rangle$.

magnetic field is to confine the carriers to narrower orbits. This effect is also observed in the semiclassical model. This one-dimensionalization and its effects are noted by Dupius and Montambaux.[21] At large magnetic fields, the carrier is confined to a very few chains; the model presented here breaks down in this limit, where the approximation of a discretized wavefunction is no longer valid (in this model, the wavefunction is only defined on the chains, at $y = nb$). The validity of the semiclassical model also becomes dubious in this limit; the magnetic field-induced confinement of a carrier to just a few unit cells modifies its behaviour in a way that cannot be accounted for in the semiclassical model.

4.2.2. Higher order hopping

Fig. 7 shows the eigenenergies and eigenstates obtained by diagonalizing $\mathcal{H}$ with $t_1 = 10\Omega$, $t_2 = t_1/10$ and max = 150. As before, the energies of the bulk states form a ladder with a separation Ω, with deviations from the ladder by the edge states. The most notable difference between the bulk states shown in Fig. 7(b) and Fig. 5(b) is that the probability density function, while still peaked at the limits, is no longer symmetrical about the central occupied chain. In the semiclassical model, the real-space velocity of the orbit now contains a second harmonic component; thus the real-space orbit path becomes somewhat saw-tooth shaped and the carrier spends more time to one side of the orbit. This is reflected in the asymmetry of the quantum-mechanical probability density function.

The presence of the second harmonic in the real space velocity gives rise to a second harmonic of the FTR in the semiclassical model. As expected, the quantum-mechanical model also predicts this. The second order transition matrix element $\langle\xi_m|\hat{y}|\xi_{m+2}\rangle$, shown dashed in Fig. 8, is now finite for bulk states. These transitions are between states with an energy difference of 2Ω. In the FTR experiment, the photon energy is kept constant (the millimetre-wave frequency is fixed by the resonator dimensions) and the magnetic field is swept. Since Ω is proportional to the magnetic field strength, these second order transitions will occur at a magnetic field that is half as strong as the field for the fundamental resonance; this is in agreement with the prediction of harmonics occuring at lower fields than the fundamental in the semiclassical model.

For this case, where $t_2/t_1 = 0.1$, the ratio of the second order transition matrix elements to first order transition matrix elements is 0.01. In fact, we find that this ratio is always $(t_2/t_1)^2$ for the bulk states. This is in agreement with the ratio of the amplitudes of the resonances in conductivity predicted by the semiclassical theory (see the paragraph following Eqn. 6).
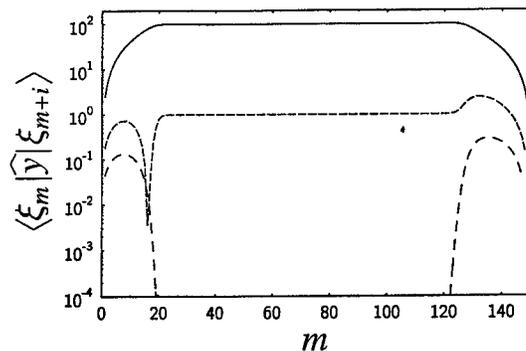
Figure 8. Transition probabilities $\langle \xi_m | \hat{y} | \xi_{m+i} \rangle$ for $i = 1$ (solid), $i = 2$ (dashed) and $i = 3$ (dotted) calculated for $t_1 = 10\Omega$, $t_2 = t_1/10$.

Fig. 8 also shows the third order transition probabilities given by the matrix elements $\langle \xi_m | \hat{y} | \xi_{m+3} \rangle$, which are zero for the bulk states, since t_3 is zero (though third order transitions occur between edge states for the reasons given above) In general we find that if t_i is non-zero, then nth order transitions are allowed between bulk states, and the transition strength is given by t_i^2, in agreement with the predictions of the semiclassical model.

5. CONCLUSIONS

We have described the origin of a new kind of magnetic resonance, FTR, using a semiclassical model of the high-frequency magneto-conductivity of metals. The existence of FTR has been confirmed by experiment. An alternative model of FTR is presented using a very natural and simple quantum-mechanical approach. The semiclassical and quantum models agree quantitatively on every feature of the new effect. The significance of these results lies in the the fact that the two models predict the effect from quite different initial assumptions. In the semiclassical limit, the granularity of the lattice is reflected only in the existence of the Brillouin zone and the Fermi surface; particles are considered to be point like in both real space and momentum space, and are allowed to move continuously. In the quantum mechanical model, the granularity of the lattice appears explicitly; we consider the occupancy of each chain individually. The prediction of FTR by both models indicates that it is a fundamental property of quasi-one-dimensional systems.

Acknowledgements

REFERENCES

1. For a review see *Electrons at the Fermi Surface*, edited by M. Springford, CUP (1980).
2. D. Shoenberg, *Magnetic oscillations in metals*, CUP, (1984).
3. S.J. Blundell and J. Singleton, *Phys. Rev. B* **53**, 5609 (1996).
4. J. Singleton *et al.*, *Phys. Rev. Lett.* **68**, 2500 (1992).
5. T. Osada, S. Kagoshima and N. Miura, *Phys. Rev. B* **46**, 1812 (1992).
6. L.P. Gor'kov and A.G. Lebed', *Phys. Rev. Lett.* **71** 3874 (1993).
7. S.J. Blundell, A. Ardavan and J. Singleton, *Phys. Rev. B Rapid Comm.* **55** 6129 (1997).
8. Bis(ethylenedithio)tetrathiafulvaline is an organic molecule also known as BEDT-TTF or ET.
9. T. Ishiguro and K. Yamaji, Organic Superconductors, *Springer Verlag*, (1990).

10. See for example M. Kurmoo, D.R. Talham, P. Day, I.D. Parker, R.H. Friend, A.M. Stringer and J.A.K. Howard, *Solid State Commun.* **61** 459 (1987); M. Oshima *et al.*, H. Mori, G. Saito and K. Oshima, *Chem. Lett.* **7** 1159 (1989).

11. N. Harrison, J. Caulfield, J. Singleton, P.H.P. Reinders, F. Herlach, W. Hayes, M. Kurmoo and P. Day, *J. Phys.: Condens. Matter* **8** 5415 (1996).

12. N. Harrison, A. House, M.V. Kartsovnik, A.V. Polisski, J. Singleton, F. Herlach, W. Hayes and N.D. Kushch *Phys. Rev. Lett.* **8** 1576 (1996); N. Harrison, M.M. Honold, M.V. Kartsovnik, J. Singleton, S.T. Hannahs, D.G. Rickel and N.D. Kushch, *Phys. Rev. B* **55** 16005 (1997).

13. M.M. Honold *et al.*, *Phys. Rev. B*, in press.

14. For a recent review see A. A. House *et al.*, *J. Phys.: Condens. Matter* **8** 8829, *ibid.* **8** 10361, *ibid.* **8** 10377 (1996), and references therein.

15. C. P. Poole, *Electron Spin Resonance*, Interscience Publishers, (1967).

16. A. Ardavan, J.M. Schrama, S.J. Blundell, J. Singleton, W. Hayes, M. Kurmoo, P. Day and P.Goy, *Phys. Rev. Lett* **81**, 713 (1998).

17. A. Polisski, J. Singleton, P. Goy, W. Hayes, M. Kurmoo and P. Day, *J. Phys.: CM* **8**, L195 (1996).

18. S. Hill *et al.*, *Proc. SPIE* **2842**, 296 (1996).

19. V.M. Yakovenko and H.-S. Goan, *Phys. Rev. B* **58**, 8002 (1998).

20. G.H. Wannier, *Phys. Rev.* **117**, 432 (1960).

21. N. Dupuis and G. Montambaux, *Phys. Rev. Lett.* **68**, 357 (1992); N. Dupuis and G. Montambaux, *Phys. Rev. B* **46** 9603 (1992).

A low power, optically controllable, THz attenuator

N.E. Hecker[a], I.H. Libon[a], M. Hempel[a], S. Baumgärtner[a], M. Koch[a,b], P.Dawson[c], and J. Feldmann[a]

[a]Photonics and Optoelectronics Group, Physics Department and CeNS, Ludwig-Maximilians-University, D-80799 Munich, Germany
[b]Institut für Hochfrequenztechnik, TU Braunschweig, D-38106 Braunschweig, Germany
[c]Department of Physics, UMIST, Manchester, M60 1QD, United Kingdom

ABSTRACT

We have demonstrated a low power, optically-controllable, THz attenuator capable of high contrast ratios using a mixed type-I/type-II quantum well sample. When high free-carrier densities are optically excited in the quantum wells by a cw-laser, the transmitted THz intensity can be controllably reduced. Normally in quantum well samples high carrier densities cannot be achieved using low power excitation densities (mW/cm^2), because the carrier lifetime is so short. This is not the case for our sample which consists of 20 periods of a narrow and a wide GaAs well. After electron-hole pairs are created via optical excitation in the narrow well, they are separated in space, because the electrons are rapidly transferred (within 30 ps) into the wide well via an X-valley in the barrier material. The carrier lifetime at low sample temperatures is therefore extremely long, 0.48 ms, leading to high carrier densities. Using an optical excitation power of 2.1 mW from a cw-HeNe laser, the transmitted THz intensity can be reduced by 60 %.

Keywords: THz spectroscopy, mixed type GaAs/AlGaAs quantum wells, THz attenuator

1. INTRODUCTION

In mixed type-I/type-II GaAs/AlAs double quantum wells, optically excited carrier lifetimes can exceed 0.4 msec[1], because electron/hole pairs are spatially separated. Such long lifetimes can be used to attain extremely high carrier densities (~10^{12} cm^{-2}) at low excitation powers (~0.09 W/cm^2). We have been able to exploit these properties of the mixed type quantum well sample to construct an optically controlled, THz attenuator. In essence, a low power cw-HeNe laser is used to externally control the carrier density in the quantum wells. Without optical excitation, the transmitted THz intensity is attenuated mainly by reflections at the air-sample surfaces. After optical excitation however, the THz beam is reflected and absorbed by the free carriers in the quantum wells where the magnitude of the reflection and absorption can be controlled by variation of the carrier density.

Our sample consists of 20 periods of a double quantum well structure. The narrow (25 Å) and the wide (68 Å) GaAs quantum wells are separated by a 103 Å thick AlAs barrier (see fig. 1). The GaAs substrate has been removed by selective chemical etching to allow for THz-transmission measurements, and the remaining film has been mounted on a sapphire substrate. Carriers are optically excited in both wells by an unfocussed cw-HeNe laser ($\lambda = 612$ nm). The electron/hole pairs in the wide well recombine on a timescale of nanoseconds. In contrast, electrons excited in the Γ-valley of the narrow well are transferred to the X-valley in the barrier material on a subpicosecond timescale[2]. The subsequent transfer of the electrons to the Γ-valley of the wider well occurs on a time scale on the order of 30 ps[3]. This spatial separation between holes remaining in the narrow well and the electrons now in the wide well leads to the 0.48 msec carrier lifetime at a sample temperature of 10 K[1]. The recombination rate of these electron-hole pairs is dominated by the tunneling rate of heavy holes from the narrow well into the wider well[4].
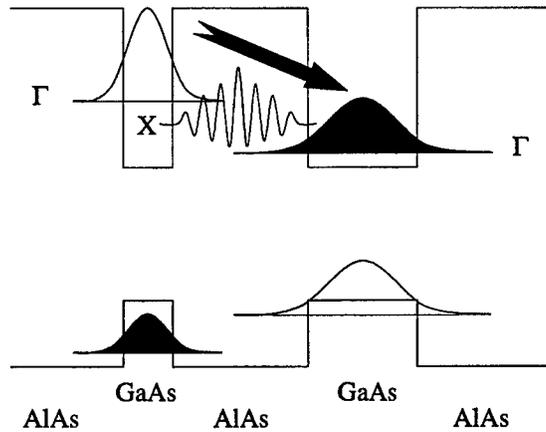
Figure 1: Schematic diagram of the conduction and valence band edges of the mixed type-I/type-II quantum wells along with the relevant n=1 electron and heavy hole energy states. The electrons after optical excitation are transferred from the narrow well to the wide well and are therefore spatially separated from the holes remaining in the narrow well.

Our THz pulses are generated using the scheme developed by Grischkowsky et al.[5] which consists of an ultrafast photoconductive switch as THz emitter and a receiver antenna as detector (see fig. 2).
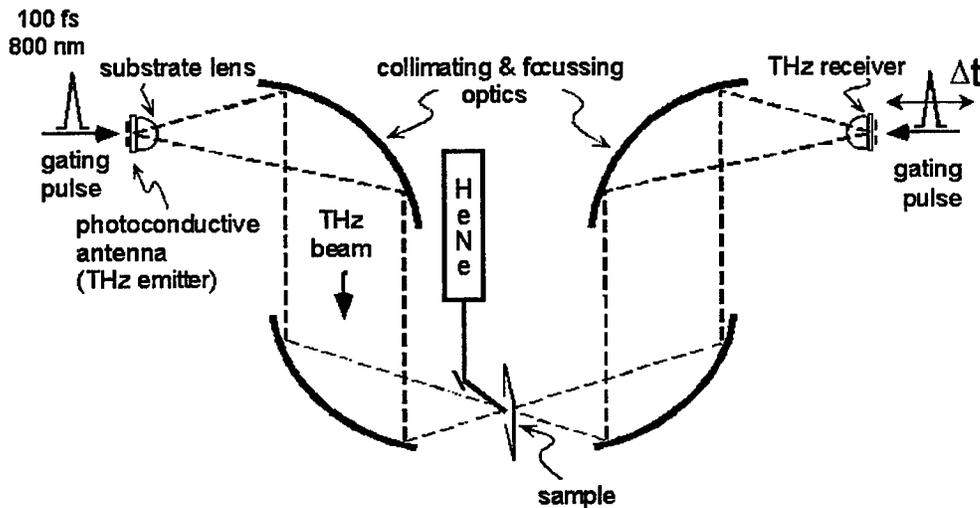
Figure 2: A sketch of the experimental setup. The quantum well sample is mounted in a cryostat.

For our measurements discussed here, we focussed with a microscope objective 20 mW of 800 nm, 100 fs laser pulses from a commercial 76 MHz Ti-sapphire laser between the striplines of a semi-insulating GaAs antenna to generate free carriers by photoexcitation. When the striplines are biased by up to 40 V, these carriers are accelerated and subsequently, because of the induced space-charge field which screens the bias, are decelerated. The emitted radiation is proportional to the time derivative of this induced photocurrent and is in the THz-frequency range. The resulting THz-pulses are detected by a

silicon-on-sapphire based antenna. Here another optical pulse gates the detector antenna by exciting carriers which are accelerated by the the biasing electric field of the THz radiation. The resulting current in the detector is proportional to the electric field of the THz pulse and is measured using the fast scan technique[6]. In order to measure the complete waveform of the THz pulse, the optical pulse used to gate the receiver antenna is delayed with respect to the THz-pulse and for each delay the detector current is determined. Typically our measurable THz spectrum ranges between 0.05-1.0 THz.

The sample has been mounted in a continuous flow liquid He cryostat for transmission experiments and for the measurements discussed here the sample temperature was held at 40 K. The cryostat's windows are composed of TPX, a plastic which is transparent both in the optical and THz frequency ranges[7].

A 2.6 mW, 612 nm, HeNe cw laser is used to optically excite carriers in the quantum wells. The laser has not been focussed in order to achieve a good overlap between the optical beam and the THz pulses. The beam waists are 1.7 and 2.0 mm, respectively. The time averaged electron and hole densities in the quantum wells optically excited by the cw-laser operated at highest power (at the sample, this value is 2.1 mW) are $\sim 10^{12}$ cm^{-2}.

2. EXPERIMENTAL RESULTS

Transmission measurements of the THz waveforms were performed for HeNe laser intensities on the sample ranging from 0–2.1 mW. In figure 3, we show the measured THz waveforms for 0, 0.6, and 2.1 mWs. The THz-peak signal decreases with increasing optical power and also shifts noticeably to shorter delay times indicating that the index of refraction $n(\omega)$ of the quantum well layers has changed. This shift will be discussed in greater detail in a future publication[8].
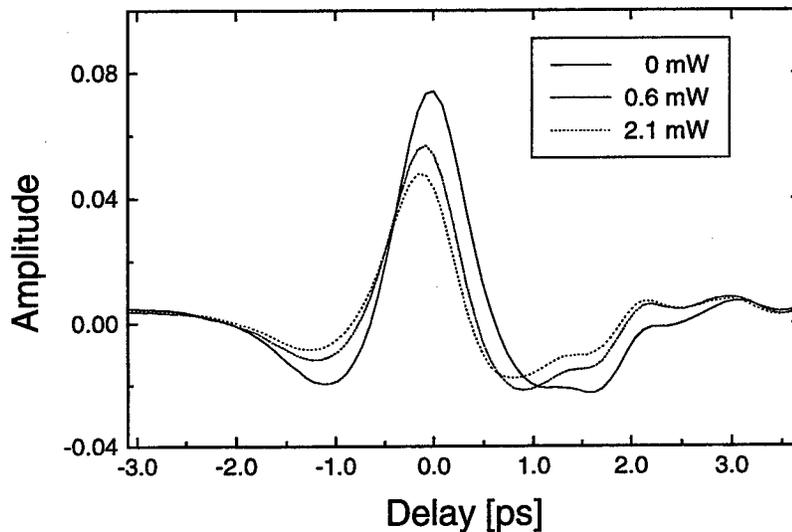

Figure 3: Measured THz-waveform transmitted through the mixed type-I/type-II quantum well sample with various HeNe laser powers exciting carriers in the quantum wells.
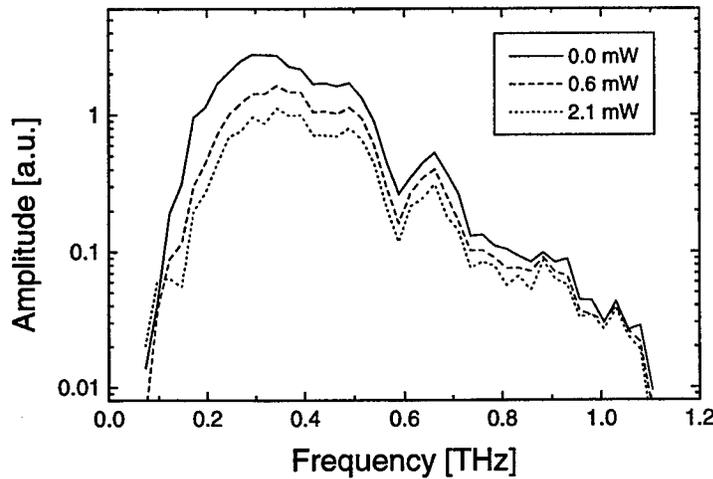
Figure 4: Spectra obtained by Fourier transforming the waveforms shown in fig. 3.

In figure 4, the corresponding Fourier transformed spectra are plotted. By integrating the spectra from 0.2-1.0 THz, we obtain the attenuation of the THz beam as it passes through the sample (see figure 5). At our highest cw-excitation power (2.1 mW), we measure a 60% decrease in the THz-intensity.
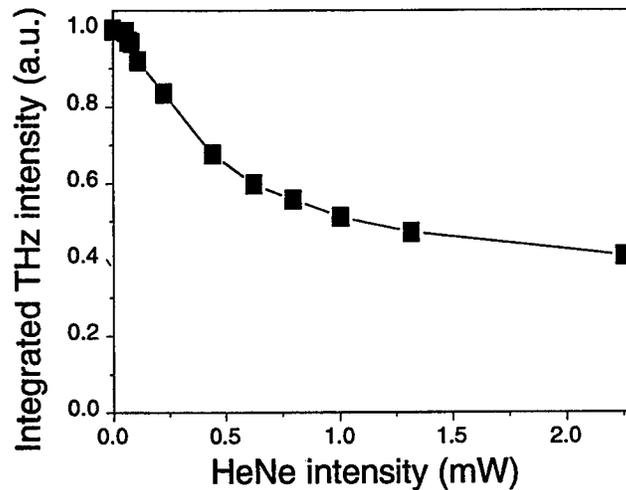

Figure 5: Dependence of the transmitted THz intensity on the HeNe laser power. The intensity has been determined from integrating the THz-spectrum at each excitation power from 0.2 – 1.0 THz.

We attribute the attenuation of the THz intensity to free carrier absorption and to an increase in the reflectivity of the sample due to changes in the index of refraction. When using a simple Drude model to fit the frequency dependent transmission for various HeNe powers, we are able to fit the data quite well with a single parameter. Although a three dimensional model of the conductivity may seem unreliable for a quantum well heterostructure, Chen et al.[9] have been able to obtain good results when comparing conductivities determined using fits to THz transmission data and Hall measurements. In our model, we

assume that the density of carriers in each of the quantum wells is constant and neglect any reflections at the quantum well/barrier material interfaces. The complex dielectric function given by the Drude model[10] is:

$$\varepsilon(\omega) = \varepsilon_\infty - \frac{\omega_p^2}{\omega\,(\omega + i\,\Gamma_{fit})}$$

where $\varepsilon_\infty = 10.9$, ω_p is the plasmon frequency which is determined by the calculated electron density, and Γ_{fit} is the carrier damping rate. By inserting the reflection of the THz radiation due to variations in the index of refraction:

$$R = \frac{(n - n')^2 + k^2}{(n + n')^2 + k}$$

where n and k are the real and imaginary parts of the index of refraction for the quantum wells and $n' = 3.6$ is the real part of the index of refraction for the surrounding GaAs material, into the THz transmission[11]:

$$T = \frac{(1 - R)^2 e^{-\alpha d}}{1 - R^2 e^{-\alpha d}}$$

where d=136 nm (the thickness of the 20 wide quantum wells), $\alpha = 4\pi k/\lambda_0$ is the absorption coefficient and λ_0 is the wavelength of the THz radiation, we are able to fit our data and determine Γ_{fit}.

In figure 6, we have plotted the normalized THz transmission versus frequency for 0.6, 0.9, and 2.1 mW of HeNe power used to excite carriers in the quantum wells. The lines are our Drude fits, and our extracted Γ_{fit} ranges from 27-40 THz. We find that the simple Drude model can be used to produce good fits. However in order to obtain more quantitative information about our THz attenuator sample, a more sophisticated model is needed which explicitly includes the effects of the band structure and therefore properly treats intraband absorption.
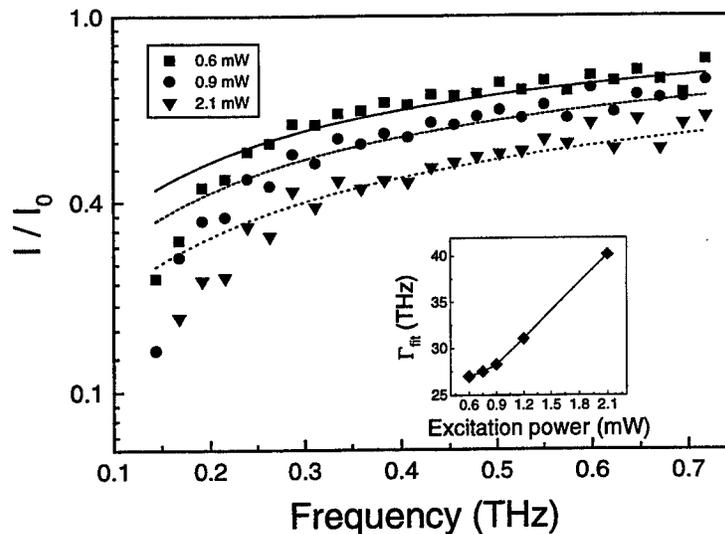

Figure 6: Normalized THz transmission I/I_0 though the mixed type quantum well sample versus frequency for HeNe powers: 0.6, 0.9, and 2.1 mW used to excite carriers in the quantum wells. The lines are fits to the theoretical model. The insert depicts the dependence of Γ_{fit} on the excitation power or carrier density.

3. CONCLUSIONS

We have demonstrated a low optical power controlled THz attenuator using a low power cw-laser and a mixed type quantum well sample. Using 2.1 mW for optical excitation, we can reduce the integrated transmitted intensities by up to 60%. Using a simple Drude model, we have shown that the attenuation of the THz radiation can be modeled by fitting the carrier damping rate Γ_{fit} which ranges from 20-40 THz.

4. ACKNOWLEDGEMENTS

5. REFERENCES

1. I. Galbraith, P. Dawson, and C.T. Fox, Phys. Rev. B **45**, 13499 (1992).
2. J. Feldmann, R. Sattmann, E.O. Göbel, J. Kühl, J. Hebling, K. Ploog, R. Muralidharan, P. Dawson, and C.T. Foxon, Phys. Rev. Lett. **62**, 1892 (1989).
3. J. Feldmann, M. Preis, E.O. Göbel, P. Dawson, C.T. Foxon, and I. Galbraith, Sol. State Comm. **83**, 245 (1992).
4. A.M. Malik, M.J. Godfrey and P. Dawson, Phys. Rev. B **59**, 2861 (1999).
5. D. Grischkowsky, Søren Keiding, Martin van Exter, and Ch. Fattinger, J. Opt. Soc. Am. B **7**, 2006 (1990).
6. D.M. Mittleman, Rune H. Jacobsen, and Martin C. Nuss, IEEE Journal of Selected Topics in Quantum Electronics **2** 679 (1996).
7. J. R. Birch *et al.*, Infrared Physics **24**, 573 (1984).
8. I.H. Libon, S. Baumgärtner, M. Hempel, P. Dawson, M. Koch, N.E. Hecker, and J. Feldmann, to be published.
9. Yue Chen, S.S. Prabhu, Stephen E. Rallph, and Dave T. McInturff, Appl. Phys. Lett. **72**, 439 (1998).
10. N. Katzenellenbogen and D. Grischkowsky, Appl. Phys. Lett. **61**, 840 (1992).
11. for a derivation, see C.T. Johnson, G.H. Sherman, and R. Weil, App. Opt. **8**, 1667 (1969).

Optimisation of pulsed GaAs IMPATT diodes for 200 GHz

Christian Benz[*] , Jürgen Freyer, Helmut Grothe

Technische Universität München
Lehrstuhl für Allgemeine Elektrotechnik und Angewandte Elektronik
Arcisstr. 21, D-80290 München, Germany

ABSTRACT

RF power generation of IMPATT diodes at mm-wave frequencies is limited mainly by thermal effects. The challenge to obtain output power at 200 GHz and above can be met only by extremely high DC current densities to push the characteristic avalanche frequency near to the oscillation frequency. The active devices have to be optimised with regard to pure IMPATT mode operation, low break-down voltage and efficient heat dissipation. Since these three conditions influence each other, a compromise is necessary. From theoretical simulations (Monte Carlo simulation and drift-diffusion model) a double-drift Read IMPATT diode structure results which is capable to be operated at DC current densities up to 225 kA/cm² for short pulses of 50 ns with maximum device temperature below 500 K. The initial material is grown by MBE technique taking special care to control the thickness and doping concentration of the different GaAs layers. The individual devices are fabricated by standard photo-resist technology with an integrated gold cone on top which adjusts the encapsulation height in the used full height inductive post waveguide resonator. Thereby, a low loss device mounting in the resonator without parasitic elements and an optimum impedance matching of diode and resonator can be realised. By means of different double-drift Read IMPATT structures the experimental results in terms of RF output power, conversion efficiency and oscillation frequency are compared. The highest output power so far is 1W at 176.5 GHz with 5.5 % conversion efficiency. At a frequency of 210 GHz 0.25 W output power and 1.8 % conversion efficiency were realised at a DC current density of 225 kA/cm². The experimental results are in good agreement with calculations applying a pulsed oscillator model.

Keywords: GaAs IMPATT diodes, RF power generation, mm-waves, pulsed operation, waveguide resonator

1. INTRODUCTION

Significant RF power levels from fundamental mode GaAs transit-time devices have been reported under CW operation up to 170 GHz which exhibit an excellent noise behaviour [1,2]. Further increase of the oscillation frequency, however, seems to be limited mainly by the thermal properties of the GaAs material, since higher current densities, which are necessary to push the characteristic avalanche frequency near to the oscillation frequency, lead to an unacceptable increase in device temperature. Therefore, for GaAs transit-time devices, recently intensive efforts have been made to extract RF power from second-harmonic operation at higher frequencies [3,4].

In the present paper, the increase in oscillation frequencies achieved using pulsed GaAs IMPATT diodes is described. The applied devices are double-drift Read IMPATT diodes, which have been already successfully realised for CW operation at upper D-band frequencies (140 GHz -170 GHz)[1]. In a first step, the devices were designed for a DC current density of 175 kA/cm² for a pulse time of 50 ns. For the design a Monte Carlo Simulation programme for the high field injection region and a large signal drift diffusion model for the drift zones were used. For higher current densities, necessary to receive RF output powers at 200 GHz and above, the devices were redesigned under the point of view to minimise the thermal resistance of the diode chip. As a result, the maximum DC current density could be further increased to 225 kA/cm². The experimental results of RF output power and conversion efficiency demonstrate the excellent performance of these powerful devices.

[*] Christian Benz: email: benz@ei.tum.de; Telephone: +49 (0)89 28922957; Fax: +49 (0)89 28922950

384

Part of the EUROPTO Conference on Terahertz Spectroscopy and Applications II
Munich, Germany ● June 1999 SPIE Vol. 3828 ● 0277-786X/99/$10.00

2. DEVICE DESIGN

The devices presented in this paper are based on double-drift Read IMPATT diodes originally realised for CW operation. To apply the devices for pulsed operation at extremely high DC current densities, the design of the structures has to involve the optimisation of both, the high field injection region and the drift zones for electrons and holes, respectively. For the calculations, the maximum device temperature is chosen to be 500 K.

The injection region is designed by Monte Carlo simulations which take into account the non-local effects of carrier generation due to impact ionisation. An optimum length of the high field region is found which represents a compromise between low DC voltage across the injection region and a minimum carrier generation due to Zener tunneling [5]. The low DC voltage positively affects the input power density and therefore the allowable DC current density to be applied to the active device, whereas a sufficiently suppression of Zener tunneling leads to higher conversion efficiency in the IMPATT mode. Using the optimised injection region from Monte Carlo simulations, the drift zones for electrons and holes, respectively, are optimised for very high current densities with the help of a large-signal drift-diffusion model [6]. To prevent drastic degradation in conversion efficiency due to carrier generation the electric field in the drift zones has to be below breakdown field. Fig. 1 shows the electric field distribution in the space
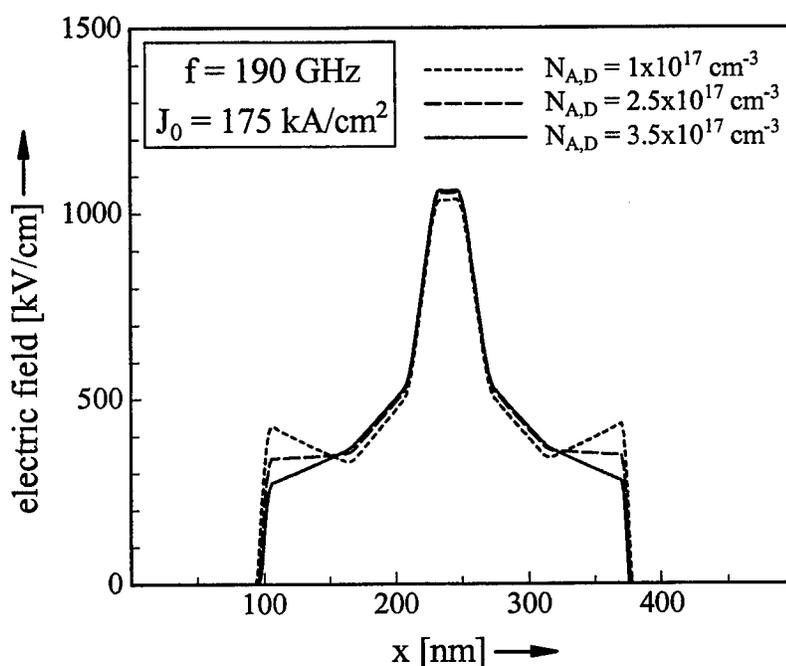
Fig. 1: Electric field distribution of the applied double-drift Read IMPATT diode. Parameter is the doping concentration of the drift zones.

charge region of the applied double-drift Read IMPATT diode. The calculations were performed at a maximum DC current density of 175 kA/cm². Parameter is the doping concentration of the drift zones. It is clearly visible that for a doping in the range of $1 \cdot 10^{17}$ cm⁻³, which represents the doping level for the CW structure, the electric field at the edge of the drift zones is significantly increased and thus leads to unwanted carrier generation. On the other hand, if the doping is increased the electric field is sufficiently suppressed. It is found, that for a doping concentration of $3.5 \cdot 10^{17}$ cm⁻³, optimum RF power densities are obtained between 170 GHz and 200 GHz at a DC current density of 175 kA/cm². With a further increase of the doping level, the RF performance could not be improved due to non depleted regions during RF modulation. This behaviour is shown in Fig. 2, where the calculated RF power density is plotted against the applied DC current density for an oscillation frequency of 190 GHz (parameter is again the doping concentration of the

drift zones). It can be seen, that the DC current density has to be significantly increased to obtain higher RF output power levels.
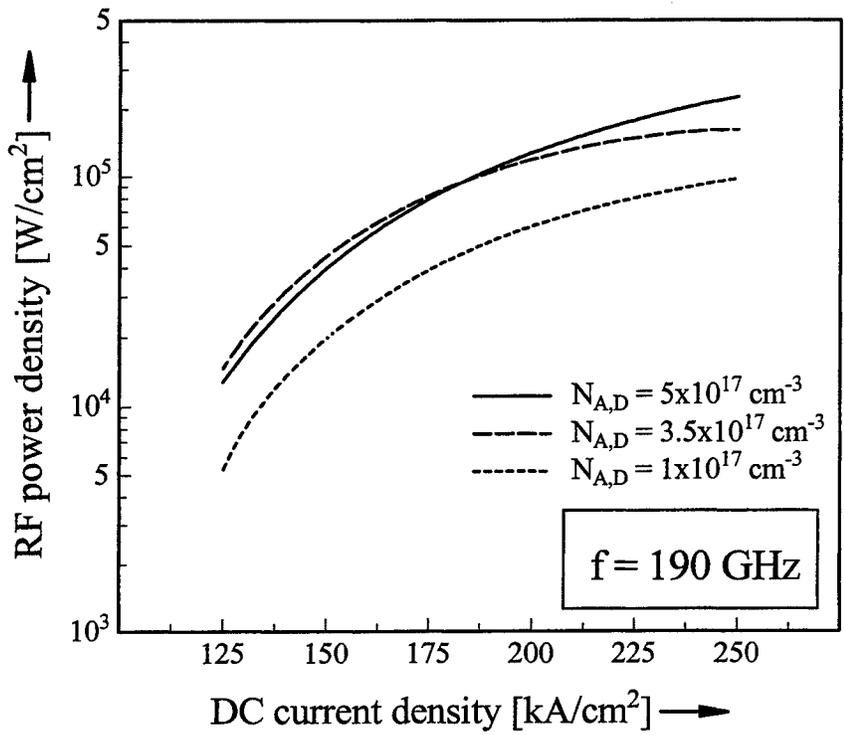

Fig. 2: Calculated RF power density against DC current density of the applied double-drift Read IMPATT diodes. Parameter is the doping concentration of the drift zones.

Starting from the electronically optimised device structure with maximum DC current density of 175 kA/cm² the double-drift Read IMPATT diode was redesigned for still higher current densities to obtain RF output power at elevated frequencies above 200 GHz. Nevertheless, the temperature increase during the pulse time must be controlled in order not to exceed the maximum allowable total device temperature of 500 K. This leads consequently to a compromise between the electronically and the thermally optimised structure. For short pulse times in the range of 50 ns to 75 ns, which are used in the experiments, the thermal behaviour of the diode is mainly affected by the thermal resistance and capacitance of the device itself and only little by the heat sink. Therefore, the maximum DC current density for a given pulse length is fairly independent of device area. In addition, an increase of the applied current density, i. e. an increase of the input power at fixed device temperature can be achieved only by reduction of the lengths next to the heat generating high field region. Fig. 3 shows the schematic structure of the GaAs double-drift Read IMPATT diode. The numbers in brackets beneath the single layers denote the values of the foregoing structure optimised for 175 kA/cm². The results of the simulation clearly show that the high-field region must not be altered as otherwise the IMPATT operation mode is changed. Also the length of the drift zones for electrons must not be changed due to a resulting strong degradation of the electronic device performance. However, as shown in Fig. 3 the remaining layers can be diminished leading to an overall improvement of the device. The final length for the hole drift zone and the p⁺-contact layer is only 30 nm. The n⁺-contact layer can be reduced only to a total thickness of about 500 nm to avoid failure during the thermocompression bonding process. Finally, the thickness of the different metallisation layers of the n⁺-contact and the p⁺-contact, respectively, are reduced to a minimum value where still optimum RF performance is

guaranteed. With this redesigned structure an increase of the maximum DC current density of about 25 % seems to be feasible. Thus, the doping concentration of the drift zones is increased to $4.5 \cdot 10^{17}$ cm^{-3} to obtain optimum RF output power levels at that elevated DC current densities.
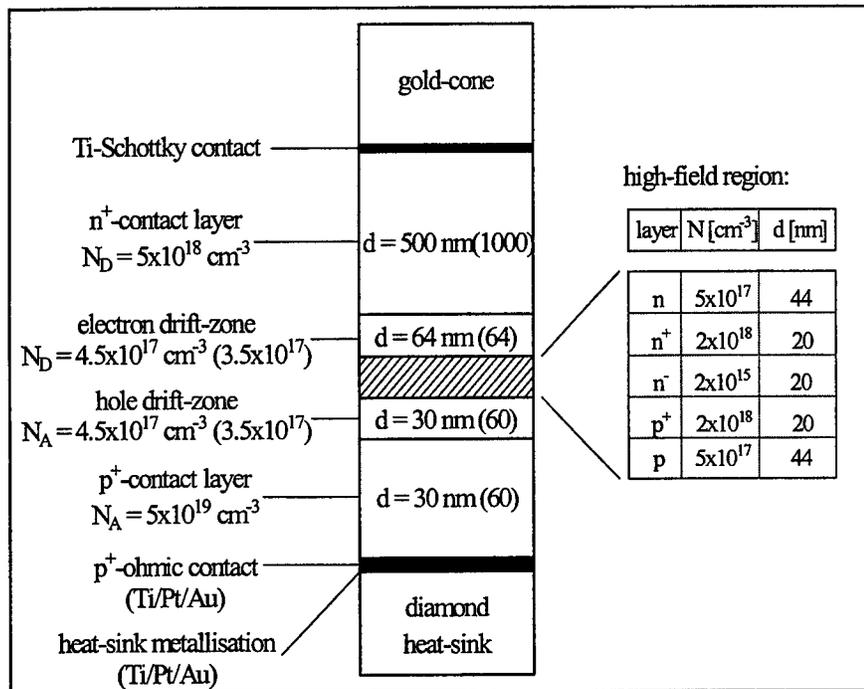

Layer structure diagram labels:

- gold-cone
- Ti-Schottky contact
- n$^+$-contact layer $N_D = 5 \times 10^{18}$ cm^{-3} — d = 500 nm (1000)
- electron drift-zone $N_D = 4.5 \times 10^{17}$ cm^{-3} (3.5×10^{17}) — d = 64 nm (64)
- hole drift-zone $N_A = 4.5 \times 10^{17}$ cm^{-3} (3.5×10^{17}) — d = 30 nm (60)
- p$^+$-contact layer $N_A = 5 \times 10^{19}$ cm^{-3} — d = 30 nm (60)
- p$^+$-ohmic contact (Ti/Pt/Au)
- heat-sink metallisation (Ti/Pt/Au)
- diamond heat-sink

high-field region:

layer	N [cm^{-3}]	d [nm]
n	5x10^{17}	44
n$^+$	2x10^{18}	20
n$^-$	2x10^{15}	20
p$^+$	2x10^{18}	20
p	5x10^{17}	44

Fig. 3: Schematic structure of the applied GaAs double-drift Read IMPATT diode for oscillation frequencies up to 210 GHz at a DC current density of 225 kA/cm^2.

3. RESONATOR STRUCTURE

Generally, the realisation of oscillators at pulsed operation is related to the application of waveguide resonators with inductive post structure, where the waveguide height is reduced to 1/3 of the normal height for impedance matching of devices with relatively large areas. Since there is a great demand on mechanical precision and tuning behaviour at G-band frequencies (140 GHz - 220 GHz, waveguide height: 650 μm), the application of this resonator structure appears quite critical. First experiments carried out at upper D-band frequencies (140 GHz -170 GHz) [7] and simulations from a finite element programme qualifies also the full height waveguide resonator with inductive post structure for pulsed operation. Impedance matching of the active device and the load resistance can be achieved for oscillation frequencies up to 210 GHz if the impedance transformation to the relatively low device impedance is carried out by appropriate choice of only the resonator post height and diameter, respectively (see Fig. 4: h$_{post}$, $\emptyset_{post}$). Conventional stand-off technology for the encapsulation of the active device is not applicable due to the relatively high values of the parasitic elements and the small degree of reproducibility. Even the module technique [1], which represents the monolithic integration of an active element and the surrounding stand-off structure with well defined parasitics can not be applied, since also the parasitics of this encapsulation technique lead to a drastic reduction of the small negative device resistance or to a quenching at all. Therefore, a new mounting technique without parasitic elements for large area devices is developed, which ensures low loss impedance transformation of the investigated double-drift Read IMPATT diodes. By the help of standard photoresist technology the active device structure and a truncated cone of gold on top of the device are fabricated. The element ensures high reproducibility and sensitive adjustment of the load resistance for

impedance matching. The single elements are thermocompression bonded on a metallised diamond heat sink on the bottom of the G-band resonator. The total applied resonator structure consists of the full height waveguide section with inductive post structure and a sliding short for tuning as illustrated in Fig. 4.
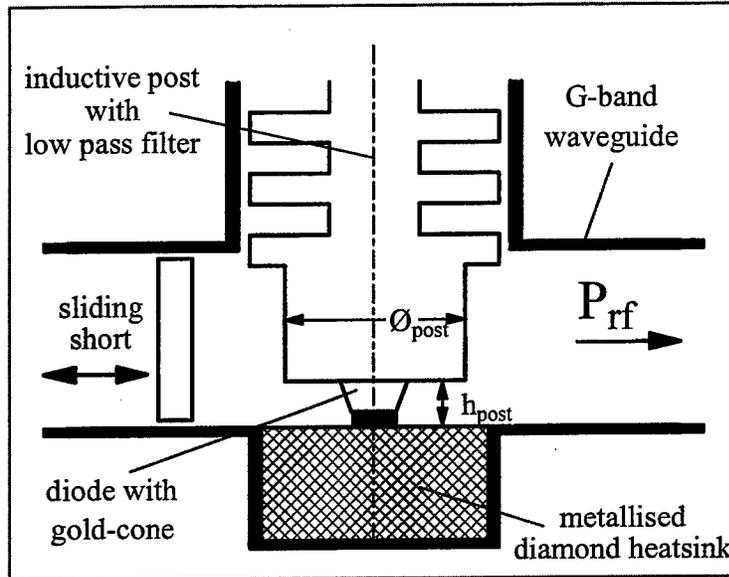

Fig. 4: Schematic cross-section of the applied resonator structure, with low loss mounting technique of the active device.

4. EXPERIMENTAL RESULTS

The applied double-drift Read IMPATT structures are grown in a molecular beam epitaxy system on GaAs n^+-substrates. During growth, attention is focused on exact compliance with the length and doping concentration of the individual layers. The diodes have been optimised with regard to low internal losses by the application of a Ti-Schottky contact on the highly doped n^+-GaAs layer [8]. For the p^+-ohmic contact, Ti/Pt/Au is used. The optimum device diameter, which follows from RF losses in both diode and resonator, is between 25 and 40 μm. The active device structure and a truncated cone of gold on top of the device are fabricated using standard photoresist technology. The gold-cone adjusts the height of the post above the waveguide bottom. The monolithic realisation of the element ensures high reproducibility and sensitive setting of the post height which in turn leads to a fine adjustment of the load impedance for matching. The single elements are bonded by thermocompression on metallised diamond heat sinks on the bottom of G-band resonators as depicted schematically in Fig. 4.

In Fig. 5 the experimental results for RF output power and conversion efficiency are given against oscillation frequency. A maximum DC current density of 225 kA/cm², which is equivalent to an applied DC input power density of 2.5 MW/cm², could be applied to the redesigned, thermally optimised device structures for a pulse length of 55 ns. In contrast to the preceding results at 150 kA/cm² and 175 kA/cm², obtained with the foregoing double-drift Read IMPATT diode [9], the improvement is quite impressive: At 200 GHz a maximum RF output power level of 0.7 W with a conversion efficiency of 4.2 % is realised. This is a progress of a factor of more than 2 as compared to the current density of 175 kA/cm². The maximum oscillation frequency achieved at 225 kA/cm² is 210 GHz with still 0.25 W RF output power and 1.8 % conversion efficiency. For a value of the total losses of 2·10⁻⁶ Ωcm² the results are in good agreement with those of a pulsed oscillator programme where oscillation frequency and RF output power can be
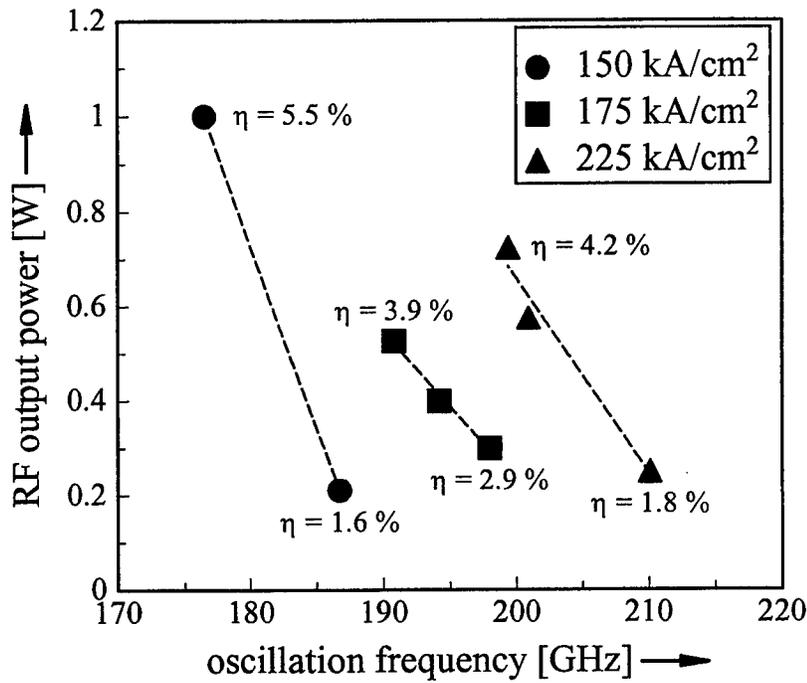
Fig. 5: Measured peak RF output power and conversion efficiency against oscillation frequency. Parameter is the applied DC current density.
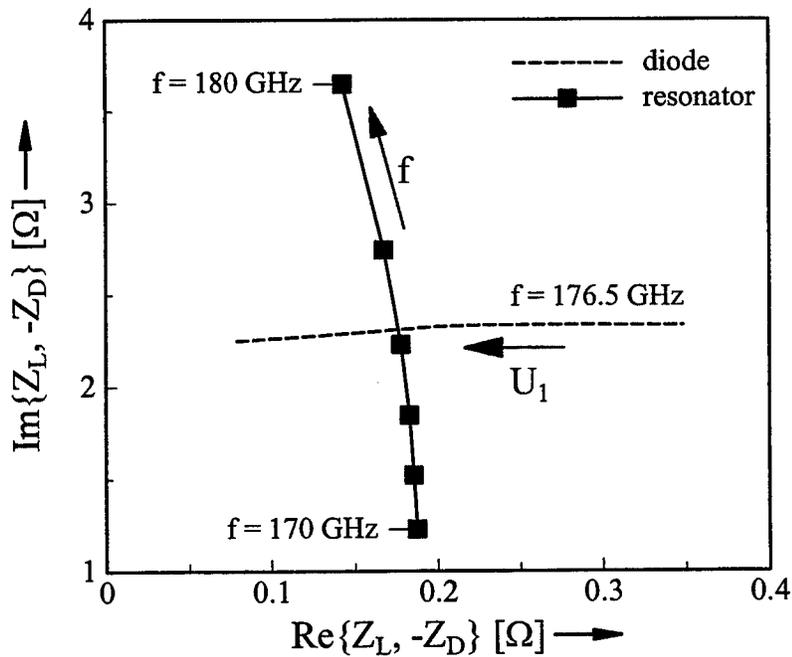

Fig. 6: Impedance locus of resonator and double-drift Read IMPATT diode.
G-band resonator: h_{post} = 18 µm, $\varnothing_{post}$ = 500 µm (see Fig. 4)
Diode: DC current density = 150 kA/cm², T = 500K

calculated as a function of the sliding short position [10]. Herein the non linear device is characterised by the drift diffusion model and the load impedance of a given resonator geometry is described by a finite element programme. Fig. 6 shows as an example the resonator and diode impedance loci in dependence of frequency and RF voltage, respectively, for the realised oscillator at 176.5 GHz. At the point of intersection, the oscillation condition is fulfilled and stable operation of the oscillator is obtained. From the calculations RF output power of 1 W is expected, which is exactly the value obtained in the experiments (see Fig. 5).

5. CONCLUSION

With the help of Monte-Carlo simulations and a large-signal drift-diffusion model, GaAs double-drift Read IMPATT diodes have been designed for pulsed operation up to 210 GHz at DC current densities of 225 kA/cm². An appropriate resonator structure consisting of a full height waveguide section with inductive post structure is realised for optimum impedance matching between active device and load resistance. Using the applied mounting technique without parasitic elements, low loss impedance transformation of the negative device resistance is ensured. RF output power of 1 W at 176.5 GHz with 5.5 % conversion efficiency is realised at a DC current density of 150 kA/cm². Since a maximum DC current density of 225 kA/cm² could be realised in the experiments which a thermally optimised structure, RF power of 0.7 W at 200 GHz and still 0.25 W at 210 GHz with conversion efficiencies of 4.2 % and 1.8 %, respectively, are obtained. The experimental results are in good agreement with the applied oscillator model.

6. ACKNOWLEDGEMENTS

7. REFERENCES

1. M. Tschernitz and J. Freyer, „140 GHz GaAs double-drift IMPATT diodes", Electron. Lett. **31** (7), pp. 582-583, 1995.
2. M. Pöbl, W. Bogner, and L. Gaul, „CW GaAs MITATT source on copper heatsink up to 160 GHz", Electron. Lett. **30** (16), pp. 1316-1317, 1994.
3. H. Böhm, J. Freyer, M. Claassen, W. Harth, and T. Bauer, „Second harmonic power generation form GaAs-IMPATT diodes at 210 GHz", Int. J. Infrared Millim. Waves **19** (4), pp. 587-593, 1998.
4. H. Eisele, „Efficient second-harmonic power extraction form GaAs TUNNETT diodes above 200 GHz", Electron. Lett. **34** (13), pp.1324-1326, 1998.
5. D. Liebig and K. Schünemann, „Cellular automation particle simulation and sensitivity analysis of GaAs-MITATT-diodes for operation at 200 GHz", Int. J. Electron. Commun. (AEÜ) **52** (5), pp. 329-334, 1998.
6. L. Gaul and M. Claassen, „Pulsed high-power operation of p⁺pnn⁺-avalanche diodes near avalanche resonance for mm-wave oscillators", IEEE Trans. **ED-41** (8), pp. 1310-1318, 1994.
7. C. Benz and J. Freyer, „Pulsed GaAs mm-wave devices", Proc. of 21ˢᵗ Int. Conf. on Infrared and Millimeter Waves, Berlin, Germany, **CT8**, 1996.
8. J. Freyer, M. Tschernitz, H. Grothe, and W. Harth, „GaAs transit time devices for frequencies above 140 GHz", Proc. of 3ʳᵈ Int. Workshop on Terahertz Electronics, Zermatt, Switzerland, pp. 17-26, 1995.
9. C. Benz and J. Freyer, „200 GHz pulsed GaAs-IMPATT diodes", Electron. Lett. **34** (24), pp. 2351-2353, 1998.
10. T. Bauer and J. Freyer, „Steady-state simulation of mm-wave multiple device oscillators", Proc. of Int. Workshop an Millimeter Waves, Orvieto, Italy, pp. 145-147, 1996.

Theoretical and Experimental Results of an Integrated mm-Wave Frequency Tripler

Renato Meola, Jürgen Freyer

Lehrstuhl für Allgemeine Elektrotechnik und Angewandte Elektronik, Technische Universität München
Arcisstr. 21, D-80333 München, Germany

ABSTRACT

A frequency tripler from 70 GHz to 210 GHz on semi-insulating GaAs substrate is characterised. Single-barrier varactors with symmetrical capacitance-voltage characteristic are chosen as non-linear devices which simplifies the total tripler circuit, i.e. no idler and bias circuits are necessary. The varactors are monolithically integrated and connected by an air bridge. The matching network is realised by a microstrip network next to the varactor and fine tuning is obtained by backshorts in input and output waveguides. The whole circuit including the varactor is computed at the fundamental and harmonic frequency using a simulation programme for the device and a finite element programme for the circuit, respectively. The aim of this work is to optimise the matching network to achieve maximum tripler performance. Two different matching networks have been calculated indicating the influence on output power and efficiency. Experimental results are presented and compared to theory.

Keywords: GaAs frequency multiplier, tripler, single-barrier varactor, mm-waves

1. INTRODUCTION

Multipliers are frequently applied for rf-power generation at mm-wave frequencies above about 170 GHz since the performance of active semiconductor devices is relatively poor at these frequencies [1]. Although satisfactory results have been achieved from whisker contacted varactors, there is a large interest in planar devices for more reproducible fabrication [2,3]. Mostly, the planar varactors are implemented in the rf-circuit by hybrid techniques [4,5]. Only little is reported in the literature on monolithically integrated devices for multipliers, though the advantage of the control of the parasitic elements for optimum impedance matching is obvious, especially at elevated frequencies. Impedance mismatch is one of the main performance limitations of frequency multipliers. In this paper, the theoretical characterisation of a frequency tripler from 70 GHz to 210 GHz on semi-insulating GaAs substrate with monolithically integrated single barrier varactor is described and experimental results are given.

2. NONLINEAR DEVICE

A single-barrier varactor (SBV) used as nonlinear device shows several advantages as compared to the commonly applied Schottky diode [3,5]. Due to its symmetric capacitance-voltage characteristic, only odd harmonics are generated, which simplifies the multiplier rf-circuit, e.g. for triplers no bias and no idler circuits are necessary. The structure of the applied GaAs/GaAlAs SBV is shown in Fig. 1. The device is optimised with respect to low leakage current across the hetero barrier and high ratio of maximum to minimum capacitance using a simulation programme which considers thermionic field emission as well as tunneling [6]. The GaAlAs barrier has an Al-concentration of 55 % and a width of 20 nm. The GaAs depletion layers on both sides of the barrier consist of two regions with stepwise constant doping profile. The high doping concentration near the barrier enhances the maximum capacitance and the lower doping concentration in the adjacent region allows larger space-charge layer modulation resulting in a smaller minimum capacitance at higher voltage. Details about the optimisation of the GaAs/GaAlAs SBV can be found elsewhere [6]. Fig. 2 shows the experimental realised current-voltage and capacitance-voltage characteristics. Variation in the voltage changes the width of the depleted layer, forming a voltage dependent capacitance. The maximum capacitance, mainly determined by the width of the GaAlAs barrier, is obtained at zero voltage. The minimum capacitance appears for maximum applied voltage. The ratio of maximum to minimum capacitance is a figure of merit for the application as frequency tripler.

Part of the EUROPTO Conference on Terahertz Spectroscopy and Applications II
Munich, Germany • June 1999 SPIE Vol. 3828 • 0277-786X/99/$10.00

391

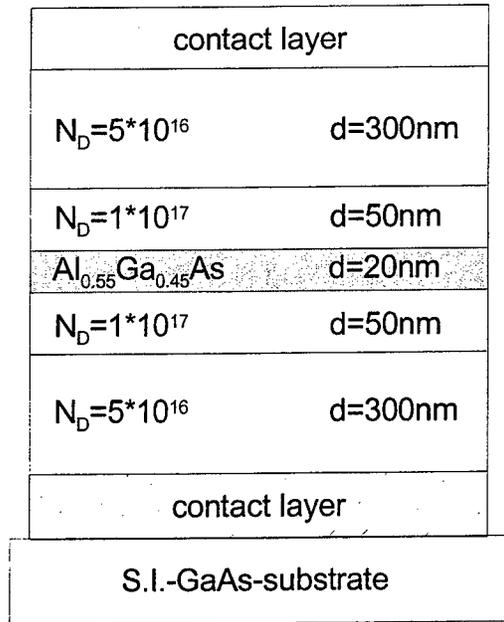| contact layer	
$N_D=5*10^{16}$	$d=300nm$
$N_D=1*10^{17}$	$d=50nm$
$Al_{0.55}Ga_{0.45}As$	$d=20nm$
$N_D=1*10^{17}$	$d=50nm$
$N_D=5*10^{16}$	$d=300nm$
contact layer	

S.I.-GaAs-substrate

Fig. 1: Structure of an optimised single-barrier varactor for frequency tripling from 70 GHz to 210 GHz

The conduction current through the SBV mainly caused by thermionic emission, is blocked by the GaAlAs-barrier at moderate voltages. For not too high voltages the conduction current is much lower than the displacement current and the device performance is dominated by reactive behaviour. With higher voltages, the increasing influence of the conduction current leads to a mixture of reactive and resistive currents and therewith to a saturation of conversion efficiency. (The results of device simulations show that this occurs for conduction current densities above about 1 kA/cm^2.)

(a)   (b)
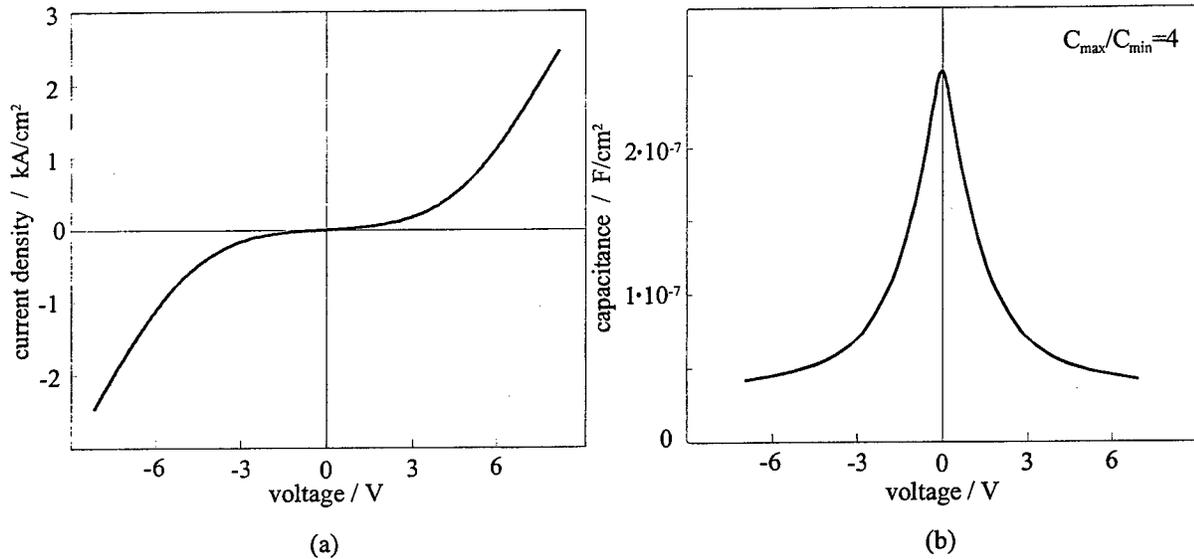
Fig. 2: Characteristics of the SBV according to Fig. 1:   a) current density-voltage   b) capacitance-voltage

3. MICROSTRIP CIRCUIT

The microstrip circuit is realised on a 100 μm thick semi-insulating GaAs substrate on which the varactor structure is grown by MBE technique. Fig. 3a schematically shows the waveguide mount with the entire rf-circuit including the GaAs chip.

(a)

(b)
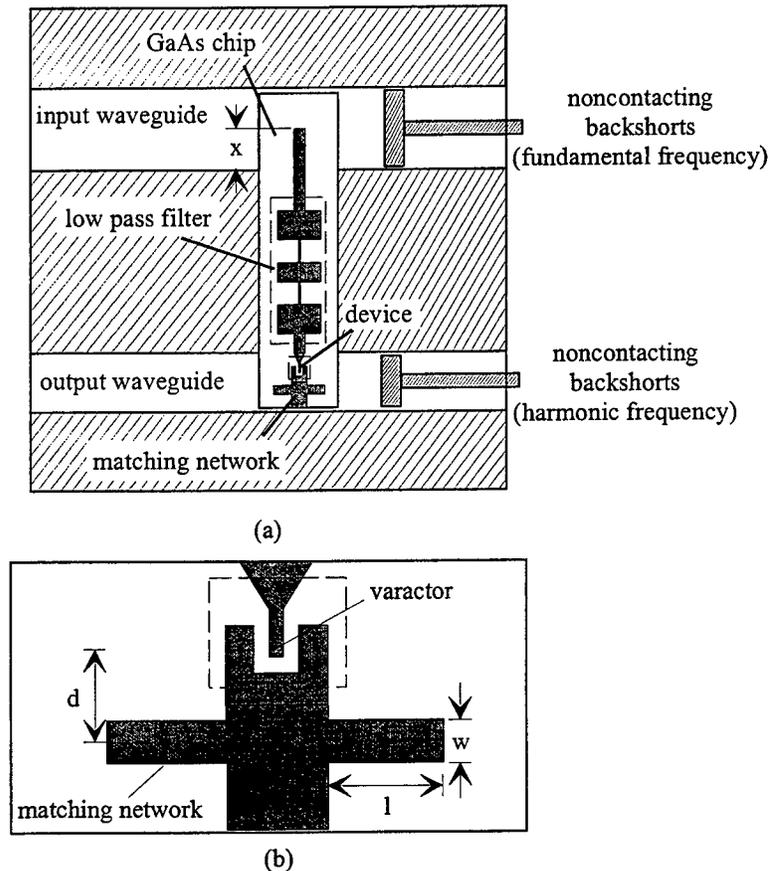
Fig. 3: a) Schematic view of the waveguide mount and GaAs chip including the rf-circuit with monolithically integrated SBV b) Matching network with optimisation parameters

The tripler consists of the monolithically integrated GaAs MMIC containing the nonlinear device positioned directly in the output waveguide and connected by an airbridge, a Tchebyshev low pass filter which provides the decoupling of input and output signal, as well as the matching network for impedance matching at input and output, and the waveguide mount. Input power is coupled from waveguide to microstrip via an E-plane transition. The waveguide mount is splitted into two mirrored symmetrical halfs with full height waveguide and backshorts for impedance fine tuning at input and output frequency, respectively. The matching network is shown in detail in Fig. 3b. Two symmetric microstrip stubs with width w and length l are positioned in the output circuit of the GaAs chip and have a certain distance d from the varactor. The parameters w, l and d are used to optimise the matching network for maximum output power.

4. CIRCUIT CHARACTERISATION AND LARGE SIGNAL ANALYSIS

For the characterisation of the tripler, the varactor is described by time-domain current/voltage solutions and its impedances at the fundamental and the harmonic frequency are determined by a large signal simulation programme based on Fourier analysis. The external circuit is described by frequency-domain current/voltage solutions and its impedances including the microstrip components, the matching network, the air-bridge, and the waveguide mount are determined by the finite-element

programme HFSS (Hewlett Packard). The non-linearity of the device is implemented by the experimental realised capacitance-voltage and current-voltage characteristics according to Fig. 2. The critical step for the design of the tripler is to dimension the matching network for optimum impedance matching at both, input and output frequency. Due to the monolithically integrated varactor, however, a detailed determination and reproducible fabrication of the device parasitics can be achieved. The entire circuit is computed including the losses of the GaAs substrate, the metallisation, and the waveguide mount.

Fig. 4 shows the equivalent circuits for input (Fig. 4a) and output frequency (Fig. 4b), respectively. At the fundamental

$f_1 = 70$ GHz	$f_3 = 210$ GHz
$Z_L^{f_1} = Z_C^{f_1} + R_{loss}^{f_1}$	$Z_L^{f_3} = Z_C^{f_3} + R_{loss}^{f_3}$
$Z_L^{f_1} = (Z_D^{f_1} + 2R_{loss}^{f_1})^*$	$Z_L^{f_3} = -Z_D^{f_3}$
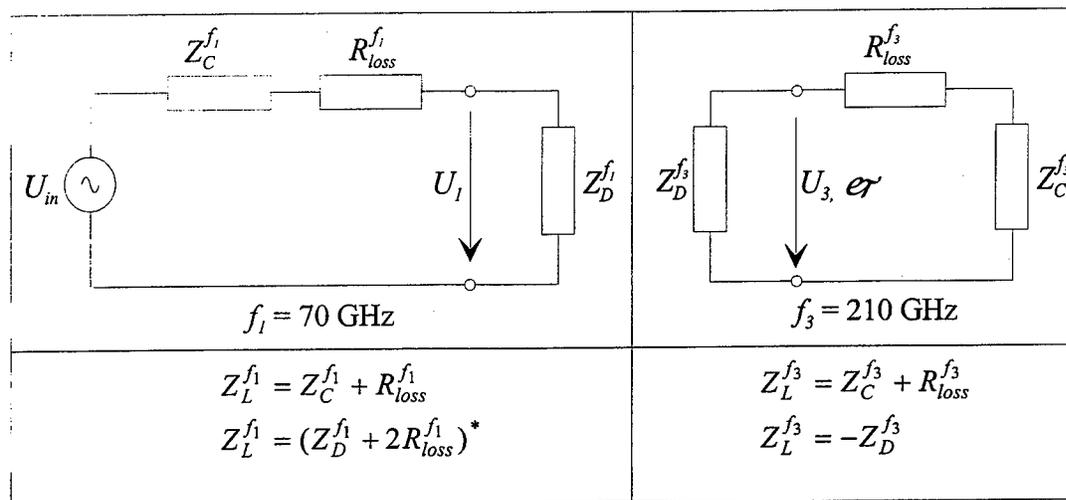
Fig. 4: Equivalent circuit for fundamental and harmonic frequency

frequency, the multiplier is pumped by an external source and for power matching the circuit impedance must be equal to the conjugate impedance of the device and the losses at the fundamental frequency. At the harmonic frequency, the varactor shows an impedance with negative real part. For maximum conversion efficiency, the optimum varactor impedance must be matched to the circuit such that the total impedance vanishes. To fulfil these conditions at input and output frequency, the parameters of the network shown in Fig. 3b must be optimised. The variation of the length l, the distance d from the diode and the width w of the matching stubs transforms the circuit impedances at fundamental and harmonic frequency in a wide range. Furthermore, the insertion depth x of the microstrip to waveguide transition (see Fig. 3a) can also be used as matching parameter. Fine tuning at the fundamental frequency is achieved by the backshort in the input waveguide decoupled at the harmonic frequency by the low pass filter, whereas the backshort in the output waveguide is only relevant for the harmonic frequency due to the high cut-off frequency of the output waveguide.

Fig. 5a shows two cases for the circuit impedances (solid lines) at the fundamental frequency in dependence of the backshort of the input waveguide. The parameters of the different matching networks are given in the insert. As can be seen a small change (20μm) in the distance of the matching network from the varactor delivers two distinct different impedance loci of the input impedance. Additionally, in Fig. 5a the optimum matching impedance locus of the varactor for varying device area considering the device losses $Z_D^{f_1} + 2R_{loss}^{f_1}$ is plotted (dashed line). Fig. 5b shows the corresponding circuit impedance loci for the two cases above in dependence of the backshort as solid curves at the harmonic frequency, too. Similar to the fundamental frequency, also at the harmonic frequency the optimum varactor matching impedance locus is depicted. Optimum conversion efficiency is reached for intersection of the load and device impedance lines at both fundamental and harmonic frequency. This intersection point defines the device area for which the tripler with the used circuit configuration shows best performance. Circuit A shows at both frequencies an intersection point, which means that optimum impedance matching could be achieved with the corresponding device area and input power.
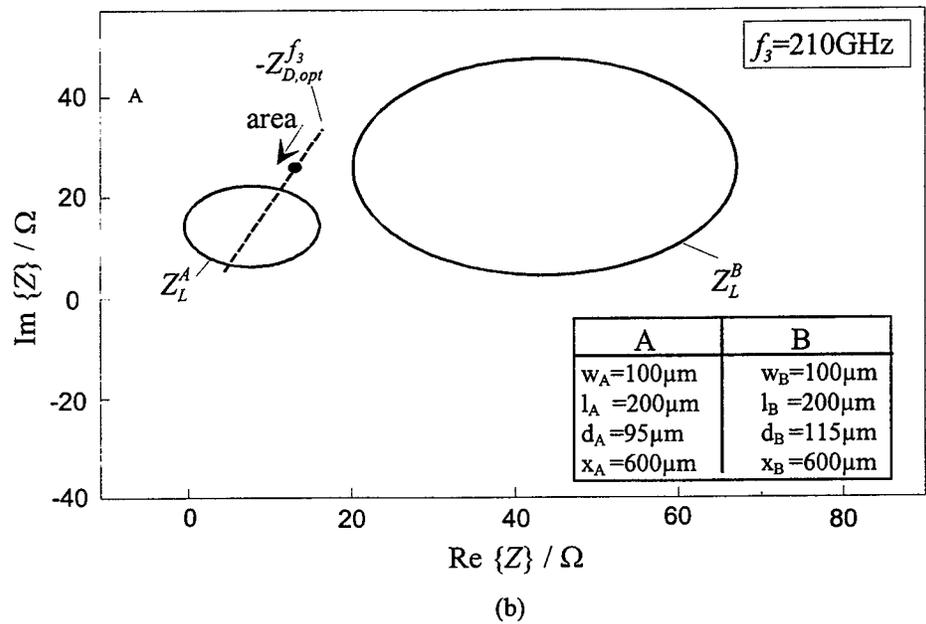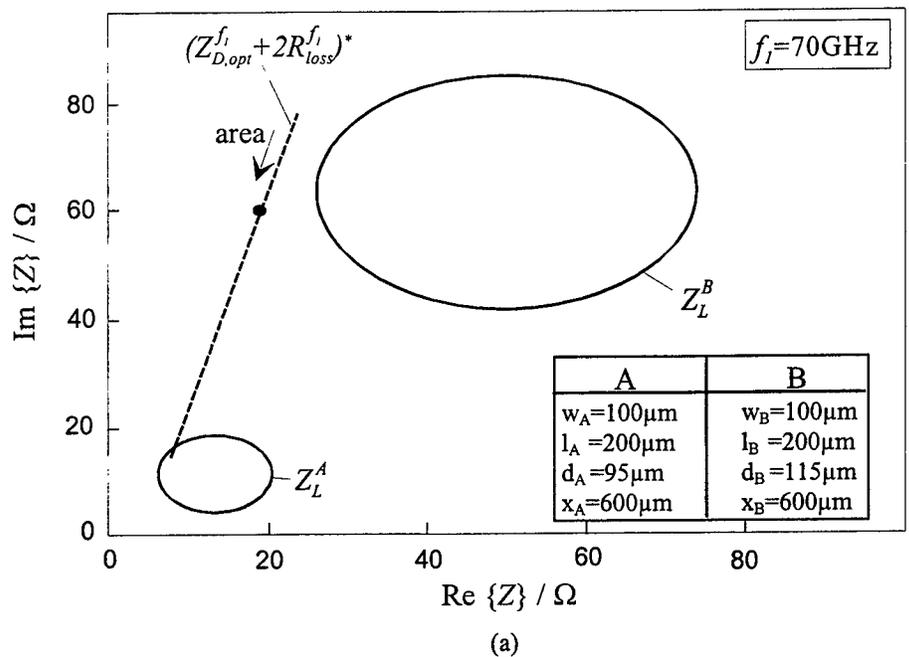
Fig. 5: Circuit impedances in dependence of the backshort for two different matching networks A and B (solid line) and optimum varactor impedance in dependence of the device area (dashed lines). The solid dots indicates the optimum device impedance for an area of 5*10-7 cm2.
a) fundamental frequency b) harmonic frequency

For comparison of the experimental results to the theory the calculations have been carried out with a realised device area of $5*10^{-7}$ cm^2. Fig. 6 shows conversion efficiency and output power of the device according to Fig. 1 with ideally matched circuit. Maximum efficiency up to 15 % with an output power more than 10 mW should be achievable for an input power of 55 mW. The corresponding device impedances are $Z_D^{f_1} = (14 - j60)\Omega$ for the fundamental and $Z_D^{f_3} = (-13.5 - j25)\Omega$ for the harmonic frequency. The optimum matching impedances are indicated in Fig. 5a and 5b by solid dots.
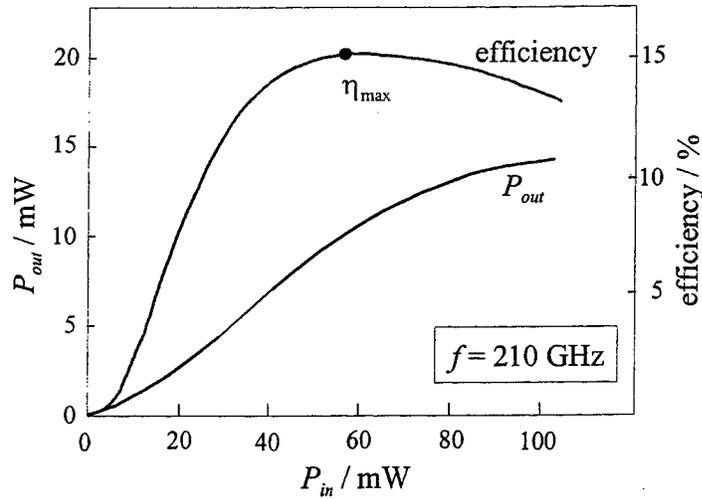
Fig. 6: Output power and conversion efficiency of the SBV with an area of $5*10^{-7}$ cm^2 according to Fig. 1 with an ideally matched circuit (Varactor impedances for maximum conversion efficiency: $Z_D^{f1} = (14 - j60)\Omega$, $Z_D^{f3} = (-13.5 - j25)\Omega$.

(a)

(b)
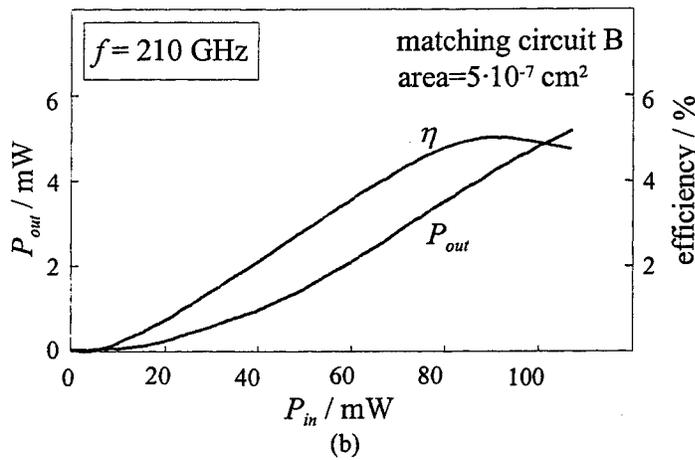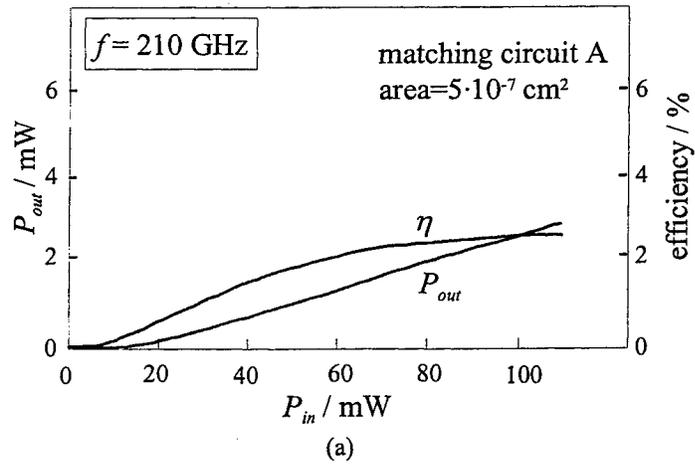
Fig. 7: Output power and efficiency of a tripler with monolithically integrated SBV (a) matching circuit A, b) matching circuit B)

The tripler performance for the two experimentally realised matching network configurations A and B from Fig. 5 calculated by harmonic balance technique using the simulation programme ADS (Hewlett Packard) is shown in Fig. 7. A maximum efficiency of about 2.5 % and an output power of more than 2 mW can be reached for type A. From Fig. 5 it can be seen that the circuit impedance line is quite far away from the optimum impedance value of the varactor with the used area (solid dots), especially at the fundamental frequency. The performance of the varactor with matching circuit B, given in Fig. 7b is better. Higher efficiency of about 5 % and a corresponding output power of about 4.5 mW can be reached since the circuit impedance loci are closer to the optimum device impedance for the used area as can be seen in Fig. 5, too.

5. EXPERIMENTAL RESULTS

Frequency triplers with monolithically integrated SBV using the above described matching circuits (A,B) have been fabricated and investigated. The used varactor shown in Fig. 1 has an area of $5*10^{-7}$ cm^{-3}, a low frequency series resistance of 8 Ω, a maximum to minimum capacitance ratio of about 4 and an onset voltage of 5.2 V for a current density of 1 kA/cm^2. The experiments indicate that the output power for the matching network A is always lower as compared to the case of B. The best results of the tripler with matching circuit B and an available input power of 50 mW show a measured flange to flange efficiency of 2.8 % and an output power of 1.4 mW at 210 GHz. The corresponding values for output and efficiency from the computation according to Fig. 7b are 1.5 mW and 3 %, respectively, which indicates the good agreement of the theoretical and experimental results. Up to an input power of 50 mW no saturation nor for efficiency neither for power has been measured. The theoretical results from Fig. 7b predict an efficiency up to 5 % with 4.5 mW output power if higher input power is available. The aim of the next work will be to alter the device area and the parameters of the matching network to reach the optimum efficiency and hence higher output power.

6. CONCLUSION

Investigations on frequency tripler from 70 GHz to 210 GHz with monolithically integrated SBV have been presented. Two circuits with different matching networks have been investigated. Theoretical and experimental results have shown that the design of the matching network is one of the most critical steps for the optimum tripler performance. A measured flange to flange efficiency of 2.8 % and an output power of 1.4 mW have been achieved with 50 mW input power. Theoretical extrapolation predicts an efficiency of about 5 % if higher input power is available. Furthermore, improvements in the circuit design should lead to higher tripler efficiency and output power.

7. ACKNOWLEDGMENT

8. REFERENCES

1. M. Tschernitz, J. Freyer, '140 GHz GaAs double-drift IMPATT diodes', Electron. Lett. 31, pp. 582-583, 1995
2. A. V. Räisänen. 'Frequency multipliers for millimeter and submillimeter wavelengths', Proceedings of IEEE, 80, (11), 1992, pp. 1842-1852
3. D. Choudhury, M. A. Frerking, P. D. Batelaan, 'A 200 GHz tripler using a single barrier varactor', IEEE Trans. MTT, 41, 1993, pp.595-599
4. X. Mélique, C. Mann, P. Mounaix, J. Thornton, O. Vanbésien, F. Mollot, D. Lippens, '5 mW and 5 % efficiency 216 GHz InP-based heterostructure barrier varactor tripler', IEEE Microwave and Guided Letters, 8, (11), 1998, pp. 384-386
5. J. R. Jones, W. L. Bishop, S. H. Jones, G. B. Tait, 'Planar multibarrier 80/240 GHz heterostructure barrier varactor triplers', IEEE Trans MTT, 45, (4), 1997, pp.512-518
6. J. Freyer, R. Meola, M. Claassen, F. Neugebauer, 'Design of GaAs/GaAlAs single-barrier varactors (SBV) for mm-wave frequency multipliers', 23rd Intern. Conf. on Infrared and Millimeter Waves, Essex, UK, 1998

FIRL: Simulations of Methanol Laser Output Power

Michael Raum

Lehrstuhl für Hochfrequenztechnik, University Erlangen-Nürnberg
Cauerstraße 9, D-91058 Erlangen, Germany

ABSTRACT

In airborne heterodyne receivers for remote sensing of the OH radical in the stratosphere, optically pumped methanol gas lasers on the 2.523 THz line are used as local oscillators. In order to optimize their performance, a new simulation concept has been developed and is described here.

A standard design procedure for SMMW ring lasers using a focussing mirror for optical pump beam guiding is scetched briefly. To make computations easier, the pump radiation distribution is averaged along the resonator. Using a quantum mechanical approach, a SMMW laser process model which takes into account the ac Stark effect, the Maxwell distribution and the Doppler effect can be derived. Transversal profiles of pump and SMMW intensity, absorption and gain coefficient, vibrational and physical temperature serve as a base for the determination of the SMMW laser output power.

Based on this model, a computer program named FIRL has been developed. Computed results obtained with the program are presented and consequences for construction of SMMW lasers are discussed. Two laser prototypes have been built and demonstrate good agreement of simulated and measured results, indicating that the described program is a qualified CAD tool for methanol laser development.

Keywords: ring resonator, SMMW laser, FIR laser, laser modelling, simulation, CAD, ERFILAS

1. INTRODUCTION

The submillimeter wave (SMMW) range from 30 μm to 1 mm is very important for spectroscopy, radioastronomy and environmental research because it contains the spectral fingerprints of many molecular, atomic and ionic transitions.

The OH radical, one of the radicals involved in stratospheric chemistry, emits radiation at 2.514 THz. For its remote sensing, airborne heterodyne receivers with a local oscillator frequency near the emission line are required.[1] Up to now, the only device delivering an appropriate frequency is a methanol gas laser on its 2.523 THz line (wavelength $\lambda_L = 119$ μm). The laser has to be pumped by a carbondioxide laser on its 9 P 36 line (wavelength $\lambda_P = 9.69$ μm).

The airborne platform puts high demands on the system concerning compactness, efficiency and reliability.[2] The goal of the ERFILAS-Project (Erlangen Far Infrared Laser) at the Lehrstuhl für Hochfrequenztechnik (LHFT) is the construction of SMMW laser heads for airborne applications. In order to optimize SMMW laser performance, the program FIRL has been developed at the LHFT.

2. DESIGN OF STANDARD RESONATORS

The ring resonator of the SMMW laser head consists of four mirrors as shown in figure 1. The pump beam is coupled into the resonator through a pinhole in mirror 1. Mirror 2 is a focussing mirror (focal length f_B) serving for pump beam guiding as well as for SMMW beam guiding. Together with a plane mirror 3 it is mounted on a positioning unit to tune the SMMW frequency. The SMMW radiation is coupled out by a hybrid hole mirror 4 and leaves the resonator in copropagating or in counterpropagating direction. The pump beam performs several roundtrips in the resonator ring, which leads to an increase of pump efficiency.

For further author information (correspondence): email: michael@lhft.e-technik.uni-erlangen.de; WWW: www.lhft.e-technik.uni-erlangen.de; Telephone: ++49 9131 85-27231; Facsimile: ++49 9131 85-27212.
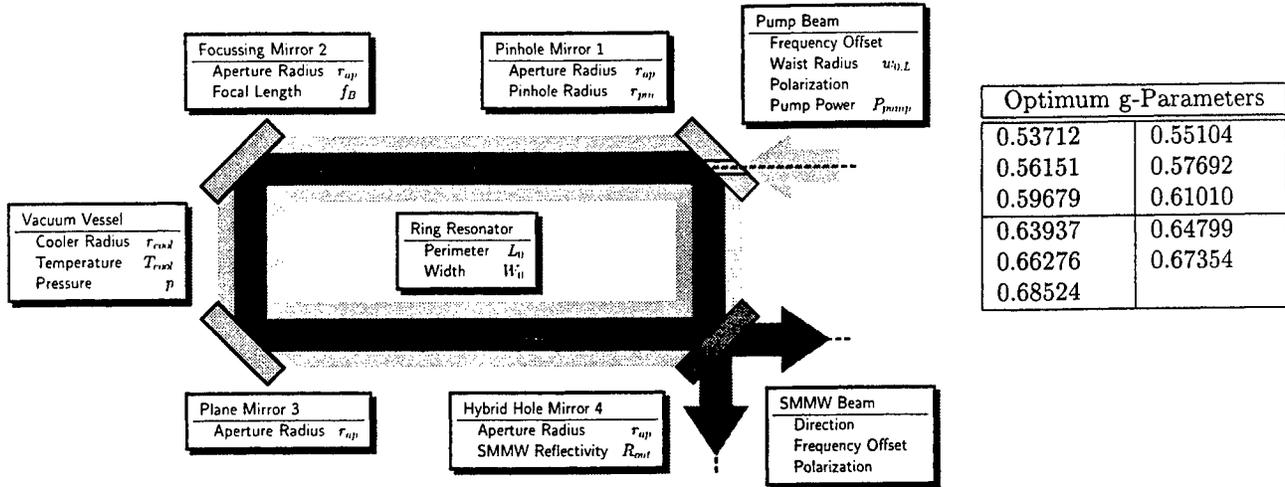
398

Part of the EUROPTO Conference on Terahertz Spectroscopy and Applications II
Munich, Germany • June 1999 SPIE Vol. 3828 • 0277-786X/99/$10.00

Figure 1. (left) Resonator geometry and parameters important for SMMW output power.
(right) Table of standard resonator g-parameters

The most important constructional parameters to be determined are focal length f_B, perimeter of the ring resonator L_0 and outcoupler reflectivity R_{out}. The g-parameter as a characteristic quantity for resonator geometry is introduced:

$$g = 1 - \frac{L_0}{2 \cdot f_B} \tag{1}$$

As has been shown,[3] not every g-parameter provides good pump beam guiding. Refocussing of the pump beam on the pinhole in the $m + 1$ roundtrip occurs when the g-parameters satisfy the condition

$$g = \cos\left[\frac{\pi \cdot i}{m + 1}\right] \tag{2}$$

with i and m integers, and the remnant pump power is lost. In the interesting region $0.5 \leq g \leq 0.7$, only the eleven g-parameters listed in the table of figure 1 are to be recommended.

For the described kind of resonator with the geometry given by the resonator perimeter L_0 and the g-parameter, the SMMW beam geometry is perfectly known. From theory of optical resonators, its Rayleigh length

$$z_{R,L} = \frac{L_0}{2} \cdot \sqrt{\frac{1 + g}{1 - g}} \tag{3}$$

can be calculated. The SMMW beam has its beam waist with a radius of

$$w_{0,L} = \sqrt{\frac{z_{R,L} \cdot \lambda_L}{\pi}} \tag{4}$$

situated on the hybrid hole mirror and its maximum radius on the focussing mirror

$$w_{L,max} = \sqrt{\frac{L_0 \cdot \lambda_L}{\pi} \cdot \left[\frac{z_{R,L}}{L_0} + \frac{L_0}{4 \cdot z_{R,L}}\right]} \tag{5}$$

The optimum pump beam waist radius is more difficult to determine. Introducing a pump beam factor f_{pb} with

$$w_{0,P} = f_{pb} \cdot \sqrt{\frac{z_{R,L} \cdot \lambda_P}{\pi}} \tag{6}$$

the maximum spot size of the pump beam on the focussing mirror can be calculated analytically:

$$w_{P,max} = \frac{1}{f_{pb}} \cdot \sqrt{\frac{L_0 \cdot \lambda_P}{\pi} \cdot \left[\frac{z_{R,L}}{L_0} + \frac{L_0}{4 \cdot z_{R,L}}\right]} \tag{7}$$

Together with $w_{L,max}$ from (5), $w_{P,max}$ from (7) determines the aperture radius r_{ap} via an aperture factor f_{ap}:

$$r_{ap} = f_{ap} \cdot \max\{w_{L,max}, w_{P,max}\} \tag{8}$$

Similarily, a pinhole factor f_{pin} relates the pinhole radius r_{pin} to the pump beam waist radius

$$r_{pin} = f_{pin} \cdot w_{0,P} \tag{9}$$

Finally, a cooler wall radius r_{cool} is defined by a factor f_{cool} referring it to the aperture radius

$$r_{cool} = f_{cool} \cdot r_{ap} \tag{10}$$

Both, r_{ap} and r_{pin}, should be kept as small as possible, and a compromise has to be found. Closer examinations show that a pump beam factor $f_{pb} = 0.18$, an aperture factor $f_{ap} = 1.7$ and a pinhole factor $f_{pin} = 1.75$ are good solutions. As the cooler should be slightly larger than the aperture, $f_{cool} = 1.1$ has been chosen.

The whole procedure from (3) to (10) shows that the ring resonator geometry can be completely characterized by g-parameter and resonator perimeter L_0. The configuration is referenced by a name like STD/61/2.0 where the 61 stands for the used g-parameter $g = 0.61$ (rounded to two digits) and 2.0 denotes the resonator perimeter L_0 in m.[4-6] If not otherwise indicated, all simulations to follow have been performed on a STD/61/2.0 resonator.

3. LASER MODELLING

The absorption of pump radiation and emission of SMMW radiation in a volume element is determined by the SMMW and pump radiation intensities the molecules of the laser gas are exposed to. The power remnant from the SMMW laser quantum process has to be brought out of the volume element by thermal conductivity and diffusion.

Therefore, mathematical descriptions of SMMW intensity, pump intensity, the SMMW laser process, thermal conduction and diffusion are required to obtain a complete description of a SMMW laser system.

3.1. Pump Radiation

Figure 2 (upper) shows the pump beam traces (i. e. the beam radii) of 20 roundtrips in a STD/61/2.0. The single traces are assumed to stay gaussian beams despite diffraction by the limited mirror apertures and the pinhole. Along the z coordinate of the resonator, several refocussings occur, leading to transversal inhomogenities of the pump radiation intensity. They are marked by bright on-axis spots in figure 2 (middle) which shows the normalized pump intensity along the resonator in a grayscale contour plot.

In order to keep computation times low, the intensities of the pump beam traces are averaged along the z-axis to obtain an averaged pump intensity profile $I_P(r, z)$. This profile is separated into an intensity structure function $\psi_P(r)$ and pump radiation power $P_P(z)$ by

$$I_P(r, z) = P_P(z) \cdot \psi_P(r) \tag{11}$$

The structure function ψ_P is calculated from all pump beam traces i, which are characterized by their power $P_{P,i}(z)$ and their beam radius $w_{P,i}(z)$ at coordinate z:

$$\psi_P(r) = \frac{\sum_{i=1}^{\infty} \int_0^{L_0} \frac{2 \cdot P_{P,i}(z)}{\pi \cdot w_{P,i}(z)^2} \cdot \exp\left\{-2 \cdot \frac{r^2}{w_{P,i}(z)^2}\right\} \cdot dz}{\sum_{i=1}^{\infty} \int_0^{L_0} P_{P,i}(z) \cdot dz} \tag{12}$$

The term contains infinite sums, but these return limited results as the pump beam trace powers are reduced by diffraction, attenuation and absorption losses during the roundtrips. Figure 2 (lower) shows the pump beam distribution described by the structure function as a grayscale contour plot. A comparison with figure 2 (middle) shows that the approximation by equation (11) is very good.

In the case of the cold resonator (i. e. without absorption by the laser gas) and totally reflecting mirrors, an averaged resonator transmission T_{wg} can be defined using the powers $P_{i,in}$ of the pump traces at the beginning of a roundtrip i and the powers $P_{i,out}$ of the traces at the end of a roundtrip:

$$T_{wg} = \frac{\sum_{i=1}^{\infty} P_{i,out}}{\sum_{i=1}^{\infty} P_{i,in}} \tag{13}$$
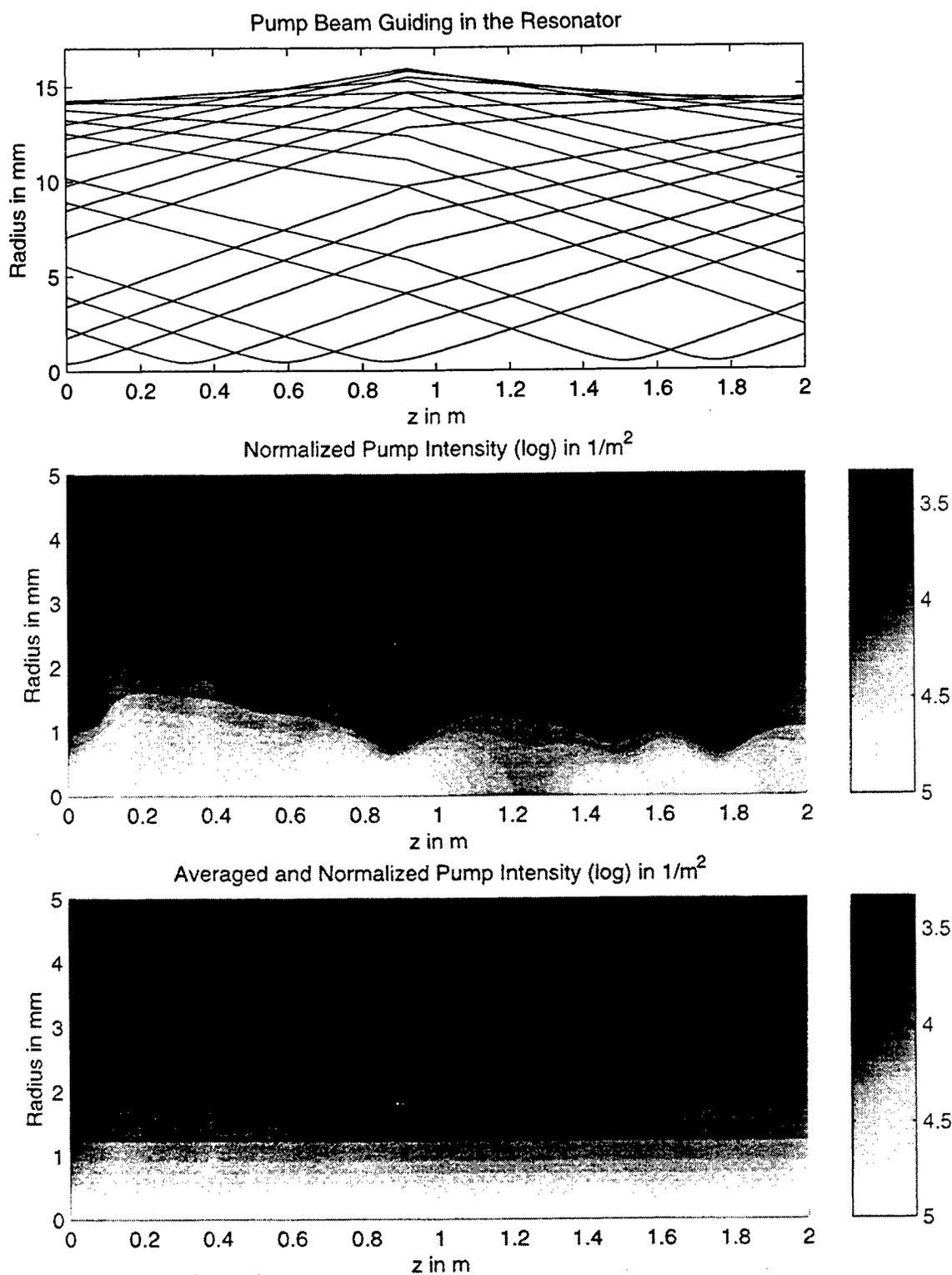
Figure 2. (upper) Pump beam traces of 20 roundtrips through STD/61/2.0 resonator.
(middle) Pump radiation intensity profile in the resonator
(lower) Approximate radiation intensity profile in the resonator

The attenuation coefficient α_P (related to amplitude) of the pump radiation is determined by averaging all losses over the resonator perimeter.[7] With the pump reflectivities $R_{P,1}$ to $R_{P,4}$ of the four mirrors one obtains

$$\alpha_P = -\frac{1}{2 \cdot L_0} \cdot \ln\{T_{wg}\} - \frac{\ln\left\{\Pi_{m=1}^4 R_{P,m}\right\}}{2 \cdot L_0} \tag{14}$$

3.2. SMMW Radiation

A similar approach using an intensity structure function ψ_L and SMMW radiation power P_L is used for the SMMW radiation intensity profile $I_L(r,z)$:

$$I_L(r,z) = P_L(z) \cdot \psi_L(r) \tag{15}$$

In contrast to the pump radiation, not the intensity but the beam size is averaged from the radius of the SMMW beam $w_L(z)$ along the resonator. The expression can be evaluated analytically:

$$w_{smmw} = \sqrt{\frac{\int_0^{L_0} w_L^2(z) \cdot dz}{L_0}} = w_{L,0} \cdot \sqrt{1 + \frac{1}{12} \cdot \left(\frac{L_0}{z_{R,L}}\right)^2} \tag{16}$$

The structure function of the SMMW beam, derived from the average beam size w_{smmw}, describes a quasi-gaussian beam with a uniform gaussian shape all along the resonator perimeter:

$$\psi_L(r) = \frac{2}{\pi \cdot w_{smmw}^2} \cdot \exp\left\{-2 \cdot \frac{r^2}{w_{smmw}^2}\right\} \tag{17}$$

As in the case for the pump radiation guiding, losses occur due to the pinhole and the mirror SMMW reflectivities of $R_{L,1}$ to $R_{L,3}$ of mirrors 1 to 3, resulting in an attenuation coefficient α_L (related to amplitude):

$$\alpha_L = -\frac{\ln\left\{\Pi_{m=1}^3 R_{L,m}\right\}}{2 \cdot L_0} + \frac{r_{pin}^2}{w_{0,L}^2 \cdot L_0} \tag{18}$$

3.3. Absorption and Emission

In the section to follow let us assume that the absorption coefficient for pump radiation $\xi(r,z)$ and the SMMW gain coefficient $\Gamma(r,z)$ are known. In order to get the effect on the total output power of the SMMW laser, both can be averaged across the respective profiles with the intensity structure functions as weights according to

$$\xi_m(z) = 2\pi \cdot \int_0^\infty \xi(r,z) \cdot \psi_P(r) \cdot r\,dr \tag{19}$$

$$\Gamma_m(z) = 2\pi \cdot \int_0^\infty \Gamma(r,z) \cdot \psi_L(r) \cdot r\,dr \tag{20}$$

The classical laser theory of the absorption coefficient[8] is now extended to the averaged absorption coefficient. Introducing the small signal absorption coefficient ξ_{m0} and the pump saturation power P_{SP}, one gets

$$\xi_m(z) = \frac{\xi_{m0}}{\sqrt{1 + \frac{P_P(z)}{P_{SP}}}} \tag{21}$$

for the case of an inhomogeniously broadened absorption line. The dependence of pump radiation power and SMMW radiation power on z in the resonator is given by the solution of the differential equations

$$\frac{dP_P(z)}{dz} = -[\xi_m(z) + 2 \cdot \alpha_P] \cdot P_P(z) \tag{22}$$

$$\frac{dP_L(z)}{dz} = [\Gamma_m(z) - 2 \cdot \alpha_L] \cdot P_L(z) \tag{23}$$

The condition under which differential equation (22) has to be solved is power conservation at the pinhole mirror. Using the pump radiation power $P_{P,A}$ at the beginning and $P_{P,E}$ at the end of the resonator, this requires

$$P_{P,A} = P_{P,E} + P_{pump} \tag{24}$$

Starting with the differential equation (22), inserting (21) and introducing abbreviations for the normalized gain

$$A_P = \frac{\xi_{m0}}{2 \cdot \alpha_P} \tag{25}$$

and for the normalized pump radiation power

$$\Pi_P(z) = \frac{P_P(z)}{P_{SP}} \tag{26}$$

(Π_A and Π_E are built from $P_{P,A}$ and $P_{P,E}$, accordingly), one gets an implicit equation for the power distribution

$$\frac{A_P^2}{1 - A_P^2} \cdot \ln \left\{ \frac{(\sqrt{1 + \Pi_E} - 1)(\sqrt{1 + \Pi_A} + 1)}{(\sqrt{1 + \Pi_E} + 1)(\sqrt{1 + \Pi_A} - 1)} \right\} + \frac{2 \cdot A_P^3}{1 - A_P^2} \cdot \ln \left\{ \frac{A_P + \sqrt{1 + \Pi_E}}{A_P + \sqrt{1 + \Pi_A}} \right\} - \frac{A_P}{1 - A_P^2} \cdot \ln \left\{ \frac{\Pi_E}{\Pi_A} \right\} = \xi_{m0} \cdot L_0 \tag{27}$$

From the solution, the normalized absorbed pump power can be calculated:

$$\Pi_{abs} = \frac{P_{abs}}{P_{SP}} = 2 \cdot A_P \cdot \left(\sqrt{1 + \Pi_A} - \sqrt{1 + \Pi_E} + A_P \cdot \ln \left\{ \frac{\sqrt{1 + \Pi_E} + A_P}{\sqrt{1 + \Pi_A} + A_P} \right\} \right) \tag{28}$$

This power serves as the base to calculate a representative pump radiation power

$$P_{P,rep} = P_{SP} \cdot \frac{\Pi_{abs}^2}{2 \cdot \xi_{m0}^2 \cdot L_0^2} \cdot \left[1 + \sqrt{1 + \frac{4 \cdot \xi_{m0}^2 L_0^2}{\Pi_{abs}^2}} \right] \tag{29}$$

which describes a representative pump radiation intensity profile at a representative coordinate z_{rep} throughout the whole resonator perimeter

$$I_{P,rep} = P_{P,rep} \cdot \psi_P(r) \tag{30}$$

and is used to determine the gain coefficient $\Gamma(r, z_{rep})$. Again, a formula from classical laser theory gives a connection between the SMMW radiation power $P_L(z)$ in the resonator and the emission coefficient with small signal gain coefficient Γ_{m0} and saturation power P_{SL}:

$$\Gamma_m(z) = \frac{\Gamma_{m0}}{1 + \frac{P_L(z)}{P_{SL}}} \tag{31}$$

According to RIGROD.[7] the SMMW output power in the resonator is

$$P_{L.out} = P_{SL} \cdot T_{out} \cdot T_w \cdot \left[\frac{L_0 \cdot \Gamma_{m0}}{2 \cdot \alpha_L \cdot L_0 - \ln\{R_{out}\}} - 1 \right] \tag{32}$$

with the outcoupler transmission T_{out} and the window transmission T_w. The outcoupler reflectivity may be optimized

$$R_{opt} = \exp \left\{ -2\alpha_L L_0 \left(\sqrt{\frac{\Gamma_{m0}}{2\alpha_L}} - 1 \right) \right\} = 1 - T_{opt} \tag{33}$$

to yield maximum SMMW output power. Shape and kind of the outcoupler determine which part of the power of a gaussian beam incident on the surface is coupled back into the same gaussian beam; fractions of power coupled into other higher order modes have to be regarded as losses of the outcoupler.

3.4. Active Medium

The goal of the chapter to follow is the calculation of SMMW gain $\Gamma(r, z)$ and absorption coefficient $\xi(r, z)$ in order to get information on the longitudinal distribution of SMMW and pump radiation. For better understanding, a short description of the SMMW laser process is given here.

The process starts with the absorption of a pump quantum by a molecule in a lower vibrational state, lifting it to a higher vibrational energy state. From this upper pump level (or upper laser level), the SMMW lasing process starts, leading to the emission of a SMMW quantum and leaving the molecule in a lower energetic rotational level within the upper vibrational energy state.

Unfortunately, the described process is interfered by other mechanisms.[9] First, rotational relaxation of the upper laser level occurs, shifting it closer to thermodynamical equilibrium with the other rotational levels and making laser amplification (gain) more difficult. The quantum efficiency η_Q expected from the Manley-Rowe equation is reduced to

$$\eta_Q = \frac{\lambda_{pump}}{2 \cdot \lambda_{smmw}} \tag{34}$$

The molecule relaxes to the lower vibrational energy state by different mechanisms,[9] transferring the vibrational power to the gas and thus closing the SMMW laser cycle. As this process is slow compared to the rotational relaxation, the population of vibrational levels changes compared to thermodynamical equilibrium; the new distribution will be described by a vibrational temperature T_{vib}.

For the quantitative determination of gain and absorption, a quantum mechanical approach by PANOCK and TEMKIN[10] is applied. The approach requires information about pump and SMMW intensities, offset frequencies and the dipole moments associated with the different processes. Pump and SMMW offsets are determined by molecular constants as well as by the Doppler shift due to the velocity distribution (Maxwell distribution) of the gas, so the molecules are sorted into velocity groups (denoted by a prime) and different orientations of their main axis related to the pump and SMMW polarization (marked by an index M). The related pump absorption and SMMW gain coefficients $\xi'_M(r, z; v_z)$ and $\Gamma'_M(r, z; v_z)$ have to be integrated across the velocity distribution and summarized over all polarization directions M in order to get pump absorption and SMMW gain coefficients $\xi(r, z)$ and $\Gamma(r, z)$:

$$\xi(r, z) = \int_{-\infty}^{\infty} \sum_{M=-J}^{J} \xi'_M(r, z; v_z) \cdot dv_z \tag{35}$$

$$\Gamma(r, z) = \int_{-\infty}^{\infty} \sum_{M=-J}^{J} \Gamma'_M(r, z; v_z) \cdot dv_z \tag{36}$$

For the dipole moments and the distributions, special molecular parameters are required. Information on dipole moments of different methanol laser lines and energy levels may be found in literature.[8,11-14]

3.5. Relaxation Mechanisms

The processes determining the physical temperature and vibrational temperature distribution $T(r)$ and $T_{vib}(r)$ in the representative laser cross section at coordinate z_{rep} can be divided into two classes: global processes like diffusion and thermal conductivity on the one hand side, which transfer the remnant pump power to the cooler walls, and local processes as the pump process and the VT-relaxation on the other hand side, which drive the global processes.

The source for the thermal conduction is the conversion of vibrational energy to kinetic energy by the VT relaxation mechanism. The power per volume converted to heat is described by the thermal power density Q_T. For power conservation, the power density transported out of the volume element by diffusion must be

$$Q_D(r) = I_{P,rep} \cdot \xi(r, z_{rep}) - Q_T(r) \tag{37}$$

Both temperature and vibrational temperature profiles can now be determined by solving the differential equations for thermal conductivity and diffusion

$$\begin{aligned} Q_T &+ \operatorname{div}\left[\kappa_{dyn} \cdot \operatorname{grad} T\right] &= 0 \\ Q_D &+ \operatorname{div}\left[\kappa_{vib} \cdot \operatorname{grad} T_{vib}\right] &= 0 \end{aligned} \tag{38}$$

The dynamic thermal conductivity κ_{dyn} is provided by the assumption that the gas is an ideal one

$$\kappa_{dyn} = \frac{2}{\pi \cdot \sigma_M \cdot T} \cdot \sqrt{\frac{(kT)^3}{m_M}} \tag{39}$$

whereas the vibrational conductivity κ_{vib} comes from transport of vibrational energy by the molecules

$$\kappa_{vib}(T_{vib}) = \frac{2}{3\pi \cdot \sigma_M} \cdot \sqrt{\frac{kT}{m_M}} \cdot \frac{1}{k \cdot T_{vib}^2} \cdot [W_{qm}^2(T_{vib}) - W_m^2(T_{vib})] \tag{40}$$

The averaged vibrational energy W_m and the root mean square of the vibrational energy W_{qm} must be derived from the vibrational energy levels of the SMMW gas. At the walls, both temperatures must equal the cooler wall temperature of $T_{cool} = 300\ K$.
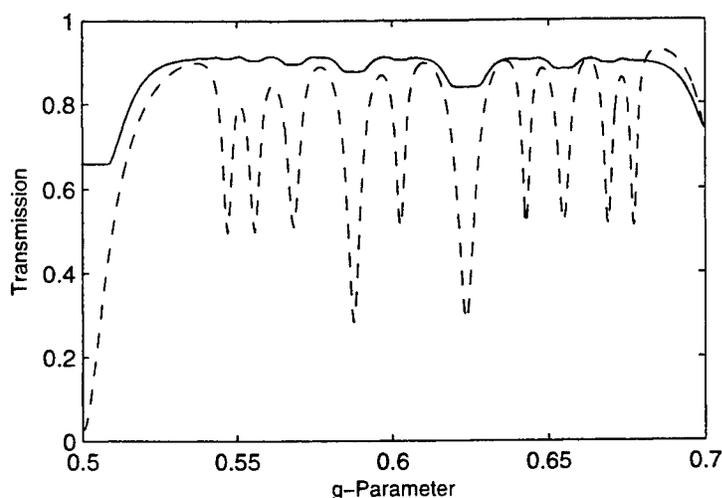
Figure 3. Pump Beam Transmission T_{wg} (solid line) and Single Beam Transmission $T_{s,20}$ (dashed line).

4. SIMULATIONS

The equations describing the SMMW laser process and determining the SMMW laser output power are not straight forward. Small loops of recursive algorithms for the solution of single equations like (27) have to be applied as well as large loops for the determination of the different profiles.

The FIRL program starts with the determination of attenuation coefficients α_L, α_P, and intensity structure functions v_L, ψ_P. Within the subsequent iterative algorithm for the pump radiation distribution, the quantum mechanical considerations are applied to single velocity groups and orientations of the molecular rotational axis and combined according to equation (35). The relaxation mechanisms described in chapter 3.5 are taken into account. From two given absorption coefficients, the small signal absorption and the saturation power from equation (21) can be calculated. After that, the representative pump power is determined according to equation (29), and the physical temperature and vibrational temperature profiles are assumed to be known.

In another iterative algorithm, the small gain coefficient and the saturation power from equation (31) are determined from two gain coefficients and inserted into equation (32) to yield the SMMW output power. On demand, the outcoupler reflectivity can be optimized according to equation (33).

The FIRL program has been implemented in the C^{++} programming language.[15] The gnu compiler which is available for many operating systems in freeware collections has been used to ensure portability. The compiler works well on the source code on IBM OS/2 Release 3.0 and Linux, with some indication that it might be ported to HP-UX as well. The major advantage of the programming language, object-oriented programming, has been used, so the program can be extended to other lines, gases and resonator geometries in future versions.

The program reads input from an instruction file and writes output to an ASCII file; the latter can be read in and postprocessed by any mathematical program (e. g. MATLAB). Any resonator and laser configuration of the parameters from figure 1 can be used for the calculations. The parameters for standard resonators can be set by a single keyword and the resonator perimeter. Configuration data of these resonators can be found in table 1.

4.1. Resonator Calculations

The pump beam transmission T_{wg} according to equation (13) is shown in figure 3 (solid line) as well as the single beam transmission for 20 roundtrips $T_{s,20}$ (dashed line) which is defined as $T_{s,n} = P_{n,out}/P_{1,in}$. The latter one served as a base for the determination of the eleven basic g-parameters listed in figure 1 in earlier publications.[4,5] They are marked by the maxima of the curve, whereas the deep dips mark positions given by equation (2). In the graph of T_{wg}, the dips are not so marked as in the single beam transmission graph because refocussings taking place in later roundtrips do not increase losses in equation (13) as much as those taking place in earlier roundtrips. As the graph of T_{wg} has been calculated for a limited aperture, it is lower than $T_{s,20}$ at higher g-parameters.

	STD/54	STD/55	STD/56	STD/58	
g	0.53712	0.55104	0.56151	0.57692	
L_0	1.00...2.00	1.00...2.00	1.00...2.00	1.00...2.00	m
f_B	1.080...2.160	1.114...2.227	1.140...2.281	1.182...2.364	m
$w_{0.L}$	5.87...8.30	5.93...8.38	5.97...8.45	6.04...8.55	mm
$w_{L,max}$	6.39...9.04	6.49...9.18	6.57...9.29	6.69...9.46	mm
f_{ps}	0.176	0.178	0.183	0.183	
$w_{0.P,opt}$	0.30...0.42	0.30...0.43	0.31...0.44	0.32...0.45	mm
$w_{P,max}$	10.38...14.67	10.44...14.76	10.26...14.51	10.44...14.77	mm
r_{pin}	0.52...0.73	0.53...0.74	0.55...0.77	0.55...0.78	mm
r_{ap}	17.64...24.95	17.75...25.10	17.45...24.67	17.75...25.10	mm
r_{cool}	19.40...27.44	19.52...27.61	19.19...27.14	19.53...27.61	mm
W_0	53.81...69.88	54.04...70.21	53.38...69.28	54.05...70.23	mm

	STD/60	STD/61	STD/64	STD/65	
g	0.59679	0.61010	0.63937	0.64799	
L_0	1.00...2.00	1.00...2.00	1.00...2.00	1.00...2.00	m
f_B	1.240...2.480	1.282...2.565	1.386...2.773	1.420...2.841	m
$w_{0.L}$	6.13...8.68	6.20...8.77	6.35...8.98	6.40...9.05	mm
$w_{L,max}$	6.85...9.69	6.96...9.85	7.24...10.24	7.33...10.37	mm
f_{ps}	0.180	0.177	0.183	0.181	
$w_{0.P,opt}$	0.32...0.45	0.31...0.44	0.33...0.47	0.33...0.47	mm
$w_{P,max}$	10.85...15.34	11.21...15.86	11.32...16.00	11.56...16.35	mm
r_{pin}	0.55...0.78	0.55...0.78	0.58...0.82	0.58...0.82	mm
r_{ap}	18.44...26.08	19.06...26.96	19.24...27.20	19.65...27.79	mm
r_{cool}	20.29...28.69	20.97...29.66	21.16...29.92	21.62...30.57	mm
W_0	55.58...72.39	56.94...74.31	57.32...74.85	58.24...76.15	mm

	STD/66	STD/67	STD/69		
g	0.66276	0.67354	0.68524		
L_0	1.00...2.00	1.00...2.00	1.00...2.00		m
f_B	1.483...2.965	1.532...3.063	1.589...3.177		m
$w_{0.L}$	6.48...9.16	6.54...9.25	6.62...9.36		mm
$w_{L,max}$	7.49...10.59	7.61...10.76	7.75...10.96		mm
f_{ps}	0.183	0.182	0.173		
$w_{0.P,opt}$	0.34...0.48	0.34...0.48	0.33...0.46		mm
$w_{P,max}$	11.67...16.50	11.97...16.93	12.82...18.13		mm
r_{pin}	0.59...0.84	0.59...0.84	0.57...0.81		mm
r_{ap}	19.84...28.06	20.35...28.78	21.79...30.81		mm
r_{cool}	21.82...30.86	22.39...31.66	23.97...33.89		mm
W_0	58.64...76.72	59.77...78.32	62.93...82.79		mm

Table 1. Standard Resonator Geometries for g-parameters from figure 1 with resonator perimeters 1...2 m

The pump beam traces from figure 2 (upper) have been obtained using the program, too. The maximum radius of the traces around 16 mm requires an aperture radius of $r_{ap} \approx 27\ mm$ (see equation (8)), a value which can be found in table 1 as well. Within the first 20 roundtrips no refocussing on the pinhole (right border) occurs.

4.2. Internal Profiles

For a given resonator configuration and pump power, the profiles of radiation, absorption and gain coefficient, physical and vibrational temperature can be computed. The pump reflectivities of the mirrors are $R_{P,1} = R_{P,2} = R_{P,3} = 0.995$. $R_{P,4} = 0.99$, the SMMW reflectivities are $R_{L,1} = R_{L,2} = R_{L,3} = 0.992$ according to manufacturer specifications. Figure 4 shows the normalized intensity structure functions of pump and SMMW radiation. For the given pump power of $P_{pump} = 20\ W$, the maximum pump intensity is around $I_{P,max} = 22.6\ MW/m^2$, whereas the maximum SMMW intensity is around $I_{L,max} = 9000\ W/m^2$. The peak of the pump power on the optical axis, corresponding to the refocussings of the pump beam, causes a dip of the absorption coefficient (maximum $\xi_{max} = 0.2484\ m^{-1} \approx \xi_0$) due to saturation. Nevertheless, good inversion is achieved as can be seen from the peak in the gain coefficient.

The SMMW gain shows the most complex behaviour. On the axis, the SMMW gain has a small dip corresponding to the pump intensity peak. This may be caused by the dynamic Stark effect. Nevertheless, the maximum of the SMMW gain is near the axis; the gain then decreases rapidly. However, there is another not very marked maximum of the gain at around 10 mm. This is due to the balance of increased SMMW saturation on the axis, leading to less SMMW gain, and increased inversion on the axis, leading to higher SMMW gain. At approximately $r \approx 16\ mm$, the gain gets negative, which denotes absorption of SMMW radiation. The maximum SMMW gain is $\Gamma_{max} = 0.1667\ m^{-1}$.

The high inversion on the optical axis does not seem to have any influence on the temperatures which do not share the heavy turbulences on the optical axis, as can be seen in figure 4. Diffusion and relaxation processes degrade the strong absorption in the pump beam center very quickly.
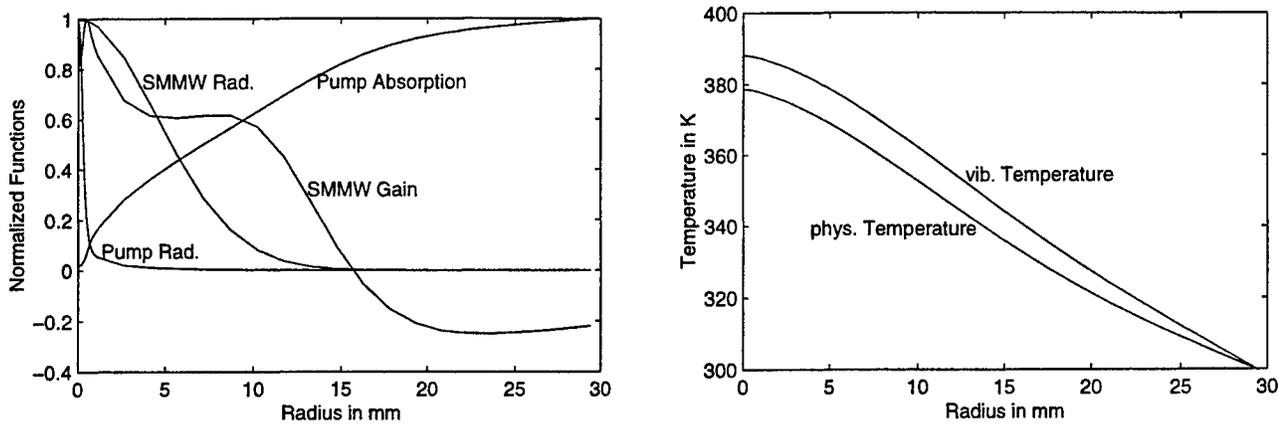
Figure 4. (left) Normalized profiles of SMMW radiation, pump radiation, SMMW gain and absorption coefficient. (right) Profiles of physical and vibrational temperature.
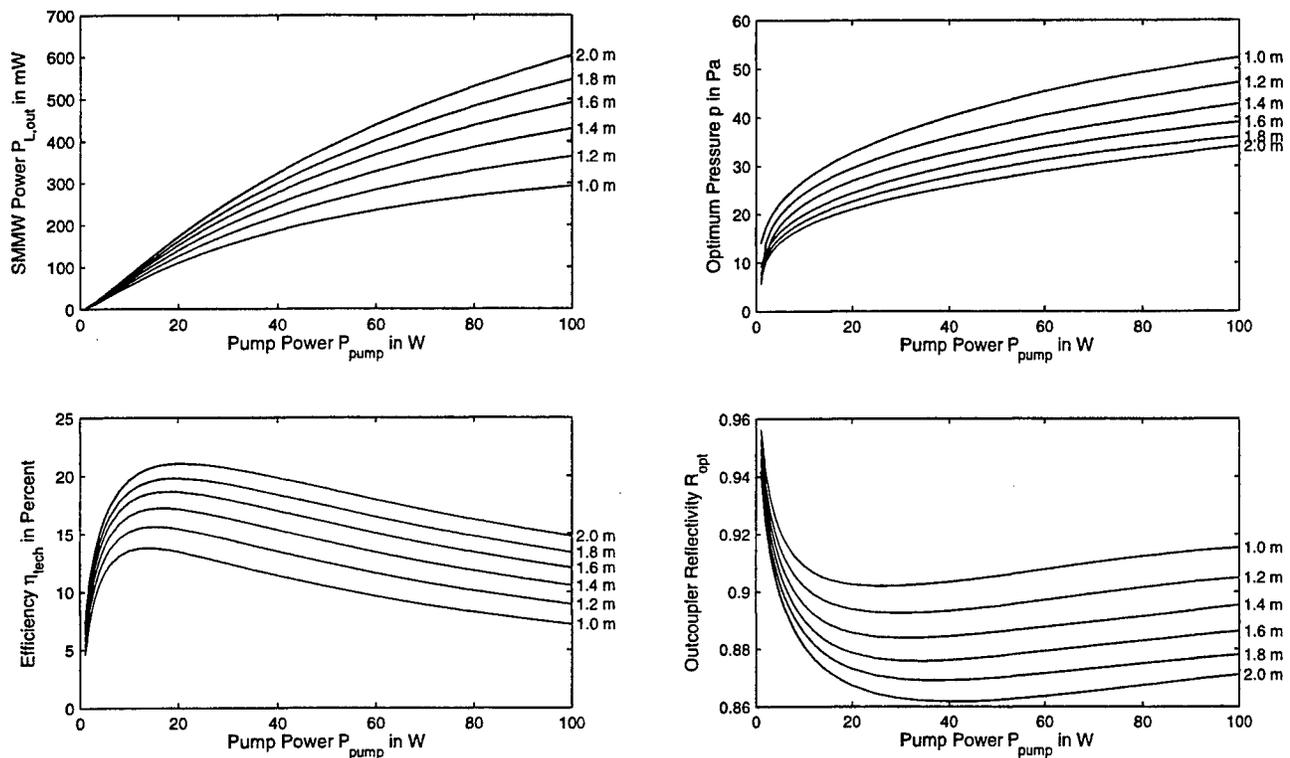

Figure 5. (left) Nomograms of SMMW output power and efficiency for STD/61 resonators with L_0 as parameter. (right) Nomograms of optimum pressure and reflectivity R_{opt} for STD/61 resonators with L_0 as parameter.

4.3. SMMW Output Power

For laser construction purposes, it is useful to know the resonator perimeter necessary to achieve a certain SMMW output from a given pump power. With the program FIRL, it is possible to calculate nomograms of the SMMW output power. Figure 5 (left) shows nomograms of the SMMW output power and efficiency versus pump power with the resonator perimeter as parameter. As is expected, the SMMW output power as well as the technical efficiency

$$\eta_{tech} = \frac{P_{SMMW}}{P_{pump} \cdot \eta_Q} \tag{41}$$
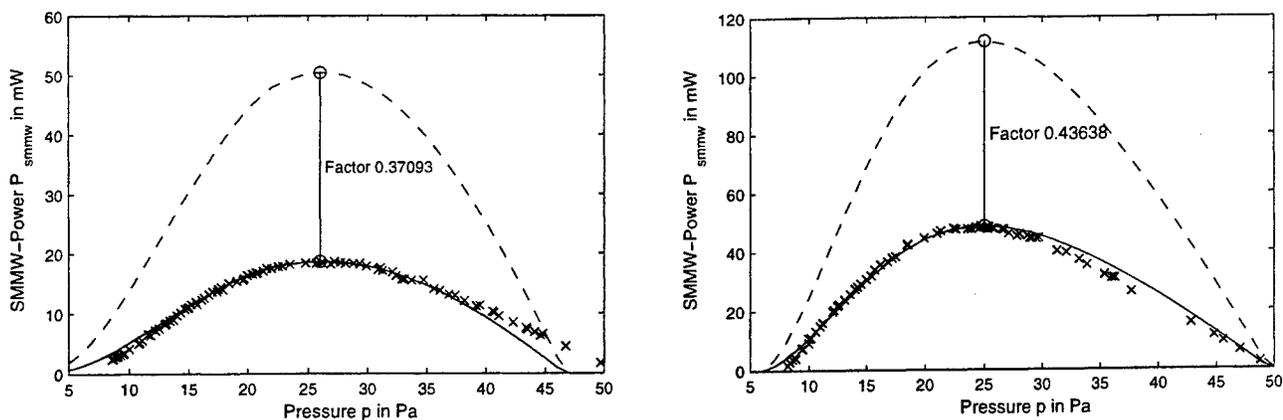
Figure 6. Experimental results in comparison to simulation results: ERFILAS-2 counterpropagating beam (left) and ERFILAS-3 copropagating beam (right).

increase with increasing resonator perimeter. In the same calculation series, which requires approximately one week of computation time on a 233 MHz Pentium processor, the optimum conditions have been determined (figure 5 right). With increasing perimeter and decreasing pump power, the operation pressure has to be reduced, a fact that has been stated repeatedly in literature from experimental results.[16] The reflectivity R_{out}, one of the most critical parameters in laser design. has been optimized in the same process.

5. EXPERIMENTAL VERIFICATION

Based on the standard resonator design approach, two SMMW laser heads have been realized. ERFILAS-2 is based on a STD/55/1.5 resonator design: ERFILAS-3 includes a STD/61/2 resonator.[17,4,5] In comparison to the standard resonators. the cooler radii r_{cool} have been reduced, with minor influence on the performance.

The pump beam has a waist radius of 0.45 mm and provides a pump power of 20 W. In the case of ERFILAS-2, an output power of 33 mW can be achieved at a pressure of 23 Pa. However, this beam is TEM_{01}, and for the counterpropagating TEM_{00} beam lower power levels have been observed. In figure 6 (left), the results of measurements are compared to simulation results. The indicated factor between simulation and experiment is due to the transmission of the hybrid hole outcoupler substrate and the vacuum window. The fact that the TEM_{01} is preferred to the TEM_{00} mode may be attributed to the outcouplers in combination with the off-axis SMMW gain maximum (see figure 4).

ERFILAS-3 delivers output powers of 49 mW in the copropagating direction and 27 mW in the counterpropagating direction under the same pump conditions.[5] The beam profile is a nearly perfect TEM_{00}. The copropagating beam was examined closer. and the results are shown in figure 6 (right). Again. the factor between simulation and experiment can be explained by outcoupler and vacuum window transmission.

In both cases, the agreement between simulation and experiment is very good. Nevertheless, the optimum pressure in theory is slightly larger ($\approx 2\ Pa$) than that one observed in experiments. This might be due to inaccuracies in the applied molecular parameters of methanol.

6. CONCLUSIONS

In this paper, the complete modelling of a SMMW laser head has been briefly scetched. Mathematical descriptions of the components resonator, pump and SMMW radiation, relaxation and active medium have been derived.

A standard design procedure of SMMW laser resonators has been summarized from earlier papers by the author.

The molecular gas and its absorption and gain characteristics have been derived including a quantum mechanical approach, the Doppler effect and the Maxwell distribution of the molecular velocities. Molecular parameters of the 2.523 THz line of methanol have been extracted from literature. These parameters might be inaccurate as they were derived from the theoretical models of the corresponding authors.

The pump radiation distribution has been averaged along the resonator perimeter to keep the model simple, but accounting for refocussing of the pump beam on the optical axis. Transversal profiles calculated in a representative cross section form the base for the determination of the SMMW output power of the SMMW laser head. Thermal conduction and diffusion are taken into account.

The simulation results were compared to measurement results and showed good agreement. This indicates that the program FIRL can be used as a tool for the computer aided design (CAD) of SMMW laser heads.

7. ACKNOWLEDGEMENTS

REFERENCES

1. R. Titz, M. Birk, D. Hausamann, R. Nitsche, F. Schreier, J. Urban, H. Küllman, H. P. Röser, "Observation of stratospheric OH at 2.5 THz with an airborne heterodyne system," *IR Phys. and Techn.* **36**, p. 883-891, 1995.

2. G. Chin, "Optically Pumped Submillimeter Gas Lasers and the Prospects for Constructing Space-Qualifiable LO Systems." *Int. Journ. Infrared and Millimeter Waves* **8**(10), p. 1219-1234, 1987.

3. M. Raum, "Design of a 2.5 THz Submillimeter Wave Laser with Optical Pump Beam Guiding," *Int. Journ. Infrared and Millimeter Waves* **16**, p. 2147-2161, 1995.

4. M. Raum, H. Brand, "SMMW Lasers with Optical Pump Beam Guiding," in *ITG-Fachbericht: Displays and Vacuum Electronics.* M. Thumm, ed., p. 411-416, VDE-ITG, (Garmisch-Partenkirchen), 1998.

5. M. Raum. "SMMW Ring Lasers with Optical Pump Beam Guiding," in *23rd International Conference on Infrared and Millimeter Waves.* T. J. Parker, ed., p. 112-113, (Colchester), 1998.

6. M. Raum, K. Huber. "Standard Design of SMMW Laser Ring Resonators with Optical Pump Beam Guiding," in *6th International Conference on Terahertz Electronics*, P. Harrison, ed., p. 238-241, (Leeds), 1998.

7. W. W. Rigrod. "Saturation effects in high-gain lasers," *Journal of Applied Physics* **36**, p. 2487-2490, 1965.

8. C. O. Weiss. "Pump Saturation in Molecular Far-Infrared Lasers," *IEEE Journ. Quant. Electr.* **QE-12**, p. 580-584, 1976.

9. R. I. McCormick. F. C. DeLucia, D. D. Scatrud. "A Time Resolved Study of Rotational and Vibrational Excitation and Relaxation in the $^{13}CH_3F$ Optically Pumped Far-Infrared Laser," *IEEE Journ. Quant. Electr.* **QE-23**, p. 2060-2067, 1987.

10. R. L. Panock. R. J. Temkin. "Interaction of two laser fields with a three-level molecular system," *IEEE Journal of Quantum Electronics* **QE-13**, p. 425-434, 1977.

11. D. G. Burghard, D. M. Dennison, "The molecular structure of methyl alcohol," *Phys. Rev.* **84**, p. 408-417. 1951.

12. J. O. Henningsen. "Assignment of Laser Lines in Optically Pumped CH_3OH," *IEEE Journ. Quant. Electr.* **QE-13**. p. 435-441, 1977.

13. M. Inguscio, L. R. Zink, K. M. Evenson, D. A. Jennings, "Accurate frequency of the 119 μm methanol laser from tunable far-infrared absorption spectroscopy," *IEEE Journ. Quant. Electr.* **26**, p. 575-579, 1990.

14. S. Zhao, S. N. Ghosh, "Vibrational frequency and force field constant calculation of CH_3OH and its 9 isotopomers by GF matrix method." *Int. Journ. Infrared and Millimeter Waves* **16**, p. 547-578, 1995.

15. H. M. Deitel, P. Deitel, *C++ How to Program*, Prentice Hall International Editions,Inc., 1994.

16. X. Huang, J. Qin, X. Zheng, Y. Bao, X. Luo, Y. Lin, "Operating parameter optimization of optically pumped CH_3OH far-infrared laser," *Int. Journ. Infrared and Millimeter Waves* **18**, p. 1539-1546, 1997.

17. M. Raum, "New results on 2.5 THz Laser with Optical Pump Beam Guiding," in *4th International Workshop on Terahertz Electronics.* H. Brand, ed., LHFT, (Erlangen), 1996.

NbN Phonon-Cooled Hot-Electron Bolometer as a Mixer for THz Heterodyne Receivers

H.-W. Hübers[a], J. Schubert[a], A. Semenov[b], G. Gol'tsman[b], B. Voronov[b], E. Gershenzon[b], and G. W. Schwaab[c]

[a]Institute of Space Sensor Technology and Planetary Exploration, DLR,
12484 Berlin, Germany
[b]Physical Department, State Pedagogical University, 29 M. Pirogovskaya Str.,
Moscow 119435, Russia
[c]Physical Chemistry Department II, Ruhr University, Universitätsstr. 150,
44801 Bochum, Germany

ABSTRACT

We have investigated a phonon-cooled NbN hot electron bolometric (HEB) mixer in the frequency range from 0.7 THz to 5.2 THz. The device was a 3.5 nm thin film with an in-plane dimension of $1.7 \times 0.2 \ \mu m^2$ integrated in a complementary logarithmic spiral antenna. The measured DSB receiver noise temperatures are 1500 K (0.7 THz), 2200 K (1.4 THz), 2600 K (1.6 THz), 2900 K (2.5 THz), 4000 K (3.1 THz), 5600 K (4.3 THz), and 8800 K (5.2 THz). The sensitivity fluctuation, the long term stability, and the antenna pattern were measured and the suitability of the mixer for a practical heterodyne receiver is discussed.

Keywords: hot-electron bolometer, NbN, superconductor, mixer, terahertz, spiral antenna

1. INTRODUCTION

High resolution heterodyne spectroscopy in the frequency range from 1 THz to 6 THz yields important information on astronomical objects as well as the atmosphere of the earth. Some prominent examples are the CII fine structure line at 1.6 THz [1] and the OI fine structure line at 4.75 THz [2], which are major coolant lines of the interstellar medium. The OH rotational transitions at 2.5 THz and 3.5 THz allow the determination of the OH volume mixing ratio in the atmosphere and yield important information on the catalytic cycles, which are responsible for the destruction of stratospheric ozone.[3] A number of on-going astrophysical and atmospheric research programs are aimed at these goals.

So far Schottky diodes are used as mixers in heterodyne receivers above a frequency of about 1.2 THz. Double sideband receiver noise temperatures range from 2500 K at 1 THz up to about 70000 K at 4.75 THz.[2,4] This is far above the quantum noise limit. However, state of the art heterodyne receivers require a sensitivity close to the quantum limit. Superconducting hot-electron bolometric (HEB) mixers are possible devices to achieve this goal. Since in a sufficiently small superconducting HEB mixer only the electrons are heated by the incoming radiation, the response time of the HEB is of the order of the electron-phonon interaction time. This results in low noise temperatures as well as in intermediate frequencies (IF) of several GHz. Another attractive feature of an HEB mixer is the small amount (≈ 100 nW) of power required from the local oscillator (LO).

Two types of HEB mixers are known: diffusion-cooled and phonon-cooled HEBs. While the first ones are fabricated from Nb the latter ones are fabricated from NbN. In this paper we present the design and performance of a NbN phonon-cooled HEB mixer in the frequency range from 0.7 THz up to 5.2 THz. Emphasis is put on noise temperature measurements, but also on those parameters which are equally important for application of a mixer in a practical heterodyne receiver, such as the sensitivity fluctuation, the long term stability, and the antenna pattern.

410

Part of the EUROPTO Conference on Terahertz Spectroscopy and Applications II
Munich, Germany • June 1999 SPIE Vol. 3828 • 0277-786X/99/$10.00

2. MIXER DESCRIPTION

2.1 HEB detector

The investigated HEB was fabricated from a 3.5 nm thin superconducting NbN film. The film was deposited by dc reactive magnetron sputtering of Nb in a N_2 atmosphere onto a 350 µm thick high resistivity Si substrate (5 kΩ cm). The details of the process are described elsewhere.[5] The bolometer itself is a 1.7 µm wide and 0.2 µm long bridge. It has a transition temperature of 9.3 K and a 870 µΩcm resistivity at room temperature. The series resistance in the superconducting state is about 3 Ω. In Fig. 1 the unpumped and pumped current-voltage (I-V) characteristic of the HEB mixer at a temperature of 4.2 K are shown. There is a first plateau at a current of 45 µA, which is followed by a second linear increase corresponding to a resistance of 40 Ω. Another plateau develops at a current of 55 µA. After the third almost linear increase, which corresponds to a resistance of 80 Ω, the maximum critical current of 90 µA is reached. This behavior is likely to be due to the existence of three patches in the superconducting film, each with a different critical current. We speculate that two of them are situated under the contact pads. The critical current in those parts is reduced due to the proximity effect between NbN and gold of the antenna
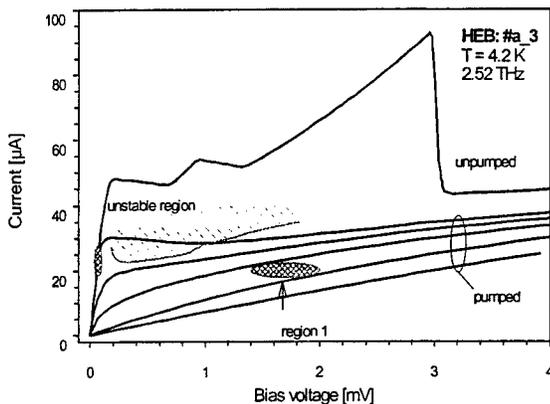
Fig. 1: Unpumped and pumped current-voltage characteristics of the HEB. The noise temperature measurements were performed with the bias voltage and LO power of region 1.
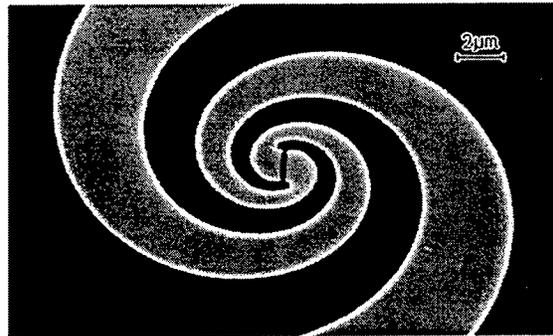
Fig. 2: SEM picture of the logarithmic spiral antenna. The HEB is located in the gap at the inner end of the spiral arms.

2.2 Logarithmic-spiral antenna

A planar two-arm logarithmic-spiral antenna is used to couple both the signal and the local oscillator (LO) radiation with the bolometer (Fig. 2). The central part of the antenna was patterned using electron beam lithography while the outer part was defined by conventional UV photolithography (for details see Ref. 5). This antenna belongs to a family of frequency independent antennas, i. e. the most important characteristics such as the antenna impedance and the beam pattern are independent on the frequency over a wide range. In order to have a frequency independent beam pattern the effective aperture scales with the wavelength. In our design, the circle that circumscribes the spiral structure is 130 µm in diameter while the circle, inside which the antenna arms form the inner terminals and cease to represent a spiral, is 2.6 µm in diameter. Between these circles, the antenna arms make two full turns. From this geometry it is possible to estimate the range where the antenna characteristics are independent of the frequency. The upper wavelength limit, λ, can be estimated by $\lambda/2 \leq D$,[6] where D is the diameter of the outer circle. The shortest wavelength where the spiral antenna is still working properly is about 10 times the inner radius at which the spiral deviates from the ideal shape.[7] In our case this yields an upper wavelength limit of 884 µm (0.34 THz) and a lower wavelength limit of 44 µm (6.8 THz). The winding of the spiral can be characterized by the angle at which a radial line from the origin of the antenna intersects a spiral arm. In our case this angle is 70°. A more tightly wound spiral will yield a more symmetric beam pattern, since the asymmetry is caused by the decaying fields along the spiral arm.

However, the effective aperture will also decrease, resulting in a wider beam, which is more difficult to couple to the RF optics. The choice of 70° is a compromise between these two effects. According to estimates,[6] such an antenna should have an RF impedance of about 75 Ω when suspended in free space. We expect an even smaller value for our antenna since it is supported by the semi-infinite dielectric half-space simulated by the Si substrate with the thickness much larger than the wavelength.

2.3 RF optics

The HEB and the planar antenna were glued onto the flat side of an extended hyperhemispheric lens. The lens was cut off from an optically polished 6 mm diameter sphere that was made from high resistivity (>10 kΩcm) silicon. No antireflection coating was used. The extension of the lens together with the thickness of the substrate yields a total extension length of 1.2 mm. This is very close to the optimal extension length at which the beam pattern of the hybrid antenna is diffraction limited, i.e. the pattern is rather determined by the diameter of the lens than by the beam properties of the planar feed antenna. In this case the side-lobes are still low. It is worth mentioning that in the range of the diameter to wavelength ratios, which we covered in the experiment, the optimal extension length varies by about 5 %.[8] The lens and the HEB were mounted in a copper holder which in turn was directly screwed to the 4.2 K cold plate of an Infrared Labs HD-3 lHe cryostat. The cryostat has a wedged 1.5 mm thick TPX pressure window. A 1.2 mm thick quartz window with an antireflection coating was mounted on the 77 K shield in order to block the background radiation. The optical losses of the lens, the quartz window, and the teflon window are given in Table 2.

2.4 IF circuit

The intermediate (IF) signal is coupled out of the HEB via the arms of the antenna. The antenna in turn terminates by a coplanar line, which was lithographed on the same substrate and has an impedance of 50 Ω. The use of RF filters is not necessary since the RF field decays by about 20 dB in the first wavelength along the spiral arm.[9] One arm of the spiral antenna is grounded. The other arm leads to a bias tee and a circulator, which was used in order to prevent standing waves between the HEB and the first amplifier. Bias tee, circulator and the HEMT amplifier were cooled to 4.2 K. The HEMT amplifier has a bandwidth of 1.2 - 1.8 GHz and a gain of 36 dB at the IF frequency of 1.5 GHz. Its noise temperature is about 3 K. The output of the amplifier was filtered at 1.5 GHz with a bandwidth of 75 MHz, further amplified and finally detected with a crystal detector.

3. EXPERIMENTAL SET-UP

The device was investigated at seven different frequencies ranging from 0.7 THz up to 5.2 THz. Two FIR gas laser systems were used to cover this frequency region. The measurements from 0.7 THz to 2.5 THz were performed using an optically pumped FIR ring laser.[10] The ring laser design prevents back-reflection of CO_2 pump radiation from the FIR cavity into the CO_2 laser cavity resulting in a stable output power of the FIR laser. Out-coupling of FIR radiation was performed through a 3 mm diameter hole in one of the laser mirrors. For the measurements between 2.5 THz and 5.2 THz a transversely excited FIR laser was used. As it is the case for the ring laser this design inhibits the back-reflection of CO_2 radiation into the pump laser. For this laser a 45° moveable mirror was used for the output coupling of the FIR radiation. This mirror can be moved transversely to the optical axis of the FIR laser and allows for optimization of the output power for each laser line separately.[11] It should be mentioned that the noise temperature measured at 2.52 THz was the same independently which laser system was used for the measurements.

For the noise temperature measurements the output radiation of the ring laser (see Fig. 3) was focussed onto the HEB mixer by two high-density polyethylene lenses (one lens for the set-up with the transversely excited FIR laser). A wire grid in the LO beam path deflected a minor fraction of the LO radiation onto a pyroelectric detector which was used for monitoring the LO power. A second wire grid could be rotated in order to optimize the LO power coupled to the HEB. The signal and the LO beam were superimposed by a 6 μm thick Mylar beamsplitter. Double sideband (DSB) receiver noise temperatures were determined by the Y-factor method. Ecosorb was used as the hot and cold load. The temperature of the hot and cold load was 293 K and 77 K, respectively. The stability of the laser systems was good enough to measure the noise temperature by putting alternately the hot load and the cold load for about ten seconds in the signal path behind the beamsplitter. The not evacuated optical path from the load to the pressure window of the cryostat was about 25 cm long. The hot and cold readings were averaged by a computer and the Y-factor as well as the noise temeperature were calculated. Due to the relatively weak laser line and the narrow line profile the noise temperature at 5.2 THz was measured by chopping (frequency: 15 Hz)

between the hot and cold load using lock-in technique. It was verified at the other frequencies that the direct technique and the chopping technique yield the same result. At frequencies above 1 THz the Rayleigh-Jeans approximation does no longer closely describe the power radiated by a black body. Therefore, we used the general form of the dissipation-fluctuation theorem (Callen and Welton) for deriving the receiver noise temperature from the measured Y-factor.[12]
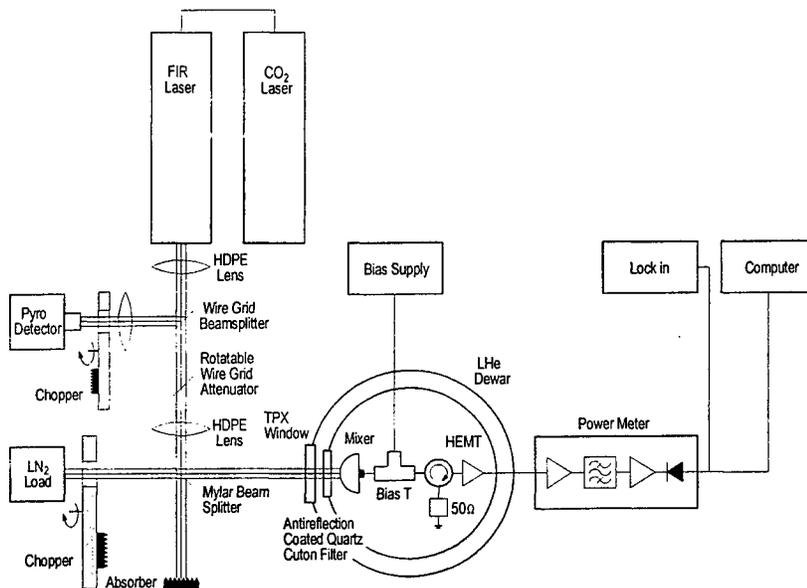

Fig. 3: The experimental set-up.

For the antenna pattern measurements the two lenses were removed. Due to the divergence of the laser beam this yielded an almost plane parallel wavefront at the position of the HEB mixer. The cryostat was fixed on a mount, which allowed to rotate it in azimuth and elevation. The mixer was operated in the direct detection regime and signal was measured as a function of the angular position of the HEB at a frequency of 2.5 THz.

4. MIXER PERFORMANCE

4.1 Receiver noise temperature

In Fig. 4 and Table 1 the DSB receiver noise temperature is given as a function of the LO frequency between 0.7 THz and 5.2 THz. Also shown in Fig. 4 is the DSB receiver noise temperature when corrected for the losses in the optical elements as given in Table 2. The optical losses were determined either from the known transmission curves (TPX window and quartz window), calculated (beamsplitter) or estimated (Si lens). The corrected receiver noise temperature increases linearly with frequency and follows closely the 10 hv/k line. This is 20 times the quantum limit hv/2k for a DSB receiver operated in the continuum detection mode. The result suggests that the hybrid antenna of the mixer is frequency independent from 0.7 THz up to 5.2 THz, in agreement with the specified design. The LO power absorbed in the HEB was evaluated from the pumped and unpumped IV characteristics. We used the isothermal method described elsewhere.[13] An absorbed LO power around 100 nW was determined at all frequencies. The optimum bias current and voltage were about 22 μA and 1.8 mV (region 1 in Fig. 1). No significant dependence of the optimal operation regime on the frequency was observed.
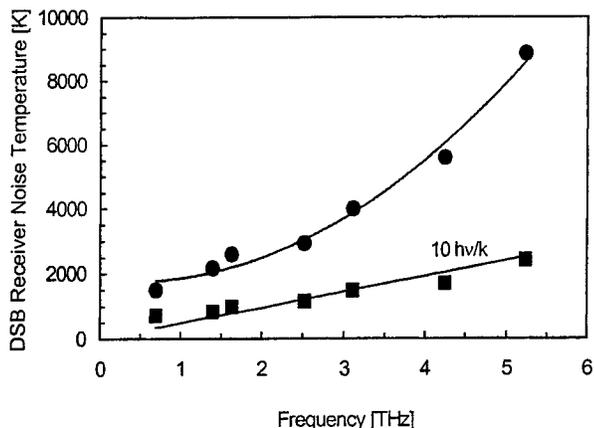
Freq. [THz]	Laser Gas	CO_2	$T_{rec,DSB}$ [K]
0.623	HCOOH	9R20	1500
1.397	CH_2F_2	9R34	2200
1.627	CH_2F_2	9R32	2600
2.523	CH_3OH	9P36	2900
3.106	CH_3OH	9R10	4000
4.252	CH_3OH	9P34	5600
5.246	CH_3OD	9R8	8800

Fig. 4: DSB receiver noise temperature as a function of frequency. The circles indicate the measured noise temperature while the squares correspond to the noise temperature corrected for losses in the optics.

Table 1: FIR laser lines[14] and DSB receiver noise temperature as a function of frequency.

According to Table 2 the quartz filter and the Si lens give the major contributions to the total losses. Using a Zitex filter instead of the quartz filter could reduce the noise temperature by about 0.6 – 1.4 dB in the frequency range from 0.7 THz to 2.5 THz. This for example would yield a DSB noise temperature of about 2400 K at 2.5 THz (loss of Zitex filter ≤0.5 dB [15]). This is comparable with other phonon cooled HEB mixers as well as with Nb diffusion cooled HEB mixers.[15,16] For the reduction of the loss in the Si lens no straightforward solution is available. One possibility to reduce the reflection could be to fabricate a Si lens with grooves of a certain shape and separation. This approach is discussed in Ref. 17.

	Loss [dB]						
Frequency	0.7 THz	1.4 THz	1.6 THz	2.5 THz	3.1 THz	4.3 THz	5.2 THz
Beamsplitter	0.1	0.2	0.3	0.6	0.7	1.2	1.2
TPX window	0.4	0.4	0.5	0.6	0.6	0.8	0.9
Quartz filter	1.1	1.8	1.9	1.2	1.3	1.5	1.9
Si lens (refl.)	1.5	1.5	1.5	1.5	1.5	1.5	1.5
Si lens (absorp.)	0.1	0.1	0.1	0.1	0.1	0.1	0.1
Sum	3.2	4.0	4.3	4.0	4.2	5.1	5.6

Table 2: Losses in the optics (data for the beamsplitter are calculated, data for the TPX window and the quartz filter are from the transmission curves as given by the manufacturer, data for the Si lens are estimated).

4.2 Sensitivity fluctuations

For a practical mixer in a heterodyne receiver the minimum detectable temperature or sensitivity fluctuation, ΔT_{min}, is of prime importance, because it describes the temperature contrast which can be resolved within a certain integration time. For an ideal total power receiver it can be derived from the receiver noise temperature, T_{rec}, the post detection bandwidth, Δv, and the integration time, τ_{int}, according to $\Delta T_{min} = T_{rec}/(\Delta v \, \tau_{int})^{1/2}$. For a non ideal receiver other sources such as gain instabilities of the amplifier can contribute to the sensitivity fluctuations and raise it above ΔT_{min}. In our set-up the postdetection bandwidth is Δv=75 MHz and the integration time is τ_{int}=2 ms, yielding a sensitivity fluctuation ΔT_{min}=6.2 K. Fig. 5 shows

the sensitivity fluctuation for the optimum bias voltage at a frequency of 1.4 THz. The first half of the scan is with the cold load in the signal path while the second half is with the hot load in the signal path. From the scan a rms sensitivity fluctuation of 7.4 K is determined. This is in a good agreement with the calculated value of 6.2 K. In addition, the scan documents the excellent stability of the laser LO.
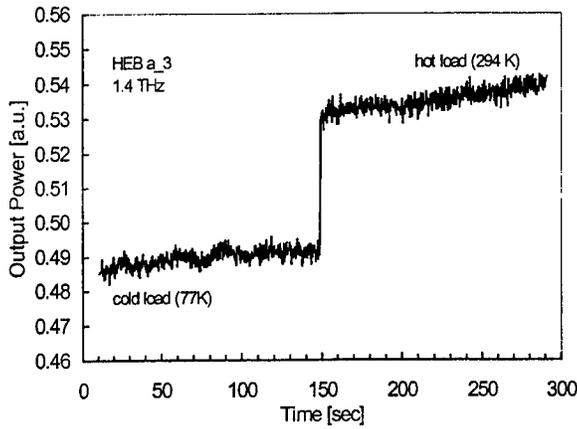
Fig. 5: Output power of the HEB as a function of time measured at a frequency of 1.4 THz. The sensitivity fluctuation (i.e. the width of the trace) is close to the theoretical minimum (see text).
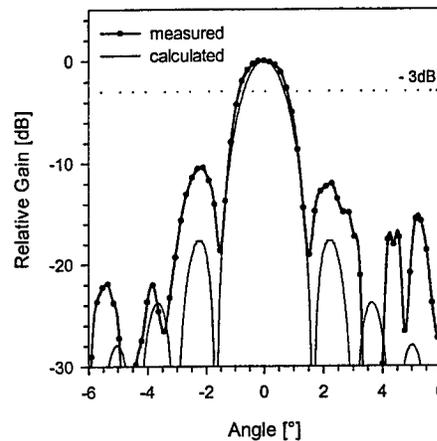
Fig. 6: Measured and calculated antenna pattern of the hybrid antenna at a frequency of 2.5 THz.

4.3 Antenna pattern

As an example, in Fig. 6 the antenna pattern in the E-plane of the hybrid antenna is shown. It was measured at a frequency of 2.5 THz. Also shown is the Airy pattern calculated for the antenna. The measured full width at half maximum (FWHM) is $\Omega_A=1.65°$ while the calculated profile yields $\Omega_A=1.4°$, in good agreement with the measurements. From this the directivity of the antenna, $D=4\pi/\Omega_A^2$, and the effective aperture, $A_{eff}=D\lambda^2/4\pi$, are calculated. It is $D\approx1.5\times10^4$ and $A_{eff}\approx17\ mm^2$. We estimate the Gaussian coupling efficiency to be about 70 %. The first side lobes occur below the −10 dB level. However, while the FWHM and the position of the side lobes are reproduced quite well by our calculations, the power level of the measured side lobes is too high. The reason for this is not quite clear. It might be a slightly too large extension length which is known to result in increased side lobes.

5. SUMMARY AND OUTLOOK

We have measured the DSB receiver noise temperature of a phonon-cooled hot-electron bolometric mixer operated in the frequency range from 0.7 THz to 5.2 THz. When corrected for optical losses, the noise temperature of the mixer increased linearly with frequency with the slope 10 hv/k. This indicates that the hybrid antenna was frequency independent in the specified frequency range. In addition, the sensitivity fluctuation and the antenna pattern are close to the theoretical expectation. The excellent performance of this HEB mixer demonstrates that the time to apply an HEB as mixer in a practical heterodyne receiver for THz frequencies has come.

6. ACKNOWLEDGEMENTS

7. REFERENCES

1. R.T. Boreiko, A. L. Betz, and J. Zmuidzinas, "Heterodyne spectroscopy of the 158 micron CII line in M42", Astrophys. J. **325**, pp. L47-L51, 1988.
2. A. L. Betz and R. T. Boreiko, "A practical Schottky mixer for 5 THz (Part II)", Proc. of the 7th Int. Symp. on Space THz Technology, pp. 503- 510, Charlottesville 1996.
3. R. Titz, M. Birk, D. Hausamann, R. Nitsche, F. Schreier, J. Urban, H. Küllman, and H. P. Röser, "Observation of stratospheric OH at 2.5 THz with an airborne heterodyne system", Infrared Phys. and Technology **36**, pp. 883-891, 1995.
4. H. P. Röser, H.-W. Hübers, T. W. Crowe, and W. C. B. Peatman, "Nanostructure GaAs Schottky diodes for far-infrared heterodyne receivers", Infrared Phys. Technol. **35**, pp. 451-462, 1994.
5. S. Svechnikov, A. Verevkin, B. Voronov, E. Menschikov, E. Gershenzon, and G. Gol'tsman, "Quasioptical pnonon-cooled NbN hot electron bolometer mixers at 0.5-1.1 THz", Proc. of the 9th Int. Symp. on Space Terahertz Technology, pp. 45-51, Pasadena 1998.
6. J. D. Kraus, "Antennas", McGraw-Hill, Inc., 1988.
7. T. H. Büttgenbach, R. E. Miller, M. J. Wengler, D. M. Watson, and T. G. Phillips, "A broad band low-noise SIS receiver for submillimeter astronomy", IEEE Trans. on Microwave Theory Tech. **36**, pp. 1720-1725, 1988.
8. T. H. Büttgenbach, "An improved solution for integrated array optics in quasi-optical mm and submm receivers: the hybrid antenna", IEEE Trans. on Microwave Theory Tech. **41**, "1750-1761, 1993.
9. J. D. Dyson, "The equiangular spiral antenna", IRE Trans. Antennas Propagat. **AP-7**, pp. 181-187, 1959.
10. H.-W. Hübers, G. W. Schwaab, and H. P. Röser, "A heterodyne receiver for the frequency range from 1 - 6 THz", Proc. 30th ESLAB Symp. 'Submillimetre and Far-Infrared Space Instrumentation', ESA **SP-388**, pp. 159-162, 1996.
11. H.-W. Hübers, L. Töben, and H. P. Röser, "A far-infrared laser magnetic resonance spectrometer with permanent magnets", Rev. Sci. Instrum. **69**, pp. 290-293, 1998.
12. A. R. Kerr, M. J. Feldman, and S. K. Pan, "Receiver noise temperature, the quantum noise limit, and the role of zero-point fluctuations", Proc. of the 8th Int. Symp. on Space Terahertz Technology, pp. 101-111, Cambridge 1997.
13. H. Ekström, E. Kollberg, P. Yagoubov, G. Gol'tsman, E. Gershenzon, and S. Yngvesson, "gain and noise bandwidth of NbN hot-electron bolometric mixers", Appl. Phys. Lett. **70**, pp. 3296-3298, 1997.
14. N. G. Douglas, "Millimetre and submillimetre wavelength lasers", Springer, Berlin, 1989.
15. B. Karasik, M. Gaidis, W. R. McGrath, B. Bumble, and H. G. LeDuc, "A low noise superconductive Nb hot-electron mixer at 2.5 THz", Proc. of the 8th Int. Symp. on Space Terahertz Technology, pp. 55-66, Cambridge 1997.
16. P. Yagoubov, M. Kroug, H. Merkel, E. Kollberg, J. Schubert, H.-W. Hübers, G. Schwaab, G. Gol'tsman, and E. Gershenzon, "Heterodyne measurements of a NbN superconducting hot electron mixer at terahertz frequencies", to appear in IEEE Trans. on Appl. Superconductivity (1999).
17. G. Schwaab, H.-W. Hübers, J. Schubert, Patrick Erichsen, G. Gol'tsman, A. Semenov, A. Verevkin, S. Cherednichenko, and E. Gershenzon, "A high resolution spectrometer for the investigation of molecular structures in the THz range", Proc. of the 10th Int. Symp. on Space Terahertz Technology, Charlottesville 1999.

KASIMIR initiative and recent results

C.-C. Lin[1], P. de Maagt[1], T. Närhi[1], P. Piironen[1], J. Mees[2], T. Weber[2], J. Mosig[3], P. Otero[3],
V. Hansen[4], T. Vaupel[4], H. Hartnagel[5], C.-I. Lin[5], A. Simon[5], V. Möttönen[6], A. Räisänen[6],
E. Kollberg[7], H. Merkel[7], P. Zimmermann[8]

[1]European Space Agency, ESTEC, PO Box 299, 2200 AG Noordwijk, The Netherlands
[2]DaimlerChrysler Aerospace, Friedrichshafen, Germany
[3]Ecole Polytechnique Fédérale de Lausanne, Switzerland
[4]Bergische Universität Gesamthochshule Wuppertal, Germany
[5]Technische Hochschule Darmstadt, Germany
[6]Helsinki University of Technology, Finland
[7]Chalmers University of Technology, Gothenburg, Sweden
[8]Radiometer Physics GmbH, Meckenheim, Germany

ABSTRACT

KASIMIR (Key Advanced Structure Investigations for MM- and Sub-MM-Wave Integrated Receivers)
initiative is a development programme started in early 1996 by the ESA in order to advance the mm-
and sub-mm-wave sensor technology for satellite-based atmospheric observations. The initial goal of
the project is to build integrated antenna/mixer frontends at 650 GHz which are qualifiable for the low
Earth orbit environment. All of the frontends will make use of the so-called integrated quasi-vertical
Schottky diodes developed at Tech. Univ. of Darmstadt in Germany.

Keywords: Earth observation, atmospheric chemistry, mm-wave, sub-mm-wave, heterodyne
receivers, mixers, integrated circuits, Schottky diodes

1. INTRODUCTION

Satellite-based observations of Earth's atmosphere necessitate sensitive receivers in the millimeterwave
(mm-wave) and sub-millimeterwave (sub-mm-wave) regions of spectrum. Especially, receivers using
heterodyne technique are best adapted for studying spectral signatures of various chemical species, thus
permitting to understand key chemical reactions which lead to changes in atmospheric compositions
such as depletion of ozone layer. Millimeterwave receivers are most suitable for tropospheric
observations from a satellite as species' signatures are not strongly masked by the background signal of
water molecules at this range of frequency. In the sub-mm-wave region however, the atmosphere
becomes opaque below the stratosphere precisely due to the presence of water vapour. Thus, the
tropospheric and stratospheric observations are best performed by two separate sensing instruments
covering complementary spectral regions with some overlap so as to optimise the observation
efficiency[1]. Instrument studies have been conducted by ESA in order to analyse the feasibility of such
satellite missions[2].

Among critical technology areas for enabling such missions, mm-wave and sub-mm-wave mixers have
been identified as one of the most crucial elements of such receivers. Due to violent mechanical
stresses during the launch as well as thermal stresses and atomic radiations in the space environment,
the reliability of such sensitive components/devices must be guaranteed by design and demonstrated
before launch.

Part of the EUROPTO Conference on Terahertz Spectroscopy and Applications II
Munich, Germany • June 1999 SPIE Vol. 3828 • 0277-786X/99/$10.00

417

KASIMIR (Key Advanced Structure Investigations for MM- and Sub-MM-Wave Integrated Receivers) initiative is a development programme started in early 1996 by the ESA in order to advance the mm- and sub-mm-wave sensor technology for satellite-based atmospheric observations (atmospheric chemistry research). The initial goal of the project is to build integrated antenna/mixer frontends at 650 GHz which are qualifiable for the low Earth orbit environment. All of the frontends will make use of the so-called integrated quasi-vertical Schottky diodes developed at Tech. Univ. of Darmstadt in Germany. A number of frontend designs are being pursued in parallel:

(1) an open-structure type, fundamentally pumped mixer using a Si-dielectric lens together with a ring-slot radiator, a single Schottky diode and a co-planar waveguide circuit;

(2) an open-structure type, fundamentally pumped mixer using a Si-dielectric lens together with a double-slot radiator, a single Schottky diode and a microstrip circuit;

(3) a waveguide type, sub-harmonically pumped mixer using integrated diagonal horn, an anti-parallel diode pair and a microstrip circuit.

2. QUASI-VERTICAL SCHOTTKY DIODES (QVD)

The QVD's[3], developed at the Technical University of Darmstadt, offer low parasitics, vertical current flow, improved heat sink capabilities and is less affected by the skin effect as compared with other planar concepts. Both single diodes and anti-parallel diodes (APD) have been fabricated[4]. The single diodes are used for the open-structure type mixers where a dielectric lens is used as a focusing element. Anti-parallel diodes are used for the waveguide integrated mixer which is sub-harmonically pumped. Based on the experience in optimising whisker-contacted diodes at 570 GHz, the following QVD parameters have been chosen for 650 GHz mixers:

Anode diameter:	0.8 μm
Epitaxial layer doping concentration:	3×10^{17} cm^{-3}
Epitaxial layer thickness:	70 nm
Air-bridge height above mesa:	2 μm
Series resistance (estimated):	16 Ω
Junction capacitance (estimated):	1 fF

Fig. 1 shows the dimensions of the APD as used in the waveguide mixer. The main efforts during the KASIMIR project have been concentrated on reducing the overall diode dimensions and improving the reliability of the fabrication processes. As a matter of fact, the physical size of the diodes is comparable to lateral dimensions of the circuit-elements such as transmission-lines and filters. Thus, undesirable discontinuities can result around the diode which degrade receiver performance.

3. OPEN-STRUCTURE MIXERS

An open-structure mixer consists of an integrated antenna/mixer chip mounted on an extended hemispherical silicon lens as a focusing device. Two technologically different concepts have been developed in the course of this project:

(1) a co-planar waveguide based frontend with a ring-slot radiator, a single Schottky diode, co-planar transmission-lines and filters;
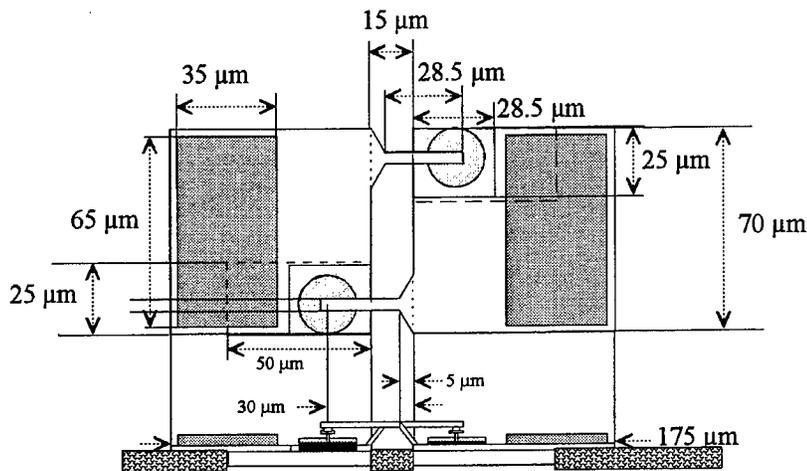
Fig. 1: Structure and dimensions of the anti-parallel diode chip

(2) a microstrip based frontend with a double-slot radiator, a single Schottky diode, microstrip transmission-lines and filters.

Both are fundamentally pumped mixers and the local oscillator signal needs to be injected through the antenna.

The co-planar waveguide based frontend is technologically simpler as only one metal layer is required for realising the radiator and the circuit. However, less freedom is offered to design the frontend as only one metal layer is available for implementing the radiator, diode and matching circuits. As the complete co-planar circuit can radiate towards the dielectric lens and not only the ring-slot radiator, the resulting radiation characteristics are very sensitive to the overall circuit topology.

In order to ensure satisfactory radiation characteristics, both scale-model measurements as well as numerical simulations have been performed. Fig. 2 depicts the layout of the 65 GHz scale-model which was fabricated at EPF-Lausanne using RT/duroid 6010 substrate with 0.635 mm thickness. A commercially available Schottky diode was mounted between the upper end of the co-planar line and the ground. Fig. 3 shows the predicted and measured radiation patterns of the 65 GHz scale-model using a synthesised elliptical lens (50 mm diameter). A simple model[5] was used in this case to compute the radiation characteristics. Both the scale-model measurements and theroretical predictions gave us confidence that the parasitic radiation can be kept below an acceptable limit. Fig. 4 depicts predicted radiation patterns of the 650 GHz frontend with a synthesised elliptical lens and a hyperhemispherical lens, which were calculated using an integral equation based spectral domain field solver[6]. A very accurate modelling of the frontend geometry was done to produce those predictions. In particular, the effects of parasitic radiations from the transmission-lines and transitions have been included in the model. This can be seen in Fig. 5 where the Gaussian coupling efficiency has been calculated as a function of the lens extension length for the co-planar frontend as well as for a simple ring-slot with a short feedline. The predicted coupling efficiency of the frontend circuit is less than 5 % worse than that of a single ring-slot radiator. The 650 GHz frontend chip is currently in fabrication at Tech. Univ. Darmstadt.
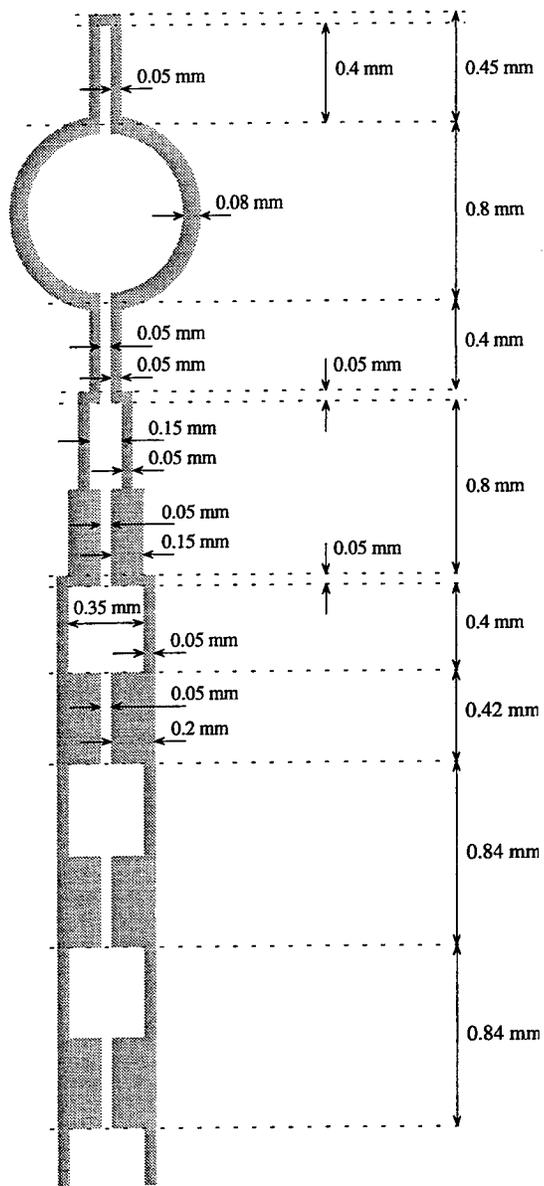
Fig. 2: Layout of the 65 GHz co-planar
frontend scale-model
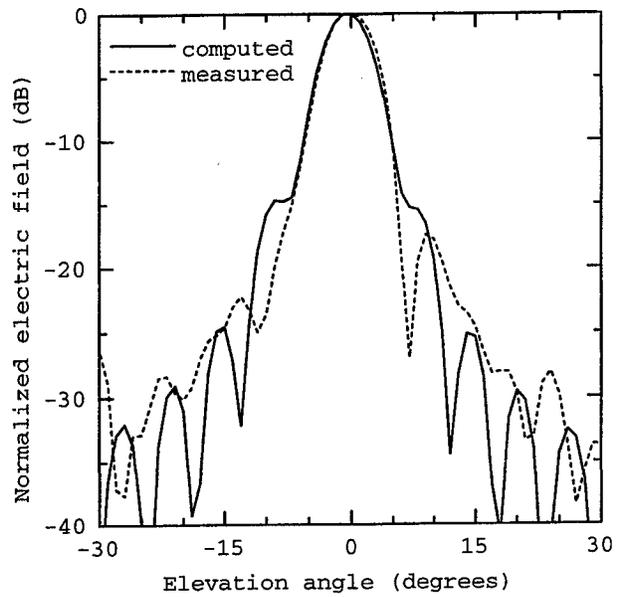
Co-polar component in E-plane
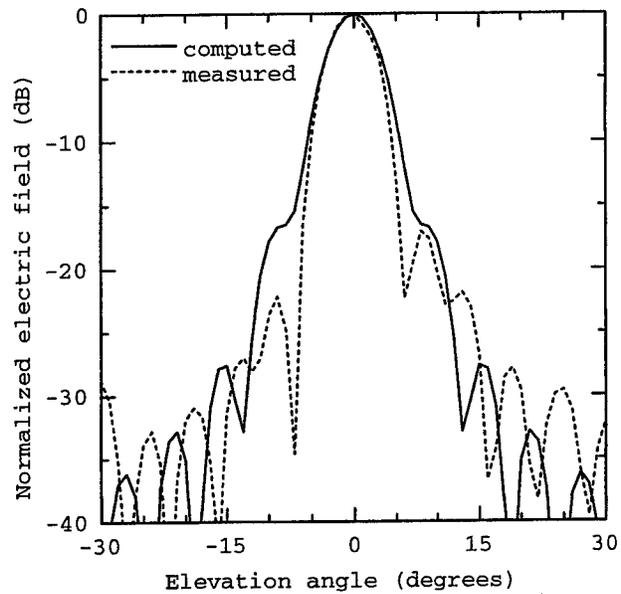
Co-polar component in H-plane

Fig. 3: Predicted and measured radiation patterns
of the 65 GHz scale-model
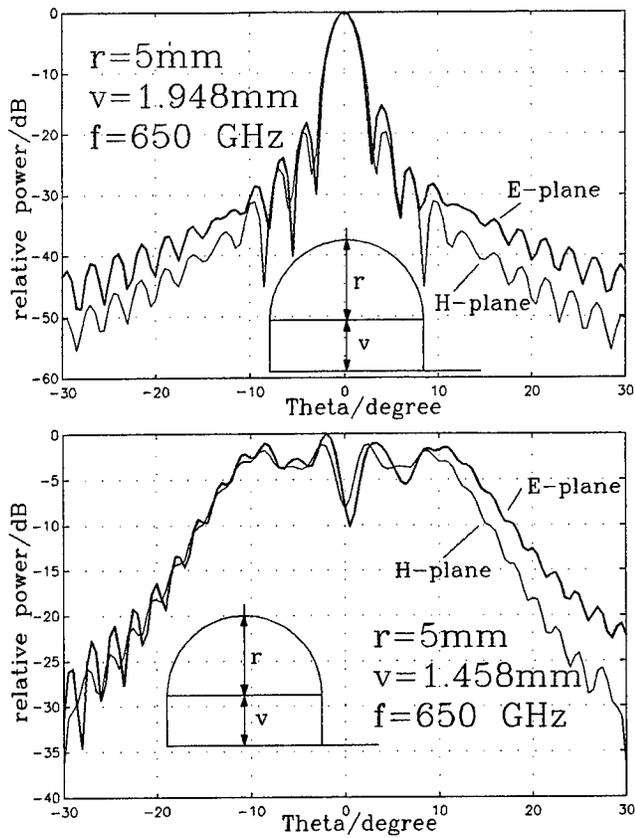
Fig. 4: Predicted radiation patterns for the co-planar waveguide frontend mounted on a synthesised elliptical lens (upper figure) and a hyperhemispherical lens (lower figure)
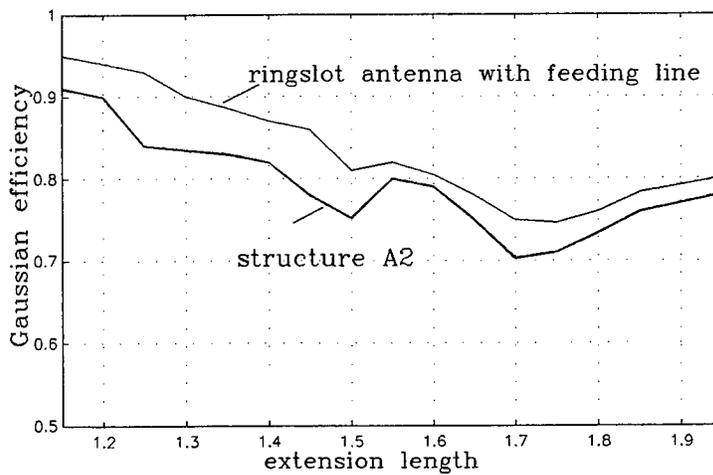
Fig. 5: Gaussian coupling efficiency of the overall structure (A2) as compared to a solitary ringslot radiator with a short feedline

The microstrip based frontend design requires additional technology steps for fabrication such as: (a) deposition of an insulating layer over the first metal layer; (b) deposition of the second metal layer; (c) a proper contacting to the anode of the diode; (d) subsequent circuit patterning. Fig. 6 depicts the layout of the microstrip based frontend in a schematic manner. For the clarity, the substrate layer is not shown in the upper-half of the figure (or assumed transparent).

Initially, polyimide material was tried as the substrate layer. However, building up to a layer thickness of 5 μm proved to be difficult, especially for attaining the required planarity for the microstrip circuit and for obtaining sufficient adhesion of the second metal layer. Therefore, SiO_2 deposition was tried and has been proven to be more adequate as a substrate layer.

The advantage of the microstrip based concept is the larger freedom offered to the designer to optimise the frontend topology as the radiator and the rest of the circuit are separated on two different metal layers. Also, the mixer circuit is shielded by the ground plane (lower metal layer) so that only the double-slot radiator would effectively see the incoming radiation. Again, scale-model measurements at 65 GHz as well as theoretical (numerical) predictions have been carried out during the design phase of the frontend. The actual 650 GHz frontend chip is currently in fabrication at Tech. Univ. Darmstadt.

Those frontend chips will be integrated, upon preliminary tests, onto silicon dielectric lenses (10 mm diameter) at Chalmers Univ. Tech. An extensive test programme is foreseen to carry out pattern and noise measurements together with vibration tests and thermal cyclings as preliminary space environmental tests.
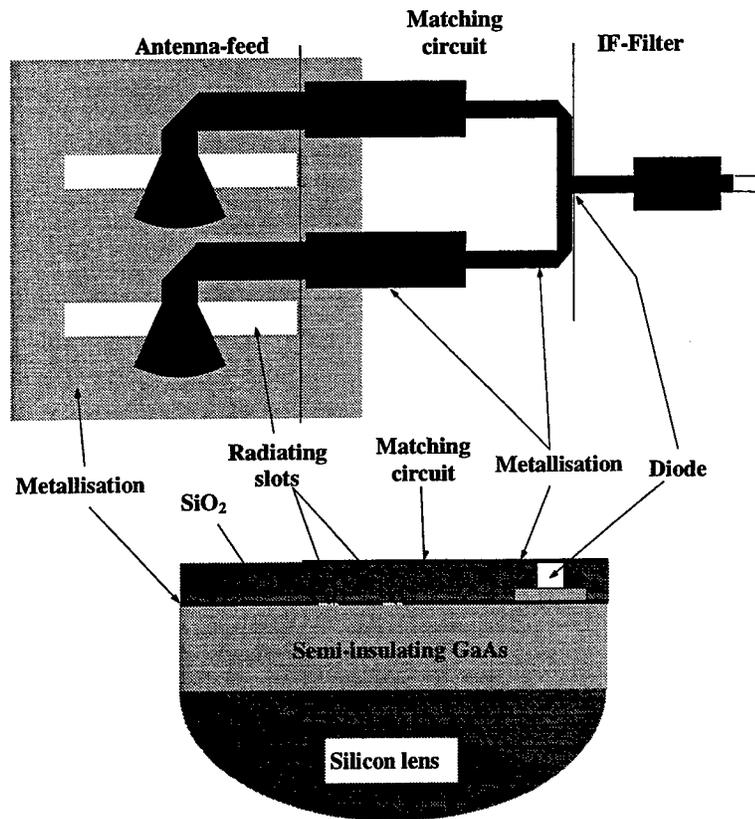
Fig. 6: Schematic presentation of the microstrip based frontend design

4. WAVEGUIDE MIXER

The design of the waveguide mixer was carried out at Helsinki Univ. Tech. After the successful fabrication of anti-parallel diodes in Darmstadt, it was decided to concentrate on the design of sub-harmonically pumped mixers as it would potentially reduce the overall receiver complexity (LO source at ½ frequency). A systematic design procedure was applied which consisted of theoretical modellings and scale-model verifications at 10 and 220 GHz.

The complete mixer block is shown in Fig. 7 which also includes a diagonal horn antenna for coupling to the incoming signal. Both two-tuner and four-tuner designs have been explored. Due to the uncertainties in predicting the actual input impedance of the diode at 650 GHz, the four-tuner design was preferred which has a wider impedance tuning range.

A picture of a 220 GHz scale-model is shown in Fig. 8, which is a two-tuner design. For this scale-model, a diode optimised for 650 GHz has been used which led to less than optimum noise performance at 220 GHz. The results of conversion loss and noise measurements on a four-tuner scale-model are summarised in Fig. 9. The conversion loss is comparable to the best published results of sub-harmonic planar diode mixers around 220 GHz. The noise performance is somewhat worse due to the above mentioned reason. The 650 GHz waveguide mixer is currently under integration.
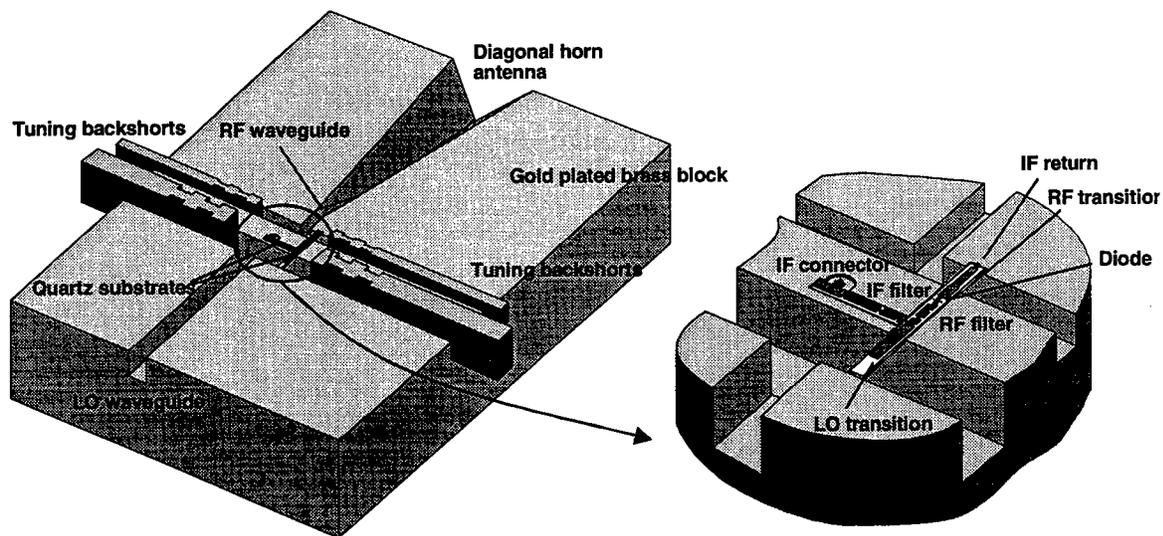
Fig. 7: 650 GHz sub-harmonically pumped waveguide mixer
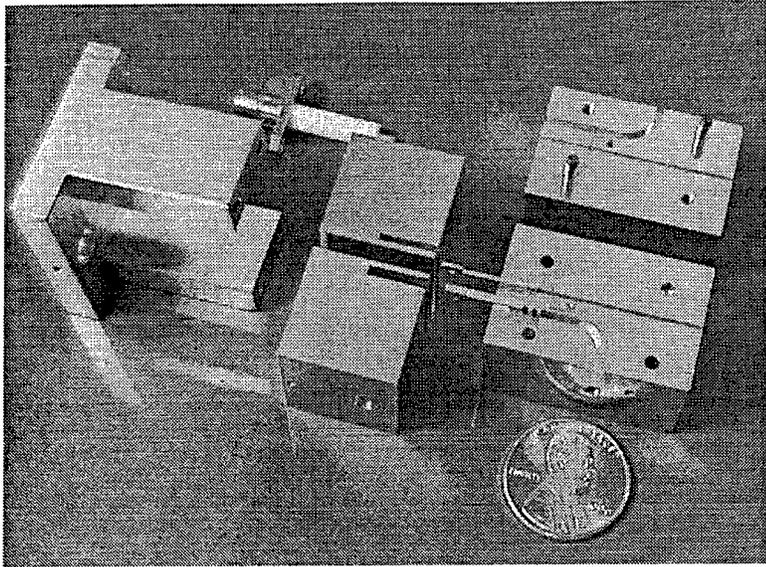
Fig. 8: Two-tuner 220 GHz scale-model mixer (tuning mechanism is at left and mixer block parts at right)
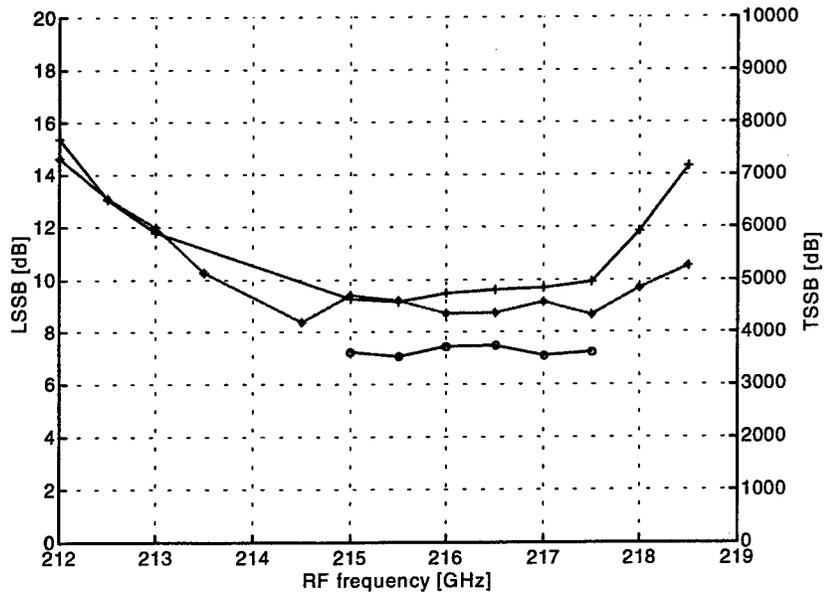
Fig. 9: SSB conversion loss and noise temparature vs. instantaneous RF frequency of a four-tuner scale model: f_{LO} = 107 GHz, P_{LO} = 3.5 mW (5.5 dBm)

+ = conversion loss obtained from noise measurement

* = conversion loss obtained from signal measurement

o = noise temperature

5. CONCLUSION

The KASIMIR project required synthetic efforts of the experts in various speciality disciplines such as space-based sensor system engineering, sub-mm-wave mixer designs, circuit and antenna numerical analyses and designs, optical techniques, device physics, sub-micron device fabrication and micro-machining techniques, high precision machining and sub-mm-wave measurement techniques. It is a unique attempt, for its novelty and ambitious goals, to advance the technology of sub-mm-wave heterodyne receivers for space-based observations. Despite numerous design and fabrication difficulties encountered in the course of the KASIMIR project, the final fabrication of the 650 GHz receiver frontends are under way and they will be tested in the time frame of Summer to Autumn 1999.

6. REFERENCES

1. The Report for Assessment – The Nine Candidate Earth Explorer Missions, Atmospheric Chemistry Mission, ESA Publication SP-1196 (6), Noordwijk, April 1996.

2. D. Lamarre et al., "ESA Technical Activities in Sub-mm-wave Limb Sounding", Int'l Workshop on Sub-mm-wave Observation of Earth's Atmosphere from Space, Tokyo, 27-29 January 1999.

3. A. Simon et al., "Improvement of Varactor Diodes for Sub-mm-wave Sources", 5th Int'l Workshop on Terahertz Electronics, Grenoble, 18-19 Sept.1997.

4. J. Mees et al., "Key Advanced Structure Investigations for MM- and Sub-MM-Wave Integrated Recievers (KASIMIR) – Integrated Schottky Receivers for Space Applications", ESA Workshop on Millimeter Wave Technology and Applications, Espoo, 27-29 May 1998.

5. P. Otero, G.V. Eleftheriades and J.R. Mosig, "Slot-Loop Antennas on Substrate Lenses for Sub-mm-Wave Open Structure Mixers", 20th ESTEC Antenna Workshop, Noordwijk, 1997.

6. T. Vaupel and V. Hansen, "Improved Spectral Domain Analysis Based on Complete Analytical Solutions of the Asymptotic System Matrix", Int'l Symposium on Electromagnetic Theory, Thessaloniki, May 1998.

Demonstration of a Millimetre-Wave Sub-harmonically excited Quantum Barrier Mixer

W.Y.Liu, D.P.Steenson, Institute of Microwaves and Photonics, School of Electronic and Electrical Engineering, The University of Leeds, U.K.

Abstract

The paper presents both our theoretical and experimental findings regarding a sub-harmonically pumped Quantum Barrier Mixer. A qualitative treatment is given with examples to demonstrate some unique features of a Quantum Barrier Device mixer, which cannot be offered by Schottky junctions, and which would be particularly suited to efficient operation at terahertz frequencies.

Keywords: Quantum Barrier Mixer, Harmonic Mixer, Millimetre-wave Mixer, sub-harmonic mixer, downconverter

1. Introduction

Sub-harmonically pumped mixers are commonly realized with a pair of anti-parallel Schottky diodes. This arrangement will theoretically suppress the odd-order mixing which can otherwise reduce the power available for even-order mixing products. Although two diodes connected in anti-parallel is conceptually simple, any physically mismatch between the two diodes will potentially degrade the mixing performance. To avoid this problem, we can instead use a single Quantum Barrier Device (QBD) that possesses not only a highly non-linear characteristic but also an anti-symmetric conductance resulting from a single junction. Another factor follows from the fact that a pair of Schottky junctions connected in parallel has two metal contacts, while and equivalent Quantum Barrier Device contains only one junction or active area within the device. In essence, the net unbiased capacitance in an equivalent Quantum Barrier Device is lower than the combined capacitance of the two Schottky junctions in parallel. Excess capacitance is highly detrimental with regard to conversion loss at terahertz frequencies, because it tends to shunt the signal past the non-linear mixing element. The other advantages that support the use of a single Quantum Barrier Device as a sub-harmonically pumped mixer at THz frequencies, will be discussed later in greater detail.

Perhaps more significantly, the barriers of a Quantum Barrier Device can be tailored during fabrication in such a way that the non-linearities associated with the device can be controlled to favor either high or low power pump requirements. For example, it is possible to choose different layer structures for a device of the same diameter to obtain different resistive non-linearities. Flexibility to modify the device non-linearities in this manner permits both the carrier supply function and the resonant transmission characteristics to be modified independently, which in turn enables the optimization of the nonlinear behavior to favor different operating conditions. This is especially so in the case of the sub-harmonic mixer where a large degree of non-linearity at low voltages permits the use of modest local oscillator powers, and also leads to improved device reliability under both continuous wave and pulsed power conditions.

The intrinsic mixing performance of related devices has been reported previously in [7], and [5]. In Ref. [6], Tait experimentally demonstrated that heterostructure devices with two and four barriers under a biased condition, can achieve conversion losses between 4 and 6 dB and noise temperature ratios between 1.5 and 2 at 300K. In the experiment reported by the authors in Ref. [7], a conversion loss of less than 9 dB was achieved for an 18GHz-to-0.9Ghz sub-harmonic mixer using a double barrier device, in the absence of any DC bias and with a low local oscillator power. Mixing with conversion gain at W-band, has also been demonstrated using QBD's biased into their negative dynamic resistance region [5]. So far, the intrinsic mixing performance of barrier devices has only been demonstrated experimentally. However, this paper qualitatively reviews the basic mixing mechanism in a

non-linear network, with particular attention being given to describing the non-linear characteristics and the resulting electrical behavior of Quantum Barrier Devices in response to excitation at many different frequencies.

2. Qualitative Treatments

Before discussing the specific aspects related to quantum barrier devices, the intrinsic frequency conversion mechanism of a typical mixing device is qualitatively reviewed. The following equivalent circuit will be used to model the intrinsic non-linearities of the device. The series impedance due to the bond wire and contacts is considered to be linear and can be taken care of if considered as part of the linear external embedding network.
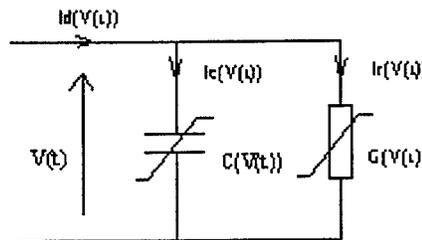
Figure 2.1 Equivalent Circuit of a Nonlinear Diode

A. Conductive Mixing

The following polynomial describes the current flow through such a non-linear conductance as a function of voltage and holds for any applied frequency simply with a change of coefficients, a_i.

$$i_g(t) = \sum_{i=0}^{\infty} a_i V(t)^i \qquad (2.1)$$

In the presence of an applied bias the operating point will be altered and the coefficients of equation 2.1 will require modification. Given that the bias is V_b, the current versus voltage characteristic will be given by:

$$i_g(t) = \sum_{i=0}^{\infty} a'_i V(t)^i \qquad \text{with} \qquad a'_i = \sum_{j=i}^{\infty} \frac{j!}{(j-i)!(i+1)!} a_j V_b^j.$$

Now, with a local oscillator applied and under a single-tone excitation, the time domain description of the voltage across the device is given by :

$$V(t) = v_{lo}\cos(\omega_{lo}t) + \sum_{k=-\infty}^{\infty} v_k \cos(\omega_{rf}t - k\omega_{lo} + \psi_k) \qquad (2.2)$$

It is assumed that the local oscillator voltage is very much greater in magnitude than the RF signal, and that under a resistive mixing regime where conversion loss is usual, it is reasonable to assume that the powers of any inter-modulation products are insignificant. It is now possible to approximate the conductive current by Taylor expansion up to the linear disturbance:

$$i_g(t) = \sum_{i=0}^{\infty} a_i v_{lo}\cos(\omega_{lo}t)^i + \frac{1}{2!}\sum_{i=0}^{\infty} i a_i \big(v_{lo}\cos(\omega_{lo}t)\big)^{i-1} \sum_{k=-\infty}^{\infty} \big\{v_k \cos(\omega_{rf}t - k\omega_{lo}t + \psi_k)\big\} + \ldots\ldots \qquad (2.5)$$

With some algebraic rearrangements, equation 2.5 can be rewritten as:

$$i_g(t) = \sum_{n-\infty}^{\infty} G_0(n)\exp(jn\omega_{lo}t) + \sum_{n=-\infty}^{\infty}\sum_{m=-\infty}^{\infty} G_1(n)V_m \exp[j(\omega_{rf}t + (n-m)\omega_{lo}t)] + \sum_{n=-\infty}^{\infty}\sum_{m=-\infty}^{\infty} G_1(n) V_m^* \exp[j((n+m)\omega_{lo}t - \omega_{rf}t)] \qquad (2.6)$$

where

$$G_0(n) = \sum_{i=|n|}^{\infty} \binom{i}{\frac{i+n}{2}} \frac{a_i v_{lo}^i}{2^i}, \quad G_1(n) = \sum_{i=|n|}^{\infty} \binom{i}{\frac{i+n}{2}} \frac{(i+1)a_i v_{lo}^i}{2^{i+1}}, \quad \text{and} \quad V_m = \frac{v_m \exp(j\psi_m)}{2}.$$

B. Capacitive Mixing

Similarly, the nonlinear capacitance of the quantum barrier device is described by a power series, as follows:

$$C(V(t)) = \sum_{j=0}^{\infty} b_j V(t)^j \quad (2.7)$$

Hence, the charge accumulated in the barriers is given by :

$$Q(V(t)) = \sum_{i=0}^{\infty} b_i V(t)^{i+1} \quad (2.8)$$

and, applying Taylor expansion to equation 2.8 in the same way as we did for the conductive current gives:

$$Q(V(t)) = \sum_{i=0}^{\infty} b_i [v_{lo}\cos(\omega_{lo}t)]^{i+1} + \sum_{i=0}^{\infty} (i+1)b_i [v_{lo}\cos(\omega_{lo}t)]^{i} \sum_{m=-\infty}^{\infty} v_m \cos(\omega_{rf}t - m\omega_{lo}t + \psi_m) \quad (2.9)$$

Replacing the trigonometric expressions of equation 2.9 by using a phasor representation, and differentiating the whole equation with respect to time gives:

$$i_c(t) = \frac{d}{dt}Q(V(t)) = \sum_{n=-\infty}^{\infty} jn\omega_{lo}C_0(n)V_n \exp(jn\omega_{lo}t) + \sum_{m=-\infty}^{\infty}\sum_{n=-\infty}^{\infty} j(\omega_{rf} - (m-n)\omega_{lo})C_1(n)V_m \exp[j(\omega_{rf}t - (m-n)\omega_{lo}t)] +$$
$$\sum_{m=-\infty}^{\infty}\sum_{n=-\infty}^{\infty} j((n+m)\omega_{lo} - \omega_{rf})C_1(n)V_m^* \exp[j((n+m)\omega_{lo}t - \omega_{rf}t)] + \dots \qquad (2.10)$$

where, $C_0(n) = \sum_{i=|n|}^{\infty} \binom{i+1}{\frac{i+1+n}{2}} \frac{b_i v_{lo}^{i+1}}{2^{i+1}}$, and $C_1(n) = \sum_{i=|n|}^{\infty} \frac{(i+1)b_i v_{lo}^i}{2^{i+1}} \binom{i}{\frac{i+n}{2}}$, and $V_m = \frac{v_m \exp(j\psi_m)}{2}$

C. Conversion Matrix and Conversion Loss

The total current flowing into the mixing device is the sum of the reactive current together with the resistive current, giving :

$$i(t) = i_g(t) + i_c(t) = \sum_{n-\infty}^{\infty} [G_0(n) + jn\omega_{lo}C_0(n)]V_n \exp(jn\omega_{lo}t) + \sum_{n=-\infty}^{\infty}\sum_{p=-\infty}^{\infty} [G_1(n) + j(\omega_{rf} - p\omega_{lo})C_1(n)]V_{p+n} \exp(\omega_{rf}t - p\omega_{lo}t) +$$
$$\sum_{n=-\infty}^{\infty}\sum_{p=-\infty}^{\infty} [G_1(n) + j(p\omega_{lo} - \omega_{rf})C_1(n)]V_{p-n}^* \exp(p\omega_{lo}t - \omega_{rf}t) \qquad (2.11)$$

It follows from the second term of equation 2.11 that the mixing products are related as:

$$\sum_{p=-\infty}^{\infty} I_p + \sum_{p=-\infty}^{\infty} I_p^* = \sum_{n=-\infty}^{\infty}\sum_{p=-\infty}^{\infty} [G_1(n) + j(\omega_{rf} - p\omega_{lo})C_1(n)]V_{p+n} + \sum_{n=-\infty}^{\infty}\sum_{p=-\infty}^{\infty} [G_1(n) + j(p\omega_{lo} - \omega_{rf})C_1(n)]V_{p-n}^* \qquad (2.12)$$

Assuming that the LO matching condition is satisfied, then each mixing product I_p can be determined, and each is associated with an appropriate embedding admittance Ye_p in the following way:

$$I_p = I'_p - V_p Ye_p \quad (2.13)$$

Hence, equation 2.12 can be rewritten as

$$I'_p + I'^*_p = \sum_{\substack{n=-\infty \\ k \neq n}}^{\infty} \left[G_1(n) + j(\omega_{rf} - p\omega_{lo})C_1(n) \right] V_{p+n} + \left\{ G_1(0) + j(\omega_{rf} - p\omega_{lo})C_1(0) + Ye_p \right\} V_p + $$
$$\sum_{\substack{n=-\infty \\ k \neq n}}^{\infty} \left[G_1(n) + j(p\omega_{lo} - \omega_{rf})C_1(n) \right] V_{p+n}{}^* + \left\{ G_1(0) + j(p\omega_{lo} - \omega_{rf})C_1(0) + Ye_p{}^* \right\} V_p{}^* \quad (2.14)$$

where p, can be any number that represents the harmonic index. The value $p = 0$, represents the RF signal. In the following analysis, we let k-th harmonic of the LO signal to be mixed with the RF signal to form an IF product, (i.e. $\omega_{if} = \omega_{lo} - k\omega_{rf}$), so that I'_k and V_k represent the IF current and voltage respectively. Subsequently, the image current and voltage at $\omega_{im} = 2k\omega_{rf} - \omega_{lo}$ will be represented as $I'_{2k}{}^*$ and $V_{2k}{}^*$ respectively. Since all frequency components other than the image, the IF, the RF and the LO are considered short-circuited, we can reformulate equation 2.15 using a matrix representation as follows :

$$\begin{bmatrix} I'_0 \\ I'_k \\ I'_{2k}{}^* \end{bmatrix} = \begin{bmatrix} y_{0,0} & y_{0,k} & y_{0,2k}{}^* \\ y_{k,0} & y_{k,k} & y_{k,2k}{}^* \\ y_{2k,0}{}^* & y_{2k,k}{}^* & y_{2k,2k}{}^* \end{bmatrix} \begin{bmatrix} V_0 \\ V_k \\ V_{2k}{}^* \end{bmatrix} \quad (2.16)$$

Or, more explicitly

$$\begin{bmatrix} I'_0 \\ I'_k \\ I'_{2k}{}^* \end{bmatrix} = \begin{bmatrix} G_1(0) + j(\omega_{rf})C_1(0) + Ye_0 & G_1(k) + j(\omega_{rf})C_1(k) & G_1(2k) - j(\omega_{rf})C_1(2k) \\ G_1(k) + j(\omega_{rf} - k\omega_{lo})C_1(k) & G_1(0) + j(\omega_{rf} - k\omega_{lo})C_1(0) + Ye_k & G_1(k) - j(\omega_{rf} - k\omega_{lo})C_1(k) \\ G_1(2k) + j(2k\omega_{lo} - \omega_{rf})C_1(2k) & G_1(k) + j(2k\omega_{lo} - \omega_{rf})C_1(k) & G_1(0) - j(2k\omega_{lo} - \omega_{rf})C_1(0) + Ye^*_{2k} \end{bmatrix} \begin{bmatrix} V_0 \\ V_k \\ V_{2k}{}^* \end{bmatrix} \quad (2.17)$$

Assuming that the terminating admittance of the image is Y_{im}, then equation 2.16 gives the minimum conversion loss under a matched condition as:

$$Lc = \frac{\left| (Y_{00} - Ye_0)(Y_{kk} - Ye_k) - Y_{0k}Y_{k0} \right|^2}{4|Y_{k0}|^2 |Ye_0 Ye_k|} \quad (2.18)$$

where $\quad Y_{00} = y_{0,0} - \dfrac{y_{0,2k}{}^* y_{2k,0}{}^*}{Y_{im}{}^* + y_{2k,2k}{}^*}, \quad Y_{kk} = y_{k,k} - \dfrac{y_{k,2k}{}^* y_{2k,k}{}^*}{Y_{im}{}^* + y_{2k,2k}{}^*}, \quad Y_{0k} = y_{0,k} - \dfrac{y_{0,2k}{}^* y_{2k,k}{}^*}{Y_{im}{}^* + y_{2k,2k}{}^*}, \quad$ and $\quad Y_{k0} = y_{k,0} - \dfrac{y_{k,2k}{}^* y_{2k,0}{}^*}{Y_{im}{}^* + y_{2k,2k}{}^*}$.

D. Implications for QBD Based k=2 sub-Harmonic Mixer

The important features of a sub-harmonic mixer based on a Quantum Barrier Device, will be deduced with respect to the previous analysis.

The Voltage-Independent Admittance and Unbiased Capacitance

From equation 2.18, the conversion loss will decrease when the magnitudes of Y_{00} and Y_{kk} decrease. This implies that the values of $\text{Re}\{Y_{00}\}, \text{Re}\{Y_{kk}\}$ and $\text{Im}\{Y_{0k}\}, \text{Im}\{Y_{k0}\}$ should be minimized. Neglecting image recovery, we have $Y_{00} = y_{00}$, $Y_{kk} = y_{kk}$, $Y_{0k} = y_{0k}$, and $Y_{k0} = y_{k0}$. However, from equation 2.17, $\text{Re}\{y_{00}\}$ and $\text{Re}\{y_{kk}\}$ are :

$$\text{Re}\{y_{00}\} = \text{Re}\{y_{kk}\} = G_1(0) = \sum_{i=|0|}^{\infty} \binom{i}{\frac{i}{2}} \frac{(i+1)a_i v_{lo}{}^i}{2^{i+1}} \qquad (2.20a)$$

which contains the coefficients $a_1, a_2 \ldots a_{k-1}$, which do not appear in Y_{0k} and Y_{k0} of equation 2.19, and similarly,

$$\text{Im}\{y_{00}\} = \text{Im}\{y_{kk}\} = C_0(0) = \sum_{i=|0|}^{\infty} \binom{i+1}{\frac{i+1}{2}} \frac{b_i v_{lo}{}^{i+1}}{2^{i+1}} \qquad (2.20b)$$

which contains the coefficients $b_0, b_1 \ldots b_{k-2}$ which do not appear in Y_{0k} and Y_{k0} of equation 2.19. Thus, the coefficients $a_1, a_2 \ldots a_{k-1}$ and $b_0, b_1 \ldots b_{k-2}$ contain only the low order non-linearities and will not contribute to the IF component. In a k=2 sub-harmonic mixer, it will be a_1 and b_0 which do not appear in both in Y_{0k} and Y_{k0} of equation 2.18, where k in this instance is 2. As can be seen in equation 2.19, the coefficient a_1 represents the linear but voltage-independent conductance, and this component has the effect of reducing the non-linear device current which could otherwise contribute to the mixing process. Similarly, the coefficient b_0, represents the unbiased capacitance which will in act to "shunt" off a proportion of the device current that would otherwise be used for mixing. In other words, both the linear conductance and the unbiased capacitance will significantly reduce the conversion efficiency of a mixer and as such, should be minimized.

Now, for very small value of $|z|$, a polynomial $P(z) = p_0 + p_1 z + p_2 z^2 + \ldots + p_n z^n$ will behave like $p_0 + p_1 z$ or $p_0 + p_m z^m$, with $m \geq 1$, where the first order coefficient p_0, is referred to here as the linear conductance, and reflects the fact that it does not contribute to the mixing process. Hence, when a sub-harmonic mixer is pumped at very low LO powers (or voltage), the effect of the linear conductance p_0, is especially significant in increasing the conversion loss. In the case of the quantum barrier device, the device non-linearity can be "tailored" as required. It is therefore desirable to grow the layers in such a way that the first order resistance at low voltages is maximized, in which case more of the resultant current is contributed by the higher order polynomial coefficients (or non-linearities), thus improving conversion loss at higher harmonic numbers.

The First and the Second Minimum Conversion Loss

If the local oscillator power is further increased beyond the negative differential resistance (NDR) regions of the current-voltage characteristic, the effect of the higher order non-linearities becomes dominant. Since the current-voltage characteristic contains negative coefficients for some of the higher order terms in the power series, resulting from the existence of the NDR regions, the conversion loss will not necessarily reach saturation in the conventional manner. Instead, it will reach an initial minimum in the conversion loss versus LO power. After the first minimum, the NDR regions, and their associated negative coefficients, will enhance the conversion loss at various harmonics of the LO. There are multiple minima in conversion loss corresponding to the regions of the QBD current-voltage characteristic, before the current peak, in the NDR region, and following on from the current minimum. Associated with these minima in conversion loss there are two maxima, which correspond to the discontinuities in the current-voltage characteristic at the peak and valley currents. The measured results shown in Figure 2.4b, illustrates these features clearly, beyond the third minimum the conversion loss characteristic is thought to saturate in a similar way as a Schottky device, although this was not measured experimentally. Another key feature shown in Figure 2.4b, is the slow degradation in conversion loss as the local oscillator power drops below –2dBm (800μW). This slow degradation in conversion loss compared to that of an unbiased Schottky based mixer is another significant feature of the QBD based mixer, and simply reflects the strong degree of non-linearity at low applied voltages in such devices. To maximize the efficient use of the LO power so that the minimum LO power is be required to attain the first and the second minima in conversion loss,

430

then the NDR regions in the current-voltage characteristic should be drawn as close to the current-axis as possible. This is achieved by growing the double barrier layers to favor a lower quasi-confined energy level, that is, a wider well. The high orders of non-linearity are achieved during growth by ensuring that high current densities are available and following from the growth of barriers with high transmission coefficients, that is, thin barriers. The structures used for this study featured, two 4.3nm, Al0.4Ga0.6As barriers and a 5.1nm, un-doped GaAs well, grown by The University of Nottingham.
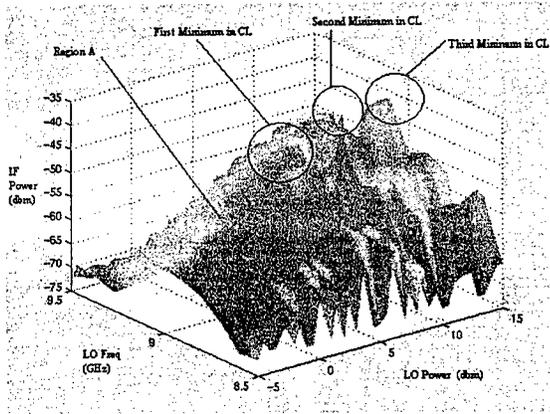
fig. 2.4a
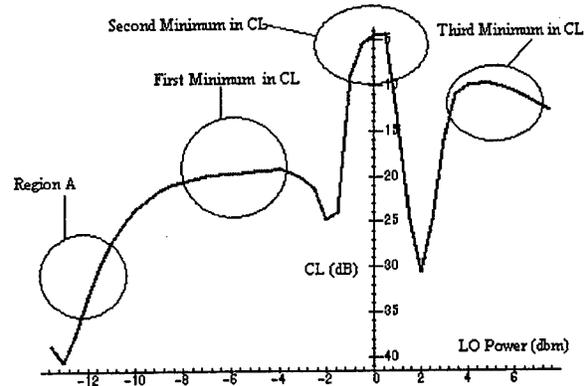
fig. 2.4b

Figure 2.4. a) Measured IF Power Versus LO Power Characteristic;   b) Simulated Conversion Loss Versus LO Power
(CL=Conversion Loss)

Distribution of Harmonic Powers

In the case of a Schottky diode, the exponential current-voltage relationship requires that $a_{i+1} < a_i$ always, in the power series. Thus, the higher the order of the sub-harmonic mixer, the lower the conversion loss. However, this is not necessary the case for the QBD sub-harmonic mixer. For example, considering the condition where the junction capacitance can be ignored, and following some algebraic substitutions in equation 2.17, we find that the conversion loss for a k-th harmonic mixer is:

$$L_c = \frac{\left|(\zeta_k + \xi_k)(\zeta_k + \xi_{kk}) - Y_{0k}Y_{k0}\right|^2}{4|Y_{k0}|^2|Y_{e0}Y_{ek}|} \qquad (2.21)$$

where, $\zeta_k = \sum_{i=|0|}^{k-1} \binom{i}{\frac{i}{2}} \frac{(i+1)a_i v_{lo}^i}{2^{i+1}}$ and $\xi_k = \sum_{i=|k|}^{\infty} \binom{i}{\frac{i}{2}} \frac{(i+1)a_i v_{lo}^i}{2^{i+1}}$ (2.22)

For the QBV the coefficient a_i of equation 2.22 can be negative to account for the negative differential conductance in the NDR regions. Hence, ζ_k will not necessarily rise monotonically for increasing LO voltages. Normally, when the LO voltage rises slightly beyond the NDR regions, the value of ζ_k reaches a local minimum. According to equation 2.22, the value of ζ_k is also a function of k, meaning that a different harmonic k, will yield different values in the minimum of ζ_k. It follows from equation 2.21 that there exists an optimal conversion loss for certain harmonic k, LO power and layer structure. The results of our simulation, for the previously mentioned device and layer structure are shown in figure 2.5, suggest that the conversion loss for the 4-th harmonic QBD mixer is comparable to that of the 2nd harmonic one. In fact, instead of restricting ourselves to the requirement of the second harmonic mixing, we can choose a more appropriate harmonic of LO to cost-effectively down-convert an RF signal to the IF frequency.
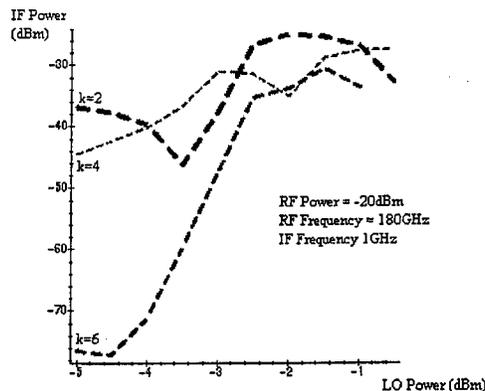
Figure 2.5 Simulated IF Power versus LO Power, for a mixer pumped by LO's of different harmonic Order, k

3. Measurements

Various Quantum Barrier Device based mixers have been measured and the results from two different devices and layers with different barrier characteristics, are used to illustrate some of the aspects mentioned above. By comparison to the first layer structure, the second device features two 1.7nm AlAs barriers and a 4.3nm GaAs well, and as previously mentioned the devices have similar diameters and similar capacitance. The test fixture employed for this investigation was a second sub-harmonically pumped down-converter [7], which is shown in figure 3.3. This mixer was designed to down-convert an RF signal at 18-19 GHz, and give an intermediate frequency of around 900 MHz, with the local oscillator input being approximately half that at 8.5-9.5 GHz. This is a frequency scaled analogue intended for a future realization at a frequency ten times higher than this.
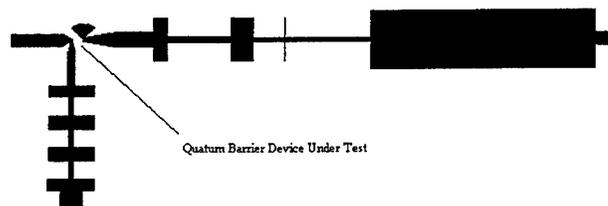
Figure 3.1. Layout of the 18-to-1 GHz Sub-harmonic Mixer (Not to Scale)

Case 1: Device of 10 Microns in Diameter, (Calculated Voltage-Independent Conductance = 0.0016 mho) Figure 3.2a shows the measured current-voltage characteristic of the Quantum Barrier Device. The best conversion loss was recorded to be 5 dB, with a local oscillator power of 0.8 dBm (1.1mW). The region of the current-voltage characteristic, which corresponds to this value of LO power, is near or just below the first minimum in conversion loss. The trend in IF power versus IF frequency for a local oscillator Power = 0dbm, and RF Power = -20dbm, is illustrated in figure 3.2b.

432
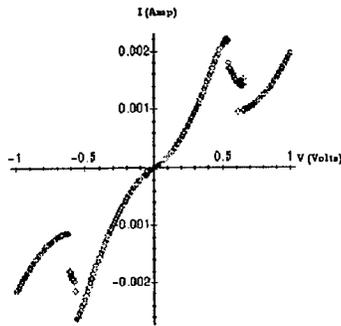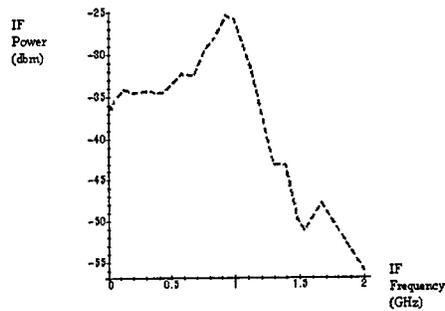
fig 3.2a   *fig3.2b*

Figure 3.2. a) Measured IV Characteristic of Quantum Barrier Device of 10 Microns in Diameter (Voltage-independent Conductance = 0.0016); b) The Measured IF Power versus LO Frequency for LO Power = 0dbm, RF Frequency=18GHz, and RF Power = -20dbm

Case 2: Device of 10 Microns in Diameter, Calculated Voltage-Independent Conductance = 0.024 mho. Figure 3.3a shows the measured current-voltage characteristic of the device. The device diameter is the same as that in the previous, but the current density is higher. The current-voltage characteristic of this device differs from the previous case in that the NDR region of this device further away from the origin. The measured IF power as a function of LO frequency and power is shown in figure 3.3b, and it is noticeable that the device appears to be operating below the NDR regions. In this region the conversion loss increases slowly with reducing LO power. The conversion efficiency, over a similar range of LO powers to the previous example, is inferior due to the noticeably reduced rate of change of current as a function of the applied voltage. Which, when considered in terms of the previously mentioned polynomial description of the current-voltage characteristic, equates to larger values for the lower order coefficients and thus a reduced conversion efficiency. However, by using significantly higher LO powers, in order to exploit a greater portion of the characteristic shown in figure 3.3a (ie. up to the current peak), it would be possible to improve on the measured values of conversion loss.
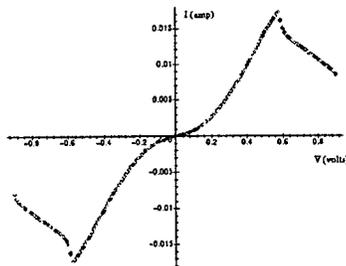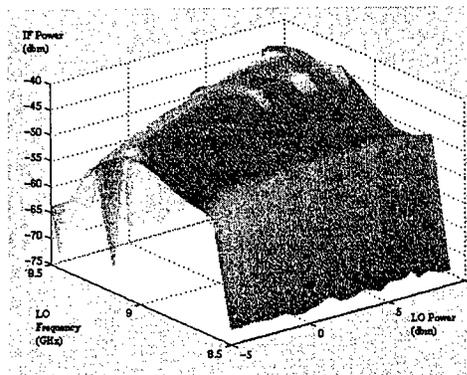
fig 3.3a   *fig 3.3b*

Figure 3.3. a) Measured IV Characteristic of Quantum Barrier Device of 10 Microns in diameter (Voltage-independent Conductance = 0.024); b) The Measured IF Power against LO Frequency for Different LO Power, RF Freq=18GHz, RF Power=-23 dbm

4. Discussions and Conclusions

A qualitative treatment has been presented to identify the significant effects of factors such as: the location of the negative dynamic resistance regions, the intrinsic voltage-independent conductance, the unbiased capacitance as well as the effect of the NDR regions on conversion efficiency at higher harmonics. Measurements of the mixing performance based on two quantum barrier devices from different layer structures have been used to illustrate some of our initial observations from this study. The experimental results, together with our analysis, reveals a number of factors for improving the intrinsic mixing performance of such devices. Namely, at the device level, the device should be fabricated so as to minimize the linear conductance and the unbiased capacitance, to optimize the conversion efficiency for low LO powers. Also, the NDR region should be drawn as close to the current-axis as possible if the intention is to minimize the LO power required to attain a minimum conversion loss. This has been demonstrated and is achieved by increasing the well width during growth, so as to lower the quasi-confined energy level in the well with respect to the fermi-energy in the emitter. Further work is in progress, to perform more measurements and to further elucidate the effects of device level non-linearities for optimum sub-harmonic mixing.

References

[1] Steenson, D.P. Miles, R.E. Pollard, R.D, "High Frequency (200-600 GHz) integration of quantum barrier devices in compound semiconductors grown by MBE", 5th European Heterostructure Technology Workshop, Cardiff, UK. 1995.

[2] Cohn, M. Degenford, J.E. Newman, B.A. "Harmonic Mixing with an Antiparallel Diode Pair", IEEE Trans. Microwave Theory Tech., vol. MTT-23, pp. 667-673, 1975.

[3] Maas, S.A. "Microwave Mixers", Artech House, Second Edition, 1993.

[4] Malik, R.J. Dixon, S. "A Subharmonic Mixer Using a Planar Doped Barrier Diode with Symmetric Conductance", IEEE Electron Devices Lett. EDL-3, pp. 205-207.

[5] Millington, G. Miles, R.E. Pollard, R.D. Steenson, D.P. and Chamberlian, J.M. "A Resonant Tunneling Diode Self-Oscillating Mixer with Conversion Gain", IEEE Microwave and Guided Wave Letters, Vol. 1., No.11. 1991.

[6] Tait, G.B. "Microwave Mixers Employing Multiple-Barrier Semiconductor Heterostructure Devices", IEEE Trans. Microwave Theory And Techniques, Vol. 4, No. 9, 1994.

[7] Liu, W.Y. Steenson, D.P. "18-to-1 GHz Subharmonically Pump Downconverter using a Quantum Barrier Device with Symmetric Conductance, Prep99, 1999.

Micromachined E-plane filter for W-band operation

A. Champion[1], F. Masot[1,2], D.P. Steenson[1], R. E. Miles[1]

[1] Institute of Microwaves and Photonics, School of Electrical and Electronic Eng., The University of Leeds, Leeds LS2 9JT, U. K.

[2] Departamento de Fisica Aplicada, ESI, Universidad de Sevilla, 41092–Sevilla, Spain

Indexing Terms

Micromachining, SU–8 photoresist, E–plane waveguide filter, W–band.

Abstract:

In this paper we describe the realization and electrical performance of a micromachined E-plane filter for operation at a central frequency of 90 GHz. The micromachining technique employed here for the filter fabrication is based on the use of an ultra–thick photoresist, the EPON SU-8, which gives precise control of 2-D and 3-D structures at the 1–100-μm level. In the work described here, the E–plane ladder was micromachined and mounted in a conventional metal waveguide for electrical characterization purposes. The results show that the performance of the micromachined filter is comparable to its metal counterpart,

with the additional advantages of a much lighter structure, greater ease of fabrication and at lower cost.

I. Introduction

As the wavelength of operation becomes increasingly small at frequencies beyond 100 GHz, so do the dimensions of the physical circuit. Integrated–circuit technology offers practical advantages for millimeter and sub-millimeter systems, but it is well known that the planar components at such high frequencies become subject to deleterious substrate modes and other loss mechanisms. Rectangular waveguide technology remains a popular choice in the millimeter band owing to its low losses, but it is difficult to fabricate at these small sizes and tight manufacturing tolerances. Consequently much research effort has recently focused on the development of micromachining techniques to allow precise, reproducible and inexpensive fabrication of waveguide-based components in the millime-

Part of the EUROPTO Conference on Terahertz Spectroscopy and Applications II
Munich, Germany • June 1999 SPIE Vol. 3828 • 0277-786X/99/$10.00

435

ter and submillimeter bands [1].

One technique is the use of photoresists to form the high–precision skeleton structures by photolithography [2,3]. The main physical limitation of this approach is primarily imposed by the maximum thickness achievable with standard positive photoresists (100 μm, to date). Despite the fact that this thickness approaches full waveguide height at increased frequencies, it is still a great handicap in the fabrication of closed waveguide circuitery such as mixer blokes and oscillators cavities.

This problem has been partially solved with the introduction of the untra–thick negative photoresist, EPON SU-8 [1,3]. There are two main properties that makes of this resin especially suitable for micromachining applications at W-band: the extremely high physical viscosity. allows high–precision control of the thickness up to 1 mm by controlling the spin velocity. Also a much small optical absortion coefficient, allowing the whole micromachining fabrication process to take place in just a few UV-exposure steps.

In this paper we present the practical realization of an E-plane filter operating at 90 GHz, as illustrated in fig. 1. The skeleton structures of the metal inserts have been fabricated in SU–8 and then metallized by gold or copper sputtering. The filter structure was then mounted in the E–plane of a conventional metal WR–10 waveguide.

Both simulation and experimental results for the micromachined filter are presented. It is shown that the electrical performance is comparable to the metal counterpart, however achieved with a much lighter struc-
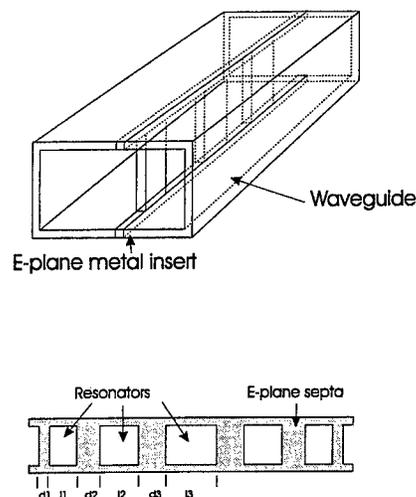
Figure 1: E–plane filter geometry (a) Waveguide (b) E–plane metal insert. Dimensions(mm): $l_1=1.602, l_2=1.642, l_3=1.644$ (resonators), $d_1=0.0994$, $d_2=0.5737$, $d_3=0.7211$ (septum)

ture, and at considerably lower manufacturing cost. A description of the micromachining procedure for the E–plane inserts, and some useful data about the control of the SU–8 thickness and tolerances are also given.

II. Waveguide E–plane Filter. Analysis & Design

The E–plane waveguide configuration consisting of ladder–type metallic inserts centered in the E–plane of a rectangular waveguide offers great potential for realising low dissipation loss millimeter–wave filters [4]. Furthermore, pure metal inserts without supporting dielectrics can be advantageous for

reducing losses in high–Q millimeter–wave circuits [6].

In this paper, a five resonator filter has been fabricated and tested for operation at W–band. The design was obtained by scaling the dimensions of a 9 GHz filter for operation at 90 GHz. The dimensions are given in fig. 1, and are simply 10 times smaller than the dimensions of the original 9 GHz filter [6], as derived in [4] by Postoyalko *et al*, based on a Cohn's equal ripple optimization procedure. The theoretical performance of the scaled version was obtained by a full–wave approach based on the finite element method, implemented by Hewlett–Packard (High Frequency Structure Simulator, v. 5.0) [7]. The simulation results together with the measured values are discussed in section IV.

Figure 3: SU–8 thickness versus spin velocity

Figure 2: Fabrication overview

III. Fabrication Procedure

The process for fabricating the E–plane in-sert is shown in fig. 2. A layer of SU–8 is applied to a glass substrate, previously coated with an evaporated sacrificial layer of aluminium (fig. 2.a,b). The thickness of the SU–8 can be controlled using the spin velocity, to a precision of $\pm$ 5 μm. The relationship between the SU–8 thickness and the spin velocity has been obtained empirically, and is ahown in fig. 3. For this application, the spin velocity was adjusted to 5200 rpm during 120 s, producing a thickness of SU–8 of 30 μm. This thickness is less than one percent of the wavelength at W–band, and is regarded as acceptable for good performance [4]. The wafer is then exposed to UV radiation for 90 s (fig. 2.c). Owing to the negative character of the SU–8, the areas exposed to the UV radiation harden, and the unexposed areas can be etched away by the development of the photoresist. The shape of the filter insert then appears attached to the glass substrate (fig. 2.d). It is finally released by inmersing the wafer in a solution of potassium hydrox-

Figure 5: Final aspect of the filter after mounted in the test–fixture

Figure 4: Photograph of the SU–8 micromachined skeleton of the E–plane insert after metallization by gold sputtering

ide (KOH) which etches away the aluminium and releases the filter element (fig. 2.e).

Once fabricated, the skeleton structures are metallized with gold or copper by sputtering, to a thickness of at least 600 μm (two skin dephs at W–band). Fig. 4 shows the photograph of the E–plane filter insert after sputtering, and in fig. 5, the final look of the filter after mounted in the test fixture. Note, the test fixture contains two lengths of waveguide, so that the filter can be compared directly with an empty section.

IV. Results

Fig. 6 shows the simulated and measured insertion and return loss curves of the micromachined filter. The simulation results in solid line correspond to the return loss, and the insertion loss is in dashed line. The calculated minimum pass–band insertion loss at the central frequency is 0.001 dB, the maximum return loss is more than 27 dB (less than

Figure 6: Scattering response of the micromachined filter. Comparison between the measured data in markers, and the predicted filter response from the full–wave analysis, in solid (S_{11}) and dashed (S_{12}) lines

0.7 dB, which is a typical value for the conventional metallic E–plane filters [8]). The relative bandwith is about 40 %. The measured minimum insertion loss is 1.5 dB, and the maximum return loss is 18 dB, being at least 15 dB in the band of interest. Also re-

markable the good rejection in the frequency stop–band, despite the high–order interaction of the inductive strips, which influences the stopband behaviour of the filter at higher frequencies.

V. Conclusions

In this paper we have demonstrated the feasibility of making an E–plane filter operating at W–band, which has been micromached based on the SU–8 photoresist. The precise control of the thickness at the 1–100-μm level achievable with the SU–8 just by a simple spin velocity adjustment allows the straightforward fabrication of the 2-D and 3-D structures required for waveguide circuits at this frequency. The results of the electrical response of the filter shows a comparable performance to the all metal counterpart, but achieved with a much lighter waveguide structure. Also of note is the ease and low cost of manufacture of the SU–8–based process, which confirms this technique as an alternative for mass production of high–performance components at W–band and terahertz frequencies.

Acknowledgements

References

[1] V. M. Lubecke, K. Mizuno, G. M. Rebeiz, Micromachining for Terahertz Applications, IEEE Trans. on Mic. & Tech. vol. 46, no. 11, pp. 1821–1831, Nov. 1998.

[2] L. P. B. Katehi, Novel Transmission Lines for the Submillimeter-Wave Region", Proc. IEEE, vol. 80, no. 11, pp. 1771–1787, Nov. 1982.

[3] C. E. Collins, J. W. Digby, G. M. Parkhurst, R. E. Miles, R. D. Pollard, J. M. Chamberlain, D. P. Steenson, A Novel Micromachined Millimeter-Wave and Terahertz Snap-Together Rectangular Waveguide Technology, IEEE, Mic. and Guided Wave Lett., vol. 9, no. 2, pp. 63–65, Feb., 1999.

[4] V. Postoyalko, D. S. Budimir, Design of Waveguide E-Plane FIlters with All-Metal Inserts by Equal Ripple Optimization, IEEE Trans. on Mic. & Tech. vol. 42, no. 2, pp. 217–222, Feb. 1994.

[5] R. Vahldieck, J. Bornemann, F. Arndt, D. Grauerholtz, Optimized waveguide E–plane metal Insert Filters for Millimeter–Wave Applications, IEEE Trans. on Mic. & Tech. vol. 31, no. 1, pp. 65–69, Jan. 1983.

[6] R. K. Hoffmann, Handbook of Microwave Integrated Circuits, Ed. Artech-House, 1987.

[7] HP–High Frequency Structure Simulator, User's Reference, Hewlett–Packard, September, 1997.

[8] B. Bhat, S. K. Koul, Analysis, Design and Applications of Fin–lines, B. Bhat, S. K. Koul, Artech House, 1987.

Author Index